WILEY-VCH

Magnetism: Molecules to Materials

Models and Experiments

Edited by Joel S. Miller and Marc Drillon

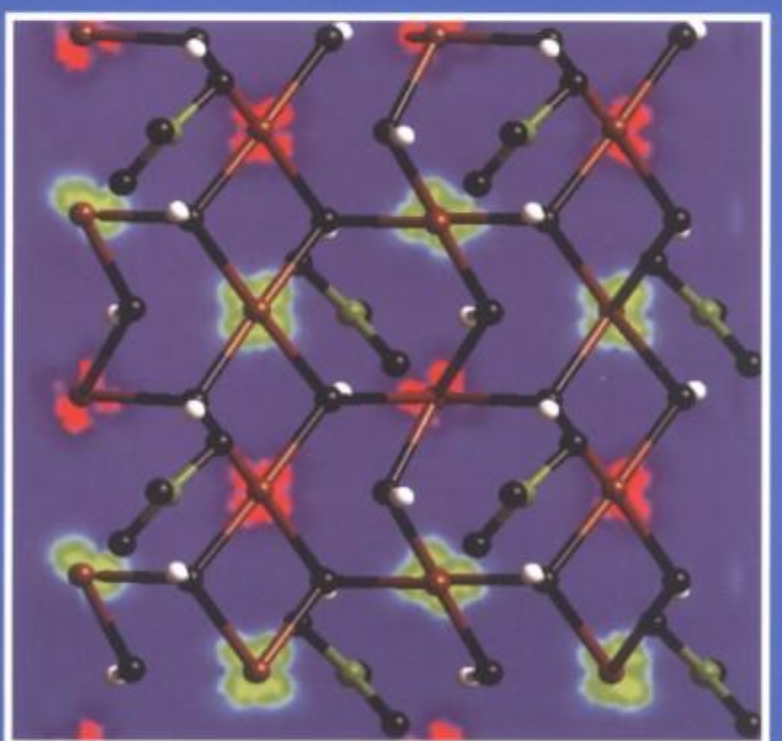

Magnetism: Molecules to Materials I: Models and Experiments.
Edited by Joel S. Miller and Marc Drillon

ISBNs: 3-527-29772-3 (Hardback); 3-527-60084-1 (Electronic)

Magnetism: Molecules to Materials I

Edited by J. S. Miller and M. Drillon

Magnetism: Molecules to Materials I: Models and Experiments.
Edited by Joel S. Miller and Marc Drillon

ISBNs: 3-527-29772-3 (Hardback); 3-527-60084-1 (Electronic)

Further Titles of Interest

J. H. Fendler (Ed.)
Nanoparticles and Nanostructured Films
1998. XX, 468 pages
Hardcover. ISBN: 3-527-29443-0

P. Braunstein, L. A. Oro, and P. R. Raithby (Eds.)
Metal Clusters in Chemistry
1999. XLVIII, 1798 pages
ISBN: 3-527-29549-6

Magnetism: Molecules to Materials I: Models and Experiments.
Edited by Joel S. Miller and Marc Drillon

ISBNs: 3-527-29772-3 (Hardback); 3-527-60084-1 (Electronic)

Magnetism: Molecules to Materials I

Models and Experiments

Edited by
Joel S. Miller and Marc Drillon

WILEY-VCH

Magnetism: Molecules to Materials I: Models and Experiments.
Edited by Joel S. Miller and Marc Drillon

ISBNs: 3-527-29772-3 (Hardback); 3-527-60084-1 (Electronic)

Prof. Dr. Joel S. Miller
University of Utah
315 S. 1400 E. RM Dock
Salt Lake City
UT 84112-0850
USA

Prof. Dr. Marc Drillon
CNRS
Inst. de Physique et Chimie
des Matériaux de Strasbourg
23 Rue du Loess
67037 Strasbourg Cedex
France

Library of Congress Card No.: applied for

A catalogue record for this book is available from the British Library.

Die Deutsche Bibliothek - CIP Cataloguing-in-Publication-Data
A catalogue record for this publication is available from Die Deutsche Bibliothek

ISBN 3-527-29772-3

Composition: EDV-Beratung Frank Herweg, Leutershausen. Printing: betz-druck GmbH, Darmstadt. Bookbinding: Wilh. Osswald + Co. KG, Neustadt
Printed in the Federal Republic of Germany.

Magnetism: Molecules to Materials I: Models and Experiments.
Edited by Joel S. Miller and Marc Drillon

ISBNs: 3-527-29772-3 (Hardback); 3-527-60084-1 (Electronic)

Magnetism: Molecules to Materials

The development, characterization, and technological exploitation of new materials, particularly as components in "smart" systems, are key challenges for chemistry and physics in the next millennium. New substances and composites including nanostructured materials are envisioned for innumerable areas including magnets for the communication and information sectors of our economy. Magnets are already an important component of the economy with worldwide sales of approximately $30 billion, twice those of semiconductors. Hence, research groups worldwide are targeting the preparation and study of new magnets especially in combination with other technologically important features, such as electrical and optical properties.

In the past few years our understanding of magnetic materials, thought to be mature, has enjoyed a renaissance as it has been expanded by contributions from many diverse areas of science and engineering. These include: 1) the discovery of bulk ferro- and ferrimagnets based on organic/molecular components with critical temperature exceeding room temperature; 2) the discovery that clusters in high, but not necessarily the highest, spin states, because of a large magnetic anisotropy or zero field splitting, have a significant relaxation barrier that traps magnetic flux enabling a single molecule/ion (cluster) to act as a magnet at low temperature; 3) the discovery of materials with large negative magnetization; 4) spin-crossover materials with large hysteretic effects above room temperature; 5) photomagnetic and 6) electrochemical modulation of the magnetic behavior; 7) the Haldane conjecture and its experimental realization; 8) quantum tunneling of magnetization in high-spin organic molecules; 8) giant and 9) colossal magnetoresistance effects observed for 3D network solids; 10) the realization of nanosized materials, such as self-organized metal-based clusters, dots and wires; and 11) the development of metallic multilayers and 12) spin electronics for the applications. This important contribution to magnetism and more importantly to science in general will lead us into the next millennium.

Documentation of the status of research, ever since the publication of William Gilbert's *de Magnete* in 1600, has provided the foundation for future discoveries to thrive. As one millennium ends and another beckons, the time is appropriate to pool our growing knowledge and assess many aspects of magnetism. This series, entitled Magnetism: *Molecules to Materials*, provides a forum for comprehensive yet critical reviews on many aspects of magnetism which are at the forefront of science today.

Joel S. Miller
Salt Lake City, USA

Marc Drillon
Strasbourg, France

Magnetism: Molecules to Materials I: Models and Experiments.
Edited by Joel S. Miller and Marc Drillon

ISBNs: 3-527-29772-3 (Hardback); 3-527-60084-1 (Electronic)

Contents

Magnetism: Molecules to Materials I: Models and Experiments.
Edited by Joel S. Miller and Marc Drillon

ISBNs: 3-527-29772-3 (Hardback); 3-527-60084-1 (Electronic)

List of Contributors

Marie A. Arrio
Laboratoire de Minéralogie-
Cristallographie de Paris
CNRS UMR7590, Case 115
4 Place Jussieu
75252 Paris
France

Stephen J. Blundell
University of Oxford
Department of Physics
Clarendon Laboratory
Parks Road
Oxford OX1 3PU
United Kingdom

Juan J. Borrás-Almenar
Instituto de Ciencia Molecular
Edificio F, 3P. Facultad de Química
Universidad de Valencia
C/ Dr. Moliner, 50
46100 Burjassot
Spain
e-mail: juan.j.borras@uv.es

Christophe Cartier dit Moulin
Laboratoire de Minéralogie-
Cristallographie de Paris
CNRS UMR7590, Case 115
4 Place Jussieu
75252 Paris
France

René Clément
Laboratoire de Chimie Inorganique,
URA 420
Université de Paris-Sud
91405 Orsay
France

Juan M. Clemente-Juan
Instituto de Ciencia Molecular
Edificio F, 3P. Facultad de Química
Universidad de Valencia
C/ Dr. Moliner, 50
46100 Burjassot
Spain

Eugenio Coronado
Instituto de Ciencia Molecular
Edificio F, 3P. Facultad de Química
Universidad de Valencia
C/ Dr. Moliner, 50
46100 Burjassot
Spain
e-mail: eugenio.coronado@uv.es

Jacques Curély
Centre de Physique Moléculaire Optique
et Hertzienne (CPMOH)
Université Bordeaux I
351 Cours de la Libération
33405 Talence Cedex
France

Marc Drillon
Institut de Physique et Chimie des
Matériaux de Strasbourg (IPCMS)
CNRS
23 rue du Loess
67037 Strasbourg Cedex
France

Roland Georges
Institut de Chimie de la Matière
Condensée de Bordeaux (ICMCB)
Université Bordeaux I
351 Cours de la Libération
33405 Talence Cedex
France

Béatrice Gillon
CEN Saclay
Labortoire Leon Brillouin
91191 Gif sur Yvette
France

Antoine Goujon
Université de Versailles-St Quentin en Yvelines
Laboratorie de Magnetisme et d'Optique
45 Avenue des Etats-Unis
78035 Versailles

Wilfried Grange
Institut de Physique et Chemie des Matériaux (ICPMS)
CNRS
23 rue du Loess
67037 Strasbourg
France

Jean Paul Kappler
Institut de Physique et Chemie des Matériaux (ICPMS)
CNRS
23 rue du Loess
67037 Strasbourg
France

Susan Kauzlarich
Department of Chemistry
University of California
One Shields Avenue
Davis, CA 95616
U.S.A.

Frank H. Köhler
Anorganisch-chemisches Institut II
Technische Universität München
Lichtenbergstasse 4
8046 Garching
Germany

Anne Leaustic
Laboratoire de Chimie Inorganique,
URA 420
Universite de Paris-Sud
91405 Orsay
France

Mireille Maret
Institut de Physique et Chemie des Matériaux (ICPMS)
CNRS
23 rue du Loess
67037 Strasbourg
France

Joel S. Miller
Department of Chemistry, HEB 2124
University of Utah
315 South 1400 East
Salt Lake City, UT 84112-0850
U.S.A.

Janice L. Musfeldt
Department of Chemistry
University of Tennessee
Knoxville, TN 37976
U.S.A.

Marc Nogues
Université de Versailles-St Quentin en Yvelines
Laboratorie de Magnetisme et d'Optique
45 Avenue des Etats-Unis
78035 Versailles

Andrew Palii
Quantum Chemistry Department
Institute of Chemistry
Moldavian Academy of Science
Academy str. 3
277028 Kishinev
Republic of Moldova

Amy C. Payne
Department of Chemistry
University of California
One Shields Avenue
Davis, CA 95616
U.S.A.

Chintamani N. R. Rao
Chemistry and Physics of Materials Unit
Jawaharhal Nehru Centre for Advanced
Scientific Research
Jakkur P.O., Bangalore 560064
India

Bernard Raveau
Laboratoire CRISMAT CNRS
UMR 6508
ISMRA/Université de Caen
6 Boulevard du Maréchal Juin
14050 Caen
France

Louis Pierre Regnault
Département de Recherche
Fondamentale sur la Matière
Condensée SPSMS/MDN
Centre d'Etudes Nucléaires
17 Rue des Martyrs
38054 Grenoble
France

Jean Pierre Renard
Institut d'Electronique Fondamentale
CNRS, Bât. 220
Université de Paris Sud
91405 Orsay
France

Eric Ressouche
Département de Recherche
Fondamentale sur la Matière
Condensée SPSMS/MDN
Centre d'Etudes Nucléaires 85X
17 Rue des Martyrs
38054 Grenoble
France

Philippe Sainctavit
Laboratoire de Minéralogie-Cristallographie
de Paris
CNRS UMR 7590, Case 115
4 Place Jussieu
75252 Paris
France

Jacques Schweizer
CEA/Grenoble
Département de Recherche
Fondamentale sur laRFMC/SPCMS/MDN
17 Rue des Martyrs
Centre d'Etudes Nucléaires 85X
38054 Grenoble
France

Boris S. Tsukerblat
Quantum Chemistry Department
Institute of Chemistry
Moldavian Academy of Science
Academy str. 3
277028 Kishinev
Republic of Moldova

Francois Varret
Université de Versailles-St Quentin en
Yvelines
Laboratorie de Magnetisme et
d'Optique
45 Avenue des Etats-Unis
78035 Versailles
France

Michel Verdaguer
Laboratoire de Chimie Inorganique et
Matériaux Moléculaires
CNRS Unit 7071
Université Pierre et Marie Curie
4 Place Jussieu
75252 Paris
France

David J. Webb
Department of Physics
One Shields Avenue
University of California
Davis, CA 95616
U.S.A.

Magnetism: Molecules to Materials I: Models and Experiments.
Edited by Joel S. Miller and Marc Drillon

ISBNs: 3-527-29772-3 (Hardback); 3-527-60084-1 (Electronic)

Subject Index

Magnetism: Molecules to Materials I: Models and Experiments.
Edited by Joel S. Miller and Marc Drillon

ISBNs: 3-527-29772-3 (Hardback); 3-527-60084-1 (Electronic)

1 One-dimensional Magnetism: An Overview of the Models

Roland Georges, Juan J. Borrás-Almenar, Eugenio Coronado, Jacques Curély, and Marc Drillon

1.1 Introduction

One-dimensional (1D) magnetism has for a long time been characterized by a close interaction between solid state physicists and chemists. Chain compounds first attracted the interest because they provide genuine examples for testing models which could not be solved in higher dimension [1]. The chemical community has been more and more involved in this field with the design and controlled synthesis of novel types of low-dimensional materials. Thus, in the 1970s, several families of magnetic compounds with linear chain structures were discovered and their properties were thoroughly analyzed from models developed a decade earlier [2]. In the 1980s, a major advance in molecular chemistry has been the discovery of bimetallic chain compounds showing alternating spin carriers [3–5]. These compounds afforded a new concept in magnetism, the so-called 1D ferrimagnetism, characterized by a minimum value of the magnetic moment at non-zero temperature, and a power law divergence at lower temperatures. Novel models, involving the spin dimensionality, were proposed to quantitatively explain such a behavior. Further, in the search for novel magnetic systems, chemists have focused on linear compounds of increasing complexity. Thus, exotic systems were isolated, as for example ladder-like chains, triangle-based chains, cluster chains, ... etc, whose interest is currently under scope, since they show in some specific cases quantum effects as an energy gap in the spin excitation spectrum [6].

Notice that, although these systems are still one-dimensional, they represent an intermediate step towards 2D networks. An important point is the variation of critical behaviors (critical exponents, for instance) in the low temperature regime, when dimensionality progressively changes. In this regard, the current researches on layered materials with varying magnetic networks [7–19] could provide some insight.

In this chapter, we will restrict the discussion to models so far reported for describing the properties (magnetic susceptibility, magnetization, magnetic specific heat ...) of genuine 1D compounds. Our main focus will concern the 1D ferrimagnets, although accurate models developed to explain the properties of exotic 1D compounds will also be discussed.

In order to clarify the forthcoming discussion, we first define the terms we will be using. The expression *linear chain* will refer to a chain within which each magnetic center interacts with two nearest neighbors only. The simplest case consists of

a single magnetic species and involves ferromagnetic (F) or antiferromagnetic (AF) exchange interactions. The terms *uniform chain*, *alternating chain* and *random chain* will refer respectively to the presence of a unique exchange interaction (Fig. 1a), two alternating interactions (Fig. 1b), or a random distribution of the interactions (Fig. 1c). The term *double* (or *triple*, etc.) *chain* will deal with 1D magnetic systems essentially made of two (or more) interacting linear chains (Figs. 1(d) to 1(g)). They often give rise to striking magnetic properties. For instance, spin frustration is expected for AF coupling in the chain 1(e). In the chain (1f) ferrimagnetism must occur, even when all the magnetic moments are equal, because of the topology of the chain. Finally, chain 1(g) may present both frustration and topological ferrimagnetism.

We must also distinguish between *regular chains* and *nonregular chains*. Basically, a regular chain is built up recurrently, by step-by-step reproduction of a given subsystem (unit cell). Such a subsystem can show any degree of complexity. We shall also include in that category finite length chains. Conversely, a *nonregular chain* will be a chain which does not present such a reproducible unit cell. Such chains may exhibit interesting complex behaviors. Since, in practical situations, the lack of reproducibility introduces some random character, we shall also use the term *random chain* to designate them. The random character may also concern the spin quantum numbers associated with the magnetic moments, and/or the related Landé factors, and/or the exchange interactions or anisotropy constants, etc. When the randomness comes from the exchange interaction, we have the situation defined in Fig. 1c.

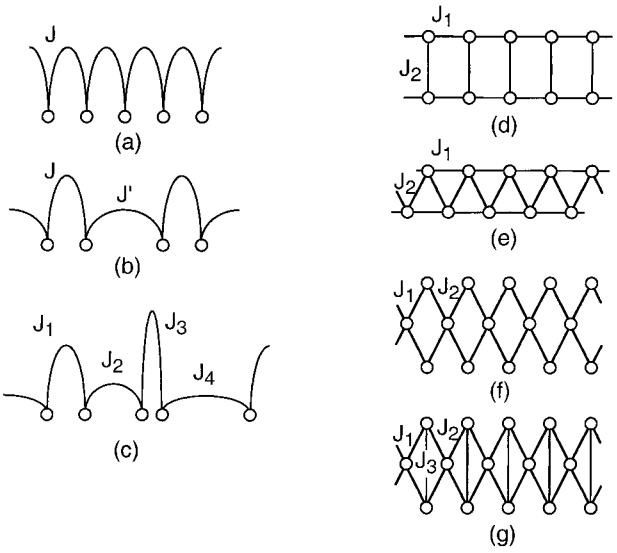

Fig. 1. Various typical exchange networks examined in the present review (the exchange couplings are assumed to be essentially antiferromagnetic): (a) uniform chain; (b) alternating chain; (c) random chain; (d) ladder-like chain; (e) spin frustrated double chain; (f) topological 1D ferrimagnet; (g) spin frustrated topological 1D ferrimagnet.

According to the anisotropy of the exchange interactions, the models currently developed in magnetism deal with the so-called Heisenberg or Ising interactions. The expression *Heisenberg coupling* is used for a fully isotropic spin hamiltonian of the form:

$$H(\boldsymbol{S}, \boldsymbol{S}') = -J\boldsymbol{S} \cdot \boldsymbol{S}' \tag{1}$$

With the present conventions, a negative J value corresponds to an AF coupling. However, Eq. (1) does not cover the overall variety of isotropic couplings, and we shall incidentally mention, for instance, the isotropic biquadratic spin hamiltonian which has the form:

$$H(\boldsymbol{S}, \boldsymbol{S}') = -j(\boldsymbol{S} \cdot \boldsymbol{S}')^2 \tag{2}$$

This term is sometimes used as a practical trick to incorporate the effects of magnon-phonon interactions [20]. More generally, we shall use the term anisotropic coupling for the hamiltonian:

$$H(\boldsymbol{S}, \boldsymbol{S}') = -\left(J_x S_x S'_x + J_y S_y S'_y + J_z S_z S'_z\right) \tag{3}$$

where J_x, J_y and J_z are the components of the exchange energy tensor which define the dimensionality of the interaction. The particular cases $J_x = J_y = 0$, $J_z \neq 0$ and $J_x = J_y \neq 0$, $J_z = 0$ correspond to the extreme cases of exchange anisotropy, namely ZZ and XY models, respectively (note that when $S = S' = 1/2$ and $J_x = J_y = 0$, $J_z \neq 0$ we are then dealing with the Ising model). As already mentioned, the isotropic case ($J_x = J_y = J_z = J$) deals with the Heisenberg model.

Incidentally, we shall be concerned with the bilinear antisymmetric (Dzialoshinski) essentially anisotropic coupling, which takes the form:

$$H(\boldsymbol{S}, \boldsymbol{S}') = (\boldsymbol{D}, \boldsymbol{S}, \boldsymbol{S}') = D\left(S_x S'_y - S_y S'_x\right) \tag{4}$$

where $\boldsymbol{D}$ is the Dzialoshinski vector (of modulus D), lying along the positive z direction.

Finally, we will sometimes find it useful to employ the so-called *classical approximation* which consists in replacing a spin operator $\boldsymbol{S}$ by a classical vector. This approximation, which rules out the difficulties associated with noncommuting operator algebra, is allowed for large spin quantum numbers, S. Then, the spin component commutators $[S_x, S_y]$, etc., which are of the order of magnitude of S, are negligible compared with the products $S_x S_y$, etc., which are of the order of magnitude of S^2. In such cases, the magnetic moment $g\boldsymbol{S}$ will be written as $M\boldsymbol{u}$, where M is the amplitude of the moment and $\boldsymbol{u}$ the unit vector along $\boldsymbol{S}$. It must be noticed that in this approximation the Landé factor actually vanishes. When both quantum and classical spins coexist in the hamiltonian, we shall use the notations $\boldsymbol{s}$, $\boldsymbol{s}'$, etc., for quantum operators, and $\boldsymbol{S}$, $\boldsymbol{S}'$, etc., for classical spin vectors.

1.2 Quantum-spin Heisenberg Chains: Numerical Models

Except for the Ising coupling, analytical solutions of these chains are only available when at least part of the spin is treated in the classical approximation. In the other cases, there is no exact solution for the infinite chain, even in the simple F or AF case (except for the ground state energy of the AF $s = 1/2$ chain [21]). In the Heisenberg model, several attempts [22–25] have been made to determine the ground state as well as the thermal and magnetic properties of the infinite chain using a computational process. We examine this treatment here. We first present the general procedure commonly followed to solve this problem numerically; then, we shall focus on the results obtained for ferrimagnetic chains.

1.2.1 General Method

First, let us consider the simple case of a linear chain with Heisenberg coupling between nearest-neighbor quantum spins, and no local anisotropy. The general method essentially uses an extrapolation procedure from the exact results obtained for increasing length finite chains. This requires diagonalizing larger and larger real matrices, in order to perform accurate enough extrapolations. Actually, significant matrix size reductions are provided by considering the various symmetry properties of the problem, using group theory representation. Since we are concerned with the fully isotropic problem, the point group operates within the spin space, and the hamiltonian may be projected onto various independent subspaces, defined by the total spin quantum number, S_{T}, and its projection along an arbitrary z direction, S_{T}^{z}. Further size reduction may result from the consideration of the specific spatial symmetries of the magnetic network itself. For instance, if instead of considering open finite chains, one assumes closed chains this makes no difference in the infinite length limit. However, this assumption allows us to include all the symmetries of the C_{N} group to which the N-cell ring belongs. A reduction of the matrix size by a factor 2 also arises for uniform chains thanks to the mirror plane operation. In this respect, it must be underlined that the introduction of next-nearest neighbor interactions does not necessarily increase the number and size of the independent matrices, and may have no significant influence on the required memory size and computing time.

When local or exchange anisotropy is introduced, favoring for instance the z axis, and/or when a magnetic field is applied along that direction, the symmetry group reduces to a C_8 group in the spin space. As a result, for a given spin, the matrices to be diagonalized are larger, limiting the computational treatment to shorter chains.

The above procedure was initiated by Bonner & Fisher in a pioneering work in which they discuss the problem of the uniform $s = 1/2$ chain, with exchange anisotropy ($J_x = J_y \neq J_z$), and either F or AF coupling [22]. Notice that they have specifically examined open chains in order to evaluate finite size effects on the magnetic properties. Their work was extended by Weng to the magnetic properties of AF Heisenberg chains with larger spin values [23], and later on by Blöte [24], who

took into account exchange and single-ion anisotropy. On the other hand, Duffy & Barr introduced alternating exchange interactions in the AF $s = 1/2$ Heisenberg chain [25]. These works have been extensively reviewed [26–28].

1.2.2 Linear Ferrimagnetic Chains

With regard to alternating spin chains made up of two quantum spin sublattices, s and s', and abbreviated as $[s–s']$, the first theoretical study was reported in 1983 [29]. In this paper the magnetic and thermal properties of the uniform [1/2–1] ferrimagnetic chain were examined in detail. It was shown that the main features for the infinite chain are conveniently given by extrapolating the results obtained up to 10-spin rings $[1/2–1]_N$ where N stands for the number of spin pairs (Fig. 2). A well-defined minimum of the product χT is observed at intermediate temperatures in the plot χT vs. T. This feature results from two conflicting tendencies namely the short-range order correlations that, due to AF coupling, tend to reduce the resulting moment of a pair of neighboring spins, and the long-range correlations that bring an increasing number of spins into coherent behavior. Since this conflict operates whatever the nature of the spins under consideration (quantum or classical), or that of the exchange coupling (isotropic or anisotropic), it is expected that such a minimum will be met in most 1D ferrimagnets. It may then be considered to some extent as the signature of this kind of system.

However, this minimum may disappear when one of the magnetic moments is too small, since this situation closely resembles that of a ferromagnetic chain, or when the two magnetic moments compensate due to the presence of two different Landé factors. Thus, for $g = g'$ the extrapolated χT product diverges at low temperature according to a $T^{-0.8}$ law, similarly to the Heisenberg $s = 1/2$ ferromagnetic chain. This leads to the very simple idea that, in the low-temperature limit, such a non-compensated chain may be considered as a pair assembly $[s = 1/2, s' = 1]$ coupled antiferromagnetically in a rigid fashion in order to afford an effective $s = 1/2$ ferromagnetic chain. In turn, for alternating Landé factors (i. e., $g \neq g'$), the chains may show an antiferromagnetic-like behavior (no divergence of χT at low temperature),

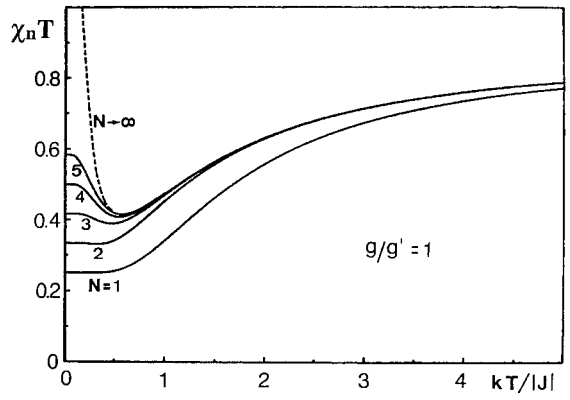

Fig. 2. Thermal variation of the χT product for the finite rings $[1/2–1]_N$, $N = 1$ to 5 and $g/g' = 1$. The normalized χT product is given in units of $N_A g^2 \mu_B^2 / k$. The dashed curve corresponds to the infinite ring extrapolation [29].

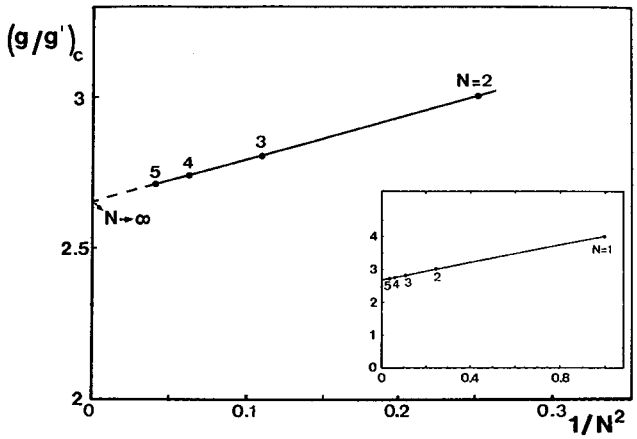

Fig. 3. Critical ratio between the g factors for the $[1/2\text{–}1]_N$ chain; extrapolation to the infinite length chain [29].

for a critical ratio g/g' which depends on N. For the infinite chain, the critical value, approximated by extrapolation, is 2.67 (Fig. 3). This value is intermediate between the Néel state value (2.0) and the spin wave theory value (3.56). As this phenomenon resembles the magnetization compensation observed in some ferrimagnets, we will refer to it as a compensation point.

The above approach has been extended [30] to the ferrimagnetic chains $[1/2\text{–}s]$ with $s = 1/2$ to $5/2$. In this paper it is shown that the critical ratio for compensation is conveniently given by $r = 4(s + 1)/3$, to be compared with the Néel state value $r = 2s$. The difference is a purely quantum effect, and results from the nature of the ground-state of the chain, which strongly differs from the Néel state in the isotropic coupling framework. This paper also extends the calculations to other thermodynamic quantities of interest, as for example the specific heat. These results are shown in Figs. 4 and 5 and the significant features of the extrapolated curves are summarized in Table 1. It is worth noticing that the convergence of the curves cor-

Table 1. Thermal and magnetic properties of ferrimagnetic Heisenberg chains. (From ref. [30]).

System	Specific heat		Magnetic susceptibility	
	C_{pmax}/k	$(kT)_{\mathrm{max}}/J$	$(\chi T)_{\mathrm{nmin}}$	$(kT)_{\mathrm{min}}/J$
[1/2–1]	0.377	0.705	1.507*	0.577*
[1/2–3/2]	0.356	0.96	2.221*	1.190*
[1/2–2]	0.351	1.2	2.609*	2.1*
[1/2–5/2]	0.35	1.4	2.80*	2.9*
[1/2–∞]	–	–	2.83†	2.98†

* Values assuming $g = g'$

† Classical spin scaled to $s' = 5/2$

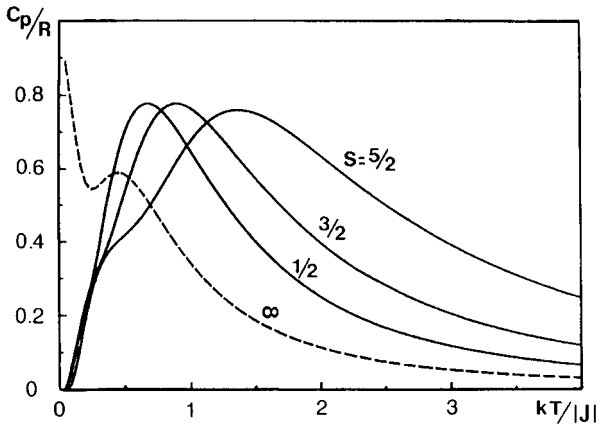

Fig. 4. Thermal variation of the specific heat for various $[1/2–s']_N$ rings (referred to a single $[1/2–s']$ cell). Due to computational limitations, N is 5 for $s' = 1$, 4 for $s' = 3/2$, and 3 for $s' = 5/2$. The dashed curve corresponds to the infinite s' limit [30].

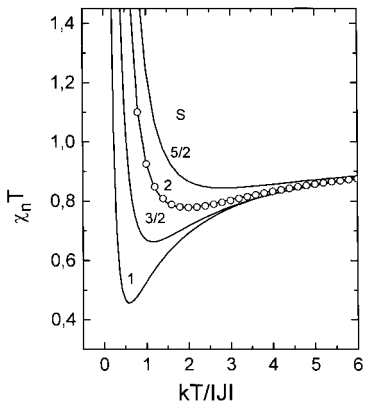

Fig. 5. Normalized χT product for various $[1/2–s]$ infinite quantum ferrimagnetic chains with Heisenberg coupling. The agreement between the theoretical curve and the fit to the polynomial expression given in Table 3 is shown for the $[1/2–2]$ chain.

responding to rings of increasing lengths is more rapid when s increases. Thus, even though we are limited to calculating shorter rings when s increases, the extrapolation results reported in this table should satisfactorily describe the infinite chain behavior.

Polynomial expressions giving the magnetic behavior of $[1/2–1]$ infinite chains for regular ($g = g'$) and alternating ($g = 2g'$) Landé factors are also given in the same paper and are summarized in Table 2. These are used to fit the experimental susceptibility data of real systems [31].

Finally, analytical expressions may be proposed for fitting the theoretical variations of the magnetic susceptibility for the ferrimagnetic chains $[1/2–s]$, by considering two contributions. First, the low temperature divergence of χT may be described by a power law variation $aT^{-\beta}$, in agreement with the findings for Heisenberg ferromagnetic chains. For such chains, β is shown to be close to 1. Further, the high-temperature behavior is well described by an Arrhenius-like law, giving as $T \to \infty$ the value of the Curie constant C:

Table 2. Polynomials giving the behavior of [1/2–1] Heisenberg chains for regular ($g = g'$) and alternating ($g = 2g'$) Landé factors.

g/g'	$\dfrac{\chi T}{(N_A\mu_B^2/k)g^2}$
1	$\dfrac{Ax^3 + Bx^2 + Cx + D}{Ex^2 + Fx + G}$ $A = -0.034146801$; $B = 2.8169306411$; $C = -7.2310013697$; $D = 11$ $E = 1.29663274$; $F = 0.69719013595$; $G = 12$
2	$\dfrac{Ax^2 + Bx + C}{Dx^3 + Ex^2 + Fx + G} + Hx$ $A = 2.944723391$; $B = -8.643216582$; $C = 20$; $D = 2.207977566$ $E = 2.210070570$; $F = 5.150935691$; $G = 12$; $H = 0.00232325$

$x = \dfrac{|J|}{kT}$

$$\chi T = a\left(\frac{|J|}{kT}\right)^{\beta} + C\ \exp\left(-b\frac{|J|}{kT}\right) \tag{5}$$

The sum of these two contributions only contains three adjustable parameters, a, b and β (see Table 3), and thus appears to be more appropriate than the commonly used polynomial expressions (see Fig. 5). It can be noted that the activation coefficient b slightly increases from 0.8 to 1 for s ranging from 1 to 5/2. On the other hand, β depends on the spin value s and differs significantly from unity, probably due to the influence of the Arrhenius contribution in the region of the χT minimum.

Table 3. Analytical expressions proposed to describe the magnetic behavior of the [1/2–s] ferrimagnetic chains.

Chains [1/2–s]	Expression of $\chi T = f(x)$, with $x = \lvert J\rvert/kT$
$s = 1$	$0.1146x^{1.69} + 1.375\ \exp(-0.811x)$
$s = 3/2$	$0.5756x^{1.80} + 2.250\ \exp(-0.882x)$
$s = 2$	$1.8120x^{1.78} + 3.375\ \exp(-0.948x)$
$s = 5/2$	$4.1249x^{1.72} + 4.750\ \exp(-1.013x)$

1.2.3 Complex Quantum-spin Heisenberg Chains

The Bonner-Fisher procedure has also been used more recently to study linear chains with alternating exchange interactions or with second-nearest neighbor interactions [32]. In the former case, the problem of alternating F–AF couplings has been treated in a linear chain of spins $s = 1/2$ and used to fit the magnetic data of both inorganic

[33] and organic [34] chain compounds. The exchange alternation has also been investigated in a chain of spins $s = 1$ including local axial anisotropy effects. This has been examined when both exchange couplings are antiferromagnetic (AF–AF alternating chain) [35] and in the F–AF case [36]. Rational unified expressions have been derived in all these cases which have been used to fit the magnetic behaviors of chain compounds. These expressions are summarized in Tables 4–6.

In the second case, the problem of second-nearest neighbor interactions in a linear chain is magnetically equivalent to the treatment of a double chain (ladder-like or triangular type). This kind of system is of interest in connection with topological ferrimagnetism or with the problem of interchain interactions and will be examined in more detail in Section 1.5.3. An example which illustrates this case is provided by the series of solid state compounds formulated as $Sr_3CuPt_{1-x}Ir_xO_6$ which exhibit a chain structure formed by two alternating sites A and B (Fig. 6a). Site A is occupied

Table 4. F/AF alternating chain ($s = 1/2$) A–H parameters for the rational expression of the susceptibility given as a function of polynomials in α, ($\alpha = J_2/|J_1|$): $X_i(\alpha) = x_0 + x_1\alpha + x_2\alpha^2 + x_3\alpha^3$.

Coefficients for the polynomials valid in the range $0 < \alpha < 2$				
	x_0	x_1	x_2	x_3
A	1	0	0	0
B	5	0	0	0
C	−1	0	0	0
D	0.05	0	0	0
E	5.2623	−0.33021	0	0
F	0.44976686	−0.99234827	−0.00881524	0.15481517
G	0.18948031	0.36766434	0.51001414	−0.2795751
H	0.28437797	−0.16749925	−0.18725364	0.09374817
Coefficients for the polynomials valid in the range $2 < \alpha < 8$				
	x_0	x_1	x_2	x_3
A	1	0	0	0
B	5	0	0	0
C	18.49535656	−6.1326294	1.63540894	−0.114937
D	−1.476022	0.238098	−0.0394290	0.001851
E	5.3195744	−0.25251758	0	0
F	20.12902219	−7.98423527	1.827504022	−0.116829819
G	−2.696851543	2.7164805741	−0.310485224	0.008341925
H	5.1120826687	−2.478242688	0.457077363	−0.02686769

$$H = -J_1 \sum_i S_{2i} S_{2i+1} - J_2 \sum_j S_{2i} S_{2i-1}$$

$$\chi_r = \frac{AT_r^3 + BT_r^2 + CT_r + D}{T_r^4 + ET_r^3 + FT_r^2 + GT_r + H};$$

$$T_r = \frac{kT}{|J_1|}; \chi_M = \frac{N_A g^2 \mu_B^2}{4|J_1|} \chi_r$$

Table 5. AF alternating Heisenberg chain $s = 1$ without local anisotropy. A–F parameters for the rational expressions of the susceptibility are given as a function of polynomials in α ($\alpha = J_2/J_1$): $X_i(\alpha) = x_0 + x_1\alpha + x_2\alpha^2$. The expressions calculated in the presence of local anisotropy can be found in Ref. [35]).

Coefficients for the polynomials valid in the range $\alpha < 0.5$			
	x_0	x_1	x_2
A	1	0	0
B	0.5	0	0
C	−0.07096	0.34191	0
D	1.136963	0.748419	0
E	1.04853272	−0.8077223	1.375320
F	0.4447955	1.162769	0
Coefficients for the polynomials valid in the range $\alpha > 0.5$			
	x_0	x_1	x_2
A	1	0	0
B	0.5	0	0
C	0.1	0	0
D	1.136963	0.748419	0
E	1.605652	−1.462219	1.668971
F	0.4447955	1.162769	0

$$\chi_r = \frac{AT_r^2 + BT_r + C}{T_r^3 + DT_r^2 + ET_r + F};\ T_r = \frac{kT}{|J_1|};$$

$$\chi_M = \frac{N_A g^2 \mu_b^2}{3|J_1|}\chi_r$$

by Cu^{II} (spin $s = 1/2$), while site B may be occupied either by Ir^{II} (spin $s' = 1/2$) or by Pt^{II} (diamagnetic $s' = 0$). In this series of linear chain compounds, the behavior changes from ferromagnetic in the [CuIr] compound to antiferromagnetic in the [CuPt] one (Fig. 6b) [37]. This evolution can be qualitatively explained by assuming F interactions between Cu^{II}–Ir^{II} first neighbors, and non-negligible AF interactions between the second neighbors (Cu^{II}–Cu^{II} and Ir^{II}–Ir^{II}). To quantitatively explain this evolution, a model consisting of a double Heisenberg chain of triangles formed by a linear Cu^{II} chain interacting with a linear Ir/Pt chain has been developed (Fig. 6c) [38]. Exact calculations on bimetallic rings with N ranging up to 8 pairs of spins $s = 1/2$ have been performed using a general computing program [39]. Such a model reproduces the experiment from the following set of parameters: $J_{\text{Ir-Cu}}/k = 160\,\text{K}$; $J_{\text{Cu-Cu}}/k = J_{\text{Ir-Ir}}/k = -20\,\text{K}$.

Table 6. F/AF alternating Heisenberg chain ($S = 1$). Parameters for the rational expressions of the susceptibility are given as a function of polynomials in α ($\alpha = J_2/|J_1|$). (From Ref. [36].)

Coefficients for the polynomials valid in the range $0 \le \alpha \le 2.5$

	x_0	x_1	x_2	x_3	x_4	x_5
A	1	0	0	0	0	0
B	−0.53179	−0.257254	2.26042	−1.80034	0.681531	−0.0939218
C	0.98989	0.118297	−0.875084	−0.957615	−0.438171	0.0690411
D	−0.00622969	−0.0105603	0.073206	−0.0889913	0.04288	−0.00699582
E	0.631753	−1.55507	1.89768	−1.27912	0.455501	−0.0609963
F	3.25342	0.375299	5.92952	−4.87702	1.79687	−0.240897
G	−2	0	0	0	0	0
H	0.709271	−0.204346	−0.72102	1.1711	−0.616891	0.105816

$$H = -J_1 \sum_i S_{2i} S_{2i+1} - J_2 \sum_i S_{2i} S_{2i-1};\ \chi_M = \frac{2N_A g^2 \mu_B^2}{3|J_1|}\chi_r;\ T_r = \frac{kT}{|2J_1|}$$

$$\chi_r = \frac{AT_r^3 + BT_r^2 + CT_r + D}{T_r^4 + ET_r^3 + FT_r^2 + GT_r + H};\ X_i(\alpha) = x_0 + x_1\alpha + x_2\alpha^2 + x_3\alpha^3 + x_4\alpha^4 + x_5\alpha^5$$

Coefficients for the polynomials valid in the range $2 \le \alpha \le 12$

	x_0	x_1	x_2	x_3	x_4	x_5
A	1	0	0	0	0	0
B	−3.2205	2.52156	−0.423	0.257234	−0.0245892	0.00063526
C	0.4509	−0.468099	−0.00515701	0.0356094	−0.0030821	6.14018e-05
D	−0.00731213	0.0140453	0.00474435	−0.00421149	0.00037082	−8.2398e-06
E	−0.00020882	7.53396e-05	−0.00015033	7.74724e-05	−6.6282e-06	1.50124e-07
F	−1.97669	1.08478	−0.181843	0.155838	−0.0152071	0.00039137
G	1.27484	4.62066	−0.819082	0.421168	−0.0396586	0.00102997
H	−10.1854	4.22695	−0.531012	0.486191	−0.0477278	0.00120624
I	3.89173	−2.14263	0.270454	−0.120208	0.0115299	−0.00030091
J	−0.529028	0.33623	−0.0438771	0.0150293	−0.00141133	3.71238e-05

$$\chi_r = \frac{AT_r^4 + BT_r^3 + CT_r^2 + DT_r + E}{T_r^5 + FT_r^4 + GT_r^3 + HT_r^2 + IT_r + J};\ X_i(\alpha) = x_0 + x_1\alpha + x_2\alpha^2 + x_3\alpha^3 + x_4\alpha^4 + x_5\alpha^5$$

Coefficients for the polynomials valid in the range $10 \le \alpha \le 25$

	x_0	x_1	x_2	x_3
A	1	0	0	0
B	11.3204	−1.21813	0.180901	−0.00221183
C	396.540	−58.2811	6.31997	−0.09586650
D	229.477	−33.3320	4.43852	−0.06972060
E	7.06542	−1.32503	0.11062	−0.00108187
F	252.580	−29.3889	4.42934	−0.0660958
G	449.351	−72.2010	5.80027	−0.0770129
H	1622.38	−209.516	30.1291	−0.457473

$$\chi_r = \frac{AT_r^3 + BT_r^2 + CT_r + D}{T_r^4 + ET_r^3 + FT_r^2 + GT_r + H};\ X_i(\alpha) = x_0 + x_1\alpha + x_2\alpha^2 + x_3\alpha^3$$

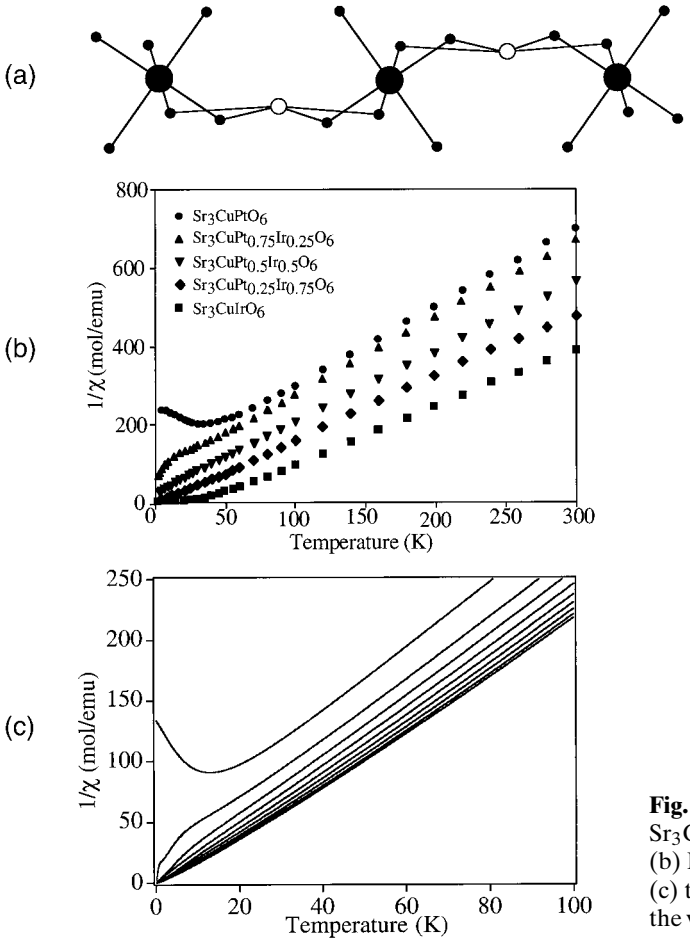

Fig. 6. (a) Structure of $Sr_3CuPt_{1-x}Ir_xO_6$. (b) Magnetic properties, and (c) theoretical predictions for the various Pt/Ir compositions.

1.3 Classical-spin Heisenberg Chains

We turn now to the first important class of magnetic chains where properties may be described by analytical expressions. We deal with chains made of classical spins and nearest-neighbor Heisenberg couplings.

1.3.1 Fisher's Model

As already mentioned, the spin component commutators become negligible for increasing spin quantum numbers, so that the spin operators commute and may be then treated as classical vectors when the spin number is large enough (usually larger than 2). In this limit, except for magnetization under an applied magnetic field, analyt-

ical expressions are provided for the thermodynamic properties. Pioneering work was done by Fisher [40] who solved the problem of the uniform F or AF chain. In this section, we first briefly present the physics of this model. As a second step, we describe its extension to various ferrimagnetic systems.

The spin hamiltonian (exchange and Zeeman terms) for a uniform chain may be written as:

$$H = -J \sum_i \boldsymbol{u}_i \boldsymbol{u}_{i+1} - M \cdot \boldsymbol{B} \sum_i \boldsymbol{u}_i \tag{6}$$

where $\boldsymbol{u}_i$ is the unit vector along the *classical spin*, $\boldsymbol{S}_i$, $M\boldsymbol{u}_i$ is the corresponding magnetic moment, and $\boldsymbol{B}$ is a magnetic field which is assumed to be applied along the z direction (note that, due to the conventional writing of the magnetostatic (Zeeman) hamiltonian, M will be implicitly expressed in units of $\mu_B/\hbar$, for the whole of this chapter); J is the exchange interaction conveniently scaled for interacting classical unit vectors. The various thermodynamic properties of the chain are derived from the partition function Z. Determination of the magnetization requires complete knowledge of the field-dependence of Z which is not available in closed form. Fortunately, the B^2 term, which is readily calculated, is enough to obtain an analytical expression of the zero-field magnetic susceptibility χ_0. The general approach of the mathematics, which is now briefly described, remains unchanged when dealing with more complex classical-spin systems.

The partition function is first calculated for a finite length chain containing N spin vectors. We have:

$$Z_N(B) = \int \mathrm{d}\Omega_0 \int \mathrm{d}\Omega_N \, \exp(-\beta H) \tag{7}$$

where β is Boltzmann's factor $1/kT$, and $\int \mathrm{d}\Omega_i$ means integrating over all the directions (defined by the usual spherical angles θ_i and ϕ_i) available to each vector $\boldsymbol{u}_i$. In order to perform the integrations, the argument of the exponential is written as a sum of terms, each one involving a pair of neighboring sites, say $\boldsymbol{u}_i$ and $\boldsymbol{u}_{i+1}$. The corresponding exponentials, which are isotropic expressions in $(\boldsymbol{u}_i, \boldsymbol{u}_{i+1})$, may then be developed in terms of spherical harmonics $Y_\ell^m(\theta_i, \phi_i)$ (or, for simplicity $Y_\ell^m(\boldsymbol{u}_i)$). The resulting integral is thus a linear combination of spherical harmonic products. In the vanishing-field limit, each one includes two harmonics of a given argument $\boldsymbol{u}_i$. Since Z must be developed up to the B^2 term in order to get χ_0, one must introduce extra spherical harmonics ($Y_1^0(\boldsymbol{u}_i)$ and $Y_2^0(\boldsymbol{u}_i)$) for each spin vector. Due to the orthonormality properties of the spherical harmonics, most of the terms in the integrals give vanishing contributions. The other ones are easily calculated, and χ_0 (per mole of spins) appears to be merely given by:

$$\chi_0 = N_\mathrm{A} \beta \frac{(\mu_\mathrm{B} M)^2}{3} \sum_{i,j} \langle \boldsymbol{u}_i, \boldsymbol{u}_{i+1} \rangle \tag{8}$$

where N_A and μ_B have their usual meanings, and $\langle \cdot \mathrm{X} \cdot \rangle$ means the thermodynamic average of the quantity within the bracket, $\cdot \mathrm{X} \cdot$. It has been pointed out [40] that the

spin–spin correlation $\langle \boldsymbol{S}_i \boldsymbol{S}_{i+n} \rangle$ ($n \geq 2$) may be expressed in terms of the intermediate correlations, $\langle \boldsymbol{S}_{i+m} \boldsymbol{S}_{i+m+1} \rangle$ ($0 \leq m \leq n-1$), due to the fact that we are dealing with classical moments:

$$\langle \boldsymbol{u}_i \boldsymbol{u}_j \rangle = \langle \boldsymbol{u}_i \boldsymbol{u}_{i+1} \rangle \langle \boldsymbol{u}_{i+1} \boldsymbol{u}_{i+2} \rangle \cdots \langle \boldsymbol{u}_{j-1} \boldsymbol{u}_j \rangle \tag{9}$$

Now, letting P be the nearest-neighbor correlation $\langle \boldsymbol{u}_i \boldsymbol{u}_{i+1} \rangle$, χ_0 is given by:

$$\chi_0 = N_\mathrm{A} \beta \frac{(\mu_\mathrm{B} M)^2}{3} \frac{1+P}{1-P} \tag{10}$$

where P appears to be nothing but the Langevin function [41]:

$$P(\beta J) = \coth(\beta J) - (\beta J)^{-1} \tag{11}$$

In order to fit experimental data, the exchange energy J must be scaled following the usual procedure:

$$J \rightarrow J S(S+1) \tag{12}$$

whereas in order to get convenient high-temperature behavior, M must be scaled to the Curie constant:

$$M = g(S(S+1))^{1/2} \tag{13}$$

In the ferromagnetic case ($J > 0$), P tends linearly to $+1$ when T is near absolute zero. Therefore, χ_0 presents a T^{-2} divergence at low temperature. Conversely, in the antiferromagnetic (AF) case ($J < 0$), P tends linearly to -1, and χ_0 has a finite limit. This agrees with the fact that under an extremely small field, the ground state of the chain is characterized by two opposite sublattices, essentially normal to the field direction.

1.3.2 Linear Ferrimagnetic Chains and Related Random Systems

The method initiated by Fisher has been extended to a large variety of more complex linear chains, most of them being ferrimagnetic [42–44]. A first study was accomplished by Thorpe [42] who considered chains involving two randomly distributed magnetic species, A and B, with concentrations c and $(1-c)$. Distinct interactions were introduced to account for the pairs (J_{aa}, $J_{\mathrm{ab}} = J_{\mathrm{ba}}$, J_{bb}). In such a model the two magnetic centers were implicitly assumed to carry equal magnetic moments, $M_\mathrm{a} = M_\mathrm{b} = M$. The initial motivation of the model was the analysis of the correlation lengths deduced from neutron diffusion experiments in TTMC chain compounds containing both magnetic cations, $\mathrm{Mn^{II}}$, and nonmagnetic ones, $\mathrm{Zn^{II}}$. The author solved the random problem for spin–spin correlations, using Eq. (9) i. e., the fact that, for an uncorrelated A/B metal distribution, the averaged value $\langle \boldsymbol{u}_i . \boldsymbol{u}_j \rangle$ over the distribution reduces to the product of the averaged intermediate correla-

tions $\langle \boldsymbol{u}_{i+m} \cdot \boldsymbol{u}_{i+m+1} \rangle$ ($m = 0, 1, \ldots, j-1$). The wave-number-dependent magnetic cross-section $S(q)$ was deduced, but the corresponding magnetic susceptibility $\chi_0(q)$ was not given. However it can be easily related to the spin–spin correlation functions in random as well as in regular systems. In this context it can be useful to mention the fragment chain model, which corresponds to a special random chain in which one of the species is nonmagnetic [42]. In this case the expression for the susceptibility is:

$$\chi_0 = N_A \beta \frac{(\mu_B M)^2}{3} \left[\frac{1+P}{1-P} - \frac{2P}{N} \frac{1-P^N}{1-P^2} \right] \tag{14}$$

where N now represents the mean length of the finite chain, and P is the Langevin function defined in Eq. (11).

The above random systems cannot be considered as true 1D ferrimagnets since, for instance, they do not show any net magnetic moment in the ground state (except for ferromagnetic coupling). The first theoretical approach concerning ferrimagnetic classical isotropic chains was motivated by experiments performed on the bimetallic chain complex MnNi(EDTA) $\cdot$ $6H_2O$ (EDTA refers to the hexadentate ligand ethylenediamine-NNN′N′-tetra-acetate) [43]. In fact this [MnNi] compound provided the first experimental observation of the characteristic minimum in χT predicted for a ferrimagnetic chain. This compound belongs to an extensive series of isostructural compounds formulated as MM′(EDTA) $\cdot$ $6H_2O$; M and M′ are two divalent metal ions (Mn, Co, Ni, Cu), which are selectively occupying two different and alternating octahedral sites, exchange-coupled by carboxylate bridges in order to form infinite zigzag chains (Fig. 7a) [3]. In this work, the magnetic properties of an exchange coupled linear chain, with two alternating magnetic sublattices (moments M_a and M_b) were investigated. The expression obtained for the zero-field magnetic susceptibility (per pair of sites) may be written as:

$$\chi_0 = N_A \beta \frac{\mu_B^2}{6} \left[M^2 \frac{1+P}{1-P} + \delta M^2 \frac{1-P}{1+P} \right] \tag{15}$$

with P defined as previously, and $M = M_a + M_b$, $\delta M = M_a - M_b$. This expression reduces to that of Fisher (Eq. (10)) when the two sublattices are equivalent ($\delta M = 0$). In the present case, the following scaling factors must be introduced to fit experimental data:

$$J \to J\left[S_a(S_a+1)S_b(S_b+1)\right]^{1/2}; \quad M_i = g_i\left(S_i(S_i+1)\right)^{1/2} \quad (i = a, b) \tag{16}$$

In Eq. (15), for F- or AF-coupling and temperature approaching absolute zero, P tends to $+1$ or -1, respectively. Accordingly, for non-vanishing δM, χ_0 diverges as T^{-2} whatever the sign of the coupling. The T^{-2} divergence essentially comes from the energy spectrum of a classical moment submitted to an external magnetic field. Therefore, it will be observed in all isotropic classical 1D systems, even when part of the spins involved in the chain are treated as quantum spins (see below). Another important point is the occurrence of the expected $\chi_0 T$ vs. T minimum, which in the present approach may be understood as follows. At high temperature, the spins are not correlated and χ_0 is governed by the Curie law which, with the present notation,

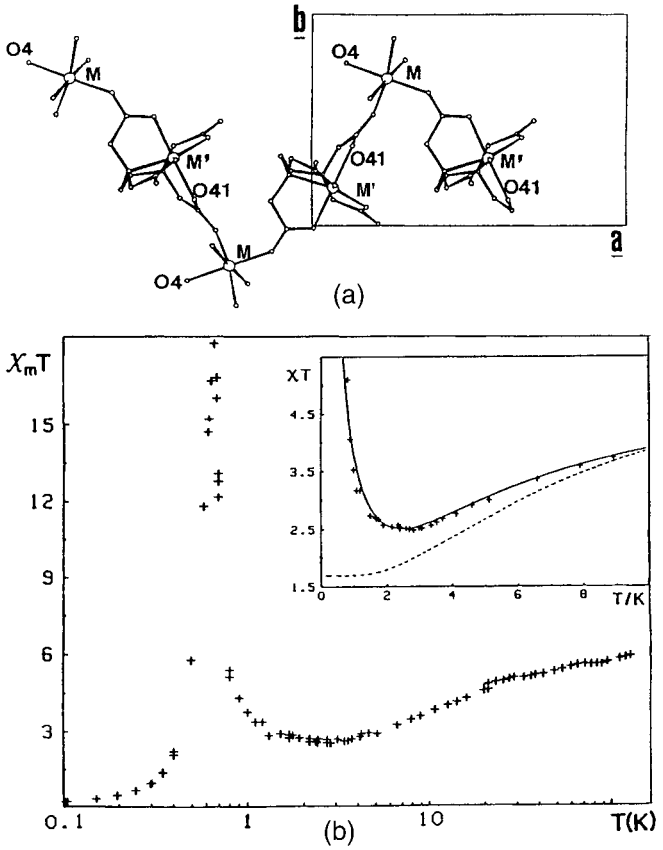

Fig. 7. (a) Structure of the series MM′(EDTA) · $6H_2O$ (M, M′ = Mn, Co, Ni, Cu). (b) Comparison between the theoretical and experimental magnetic behavior of MnNi(EDTA) · $6H_2O$. The solid line corresponds to the fit from the uniform chain model: $J/k = -1.5$ K, $g_{Mn} = 1.96$, and $g_{Ni}/g_{Mn} = 1.23$. The behavior of an isolated dimer is shown by the dashed line [48,49].

is given by:

$$\chi_0 = N_A \beta \frac{\mu_B^2}{6}[M^2 + \delta M^2] \tag{17}$$

As the system is cooled down, for AF-couplings the chain tends to behave approximately as a set of elementary pairs with moments δM (or for F-couplings, respectively, M) due to short-range correlations, thus giving rise to the following value of χ_0:

$$\begin{aligned} \chi_0 &\sim N_A \beta \frac{\mu_B^2}{6} \delta M^2; \quad \text{(AF – case)} \\ \chi_0 &\sim N_A \beta \frac{\mu_B^2}{6} M^2; \quad \text{(F – case)} \end{aligned} \tag{18}$$

Near absolute zero, which plays the role of critical temperature, the moments become strongly correlated on larger distances (the correlation length ξ increases) and the chain may be qualitatively viewed as a set of rigid fragments, each one of length ξ and carrying the net moment $\xi\delta M$ for AF-couplings (or ξM for F-couplings). As a result, we get:

$$\begin{aligned} \chi_0 &\sim N_A\beta\frac{\mu_B^2}{6}\xi\delta M^2; \quad \text{(AF – case)} \\ \chi_0 &\sim N_A\beta\frac{\mu_B^2}{6}\xi M^2; \quad \text{(F – case)} \end{aligned} \tag{19}$$

Thus, in the AF case, when δM does not vanish, the $\chi_0 T$ product shows the same divergence as the correlation length (Fig. 8), as always occurs for the F-case. This similarity between the low temperature behaviors of $\chi_0 T$ and ξ is a quite general result, and does not depend on the detailed nature of the moments (quantum or classical spins) or of the exchange coupling (Ising or Heisenberg).

For AF-couplings, if δM vanishes at absolute zero, the behavior of $\chi_0 T$ results from a delicate balance between the increase of ξ, and the decrease of δM. It is expected that the behavior will be then strongly dependent on the detailed features of the spin hamiltonian. Indeed, as a first piece of evidence, it is well known that an Ising 1D antiferromagnet exhibits an exponentially vanishing susceptibility at absolute zero, whereas the Heisenberg-coupled classical spin one gives a finite value. Moreover, apart from standard antiferromagnetism, exact compensation at absolute zero is not realistic. A more interesting situation arises when the moments carried by the two sites are slightly different. A thermal compensation may then occur at finite temperature, which is the 1D equivalent of the well-known compensation point

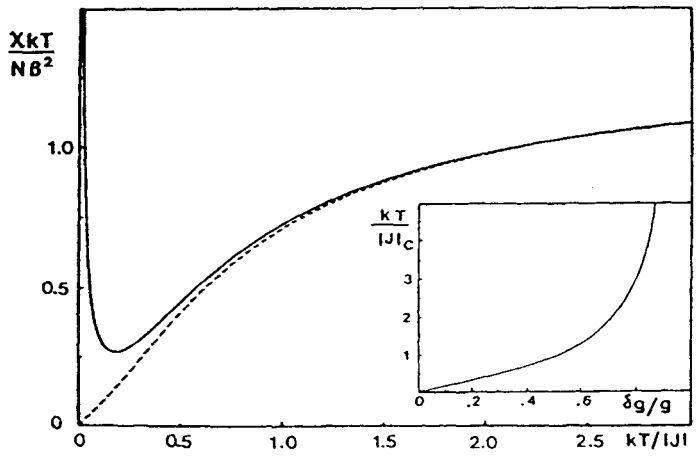

Fig. 8. χT product of a linear classical spin chain showing site alternation $M_a = 1.8$, $M_b = 2.2$ (solid line). The behavior of the uniform chain ($M_a = M_b$) is shown for comparison (dashed line). Inset: position of the χT minimum versus $\delta M/M$ [43].

occurring in 3D ferrimagnets [45]. In this case, a more complex behavior is expected, which is essentially characterized by strong oscillations of the susceptibility. This has been examined in more detail within the Ising coupling scheme [46,47] (see Section 1.5).

Using Eq. (15), together with exchange and moment scaling factors (c. f. Eq. (16)), a very satisfying description for the experimental data of $MnNi(EDTA) \cdot 6H_2O$ has been obtained in the region of the $\chi_0 T$ minimum (Fig. 7b) [43,48,49]. However, it must be pointed out that the relatively small spin value for the Ni^{II} ion ($s = 1$) is not very well adapted for a classical treatment, and that some single-ion zero-field splitting and J-alternating parameters may be expected for this chain. These points can lead to some uncertainty about the values of the fitting parameters.

The classical spin approximation also allows the introduction of alternating or random exchange coupling into the two-sublattice Heisenberg chain [50]. The expression for the random exchange is given by:

$$\chi_0 = N_A \beta \frac{\mu_B^2}{6} \left[M^2 \frac{1+\overline{P}}{1-\overline{P}} + \delta M^2 \frac{2P}{N} \frac{1-\overline{P}}{1+\overline{P}} \right] \tag{20}$$

where M and δM are defined as previously, and $\overline{P}$ is the average value of P over the J distribution. For simplicity, a uniform distribution of the exchange constant was assumed over a domain ranging from $J - \lambda$ to $J + \lambda$ ($\lambda \geq 0$), leading to the expression:

$$\overline{P} = (2\beta\lambda)^{-1} Ln \frac{(J-\lambda)}{(J+\lambda)} \frac{\sinh(\beta(J+\lambda))}{\sinh(\beta(J-\lambda))} \tag{21}$$

For the regular AF chain ($J < 0, \lambda = 0, g_a = g_b$), the susceptibility shows a rounded maximum at finite temperature and a nonvanishing value at absolute zero (Fisher's model; Fig. 9). As the distribution width increases, we note a shift of the maximum towards lower temperatures. As soon as the distribution includes F as well as AF values ($\lambda > |J|$), the maximum disappears, and the susceptibility shows a T^{-2} divergence. These features should also hold for nonuniform distributions, and for $g_a \neq g_b$. The above model has been used to describe the magnetic behaviors of amorphous $CoNi(EDTA) \cdot 6H_2O$ and $Ni_2(EDTA) \cdot 6H_2O$. Despite the amorphous character, the chains are well isolated and show a well-defined site alternation. In order to take into account the amorphous character which gives rise to a distribution in interaction angles and metal distances, a random character of the exchange interaction was introduced. The best result for the [CoNi] compound is shown in Fig. 10. For the [NiNi] compound, the present model also gives a good fit from the following set of parameters: $J/k = -3.5\,K$, $\lambda/k = 10.4\,K$, $g_{Ni} = 2.03$ and 2.35. For this last compound, the chain fragment model was also used, giving similar exchange parameters but the fit was not as good.

Further improvements to the problem of a linear chain with by two alternating sites have been reported within the classical spin approximation. A first model assumes that the two metal species are present with an arbitrary concentration and show different site affinities [51–53]. This model actually includes, as special cases, most of

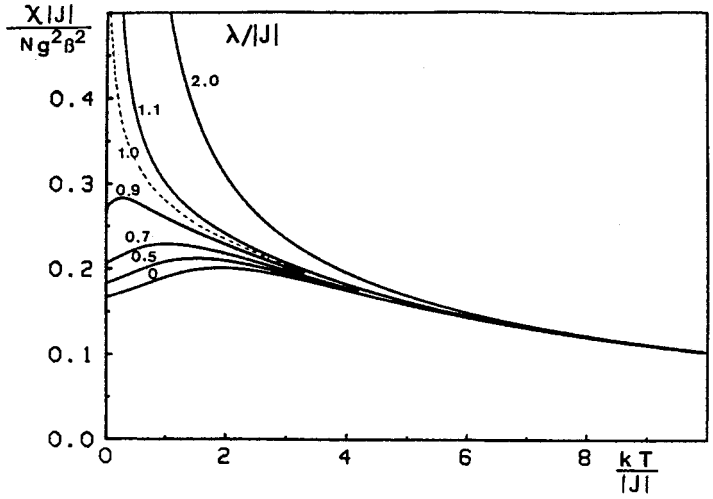

Fig. 9. Normalized magnetic susceptibility of random classical Heisenberg chain showing a uniform exchange distribution (J is the centre of the distribution and 2λ the distribution width). All curves correspond to $J < 0$ [50].

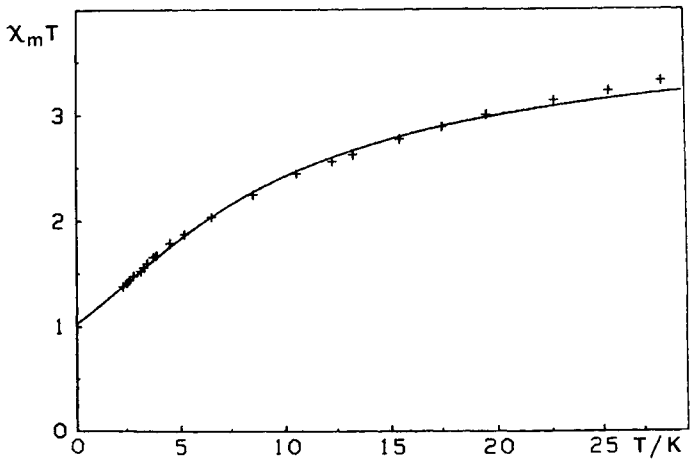

Fig. 10. Fitting of the experimental magnetic behavior of the compound $CoNi(EDTA) \cdot 6H_2O$ in the amorphous state ($J/k = -8.6\,\mathrm{K}$, $\lambda/k = 19.4\,\mathrm{K}$, $g_{Co} = 4.76$, $g_{Ni} = 2.10$) [50].

the previous ones concerning random effects. Although it is not of practical use from a general point of view, it may be an efficient tool for handling disordered systems. More specifically, it offers the interesting possibility of analyzing the finite length aspects in ferrimagnetic chains, which are often of importance due to lattice defects, by merely allowing one of the metallic species to be nonmagnetic.

A second improvement concerning the metal disorder has been proposed [51,54] when a single site may be occupied by n possible metal species m_i $(i = 1, \ldots, n)$, each one with concentration c_i, and moment M_i. The specific aspect here is that the probability for a metal to occupy a given site is determined by the nature of the metals occupying the neighboring ones. This introduces an occupation correlation superimposed onto the spin–spin correlation.

1.3.3 Complex Classical-spin Heisenberg Chains

Several attempts have been made to solve more complex 1D magnetic systems, as for example the chain of rings [44] schematized in Fig. 11. In these chains the ith ring contains n_i magnetic sites $(u = 1, \ldots, n_i)$ and shares the sites $u = 1$ and $u = c_i$ (nodes) with the neighboring rings, $i-1$ and $i+1$. The exchange constant between the uth and $(u+1)$th sites of the ith ring is $J_{i,u}$. Various ring quantities are simultaneously considered as randomly distributed: the number of magnetic sites on each ring, the positions of the nodes, the magnetic moments, the various exchange coupling parameters, etc. Again, the method is based on the orthonormality properties of the spherical harmonics, but it is less straightforward due to the existence of two interaction paths, instead of one, between two nodes on the same ring. A general expression for the zero-field susceptibility has been proposed. Actually this model applies to a large variety of complex 1D magnetic systems, and the general expression which is involved, reduces to easily handled forms in most practical cases.

This work was initially intended to interpret the magnetic properties of the fluoride $Ba_2CaMnFe_2F_{14}$ [51,55]. The crystal structure of this compound (Fig. 12) shows chains of lozenges sharing opposite corners occupied by Mn^{II} ions. The remaining sites are occupied by Fe^{III}. Such a structure is an example of 1D topological ferrimagnetism (Fig. 1f), as deduced from the rounded minimum in the χT vs. T plot

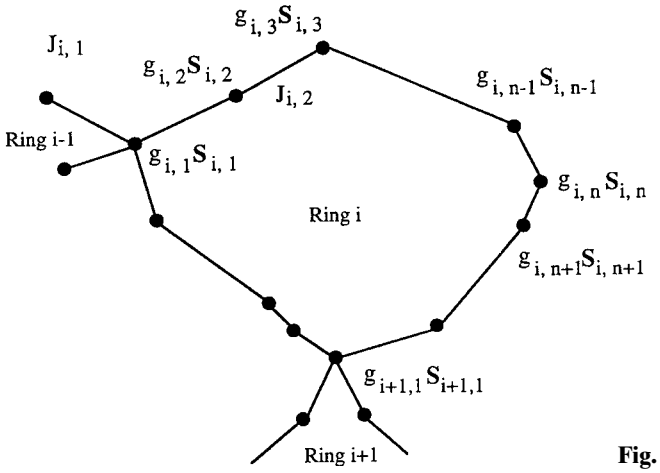

Fig. 11. Chains of rings [44].

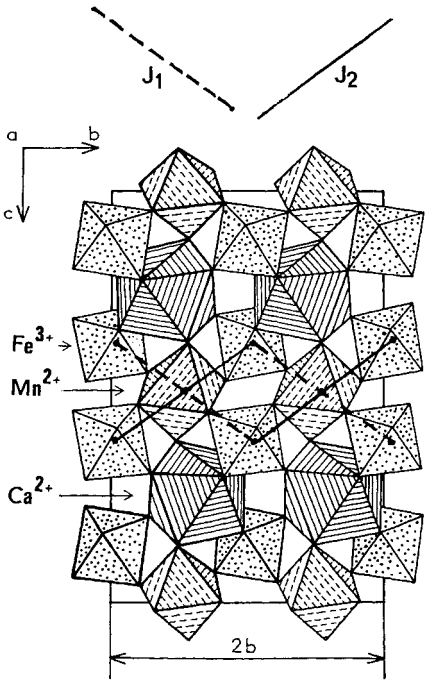

Fig. 12. Schematic representation of usovite structure $Ba_2CaMM'_2F_{14}$; M = Mn, M′ = Fe.

around 60 K (see inset of Fig. 13). At lower temperatures, χT shows a maximum at around 30 K, indicating the onset of long-range magnetic ordering. The $3d^5$ ($S = 5/2$) electronic structure of both metals justifies the use of a classical Heisenberg-type treatment [56]. Owing to the nature of the magnetic paths, two interaction constants, J_1 and J_2, are needed. A general expression of the zero-field susceptibility has been derived, from which the experimental results have been conveniently fitted in the paramagnetic region (Fig. 13).

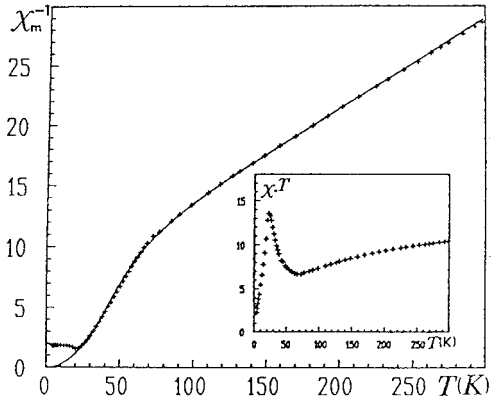

Fig. 13. Fitting of the experimental susceptibility of the compound $Ba_2CaMnFe_2F_{14}$: $J_1/k = -6.7$ K, $J_2/k = -2.7$ K [51].

Recently, a similar approach has been developed to describe the magnetic properties of MnMn(CDTA) · $7H_2O$, (CDTA = 1,2-cyclohexanediamine-NNN′N′-tetraacetate), which contains two different metal sites connected by carboxylate groups formating chains of Mn^{II} triangles [57,58] as shown in the inset of Fig. 14, where J_1, J_2 and J_3 refer to the three exchange. Since all these couplings are AF, this compound offers a nice example of spin-frustration in one dimension. The magnetic properties show a continuous decrease of χT upon cooling (Fig. 15). However, the plot of χ vs. T does not show the characteristic maximum down to 2 K, in agreement with the fact that frustration tends to reduce short-range order. Thus, the classical spin model predicts that the susceptibility maximum of the linear chain, observed at $kT/|J| = 0.5$, tends to disappear when spin-frustration is introduced (antiferromagnetic J_1) (Fig. 15). This model provides a satisfying fit of the experimental data with the following exchange parameters: $J_1/k = -0.94$ K, $J_2/k = -1.10$ K and $J_3/k = -0.23$ K.

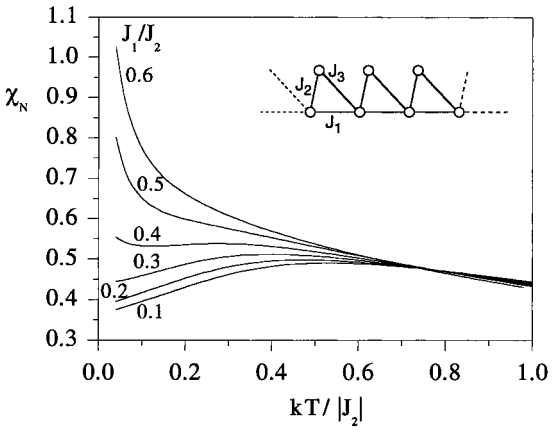

Fig. 14. Theoretical magnetic behavior of the triangular Heisenberg chain for $J_2 = J_3$ and different ratios between J_1 and J_2.

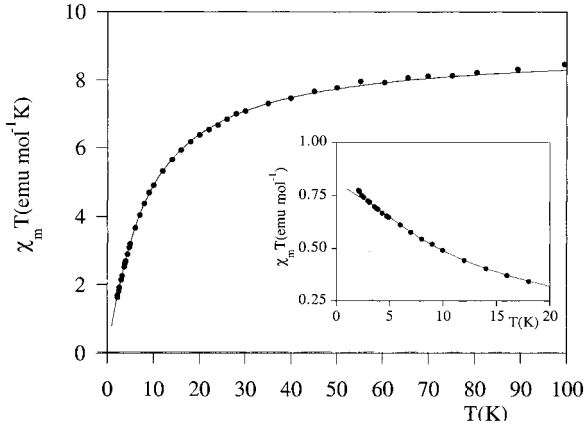

Fig. 15. Magnetic behavior of MnMn(CDTA) · $7H_2O$. The solid line represents the best fit to the triangular chain model [57,58].

1.4 Quantum-classical Heisenberg Ferrimagnetic Chains

1.4.1 Alternation of Quantum and Classical Spins: Uniform and Alternating Quantum-classical Chains

The first study of a quantum-classical Heisenberg chain was reported by Dembinski & Wydro [59] for the analysis of the correlation functions and specific heat properties. Blöte [60] further determined the expression of the susceptibility, but he neglected the magnetic contribution of the quantum sublattice with respect to the classical one, making his result useless for real systems. The first calculation in which the two spin sublattices were considered was reported by Seiden [61]. This author developed a model in order to interpret the magnetic properties of the compound $CuMn(S_2C_2O_2)_2 \cdot 7.5H_2O$ which shows a regular alternation of Mn^{II} ($S = 5/2$) and Cu^{II} ($s = 1/2$) along the chains (Fig. 16). Due to the specific spin values, he was led to consider the chain $\boldsymbol{S}_{i-1}, \boldsymbol{s}_i, \boldsymbol{S}_i, \boldsymbol{s}_{i+1}$ etc., where $\boldsymbol{s}_i$ is a $s = 1/2$ quantum operator and $\boldsymbol{S}_i$ a classical spin (directed by the unit vector $\boldsymbol{u}_i$). The hamiltonian may be written as:

$$H = -J \sum_i \boldsymbol{s}_i(\boldsymbol{u}_{i-1} + \boldsymbol{u}_i) - \boldsymbol{B}(M\boldsymbol{u}_i + g\boldsymbol{s}_i) \tag{22}$$

where M is the moment carried by the classical spins and g is the Landé factor for the quantum ones. The calculation of the partition function requires evaluating

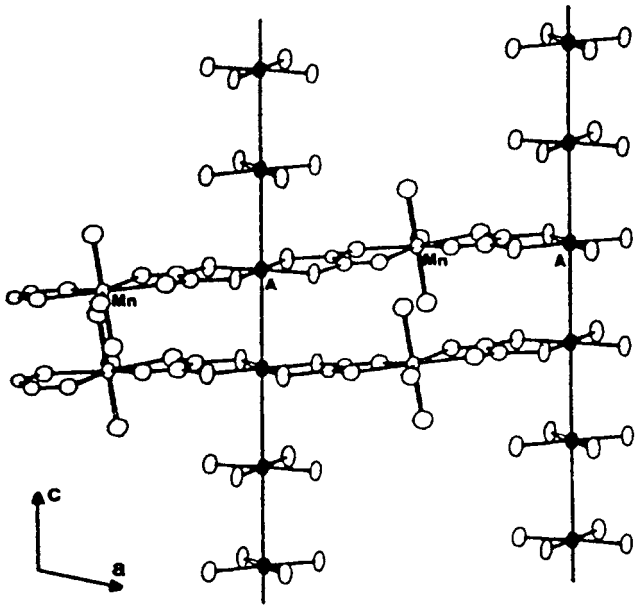

Fig. 16. Perspective view of a section of the chain in $CuMn(S_2C_2O_2)_2 \cdot 7.5H_2O$ [62].

the hamiltonian trace for each quantum spin $\boldsymbol{s}_i$ submitted to the exchange field $(J/g)(\boldsymbol{u}_{i-1} + \boldsymbol{u}_i)$ created by its neighbors $\boldsymbol{S}_{i-1}$ and $\boldsymbol{S}_i$. Then, an integration must be performed over all classical spin orientations. The double derivation with respect to $\boldsymbol{B}$, necessary for calculating the zero-field susceptibility, introduces two types of terms: single-site terms, which are directly related to the individual Curie constants, and pair-correlation ones, between localized spins. The nearest-neighbor correlations $\langle \boldsymbol{u}_{i-1}.\boldsymbol{s}_i \rangle$ or $\langle \boldsymbol{s}_i.\boldsymbol{u}_i \rangle$, and classical-classical next nearest-neighbor ones $\langle \boldsymbol{u}_{i-1}.\boldsymbol{u}_i \rangle$ are easily determined within the trimer $(\boldsymbol{S}_{i-1}, \boldsymbol{s}_i, \boldsymbol{S}_i)$, which may be considered separately in this respect. As a result, all pair correlations are available and the zero-field susceptibility may be calculated. The final expression is:

$$\chi_0 = N_A \beta \frac{\mu_B^2}{3} \left[M^2 \frac{S+1}{S} + g^2 s(s+1) + 2(1-P)^{-1} \left(PM^2 - 2QgsM + Q^2 g^2 s^2 \right) \right] \tag{23}$$

with:

$$P = \frac{\left(1 + 12\gamma^{-2}\right) \sinh \gamma - \left(5\gamma^{-1} - 12\gamma^{-3}\right) \cosh \gamma + 12\gamma^{-3} - \gamma^{-1}}{\sinh \gamma - \gamma^{-1} \cosh \gamma + \gamma^{-1}} \tag{24}$$

$$2Q = \frac{\left(1 + 2\gamma^{-2}\right) \cosh \gamma - 2\gamma^{-1} \sinh \gamma - 2\gamma^{-2}}{\sinh \gamma - \gamma^{-1} \cosh \gamma + \gamma^{-1}} \tag{25}$$

with $\gamma = \beta J$.

Equation (23) has several similarities with previously quoted ones. Clearly, γ, P and Q vanish in the high-temperature range and the susceptibility then follows the Curie law. Conversely, at low temperature, γ diverges; P, which is nothing but the correlation $\langle \boldsymbol{u}_i.\boldsymbol{u}_{i+1} \rangle$, tends linearly to unity in absolute value; finally, Q, which represents the nearest-neighbor correlation $\langle \boldsymbol{u}_i.\boldsymbol{s}_i \rangle$, tends to ± 1 (depending on the sign of J, as P). The susceptibility is then essentially governed by the term $(1-P)^{-1}$. The corresponding factor appears to be a sum of three terms: one of purely classical origin, another one which is purely quantum, and a mixed quantum-classical one. This factor can only accidentally vanish. Thus, this model predicts a T^{-1} divergence law for the $\chi_0 T$ product, as expected when classical moments are present along a linear Heisenberg-type chain. This has already been related to the structure of the energy spectrum of the classical moments submitted to their exchange field, since, in contrast with the quantum spin case, it presents no gap, being in the main responsible for the low temperature properties. This model has been successfully applied [62] to analyzing the magnetic properties of the uniform chain $CuMn(S_2C_2O_2)_2 \cdot 7.5H_2O$.

In a series of papers [63–66] this model has been extended to chains showing various random characters (exchange energies, spin quantum numbers, classical moment amplitudes, quantum spin Landé factors). This was motivated by the synthesis of new 1D ferrimagnetic compounds with alternating exchange interactions between nearest neighbors, as for example $MnCu(obp)(H_2O)_3 \cdot 2H_2O$ (obp = oxamido-bis(N,N′-propionato)) [66], which shows alternating spins $s_{Cu} = 1/2$, $S_{Mn} = 5/2$, as well as alternating exchange constants (Fig. 17a). Now, the exchange hamiltonian is given

by:

$$H = \sum_i \big[- J_i \boldsymbol{s}_i \left[(1-\alpha_i)\boldsymbol{u}_{i-1} + (1+\alpha_i)\boldsymbol{u}_i \right] - \boldsymbol{B}(M_i \boldsymbol{u}_i + g_i \boldsymbol{s}_i) \big] \tag{26}$$

where α_i allows us to distinguish the left and right interactions of a general quantum spin $\boldsymbol{s}_i$ with a classical one $\boldsymbol{u}_i$. The calculations essentially follow the same process as previously and, in the most general case, the final expression for χ_0 is:

$$\begin{aligned} \chi_0 \;=\; & N_{\mathrm{A}} \beta \frac{\mu_{\mathrm{B}}^2}{3} \big[M_i^2 + g_i^2 s_i (s_i + 1) \\ & + 2(1 - P_i)^{-1} \big[M_i P_i M_i + g_i Q_{i+} g_i Q_{i-} + M_i g_i Q_{i+} \\ & - P_i M_i g_i Q_{i+} + M_i g_i Q_{i-} + M_i P_i g_i Q_{i+} \big] \end{aligned} \tag{27}$$

with

$$P_i = \frac{A_{1,i}}{A_{0,i}} \tag{28}$$

$$Q_{i,\varepsilon} = \beta J_i \frac{(1 + \varepsilon\alpha_i) B_{0,i} + (1 - \varepsilon\alpha_i) B_{1,i}}{A_{0,i}} \tag{29}$$

$$A_{0,i} = \frac{4\pi}{\lambda_i^2 \eta_i} \sum_{\sigma_i = -s_i}^{+s_i} \sum_{\varepsilon = \pm 1} \frac{\varepsilon}{\sigma_i^2} (\vartheta_{i,\sigma_i,\varepsilon} - 1) \, \exp(\vartheta_{i,\sigma_i,\varepsilon}) \tag{30}$$

$$\begin{aligned} A_{1,i} \;=\; & \frac{4\pi}{(\lambda_i^2 \eta_i)^2} \sum_{\sigma_i = -s_i}^{+s_i} \sum_{\varepsilon = \pm 1} \frac{\varepsilon}{\sigma_i^4} \\ & \times \left(\vartheta_{i,\sigma_i,\varepsilon}^3 - 3\vartheta_{i,\sigma_i,\varepsilon}^2 + \left(6 - (\sigma_i \lambda_i)^2 \right) \left(\vartheta_{i,\sigma_i,\varepsilon} - 1 \right) \right) \exp(\vartheta_{i,\sigma_i,\varepsilon}) \end{aligned} \tag{31}$$

$$B_{0,i} = \frac{4\pi}{\lambda_i^2 \eta_i} \sum_{\sigma_i = -s_i}^{+s_i} \sum_{\varepsilon = \pm 1} \varepsilon \cdot \exp(\vartheta_{i,\sigma_i,\varepsilon}) \tag{32}$$

$$\begin{aligned} B_{1,i} \;=\; & \frac{4\pi}{(\lambda_i^2 \eta_i)^2} \sum_{\sigma_i = -s_i}^{+s_i} \sum_{\varepsilon = \pm 1} \frac{\varepsilon}{\sigma_i^2} \\ & \times \left(\vartheta_{i,\sigma_i,\varepsilon}^2 - 2\vartheta_{i,\sigma_i,\varepsilon} + 2 - (\sigma_i \lambda_i)^2 \right) \exp(\vartheta_{i,\sigma_i,\varepsilon}) \end{aligned} \tag{33}$$

with

$$\vartheta_{i,\sigma_i,\varepsilon} = \sigma_i \lambda_i \sqrt{1 + \varepsilon \eta_i}; \quad \lambda_i = \beta J_i \sqrt{2(1+\alpha_i^2)}; \quad \eta_i = \frac{1-\alpha_i^2}{1+\alpha_i^2} \tag{34}$$

where P_i is the correlation $\langle \boldsymbol{u}_i \boldsymbol{u}_{i+1} \rangle$ and is now i-dependent. Furthermore, Q_{i+} and Q_{i-} are the correlations $\langle \boldsymbol{s}_i \boldsymbol{u}_i \rangle$ and $\langle \boldsymbol{u}_{i-1} \boldsymbol{s}_i \rangle$ which must now be distinguished. This result clearly reduces to Seiden's result when the quantum spin is $s = 1/2$, and uniform exchange and magnetic moments are considered. The T^{-1} divergence law for $\chi_0 T$ is maintained when all the exchange parameters $J_i(1 \pm \alpha_i)$ have the same sign. In the case of exchange sign alternation, χ_0 exhibits a rather misleading Curie-type behavior at low temperature. It has been shown [64] that this behavior may be interpreted as a collective exaltation of a Van Vleck-type susceptibility contribution arising from the presence of distinct Landé factors, since when a spin is treated as classical its Landé factor actually vanishes.

In the particular case of alternating exchange parameters, Eq. (27) reduces to:

$$\chi_0 = N_A \beta \frac{\mu_B^2}{3} \Big[M^2 + g^2 s(s+1) + 2(1-P)^{-1} \big[M^2 P + g^2 Q_+ Q_- + Mg(Q_+ + Q_-) \big] \Big] \tag{35}$$

where the indices have been dropped; P, Q_+ and Q_- are directly derived from Eqs. (28)–(34) by dropping the i indices. Conveniently scaled, Eq. (35) (see Eqs. (12) and (13)) has allowed the reproduction of the experimental magnetic behavior of $MnCu(obp)(H_2O)_3 \cdot 2H_2O$ from the following parameters: $J/k = -28\,K$, $\alpha = 0.65$ (solid line in Fig. 17b). This result reveals a relatively large α value, in agreement with the very different nature of the left and right exchange pathways [65,66].

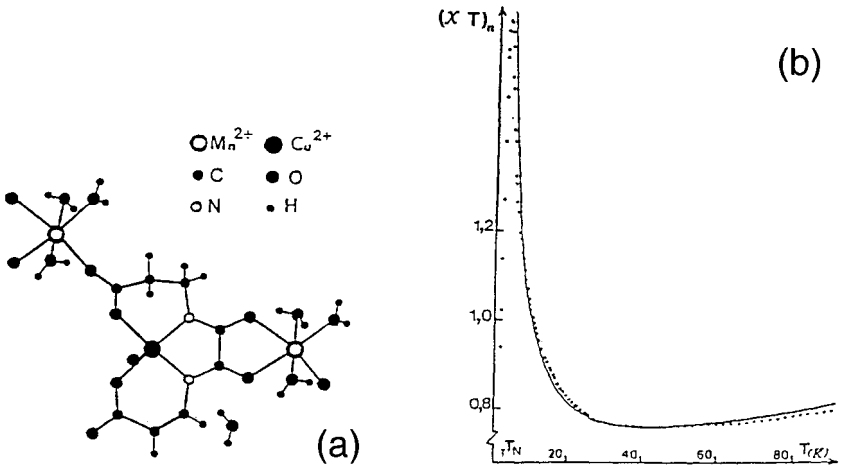

Fig. 17. (a) Perspective view of a section of the chain in $MnCu(obp)(H_2O)_3 \cdot 2H_2O$; (b) Fitting of the experimental susceptibility [66].

1.4.2 Alternation of a Classical Spin with a Quantum System

A further generalization of this model has been proposed [67] to analyze the magnetic properties of the compound $MnCu_2(bapo)(H_2O)_4 \cdot 2H_2O$ (bapo = N,N′ (3-amino-propylene)oxamidato), in which the magnetic ions form the regular sequence: ... MnCuCuMnCuCuMn .... This arrangement introduces a new class of isotropic ferrimagnetic chains, in which a classical spin alternates with a more or less complex quantum spin system, ζ_i. The chain hamiltonian may be written in the general form as:

$$H = \sum_i [H(\zeta_i, \boldsymbol{u}_{i-1}, \boldsymbol{u}_i, B) - M \cdot B\boldsymbol{u}_i^z] \tag{36}$$

where $H(\zeta_i, \boldsymbol{u}_{i-1}, \boldsymbol{u}_i, B)$ is the hamiltonian for the ith isotropic quantum subsystem submitted to the external field $\boldsymbol{B}$, and to the exchange field created by the neighboring classical spins $\boldsymbol{S}_{i-1}$ and $\boldsymbol{S}_i$. The last part is the Zeeman term for the classical spins. The main lines of the mathematical treatment are as follows.

The B-dependent partition function is written as:

$$Z_N(B) = \int \mathrm{d}\Omega_0 U_0 \int \mathrm{d}\Omega_1 V_0 V_1 \cdots \int \mathrm{d}\Omega_i V_{i-1} U_i \cdots \int \mathrm{d}\Omega_N V_{N-1} U_N \tag{37}$$

where

$$U_i = \exp(\beta M_i u_i^z) \tag{38}$$

$$V_i = \text{trace}\left(\exp(-\beta H(\zeta_i, \boldsymbol{S}_{i-1}, \boldsymbol{S}_i, \boldsymbol{B})\right) \tag{39}$$

The trace V_i deals with the hamiltonian of the subsystem ζ_i submitted to the exchange field of its classical neighbors $\boldsymbol{S}_{i-1}$ and $\boldsymbol{S}_i$. For vanishing B, it only depends on the angle between these vectors. This property affords the calculation of the zero-field partition function and its first two derivatives with respect to B. As a result, one gets the susceptibility:

$$\begin{aligned}\chi_0 = {} & \chi_{VV} + N_A \beta \frac{\mu_B^2}{3} \\ & \times \left[M_i^2 + G_i^2 + 2(1 - P_i)^{-1}[M_i P_i M_i + Q_{i+} Q_{i-} + M_i Q_{i+} \right. \\ & \left. - P_i M_i Q_{i+} + M_i Q_{i-} + M_i P_i Q_{i+}]\right]\end{aligned} \tag{40}$$

where M_i and P_i are defined as previously, whereas G_i^2 is the mean square moment carried by ζ_i; Q_{i+} and Q_{i-} are the correlations between $\boldsymbol{u}_i$ and the total moments on ζ_i and ζ_{i-1}, respectively. Except for χ_{VV}, this expression is very similar to Eq. (27), to which it reduces when each ζ_i contains a single spin. The Van Vleck susceptibility, χ_{VV}, arises from the presence of distinct Landé factors associated with the quantum spins forming the ζ_i subsystems. The calculation of the various terms in Eq. (40) requires the knowledge of the traces V_i which are not always available in

analytical form and must then be obtained numerically. This work has been generalized to more complicated unit cells, including notably the introduction of a spin–orbit coupling [68].

For the regular chain case, Eq. (40) reduces to:

$$\chi_0 = \chi_{VV} + N_A\beta\frac{\mu_B^2}{3}\Big[M^2 + G^2 + 2(1-P)^{-1} \times \big[MPM + Q_+Q_- + M(Q_+ + Q_-)\big]\Big] \tag{41}$$

where the indices have been dropped. This expression was used [67,69] to fit the experimental results obtained for the compound $MnCu_2(bapo)(H_2O)_4 \cdot 2H_2O$. The parameters Q_+ and Q_- were set as equal because of crystal symmetries. The best-fitting exchange values ($J_{Mn\text{-}Cu}/k = -50\,K$, $J_{Cu\text{-}Cu}/k = -100\,K$) appear to be in agreement with independent estimates.

To finish this section, three remarks can be made. First, from a theoretical point of view, the bilinear Heisenberg-type coupling is not essential, and could be replaced by (or combined with) any isotropic coupling scheme, including for instance biquadratic terms. Second, from the modeling point of view, the presence of classical spins bridging more or less complex quantum subsystems is fundamental in the isotropic interaction framework; it isolates the subsystems and allows them to be treated separately before performing the usual integrations which are facilitated by the orthonormality properties of the spherical harmonics. Thirdly, the generally observed low temperature T^{-1} divergence of the $\chi_0 T$ product is a fundamental characteristic of 1D isotropic exchange interactions whatever the chain unit-cell structure.

1.4.3 Other Complex Quantum-classical 1D Systems

More complex ferrimagnets with 1D structures are known; for example the coordination compound $Gd_2(ox)[Cu(pba)]_3[Cu(H_2O)_5] \cdot 20H_2O$ (pba = 1,3-N,N′-propylenebis(oxamato), ox = oxalato) is of particular interest [70]. In the structure, the dications $[Cu(H_2O)_5]^{+2}$ are isolated so that their contribution to the magnetic susceptibility corresponds to a Curie behavior. The remaining magnetic cations form ladder-like motifs; the Gd^{III} ions (spin 7/2), considered as classical moments lie at the intersect of the uprights and the ranges, whereas the Cu^{II} ions (1/2 spins) separate any pair of neighboring Gd^{III} (Fig. 18). The structure and chemical considerations allow all the $[Gd^{III}Cu^{II}Gd^{III}]$ moieties to be regarded as nearly similar.

Georges et al. [71] extended the previous theoretical treatment to larger values of the quantum spins and less symmetrical structures. Essentially, in the vanishing field limit, they considered the partition function involving N unit cells (each one comprising two Gd^{III} and three Cu^{II}) as a function of the scalar product $\boldsymbol{S}_N\boldsymbol{S}'_N$ of the last two Gd^{III} cations. They developed this function as a series of Legendre polynomials with respect to $\boldsymbol{u}_N\boldsymbol{u}'_N$, where $\boldsymbol{u}_N$ and $\boldsymbol{u}'_N$ are the unit vectors along $\boldsymbol{S}_N$ and $\boldsymbol{S}'_N$ respectively. The coefficients of the development form the components of the

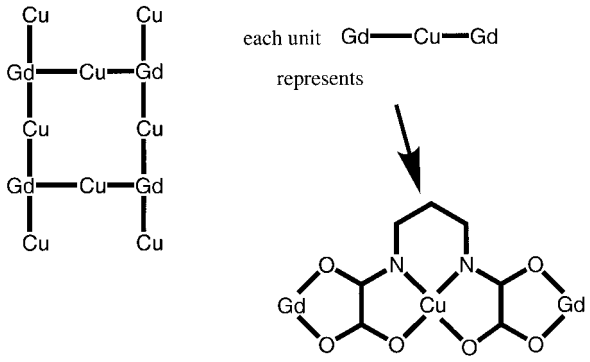

Fig. 18. Structure of the compound $Gd_2(ox)[Cu(pba)]_3[Cu(H_2O)_5] \cdot 20H_2O$ [70].

vectors linked by a transfer matrix. In fact, these authors also introduced a weak magnetic field in order to compute the magnetic susceptibility. This results in a reduction of the spin space symmetry from the full rotation group to the C_∞ one. As a consequence, the basis functions must take the form $Y_l^0(\boldsymbol{u}_N)Y_{l'}^0(\boldsymbol{u}'_N)P_{l''}(\boldsymbol{u}_N\boldsymbol{u}'_N)$, where $Y_l^m(\boldsymbol{u})$ is the spherical function for the standard angles θ and ϕ associated with the direction of the unit vector. Since only second derivatives with respect to the field amplitude are required, only spherical l or l' indices up to 2 are used within this basis.

It is an obvious step, although extremely tedious, to determine the structure of the transfer matrix and to compute the partition function as its largest eigenvalue. This has been done for instance with the ladder-type bimetallic compound just mentioned above, giving a remarkable agreement with the experimental susceptibility. The only fitting parameter used, namely the $Gd^{III}Cu^{II}$ exchange coupling, was shown to be ferromagnetic ($J/k = 0.40\,\mathrm{K}$). Such an agreement is consistent with the fact that considering the spin of the Gd^{III} cations as classical is a very convenient approximation, owing to its large spin quantum number. Also, the isotropic coupling scheme fits well the magnetic characteristics of the two interacting cations.

Finally, it has been shown [71] that, for a ladder-type Heisenberg double chain composed of classical spins (interacting between themselves with or without the presence of quantum spins), the correlation length ξ behaves as T^{-1} near absolute zero, as the product χT does. This means that double chains isotropically coupled have a 1D magnetic behavior independently of the (classical or quantum) nature of the spin moments involved. At this juncture, it must be noticed that this work has been the starting point of a series of papers dealing with 2D magnetic systems composed of classical spins isotropically coupled, and characterized by a square [72–75] or a hexagonal unit cell [76]; all the thermodynamic functions of interest have been derived in the zero field limit.

1.5 Ising Chains

We have shown that in fully isotropic 1D ferrimagnets, the presence of classical spins at *strategic* positions is very useful for modeling thermodynamic properties. In systems showing some amount of exchange or local anisotropy, the restrictions are somewhat similar to those noticed for the fully isotropic case and, in general, no exact solutions are available. Only the ZZ-type anisotropic coupling allows a rigorous treatment for quantum as well as for classical spins. Exact models were developed early on, since their mathematical aspects (at least in the purely F or AF 1D systems) are very easy to handle [77–79]. We shall first present the procedure originally proposed by Kramers & Wannier (transfer-matrix method) for the linear $1/2$ spin chains [80]. Extensions to ferrimagnetic systems will then be described.

1.5.1 The Transfer-matrix Method

Conceptually, the chains described by an Ising coupling are the opposite of isotropic ones. They have been generally developed to describe strongly anisotropic systems, involving for instance cations with a large zero-field splitting which confines the z component of a spin ($s = 1$) to its extreme values $\pm s$. Cobalt(II) in distorted octahedral environments is often a good example of an Ising ion. In this model, advantage is taken of the commutation of the spin operators. Now, this does not result from the classical approximation, but from the fact that only the z component is involved for each spin. This excludes looking for the normal susceptibility $\chi_{0\perp}$ (applied magnetic field normal to the z direction) except when a classical spin alternates with the quantum one, and we shall essentially restrict ourselves to the discussion of the zero-field parallel susceptibility ($\chi_{0\parallel}$). From a practical point of view, it appears that $\chi_{0\perp}$ remains finite at low temperature, whereas $\chi_{0\parallel}$ diverges for ferrimagnetic or antiferromagnetic noncompensated chains, and is easily estimated with a convenient accuracy in the whole temperature range. Thus, in this context, the lack of an exact expression for $\chi_{0\perp}$ does not really hinder the fitting of experimental data obtained for crystal or powder samples.

The general mathematical procedure is governed by the discreteness of the z-spin components. The integrations over the directions available to the classical spins are now replaced by summations over the s_z values. This favors a matrix formalism which gives rise to the so-called transfer-matrix method. The approach initially developed for linear $1/2$ spin chains may be immediately generalized to an arbitrary spin quantum number. In the present context, the hamiltonian may be written:

$$H = -J \sum_i m_i m_{i-1} - gB \sum_i m_i \tag{42}$$

where B is the amplitude of the applied magnetic field and m_i the z component of the current spin operator $\boldsymbol{s}_i$.

Let Z_N be the partition function for a finite chain beginning at site 0 and ending at site N. We introduce the related vector $\boldsymbol{Z}_N$ defined as follows: it has $2s+1$ compo-

nents, Z_{N,m_N}, associated with each m_N component. The value of Z_{N,m_N} results from the contributions to Z_N of all the chain configurations, for which the z component of $\boldsymbol{s}_N$ is m_N. Adding an $(N+1)$th spin to the N-spin chain, we can similarly define Z_{N+1}, and $\boldsymbol{Z}_{N+1}$. Clearly, $\boldsymbol{Z}_{N+1}$ is directly related to $\boldsymbol{Z}_N$ through a $(2s+1)\times(2s+1)$ matrix, namely the transfer matrix T:

$$\boldsymbol{Z}_{N+1} = (\mathrm{T})\boldsymbol{Z}_N \tag{43}$$

The current term of (T) is:

$$(\mathrm{T})_{m_N,m_{N+1}} = \exp(\beta(Jm_N + g\mu_\mathrm{B}B)m_{N+1}) \tag{44}$$

which takes into account the exchange coupling between $\boldsymbol{s}_N$ and $\boldsymbol{s}_{N+1}$, and the Zeeman effect on $\boldsymbol{s}_{N+1}$. Clearly, (T) does not depend on N. This recurrence property permits the calculation of the partition vector $\boldsymbol{Z}_N$ for arbitrary N, starting from $\boldsymbol{Z}_0$ which is easily determined. Let us now consider the dominant (largest modulus) eigenvalue t_+ of the transfer matrix, and call $\boldsymbol{Z}_+$ the corresponding (dominant) eigenvector. Upon successive applications of the transfer matrix (T) on $\boldsymbol{Z}_0$, its component along the dominant eigenvector, say $\boldsymbol{Z}_{0+}$, is progressively selected. As a result, for very long chains, the partition function reduces to:

$$Z_N \approx (t_+)^N Z_{0+} \tag{45}$$

Then, the partition function of the infinite chain, referred to the unit cell, appears to be merely given by t_+ (to within a constant factor).

For example, in the $s = 1/2$ case, the transfer matrix is easily shown to be:

$$(\mathrm{T}) = \begin{vmatrix} \exp(\beta(J/4 + g\mu_\mathrm{B}B/2)) & \exp(\beta(-J/4 + g\mu_\mathrm{B}B/2)) \\ \exp(\beta(-J/4 - g\mu_\mathrm{B}B/2)) & \exp(\beta(J/4 - g\mu_\mathrm{B}B/2)) \end{vmatrix} \tag{46}$$

leading to the partition function $Z(B)$:

$$\begin{aligned} Z(B) \;=\; & \exp(\beta J/4)\cosh(\beta g\mu_\mathrm{B}B/2) \\ & + \left[(\exp(-\beta J/2) + \exp(\beta J/2)\sinh^2(\beta g\mu_\mathrm{B}B/2)\right]^{1/2} \end{aligned} \tag{47}$$

After convenient derivation, we get the zero-field parallel susceptibility (per mole of spins):

$$\chi_{0\parallel} = N_\mathrm{A}\beta(g\mu_\mathrm{B}/2)^2\,\exp(\beta J/2) \tag{48}$$

As can be seen, $\chi_{0\parallel}T$ diverges (or vanishes) exponentially at low temperature for F (or AF) exchange coupling. Now, introducing the zero-field partial derivative of Z with respect to βJ, i. e., the nearest-neighbor correlation function P:

$$P = \langle m_i m_{i+1}\rangle = \tanh(\beta J/4) \tag{49}$$

we may write:

$$\chi_{0\parallel} = N_A \beta \left(\frac{g\mu_B}{2}\right)^2 \frac{1+P}{1-P} \tag{50}$$

It is useful to briefly compare this result with Eq. (10), obtained for the classical-spin Heisenberg chain. Both show a square dependence of the individual moment. The factor 1/3, which is only present for the isotropic chain, accounts for the distinct dimensionalities of the spaces actually available to the spins in the low-temperature range. The formal temperature dependence of the product $\chi_{0\parallel} T$ is similarly governed by the nearest-neighbor correlation P. However, for the classical-spin Heisenberg model, there is no energy gap above the ground state. This gives rise to the usual linear T-dependence of P at low temperature. Conversely, in the ZZ coupling 1/2-spin case, any departure from the ground state requires the reversal of a spin and a finite excitation energy. As a result, $|P|$ exponentially approaches unity in the low-temperature range, leading to an exponential behavior for $\chi_{0\parallel} T$.

1.5.2 Ferrimagnetic Ising Chains and Related Random Systems

The transfer-matrix method has been extended to a large variety of more complex chains, most of them being ferrimagnetic like. The simplest step towards a general presentation of the ferrimagnetic Ising chain models deals with a linear chain exhibiting a regular alternation of two cations M and M' with identical spins 1/2 but distinct Landé factors, g and g'. Thus, for a nonvanishing field, distinct transfer matrices (T) and (T′) are used when an s (or s') spin is added to the chain. Actually, one may add the spins pair by pair, and hence one may use the product (T)(T′) as the effective transfer matrix. When this operates on the vector $\boldsymbol{Z}_i$, associated to the chain ending at $\boldsymbol{s}_i$, it gives $\boldsymbol{Z}_{i+1}$ which is related to $\boldsymbol{s}_{i+1}$. Since the product is again a (2×2) matrix, we are left with the same eigenvalue problem. Further, this process allows to introduce an exchange coupling alternation (J, J'), and to study dimerized spin lattices. This model has been developed [81] for analyzing the magnetic and specific heat properties of the chain compounds $Co_2(EDTA) \cdot 6H_2O$ and $CoCu(EDTA) \cdot 6H_2O$ characterized by two different sites for the metal ions, and two distinct interaction paths. The expression obtained for $\chi_{0\parallel}$ is (per pair of sites):

$$\chi_{0\parallel} = N_A \beta \frac{\mu_B^2}{2} \frac{g_+^2 \exp(\beta J_+/2) + g_-^2 \exp(\beta J_-/2)}{\cosh(\beta J_-/2)} \tag{51}$$

where $g_\pm = (g \pm g')/2$, and $J_\pm = (J \pm J')/2$. As for the isotropic case, for distinct Landé factors and purely AF coupling, a minimum generally occurs in the thermal variation of the $\chi_{0\parallel} T$ product with a divergence in the low temperature range, even for strong dimerization of the chain, $|J_-| < |J_+|$ (Fig. 19).

The same procedure [82,83] has been extended to the [s–s'] alternating chain with $s = 1/2$ and arbitrary s', and a regular J value. The method also allows the

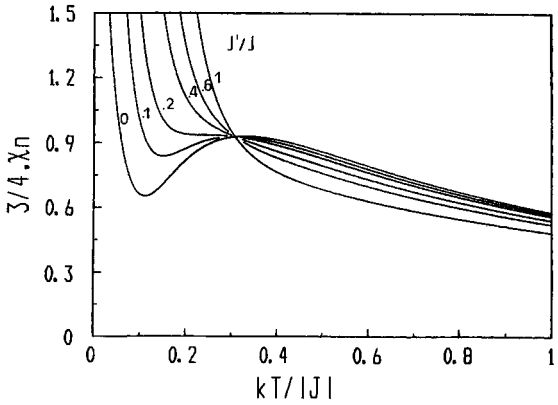

Fig. 19. Thermal variation of the parallel susceptibility for a ferrimagnetic [1/2–1/2] Ising chain in a noncompensated case ($g'/g = 1.5$), for various values of the J'/J ratio [81].

introduction of some zero-field splitting effect (along the z direction) on the spins s'. The starting matrices (T) and (T′) are now rectangular, $2 \times (2s'+1)$ and $(2s'+1) \times 2$, giving a square (2×2) matrix product, when performed in the convenient order. The partition function is given in terms of the trace and determinant (S and P, respectively) of the transfer matrix:

$$Z(B) = S + (S^2 - 4P)^{1/2} \tag{52}$$

with

$$S = \sum_{\varepsilon=\pm 1} \exp\left(\frac{\varepsilon\beta g B}{2}\right) \frac{\sinh\left[\dfrac{\beta}{2}(2s'+1)[\varepsilon J + g'B]\right]}{\sinh\left[\dfrac{\beta}{2}[\varepsilon J + g'B]\right]} \tag{53}$$

$$P = \frac{\sinh\left[\dfrac{\beta}{2}(2s'+1)[J - g'B]\right]}{\sinh\left[\dfrac{\beta}{2}[J - g'B]\right]} \frac{\sinh\left[\dfrac{\beta}{2}(2s'+1)[J + g'B]\right]}{\sinh\left[\dfrac{\beta}{2}[J + g'B]\right]} - \left(\frac{\sinh\left[\dfrac{\beta}{2}(2s'+1)gB\right]}{\sinh\left[\dfrac{\beta}{2}gB\right]}\right)^2 \tag{54}$$

From here, it is straightforward to derive the thermodynamic functions of interest. For example, the zero-field specific heat is given by:

$$\frac{C_p}{R} = \beta^2 \left(\frac{Z_0''}{Z_0} - \left(\frac{Z_0'}{Z_0}\right)^2\right) \tag{55}$$

where Z_0 is the zero-field partition function, and Z_0' and Z_0'' the first and second derivatives with respect to β. In a similar way, parallel magnetization and zero-field susceptibility are given by:

$$M_{\parallel}(B) = \frac{N_{\mathrm{A}}}{\beta} \frac{S' + \dfrac{SS' - 2P'}{(S^2 - 4P)^{1/2}}}{S + (S^2 - 4P)^{1/2}} \tag{56}$$

$$\chi_{0\parallel} = \frac{N_{\mathrm{A}}}{\beta} \frac{S_0'' + \dfrac{S_0 S_0'' - 2P_0''}{(S_0^2 - 4P_0)^{1/2}}}{S_0 + (S_0^2 - 4P_0)^{1/2}} \tag{57}$$

where S' and P' are the first derivatives of S and P with respect to B and S_0'' and P_0'' the second derivatives expressed in the vanishing field limit. The corresponding expressions are given in Table 7, for a regular alternation (J, J').

The Ising model has been used [49,81] to interpret the magnetic properties of the compound $MnCo(EDTA) \cdot 6H_2O$, wherein the anisotropic Co^{II} ion ($g_{\parallel} = 9$ and $g_{\perp} = 1.3$) may be treated as a Kramers doublet at low enough temperatures

Table 7. J-alternating [1/2–s'] ferromagnetic Ising chain. Expressions used to calculate the thermodynamic functions of interest (Eqs. (55)–(57)). (From Ref. [82]).

$$Z = \sum_{j}^{S} (2 - \delta_{j_0}) \Big[\cosh(\beta j J_+) + \cosh(\beta j J_-) \Big]$$

$$Z_0' = \sum_{j}^{S} j (2 - \delta_{j_0}) \Big[J_+ \sinh(\beta j J_+) + J_- \sinh(\beta j J_-) \Big]$$

$$Z_0'' = \sum_{j}^{S} j^2 (2 - \delta_{j_0}) \Big[J_+^2 \cosh(\beta j J_+) + J_-^2 \cosh(\beta j J_-) \Big]$$

$$S_0 = 2 \sum_{j}^{S} (2 - \delta_{j_0}) \cosh(\beta j J_+)$$

$$S_0'' = 2 \sum_{j}^{S} (2 - \delta_{j_0}) \Big\{ [g_{\mathrm{a}} \mu_{\mathrm{B}} \beta / 2]^2 + j^2 (g_{\mathrm{b}} \mu_{\mathrm{B}} \beta)^2 \Big\} \cosh(\beta j J_+) + j g_{\mathrm{a}} g_{\mathrm{b}} \mu_{\mathrm{B}}^2 \beta^2 \sinh(\beta j J_+)$$

$$P_0 = \sum_{j,k}^{S} (2 - \delta_{j_0})(2 - \delta_{k_0}) \Big[\cosh(\beta j J_+) \cosh(\beta k J_+) - \cosh(\beta j J_-) \cosh(\beta k J_-) \Big]$$

$$\begin{aligned} P_0'' = {} & (g_{\mathrm{b}} \mu_{\mathrm{B}} \beta)^2 \sum_{j,k}^{S} (2 - \delta_{j_0})(2 - \delta_{k_0})(j^2 + k^2) \\ & \times \Big[\cosh(\beta j J_+) \cosh(\beta k J_+) - \cosh(\beta j J_-) \cosh(\beta k J_-) \Big] \\ & - 2jk \Big[\sinh(\beta j J_+) \sinh(\beta k J_+) - \sinh(\beta j J_-) \sinh(\beta k J_-) \Big] \end{aligned}$$

With $J_{\pm} = (J \pm J')/2$. The summations extend over $j, k = 0\ (1/2)$ to S; j_0 and k_0 correspond to Kronecker symbols.

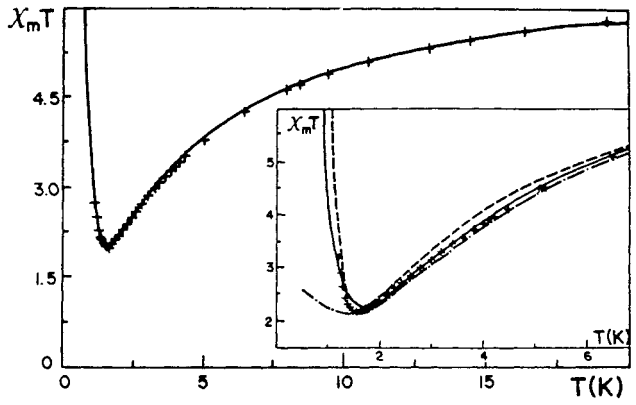

Fig. 20. Experimental and theoretical magnetic behavior of $MnCo(EDTA) \cdot 6H_2O$. Solid lines correspond to the best fit from the alternating Ising model ($J/k = -2.7\,K$, $J'/k = -0.6\,K$). A comparison with uniform chain (– – –) and dimer (– · – · –) limits is shown in the inset [49,81].

($T < 30\,K$). The best fitting of the experimental results reveals a significant exchange alternation in the ferrimagnetic chain with a ratio $J'/J = 0.22$ (Fig. 20).

It is worth underlining the simplicity and the flexibility of this model, which also allows the introduction of a z-axial anisotropy. A detailed discussion of local uniaxial anisotropy effects has been done for the [1–1] Ising chain, which involves (3×3) transfer matrices. Such a system needs a mathematical treatment through the so-called Cardan method for finding the roots of a third-degree polynomial [47]. This model has been used [84] to discuss the magnetic behavior of $NiNi(EDTA) \cdot 6H_2O$.

On the other hand, a detailed discussion of the compensation problem has also been reported in the framework of the Ising model. Such a compensation between the magnetic moments has been suggested to occur in the bimetallic chain $CoNi(EDTA) \cdot 6H_2O$ [85]. In spite of its two-sublattice structure, the magnetic behavior of this compound does not exhibit any χT divergence in the low temperature range (Fig. 21). The compensation problem (for purely AF coupling) has already been mentioned in connection with both quantum and classical isotropic models. In the classical context, it has been pointed out that the low-temperature behavior results from a subtle conflict between the short-range ordering, which reduces the effective moment carried by a pair of consecutive spins, and the long-range one, which assembles these spins into quasi-rigid fragments. This problem has been also solved within the Ising model for a quantum-classical spin chain [46]. In this last case, it has been shown that, in contrast with the previous results, the parallel susceptibility diverges at absolute zero, even when the ground state does not show any net magnetic moment due to compensation. These opposite behaviors raise the question of the critical spin number, s'_c, at which the susceptibility behavior turns. The calculation for ($1/2$–s') Ising chains, with arbitrary s', shows that under compensation the susceptibility vanishes for $s' < 2$, and diverges exponentially for $s' > 2$. For the critical value, 2, the behavior is characterized by a slower, T^{-1}, divergence (Fig. 22). This discussion has been extended to arbitrary s and s' values [86]. The low-temperature behavior

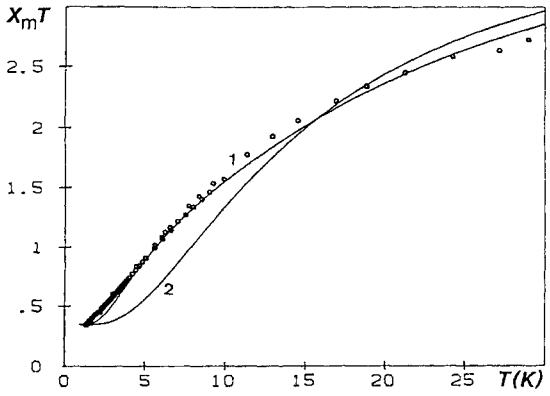

Fig. 21. Experimental and theoretical magnetic behavior of CoNi(EDTA) · $6H_2O$. Line 1 corresponds to the best fit from the uniform Ising chain model ($J/k = J'/k = -20\,\mathrm{K}$; $D_{\mathrm{Ni}}/k = -9\,\mathrm{K}$; $g_{\mathrm{Co}} = 5.2$; $g_{\mathrm{Co}}/g_{\mathrm{Ni}} = 2$). Line 2 shows a comparison with the dimer limit ($J/k = -26\,\mathrm{K}$; $J'/k = -1\,\mathrm{K}$; $D_{\mathrm{Ni}}/k = 0$; $g_{\mathrm{Co}} = 5.2$; $g_{\mathrm{Co}}/g_{\mathrm{Ni}} = 2$) [85].

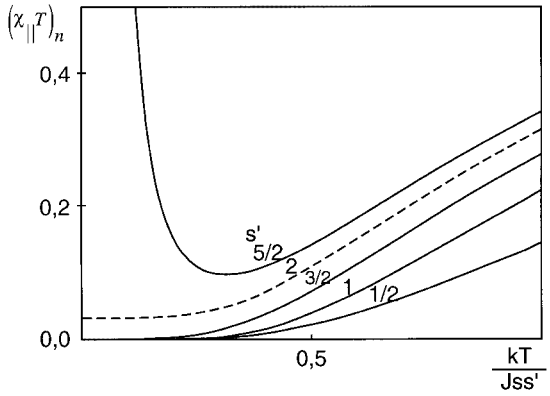

Fig. 22. Magnetic behavior of [1/2–s'] Ising chains for compensated magnetic moments [46].

then becomes a complex function of s and s'. The general trend is summarized in Table 8.

Dealing now with the problem of random linear chains, it is worth mentioning that under certain conditions, the transfer-matrix method may also apply to this kind of system. This aspect has been examined for alternating quantum-classical Ising

Table 8. Low temperature behavior of $\chi_{0\parallel}T$ for [s–s'] compensated Ising chains (AF coupling). (From Ref. [86].)

	$S' = 1/2$	1	3/2	2	5/2	3	7/2
$S = 1/2$	0	0	0	F	∞	∞	∞
1	0	0	0	F	∞	∞	∞
3/2	0	0	0	F	∞	∞	∞
2	F	F	F	0	∞	∞	∞
5/2	∞	∞	∞	∞	0	∞	∞
3	∞	∞	∞	∞	∞	0	∞
7/2	∞	∞	∞	∞	∞	∞	0

0, vanishing limit; F, finite limit; ∞, divergence.

chains with random exchange distribution [87,88]. It has been shown that the low-temperature behavior of parallel susceptibility depends on the dimensionality of the space available to the classical spins, as well as on the exchange constant distribution [89]. In particular, if the distribution includes F and AF values, a T^{-1} (that is, a Curie-type) behavior is predicted, which may be misleading in experimental data analysis.

1.5.3 Exotic Chains Showing Ising Coupling

Specific models based on the transfer-matrix method have been proposed for studying various exotic 1D systems. It is not necessary to describe them in detail, but it may be useful to indicate their main trends. One of the interesting directions concerns the so-called double chains, for example ladder-like chains, frustrated double chains, or topological ferrimagnetic chains (Figs. 1d to 1g). Although the problem is treated within the simple Ising scheme [90] this work gives exact answers to the important question of weak interchain coupling. It nicely confirms the generally admitted point of view that interchain coupling must be taken into account as soon as an interchain energy larger than kT is required for reversing all the spins along a correlation length ξ. On the other hand, the Ising model provides exact expressions of the thermodynamic quantities of interest. For example, closed-form expressions for the parallel susceptibility have been derived for various double chains of spins $s = 1/2$ (Table 9).

In connection with the problem of spin frustration, the Ising model has been used to explain the magnetism of the hydroxide nitrate $Co(OH)(NO_3) \cdot H_2O$ [91]. The structure of this compound exhibits infinite double chains of edge-sharing cobalt(II) octahedra (Fig. 23). From a magnetic point of view this system consists of infinite

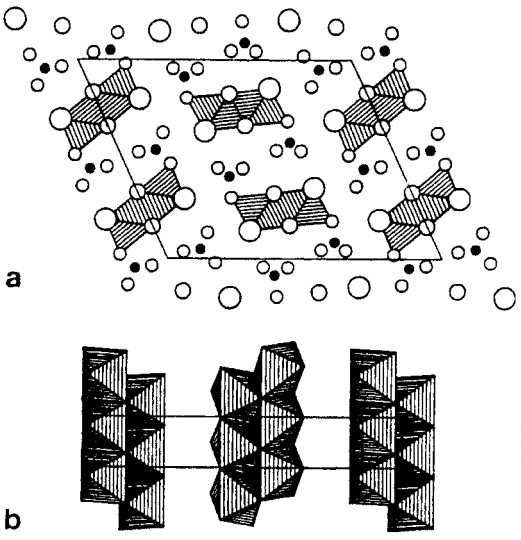

Fig. 23. Structure of $Co(OH)(NO_3) \cdot H_2O$ showing the isolated chains of cobalt (II) octahedra, (a) in the ac plane, and (b) in the perpendicular direction.

Table 9. Magnetic susceptibility and specific heat for Ising double chains with different topologies.

1. Ladder-like chain (Fig. 1d)

$$\chi_{\parallel} = \left(\frac{N_A g^2 \mu_B^2}{2kT}\right)\left(\frac{abE_+ - 2a\,\sinh(\alpha)}{E_+^2 - 2E_+(ab - \cosh(\alpha)\,\sinh(\alpha)) + 2(1+b^2)\,\sinh(\alpha)\,\cosh(\alpha)}\right)$$

$$E_+ = 2\,\cosh(\alpha)\,\cosh(\beta) + 2\Big[\cosh^2(\alpha)\,\sinh^2(\beta) + 1\Big]^{1/2}$$

with:

$\alpha = J_1/2kT$; $\beta = J_2/4kT$
$a = \exp(\alpha)$; $b = \exp(\beta)$

2. Topological 1D ferrimagnet (Fig. 1g)

Magnetic susceptibility

$$\chi_{\parallel} = \left[\frac{N_A g^2 \mu_B^2}{2kT}\right]\left(\frac{A}{B}\right)$$

$$A = U\,\exp(K_3)\Big[4\,\exp(K_+) + \cosh(K_+) + \exp(-2K_3)\Big] - 4\Big[\cosh(K_+) - \cosh(K_-)\Big]$$

$$B = 2U\Big\{U - \exp(K_3)\Big[\cosh(K_+) + \exp(-2K_3)\Big]\Big\}$$

with:

$U = \exp(K_3)\,\cosh(K_+) + \exp(-K_3)\,\cosh(K_-) + 2\,\cosh(K_3)$
$K_\pm = (J_1 \pm J_2)/2kT$; $K_3 = J_3/4kT$

Specific heat

$$C_p/R = \Big(P/U - Q^2/U^2\Big)$$

$$P = 16K_3^2\Big[\exp(K_3)\,\cosh(K_+) + \exp(-K_3)\,\cosh(K_-) + 2\,\cosh(K_3)\Big] +$$
$$8K_3\Big[K_+\,\exp(K_3)\,\sinh(K_+) - K_-\,\exp(-K_3)\,\sinh(K_-)\Big] +$$
$$K_+^2\,\exp(K_3)\,\cosh(K_+) + K_-^2\,\exp(-K_3)\,\cosh(K_-)$$

$$Q = 4K_3\Big[\exp(K_3)\,\cosh(K_+) - \exp(-K_3)\,\cosh(K_-) + 2\,\sinh(K_3)\Big] +$$
$$K_+\,\exp(K_3)\,\sinh(K_+) + K_-\,\exp(-K_3)\,\sinh(K_-)$$

double chains of spin $s = 1/2$ exchange-coupled by both in-chain (J_1) and interchain (J_2) interactions (Fig. 1e) The calculated expressions for parallel susceptibility and specific heat are given in Table 9. The model predicts spin frustration effects when J_1 is antiferromagnetic, whatever the sign of J_2. Thus, the double chain behaves as a 1D ferromagnet when $J_2 > 2|J_1|$, or as a 1D antiferromagnet when $J_2 < 2|J_1|$ (Fig. 24a). For $J_2 = 2|J_1|$ the system looks like a set of magnetically isolated 1/2 spins giving rise to a Curie-like behavior. The cobalt(II) nitrate appears to belong to the ferromagnetic case with $J_1/k = -19.5\,\mathrm{K}$ and $J_2/k = 45.6\,\mathrm{K}$ (Fig. 24b). Such a model has been generalized to the (1/2–s') Ising double chain through numerical [92] and analytical [90] treatments of the transfer matrix.

In connection with ferrimagnetism, double chains also provide the opportunity to study topological 1D ferrimagnetism (Fig. 1f), i. e., the occurrence of ferrimagnetic behavior in a homometallic double chain due to the exchange pathway topology.

Table 9. Continued.

3. Frustrated double chain (Fig. 1e)

Magnetic susceptibility

$$\chi_{\parallel} = \left[\frac{N_A g^2 \mu_B^2}{8kT}\right]\left(\frac{A}{B}\right)$$

$$A = U^2 \exp(K_1)\exp(K_2) + 2\Big[1 - \exp(2K_1)\Big]U + \exp(3K_1)\exp(-K_2) + \exp(-K_1)\exp(-K_2) - 2\exp(K_1)\exp(-K_2)$$

$$B = ER$$

with

$$E = \exp(-2K_1) + \cosh(K_2) + \exp(-K_1)R$$

$$R = \Big[\exp(2K_1)\sinh^2(K_2) + 2\cosh(K_2) + 2\Big]^{1/2}$$

$$U = \exp(K_1)\cosh(K_2) + \exp(-K_1) + \Big[\exp(2K_1)\sinh^2(K_2) + 2\cosh(K_2) + 2\Big]^{1/2}$$

Specific heat

$$C_p/R = (B/Z - A^2/Z^2)$$

$$Z = \exp(-K_1) + \exp(K_1)\cosh(K_2) + U^{1/2}$$

$$A = V + P/U^{1/2}$$

$$B = W + (UQ - P^2)/U^{3/2}$$

$$U = \exp(2K_2)\sinh^2(K_1) + 2\cosh(K_1) + 2$$

$$V = -K_1\exp(-K_1) + K_1\exp(K_1)\cosh(K_2) + K_2\exp(K_1)\sinh(K_2)$$

$$W = K_2^2\Big[\exp(K_2)\cosh(K_1) + \exp(-K_2)\Big] + K_1K_2\exp(K_1 + K_2) + K_1\exp(K_2)\sinh(K_1)$$

$$P = K_2\exp(2K_2)\sinh^2(K_1) + (1/2)K_1\exp(2K_2)\sinh(2K_1) + K_1\sinh(K_1)$$

$$Q = 2K_2^2\Big[\exp(K_2)\sinh(K_1) + 2K_1K_2\exp(2K_2)\sinh(2K_1)\Big] + K_1^2\exp(2K_2)\cosh(2K_1) + K_1^2\cosh(K_1)$$

with

$$K_i = J_i/2kT;\ i = 1, 2$$

This problem has been encountered in the Cu(II) compounds $A_3Cu_3(PO_4)_4$ (A = Ca^{II} and Sr^{II}) and Cu_2OSO_4. In the phosphate derivatives the copper (II) ions are connected by oxygen atoms so as to form infinite ribbons of trimer species (Fig. 25a) [93,94]. The interaction network contains two different exchange couplings, J_1 and J_2 (Fig. 1f). In turn, in Cu_2OSO_4, the structural features lead to the introduction of a further interaction (J_3) between outer copper(II) ions belonging to adjacent trimers (Fig. 25b). If this interaction is antiferromagnetic, spin frustration also occurs (Fig. 1g). Comparisons between theory and experiment are displayed in Figs. 26 and 27. For these two types of chains, the magnetic data show a rounded minimum in χT around 25 K, which is typical of 1D ferrimagnetism. In the phosphate derivatives the data have been fitted with $J_1/k = -150\,\mathrm{K}$ and $J_2/k = -2.5\,\mathrm{K}$ (Fig. 26). Conversely, in Cu_2OSO_4 all the interaction constants are shown to be close ($J_1/k = -66\,\mathrm{K}$, $J_2/k = -72\,\mathrm{K}$ and $J_3/k = -68\,\mathrm{K}$), giving rise to a good example of frustrated 1D topological ferrimagnet [95] (Fig. 27).

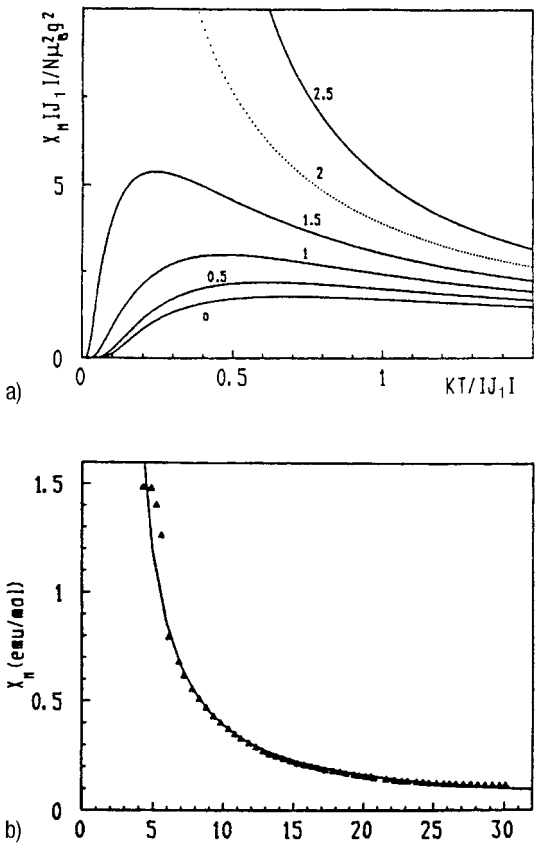

Fig. 24. (a) Scaled magnetic susceptibility vs. reduced temperature for different $J_2/|J_1|$ ratios ($J_2 > 0$). (b) Experimental and theoretical magnetic susceptibility for $Co(OH)(NO_3)\cdot H_2O$ [91].

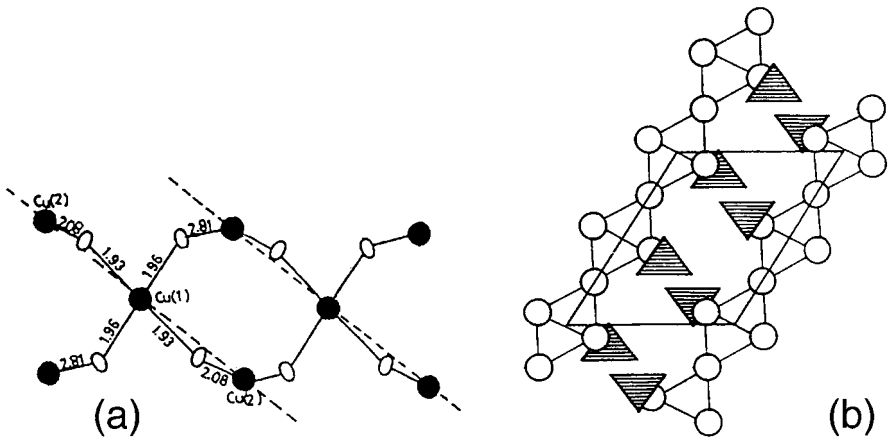

Fig. 25. (a) Structure of $Ca_3Cu_3(PO_4)_4$ showing copper(II) trimers spreading in the b direction. (b) Structure of $Cu_2O(SO_4)$.

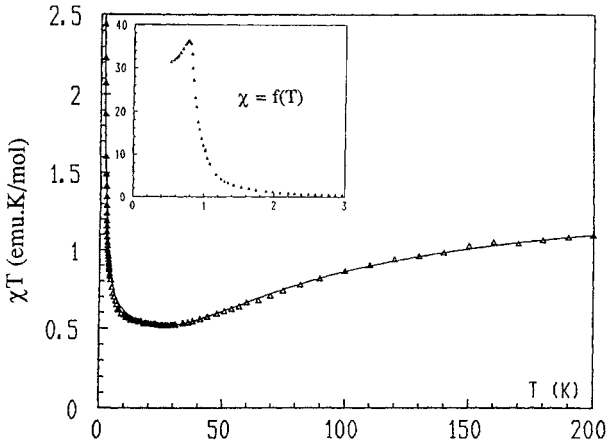

Fig. 26. Fitting of the experimental susceptibility of $Ca_3Cu_3(PO_4)_4$ [93].

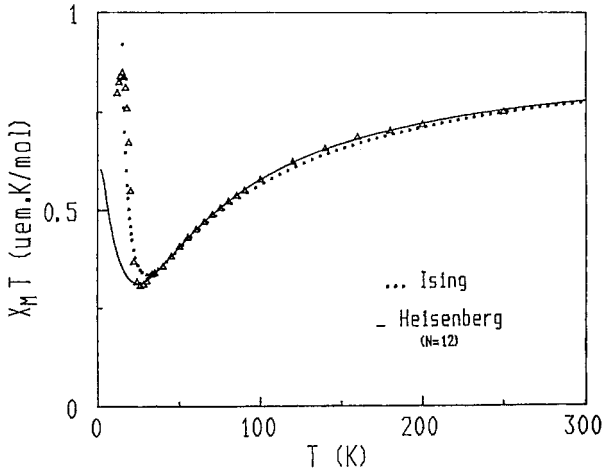

Fig. 27. Fitting of the experimental susceptibility of $Cu_2O(SO_4)$ [95].

1.6 Spin Chains with Anisotropic Exchange Interactions

In molecular 1D systems, large spin values allowing for the use of a classical-spin approximation are often met with metal ions exhibiting half-filled magnetic shells (for example Mn^{II} and Gd^{III}). Due to the related isotropic orbital properties, a Heisenberg type hamiltonian appears to be generally convenient for analyzing their magnetic properties. However, large spin values are not necessarily related to isotropic cations. Moreover, even half-filled shells may give rise to weak, nevertheless sometimes essential, anisotropic properties to a higher perturbation degree. Weak ferromagnetism in αFe_2O_3 has been known for a long time as an example of such a

situation. It must also be pointed out that, in molecular 1D systems, the magnetic sites exhibit low symmetries with often no inversion center, thus favoring antisymmetric Dzialoshinski coupling [95].

In a pioneering paper Wegner [97] solved the 1D XY coupling problem. Later on, Joyce [98] suggested the use of spheroidal functions for solving the problem of a chain showing anisotropic nearest neighbor coupling. He treated the problem for the symmetrical part of the exchange, only, using the transfer matrix method. More recently Curély and Georges [99] have considered the 1D problem described by the following nearest neighbor exchange hamiltonian:

$$H = -J_{\perp}(S_i^x S_{i+1}^x + S_i^y S_{i+1}^y) - J_{\parallel}(S_i^z S_{i+1}^z) + \varepsilon_i \boldsymbol{D}(S_i \wedge S_{i+1}) \tag{58}$$

In this expression, the Dzialoshinski vector $\varepsilon_i \boldsymbol{D}$ is assumed to lie along the z direction, but its orientation may change from pair to pair owing to the value of $\varepsilon_i(\pm 1)$. Considering only the even part of the coupling, the signs attributed to the exchange constants $J_{\perp}$ and $J_{\parallel}$ and their relative amplitudes, a large number of distinct configurations may be obtained at absolute zero.

Three different situations are considered by the authors, namely, (i) the in-plane and (ii) out-of-plane ferromagnetic cases, (iii) the in-plane antiferromagnetic case. Expressions for the spin correlation functions are derived in terms of the radial and angular spheroidal functions. Analytical expressions for the parallel and perpendicular susceptibilities are also deduced. All three cases are expected to occur in practical situations. In the first case, the susceptibility diverges at low temperature occuring to T^{-2}, as for a purely Heisenberg coupling. Meanwhile, the axial susceptibility keeps a finite (nonvanishing) value. Conversely, in the second case, the axial susceptibility diverges now following an exponential law, whereas the in-plane susceptibility keeps a finite value. The last case allows discussion of the crossover effects occurring at temperatures for which the correlation length compares with the helical path. The related conclusions may be extended to 1D systems in which a helical structure would result from a frustration phenomenon, due to competing nearest and next-nearest neighbor exchange couplings.

An extrusion is provided by chains showing mixed anisotropy interactions. For example, the compound $Ba_2MnCoAl_2F_{14}$ involves two kinds of magnetic cations with distinct anisotropies: the isotropic high-spin Mn^{II}, and the strongly anisotropic Co^{II}. These cations are randomly distributed among sixfold and eightfold coordinated sites, giving rise to a mixture of pairwise interactions with different anisotropies (Mn–Mn, Mn–Co and Co–Co). This problem has been solved [100] by considering an Ising chain with spins 1/2 from Co^{II} located in the octa-coordinated sites and separated by a random number of classical spins with random Landé factors (Co^{II} in octahedral sites, and Mn^{II} on both sites).

1.7 Conclusion

Since the end of the 1970s, numerous linear as well as exotic chain systems have been thoroughly investigated from a magnetic point of view. One can note linear chains with alternating F and AF interactions, double chains with ladder-like structure or with competing interactions (frustrated chains), random-exchange chains, etc. As a result, a great variety of models are now available which quantitatively describe the physics of 1D systems. In this chapter, the different models are reviewed and the theoretical expressions derived for describing the thermal dependence of the thermodynamic properties. The solutions are obtained either numerically or analytically depending on the nature and symmetry of the spin chain. Analytical expression are only available for the quantum Ising models, and the classical or quantum-classical isotropic spin models, when the spin hamiltonian H may be developed as an infinite sum of commuting partial hamiltonians H_i. In that case, it is demonstrated that the dynamic variables which are involved in H_i's are distributed into three subsets: those common to H_i and H_{i-1}, those common to H_i and H_{i+1}, and those belonging to H_i. In other word, the set of variables connecting the unit cells $i-1$ et $i+1$ through the unit cell i play a role of relay. Under these conditions, the partition function may be deduced by an analytical mathematical treatment involving the transfer matrix technique.

From a physical point of view, 1D magnetic systems are characterized by a quasi-infinite critical domain, the absolute zero playing the role of critical temperature, T_c [101]. In addition, it must be noticed that 2D isotropic (or Heisenberg) systems are also characterized by a vanishing critical temperature. However, T_c becomes finite if any type of anisotropy (exchange or dipolar-like, magneto-crystalline) is introduced. For instance, in actual materials, the in-plane anisotropy related to dipolar interactions is sufficient to promote a non-zero ordering temperature [102]. The magnetic properties of low dimensional materials are governed in the paramagnetic regime (above T_c) by the short-range correlations, and the spin space symmetry. Of course, the properties differ below T_c where a long-range order takes place. This is an additional reason for interest in 1D magnetic systems. Under these conditions, one can easily assume that the chain correlation length ξ becomes an important physical tool. Near absolute zero, the spin chain behaves as an assembly of quasi-independent blocks of length ξ; if M is the unit cell moment, the product χT may be written as ξM^2. Interestingly, for non-compensated sublattices χT always behaves as ξ, while for compensated sublattices χT is mainly governed by the competition between ξ (divergence) and M (decrease) upon cooling down. In other words, from knowledge of the χT and ξ variations, one can derive the temperature law which M obeys near absolute zero. At this point, it becomes important to know the temperature at which the 2D or 3D ordering occurs. Thus, the chain behavior will be observed as long as the inter-chain exchange energy of blocks of length ξ is smaller than kT. If J' is this interchain interaction, the crossover temperature appears to be a solution of the following equation:

$$kT_c^{2D} \sim \xi |J'| \tag{59}$$

When T_c^{2D} is reached, the interchain coupling J' becomes efficient and we are dealing with a stable 2D spin network. Near the 3D ordering temperature, the 2D-spin system behaves as quasi-independent rectangular blocks, the sides of which are ξ_1 and ξ_2, ξ_1 being the in-chain correlation length and ξ_2 the correlation length in the perpendicular direction. Consequently, if M' is the temperature-dependent moment of the unit cell, the χT variation near T_c is governed by $\xi_1\xi_2 M'^2$. As for the chain, if one deals with non-compensated sublattices, χT always behaves as $\xi_1\xi_2$ and thus diverges. For compensated sublattices, the χT behavior is governed by the competition between $\xi_1\xi_2$ and M'. Of course, the 3D ordering unavoidably appears upon cooling down. This ordering occurs when the interlayer energy (interaction J'') of the quasi-independent blocks of surface $\xi_1\xi_2$ becomes similar to kT, i. e.:

$$kT_c \sim \xi_1\xi_2|J''| \tag{60}$$

As the correlation lengths depend on several factors as for example the isotropic or anisotropic character of the exchange coupling, the crossover temperature will be affected by the nature of the chain under consideration. These considerations will be essential to the understanding of the long-range ordering in real systems.

Acknowledgments

We gratefully acknowledge the contributions of our co-workers and colleagues whose names appear in the references. Financial support from the European Union (TMR Network and ESF program on Molecular Magnetism) is acknowledged.

References

[1] L. J. De Jongh, A. R. Miedema, *Adv. Phys.* **1974**, *23*, 1.
[2] E. W. Hatfield, W. E. Estes, W. E. Marsh, M. W. Pickens, L. W. Ter Haar, R. R. Weller in *Extended Linear Chain Compounds, Vol. 3* (Ed.: J. S. Miller), Plenum Press, New York, **1983**, p. 43.
[3] E. Coronado, M. Drillon, R. Georges in *Research Frontiers in Magnetochemistry* (Ed.: C. J. O'Connor), World Scientific, Singapore, **1993**, p. 27.
[4] E. Coronado in *Magnetic Molecular Materials, Vol. E 191* (Eds.: D. Gatteschi, O. Kahn, J. S. Miller, F. Palacio), Kluwer Academic Publishers, Dordrecht, **1991**, p. 267.
[5] O. Kahn, *Molecular Magnetism*, VCH Publishers, New York, **1993**, p. 379.
[6] C. K. Majumdar, D. K. Ghosh, *J. Math. Phys.* **1969**, *10*, 1388
[7] S. G. Carling, C. Mathonière, P. Day, K. M. Abdul Malik, S. J. Coles, M. B. Hursthouse, *J. Chem. Soc. Dalton Trans.* **1996**, 1839.
[8] S. Decurtins, H. W. Schmaller, H. R. Oswald, A. Linden, J. Ensling, P. Gütlich, A. Hauser inorg. *Chim. Acta* **1994**, *216*, 65.

[9] C. Mathonière, S. G. Carling, D. Yusheng, P. Day, *J. Chem. Soc. Chem. Commun.* **1994**, 1551.
[10] C. Mathonière, C. J. Nuttall, S. G. Carling, P. Day in *Org. Chem.* **1996**, 1201.
[11] C. J. Nuttall, C. Bellito, P. Day, *J. Chem. Soc. Chem. Com* **1995**, 1513.
[12] H. Okawa, N. Matsumoto, H. Tamaki, M. Ohba, *Mol. Cryst. Liq. Cryst* **1993**, *233*, 257.
[13] R. Pellaux, H. W. Schmalle, R. Huber, P. Fisher, T. Hauss, B. Ouladdiaf, S. Decurtins in *Org. Chem.* **1997**, *36*, 2301.
[14] H. Tamaki, Z. J. Zhong, N. Matsumoto, S. Kida, M. Koikawa, N. Achiwa, Y. Hasimoto, H. Okawa, *J. Am. Chem. Soc.* **1992**, *114*, 6974.
[15] M. Clemente-León, E. Coronado, J. R. Galán-Mascarós, C. J. Gómez-García, *Chem. Commun.* **1997**, 1727.
[16] E. Colacio, J. M. Domínguez-Vera, M. Ghazi, R. Kikeväs, F. Lloret, J. Moreno, H. Stoeckli-Evans, *Chem. Commun* **1999**, 987.
[17] S. Ferlay, T. Mallah, J. Vaissermann, F. Bartolomé, P. Veillet, M. Verdaguer, *Chem. Commun* **1996**, 2841.
[18] M. Ohba, N. Maruono, H. Okawa, *J. Am. Chem. Soc.* **1997**, *119*, 1011.
[19] O. Kahn in *Molecular Magnetism: From Molecular Assemblies to the Devices, Vol. E-321* (Eds.: E. Coronado, P. Delhaès, D. Gatteschi, J. S. Miller), Kluwer Academic, Dordrecht, **1996**, p. 590.
[20] P. W. Anderson, *Phys. Rev.* **1959**, *115*, 2.
[21] H. A. Bethe, *Z. Physik* **1931**, *71*, 205.
[22] J. C. Bonner, M. E. Fisher, *Phys. Rev. A* **1964**, *135*, 640.
[23] C. Y. Weng, PhD. thesis, Carnegie-Mellon University (US), **1968**.
[24] H. W. Blöte, *Physica* **1975**, *B79*, 427.
[25] W. Duffy, K. P. Barr, *Phys. Rev.* **1968**, *A165*, 647.
[26] W. E. Hatfield, W. E. Estes, W. E. Marsh, M. W. Pickens, L. W. Ter Haar, R. R. Weller in *Extended Linear Chain Compounds* (Ed.: J. S. Miller), Plenum, New York, **1983**, p. 43.
[27] R. D. Willett, R. M. Gaura, C. P. Landee in *Extended Linear Chain Compounds* (Ed.: J. S. Miller), Plenum, New York, **1983**, p. 143.
[28] J. C. Bonner in Magneto-Structural Correlations in *Exchange-Coupled Systems* (Eds.: R. D. Willett, D. Gatteschi, O. Kahn), Reidel, **1985**, p. 157.
[29] M. Drillon, J. C. Gianduzzo, R. Georges, *Phys. Lett.* **1983**, *96A*, 413.
[30] M. Drillon, E. Coronado, R. Georges, J. Curély, J. C. Gianduzzo, *Phys. Rev.* **1989**, *B40*, 10992.
[31] M. Drillon, E. Coronado, D. Beltrán, R. Georges, *J. Appl. Phys.* **1985**, 57, 3353.
[32] J. J. Borrás-Almenar, PhD thesis, University of Valencia (Spain), **1992**.
[33] J. J. Borrás-Almenar, E. Coronado, J. Curély, R. Georges, J. C. Gianduzzo, *Inorg. Chem.* **1994**, *33*, 5171.
[34] E. Hernández-Gasio, M. Mas, E. Molins, C. Rovira, J. Veciana, J. J. Borrás-Almenar, E. Coronado, *Chem. Mater.* **1994**, *6*, 2398.
[35] J. J. Borrás-Almenar, E. Coronado, J. Curély, R. Georges, *Inorg. Chem.* **1995**, *34*, 2699.
[36] J. J. Borrás-Almenar, J. M. Clemente-Juan, E. Coronado, F. Lloret, *Chem. Phys. Lett.* **1997**, *275*, 79.
[37] T. N. Nguyen, P. A. Lee, H. C. zur Loye, *Science* **1996**, *271*, 489.
[38] J. M. Clemente, PhD thesis, University of Valencia (Spain), **1998**.
[39] J. J. Borrás-Almenar, J. M. Clemente-Juan, E. Coronado, B. S. Tsukerblat *Inorg. Chem.* **1999**, *38*, 6081.
[40] M. E. Fisher, *Am. J. Phys.* **1964**, *32*, 343.
[41] A. H. Morrish, *The Physical Principles of Magnetism*, J. Wiley, New York, **1965**
[42] M. F. Thorpe, *J. Phys. Paris* **1975**, *36*, 1177.

[43] M. Drillon, E. Coronado, D. Beltrán, R. Georges, *Chem. Phys.* **1983**, *79*, 449.
[44] X. Qiang, J. Darriet, R. Georges, *J. Mag. Mag. Mat.* **1988**, *73*, 379.
[45] L. Néel, R. Pauthenet, B. Dreyfus, J. C. Gorter, *Progr Low Temperature Phys.* **1964**, *4*, 344.
[46] J. Curély, R. Georges, M. Drillon, *Phys. Rev.* **1986**, *B33*, 6243.
[47] R. Georges, J. Curély, M. Drillon, *J. Appl. Phys.* **1985**, *58*, 914.
[48] M. Drillon, E. Coronado, D. Beltrán, J. Curély, R. Georges, P. R. Nugteren, L. J. de Jongh, J. L. Genicon, *J. Magn. Magn. Mater.* **1986**, *54–57*, 1507.
[49] E. Coronado, M. Drillon, P. R. Nugteren, L. J. de Jongh, D. Beltrán, R. Georges, *J. Am. Chem. Soc.* **1989**, *111*, 3874.
[50] A. Mosset, J. Galy, E. Coronado, M. Drillon, D. Beltrán, *J. Am. Chem. Soc.* **1984**, *106*, 2864.
[51] X. Qiang, PhD thesis, University of Bordeaux I (France), **1990**.
[52] J. Curély, R. Georges, *J. Math. Phys.* **1994**, *35*, 3998.
[53] J. Curély, Ph. D. Thesis, *University of Bordeaux I* **1990**.
[54] R. Georges, X. Qiang, *Chinese Phys. Lett.* **1989**, *6*, 518.
[55] M. Drillon, J. Darriet, *Struct. Bonding* **1992**, *79*, 79.
[56] X. Qiang, J. Darriet, J. L. Soubeyroux, R. Georges, *J. Magn. Magn. Mater.* **1988**, *74*, 219.
[57] J. J. Borrás-Almenar, E. Coronado, R. Georges, C. J. Gómez-García, C. Muñoz-Roca, *Chem. Phys. Lett.* **1991**, *186*, 410.
[58] J. J. Borrás-Almenar, E. Coronado, J. C. Gallart, R. Georges, C. J. Gómez-García, *J. Magn. Magn. Mater.* **1992**, *104–107*, 835.
[59] T. Dembinski, T. T Wydro, *Phys. Status Solidi* **1975**, *67*, K123.
[60] H. W. Blöte, *J. Appl. Phys.* **1979**, *50*, 7401.
[61] J. Seiden, *J. Phys.* **1983**, *44*, L947.
[62] M. Verdaguer, A. Gleizes, J. P. Renard, J. Seiden, *Phys. Rev.* **1984**, *B29*, 5144.
[63] J. Curély, R. Georges, J. C. Gianduzzo, X. Qiang, O. Kahn, Y. Pei, J. Sletten in *Organic and Inorganic Low Dimensional Crystalline Materials*, NATO ASI Series, *Vol. B168* (Eds.: P. Delhaes, M. Drillon), Plenum Press, New York, **1987**, p. 413.
[64] J. Curély, R. Georges, *J. Phys. I (Paris)* **1995**, *5*, 485.
[65] R. Georges, J. Curély, J. C. Gianduzzo, X. Qiang, O. Kahn, Y. Pei, *Physica* **1988**, *B153*, 77.
[66] Y. Pei, O. Kahn, J. Sletten, J. P. Renard, R. Georges, J. C. Gianduzzo, J. Curély, Q. Xu, *Inorg. Chem.* **1988**, *27*, 47.
[67] R. Georges, O. Kahn, Mol. Cryst. *Liq. Cryst.* **1989**, *176*, 473.
[68] J. Curély, R. Georges, *Phys. Rev.* **1992**, *B46*, 3250.
[69] Y. Pei, J. Sletten, O. Kahn, *J. Am. Chem. Soc.* **1984**, *106*, 3727.
[70] O. Guillou, O. Kahn, R. Oushoorn, K. Boubeker, P. Batail, *Inorg. Chim. Acta* **1992**, *119*, 198.
[71] R. Georges, O. Guillou, O. Kahn, *Phys. Rev.* **1994**, *B49*, 3235.
[72] J. Curély, *Europhys. Lett.* **1995**, *32*, 529.
[73] J. Curély, *Physica* **1998**, *B245*, 263.
[74] J. Curély, *Physica* **1998**, *B254*, 277.
[75] J. Curély, J. Rouch, *Physica* **1998**, *B254*, 298.
[76] J. Curély, F. Lloret, M. Julve, *Phys. Rev.* **1998**, *B58*, 11465.
[77] E. Z. Ising, *Phys.* **1925**, *31*, 253.
[78] M. E. Fisher, *J. Math. Phys.* **1963**, *4*, 124.
[79] M. Suzuki, B. Tsujiyama, S. Katsura, *J. Math. Phys.* **1967**, *8*, 124.
[80] H. A. Kramers, G. H. Wannier, *Phys. Rev.* **1941**, 252.

[81] E. Coronado, M. Drillon, P. R. Nugteren, L. J. de Jongh, D. Beltrán, *J. Am. Chem. Soc.* **1988**, *110*, 3907.
[82] F. Sapiña, E. Coronado, M. Drillon, R. Georges, D. Beltrán, *J. Phys. (Paris)* **1988**, *C8*, 1423.
[83] F. Sapiña, PhD thesis, University of Valencia (Spain), **1991**.
[84] E. Coronado, M. Drillon, A. Fuertes, D. Beltrán, A. Mosset, J. Galy, *J. Am. Chem. Soc.* **1986**, *108*, 900.
[85] E. Coronado, F. Sapiña, M. Drillon, L. J. de Jongh, *J. Appl. Phys.* **1990**, *67*, 6001.
[86] J. Curély, R. Georges, *Phys. Rev.* **1992**, *B46*, 6240.
[87] J. Curély, R. Georges, *Phys. Rev.* **1994**, *B49*, 1146.
[88] J. Curély, R. Georges, *Phys. Rev.* **1994**, *B49*, 1158.
[89] J. Curély, R. Georges, *Physica* **1997**, *B233*, 43.
[90] J. Curély, R. Georges, M. Drillon, M. Belaiche, K. Benkhouja, *Phys. Rev.* **1992**, *B46*, 3527.
[91] S. Angelov, M. Drillon, E. Zhecheva, R. Stoyanova, M. Belaiche, A. Derory, A. Herr, *Inorg. Chem.* **1992**, *31*, 1514.
[92] C. Benelli, A. Caneschi, D. Gatteschi, L. Pardi, P. Rey, *Inorg. Chem.* **1990**, *29*, 4223.
[93] M. Drillon, E. Coronado, M. Belaiche, R. L. Carlin, *J. Appl. Phys.* **1988**, *63*, 3551.
[94] M. Drillon, M. Belaiche, P. Legoll, J. Aride, A. Boukhari, A. Moquine, *J. Magn. Magn. Mat.*, **1993**, *128*, 83.
[95] M. Belaiche, M. Drillon, J. Aride, A. Boukhari, T. Biaz, P. Legoll, *J. Chim. Phys.* 1991, 88, 2157.
[96] T. Moriya in *Magnetism* (Eds.: G. T. Rado, H. Suhl, New York), **1962**, 86
[97] F. Wegner, *Z. Phys.* **1964**, *206*, 465.
[98] G. S. Joyce, *Phys. Rev. Lett.* **1967**, *19*, 581.
[99] J. Curély, R. Georges, *Phys. Rev.* **1994**, *B49*, 12839.
[100] A. Le Lirzin, J. Darriet, R. Georges, J. C. Soubeyroux, *J. Magn. Magn. Mat.* **1992**, *109*, 47.
[101] N. D. Mermin, H. Wagner, *Phys. Rev. Lett.* **1996**, *17*, 1133.
[102] P. Bruno, *Phys. Rev. B*, **1991**, *43*, 6015.

Magnetism: Molecules to Materials I: Models and Experiments.
Edited by Joel S. Miller and Marc Drillon

ISBNs: 3-527-29772-3 (Hardback); 3-527-60084-1 (Electronic)

2 Haldane Quantum Spin Chains

Jean-Pierre Renard, Louis-Pierre Regnault, and Michel Verdaguer

2.1 Introduction

One-dimensional (1D) magnetic systems are very attractive because they exhibit magnetic properties which are rather different from those encountered at higher dimensionality, $D = 2$ or 3 [1,2]. In 1D antiferromagnets (AF), in particular, the role of quantum magnetic fluctuations is expected to be very important. Quite generally, in ferromagnets (F), the quantum effects are strongly reduced by the increase of the correlation length as the temperature decreases, since a block of N ferromagnetically coupled spins is likely to behave as a single large spin NS. In AF, with isotropic short-range interactions, quantum effects are sizable even for $D = 3$. Indeed in Heisenberg AF with nearest neighbor interactions, the spontaneous magnetization has a zero point relative reduction of about $1/zS$, where z is the number of nearest neighbors and S the spin value. At $D = 1$, the spin fluctuations have more drastic effects which were first pointed out by F.D.M. Haldane [3]. Haldane conjectured that the 1D Heisenberg antiferromagnet (1D-HAF) with integer spin, in contrast to the case of half-integer spin, has a singlet ground state separated from the excited states by an energy gap, Δ. The spatial correlation function of the 1D-HAF with half-integer spin has a power law decay, while that for integer spin shows an exponential decay. Although fairly controversial at first, the Haldane conjecture was rapidly supported by numerical simulations on finite AF chains and by experiments on quasi-1D antiferromagnets [4,5]. Such findings renewed the interest in 1D magnetism and induced a large amount of theoretical and experimental work, which is reviewed here.

Following this Introduction, a theoretical survey of the Haldane gap problem, including the results of the numerical simulations on finite systems with integer spin, is given in Section 2. We mainly focus on the theoretical results which are important for real magnetic systems and refer to the review paper of Affleck [6] for general theory. In Section 3, a description of the quasi-1D antiferromagnets which exhibit a Haldane gap is given and their static and dynamic magnetic properties are described in Sections 4 and 5 respectively. The effect of chain breaking by impurities is discussed in Section 6 and concluding points are made in Section 7.

2.2 Theoretical Survey

2.2.1 The Hamiltonian

A convenient general spin hamiltonian for a Haldane gap 1D system (chain) can be written as follows:

$$H = J \sum_i \left[\boldsymbol{S}_i \boldsymbol{S}_{i+1} + \beta (\boldsymbol{S}_i \boldsymbol{S}_{i+1})^2 \right] + \sum_i \left[D (S_i^z)^2 - g \mu_B S_i^\alpha H^\alpha \right] \tag{1}$$

where the z axis is along the chain and the field is applied along the direction α ($\alpha = x, y, z$). The first two isotropic terms are, respectively, the nearest neighbor Heisenberg exchange interaction H_H ($J > 0$ for AF chain) and the biquadratic exchange term H_B. The latter is usually rather small in real magnetic compounds (i. e. $|\beta| \ll 1$); however some models with specific values of β (such as $\beta = -1, 1/3$) are of current interest for theory. The third term H_D represents a uniaxial single ion anisotropy which breaks the spherical symmetry. For positive D, a perpendicular spin orientation to the z axis is favored (easy-plane or XY-like anisotropy), whereas for negative D, the spin orientation along z is favored (easy-axis or Ising-like anisotropy). The fourth term is the usual Zeeman energy, H_Z, in an applied field, in which μ_B is the Bohr magneton and g the Landé factor.

In real systems, it may be necessary to consider some additional terms. Nonuniaxial orthorhombic anisotropy can be considered by adding to H_D a supplementary single ion anisotropy term, $H_E = \sum_i E\left[(S_i^x)^2 - (S_i^y)^2 \right]$. There is an interchain exchange interaction $H' = J' \sum_{k,l} \boldsymbol{S}_k \boldsymbol{S}_l$ where $\boldsymbol{S}_k$ and $\boldsymbol{S}_l$ are neighboring spins belonging to neighboring chains. For good quasi-1D systems $|J'/J| \ll 1$; typical values of this ratio for model 1D systems lie in the range 10^{-4}–10^{-3}.

In some theoretical work, anisotropic exchange interactions have also been taken into account by replacing in the Heisenberg exchange interaction in Eq. (1) by the so-called XXZ hamiltonian:

$$H_{AE} = J \sum_i (S_i^x S_{i+1}^x + S_i^y S_{i+1}^y + \lambda S_i^z S_{i+1}^z) \tag{2}$$

Generally, in real magnetic compounds, the anisotropic exchange is negligible (i. e. $|\lambda - 1| \ll 1$) when compared to single ion anisotropy, except for $S = 1/2$ and for ions without orbital moment (for instance Mn^{II}, $S = 5/2$).

2.2.2 Isotropic Case: the Haldane Conjecture

The general hamiltonian, Eq. (1), is not solvable exactly. Even restricting the calculations to the Heisenberg exchange term ($\beta = D = H = 0$), exact Bethe ansatz results are only available for the $S = 1/2$, 1D-HAF, giving, for instance, for the lower edge of the continuum of magnetic excitations [7,8]:

$$\varepsilon_1(q) = \frac{\pi}{2} J |\sin q| \tag{3}$$

in which q is the reduced wavevector of the excitation, defined as the product of the wave vector by the chain lattice parameter, d. The excitation spectrum exhibits no energy gap and is qualitatively similar to the one for $S \to \infty$ (classical limit). In both cases, $S = 1/2$ and $S \to \infty$, the spin correlation length diverges as $T \to 0$, and at $T = 0$, quasi-Néel AF long-range magnetic order (LRO) is established. Owing to these qualitatively similar behaviors for $S = 1/2$ and $S \to \infty$, it was believed, prior to 1983 that the spin value had no drastic effects on the magnetic properties of the 1D-HAF.

The Haldane conjecture is contrary to this tacitly assumed idea. By using a quantum field treatment of the 1D-HAF in the limit of large spins, Haldane [3] predicted that the properties of the model depend profoundly on the spin quantum number. For half-integer S, they are similar to those for $S = 1/2$, namely, gapless excitation spectra and asymptotic spin–spin correlation function decay at $T = 0$, given by the following power law (neglecting logarithmic corrections):

$$\langle \boldsymbol{S}_n \cdot \boldsymbol{S}_0 \rangle \approx (-1)^n |n|^{-\eta} \tag{4}$$

In Eq. (4) the exponent η depends on S, i. e. $\eta \approx 1$ for $S = 1/2$ and $\eta \approx 0$ for $S = \infty$. On the other hand, for integer S, the ground state is a singlet separated from the excited states spectrum by a gap $\Delta \sim 2JS \exp(-\pi S)$, and the spin–spin correlations have an exponential decay [3,6]:

$$\langle \boldsymbol{S}_n \cdot \boldsymbol{S}_0 \rangle \approx (-1)^n |n|^{-1/2} \exp(-\kappa |n|) \tag{5}$$

In Eq. (5) κ is the inverse number of correlated spins, $\kappa = 1/\xi_0$. κ is expected to decay rapidly when increasing S as $\kappa \sim \exp(-\pi S)$ [3,6]. The finite value of the correlation length, $d\xi_0$, reflects the absence of long-range order at $T = 0$.

For $S = 1$, the 1D-HAF is not solvable, but rigorous results have been obtained on models including biquadratic terms: i. e. $\beta \neq 0$, $D = 0$, $H = 0$ in the hamiltonian, Eq. (1). For $\beta = -1$, the model was solved exactly by Takhtajan [9] and Babujian [10] using the Bethe ansatz. In this case, the spectrum of excitations is similar to that for the $S = 1/2$, 1D-HAF (Eq. (3)). For $\beta = 1$, the model, which is equivalent to the three-component lattice gas model on the SU (3) chain solved by Sutherland [11], is also gapless with soft modes at wave vectors $q = 0$ and $q = \pm 2\pi/3$. In contrast to these gapless models, Affleck, Kennedy, Lieb and Tasaki [12] have shown that, for $\beta = 1/3$, the ground state is a unique singlet that they called valence-bond solid (VBS) separated from the excited states by a gap $\Delta = 0.75\, J$. This model has also been studied by Arovas et al. [13]. The pure antiferromagnetic biquadratic chain model has been solved by Barber and Batchelor [14]. They found that this model has a twofold degenerate ground state with a finite excitation gap, which corresponds to a dimerized state. Finally, the phase diagram of the $S = 1$ bilinear-biquadratic chain can be pictured in the angular diagram of Fig. 1, for the general hamiltonian [15]:

$$H = \sum_i \left[(\cos\theta) \boldsymbol{S}_i \cdot \boldsymbol{S}_{i+1} + \sin\theta (\boldsymbol{S}_i \cdot \boldsymbol{S}_{i+1})^2 \right]. \tag{6}$$

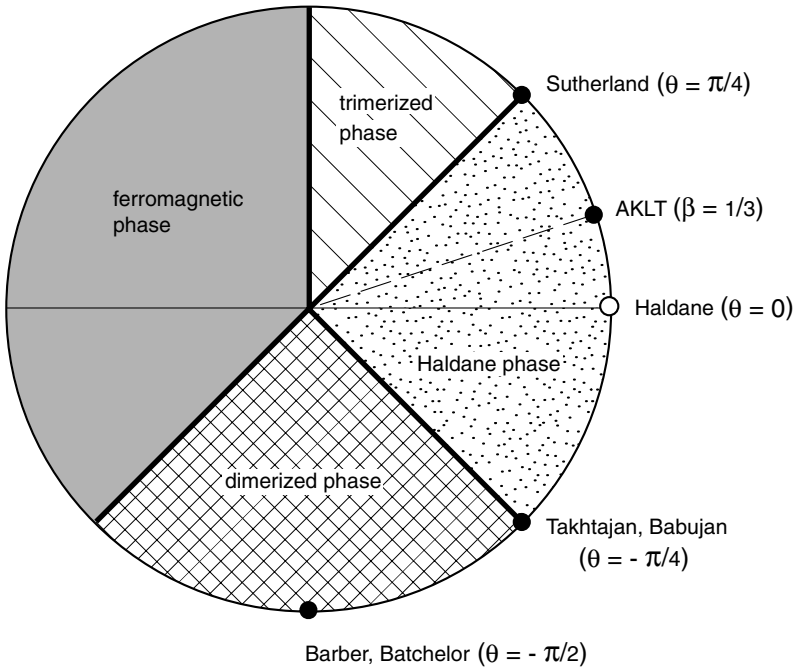

Fig. 1. Angular representation of the phase diagram of the $S = 1$ bilinear biquadratic hamiltonian. (Adapted from Ref. [16].)

In this representation, the exact solutions discussed above correspond to $\theta = \pi/4$ (Sutherland), $\theta = -\pi/4$ (Takhtajan, Babujian), $\theta = \text{arctg}(1/3)$ (Affleck et al.), $\theta = -\pi/2$ (Barber, Batchelor) and the Haldane point is for $\theta = 0$. In this diagram the Haldane phase should occur in the region $-\pi/4 < \theta < \pi/4$; the points $\theta = -\pi/4$ and $\theta = \pi/4$ at which the gap vanishes, should be critical points separating the Haldane phase from, respectively, the dimerized and trimerized AF phases [16]. The Haldane phase at $\beta = 0$ can be intuitively interpreted as being similar to the VBS phase, which is the exact ground state for $\beta = \text{tg}\,\theta = 1/3$. In this frame, spin 1 at each lattice site is obtained by symmetrization of two $S = 1/2$ variables at the same site. The VBS ground state is realized as a symmetrical linear superposition of states where one of the two $S = 1/2$ variables at each site is paired in a singlet state (valence bond) with one of the two $S = 1/2$ variables at the neighboring site. This picture clearly reveals the difference between integer spin chains, which may have a VBS ground state of unbroken symmetry with a gap, and half-integer spin chains, which are necessarily partially dimerized. In this latter case, if the translational symmetry is restored by quantum fluctuations leading to a unique resonating-valence-bond (RVB) state [17], the gap vanishes [18].

The VBS state of the $S = 1$ AF chain is characterized by the development of string correlations which reflect a hidden topological long-range order [19,20]. The string correlations have been extensively studied for the general hamiltonian, Eq. (6),

and the string order parameter as well as the gap and the correlation length were determined for $-\pi/4 \leq \theta \leq \pi/4$ [21]. From this study, it is clearly established that the Heisenberg hamiltonian $\theta = 0$ shares the same physics as the VBS hamiltonian $\theta = \text{arctg}(1/3)$.

Another interesting approach giving a physical insight into the Haldane phase was introduced by Gomez-Santos [22] and developed by Köhler and Schilling [23] and Meshkov [24]. It consists of introducing disorder in the long range AF state by means of spin-zero defects (SZD), which can be treated as fermions in a Hartree-Fock approximation. In this approach, the correlation length is simply the mean distance between two SZD.

Numerical calculations on finite chains or rings are very useful as a test of the Haldane conjecture and to quantitatively estimate the gap, Δ, and the correlation length, ξ_0. They have mostly been performed on the $S = 1$ AF chains which give rise to the largest Haldane gap. The pioneering work of Botet, Jullien and Kolb [4], performed on rings with N up to 12 using the Lanczös techniques, allowed a lower limit determination of the gap, $\Delta/J \approx 0.25$, and led to the first results on the effect of a uniaxial magnetic anisotropy on the gap (see Section 2.3). A more precise value of Δ was obtained by Nightingale and Blöte [25] by means of quantum Monte Carlo calculations for N up to 32. Their results for Δ versus $1/N$ (Fig. 2) clearly show the existence of the Haldane gap as $N \to \infty$; the extrapolated value for the infinite chain is estimated to be $\Delta \approx 0.41$ J.

Since these early studies, many numerical calculations have been devoted to the $S = 1$, 1D-HAF, in order to determine not only the ground state energy, the Haldane gap and the correlation length at $T = 0$ but also the dispersion law of the excitations and some thermodynamic properties such as the specific heat. The results for correlation length ξ_0 and gap Δ are given in Table 1.

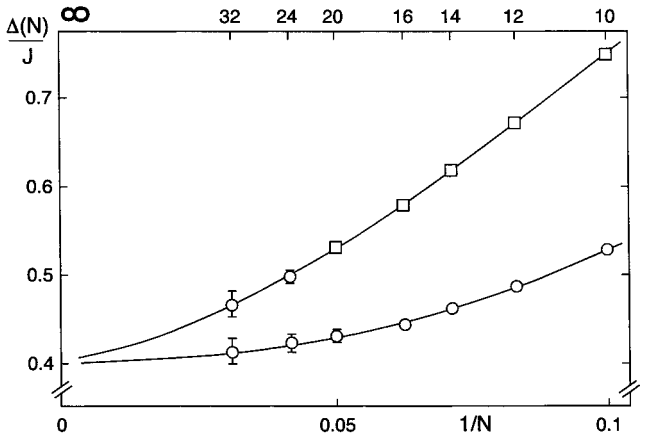

Fig. 2. Finite chain gap $(E_1 - E_0)/J$ (circles) and $(E_2 - E_0)/2J$ (squares) versus $1/N$ for $S = 1$, 1D HAF. The curves are visual guides. From Ref. [25].

Table 1. Haldane gap Δ and reduced correlation length ξ_0 at $T = 0$ for spin 1 antiferromagnetic Heisenberg chain.

Δ/J	ξ_0	Calculation method	Reference
0.41		Quantum Monte Carlo	[25]
	8	Transfer matrix	[26]
0.402		Diagonalization-valence bond solid (VBS) extrapolation	[27]
0.36	5.5 ± 2	Quantum Monte Carlo	[28]
	3.5	Quantum Monte Carlo	[29]
	6.3	Quantum Monte Carlo	[30]
0.411	5.2	Diagonalization – Lanczös	[31]
0.410	7	Density-matrix renormalization group	[32]
0.4105	6.03	Density-matrix renormalization group	[33]

The best current values are $\Delta/J = 0.411$ and $\xi_0 \approx 6$. The dispersion law for the magnetic excitations is especially interesting since it can be readily checked in real magnetic systems by inelastic neutron scattering (INS). Near $q = \pi$ (i. e. the limit of the AF Brillouin zone boundary), the dispersion law has the following form:

$$\varepsilon(q) = \sqrt{\Delta^2 + c^2 q^{*2}} \tag{7}$$

with $|q^*| = |\pi - q| \ll 1$ and where c is the quantum spin-wave velocity. Equation (7) is an approximation for small q^* of the relation $\varepsilon(q) = (\Delta^2 + c^2 \sin^2 q^*)^{1/2}$, which was thought classically to hold within the whole range of q values. Theoretical [6,22,34] and numerical [35,36] results strongly suggest however, that the gap at $q = 0$ is twice the gap at $q = \pi$, i. e. $\varepsilon(0) = 2\Delta$, the lowest excitation at $q = 0$ being a pair of magnons. It should be noticed that the correlation length ξ_0 is related to c and Δ as $\xi_0 \approx c/\Delta$. Taking for spin wave velocity, $c = 2JS$, leads to the relation $\xi_0 = 2JS/\Delta$ which is reasonably fulfilled by the ξ_0 and Δ/J values of Table 1 [37].

The $S = 2$ Heisenberg AF chains were also investigated by using the density matrix renormalization group techniques which proved to be very efficient at $S = 1$ [32,33]. They support the existence of a Haldane phase for $S = 2$ with a gap $\Delta/J = 0.085$ and a correlation length $\xi_0 \approx 49$ [38, 39]. These values are, at least qualitatively, in agreement with the exponential asymptotic behavior of Δ and ξ_0 conjectured by Haldane.

2.2.3 Effect of Anisotropy and Interchain Interactions on the Haldane Gap

The anisotropic chain of integer spin (mainly $S = 1$) either described by the hamiltonian Eq. (1) with $\beta = H = 0$, $D \neq 0$ or by the XXZ hamiltonian Eq. (2), with or without additional single ion anisotropy, was theoretically investigated by several authors [4,22,27,36,40–49]. The first results were obtained for $S = 1$ by Botet et al. [4] using Lanczös techniques and finite size scaling. They were able to sketch the

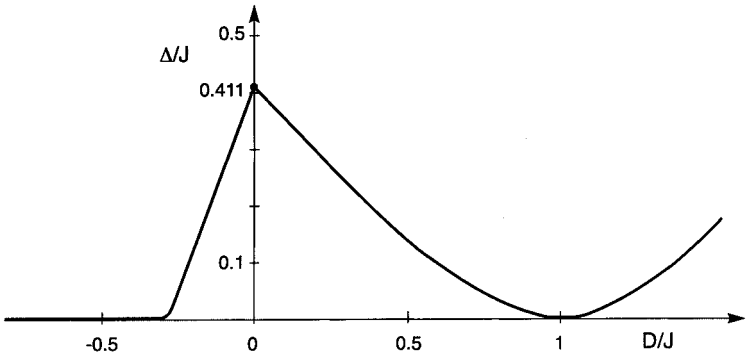

Fig. 3. Schematic view of the dependence of energy gap Δ/J on single-ion anisotropy D/J for the $S = 1$ anisotropic chain.

phase diagram in the (λ, D) plane, discussed in detail by Bonner [50]. We focus here on the case of only single-ion anisotropy which is relevant for real chain systems. The dependence of the gap on D is shown in Fig. 3.

The gap is maximum for the pure Heisenberg chain ($D = 0$), the first excited state being a degenerate triplet $S = 1$. Under the symmetry breaking term $D(S^z)^2$, the triplet is split into a singlet $S^z = 0$ and a doublet $S^z = \pm 1$. For $D > 0$ (easy-plane anisotropy), the lowest excited state is the doublet while for $D < 0$ (easy-axis anisotropy) the lowest excited state is the singlet. This splitting of the excited triplet by single-ion anisotropy was precisely determined by Golinelli, Jolicoeur and Lacaze [49], by Lanczös method up to $N = 16$ and by quantum Monte Carlo calculations up to $N = 32$. It is well reproduced for positive D/J values up to 0.25 by the following linear relations:

$$\begin{aligned} \Delta_z &= \Delta_0 + 1.41D \\ \Delta_{xy} &= \Delta_0 - 0.57D \end{aligned} \tag{8}$$

where $\Delta_0 \approx 0.41J$ is the gap value for the isotropic system. Quite generally, one should expect that the prefactor of the D linear term of Δ_z is twice that of Δ_{xy}. The discrepancy is likely due to a D^2 contribution which is not negligible in the range of fit [46]. As shown in Fig. 3, the Haldane phase for $S = 1$ AF chains exists in a relatively wide range of D values, $D_{c1} - D_{c2}$. These critical D values as well as the related critical exponents were determined by Lanczös techniques: $D_{c1}/J = -0.29 \pm 0.01$ [48] and $D_{c2}/J = 0.99(2)$ [51]. For $D > D_{c2}$ the ground state is a singlet separated by a gap from a band of excited states of width about $4J$. This large-D phase is different from the Haldane one, the gap being an anisotropy gap in this case.

Another interesting feature is the excitation spectrum obtained by Golinelli et al. [51] for different D/J ratios. At $q = 0$, the gap should be equal to $\Delta_z + \Delta_{xy}$, the excitation consisting of the sum of one excitation with $q = \pi$, $S^z = 0$ and one excitation with $q = -\pi$, $S^z = \pm 1$. Such a calculated excitation spectrum for

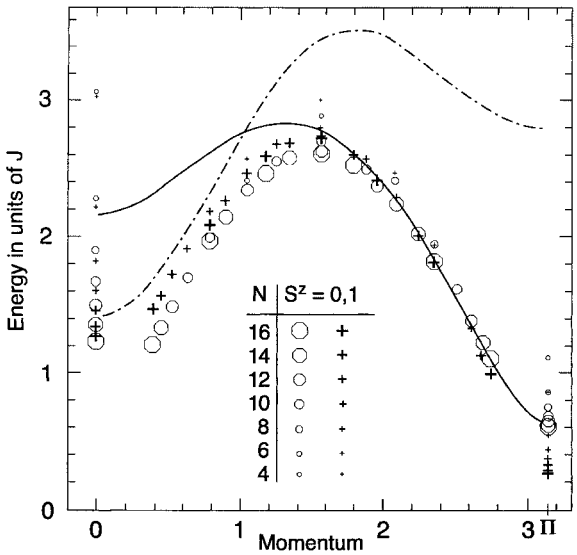

Fig. 4. Dispersion of magnetic excitations $S^z = 0$ and $S^z = \pm 1$ from the Lanczös calculations for chain lengths N=4, 6, 8, 10, 12, 14, 16. The energy is in units of J and the momenta (reduced wave vectors) range from 0 to π. The continuous line is the result of a variational calculation. The dashed line is the corresponding edge of two-particle excitations. From Ref. [36].

$D/J = 0.18$, corresponding to the case of the real Haldane gap system NENP, is shown in Fig. 4.

In real quasi-1D systems, interchain interactions are present. They can destroy the Haldane phase if they are large enough. The simplest approach to their inclusion consists of treating the interchain interactions in the mean field approximation. The interchain energy of 1D blocks of ξ correlated spins is about $z'|J'|\xi$ where z' is the number of neighboring chains and J' the interchain interaction. One should expect 3D long-range order and destruction of the Haldane phase for a critical value of $|J'|$ given by Eq. (9):

$$z'|J'|\xi \simeq \Delta \tag{9}$$

With $\xi = \xi_0 \approx 6$ and $\Delta = 0.41J$, Eq. (9) leads to $|J'/J|_c \approx 0.068/z'$, thus for $z' = 4$–6, the Haldane phase can be maintained for $|J'/J|$ up to about 10^{-2}. For $|J'/J| \geq |J'/J|_c$, Néel LRO is achieved and the Haldane phase is destroyed at low T. The phase diagram of quasi-1D AF was theoretically studied, first in general by Kosevich and Chubukov [52]. Later, triangular lattices of chains [53] and 2D square lattices [54,55] were studied. The predicted values of $|J'/J|_c$, respectively 0.013 for $z' = 6$ [53] and 0.025–0.026 for $z' = 2$ [54], support the simple mean field approximation described above. This situation is drastically different from the one of gapless chains for which 3D Néel LRO is always established at nonzero temperature, T_N being given by $k_B T_N \approx z'|J'|\xi(T_N)$ no matter what the interchain interactions may be.

2.2.4 Haldane-gap Antiferromagnet in Applied Fields

The excited triplet state of 1D-HAF is split by an applied field H and closure of the Haldane gap is expected for a critical field $H_{c1} = \Delta/g\mu_B$. At H_{c1}, the correlation length should diverge and the magnetization suddenly increases as $(H - H_{c1})^{0.5}$ up to a second critical field $H_{c2} = 4J/g\mu_B$ [42,56]. This behavior, shown in Fig. 5, was clearly established from numerical simulations on finite chains using Lanczös and size-scaling techniques [56–58]. The hamiltonian (1) with $\beta = 0$ was also studied from field theory treatment using free boson [59] or free fermion [60] approximations.

In the Haldane chain with single-ion anisotropy, the critical field of Haldane gap closure depends on field orientation. The values of the critical fields for H parallel and perpendicular to the chain axis have been obtained, as well as the field dependence of the first energy levels, and the H–D phase diagram has been thoroughly investigated for negative D and H along the easy axis [61]. The effect of nonaxial single ion anisotropy has also been considered [36,57,59]. These theoretical results on the anisotropic $S = 1$, antiferromagnetic chain will be described in more detail and compared with experimental results in Sections 4 and 5.

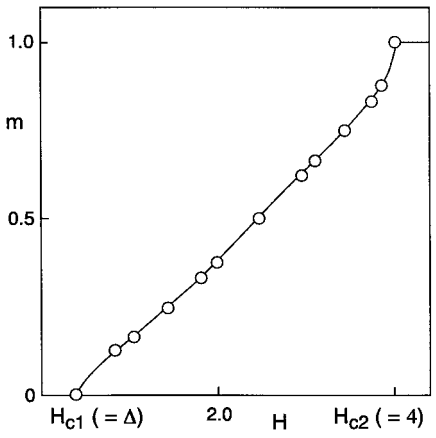

Fig. 5. Reduced magnetization $m = M(H)/M(\infty)$ versus magnetic field H in $J/g\mu_B$ units, of the $S = 1$ 1D HAF at $T = 0$. From Ref. [56].

2.2.5 *S* = 1/2 Spin Chains with Alternating F and AF Interactions

In the preceding sections, we restricted the discussion to uniform chains with first neighbor AF interactions. These exhibit a Haldane gap for integer spin and are gapless for half-integer spin. The situation of uniform AF chains with large AF second neighbor interactions or non-uniform chains with alternating exchange is quite different. For $S = 1/2$, the uniform chain with AF second neighbor interaction, J_2, larger than $0.241J_1$, has a singlet ground state and a gap [62]. The non-uniform $S = 1/2$ AF chain with alternating exchange is also gapped and was extensively studied theoretically in connection with the spin-Peierls transition [63–66]. An in-

teresting case closely related to the Haldane gap is that of alternating F and AF exchange treated by Hida [67]. When the F exchange dominates the AF one, i. e. $|J_F| \gg J_{AF}$, the dimer of F coupled spins 1/2 behaves at $T < |J_F|/k_B$ as a single spin 1 and the non-uniform F–AF chain is similar at low T to the uniform $S = 1$ Haldane chain. The calculated gap depends on the ratio $J_{AF}/|J_F|$ and tends to the Haldane gap value for $S = 1$, $0.41 J_{AF}$, as $|J_F| \to \infty$.

2.3 Quasi-1D Antiferromagnets for Haldane Gap Experiments

2.3.1 Conditions for Obtaining Haldane Systems

The presence of a Haldane gap in quasi-1D AF has a striking effect on the magnetic properties. Indeed, since the ground state is a singlet, the magnetic susceptibility should strongly decrease when the temperature becomes lower than Δ/k_B, independent of the orientation of the measuring magnetic field with respect to the crystal axes. If the interchain interactions are small enough, 3D Néel LRO cannot be established, as the temperature approaches zero. Inelastic neutron-scattering experiments at temperatures $T \ll \Delta/k_B$ should reveal a gap at $q = \pi$ in the magnetic excitations spectrum.

Owing to this specific behavior which is rather different from that of gapless chain systems, it can appear surprising that no clear experimental observation of a Haldane gap was reported prior to 1987. Different reasons can be given to explain this situation. The first is that, in fact, most of the studies of quantum effects in magnetic chains were originally focused on $S = 1/2$, AF for which such effects were expected to be larger than the $S = 1$ case. The second is that the experimental observation of the Haldane gap relies on the availability of uniform linear chains which fulfil specific conditions: (i) integer spins, i. e. $S = 1, 2, 3, \ldots$; (ii) antiferromagnetic coupling between the spins, i. e. $J > 0$; (iii) uniform chains, i. e. $J_{i,i+1} \equiv J_{i+1,i+2}$ whatever value of i in the chains; (iv) weak interchain coupling or quasi one-dimensional systems, i. e. $|J_{inter}/J_{intra}| < 10^{-2}$; and (v) relatively small local anisotropy on the integer spins. This last condition is not too severe for $D > 0$ since the Haldane phase persists up to $D/J \approx 1$. But gathering by chance, without specifically looking for them, all the necessary conditions for observing the gap in a real system is not easy. Indeed, among the few quasi-1D systems studied prior to the Haldane conjecture [68], some were ferromagnetic chains, others although antiferromagnetic such as $CsNiCl_3$ [69,70], had too large interchain interactions to allow a clear observation of the gap since a 3D Néel LRO occurred at low temperature ($T_N = 4.6$ K).

Since the Haldane conjecture was expressed, a joint effort by experimenters in chemistry and physics has resulted in the discovery and the characterization of several Haldane gap compounds, listed in Table 2. The basic structure of quasi one-dimensional spin 1 chains, well-insulated magnetically from each other, and three examples are shown in Fig. 6.

Table 2. Quasi-1D antiferromagnets with spin 1: chemical formula, crystal structure and space group at low temperature.

Compound	Chemical formula	Structure; space group	Ref.
	$CsNiCl_3$	Hexagonal; $P6_3/mmc$	[69,70]
NENP	$Ni(C_2H_8N_2)_2NO_2ClO_4$	Orthorhombic; Pnma	[5,71]
NENF	$Ni(C_2H_8N_2)_2NO_2PF_6$	Orthorhombic; P21/a	[71]
NINO	$Ni(C_3H_{10}N_2)_2NO_2ClO_4$	Orthorhombic; Pbn21	[72,73]
NINAZ	$Ni(C_3H_{10}N_2)_2N_3ClO_4$	Orthorhombic; Pn2n	[74,75]
NDMAZ	$Ni(C_5H_{14}N_2)_2N_3ClO_4$	Monoclinic; C2	[76,77]
NDMAP	$Ni(C_5H_{14}N_2)_2N_3PF_6$	Monoclinic; C2	[78,79]
TMNIN	$(CH_3)_4NNi(NO_2)_3$	Hexagonal; P3m1	[80,81]
YBANO	Y_2BaNiO_5	Orthorhombic; Immm	[82, 83]
	$AgVP_2S_6$	Monoclinic; P2/a	[84]

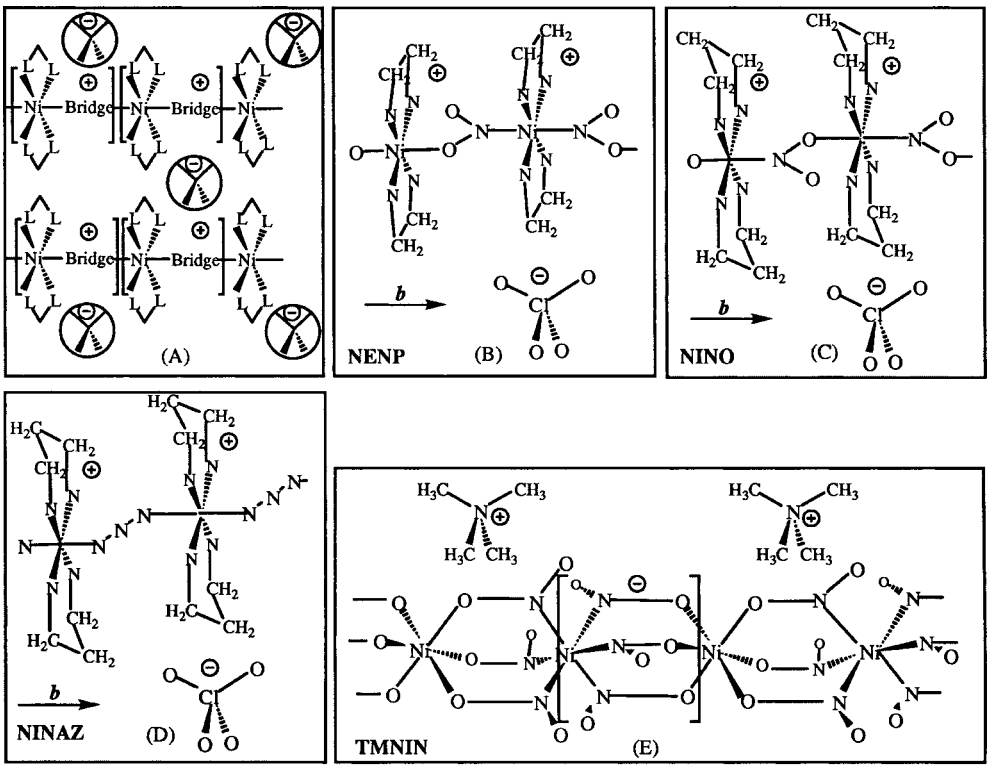

Fig. 6. Schematic structures of Haldane gap systems. (A) General scheme of quasi 1D Ni(II) chains well insulated from each other by bulky counterions; (B) NENP; (C) NINO; (D) NINAZ; (E) TMNIN.

2.3.2 Fulfilling the Structural and Electronic Conditions for Obtaining Haldane Systems

In this Section we examine how it is possible to gather in a chemical system all the experimental characteristics for the observation of the Haldane gap: integer spin, antiferromagnetic interaction, one-dimension, uniform interaction, and weak anisotropy.

2.3.2.1 Integer Spin Systems (Spin-bearing Species)

Transition metal ions

The simplest way to obtain integer spin systems is to look at the transition metal ions. Table 3 presents some possible candidates.

Fig. 7 displays how the octahedral ligand field (A) splits the d levels and leads to a $(t_{2g})^6(e_g)^2$ electronic configuration of the nickel(II) ion with $S = 1$ (B). Fig. 8 shows

Table 3. Integer spin transition metal ions.

First row :	Ti	V	Cr	Mn	Fe	Co	Ni	Cu
Electronic configuration	d^2	d^2	d^4	d^4	d^6	d^6	d^8	d^8
Oxidation state II:	Ti^{II} [(a)]		Cr^{II} [(b)]		Fe^{II} [(c)]		Ni^{II} [(d)]	
Oxidation state III:		V^{III} [(e)]		Mn^{III} [(f)]		Co^{III} [(g)]		Cu^{III} [(h)]
High spin state (HS)	1	1	2(HS)[(b)]	2(HS)[(f)]	2(HS)[(c)]	2(HS)[(g)]	1(HS)[(d)]	1(HS)[(h)]
Low spin state (LS)			1(LS)[(b)]	1(LS)[(f)]	0(LS)[(c)]	0(LS)[(g)]	0(LS)[(d)]	0(LS)[(h)]
Second and third rows	Too-large spin-orbit and zero-field splitting expected							
Lanthanides	Too weak exchange coupling constants expected							

Remarks [(a)] Ti^{II} is a species which reduces too much. No Haldane systems reported. [(b)] Cr^{II} is also a reducing species. It can be high spin (HS, $S = 2$) or low spin (LS, $S = 1$). Only one chain system ($S = 2$) has been reported [85] in which the other conditions for Haldane gap observation were not fulfilled. [(c)] Fe^{II} (HS) presents a spin-orbit coupling which is too large for the observation of the Haldane gap; intermediate spin 1 is rather rare. [(d)] Ni^{II} in octahedral configuration is the most useful for obtaining Haldane systems; in square planar geometry it is nonmagnetic and useless. [(e)] V^{III}: one example is known [84]. [(f)] Mn^{III}: the only claimed $S = 2$ Haldane gap system is made of chains of Mn^{III} [86]; most often nevertheless, the Mn^{III}, distorted by the Jahn-Teller effect gives rise to canted ferromagnetism which impedes the low-temperature observation of the Haldane gap. [(g)] Co^{III} is a very oxidizing species; furthermore it appears most often under the low spin form. [(h)] Cu^{III} is also a very oxidizing species; it always appears in the square planar, low spin, diamagnetic form.

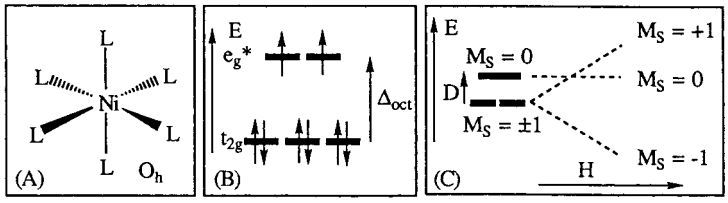

Fig. 7. (A) Octahedral Ni(II) complex, O_h symmetry. (B) Ligand field splitting in the octahedral field for a d^8 Ni(II). (C) Local anisotropy and zero-field splitting in a $S = 1$, triplet ground state (D negative).

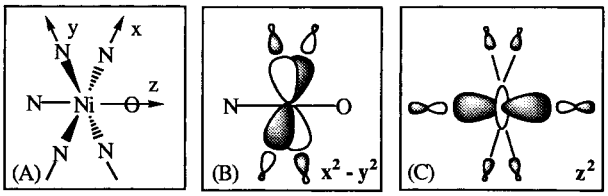

Fig. 8. Magnetic antibonding e_g^* orbitals $x^2 - y^2$ and z^2 in a mononuclear fragment of a Ni(II) chain.

the two antibonding singly occupied e_g^* orbitals, as they are present in a mononuclear fragment of a nickel(II) chain (A) extending along the z axis: orbitals $x^2 - y^2$ (B) and z^2 (C). It is convenient to name as magnetic orbitals such singly occupied molecular orbitals (d orbital partially delocalized on the ligands).

Molecules: ferromagnetically coupled radicals

The best candidate is evidently the dioxygen molecule which bears a spin 1, since the two unpaired electrons are in two orthogonal orbitals (see below). The difficulty is in organizing 1D chains of dioxygen in the condensed phase and demonstrating them [87].

One could also envisage binuclear complexes with ferromagnetically coupled spins $S = 1/2$ (see Section 2.5 and Fig. 9); in this case, the ferromagnetic coupling J_F within the copper(II) pair (due once more to the orthogonality of the singly occupied orbitals) must be larger that the antiferromagnetic coupling J_{AF} between the pairs to give rise to the Haldane behavior. This is unfortunately not the case in the reported experimental examples [88].

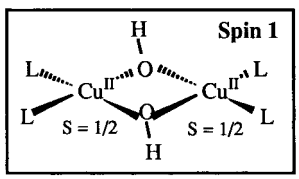

Fig. 9. Spin 1 built from ferromagnetically coupled $S = 1/2$ in a bis-μ-(hydroxo)dinuclear Cu(II) unit.

2.3.2.2 Antiferromagnetic Coupling Between Neighbors Along the Chain

An orbital model is useful in predicting the antiferromagnetic coupling between the spins of value 1 in the chain. The analysis can be performed on a dinuclear unit since the exchange interactions are short range in nature. Two orbital models are available in molecular magnetism, which lead to similar conclusions: the Kahn model (nonorthogonalized magnetic orbitals) [89] and the Hoffmann model (orthogonalized magnetic orbitals) [90]. Both models predict that orthogonal orbitals give rise to ferromagnetism and that overlaps give rise to antiferromagnetism. One relation in each model summarizes the conclusions in the case of two electrons 1 and 2 on two sites, described by two identical orbitals a and b: the singlet–triplet energy gap, equal to $J(J = E_S - E_T)$, is given by Eq. (10):

$$\text{Kahn model} \qquad J = 2k + 4\beta S \tag{10a}$$

$$\text{Hoffmann model} \qquad J = 2K_{ab} - (\varepsilon_1 - \varepsilon_2)^2/(J_{aa} - J_{ab}) \tag{10b}$$

In Eq. (10a), k is the bielectronic exchange integral (negativ) between the two nonorthogonalized magnetic orbitals a and b; β is the corresponding monoelectronic resonance or transfer integral (positive), and S the monoelectronic overlap integral (negative) between a and b. In Eq. (10b), K_{ab} is the bielectronic exchange integral (negative) between two identical orthogonalized magnetic orbitals a′ and b′; $(\varepsilon_1 - \varepsilon_2)$ is the energy gap between the molecular orbitals Ψ_1 and Ψ_2 built from a′ and b′; J_{aa} is the bielectronic interelectronic repulsion on one center and J_{ab} the equivalent on two centers.

Both expressions contain a negative term J_F, favoring parallel alignment of the spins and a positive term J_{AF}, favoring antiparallel alignment of the spins and a short-range antiferromagnetism. The total interaction results from the addition of the two terms $(J = J_F + J_{AF})$. In the case of nickel(II), two electrons are present on each center and J can be described by the sum of the different "orbital pathways" $J_{\mu\nu}$, weighted by the number of electrons [91,92]:

$$J = \left(\Sigma_{\mu\nu} J_{\mu\nu}\right)/4 \tag{11}$$

To get an antiferromagnetic coupling between two nickel(II) neighbors, an overlap must occur between the magnetic orbitals borne by the neighboring nickel(II) ions in the chain. Figs. 10 and 11 schematize the interaction in the case of NENP ($Ni(C_2H_8N_2)_2NO_2ClO_4$) and NINO.

Following Eq. (11), one finds for NENP:

$$J = (J_{z^2,z^2} + J_{x^2-y^2,x^2-y^2} + J_{x^2-y^2,z^2} + J_{z^2,x^2-y})/4 \tag{12}$$

If we neglect the two last bielectronic ferromagnetic terms, we observe that the z^2 orbitals overlap through the nitrito bridge $J_{z^2z^2} \propto (\varepsilon_1 - \varepsilon_2)^2$ (Fig. 10) whereas the $x^2 - y^2$ orbitals do not (Fig. 11), the MOs built from $x^2 - y^2$ orbitals are degenerate and $J_{x^2-y^2,x^2-y^2} \approx 0$; only the z^2 pathway contributes significantly to the coupling $J \approx J_{AF} \approx J_{z^2,z^2}/4$. This orbital mechanism of interaction through the bridging

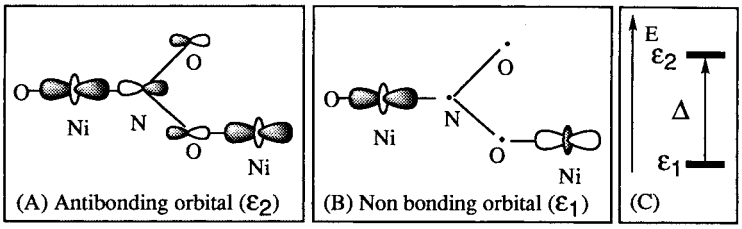

Fig. 10. Interaction between z^2 magnetic orbitals (MOs) in a dinuclear fragment of NENP chain: (A) antibonding MO; (B) nonbonding MO; (C) energy gap Δ between the two MOs.

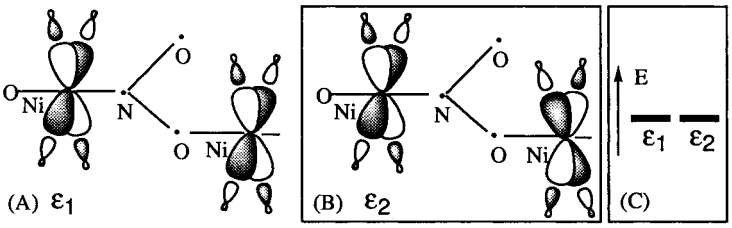

Fig. 11. Negligible interaction between $x^2 - y^2$ magnetic orbitals in a dinuclear fragment of NENP chain: (A) and (B) MOs; (C) energy degeneration of the two MOs.

ligand is often called superexchange. The tuning of the overlap between the magnetic orbitals on neighboring centers allows variation in the coupling constant in the chain (it will be stronger in NINAZ (Fig. 6D) and weaker in TMNIN (Fig. 6E). It will be much stronger with monoatomic oxide bridges in YBaNO (see below).

2.3.2.3 Uniform Chains

To get uniform chains, one must have the same coupling constant whatever the position of the metallic ion in the chain. This condition can be fulfilled when similar bridges (such as the nitrite ion NO_2^- in NENP, NINO and TMNIN and the azide N_3^- in NINAZ; see Fig. 6) and identical geometries are used along the chain. In the attempts to obtain new Haldane systems, many one-dimensional systems were obtained where the uniform character along the chain is not followed, as schematized in Fig. 12.

Nevertheless, more precise crystallographic details must be controlled. For example, in TMNIN (Fig. 6E), the coupling constant is uniform along the chain, but two neighboring nickel(II) centers are different (one surrounded by six oxygen atoms, the other by six nitrogen atoms), leading to different local values for g and D, for example. Even more subtle details, relating to the magnetic properties of NENP, will be discussed in Sections 4 and 5. Moreover, experience shows that even when the chains are uniform at high temperature, crystallographic phase transitions can appear and have some influence on the magnetic properties. Even if a spin–Peierls

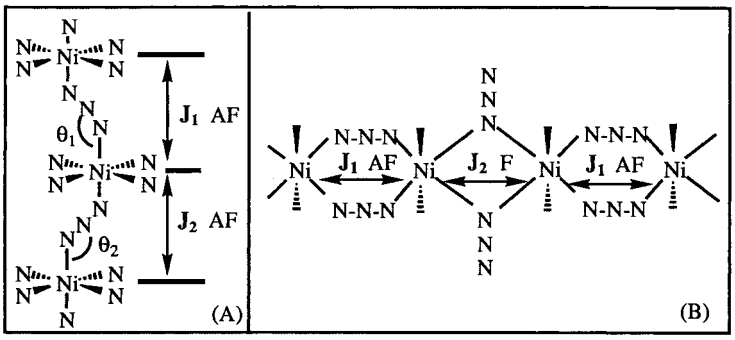

Fig. 12. Schemes of non uniform chains: (A) alternating antiferromagnetic chain; (B) alternating ferro- and antiferro-chain.

transition can be ruled out theoretically in Haldane systems [93], one must be careful about the nature of the transitions.

2.3.2.4 Weak Interchain Coupling or Quasi-one-dimensional Systems

This is one of the important conditions for allowing Haldane behavior when all the other structural conditions are already fulfilled. The best way to obtain a quasi-one-dimensional system is to magnetically insulate the chains from each other by separating them with bulky counter-ions. This necessitates that, in the chain itself, the repeating units are charged. In Fig. 6 (A–D), we have shown how this can be realized in the NENP, NINO and NINAZ chains: the repeating unit Ni(bridge)(diamine)$_2$ of the chain bears a positive charge (2+ for the nickel(II) and 1− for the bridging ion). A counter-anion is necessary to ensure the electroneutrality of the solid. Perchlorate $\{ClO_4\}^-$ is present in NENP, NINO, and NINAZ (and hexafluorophosphate in NENF). The opposite situation is found in TMNIN (Fig. 6E) where the repeating unit bears a single negative charge (2+ for the nickel(II) and 3− for the three nitrito bridging anions). The counter-ion is now the bulky tetramethylammonium cation $\{N(CH_3)_4\}^+$. The choice of counter-ion is not immaterial, since when the ion is too bulky the chain can be cut and give a dinuclear species [94].

2.3.2.5 Weak Local Anisotropy

This condition is less constraining as already mentioned, but also the most difficult to predict since there is no well-established correlation between the geometric structure and the value of the anisotropy D of the ion (Fig. 7C). Intuitively, it can be understood that the more symmetric the complex, the lower its anisotropy will be. However it is difficult to predict in detail the magnitude and even the sign of the local anisotropy D. Some experimental data show nevertheless that in octahedral nickel(II) complexes, a positive D value is obtained when the octahedron presents an elongation along a trigonal axis and a negative one in the case of a compression.

2.3.3 Some Haldane Gap Systems

2.3.3.1 NENP

The first we shall deal with is $Ni(C_2H_8N_2)_2NO_2ClO_4$ [5,71], abbreviated as NENP, which is now considered as the archetype of Haldane gap systems. It was synthesized before the Haldane conjecture was developed [95] and its magnetic properties, although presenting all the features of a Haldane gap system, were first interpreted as resulting from local anisotropy [71].

Its crystal structure, shown in Fig. 13, gathers all the features necessary for the observation of the gap: it consists of nickel(II) ions, in octahedral geometry, i. e. with spin 1, arranged in chains along the b crystal axis. The four equatorial positions of the nickel ions are occupied by the nitrogen atoms of the diamine 1,2-ethanediamine, whereas along the chains, the nickel ions are covalently linked by bridging nitrite groups $\{NO_2\}^-$. The nitrite ions are bonded, on one side, by the nitrogen atom and on the other side by one of the oxygen atoms (Fig. 13(A)). These bonds provide a relatively large intrachain AF interaction between neighboring nickel(II) ions, as shown above, in the Section 3.2.2. On the other hand, there is no efficient

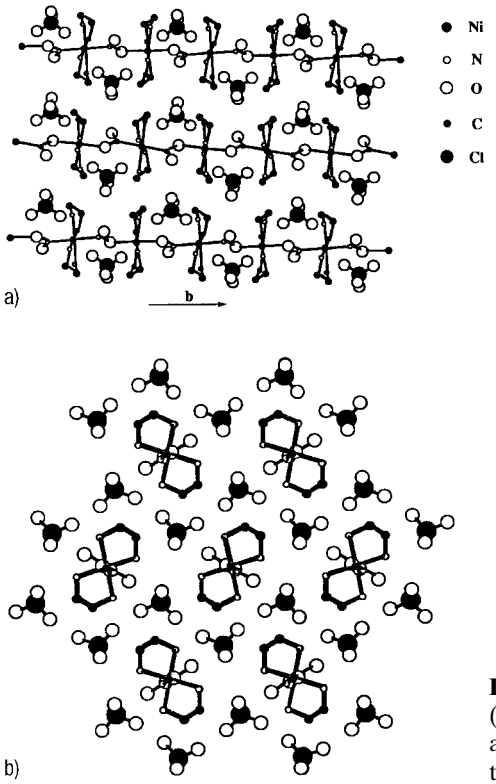

Fig. 13. Crystallographic structure of NENP: (A) perspective view showing the bonding along the chains; (B) perspective view down the b axis showing the interchain distances.

exchange path between nickel(II) ions of neighboring chains, well isolated from each other by the perchlorate $\{ClO_4\}^-$ anions (Fig. 13b), thus, the interchain interaction is extremely small compared with the intrachain one.

2.3.3.2 Related Molecular Haldane Gap Systems

NENP is the first member of a family of closely related Haldane gap systems. One of them, NENF, is obtained by replacing the $\{ClO_4\}^-$ anion of NENP by $\{PF_6\}^-$ [71]. NINO [72,73], with a chemical formula given by $Ni^{II}(C_3H_{10}N_2)_2NO_2ClO_4$ is obtained by replacing 1,2-ethanediamine, $C_2H_8N_2$, by 1,3-propanediamine $C_3H_{10}N_2$ (Fig. 6C). This substitution modifies the local stereochemistry of the nickel(II) ion and leads to a more ordered structure than that of NENP. The MO analysis is the same as in NENP.

NINAZ [74, 75] is obtained by replacing the nitrite group, NO_2, in NINO by the azido anion $\{N_3\}^-$ (Fig. 6D). The MO analysis is given in Fig. 14. In TMNIN, $(CH_3)_4NNi^{II}(NO_2)_3$, the crystal structure is reminiscent of that of TMMC, $(CH_3)_4NMn^{II}Cl_3$ [96,97] which is the archetype of a $S = 5/2$, gapless antiferromagnetic chains (Fig. 6E). The MO analysis is given in Fig. 15. Three nitrito groups bridge the nickel(II) ions but the orbital overlap is weak and TMNIN then has a relatively small J value compared with that of NENP, and consequently a smaller Haldane gap [80,81].

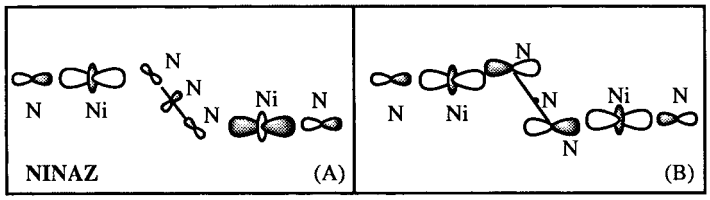

Fig. 14. Bonding and antibonding singly occupied MOs in NINAZ. The interaction through the azido bridge is strong and the energy splitting between the two orbitals is much more important than in NENP or NINO.

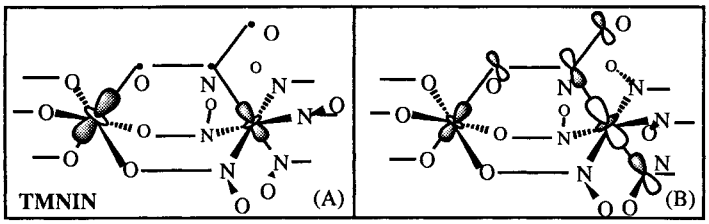

Fig. 15. Bonding and antibonding singly occupied MOs in TMNIN. The interaction through the three nitrito bridge is weak and the energy splitting between the two orbitals is much weaker than in NENP.

2.3.3.3 Solid-state Haldane Systems

YBANO, $Y_2BaNi^{II}O_5$ [82,83,98] is another nickel(II) quasi-1D AF exhibiting a Haldane gap. YBANO is obtained by means of solid-state chemistry, and represents a new type of inorganic AF chain system with rather large J and Δ values, due to a μ-oxo bridge between the nickel(II) ions. The corresponding values of J and Δ are listed in Table 4.

Another quite different Haldane gap system is $AgV^{III}P_2S_6$ [84,99,100]. It derives from the lamellar structure of MPS_3 by substitution of two M^{II} ions by the couple $Ag^I + V^{III}$. The vanadium(III) ions (electronic configuration d^2, $(t_{2g})^2$, $S = 1$), form zigzag chains isolated from each other by silver(I) chains, within a magnetic layer. This compound is characterized by a very large exchange interaction constant, $|J/k_B| \approx 600\,K$.

The main magnetic characteristics of many of the $S = 1$, quasi-1D AF mentioned above are listed in Table 4.

Table 4. Magnetic characteristics of a few Haldane gap compounds: intrachain exchange J, uniaxial single ion anisotropy D, and Haldane gaps Δ_{xy}, Δ_z.

Compound	J/k_B (K)	D/k_B (K)	Δ_{xy}/k_B (K)	Δ_z/k_B (K)	Ref.
NENP	48	12	14	30	[5,72]
	44	9			[97]
NINO	52	18			[74]
NINAZ	145	44			[74]
TMNIN	12	4			[80]
YBANO	285	−9.4	105	87	[83,98]
$AgVP_2S_6$	670	300			[84,99]

2.4 Static Magnetic Properties of Haldane Gap Systems

Measurements of susceptibility and specific heat versus temperature, and magnetization measurements versus applied magnetic field at $T \ll \Delta/k_B$ must clearly give evidence of the existence of a singlet ground state, separated from the first excited states by an energy gap, and give information about the size of this gap. Since the first susceptibility measurements on NENP showing the Haldane gap effect in this system [5], an increasing number of experiments have been performed on Haldane gap compounds. In the following sections we discuss some prominent experimental results.

2.4.1 Magnetic Susceptibility

The sharp drop of magnetic susceptibility as T decreases below Δ/k_B is the clearest signature of the Haldane gap. This behavior is observed for all directions of measuring

field; the residual susceptibility $\chi(0)$, at $T = 0$, is very small with respect to the maximum value of χ, $\chi_{\max}$, but depends on field orientation [59,60]. For perfect axial symmetry, $\chi^z(0) = 0$, whereas $\chi^{xy}(0)$ is proportional to $[(\Delta_z - \Delta_{xy})/(\Delta_z + \Delta_{xy})]^2$. If the axial symmetry is broken, $\chi^z(0)$ is no longer null. In this case, the twofold degenerate excited level is split into two singlets. For a splitting $\delta \ll |\Delta_z - \Delta_{xy}|$, $\chi^z(0)$ is given by $\chi^z(0)/\chi^{xy}(0) \approx [\delta/(\Delta_z - \Delta_{xy})]^2$ [59]. At low temperature, the susceptibility increase is mainly governed by the lowest energy gap, leading, for $D > 0$, to the following T dependence: $T^{-1/2}\exp(-\Delta_{xy}/k_B T)$ which is quite general for gapped 1D AF [101].

The salient features of the temperature dependence of magnetic susceptibility are well illustrated by the experimental data for NENP (Fig. 16).

As T decreases, the susceptibility first exhibits a maximum as expected for a 1D-AF. A sharp drop of χ is then observed as T becomes smaller than Δ_{xy}/k_B. The effect of single-ion anisotropy is clearly apparent from the different slopes, $d\chi/dH$, at the inflection point for H applied along z axis (b crystal axis), or perpendicular to z (a and c crystal axes). The predicted differences of residual values of χ for these two orientations as T tends to zero are also clearly observed. The experimental data for the susceptibility of NENP are in good agreement with the theoretical predictions, as shown in Fig.17.

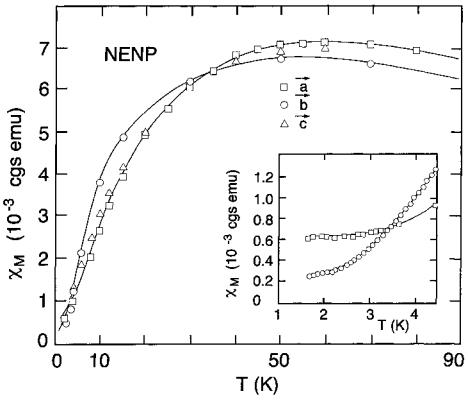

Fig. 16. Molar susceptibility of NENP along the three crystal axes, a (squares), b (circles) and c (triangles), as a function of temperature. Notice the net difference between susceptibility along b (z axis of single-ion anisotropy), and along a and c. From Ref. [5].

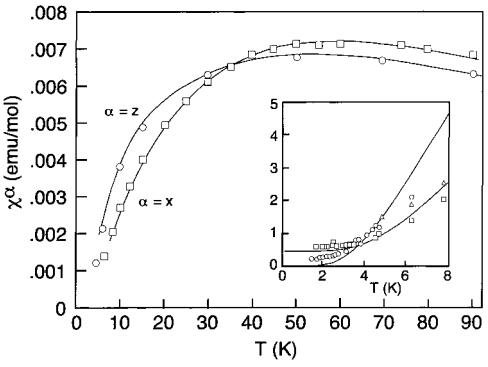

Fig. 17. Magnetic susceptibilities of the $S = 1$ AF with single-ion anisotropy for applied field along z (single-ion anisotropy axis) and along x. Comparison between experiment and calculation from numerical transfer matrix method (from Ref. [97]) and calculation from free boson model, full curve in the inset (from Ref. [59]).

For $k_B T/J \geq 0.15$, the experimental data are well fitted by the calculations of Delica et al. [97], based on a numerical transfer-matrix method. At low temperatures, i. e. $k_B T/J < 0.15$, a satisfactory agreement with the free boson model predictions [59] is obtained, but the experimental data, in particular for $\chi^z(T)$, are located slightly above the theoretical curves. This is due partly to a small axial symmetry breaking term, evidenced by a small difference between $\chi^x(T)$ and $\chi^y(T)$ and by the splitting of the Δ_{xy} gap discussed in Section 5.1 and, most likely, to structural defects or impurities which break the magnetic chains into finite segments. The effect of these chain breaks will be discussed in detail in Section 6. They bring a $1/T$ extrinsic contribution to the susceptibility. This defect-spin paramagnetism complicates the analysis of the experimental data as T tends to zero. Even for NENP, which can be obtained in nearly perfect single crystals, the magnetic susceptibility below 1 K is completely dominated by a small number of chain breaks (about one chain break per 4000 Ni spins) [102]. The low T susceptibility drop has been observed in all the other Haldane gap compounds listed in Table 3. However, the spoiling effect of defect-spin paramagnetism is rather important in compounds with large J, i. e. NINAZ, $AgVP_2S_6$ and YBANO, and often prevents a pertinent analysis of the low T data. An interesting way to avoid this difficulty is to deduce the static susceptibility from the shift of nuclear magnetic resonance (NMR) lines. In fact, the defect-spin paramagnetism broadens the NMR line but does not contribute to the NMR shift tensor. The temperature dependence of the shifts of ^{51}V and ^{31}P NMR lines was found to be in good agreement with that of the corrected magnetic susceptibility in a single crystal of $AgVP_2S_6$ [103]. The low T data are well fitted to the law $T^{-1/2} \exp(-\Delta/k_B T)$ with $\Delta/k_B = 320$ K. This value of Δ (27.5 meV) is in good agreement with that from inelastic neutron scattering experiments on polycrystalline samples ($\Delta = 26$ meV) [99]. A similar determination of the energy gap from the shift of ^{89}Y NMR lines was carried out on Y_2BaNiO_5 [104].

2.4.2 Magnetic Specific Heat

In gapless 1D AF, it is well established, both from theory and experiment, that the magnetic specific heat, C_m, has a low T linear dependence $C_m = AT$ [1]. For a 1D AF with a gap Δ, the free boson approximation leads to the following low T dependence of C_m [105]:

$$C_m = AT^{-3/2} \exp(-\Delta/k_B T) \tag{13}$$

Another low T dependence has been suggested for the $S = 1$, 1D HAF, namely $C_m = C_0(k_B T/J)^{1.6}$ from analytical extrapolation to zero of the high temperature thermodynamic functions [106]. It clearly differs from the linear dependence and thus reflects the existence of the Haldane gap, but its validity down to $T = 0$ is doubtful.

There are still few experimental studies of the specific heat of Haldane gap compounds. Such experiments are tedious due to the smallness of C_m at temperatures $T \ll \Delta/k_B$ and to the necessity of correctly removing the lattice contribution to

specific heat. So far, the magnetic specific heat of NENP, NENF and NINAZ has been indirectly deduced from the derivative of linear birefringence versus T [107]. C_{m} exhibits the broad maximum predicted for $S = 1$, AF chains at about $0.8J/k_{\mathrm{B}}$ [108,109]. The low T dependence of C_{m} can be described either by a power law T^{α} with $\alpha > 1$ ($\alpha = 1.4$ for NENP [107]), or by an exponential law with an energy gap $\Delta/k_{\mathrm{B}} \approx 16\,\mathrm{K}$ for NENP and NENF. This gap value is consistent with the value obtained by neutron scattering in NENP, i. e. $\Delta_{xy}/k_{\mathrm{B}} \approx 14\,\mathrm{K}$. The specific heat of TMNIN has been investigated by the usual adiabatic methods down to 0.6 K [110]. The experimental data fit reasonably with Eq. (13), with $\Delta/k_{\mathrm{B}} = 4.2\,\mathrm{K}$, consistent with the gap value deduced from susceptibility, magnetization and nuclear magnetic resonance measurements [80].

2.4.3 High-field Magnetization

High-field magnetization measurements have been performed in a few Haldane gap compounds, including NENP, NINO, NINAZ and TMNIN. The experimental data for a powdered sample of TMNIN are shown in Fig. 18.

Since the J of TMNIN is not too large, the whole magnetization curve, $M(H)$, was obtained up to the saturation field [111]. The general shape of $M(H)$ is in good agreement with the theoretical predictions for the $S = 1$, 1D HAF [42,56]. In particular, a well-defined jump of the slope $\mathrm{d}M/\mathrm{d}H$ of $M(H)$ is observed at the critical field, $H_{\mathrm{c1}} = \Delta/g\mu_{\mathrm{B}}$, followed by a nearly linear increase of $M(H)$ up to the saturation field, $H_{\mathrm{c2}} = 4J/g\mu_{\mathrm{B}}$. High-field magnetization measurements have been performed on single crystals of NENP [112,113] and NINO [114] along different crystal axes. For all field directions and at low temperature, the magnetization is rather small in the low field region and begins to increase abruptly at the critical field corresponding to the closure of the Haldane gap. This critical field is indicated by a maximum of $\mathrm{d}M/\mathrm{d}H$. As a result of single-ion anisotropy, it depends on field orientation in agreement with the theoretical treatment of Tsvelik [60]. For axial symmetry, the expected values of critical fields are $H_{\mathrm{c1}}^{z} = \Delta_{xy}/g_z\mu_{\mathrm{B}}$ and $H_{\mathrm{c1}}^{xy} = (\Delta_{xy}\Delta_z)^{1/2}/g_x\mu_{\mathrm{B}}$. Taking for Δ_{xy} and Δ_z the values in Table 4, obtained by inelastic

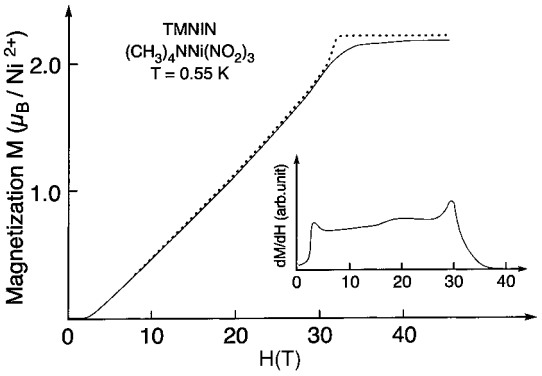

Fig. 18. High-field magnetization of TMNIN at 0.55 K. The dotted curve is the calculated one for $J/k_{\mathrm{B}} = 12\,\mathrm{K}$ and $g = 2.25$. The derivative of the magnetization curve, $\mathrm{d}M/\mathrm{d}H$, is shown in the inset. Taken from Ref. [111].

neutron scattering, one obtains $H_{c1}^{z} = 9.7T$ and $H_{c1}^{xy} = 13.7T$, which are close to the experimental values, respectively, of $H_{c1}^{b} = 9.2T$–$9.8T$, $H_{c1}^{a} = 14T$, $H_{c1}^{c} = 12.5T$, assuming for H_c the field value at which dM/dH is maximum. The slight difference between the critical field values for a and c crystal axes of NENP is due to the small nonaxial orthorhombic single-ion anisotropy also shown by the susceptibility curves (Fig. 16). In NINO, this difference is much larger than in NENP, namely $H_{c1}^{b} = 9.2T$, $H_{c1}^{a} = 9.2T$ and $H_{c1}^{c} = 12T$. This would suggest a large nonaxial anisotropy with respect to the chain axis. On the other hand, this is not shown by the susceptibility data, which yield $\chi^{a} \approx \chi^{c}$ as for NENP.

2.4.4 Long-range Order

The experiments described above clearly show, in several quasi 1D AFs, the existence, at low temperature, of a Haldane phase characterized by a singlet ground state separated by an energy gap from the excited states. Due to the finite correlation length, no Néel 3D LRO can develop at low T if interchain interactions are small enough. The occurence of 3D LRO should be revealed by a kink in the temperature variation of susceptibility and by a lambda type peak of specific heat at the 3D ordering temperature T_N. None of the Haldane gap compounds listed in Table 4 exhibits such behavior. The interchain interaction is reasonably well known for NENP where $|J'/J| \approx 4 \times 10^{-4}$ (see Section 5.1). For a gapless $S = 1$, quasi-1D HAF, T_N can be approximated by $k_B T_N \approx (8J|J'|)^{1/2}$ which leads to $T_N \approx 2.7$ K for NENP. As shown in Fig. 16, no susceptibility kink is observed down to 1.6 K. These susceptibility measurements have been extended down to 300 μK, by Avenel et al. [102], without revealing any LRO. This absence of LRO is confirmed by specific heat measurements down to 0.2 K [115] and by elastic neutron scattering down to 1.2 K (Section 5.1).

Under an applied magnetic field which closes the gap, the correlation length is expected to diverge at low temperature, and then 3D LRO should be established at low temperature. A transition to 3D LRO in an applied field was clearly observed from specific heat measurements in NDMAZ [116] and NDMAP [117], and an experimental H–T phase diagram was obtained in this latter compound. The low-T and high-H phase is probably a flopped antiferromagnetic phase. Curiously, no 3D LRO has been reported in NENP at low T and high H. This absence of transition might be due to an imperfect closure of the gap revealed by neutron scattering experiments in high fields (Section 5.1).

2.5 Dynamic Properties of Haldane Gap Systems

The existence of both the singlet ground state and a gap Δ between the ground state and the first excited state has important consequences for the spin-dynamics at low ($E \ll \Delta$) and intermediate ($E \approx \Delta$) energies, which can be checked exper-

imentally. Techniques which probe spin dynamics on a microscopic scale, such as nuclear magnetic resonance (NMR), inelastic neutron scattering (INS) or electron spin resonance (ESR), have long been demonstrated as essential and highly complementary methods for studying the physics of magnetic systems. NMR probes the excitation spectrum mainly at very low energies ($E \approx 0$), whereas INS can be used to investigate both the wave vector and energy dependencies of excitations at energies $E \approx \Delta$. On the other hand, ESR is expected to probe magnetic transitions in which the absorption of energy is realized without wave vector transfer, corresponding to the condition $\Delta q = 0$.

As previously mentioned in the first part of this chapter, for a Haldane system at $T = 0$ the excitation spectrum has been predicted to display quite different features, depending on the value of the wave vector q (see Fig. 4). Around the antiferromagnetic point k_{AF} (corresponding to $q = \pi$ in the notation adopted in the theoretical papers) and down to about $0.3k_{\mathrm{AF}}$, the excitation spectrum consists of well-defined magnons with relatively long lifetimes. The spectrum displays, in the most general case, three gaps at $q = k_{\mathrm{AF}}$ (defined in the following by Δ_n with $n = 1, 2, 3$), corresponding to the three modes associated with the first triplet excited state. However these modes can be more or less degenerated, depending on the symmetry of perturbative terms such as anisotropy terms, Zeeman terms, etc. There does not exist any exact analytical expression for the dispersion relation of magnetic excitations in the $S = 1$ HAF chain. For sufficiently small values of the reduced wave vector $q - k_{\mathrm{AF}}$, the dispersion relation of mode n can be well approximated by the following quadratic expression, which is in fact a generalization of Eq. (7) to the anisotropic case:

$$E_n(q) \approx \sqrt{(\Delta_n)^2 + c^2(q - k_{\mathrm{AF}})^2} \tag{14}$$

where c is the quantum spin wave velocity, given by the relation $c \approx 2.7Jd$ for a spin $S = 1$, d being the intrachain distance between two adjacent spins [24,35,36]. The maximum energy is located near $k_{\mathrm{AF}}/2$ at an energy $E_{\mathrm{M}} \approx 2.7J$ which differs by 35% from the classical prediction. Below $0.3k_{\mathrm{AF}}$ the nature of magnetic excitations is expected to change drastically. The theory for the isotropic system predicts the existence of a continuum of two-particle excitations which should display at $q = 0$ a gap twice the gap at $q = k_{\mathrm{AF}}$. This asymmetry in the excitation spectrum is in fact a signature of the absence of broken translational symmetry in the ground state of an integer-spin system, unlike the half-integer spin case. Anisotropy terms are expected to modify this picture only slightly, as previously mentioned in Section 2. In the analysis of the experimental data, the fundamental quantities which are relevant are the various components of the spin–spin dynamic correlation function (alias structure factor), $S_{n\nu}(q, E)$, which should in principle contain all the physics of magnetic excitations. Following our notation, n and ν label the mode number ($n = 1, 2, 3$) and the spin-component ($\nu = x, y, z$), respectively. There is, up to now, no exact expression for $S_{n\nu}(q, E)$. However for temperatures sufficiently small such that $T \ll \Delta/k_{\mathrm{B}}$ and wave vectors $q \approx k_{\mathrm{AF}}$, field-theory treatments of the Heisenberg chain [59,60] have given approximate expressions of lorentzian type, which can be generalized to the anisotropic case according to Eq. (15):

$$S_{n\nu}(q, E) \approx S_{n0} \frac{P_{n\nu}}{\kappa_{n\nu} \cdot \Gamma_n} \frac{1}{1 + \left(\frac{q - k_{\mathrm{AF}}}{\kappa_{n\nu}}\right)^2 + \left(\frac{E - E_n(q)}{\Gamma_n}\right)^2} \tag{15}$$

in which $E_n(q)$ is the energy of mode n, $\kappa_{n\nu}$ are coefficients characterizing the scale in q associated with the various spin components and $P_{n\nu}$ are the polarization factors. In Eq. (15) the prefactor S_{n0} contains the statistics of elementary excitations. In zero field, each mode is polarized along a single direction ν ($P_{n\nu} = 1$ or 0) and the coefficients $\kappa_{n\nu}$ are directly related to the inverse of correlation lengths ξ_ν associated with the correlation function $\langle S_0^\nu S_r^\nu \rangle$. Moreover one expects, as for the isotropic case, ξ_ν to be related to the gap value Δ_ν through the relation $\Delta_\nu \xi_\nu \approx c$, although no rigorous proof exist for such a relation. From general arguments the fluctuation rates Γ_n are expected to depend more or less exponentially on the temperature, following a relation of the type:

$$\Gamma_n(T) \approx C_n \cdot \exp(-\Delta_n / k_{\mathrm{B}} T) \tag{16}$$

In Eq. (16) the C_n coefficients are also expected to depend both on field and temperature. As a consequence of the existence of both gaps and a singlet ground state, $S_{n\nu}(q, E)$ should exhibit a well-defined maximum at an energy $E \approx \Delta_n$, whereas the magnetic fluctuations at $E \approx 0$ are expected to vanish as T tends to 0. These two features can be checked experimentally from INS or NMR experiments. However it is important to note that Eq. (14) is certainly wrong when $E/k_{\mathrm{B}}T \ll 1$, as is the case for NMR. We will come back to this point later. A very relevant quantity, which can be probed directly by INS, is the static structure factor defined by the integral over the energy: $S_{n\nu} = \int S_{n\nu}(q, E)\, \mathrm{d}E$. At temperatures sufficiently low, $S_{n\nu}(q)$ is simply given by a square-root lorentzian function:

$$S_{n\nu}(q) \approx S_{n0} \frac{P_{n\nu}}{\kappa_{n\nu}} \frac{1}{\sqrt{1 + \left(\frac{q - k_{\mathrm{AF}}}{\kappa_{n\nu}}\right)^2}} \tag{17}$$

This behavior can be derived directly by Fourier transforming the equal time correlation function defined by Eq. (5) in Section 2.2. The square-root lorentzian behavior is another signature of the Haldane ground state, which can be checked by measuring $S_{n\nu}(q, E)$ by INS.

Near zero wave vector, the dynamic structure factor $S_{1z}(q, E)$ has been calculated for the isotropic case by Affleck and Weston [34], within the framework of the free-boson field theory. For fixed energy, the dynamic structure factor is found to vanish quadratically in q as $q \to 0$. However in the presence of finite anisotropies, the dynamic structure factors are expected to take finite values at $q = 0$. For a system displaying both XY ($D > 0$) and in-plane ($E \neq 0$) anisotropies with $D \gg E$ (as is the case in NENP or NINO), three gaps should be seen at $q \approx k_{\mathrm{AF}}$, namely, Δ_1 and Δ_2 (both associated with fluctuations perpendicular to the chain), and Δ_3 (associated with fluctuations parallel to the chain). At $q = 0$, gaps at $\Delta_1 + \Delta_2$

(associated with fluctuations along the chain), $\Delta_1 + \Delta_3$ and $\Delta_2 + \Delta_3$ (both associated with fluctuations perpendicular to the chain) are predicted to exist, with intensities mainly controlled by the factors $(E/J)^2$ and $(D/J)^2$, respectively [34]. Numerical calculations on finite size systems [24,30,36] have confirmed very tiny values for the static structures at small q, which are found below $0.2k_{\mathrm{AF}}$, more than two orders of magnitude smaller than those at $q = k_{\mathrm{AF}}$. These tiny intensities will certainly prevent any precise experimental investigation of this part of the spectrum, at least by INS: unlike the case of half-integer spin [118], for integer-spin the continuum at $q = 0$ is found to carry little spectral weight.

2.5.1 Spin Dynamics at Intermediate Energy ($E \approx \Delta$)

The experimental results described in the previous sections, obtained essentially from macroscopic measurements, give strong evidence for the existence of a quantum gap in the excitation spectrum of Haldane gap systems. Other direct and quantitative information can be obtained from INS experiments, which probe the dynamic structure factors over the full Brillouin zone (0–k_{AF}) and energy range (0–E_{M}). In particular one can obtain crucial information on the dependencies of gaps with variables, for instance the wave vector, the temperature, the field or the anisotropy, which can be directly compared with the theoretical predictions described in Section 2.

2.5.1.1 Gaps at $q = \pi$

The first attempts to prove the veracity of the Haldane conjecture have been performed on the system $CsNiCl_3$, using both unpolarized and polarized neutron scattering [118–122]. We have seen in Section 3 that this compound was an easy-axis ($D < 0$) spin 1 antiferromagnetic chain system with relatively large interchain exchange interactions, which induce a 3D phase transition below a Néel temperature $T_{\mathrm{N}} \approx 4.6\,\mathrm{K}$. Above T_{N}, in the 1D regime, INS studies have clearly demonstrated the existence of an energy gap in the excitation spectrum and the absence of magnetic fluctuations at low energy, in agreement with the theoretical predictions. The gap is found to soften when approaching T_{N}, as a consequence of the growing 3D fluctuations. This softening, very reminiscent of the behavior generally observed in singlet ground state systems, is well comprehended by the Haldane gap theory, slightly modified to incorporate the non-negligible interchain coupling [52,53]. However, $AgVP_2S_6$, YBANO or NENP are better systems; all three present no long-range ordering down to almost $T = 0$. The former compound has been extensively studied by INS on polycrystalline samples, due to some difficulties in obtaining single crystals [99,100]. In $AgVP_2S_6$ scans in energy recorded at low temperature have unambiguously shown the existence of a spin gap at an energy $\Delta \approx 26\,\mathrm{meV} \approx 300\,\mathrm{K}$, which corresponds to a ratio $\Delta/J \approx 0.45$. The line shape of the inelastic response has been analyzed from the scattering function:

$$S(q, E) \approx \frac{\xi}{\sqrt{1 + (q - k_{\mathrm{AF}})^2 \xi^2}} \delta(E - E(q)),$$

which can be deduced easily from Eq. (15) taking the limit $\Gamma \to 0$. The best fit is obtained with a reduced correlation length value $\xi/d \approx 5.5$, which corresponds quantitatively to the prediction for the ideal 1D-HAF system and, moreover, which satisfies the expected relation $\xi \approx c\Delta^{-1}$, with a spin wave velocity $c \approx 2.5Jd$. Unfortunately the huge value of the exchange coupling observed in this compound should greatly limit further investigation, such as studies under field ($H_c \approx \Delta/g\mu_B \approx$ 200 T).

Convincing evidence for the existence of gaps at the antiferromagnetic point has been obtained with NENP from INS experiments on single crystals [5,72,124–127]. Single-crystal experiments are essential because they allow an accurate determination of the eigenvectors associated with each one of the three modes forming the excited triplet. We show in Fig. 19a typical results recorded at two scattering vectors, $\vec{Q} = (0.2, 1, 0)$, located nearly along the chain axis, and $\vec{Q} = (3.2, 1, 0)$, making a substantial angle with the chain axis. Two gaps are visible at energies $\Delta_{xy} \approx 1.2$ meV ≈ 14 K and $\Delta_z \approx 2.5$ meV ≈ 30 K (mode 3). The former corresponds to the one observed in the susceptibility and magnetization measurements. From their dependencies with the component Q_y of the scattering vector, these two modes have been unambiguously attributed to magnetic fluctuations in the xy plane and along the chain axis, respectively. With a better instrumental resolution in energy, it is found that the xy mode is split into two distinct components. Fig. 19b shows the results of a scan in energy recorded on a cold neutron spectrometer at a scattering vector $\vec{Q} = (0.3, 1, 0)$, chosen in order to suppress the fluctuations along the chain. Two gap-modes are unambiguously observed at energies $\Delta_x \approx 1.16$ meV and $\Delta_y \approx 1.34$ meV. The polarization of these modes has been determined by analyzing their dependencies with the scattering vector. The low-energy mode 1 contributes mainly to $S_{1y}(q, E)$ whereas mode 2 contributes mainly to $S_{2x}(q, E)$. Thus, three gaps are unambiguously observed in NENP, with well-defined polarization. This experimental fact demonstrates the triplet nature of the first excited state, in agreement with the theoretical predictions (see Section 2). The splitting of the triplet is interpreted as an effect of the finite orthorhombic single ion anisotropy present in NENP. The average value $\Delta_0 = (\Delta_x + \Delta_y + \Delta_z)/3$ which cancels at first order the effect of the anisotropy, is expected to be a reasonable estimate of the gap value for the ideal $S = 1$ 1D HAF system. In NENP, the experimental determination gives $\Delta_0 \approx 1.67$ meV ≈ 19 K, which leads to a ratio $\Delta_0/J \approx 0.42$ (using $J \approx 4$ meV ≈ 46 K) in quantitative agreement with the best numerical determinations (Table 2). When the xy gap is defined in the absence of in-plane anisotropy by $\Delta_{xy} = (\Delta_x + \Delta_y)/2$, values for the splitting resulting from the out-of-plane (D) and in-plane (E) anisotropies, $\Delta_z - \Delta_{xy} \approx 1.25$ meV ≈ 14.5 K and $\Delta_x - \Delta_y \approx 0.18$ meV ≈ 2.1 K, can be deduced. Golinelli et al. [128] gave precise expressions for both splittings found to depend linearly on D and E at first order: $\Delta_z - \Delta_{xy} \approx 1.9D$, $\Delta_x - \Delta_y \approx 4E$. These relations yield precise determinations of parameters $D(\approx 8$ K, $D/J \approx 0.17)$ and $E(\approx 0.5$ K, $E/J \approx 0.012)$ which agree quantitatively with those determined from the analysis of susceptibility measurements (see Section 4.1).

The same kind of measurements have been performed on YBANO single crystals [98,129,130]. INS revealed, as in NENP, the existence of three gaps due to the splitting

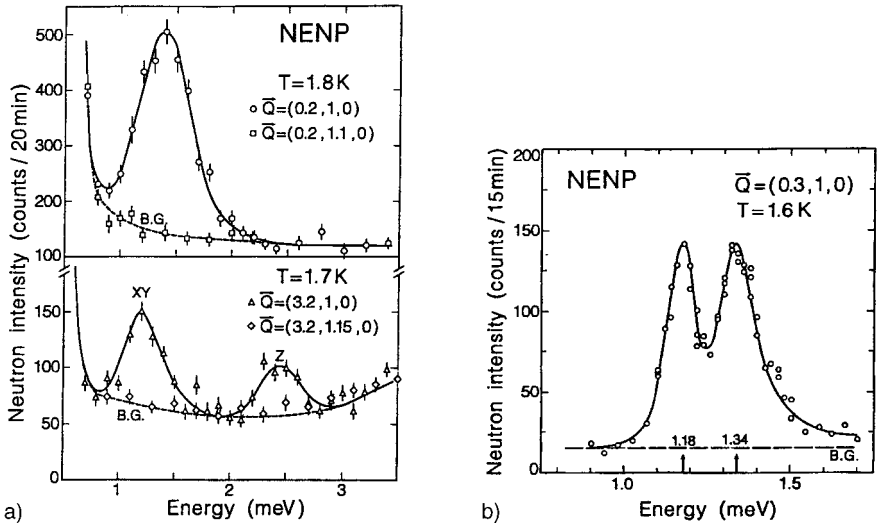

Fig. 19. (A) Scans in energy at low temperature for NENP showing the existence of two gaps in the excitation spectrum associated with xy and z fluctuations. (B) High-resolution scan in energy showing the splitting of the xy mode in NENP.

of the excited triplet by orthorhombic single-ion anisotropy. The neighboring values of these gaps, respectively $\Delta_a = 7.5\,\text{meV}$, $\Delta_b = 8.6\,\text{meV}$ and $\Delta_c = 9.6\,\text{meV}$, explain why only a single gap at the average value, $\Delta_0 = (\Delta_a + \Delta_b + \Delta_c)/3$, of about 8.5 meV was observed in the INS of powder [83]. The gap values correspond to $D = -0.81\,\text{meV}$ and $E = 0.25\,\text{meV}$ which are much smaller than the interchain exchange $J \approx 24.6\,\text{meV}$ (285 K) deduced from susceptibility. The ratio $\Delta_0/J \approx 0.35$ obtained in YBANO is slightly smaller than the theoretical prediction for the ideal Heisenberg model.

2.5.1.2 Wave Vector Dependencies of the Excitation Spectrum

The dependencies of magnetic excitations with the wave vector are important for characterizing a Haldane system. They should exhibit two features characteristic of the Haldane ground state: the finite value of the correlation lengths at $T = 0$ and the 2π-periodicity of the excitation spectrum. The latter implies in particular completely different behaviors at $q = 0$ and $q = k_{\text{AF}}$.

Accurate determinations have been obtained mainly on the prototype system NENP from INS experiments on single crystals [5,72,125]. Near the antiferromagnetic wave vector, the dispersion relation of magnetic excitations is well accounted for by Eq. (14), with a spin wave velocity $c \approx 50\,\text{meV} \approx 2.5Jd$, only 8% smaller than the theoretical prediction. A comparison between the neutron data [72] and the theoretical prediction as calculated from Eq. (14) (solid lines) is shown in Fig. 20. At larger wave vectors, the dispersion relation and the static structure factors of both the xy and z modes have been determined by Ma et al. [125] down to $0.3k_{\text{AF}}$, using fully

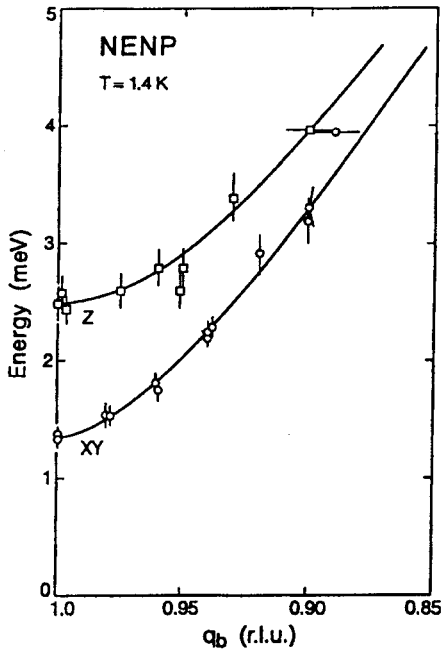

Fig. 20. Dispersion relation of magnetic excitations in NENP. The solid lines are calculated from Eq. (10). From Ref. [72].

deuterated samples. A quantitative agreement with the corresponding numerical calculations [24,30,36] was observed. The maximum energy of the excitation spectrum occurs near the wave vector $k_{\mathrm{AF}}/2$, with a value $E_{\mathrm{M}} \approx 11$ meV, consistent with the quantum prediction $E_{\mathrm{M}} \approx 2.7Jd$, taking $J \approx 4.1$ meV [125]. More interestingly, the excitation spectrum is not found to be symmetrical with respect to $k_{\mathrm{AF}}/2$, the mode at $(k_{\mathrm{AF}}/2) - q$ displaying a slightly higher energy than the mode at $(k_{\mathrm{AF}}/2) + q$. This asymmetry nicely demonstrates the absence of broken translational symmetry in the ground state of NENP. A similar conclusion seems to emerge from an analysis of both the energy and the width of the gap mode in $CsNiCl_3$ at 10 K (i. e. in the 1D regime) [121]. Below $0.3k_{\mathrm{AF}}$ the signal vanishes rapidly and it is impossible to confirm either the continuum or the doubling of the gap near $q = 0$. At least the absence of sizable neutron intensity at low q [125,95] is consistent with the existence of tiny structure factors as $q \to 0$ [24,30,36].

The dynamic correlation length ξ_v ($v = xy, z$) was determined in NENP from an analysis of the wave vector dependencies of the static structure factors around the antiferromagnetic wave vector [124,125]. Results are reported in Fig. 21 for the in-plane fluctuations. Although it seems difficult to distinguish between a simple lorentzian function and a square-root lorentzian function in this range of q values, the experimental results for NENP suggest in both cases a finite value for the dynamical correlation length ξ_{xy}. The best fit to the theoretical prediction gives a reduced value $\xi_{xy}/d \approx 8$, which can be well understood from the relation $\xi_{xy} \approx c/\Delta_{xy}$. Quite similarly, the relation $\xi_z \approx c/\Delta_z$ is also verified from an analysis of the energy integrated intensity, with $\xi_z/d \approx 4$.

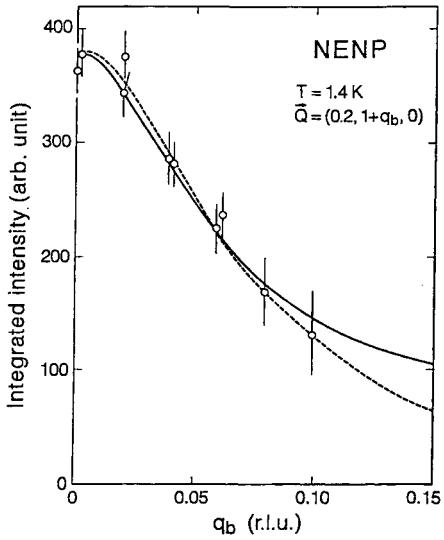

Fig. 21. Wave vector dependencies of the integrated intensity in NENP. The solid line is a fit to the theoretical square-root lorentzian prediction. Taken from Ref. [124].

In the weakly anisotropic Haldane compounds $AgVP_2S_6$ and YBANO, the measured correlation lengths, respectively 5.5 [100] and 6.9 [130], are in satisfactory agreement with the predicted value for the isotropic chain, $\xi/d \approx 6$.

2.5.1.3 Temperature Dependencies of Gaps and Damping

Thermal effects on spin dynamics were investigated in NENP and YBANO by means of INS experiments. The two interesting features observed in NENP are summarized in Fig. 22. First, the energy of the gap mode increases slightly when the temperature increases. Secondly, in addition to this shift in energy, a strong damping of the magnetic excitation is observed. Quite similar features have been observed in YBANO [130]. The increase of the gap on increasing T was also observed in $CsNiCl_3$ [131] and NINAZ [132]. For the quantum nonlinear σ model, Jolicoeur 7 Golinelli derived in the isotropic case the low-T dependence $\Delta(T) = \Delta_0 + (\alpha T)^{1/2} \exp(-\Delta_0/T)$ which

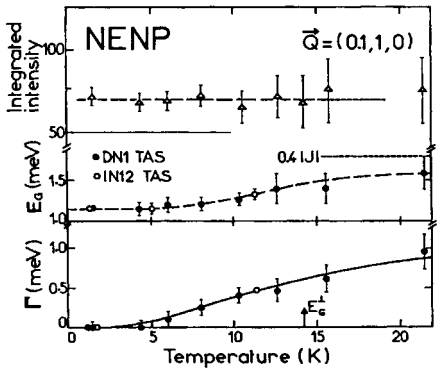

Fig. 22. Temperature dependencies of the gap, the damping and the integrated intensity in NENP. The solid line is a calculation as described in the text. After Ref. [72].

is in good agreement with the measurements in YBANO [130] and NINAZ [132], but with an α value smaller than the predicted one, $\alpha = 2\pi\Delta_0$. The experimental data on the damping of the magnetic excitations in NENP [72] are quite consistent with the activated behavior $\Gamma_n = \Gamma_{n0}\exp(-\Delta_n/T)$. As shown in Fig. 22, the data for the lowest energy mode are well fitted to this exponential law (solid curve) with $\Delta_{xy} \approx 14\,\mathrm{K}$ and $\Gamma_0 \approx 20\,\mathrm{K}$. For NINAZ the corresponding values obtained are $\Delta_{xy} \approx 42\,\mathrm{K}$ and $\Gamma_0 \approx 24\,\mathrm{K}$ [132].

2.5.1.4 Field Dependencies of Gaps

A magnetic field applied on a Haldane system suppresses the gap and restores a conventional ground state above the characteristic field $H_c = \Delta/g\mu_B$ (see Section 4.3). The effect of a magnetic field is to split the Haldane triplet and the energy of one state of this triplet is expected to vanish at a critical value H_c^y which depends, in case of anisotropy, on the field orientation. Quantum field theory treatments [59,60,133] and numerical calculations [128] have proposed expressions for the field dependencies of the gaps, $\Delta_n(H)$ [59,60] and for their respective polarizations [133]. On the experimental side, a complete and consistent set of data has been collected on NENP from both INS [124,126] and ESR [134–136] measurements on single crystals, in agreement with the theoretical predictions.

Inelastic neutron scattering allowed a direct determination of the field dependencies of the gaps Δ_n for configurations of the field both parallel (up to 5 T) and perpendicular (up to 12 T) to the chain axis [126,127,137]. Scans in energy recorded at several values of the field applied along the chain axis have shown the Zeeman splitting of gap-modes Δ_1 and Δ_2 associated with xy fluctuations. The third gap Δ_3 associated with z fluctuations, has never been measured within this configuration of the field. This mode is expected to remain roughly constant [59,60]. The experimental field dependencies of the various modes are shown in Fig. 23, with the field-theory predictions calculated from Eq. (18) [128,133]:

$$\Delta_{1,2}(H_z) \approx \frac{\Delta_x + \Delta_y}{2} \mp \sqrt{\left(\frac{\Delta_x - \Delta_y}{2}\right)^2 + (g_z\mu_B H_z)^2} \qquad (18)$$

$$\Delta_3(H_z) \approx \Delta_z$$

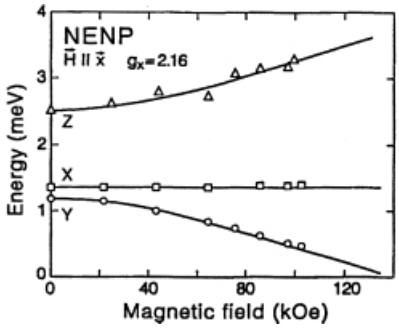

Fig. 23. Field dependencies of gaps in NENP at the antiferromagnetic point for $\vec{H}//b$. The solid lines are calculations as described in the text.

As first pointed out by Golinelli et al. [128], these expressions are formally identical to those derived from a simple perturbative treatment of the $S = 1$ anisotropic antiferromagnetic chain under field. The experimental behavior is quantitatively accounted for by the theory. The critical field, within this configuration of the field, is essentially controlled by the xy gaps and is expressed as [133]: $H_c^z = \sqrt{\Delta_x \Delta_y}/g_z\mu_B \approx \Delta_{xy}/g_z\mu_B$.

From the experimental values $\Delta_{xy} \approx 1.25\,\text{meV}$ and $g_z \approx 2.08$, which result from the best fit of the experimental data to Eq. (18), a critical field is calculated which is in quantitative agreement with high-field magnetization and specific heat measurements [115,138]. In the configuration for which the magnetic field is applied perpendicular to the chain axis, the situation turns out to be more complex. The obtained field dependencies of the various gaps are summarized in Fig. 24. Again mode 1 is found to soften, but in contrast to the previous field configuration, mode 2 is now found to be weakly field-dependent, whereas mode 3 is found to increase continuously in the same range of field [124]. In Fig. 24, the solid lines result from a calculation based on the fermionic field-theory treatment extended by Affleck in order to take into account the in-plane anisotropy term [59,133], according to Eq (19) (H/x):

$$\begin{aligned} \Delta_{1,3}(H_x) &\approx \frac{\Delta_z + \Delta_y}{2} \mp \sqrt{\left(\frac{\Delta_z - \Delta_y}{2}\right)^2 + (g_x\mu_B H_x)^2} \\ \Delta_2(H_x) &\approx \Delta_x \end{aligned} \tag{19}$$

Again the experimental behavior is quantitatively accounted for by the fermionic field-theory, suggesting that the elementary excitations of an Haldane-gap system are more likely fermions than bosons, at least in this range of field values. This point of view is strongly supported by the "spin-zero defect" approach [22,23]. The critical field at which the lowest energy gap $\Delta_1(H_x)$ vanishes is now given by the relation: $H_c^x \approx \sqrt{\Delta_z \Delta_y}/g_x\mu_B$. As previously mentioned, the critical field depends on both gaps, Δ_x and Δ_y. From the experimental values $\Delta_y \approx 1.16\,\text{meV}$, $\Delta_z \approx 2.5\,\text{meV}$ and $g_x \approx 2.16$, we estimate a critical field $H_c^x \approx 13.6\,\text{T}$, slightly larger than the determination obtained from high-field magnetization measurements [138], but in quantitative agreement with the high-field specific heat [115]. However, when approaching the critical field, a departure from Eq. (19) was observed [137]. It shows the imperfect closure of the gap due to the effect of staggered fields.

The determination of polarizations of the various modes is an additional important test for the theory. In the configuration where the field is applied parallel to the chain axis, the axial symmetry is conserved and no important changes are expected for symmetry reasons: modes 1 and 2 are xy-polarized, whereas mode 3 remains z-polarized. In the other configuration, the polarization of modes is predicted to change with the field, due to the symmetry breaking induced by the field. Affleck [133] has given analytical expressions for the field dependencies of the various polarization factors $P_{nv}(H)$ using the bosonic field-theory treatment. In the real case where the field is applied along the x axis, the 1 and 3 branches should display mixed yz polarizations, whereas mode 2 is expected to remain polarized along the x direction. The experimental data obtained with NENP are in good agreement with

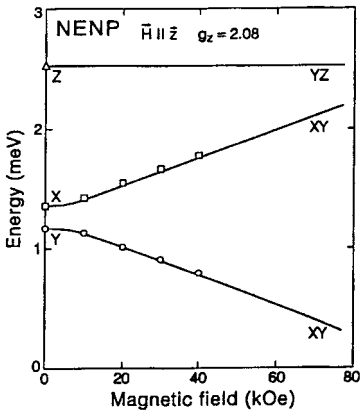

Fig. 24. Field dependencies of gaps in NENP at the antiferromagnetic point for fields perpendicular to the chain axis. The solid lines are calculations as described in the text.

these theoretical predictions, especially for mode 3. This is well illustrated by the comparison between the neutron data and the theoretical dependencies obtained by Affleck, shown in Fig. 25.

Further information on the field dependencies of gaps has been obtained from ESR measurements [134–136]. Magnetic transitions for which the absorption of energy is realized without wave vector transfer (i. e. $\Delta q = 0$) can be probed by ESR. Two types of transitions are expected to be observed: those induced from the ground state and those induced between excited states, the former corresponding to excitations at $q = 0$, whereas the latter can be generated anywhere in the Brillouin zone. The first ESR measurements in NENP have been carried out by Date and Kindo [134] in a field perpendicular to the chain axis, at a fixed frequency, $\nu = 47\,\mathrm{GHz} \approx 0.19\,\mathrm{meV}$, corresponding precisely to the difference between the two first modes observed by INS. The fact that the absorption intensity decreases at low temperature has been considered as proof that these transitions were arising

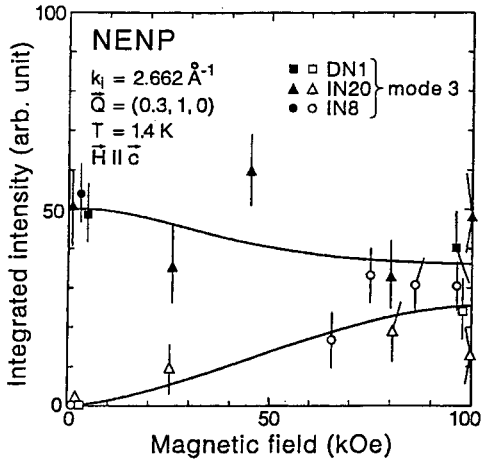

Fig. 25. Field dependencies of polarizations for mode 3 in NENP, showing the mixing between the y and z polarizations.

mainly from excited states and not from the ground state. A more systematic and accurate study has been undertaken at higher frequencies by Brunel et al. [136], for configurations of the field $\vec{H}//a$, $\vec{H}//b$ and $\vec{H}//c$. Fig. 26 shows a comparison between the observed ESR transitions, the calculated energy level diagram at the antiferromagnetic point [133] and the INS data. Except near the critical field where small deviations are observed, there is a quite good agreement between the experimental data and the theoretical results, which confirms the interpretation in terms of transitions between excited states at $q = k_{\mathrm{AF}}$ [133,136]. This is also clearly shown from the temperature dependencies of the integrated intensities of ESR signals [136], which are found to follow exponential dependencies at low temperatures, $\exp(-\Delta_1(H)/k_{\mathrm{B}}T)$. In addition these ESR measurements have provided determinations of critical fields $H_{\mathrm{c}}^x \approx 14\,\mathrm{T}$, $H_{\mathrm{c}}^y \approx 13.5\,\mathrm{T}$, $H_{\mathrm{c}}^z \approx 10\,\mathrm{T}$ (using $g_x = 2.13 \pm 0.06$, $g_y = 2.38 \pm 0.1$ and $g_z = 2.11 \pm 0.06$) in good agreement with the neutron results.

In addition to these transitions induced between excited states, ESR lines associated with transitions from the singlet ground state were observed for the first time by far infrared spectroscopy in NENP by Lu et al. [135]. The quite different nature of these transitions was demonstrated by the temperature dependence of their intensity, which decreases rapidly with increasing temperature, reflecting the depopulation of the ground state [139]. Taking into account the correct crystal symmetry of NENP (see Fig. 13), Mitra and Halperin [140] have derived a slightly different spin-hamiltonian which could explain the high-field ESR spectrum in NENP. In addition, the presence of a staggered anisotropic g tensor produces a staggered field when a uniform magnetic field is applied, consequently preventing the gap from vanishing at H_{c}.

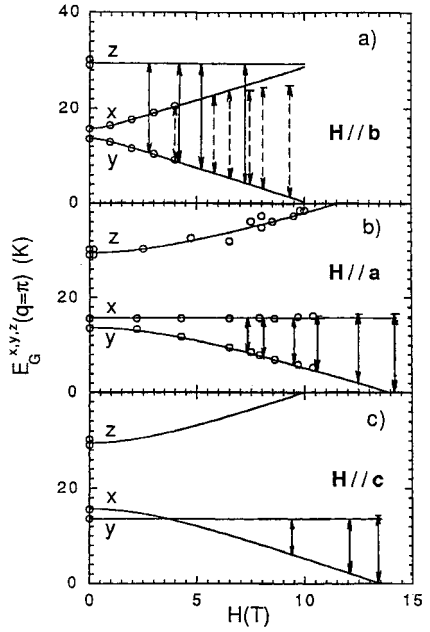

Fig. 26. Comparison between the observed ESR transitions in NENP (double arrows) and the energy level diagram at the antiferromagnetic point as a function of field, for different field orientations. Taken from Ref. [136].

2.5.2 Spin Dynamics at Low Energy ($E \ll \Delta$)

As shown in Section 5.1, the experimental data on spin dynamics at intermediate energies are in good agreement with theory. Specific features of a Haldane system, such as the triplet nature of the first excited state, the presence of gaps in the magnetic excitation spectrum or the effects of a magnetic field have been unambiguously identified in a large number of compounds. However a fundamental characteristic of such systems concerns the disappearance of all magnetic fluctuations at low energy when the temperature decreases to zero (i. e. $T \ll \Delta/k$). This is a direct consequence of the singlet ground state at $T = 0$. The magnetic fluctuations at low energy can be probed very accurately from NMR or quasi-elastic neutron scattering.

The low frequency spin dynamics has been exhaustively studied in NMR experiments performed on several Haldane gap compounds, through measurements of the spin-lattice relaxation time, T_1. As is well known, the relaxation rate T_1^{-1} is related to the dynamic structure factors $S_{n\nu}(q, E)$ defined by Eq. (15):

$$T_1^{-1} \approx \sum_q \sum_{n\nu} (A_\nu(q))^2 S_{n\nu}(q, E_N) \tag{20}$$

where the $A_\nu(q)$ are the Fourier transforms of the hyperfine coupling constants and where the Larmor energy E_N is expected to be much smaller than the characteristic energy scale Δ (typically $E_N \approx 10^{-3}\Delta$ to $10^{-5}\Delta$). Assuming a damped oscillator function for the dynamic susceptibility $\chi(q, E)$ around $q \approx k_{AF}$, for sufficiently low temperatures one could expect $T_1^{-1} \propto T\Gamma_1 \propto T \exp(-\Delta_1/k_B T)$. Within this approach, the spin-lattice relaxation rate should exhibit an activated T dependence with an activation energy likely to be equal to the lowest energy gap, Δ_1.

On the experimental side, accurate data were obtained by several groups [141–144] from measurements of the proton spin-lattice relaxation rate in the prototype system NENP. As an illustration, Fig. 27a shows the dependencies with temperatures of T_1^{-1} obtained by Goto et al. [141] at operating frequencies ν_N between 4 MHz ($E_N \approx 1.6 \times 10^{-5}$ meV) and 21 MHz ($E_N \approx 0.8 \times 10^{-4}$ meV) in fields parallel to the chain axis. In this case, as well as for perpendicular fields, the relaxation rates are found to be continuously decreasing over more than two orders of magnitude between 50 K and 5 K. This behavior supports the disappearance of all magnetic fluctuations at very low energy and the existence of a singlet ground state in NENP. In Fig. 27a, the solid lines represent the best fit of the experimental data to the activation law, with an activation energy $\Delta_1/k_B \approx \Delta_{xy}/k_B \approx 14$ K, which is apparently consistent with previous determinations of the lowest energy gap in this compound. However the fit does not extend below 5 K since T_1^{-1} exhibits a rounded maximum around 3 K, attributed to the presence of magnetic impurities (intrinsic or extrinsic). Very similar results were reported by Gaveau et al. [143].

The data for NENP as well as for TMNIN [80,145] were obtained in a relatively narrow range of temperatures which were not very small with respect to the gap. This prevents quantitative comparison with theoretical models. In contrast, reliable T_1^{-1} measurements have been performed over a wide range of low temperatures in the large gap inorganic compounds YBANO [104] and $AgVP_2S_6$ [146], respectively

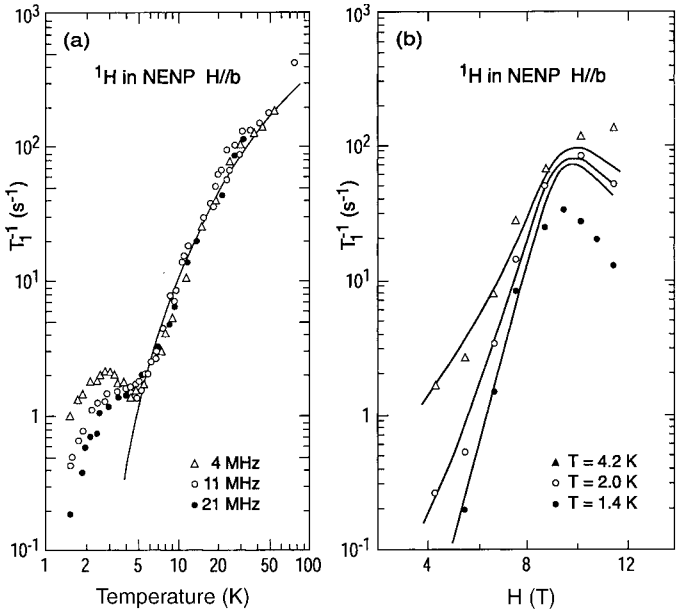

Fig. 27. (a) Temperature dependencies of the spin-lattice relaxation rate for $H//b$, showing the disappearance of magnetic fluctuations at low temperature. The solid line is calculated from exponential dependencies as described in the text. (After Ref. [80].) (b) Field dependencies of below 4.2 K. The solid lines represent calculations as described in the text. After Ref. [144].

on ^{89}Y and on ^{31}P and ^{51}V. An activated T dependence of T_1^{-1} was observed over more than two decades but with an activation energy $\Delta(T_1)$ definitely larger than Δ_1 obtained from static susceptibility or inelastic neutron scattering measurements; $\Delta(T_1)/\Delta_1 \approx 1.5$ and 1.3 respectively for YBANO and $AgVP_2S_6$. This discrepancy which was also observed in two-leg spin ladder systems [147] remained unexplained by theory [105,148] until the work of Damle and Sachdev [149] on the dynamic properties at $T > 0$ of the Heisenberg chains with a gap, Δ. These authors showed that the low-T spin diffusion constant, D_s, has an exponential T dependence, $\exp(\Delta/k_B T)$. It leads through the relation $T_1^{-1} \propto T\chi/(D_s)^{1/2}$ to an activated temperature dependence of T_1^{-1} with an activation energy 1.5Δ instead of Δ, in good agreement with experiment [104,146].

The field dependencies of T_1^{-1} in NENP have been extensively studied [143,144]. Characteristic data obtained at low temperature by Fujiwara et al. [144], in the configuration $H//b$ are shown in Fig. 27b. At temperatures $T \ll \Delta/k_B$, the relaxation rate increases with the field and exhibits a maximum at about 9.5 T, which corresponds precisely to the critical field observed in other experiments. This behavior reflects the increase of the low energy fluctuations arising from the softening of the lower energy gap Δ_1 under field, predicted theoretically and observed by INS. An example of comparison between experiment and theory is given in Fig. 27b, where the solid

lines have been obtained following the analysis procedure introduced by Gaveau et al. [143]. Quite similar behavior of $1/T_1$ was observed in TMNIN [145].

In the case of large gap Haldane chains, i. e. $\Delta \gg g\mu_B H$, a relatively smooth variation of $1/T_1$ versus H was observed. The experimental data for the ^{31}P relaxation rate [146] in $AgVP_2S_6$ were fitted to $1/T_1 = A + BH^{1/2}$ in the T range $0.4 \leq k_B T/\Delta \leq 1$, which is characteristic of 1D diffusive spin dynamics. At lower temperatures, $1/T_1$ departs from the diffusive power law, the experimental data being in better agreement with a logarithmic divergence with H decreasing to zero. These relaxation rate measurements are in good agreement with the theoretical predictions of Damle and Sachdev [149] in the high-T range. The low-T data were fitted by the same authors by introducing a cut off in the long time tail of the autocorrelation function. This cut off is a simple way for taking into account both interchain coupling and intrachain anisotropy which are expected to contribute to the spin dissipation rate.

2.6 Effect of Chain Breaking by Impurities

One-dimensional magnetic systems are very sensitive to impurities substituted for magnetic ions because they break the exchange link within the magnetic chain. In gapless quasi 1D AF, the main effect of impurities is to reduce the correlation length and thus the 3D ordering temperature and to bring an additional contribution to the susceptibility. For nonmagnetic impurities, which provide a full break of the exchange path, this additional contribution is afforded by the finite chain units with an odd number of spins which behave at low temperature like a unique uncompensated free spin. These impurity effects in classical 1D AF have been well evidenced in impurity-doped TMMC [150]. The case of Haldane gap compounds is quite different since the correlation length remains finite at low T. The ground state of the $S = 1$, HAF open chain of L spins studied theoretically by Kennedy [151], consists in a singlet and a triplet. Their energy splitting decays exponentially to zero as $\exp(-L/\xi_0)$ where ξ_0 is the spin–spin correlation length of the infinite Haldane chain. This fourfold degeneracy suggests that the open chain has a spin-1/2 degree of freedom at each end. A simple physical interpretation can be given from the VBS picture of the Haldane phase. In the latter, the spin $S = 1$ at each lattice site is obtained by a combination of two $S = 1/2$ spins and the ground state is represented by the product of valence bonds between all pairs of neighboring spins. If a host atom is substituted by a nonmagnetic impurity, the valence bonds are broken at the impurity site. This gives rise to two free $S = 1/2$ spins, each located at each chain end adjacent to the impurity site [152] as shown in Fig. 28. To this $S = 1/2$ edge spin, a staggered magnetic moment which has an exponential decay $\exp(-j/\xi_0)$, where j is the site from the chain end is associated [33,153,154].

Experimentally, the effect of impurities was first observed on the magnetic susceptibilities of Cu-doped NENP single-crystals with low Cu atomic concentration (i. e. $x = 3.6 \times 10^{-3}$ and 6.2×10^{-3}) [74]. Below 5 K, the susceptibility is dominated by

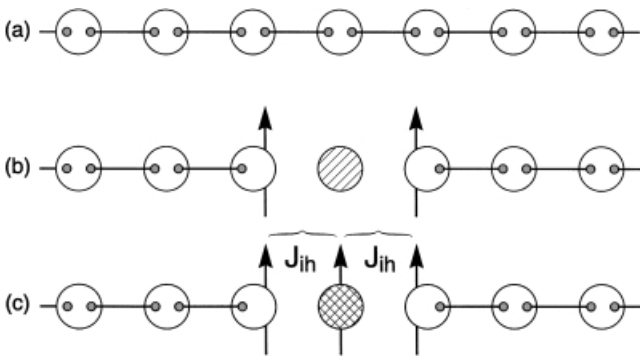

Fig. 28. (a) Valence bond solid (VBS) representation for the $S = 1$ 1D Heisenberg antiferromagnet. The larger circles show the atomic sites and the smaller circles the $S = 1/2$ spins. The lines represent valence bonds. (b) A host atom is substituted by a nonmagnetic impurity resulting in two $1/2$ spins at host sites neighboring the impurity. (c) Same situation as (b) for a $S = 1/2$ magnetic impurity corresponding to the case of Cu-doped NENP. From Ref. [152].

the impurity contribution, roughly varying as T^{-1}. This contribution is much larger than that attributed to the free Cu (II) ion with $S = 1/2$, due to the effect of chain ends. Furthermore, it does not strongly depend on field orientation, in spite of the large single-ion anisotropy of Ni (II) in NENP. This fully supports edge magnetic moments associated with spins $S = 1/2$, which have nearly isotropic magnetic behavior. A more detailed study has been performed by Hagiwara et al. [152], using the very sensitive technique of electron spin resonance (ESR). A complex ESR spectrum, well explained by a model of three $S = 1/2$ spins: a central Cu (II) spin weakly coupled to two chain end spins (Fig. 28), is observed at very low temperature. Thermal spin excitations lead to rapid vanishing of this ESR signal at $T \approx \Delta_{xy}/2k_{\mathrm{B}}$ [155]. The high-field magnetization curve of strongly Cu-doped NENP samples is also consistent with the VBS model of chain ends [75,156]. Furthermore, a careful analysis of the magnetization behavior near the critical field reveals an increase of the energy gap [75] in agreement with the Monte Carlo results on finite chains (see Fig. 2). The low-temperature heat capacity of Cu-doped NENP [157] is also in agreement with the model of three weakly coupled spins of $1/2$, using the parameters determined by ESR. Glarum et al. [158] also performed ESR experiments, on samples of NENP doped by diamagnetic impurities. These are well interpreted using the model of two independent free spins with $S = 1/2$. Similarly, the susceptibility and magnetization measurements done at low temperature in $Ni_{1-x}Mg_xNiCl_3$ [159] are quite consistent with two $S = 1/2$ degrees of freedom induced by each Mg ion substituted to Ni. Interestingly, the decrease of the 3D Néel temperature produced by the Mg impurities reveals the Haldane behavior of $CsNiCl_3$. The experiments on YBANO [160] and TMNIN [161] with Zn substitution are less clear since the heat capacity was interpreted by $S = 1$ low-lying excitations but also, for Zn-doped YBANO, by $S = 1/2$ excitations [162].

As already mentioned, the $S = 1/2$ degrees of freedom of the $S = 1$ open Haldane chain should spread over several spin sites. They are localized at the ends of the chain [163] and develop a staggered magnetization which decays as the spin–spin correlation function of the infinite chain. Tetoldi et al. [164] were the first to perform imaging of the staggered magnetization in $Y_2BaNi_{1-x}Mg_xO_5$ by ^{89}Y NMR, and obtained a good agreement with the theoretical predictions for the mean value of the edge spins ($S = 1/2$) and the correlation length.

The $S = 2$ finite chain system $CsCr_{1-x}Mg_xCl_3$ was investigated at low T by susceptibility and ESR measurements [165]. The experiments revealed the existence of $S = 1$ degrees of freedom, in agreement with the VBS model and with Monte Carlo calculations in $S = 2$ antiferromagnetic Heisenberg chains [166].

2.7 Conclusion

For a few years following its announcement, the Haldane conjecture was strongly contested because the drastic difference between integer and noninteger spin chains was not anticipated and had not been experimentally observed previously. This conjecture is now firmly supported both by increasingly accurate numerical simulations on finite $S = 1$ and 2 antiferromagnetic chains and by experiments on real compounds which are good approximations to ideal models. Simple theoretical models such as the valence-bond solid (VBS) have provided a physical insight into the Haldane phase. Some of them are of interest for physical problems other than those of quantum chains, for instance, for surface phase transitions [19].

A remarkable feature is the stability of the Haldane phase to perturbations such as chain breaking by impurities. The latter create impurity states within the gap without appreciably changing the gap value. This is markedly different from the spin-Peierls phase which is easily destroyed by impurities at low concentrations [167]. In both Haldane and spin-Peierls phases, staggered $S = 1/2$ edge spins are induced by chain breaks. In the doped spin-Peierls compound $CuGeO_3$, these order into a 3D AF phase, even at very low impurity concentrations, under the effect of interchain interactions. This attractive phenomenon of "order induced by disorder" has not yet been observed in Haldane compounds.

Interesting recent developments concern the effect of staggered fields on the Haldane compounds. In the R_2NiO_5 compounds, the magnetic rare earth ions R(III) induce staggered fields on the Ni (II) chains. The latter increase the gap and give rise to a 3D AF phase at low temperature [168]. Quite generally, the competition between the Haldane phase and other phases of different physical origin remains of interest. An example is the $S = 1$ AF chain with exchange alternation. Affleck and Haldane predicted [169] that the gap vanishes for a critical value of alternation, estimated to about 0.26 from numerical calculations [170], but there are still few experiments on this topic [171]. Other theoretically studied questions are the effects of frustration by second neighbor interaction [172] and that of bond randomness [173], which deserve further experimental investigation.

Finally, one should mention the strong similarity between the $S = 1$ Heisenberg chain and the $S = 1/2$ Heisenberg ladder [174] which opens a large field of new experimental investigations.

Acknowledgments

The authors dedicate this chapter to the memory of their dear friend J. Rossat-Mignod. They wish to thank Drs T. Jolicoeur and I. Zaliznyak, for illuminating discussions and suggestions about the theory of Haldane gap systems and Dr. M. Mulloy for critical reading of the manuscript. They are grateful to their co-workers in Haldane gap experiments, in particular to Drs C. Vettier, W.A.C. Erkelens and V. Gadet. The help of Miss A. Charrier in the preparation of the manuscript was greatly appreciated.

References

[1] L.J. de Jongh, A.R. Miedema, *Adv. Phys.* **1974**, *23*, 1–260.
[2] J.C. Bonner in *Magneto-structural Correlations in Exchange Coupled Systems*, (Eds.: R.D. Willett, D. Gatteschi, O. Kahn), D. Reidel, **1985**, *NATO ASI Series 140*, 157–205.
[3] F.D.M. Haldane, *Phys. Lett. A* **1983**, *93*, 464–466; *Phys. Rev. Lett.* **1983**, *50*, 1153–1156.
[4] R. Botet, R. Jullien, M. Kolb, *Phys. Rev. B* **1983**, *28*, 3914–3921; R. Botet, R. Jullien, *Phys. Rev. B* **1983**, *27*, 613–615.
[5] J.P. Renard, M. Verdaguer, L.P. Regnault, W.A.C Erkelens, J. Rossat-Mignod, W.G. Stirling, *Europhys. Lett.* **1987**, *3*, 945–951.
[6] I. Affleck, *J. Phys. Cond. Matt.* **1989**, *1*, 3047–3072.
[7] J. des Cloizeaux, J.J. Pearson, *Phys. Rev.* **1962**, *128*, 2131–2135.
[8] T. Yamada, *Progr. Theoret. Phys. Jpn.* **1969**, *41*, 880–890.
[9] L. A. Takhtajan, *Phys. Lett. A* **1982**, *87*, 479–482.
[10] H.M. Babujian, *Phys. Lett. A* **1982**, *90*, 479–482.
[11] B. Sutherland, *Phys. Rev. B* **1975**, 12, 3795–3805.
[12] I. Affleck, T. Kennedy, E.H. Lieb, H. Tasaki, *Phys. Rev. Lett.* **1987**, *59*, 799–802; *Comm. Math. Phys.* **1988**, *115*, 477–528.
[13] D.P. Arovas, A. Auerbach, F.D.M. Haldane, *Phys. Rev. Lett.* **1988**, *60*, 531–534.
[14] M. N. Barber, M.T. Batchelor, *Phys. Rev. B* **1989**, *40*, 4621–4626.
[15] A.V. Chubukov, *Phys. Rev. B*, **1991**, *43*, 3337–3344.
[16] K. Nomura, S. Takada, *J. Phys. Soc. Jpn.* **1991**, *60*, 389–392.
[17] P. W. Anderson, *Mater. Res. Bull.* **1973**, *8*, 153–160.
[18] I. Affleck, E. Lieb, *Lett. Math. Phys.* **1986**, *12*, 57–69.
[19] M. den Nijs, K. Rommelse, *Phys. Rev. B* **1989**, *40*, 4709–4734.
[20] T. Kennedy, H. Tasaki, *Phys. Rev. B* **1992**, *45*, 304–307.
[21] U. Schollwöck, T. Jolicoeur, T. Garel, *Phys. Rev. B* **1995**, *54*, 4038–4051.
[22] G. Gomez-Santos, *Phys. Rev. Lett.* **1989**, *63*, 790–793.
[23] H. Köhler, R. Schilling, *J. Phys.: Condens. Matter* **1992**, *4*, 7899–7912.

[24] S.V. Meshkov, *Phys. Rev. B* **1993**, *48*, 6167–6178.
[25] M.P. Nightingale, H.W. Blöte, *Phys. Rev. B* **1986**, *33*, 659–661.
[26] K. Kubo, S. Takada, *J. Phys. Soc. Jpn.* **1986**, *55*, 438–441.
[27] H. Betsuyaku, *Phys. Rev. B* **1987**, *36*, 799–802.
[28] M. Takahashi, *Phys. Rev. B* **1988**, *38*, 5188–5191.
[29] M. Uchinami, *Phys. Rev. B* **1989**, 39, 4554–4562.
[30] K. Nomura, *Phys. Rev. B* **1989**, *40*, 2421–2425.
[31] T. Sakai, M. Takahashi, *Phys. Rev. B* **1990**, *42*, 1090–1092.
[32] E.S. Sorensen, I. Affleck, *Phys. Rev. Lett.* **1993**, *71*, 1633–1636.
[33] S.R. White, D.A. Huse, *Phys. Rev. B* **1993**, *48*, 3844–3852.
[34] I. Affleck, R.A. Weston, *Phys. Rev. B*, **1992**, *45*, 4667–4671.
[35] M. Takahashi, *Phys. Rev. Lett.* **1989**, *62*, 2313–2316.
[36] O. Golinelli, T. Jolicoeur, R. Lacaze, *J. Phys.: Condens. Matter.* **1983**, *5*, 1399–1410.
[37] For the $S = 1$, HAF, the spin wave velocity is probably larger than $2J$. The numerical result of Ref. 29 is $c = 2.49J$, leading to $c/\Delta = 6.06$ in excellent agreement with $\xi_0 = 6.03$ [33].
[38] U. Schollwöck, T. Jolicoeur, *Europhys. Lett.* **1995**, *30*, 493–498.
[39] U. Schollwöck, O. Golinelli, T. Jolicoeur, *Phys. Rev. B* **1996**, *54*, 4038–4051.
[40] S.T. Chui, K.B. Ma, *Phys. Rev. B*, **1984**, *29*, 1287–1291.
[41] U. Glaus, T. Schneider, *Phys. Rev. B* **1984**, *30*, 215–225.
[42] J.B. Parkinson, J.C. Bonner, *Phys. Rev. B* **1985**, *32*, 4703–4724.
[43] H.J. Schulz, *Phys. Rev. B* **1986**, *34*, 6372–6385.
[44] J. Solyom, J. Timonen, *Phys. Rev. B* **1989**, *40*, 7150–7161.
[45] K. Nomura, *Phys. Rev. B* **1989**, *40*, 9142–9146.
[46] T. Sakai, M. Takahashi, *Phys. Rev. B* **1990**, *42*, 4537–4543.
[47] H. Tasaki, *Phys. Rev. Lett.* **1991**, *66*, 798–801.
[48] T. Sakai, M. Takahashi, *Phys. Rev. B* **1991**, *44*, 10385–10388.
[49] O. Golinelli, T. Jolicoeur, R. Lacaze, *Phys. Rev. B* **1992**, *45*, 9798–9805.
[50] J. C. Bonner, *J. Appl. Phys.* **1987**, *61*, 3941–3946.
[51] O. Golinelli, T. Jolicoeur, R. Lacaze, *Phys. Rev. B* **1992**, *46*, 10854–10857.
[52] Y.A. Kosevich, A.V. Chubukov, *Sov. Phys. JETP* **1986**, *64*, 654–667.
[53] I. Affleck, *Phys. Rev. Lett.* **1989**, *62*, 474–477; *Phys. Rev. Lett.* **1990**, *65*, 2477–2481.
[54] M. Takahashi, *Phys. Rev. B* **1989**, *40*, 2494–2501.
[55] M. Azzouz, B. Douçot, *Phys. Rev. B* **1993**, *47*, 8660–8666.
[56] T. Sakai, M. Takahashi, *Phys. Rev. B* **1991**, *43*, 13383–13393.
[57] T. Sakai, M. Takahashi, *J. Phys. Soc. Jpn.* **1993**, *62*, 750–758.
[58] T. Sakai, M. Takahashi, *Phys. Rev. B* **1998**, *57*, R8091–8094.
[59] I. Affleck, *Phys. Rev. B* **1990**, *41*, 6697–6702; *Phys. Rev. B* **1991**, *43*, 3215–3222.
[60] A.M. Tsvelik, *Phys. Rev. B* **1990**, *42*, 10499–10504.
[61] T. Sakai, *Phys. Rev. B* **1998**, *58*, 6268–6272.
[62] K. Okamoto, K. Nomura, *Phys. Lett. A* **1993**, *169*, 433–435.
[63] L.N. Bulaevskii, *Sov. Phys. JETP* **1967**, *17*, 684–687; *Sov. Phys. Solid State* **1969**, *11*, 921–924.
[64] W. Duffy, Jr, K.P. Barr, *Phys. Rev.* **1968**, *65*, 647–654.
[65] M.C. Cross, D.S. Fisher, *Phys. Rev. B* **1979**, *19*, 402–419.
[66] J.C. Bonner et al, *J. Appl. Phys.* **1979**, *50*, 1808–1812.
[67] K. Hida, *Phys. Rev. B* **1992**, *45*, 2207–2212; *Phys. Rev. B* **1992**, *46*, 8268–8275.
[68] W.E. Hatfield, W.E. Estes, W.E. Marsh, M.W. Pickens, L.W. ter Haar, R.R. Weller in *Extended Linear Chain Compounds Vol. 3* (Ed.: J.S. Miller), Plenum Press, New York, **1983**, pp 43–142.

[69] A. Achiwa, *J. Phys. Soc. Jpn.* **1969**, *27*, 561–574.
[70] P.B. Johnson, J.A. Rayne, S.A. Friedberg, *J. Appl. Phys.* **1979**, *50*, 1853–1855.
[71] A. Meyer, A. Gleizes, J.J. Girerd, M. Verdaguer, O. Kahn, *Inorg. Chem.* **1982**, *21*, 1729–1739.
[72] J.P. Renard, M. Verdaguer, L.P. Regnault, W.A.C. Erkelens, J. Rossat-Mignod, J. Ribas, W.G. Stirling, C. Vettier, *J. Appl. Phys.* **1988**, *63*, 3538–3542.
[73] T. Yosida, M. Fukui, *J. Phys. Soc. Jpn.* **1992**, *61*, 2304–2308.
[74] J.P. Renard, L.P. Regnault, M. Verdaguer, *J. Phys. (Paris)* **1988**, *49*, C8–1425–1429.
[75] J.P. Renard, V. Gadet, L.P. Regnault, M. Verdaguer, *J. Magnet. Magnet. Mater.* **1990**, *90–91*, 213–216.
[76] M. Yamashita, K. Inoue, T. Ohishi, H. Miyamae, T. Takeuchi, T. Yosida, *Synthetic Metals* **1995**, *71*, 1961–1964.
[77] T. Takeuchi, T. Yosida, K. Inoue, M. Yamashita, T. Kumada, K. Kindo, S. Merah, M. Verdaguer, J.-P. Renard, *J. Magnet. Magnet. Mater.* **1995**, *140–144*, 1633–1634.
[78] M. Momfort, J. Ribas, X. Solans, M. F. Bardia, *Inorg. Chem.* **1996**, *35*, 7633–7638.
[79] Z. Honda, H. Asakawa, K. Katsumata, *Phys. Rev. Lett.* **1998**, *81*, 2566–2569.
[80] V. Gadet, M. Verdaguer, V. Briois, A. Gleizes, J.P. Renard, P. Beauvillain, C. Chappert, T. Goto, K. Le Dang, P. Veillet, *Phys. Rev. B* **1991**, *44*, 705–712.
[81] L.K. Chou, K.A. Abboud, D.R. Talham, W.W. Kim, M.W. Meisel, *Physica B* **1993**, *194–196*, 311–312.
[82] S.W. Cheong, A.S. Cooper, L.W. Rupp Jr., B. Batlogg, *Bull. Am. Phys. Soc.* **1992**, *37*, 116.
[83] J. Darriet, L.P. Regnault, *Solid State Commun.* **1993**, *86*, 409–412.
[84] S. Lee, P. Colombet, G. Ouvrard, R. Brec, *Mat. Res. Bull.* **1986**, *21*, 917–928; P. Colombet, S. Lee, G. Ouvrard, R. Brec, *J. Chem. Res. (S)* **1987**, 134–35.
[85] C. Bellitto, J.P. Renard, L.P. Regnault, *J. Magnet. Magnet. Mater.* **1991**, *102*, 116–120.
[86] G.E. Granroth, M.W. Meisel, M. Chaparala, T. Jolicoeur, B.H. Ward, D.R. Talham, *Phys. Rev. Lett.* **1996**, *77*, 1616–1619.
[87] W. Mori, F. Inoue, K. Yoshida, H. Nakayama, S. Takamizawa, M. Kishita, *Chem. Lett.* **1997**, 1219.
[88] G. de Munno, M. Julve, F. Lloret, J. Faus, M. Verdaguer, A. Caneschi, *Angew. Chem. Int. Ed. Engl.* **1993**, *32*, 1046–1048.
[89] J.J. Girerd, Y. Journeaux, O. Kahn, *Chem. Phys. Lett.* **1981**, *82*, 534–537.
[90] P.J. Haÿ, J.C. Thibeault, R. Hoffmann, *J. Am. Chem. Soc.* **1975**, *97*, 4884–4899.
[91] M.F. Charlot, O. Kahn, *Nouv. J. Chim.* **1980**, *4*, 567–576.
[92] O. Kahn, *Struct. Bonding* **1987**, *68*, 89–167.
[93] D. Guo, T. Kennedy, S. Mazumdar, *Phys. Rev. B* **1990**, *41*, 9592–9595.
[94] A. Gleizes, A. Meyer, M.A. Hitchman, O. Kahn, *Inorg. Chem.* **1982**, *21*, 2257–2263.
[95] F.J. Llewellyn, J.M. Waters, *J. Chem. Soc. A* **1962**, 3845–3848
[96] M.T. Hutchings, G. Shirane, B.J. Birgeneau, S.L. Holt, *Phys. Rev. B* **1972**, *5*, 1999–9595.
[97] T. Delica, K. Kopinga, H. Leschke, K.K. Mon, *Europhys. Lett.* **1991**, *15*, 55–61.
[98] G. Xu, J.F. DiTusa, T. Ito, K. Oka, H. Takagi, G. Broholm, G. Aeppli, *Phys. Rev. B* **1996**, *54*, R6827–6830.
[99] H. Mutka, J.L. Soubeyroux, G. Bourleaux, P. Colombet, *Phys. Rev. B* **1989**, *39*, 4820–4823.
[100] H. Mutka, C. Payen, P. Molinié, J.L. Soubeyroux, P. Colombet, A.D. Taylor, *Phys. Rev. Lett.* **1991**, *67*, 497–501.
[101] M. Troyer, H. Tsunetsugu, D. Würtz, *Phys. Rev. B* **1994**, *50*, 13315–13527.
[102] O. Avenel, J. Xu, J.S. Xia, M.F. Xu, B. Andraka, T. Lang, P.L. Moyland, W. Ni, P.J.C. Signore, C.M.C.M. Van Woerkens, E.D. Adams, G.G. Ihas, M.W. Meisel, S.E. Nagler,

N.S. Sullivan, Y. Takano, D.R. Talham, T. Goto, N. Fujiwara, *Phys. Rev. B* **1992**, *46*, 8655–8658.
[103] M. Takigawa, T. Asano, Y. Ajiro, M. Mekata, *Phys. Rev. B* **1995**, *52*, 13087–13090.
[104] T. Shimizu, D.E. MacLaughlin, P. C. Hammel, J. D. Thompson, S.-W. Cheong, *Phys. Rev. B*, **1995**, *52*, R9835–9838.
[105] T. Jolicoeur, O. Golinelli, *Phys. Rev. B* **1994**, *50*, 9265–9273.
[106] H. Igarashi, *J. Phys. Soc. Jpn.* **1985**, *54*, 516–528.
[107] J. Ferré, J.P. Jamet, C.P. Landee, K.A. Reza, J.P. Renard, *J. Phys. (Paris)* **1988**, *49*, C8–1441–1442.
[108] H.W.J. Blöte, *Physica B* **1975**, *79*, 427–466.
[109] T. de Neef, *Phys. Rev. B* **1976**, *13*, 4141–4158.
[110] H. Deguchi, M. Itoh, K. Takeda, *J. Phys. Soc. Jpn.* **1992**, *61*, 3470–3473.
[111] T. Takeuchi, H. Hori, T. Yosida, A. Yamagishi, K. Katsumata, J.P. Renard, V. Gadet, M. Verdaguer, M. Date, *J. Phys. Soc. Jpn.*, **1992**, *61*, 3262–3266.
[112] K. Katsumata, H. Hori, T. Takeuchi, M. Date, A. Yamagishi, J.P. Renard, *Phys. Rev. Lett.* **1989**, *63*, 86–89.
[113] Y. Ajiro, T. Goto, H. Kikuchi, T. Sakakibara, T. Inami, *Phys. Rev. Lett.* **1989**, *63*, 1424–1427.
[114] T. Takeuchi, M. Ono, H. Hori, T. Yosida, A. Yamagishi, M. Date, *J. Phys. Soc. Jpn.* **1992**, *61*, 3235–3261.
[115] T. Kobayashi, Y. Tabuchi, K. Amaya, Y. Ajiro, T. Yosida, M. Date, *J. Phys. Soc. Jpn.* **1992**, *61*, 1772–1776.
[116] Z. Honda, K. Katsumata, H. Aruga Katori, K. Yamada, T. Ohishi, T. Manabe, M. Yamashita, *J. Phys.: Condens. Matter.* **1997**, *9*, L83–87.
[117] Z. Honda, H. Asakawa, K. Katsumata, *Phys. Rev. Lett.* **1998**, *81*, 2566–2569.
[118] G. Muller, H. Beck, J.C. Bonner, *Phys. Rev. Lett.* **1979**, *43*, 75–78.
[119] W.J.L. Buyers, R.M. Morra, R.L. Armstrong, M.J. Hogan, P. Gerlach, K. Hirakawa, *Phys. Rev. Lett.* **1986**, *56*, 371–374.
[120] R.M. Morra, W.J.L. Buyers, R.L. Armstrong, K. Hirakawa, *Phys. Rev. B* **1988**, *38*, 543–555.
[121] Z. Tun, W.J.L. Buyers, R.L. Armstrong, K. Hirakawa, B. Briat, *Phys. Rev. B* **1990**, *42*, 4677–4681.
[122] M. Steiner, K. Kakurai, J.K. Kjems, D. Petitgrand, R. Pynn, *J. Appl. Phys.* **1987**, *61*, 3953–3955.
[123] K. Kakurai, M. Steiner, R. Pynn, J.K. Kjems, *J. Phys.: Condens. Matter* **1991**, *3*, 715–726.
[124] L.P. Regnault, J. Rossat-Mignod, J.P. Renard, *J. Magnet. Magnet. Mater.* **1992**, *104* and *107*, 869–870.
[125] S. Ma, C. Broholm, D.H. Reich, B.J. Sternlieb, R.W. Erwin, *Phys. Rev. Lett.* **1992**, *69*, 3571–3574.
[126] L.P. Regnault, C. Vettier, J. Rossat-Mignod, J.P. Renard, *Physica B* **1992**, *180* and *181*, 188–190.
[127] L.P. Regnault, I. Zaliznyak, J.P. Renard, C. Vettier, *Phys. Rev. B* **1994**, *50*, 9174–9187.
[128] O. Golinelli, T. Jolicoeur, R. Lacaze, *J. Phys.: Condens. Matter.* **1993**, *5*, 7847–7858.
[129] T. Yokoo, T. Sakaguchi, K. Kakurai, J. Akimitsu, *J. Phys. Soc. Jpn.* **1995**, *64*, 3651–3655.
[130] T. Sakaguchi, K. Kakurai, T. Yokoo, J. Akimitsu, *J. Phys. Soc. Jpn.* **1996**, *65*, 3025–3031.
[131] W.J.L. Buyers, Z. Tun, A. Harrison, J.A. Rayne, R.M. Nicklow, *Physica B* **1992**, *180* and *181*, 222–224.
[132] A. Zheludev, S.E. Nagler, S.M. Shapiro, L.K. Chou, D.R. Talham, M.W. Meisel, *Phys. Rev. B* **1996**, *53*, 15004–15009.
[133] I. Affleck, *Phys. Rev. B* **1992**, *46*, 9002–9008.

[134] M. Date, K. Kindo, *Phys. Rev. Lett.* **1990**, *65*, 1659–1662.
[135] W. Lu, J. Tuchendler, M. von Ortenberg, J.P. Renard, *Phys. Rev. Lett.* **1991**, *67*, 3716–3719.
[136] L.C. Brunel, T.M. Brill, I. Zaliznyak, J.P. Boucher, J.P. Renard, *Phys. Rev. Lett.* **1992**, *69*, 1699–1702.
[137] L.P. Regnault, J.P. Renard, *Physica B* **1997**, *234–236*, 541–543.
[138] T. Goto, H.A. Katori, Y. Ajiro, *J. Phys. Soc. Jpn.* **1992**, *61*, 4155–4163.
[139] W. Palme, H. Kriegestein, B. Luthi, T.M. Brill, T. Yosida, M. Date, *Int. J. Mod. Phys. B* **1993**, 1016.
[140] P.P. Mitra, B.I. Halperin, *Phys. Rev. Lett.* **1994**, *72*, 912–915.
[141] T. Goto, N. Fujiwara, T. Kohmoto, S. Maegawa, *J. Phys. Soc. Jpn.* **1990**, *59*, 1135–1138.
[142] J.P. Boucher, *Hyperfine Interactions* **1989**, *49*, 423–438.
[143] P. Gaveau, J.P. Boucher, L.P. Regnault, J.P. Renard, *Europhys. Lett.* **1990**, *12*, 647–652.
[144] N. Fujiwara, T. Goto, S. Maegawa, T. Kohmoto, *Phys. Rev. B* **1992**, *45*, 7837–7840; *Phys. Rev. B* **1993**, *47*, 11860–11869.
[145] P. Gaveau, J.P. Boucher, L.P. Regnault, T. Goto, J.P. Renard, *J. Appl. Phys.* **1991**, *69*, 5956–5958.
[146] M. Takigawa, T. Asano, Y. Ajiro, M. Mekata, Y.J. Uemura, *Phys. Rev. Lett.* **1996**, *76*, 2173–2176.
[147] Y. Itoh, H. Yasuoka, *J. Phys. Soc. Jpn.* **1997**, *66*, 334–336.
[148] J. Sagi, I. Affleck, *Phys. Rev. B* **1996**, *53*, 9188–9203.
[149] K. Damle, S. Sachdev, *Phys. Rev. B* **1998**, *57*, 8307–8339.
[150] C. Dupas, J.P. Renard, *Phys. Rev. B* **1978**, *18*, 401–407.
[151] T. Kennedy, *J. Phys.: Condens. Matter* **1990**, *2*, 5737–5745.
[152] M. Hagiwara, K. Katsumata, I. Affleck, B.I. Halperin, J.P. Renard, *Phys. Rev. Lett.* **1990**, *65*, 3181–3184.
[153] S. Miyashita, S. Yamamoto, *Phys. Rev. B* **1993**, *48*, 913–919.
[154] E.S. Sorensen, I. Affleck, *Phys. Rev.* **1995**, *B51*, 16115–16127.
[155] P.P. Mitra, B.I. Halperin, I. Affleck, *Phys. Rev. B* **1992**, *45*, 5299–5306.
[156] M. Hagiwara, K. Katsumata, H. Hori, T. Takeuchi, M. Date. A. Yamagishi, J.P. Renard, I. Affleck, *Physica B* **1992**, *177*, 386–388.
[157] T. C. Kobayashi, H. Honda, A. Koda, K. Amaya, *J. Phys. Soc. Jpn.* **1995**, *64*, 2609–2613.
[158] S.J. Glarum, S. Geschwind, K.M. Lee, M.L. Kaplan, J. Michel, *Phys. Rev. Lett.* **1991**, *67*, 1614–1617.
[159] T. Asano, Y. Ajiro, M. Mekata, K. Kamishima, K. Koui, T. Goto, M. Furusawa, H. Hori, *J. Phys. Soc. Jpn.* **1997**, *66*, 460–465.
[160] A.P. Ramirez, S.W. Cheong, M.L. Kaplan, *Phys. Rev. Lett.* **1994**, *72*, 3108–3111.
[161] T. Kawae, M. Ito, M. Mito, K. Takeda, *J. Phys. Soc. Jpn.* **1999**, *68*, 740–743.
[162] C.D. Batista, K. Hallberg, A.A. Aligia, *Phys. Rev. B* **1998**, *58*, 9248–9251.
[163] E. Polizzi, F. Mila, E.S. Sorensen, *Phys. Rev. B* **1998**, *58*, 2407–2410.
[164] F. Tedoldi, R. Santachiara, M. Horvatic, *Phys. Rev. Lett.* **1999**, *83*, 412–415.
[165] H. Yamazaki, K. Katsumata, *Phys. Rev. B* **1996**, *54*, R6831–6834.
[166] S. Yamamoto, *Phys. Rev. B* **1996**, *53*, 3364–3373.
[167] See J.L. Musfeldt, *Spin-Peierls Materials* in this book.
[168] S. Maslov, A. Zheludev, *Phys. Rev. B* **1998**, *57*, 68–71; A. Zheludev, E. Ressouche, S. Maslov, T. Yokoo, S. Raymond, J. Akimitsu, *Phys. Rev. Lett.* **1998**, *80*, 3630–3633; S. Raymond, T. Yokoo, A. Zheludev, S.E. Nagler, A. Wildes, J. Akimitsu, *Phys. Rev. Lett.* **1999**, *82*, 2382–2385.
[169] I. Affleck, F.D.M. Haldane, *Phys. Rev. B* **1987**, *36*, 5291–5300.
[170] M. Kohno, M. Takahashi, M. Hagiwara, *Phys. Rev. B* **1998**, *57*, 1046–1051 and references therein.

[171] M. Hagiwara, Y. Narumi, K. Kindo, M. Kohno, H. Nakano, R. Sato, M. Takahashi, *Phys. Rev. Lett.* **1998**, *80*, 1312–1315.
[172] A. Kolezhuk, R. Roth, U. Schollwöck, *Phys. Rev. B* **1997**, *55*, 8928–8939.
[173] C. Monthus, O. Golinelli, T. Jolicoeur, *Phys. Rev. Lett.* **1997**, *79*, 3254–3257; *Phys. Rev. B* **1998**, *58*, 805–815.
[174] S.R. White, *Phys. Rev. B* **1996**, *53*, 52–55 and references therein.

Magnetism: Molecules to Materials I: Models and Experiments.
Edited by Joel S. Miller and Marc Drillon

ISBNs: 3-527-29772-3 (Hardback); 3-527-60084-1 (Electronic)

3 Spin-Peierls Materials

Janice L. Musfeldt

3.1 Introduction

A spin-Peierls (SP) transition is the magnetic analog of the electronic Peierls transition [1]. Whereas an electronic Peierls transition is driven by electron–phonon coupling, which opens a gap in the electronic spectrum, the SP transition is driven by magnetoelastic coupling. Here, the coupling is between the one-dimensional spin system and the three-dimensional lattice, with gap formation in the magnetic excitation spectrum. The important parameters are $J_{\parallel}$ and $J_{\perp}$, the in-chain and interchain exchange constants, and Δ, the spin gap. Of course, in the SP ground state, the distorted lattice results in alternating values of $J_{\parallel}$. SP materials have a characteristic magnetic field-temperature (H–T) phase diagram, first described by Cross [2,3].

Several new developments account for the resurgence of interest in this field of solid-state chemistry and condensed matter physics. The discovery of new inorganic SP materials has been of singular importance [4–8], because the SP ground state itself is fairly rare. Large, high-quality single crystals are available, facilitating neutron scattering and other measurements. That doping of these new inorganic chain materials can be accomplished without structural modification aids in overall tunability of these systems also. This kind of microscopic manipulation has allowed the investigation of a wide variety of phenomena and provided a molecular level "playground" to both experimentalists and theorists. The relevance to the copper oxide superconductors has also been noticed, because these materials also have low-dimensional spin interactions. At the same time, the development of more sensitive measurement technologies, new high-field resistive magnets, and faster computers has enabled the investigation of materials under more complex experimental conditions and exploration of more elaborate theoretical models.

The most comprehensive theory for the description of SP materials is still that of Cross and Fischer [1–3]. Here, the essential point is that a spin-1/2 one-dimensional Heisenberg antiferromagnetic system is unstable toward a $2k_{\mathrm{F}}$ perturbation driven by a three-dimensional phonon field. A $2k_{\mathrm{F}}$ perturbation is a dimerization of the lattice. The new SP ground state is characterized by alternating exchange constants (J_1 and $J_2 = \alpha J_1$); where α is the alternation parameter and a measure of the relative frustration in the magnetic system. These exchange constants are intimately related to the dimerized lattice as $J_{1,2} = J(1 \pm \delta)$, where J is the average exchange value and

δ is the lattice distortion. Then, $T_{SP} = 0.8J\eta'$, where η' is the spin–lattice coupling constant. Cross and Fischer find that the SP gap goes as $\sim 2J\delta^{2/3}$, which yields

$$2\Delta = 3.53kT_c \tag{1}$$

in the weak-coupling limit of the mean-field approximation. Energy loss due to dimerization $\sim\delta^2$, whereas energy gain due to the gap in the low-dimensional magnetic system $\sim -\delta^{2/3}$. Thus, the overall energy charge at this magnetoelastic transition goes as $\sim \delta^{4/3}$, which is the ratio of the two aforementioned terms. δ is small for real materials.

This chapter is organized as follows. First, I overview ongoing work in the inorganic chain solids; $CuGeO_3$, α'-NaV_2O_5, and the associated doped materials are of interest here. Second, I explore new results on the more traditional organic molecular conductor-based SP systems and point out new synthetic work. Recent theoretical developments and approaches to understanding the phase transition are also discussed. My goals are to provide the reader with an overview of the recent work in the area of SP materials [1,9], give a number of current references for the interested student, and identify the challenges for the future.

3.2 Inorganic SP Materials

3.2.1 $CuGeO_3$

The recently discovered $CuGeO_3$ is the first *inorganic* SP system; as such, the initial report by Hase, Terasaki, and Uchinokura generated much activity [4,9]. In this compound, the quasi-one dimensional spin system comprises localized Cu $S = 1/2$ electrons, rather than unpaired π electrons (as with the more well-studied organic SP systems based on TCNQ and TTF) [10–14]. Further, the value of $J_\perp$ is much larger than in the corresponding organic systems, fully 10% of $J_\parallel$ leading to many interesting effects; the spin-gap, Δ, is 24 K [15–17]. The fundamentally different spin system of $CuGeO_3$ has very interesting mechanistic consequences, and ongoing work to compare this material with organic SP compounds has been useful for the development of chemical structure–property concepts in low-dimensional magnetic solids [18]. These distinctions, along with the amenability to doping without structural modification [6], has made $CuGeO_3$ a prototype of a new class of inorganic SP systems.

The value of Δ is very close to the mean field value, likely reflecting the aforementioned strong interchain coupling. The latter is presumably the reason why the susceptibility of $CuGeO_3$ is "non-Bonner–Fischer-like". Indeed, to account for the various physical property measurements in this quantum spin material, including next-nearest neighbor interactions in the Hamiltonian appears to be essential and even competing with other effects [16,17,19]. Castilla et al. justify these large interactions in terms of superexchange pathways, and point out the possibility of a

frustration-induced gap [19]. They conclude that $\alpha \approx 0.24 \leq \alpha_c$ in $CuGeO_3$, leading to a dimerization-induced gap. In contrast, Riera and Dobry find $\alpha \approx 0.36$, leading to a frustration-induced gap without dimerization [17]. The sizeable interchain interactions also motivated the extension of mean-field theory to two dimensions for $CuGeO_3$ [20,21]. Here, both the gap and the lattice distortion go as $(T_c - T)^{1/2}$, and a finite value of the gap is predicted as the lattice distortion approaches zero.

Sandvik et al. show that the adiabatic model might not be relevant to $CuGeO_3$, because the phonons relevant for the dimerization do not soften while the spin gap is so small [22,23]. Using a dynamical Monte Carlo model, they show that unless the coupling exceeds a critical value (α_c), transition to the SP state will not occur. For $\alpha \geq \alpha_c$, the phonon spectral function displays a delta function component (corresponding to long-range order) separated from the rest of the oscillator strength by a soliton gap. Bursill et al. also point out that a realistic model for SP materials should include quantum phonon effects because a spin chain with static dimerization is not justified for a real material [16,24]. The authors find that above a critical value of the spin–phonon coupling, the system moves from a gapless spin-fluid state to a gapped dimerized state. The critical coupling is [16,24]:

$$g_c^2/\omega = \frac{\alpha_c J}{1/2 - \alpha_c + 3(1 + 2\alpha_c)J/8\omega} \,. \tag{2}$$

The phase diagram of the system at $T = 0$ is mapped out in g/ω vs J/ω space. Note that for classical phonons, one always finds a gapped dimerized phase.

In SP compounds, interest has focussed on the understanding of the magnetic field–temperature phase (H–T) diagram, because of the striking similarity of these plots for several different organic and inorganic materials [1,5,25]. A typical H–T diagram (Fig. 1) can be divided into three distinct parts, with the second-order uniform $\rightarrow$ dimerized SP transition at T_c described by the theory of Cross [2,3]. For low values of the field, T_c scales with the square of the field [2,3]:

$$1 - \frac{T_c(H)}{T_c(0)} \sim \alpha \left(\frac{\mu_B H}{k_B T_c(0)} \right)^2 , \tag{3}$$

because of the suppression of spin fluctuation with increasing Zeeman energy. $T_c(0) = 14\,\mathrm{K}$ for $CuGeO_3$. The low-temperature phase typically has another boundary near the critical field (H_c), dividing the regime into "low-field nonmagnetic" and "higher-field magnetic" phases. Within the mean-field approximation [2,26], such a transition is expected at:

$$\frac{g\mu_B H_c}{2kT_c} \approx 0.74 \,, \tag{4}$$

or equivalently using Eq. (1), at:

$$\frac{g\mu_B H_c}{\Delta} \approx 0.84 \,. \tag{5}$$

This phase boundary line (at $H_c = 12.5\,\mathrm{T}$) has been shown to have both first- and second-order character in $CuGeO_3$, depending on the temperature where the dimerized $\rightarrow$ incommensurate phase boundary is traversed [4,5], and is theoretically related to the competition between the Zeeman and exchange terms in the SP Hamiltonian [2,27]. While DC and AC susceptibility measurements have clearly shown that the high-field phase of both $CuGeO_3$ and the prototypal organic SP materials have finite magnetization [1,4,5], little was known about the microscopic nature of this exotic phase until quite recently when X-ray measurements in the high-field phase of both $CuGeO_3$ and TTFCu(BDT) found that the lattice takes on a field-dependent incommensurate modulation above the dimerized $\rightarrow$ magnetic phase boundary [28,29].

The room-temperature structure of $CuGeO_3$ is orthorhombic with a *Pbmm* space group [30,31], as shown in Fig. 2. Essentially, it comprises both distorted CuO_6 octahedra and GeO_4 tetrahedra, running along the *c*-axis. Below T_c, the Cu^{2+} chain dimerizes, and a shift of the *ab* plane bridging oxygens gives rise to additional superlattice Bragg scattering at $(h/2,\ k,\ l/2)$ with h, k, l equal to odd integers. This lattice dimerization results in spin pairing to form a singlet ground state [32]. The temperature-dependence of lattice constants near the 14 K transition in $CuGeO_3$ has been extracted from thermal expansion data [33]. The spontaneous strain along *b* was reported early on [34], and a soft LA phonon branch has also been reported along the b^* direction. Recently, Nishi et al. showed that this broad dispersion is actually composed of two branches with other possible excitations nearby [15]. Pouget et al. observed structural fluctuations below 40 K via X-ray diffuse scattering [35]. They also show that the inverse correlation length for structural fluctuations goes as $(T - T_{sp})^{1/2}$, diverging upon approach to 14 K. Very near T_c, extremely large length-scale fluctuations are attributed in part to random field defects near the surface [36]. Raman scattering experiments confirm the aforementioned lattice distortions at T_c, and the magnetic correlation length tracks the structural correlations well [37].

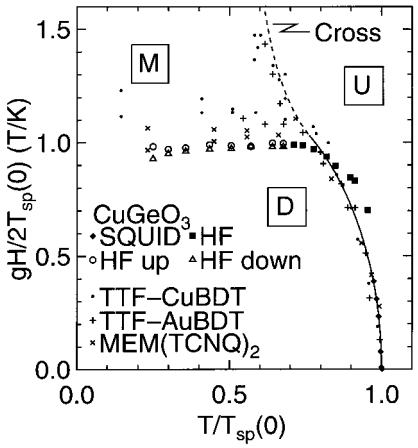

Fig. 1. Typical H–T phase diagram for SP Materials. Note the similarity between that obtained for $CuGeO_3$ and the organic prototypes. Reprinted with permission from Ref. [5], Copyright 1993 by the American Physical Society.

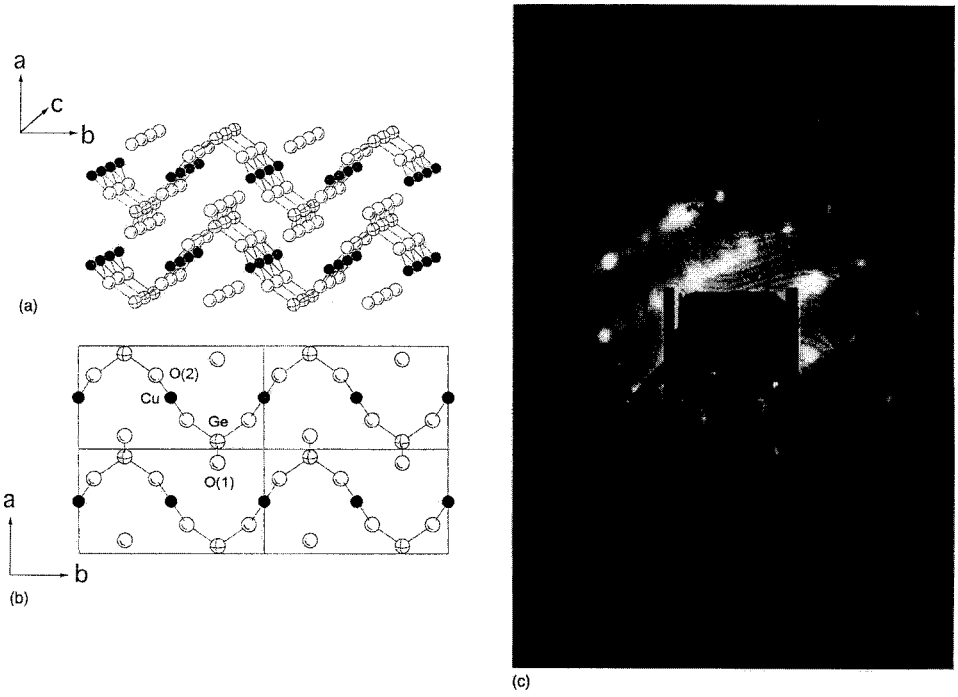

Fig. 2. (a) Crystallographic structure of $CuGeO_3$. (b) View of the structure along the c-axis. (c) LEED pattern at an electron beam density of ≈ 150 eV. Reprinted with permission from Ref. [70], Copyright 1997 by the American Physical Society.

Several neutron-scattering experiments also probed the lattice instability and magnetic driving forces for the SP transition [15,31,38–45], and Boucher and Regnault have reviewed many of the structural and magnetic properties of $CuGeO_3$ fairly recently [9]. The zone center spin energy gap was first reported by Nishi et al. as 2.1 meV, and a value of $\beta = 0.33$ has been extracted by several authors. Later an additional sharp excitation was observed at the edge of the Brillouin zone [39,40]. The spectrum of the double spinon excitation has been mapped out as a function of temperature [39–41], although the dynamics of the various features evolve quite differently. The solitonic midgap gap feature and the magnetic continuum are attributed to dissociation of a dimeric spin pair into a delocalized triplet and the further separation of that triplet into well-separated $S = 1/2$ solitons, respectively. Inelastic neutron scattering measurements combined with shell model calculations have also been used to probe the nature of spin–phonon coupling in $CuGeO_3$ [44]. Although no evidence for soft mode behavior was found, two low-energy modes symmetry of the distortion (3.5 and 6.8 THz, corresponding to Ge–O and Cu–O2–Cu motion, respectively) were found to couple with the magnetic system at temperature scales above T_c (14 K). The absense of soft mode behavior has important consequences for the mechanism of the SP transition in $CuGeO_3$. Inelastic light scattering has also been used to probe the low-energy excitations in $CuGeO_3$ [37]. A three-magnon

process has also been observed (appearing as a shoulder on the 30 cm^{-1} mode) and attributed to scattering between excited triplet states [46].

There has been much controversy about the nature of the high-field magnetic phase and the mechanism of the associated field-induced commensurate → incommensurate transition. From a theoretical point of view, the transition is driven by the competition between the Zeeman and exchange terms in the SP Hamiltonian [10]. High-resolution X-ray measurements of Kiryukhin et al. are interpreted within a localized spin picture, where dimerized domains are separated by soliton-like walls of unpaired spin [28,29]. The soliton width is estimated to be 13.6 lattice spacings near the boundry, somewhat larger than theoretical expectations. The change of dimerization peak intensities are also related to the order parameter of the field-induced transition, as shown in Fig. 3, and indicate that the distance between spin defects approaches zero in a first-order manner at the phase boundary. Fagot-Revurat et al. confirm this interpretation of the the high-field phase via NMR spectra and spin–echo measurements which are consistent with an incommensurate static modulation of the local spin density, with an amplitude of 0.065 at 1.4 K and 16.3 T [47]. A field-induced 3D magnetic soliton lattice is proposed. More recent ^{65}Cu NMR experiments by the same group have probed the solitonic profile with an eye toward using the polarization and size of the signatures to test the appropriateness of various Hamiltonians [48]. The pressure dependence of the critical field was probed by both magnetostriction and inelastic neutron scattering data [49,50].

Heat-capacity measurements of $CuGeO_3$ have presented a particular challenge, because the data are equally well-described by a mean-field model with Gaussian fluctuations and a 3D critical behavior model (Ising or XY) [51,52]. A possible resolution of this problem is presented by Birgeneau et al., who suggest a mean-

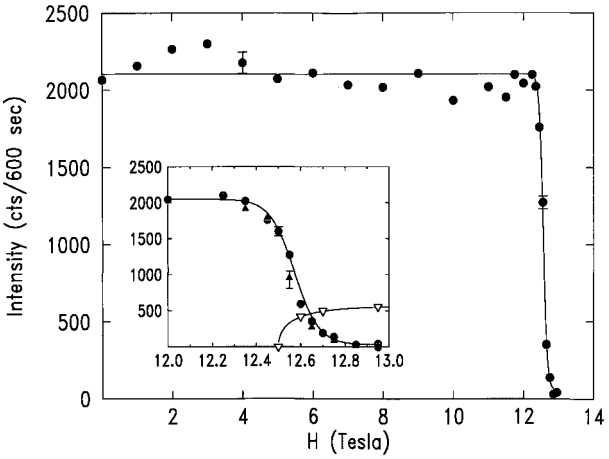

Fig. 3. Intensities of the commensurate (closed symbols) and incommensurate (open symbols) reflections as a function of magnetic field. The lines are guides to the eye. Compared with the organic SP materials, a very small hysterisis regime is reported. Reprinted with permission from Ref. [29], Copyright 1995 by the American Physical Society.

field framework with a tricritical to mean-field crossover in the transition regime [53]. The sensitivity of this thermodynamic quantity to crystalline quality, aging, and quenching has also been noted [52]. High-field results indicate that the specific heat is dominated by magnetic excitations and a phonon contribution at low temperatures; no gap is observed, in contrast to zero field data [54].

Low energy excitations of $CuGeO_3$ have also been explored by sub-millimeter wave spectroscopy. Yamamoto et al. find that upon passing through the uniform $\rightarrow$ dimerized transition on the H–T phase diagram, ESR-derived g-shifts are extraordinarily large compared with the organic SP materials, suggesting that electronic interactions are important [55]. The angular dependence of the g value is best accounted for by a tetragonal crystal field surrounding the Cu^{2+}, although NMR Knight-shift measurements argue for rhombic crystal field [56,57]. Further, a significant drop in the absorption intensity is found on passing through the 14 K transition. High-field ESR results were reported by Brill et al. [58]. In this work, two types of absorption were observed – transitions between excited states and transitions from the ground state to an excited state. Both are attributed to Zeeman splitting of spin-Peierls gaps located at different points in the Brillouin zone. The lower energy gap is at 20 K (2.1 meV), whereas the higher energy gap is at 63.5 K. The lower branch of the 2.1 meV gap goes to zero at a critical field near 12.5 T, as shown in Fig. 4.

Far-infrared reflectance and transmission measurements have been used to explore the characteristics of the H–T phase diagram of $CuGeO_3$ [59–65]. Weak folded modes are observed at 284, 312, and 800 cm^{-1} below T_c [60]. Data through

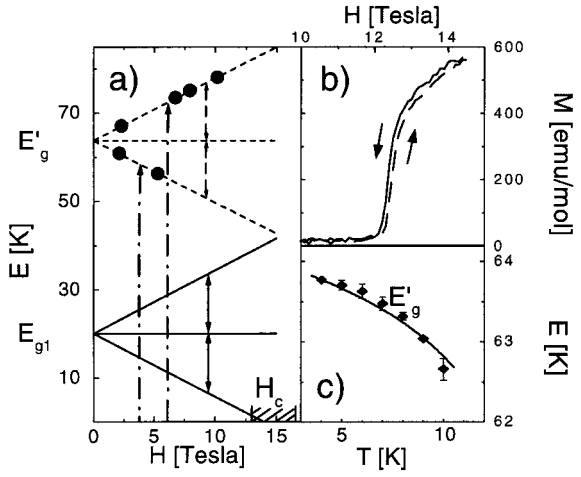

Fig. 4. (a) Energy-level diagram as a function of field for ESR transitions in $CuGeO_3$. The Zeeman splitting of two triplet states with SP gaps E_{g1} and $E_{g'}$ is shown as solid and dashed lines, respectively. These states are located at different points in the Brillouin zone. Both high-field and low-field excitations are indicated. (b) Magnetization as a function of field at $T = 1.53$ K, showing the jumplike behavior around H_c and a small hysterisis effect. (c) Temperature-dependence of the SP gap $E_{g'}$. Reprinted with permission from Ref. [58], Copyright 1994 by the American Physical Society.

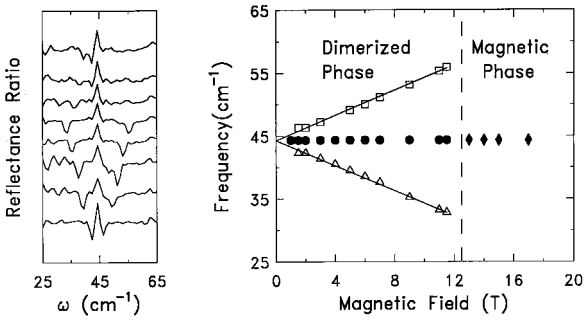

Fig. 5. Left panel: reflectance ratios of $CuGeO_3$ in the far-infrared which characterize the dimerized → magnetic phase transition at 5 K. From bottom to top: 2 T/0 T, 5 T/0 T, 7 T/0T, 9 T/0 T, 11 T/0 T, 13 T/0 T, 15 T/0 T, and 17 T/0 T. The curves have been off-set for clarity. Right panel: dependence of frequency on magnetic field for the phonon structure shown in the left panel. Reprinted with permission from Ref. [63], Copyright 1996 by the American Physical Society.

the dimerized → incommensurate transition is particularly striking [63,64]. Here, Zeeman splitting of the 63.5 K SP gap is observed; the lower and upper branches disappear in the incommensurate phase due to destruction of the singlet ground state (Fig. 5). Careful far-infrared measurements by Takehana et al. identify several additional structures in the spectra of $CuGeO_3$ [65]. For instance, a 98 cm^{-1} zone folding mode (of B_{3u} symmetry) has weak doublet character in the incommensurate phase; this doublet structure seems to be related to the degree of incommensurability. Further, the authors observed a broad absorption centered near 63 cm^{-1} which is assigned as a magnetic excitation from the singlet ground state to a continuum state.

Polarized optical spectroscopy has also been used to characterize the optical constants of $CuGeO_3$ and follow changes through the various phase boundaries of the H–T phase diagram [66–72]. In particular, the intensity and temperature-dependence of the color band suggest assignment as a phonon-assisted d → d transition [67]. Using the partial sum rule on the absorption, Bassi et al. extract the temperature dependence of the oscillator strength (f) of this band and successfully fit it to the form:

$$f = f_0 \coth\left(\frac{h\nu_p}{2kT}\right). \tag{6}$$

Characteristic phonon energies of 238 and 245 cm^{-1} were extracted for the b and c polarizations, respectively. Electron spectroscopy measurements confirm this origin of the blue color [70]. Thus, band structure calculations provide little information about the visible optical properties of $CuGeO_3$, although the 3.7 eV charge-transfer gap is in-line with band structure estimates and attributed to transitions between O 2p states and Cu d states [69,70,73–77]. A small, sharp feature at 1.47 eV (near the leading edge of the Cu^{2+} d → d band) in the optical spectrum has systematic

temperature- and field-dependence; this structure can be integrated to identify T_c and H_c (Fig. 6). Recent optical measurements under hydrostatic pressure by Zeman et al. confirm the sensitivity of this feature to the transition [72]. Interestingly, the phase diagrams at various pressures do not seem to scale according to the Cross–Fischer theory; this is probably attributable to next-nearest neighbor frustration. Better scaling is obtained when the field axis is scaled by the singlet–triplet gap energy (Fig. 7); note that an H^2 dependence on $T_{SP}(H)/T_{SP}(0)$ is still observed. Interchain exchange interactions, which are well-known to affect the high-field state of a quasi-one-dimensional Heisenberg antiferromagnet couple with a lattice distortion [78,79], are likely to play a major role, because the transverse interactions increase with pressure. A complete understanding of this and other scaling issues is still elusive.

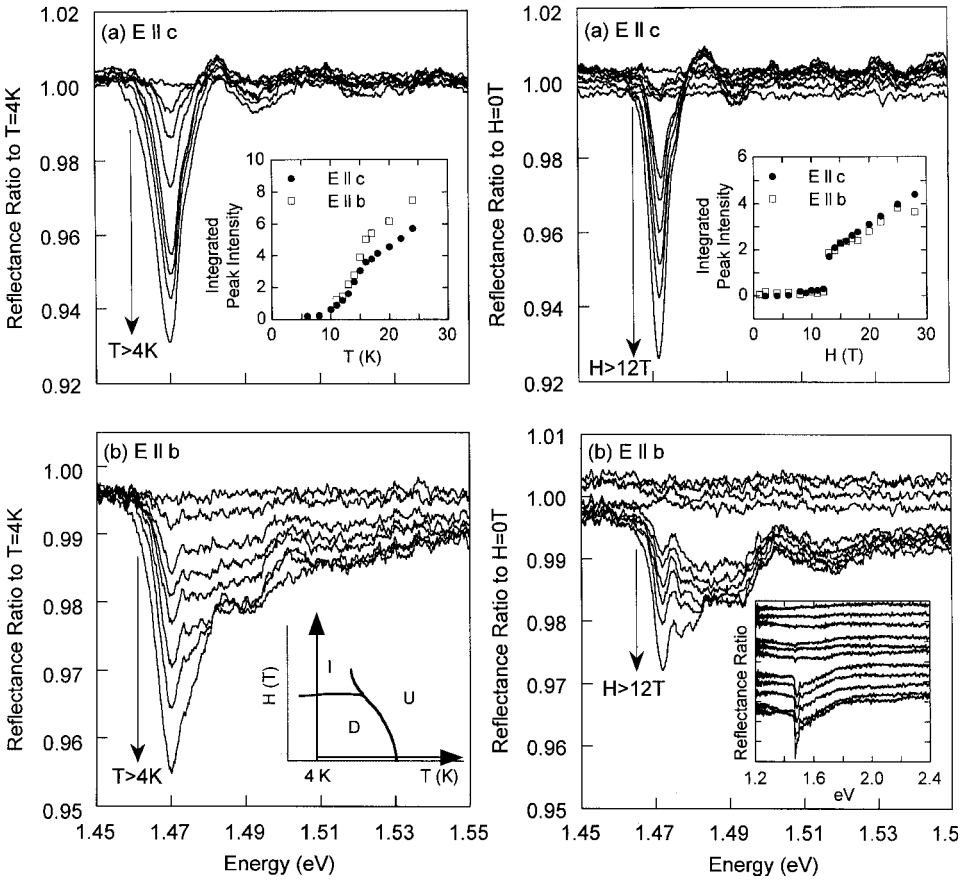

Fig. 6. Left plot: temperature-dependence of zero-field reflectance ratio spectra for $CuGeO_3$, $R(T)/R(T = 4\,\mathrm{K})$, with (a) $E\|c$ and (b) $E\|b$. Right plot: field dependence of 4 K reflectance ratio spectra of $CuGeO_3$, $R(H)/R(0)$, with (a) $E\|c$ and (b) $E\|b$. Reprinted with permission from Ref. [71], Copyright 1997 by the American Physical Society.

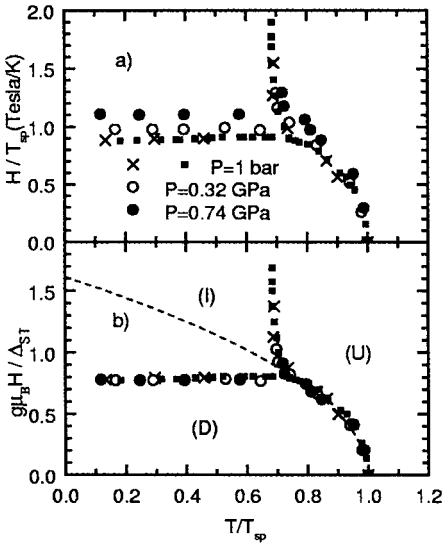

Fig. 7. Phase diagram of $CuGeO_3$ for different pressures plotted against T/T_{sp}. (a) scaling of H with T_c; (b) scaling of H with Δ. The solid squares are magnetostriction thermal expansion data from Ref. [82]. Reprinted with permission from Ref. [72], Copyright 1999 by the American Physical Society.

There is actually a good deal more to the behavior of $CuGeO_3$ in temperature–field space than is given by the aforementioned H–T diagram (Fig. 1). For instance, Raman measurements by van Loosdrecht et al. show that the uniform phase is divided into a high-temperature regime and a short-range order phase which sets in near 60 K [80,81]. The high-temperature phase has low-dimensional diffusive fluctuations, whereas the short-range order regime has signatures of a spin-wave continuum, as expected for a one-dimensional quantum Heisenberg chain. Thermal expansion and magnetostriction experiments also indicate that although the soliton picture might be the most appropriate description for the spin excitations close to the 12.5 T phase boundary, an incommensurate sinusoidal modulation of the spin gives a better fit to the data for fields well above H_c (28 T) [2,27,82]. In the soliton domain-wall model, the dimerization amplitude is given as:

$$A(l, H) = (-1)^l A_0 k \mathrm{sn}\left(\frac{lc}{k\xi}, k\right), \tag{7}$$

where $\mathrm{sn}(x, k)$ is a Jacobi elliptic function of modulus k, determined by the field-dependent intersoliton distance and the soliton width. Within the sinusoidal modulation picture, the spacial character of the dimerization amplitude is given as:

$$A(l, H) = (-1)^l A_0(H)\ \sin[q(H)lc], \tag{8}$$

where $q(H)$ is the field-dependent modulation vector and c is the lattice constant along the magnetic chain direction. The development of one form from the other (solitonic $\rightarrow$ sinusoidal) seems to be continuous. These results are supported by numerical density matrix renormalization group calculations and simulations. It is notable that neither model fits thermal expansion or structural data perfectly, making

this discrepancy an important issue for future work. Other authors have pointed out the large and changable spin–phonon interactions at high fields also [83,84].

Finally, the pressure-dependence of the $CuGeO_3$ phase diagram has been studied by Raman scattering techniques [85]. van Loosdrecht et al. map out a new T–P phase diagram, characterized by three different phases, two of which have both "regular" and low-temperature SP regimes. Trends in the important SP parameters, such as the increase in the SP gap with pressure, are attributed to the effect of next-nearest neighbor interactions.

3.2.2 Impurity-doped $CuGeO_3$ Systems

Recent studies have demonstrated the facile and interesting impurity substitution possibilities in $CuGeO_3$. Several elements, including Zn, Si, Ni, Ca, Al, Sn, Cd, Ga, and Mg, have been successfully incorporated into the crystallographic structure, with the dopant ion being substituted for Cu or Ge in the octahedral lattice [6,86]. Among these, the Zn, Mg, and Si doped systems are the most well characterized. In the case of Zn and Mg doping, the impurity species is nonmagnetic, and is substituted for the d^9 Cu atoms in the magnetic chain. Thus, systems with the formula $Cu_{1-x}Zn_xGeO_3$ or $Cu_{1-x}Mg_xGeO_3$ can be prepared and provide an ideal model to study "spin interruptions" in a linear magnetic chain system. In contrast, Si replaces Ge to yield $CuGe_{1-x}Si_xO_3$, which primarily effects interchain coupling. One of the most attractive aspects of these doped compounds is that the cationic substitution takes place without severe modification of the linear chain structure [6]. Therefore, the magnetic interactions along (and between) the chains can be modulated without a change in the structural properties. Because of this unique aspect, the $CuGeO_3$ system represents a rich testing ground to study the effects of chemical structure on the magnetic properties.

The competing ground states of impurity-substituted $CuGeO_3$ have attracted a great deal of attention. Early studies by Hase et al. showed that with increasing Zn concentration, the SP transition temperature decreases and ultimately disappears [6]. More recent work has shown that the SP transition temperature levels off at about 9 K and remains stable up to at $\approx 3\%$ doping [87,88]. Further, an antiferromagnetic Néel state is stabilized at lower temperature [88], which seems to need no critical concentration for its appearance. Thus, there is a regime where both SP lattice distortions and long-range antiferromagnetic effects coexist near 4 K (Fig. 8) [89]. μsr measurements on both Zn and Si-doped $CuGeO_3$ support this interpretation [90,91]. Recently, Büchner et al. used thermal expansion, magnetostriction, and specific heat techniques to probe properties of various phases in H–T space for a series of Zn-doped samples [92]. They also found evidence for competing SP and antiferromagnetic order. Mg doping of Cu sites also causes the SP state to disappear [93], but the effects are generally weaker than that observed with Zn. A similar temperature-concentration phase diagram is obtained for $Cu_{1-x}Mg_xGeO_3$ [94]. With Si doping, the SP temperature decreases slightly and 3D antiferromagnetic order sets in at lower temperature [95,96]. In fact, the SP phase coexists with the antiferromagnetic phase in this compound also, and a magnetic phase is present

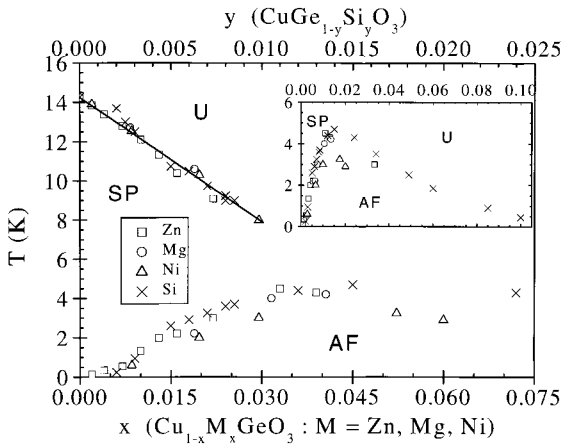

Fig. 8. Temperature-concentration phase diagram for $Cu_{1-x}M_xGeO_3$ with M = Zn, Mg, Ni, and $CuGe_{1-y}Si_yO_3$, using the scaling $y = 3x$. Within this scaling, one notes the universal character of the T–x diagram, except for the $T_N(x)$ data in Ni-doped $CuGeO_3$. The solid line is described by the equation $T_{SP}(x) = T_{SP}(0)[1 - 15x]$. Reprinted with permission from Ref. [88], Copyright 1998 by the American Physical Society.

above 8 T. For the magnetic field aligned along the chain axis, a spin–flop phase is also observed [97]. Several techniques have been used to map out H–T phase diagrams for Zn- and Si-doped crystals of particular concentrations [97–100]. For Al and Sn doping, addition of impurities does not stabilize any "extra" low-temperature competing phases. Here, the main effect of the dopant is to increase the hysteresis around the dimerized → incommensurate boundary at low temperature and to broaden the transition [101].

Recent theoretical work by Fukuyama et al. accounts for the unexpected SP–antiferromagnetic coexistence in the Si-based system [89]. The authors present antiferromagnetic and SP dimerization amplitudes as a function of doping concentration for a series of impurity displacements, and show that impurity-induced antiferromagnetic long-range order is a universal phenomena in gapped quantum spin liquids. A critical impurity concentration, above which SP distortions are expected to vanish, is estimated based upon dimensionality arguments. This coexistence of coherent antiferromagnetic long-range order and dimerization is predicted to persist even if the distribution of impurities along the chain is random. Other authors have addressed the role of disorder at very low doping levels as well [102].

The neutron scattering investigations by Regnault et al. and Martin et al. on $Cu_{1-x}Zn_xGeO_3$ were particularly important for confirming the coexistence of SP and antiferromagnetic ordering [96,103]. Following the temperature dependence of the lattice dimerization (which is related to the square of the order parameter), the authors found it was still finite below the Néel temperature, even for very small Zn concentrations. The sharp excitations of the antiferromagnetic state are robust at all doping levels (and fairly insensitive to doping), whereas the signatures of the SP state display increasing disorder with increased doping. Both b^* and c^* dispersions

were measured in Ref. [103]. A weak correlation between the energy gap and the dopant concentration was also observed. Neutron scattering studies on Si substituted crystals have also been pursued, most recently in high magnetic fields [104].

More recently, structural investigations by Wang et al. of $Cu_{1-x}Mg_xGeO_3$ show that the spin gap and the short-range order SP dimerization peaks appear to be well established before long-range SP dimerization sets in [94]. This suggests that two temperature scales, one related to small domain formation and another related to long-range three-dimensional coherence, might be appropriate for modeling the transition behavior of doped systems. Such a scenario also holds out a reasonable explanation for the disappearance of the SP transition above a critical dopant concentration; the authors ascribe it to a drastically reduced SP coherence length above a critical concentration driven by interchain interactions. Thermal conductivity measurements by Takeya et al. support the progression of short-range SP order to long-range SP order in doped samples [105]. Further, they establish that the mean free path of the spin excitations should exceed the impurity distance to realize long-range SP order.

X-ray scattering studies have extended the aforementioned neutron scattering work on Zn- and Ni-substituted samples into the high-field incommensurate phase [106]. At low doping concentrations, a short-range ordered incommensurate phase is stabilized; this is attributed to strong pinning of the spin-solitons to impurities. At higher doping levels, long-range order is in competition with the antiferromagnetic phase. Quantitative description of the experimentally observed lattice modulation (and defect width) with field remains an important challenge.

Several ESR measurements have focussed on the Zn and Si doped systems [107–110]. The multifrequency high-field spectra of Hassan et al. show particularly rich results, with a number of concentration dependent doping-induced features [109]. These effects are attributed to local enhancement of antiferromagnetic correlations near the Zn impurities, which give rise to transitions between states inside the SP gap. These results are in-line with predictions for in-gap states in doped $CuGeO_3$ by Martins et al. [111]. Temperature dependence of the in-gap states resonant fields is attributed to increasing short-range order as the temperature is lowered. Nojiri et al. show that minute Si doping significantly broadens the singlet–triplet absorption excitation, because of spectral weight shift away from the triplet branch to the antiferromagnetic resonance mode [110].

The aforementioned theoretical work on the suppression of the SP gap in Zn-doped $CuGeO_3$ [111] is based on an analysis of different spin interactions on various chain segments. Both low and high-frequency spectral weight features are introduced with doping, as the original SP gap itself is closed, because of the breaking of spin singlets. The authors postulate that at low temperatures, random unpaired spins in each segment can be replaced by a single effective spin, with coupling which depends on fragment length. Experiments which probe the low-energy response of doped $CuGeO_3$ systems are thus likely to be described best by a random exchange Heisenberg model, although the length scale of the experimental technique will be important to the analysis.

Low-energy excitations in doped $CuGeO_3$ have also been studied by far-infrared spectroscopy. Several very low-frequency absorption lines appear with progressive

Zn doping ($10\,cm^{-1}$, $20\,cm^{-1}$), and a broader temperature-independent absorption [112]. The $10\,cm^{-1}$ feature, assigned as a librational motion of the GeO_4 tetrahedra, is absent in Si-doped samples. The temperature dependence of the $20\,cm^{-1}$ structure is consistent with a three-level model, in which the two excited states are slightly above the energy of the ground state. In Si- and Mg-doped $CuGeO_3$, Damascelli et al. observed a change in the $800\,cm^{-1}$ b-polarized B_{2u} zone-boundary phonon mode on passing through the SP transition [113]. Integrated intensities as a function of temperature show a decrease and broadening of the transition temperature compared with the undoped crystal. Surprisingly, the spectra of Zn-doped $CuGeO_3$ reveals no field dependence in the 5–35 cm^{-1} regime [112], although the $98\,cm^{-1}$ zone-folding mode does have an unusual doping dependence, which seems to be related to the strength of lattice distortion in the doped systems combined with impurity-induced violation of selection rules [114].

3.2.3 α′-NaV_2O_5

Among the many vanadate compounds with low-dimensional and spin-gap features, α'-NaV_2O_5 has attracted attention as the second possible inorganic SP system [8]. This behavior was originally recognized in 1996 by Isobe and Ueda from a pronounced decrease in the susceptibility of powder samples near 35 K [7,8]. From a fit of the data to the Bonner–Fisher model, the authors extracted a near-neighbor exchange interaction of $J = 560$ K. These results were confirmed by Weiden et al. on single crystals a short time later [115]. The decrease of the susceptibility with temperature is independent of field direction, as shown in Fig. 9. From a fit of $\chi(T)$ to the theory of Bulaevskii, the gap energy (Δ) and the exchange coupling constant (J) are extracted as 85 ± 15 K and 441 K, respectively. A Heisenberg-type fit to the susceptibility also works well, although the fit quality is best at high temperature. Interchain interactions and magnetic frustrations are found to be almost negligible in this material, in contrast to $CuGeO_3$. Thus, $\alpha_c = J'/J \approx 0$. The lattice distortion of α'-NaV_2O_5 at the 35 K transition is much larger than that of $CuGeO_3$. Theoretical models therefore predict that the spin–phonon coupling is 2 or 3 times larger in α'-NaV_2O_5 than $CuGeO_3$ [116,117], with important consequences for the inelastic neutron scattering, photoemission, and Raman scattering results. Recent quantum Monte Carlo calculations also point to the importance of including dynamical phonons in order to obtain a quantitative description of the magnetic properties of α'-NaV_2O_5 [22,23].

The 300 K structure of α'-NaV_2O_5 is orthorhombic, with a Pmmm space group as shown in Fig. 10 [118–120]. In the ab plane, layers of VO5 square pyramids share edges and corners. These "connected pyramid" layers in the ab plane are separated by Na atoms along c. The ladder analogy (with legs and V–O–V rungs) is helpful here. Early 300 K structural studies overlooked an inversion center and mistakenly identified the space group as $P2_1mn$. Such a rendering gave rise to crystallographically inequivalent vanadium sites defining two very different types of chain running along the b direction. In this picture, the magnetic chains, which contain $S = 1/2$ V^{4+} ions, are surrounded by nonmagnetic $S = 0$ V^{5+} chains and the one-dimensional

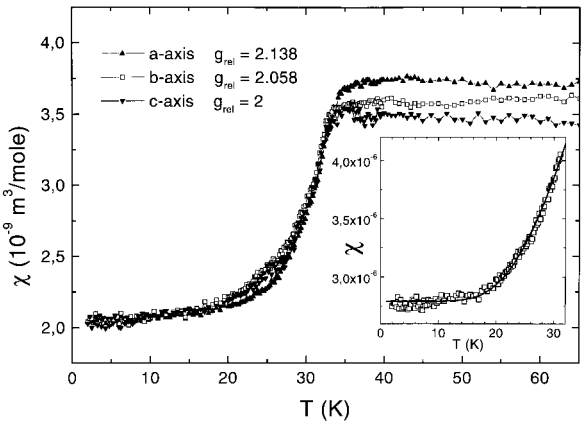

Fig. 9. Susceptibility of α'-NaV_2O_5 along the three major crystallographic axes. The values for the magnetic field parallel to the three axes are shifted to reach the same value at $T = 2\,\mathrm{K}$. Inset: Analysis of the susceptibility of the single crystals for $B \| b$ using the theory of Bulaevskii. Reprinted with permission from [115], Copyright 1997 by Springer.

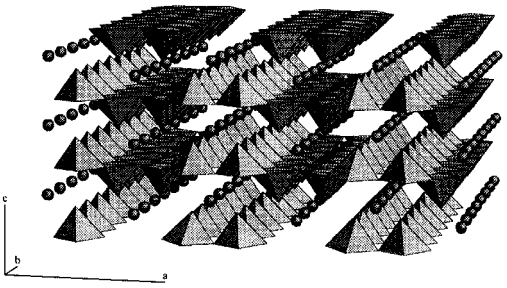

Fig. 10. Crystal structure of orthorhombic α'-NaV_2O_5 in the Pmmm space group. Note the VO_5 square pyramids and the rows of Na atoms. Reprinted with permission from Ref. [119], Copyright 1998 by the International Union of Crystallography.

spin structure arises naturally. However, it has recently been found that α'-NaV_2O_5 is actually described by the Pmmm space group at 300 K [118–120]. The Pmmm centrosymmetric rendering implies that all vanadium sites are crystallographically equivalent, giving a formal valence of +4.5 for each V site [118–120]. Such an interpretation is supported, for instance, by recent V NMR work [121,122]. Thus, at 300 K, it is currently thought that α'-NaV_2O_5 has a single $V^{4.5+}$ site and centrosymmetric symmetry, which has raised raised the important question of whether α'-NaV_2O_5 should be considered at SP material.

X-ray diffraction has been used to probe the change in structure associated with the 35 K transition in α'-NaV_2O_5. The superlattice reflection data of Fujii et al. clearly show the lattice dimerization along the chain direction [123]. Many studies have focussed on the nature of the low-temperature superstructure. These superlattice reflections occur with a lattice modulation vector $\mathbf{q} = (1/2, 1/2, 1/4)$ [123]. In $CuGeO_3$, unit cell distortion below the 14 K transition is observed in only two directions. The modulated ladder in α'-NaV_2O_5 might have some charge disproportionation (V^{4+} and V^{5+} sites), and a zig-zag charge order is one of the leading structural

candidates [124]. Recent calculations show that such a pattern is also energetically favorable [125,126]. Note that in the zig-zag spin lattice, the paired spins do not reside in the ladder chains but in between the ladder chains. This transverse pairing makes α'-NaV_2O_5 different than a simple SP system. It is notable that theoretical models both with and without explicit correlation effects make this prediction [125,126]. Although microwave dielectric anomalies also seem to be consistent with zig-zag charge ordering in the ab plane below T_c [127], the most recent low-temperature structural refinement by Lüdecke et al. reveals much more complex behavior with a modulated acentric Fmm2 structure on the $2a \times 2b \times c$ supercell. Here half of the vanadium ions are not involved in the distortion, leading to both modulated (magnetic) and unmodulated (nonmagnetic) chains [128]. The susceptibility of the remaining $V^{4.5+}$ below 35 K remains unaccounted for.

In the low-temperature phase, inelastic neutron scattering measurements have been used to extract the energy gap in the magnetic excitation spectrum directly. Fujii et al. found $\Delta/k = 114\,\mathrm{K} = 3.4T_c$, which is twice the mean-field value [123]. This suggests that fluctuation effects in α'-NaV_2O_5 will play an important role in the transition, especially in comparison with $CuGeO_3$, the critical behavior of which is described quite well by mean-field theory. This estimate of the gap amplitude of α'-NaV_2O_5 is in line with that of other techniques, including ESR [129]. The temperature-dependence of the gap, obtained both from inelastic neutron scattering studies and from ultrasound velocity measurements is shown in Fig. 11 [130]. Modeling this behavior as $\Delta(T) = \Delta(0)(1 - T/T_{sp})^{\beta}$ yields a critical exponent of 0.34 ± 0.08, similar to that observed for $CuGeO_3$.

Indeed, both specific heat and thermal conductivity measurements of α'-NaV_2O_5 point to the importance of fluctuation effects in the transition regime. In the specific

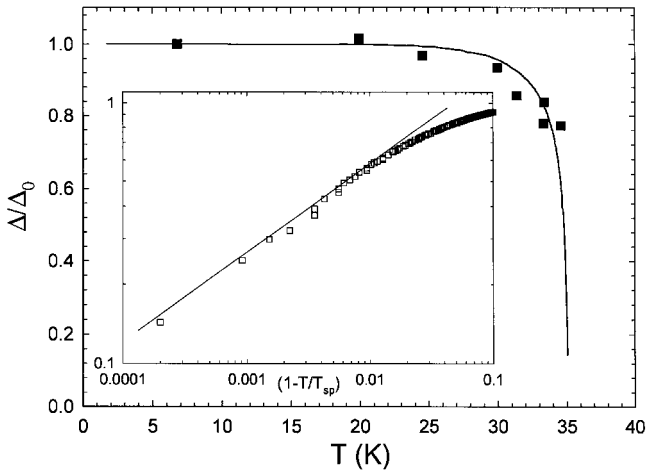

Fig. 11. Temperature profile of the gap determined from the relative velocity variations along the chain axis. Filled squares are the gap values deduced from the inelastic neutron scattering data of Ref. [123]. Reprinted with permission from Ref. [130], Copyright 1998 by the American Physical Society.

heat data of Powell et al. the thermal signature of the 35 K transition is more than twenty times that expected from mean-field theory, and it is much sharper than the response from $CuGeO_3$ [131]. Analysis places the Debye temperature between 345 and 414 K. Very recent experiments indicate possible tricritical behavior in α'-NaV_2O_5 [132]. The thermal conductivity results of Vasil'ev et al. are also highly anomalous, with a huge increase in κ at the SP transition temperature [133]. The striking difference between the thermal conductivity signature in α'-NaV_2O_5 and $CuGeO_3$ is attributed to the stronger spin–phonon coupling in the vanadate material combined with the more complicated nature of the transition.

Ultrasonic techniques are also extraordinarily useful for probing the precursor effects in α'-NaV_2O_5 above T_c [130,134]. They are quite strong, whereas there is no persistent softening in the low-temperature SP phase, in contrast to what is observed for $CuGeO_3$. This suggests that magnetoelastic coupling is more effective in α'-NaV_2O_5 than in $CuGeO_3$, in agreement with the aforementioned thermal conductivity measurements. The temperature dependence of the gap is calculated (Fig. 11), and a zero temperature value of $\Delta = 90$ K is extracted. Originally, the field dependence of T_c from susceptibility measurements on α'-NaV_2O_5 was reported to be in line with that expected from theories of Bulaevskii and Cross. Recent ultrasonic results in fields up to 14 T, however, indicate a much smaller than expected reduction of the transition temperature in the applied field; this suggests that further investigation at higher magnetic fields are required to resolve this issue and to map out the full H–T phase diagram [130]. Also, propagation of the C_{66} shear mode has been related to a low temperature charge fluctuation of B_{1g} symmetry [134].

There have been several computational attempts to understand the electronic structure of α'-NaV_2O_5. Methods ranging from local density approximation (LDA + U), spin density approximation (SDA + U), Hartree–Fock, cell perturbation method, t–J ladder model, and extended Hückel have been employed [135–138]. Extended Hückel band structure techniques have also been used [137]. Wu et al. and Nishimoto et al., on the other hand, take a more localized approach, computing the electronic structure of α'-NaV_2O_5 within the LDA + U picture and trellis lattice t–J models, which enable assessment of correlation parameters [135,136]. Many of these aforementioned models provide a framework for understanding the frequency-dependent conductivity [136,138]. For instance, the trellis t–J model affords reasonable agreement with the experimental spectra only under the assumption of a charge-disproportionated ground state [136].

The nature of the electronic excitation near 1 eV in α'-NaV_2O_5 has been a subject of special controversy (Fig. 12). This structure was originally interpreted as resulting from phonon-assisted d–d transitions within the crystal field manifold for the V^{4+} site [139]. Such an explanation is similar in spirit to what is observed for $CuGeO_3$. Alternatively, the near-infrared excitation in α'-NaV_2O_5 has been interpreted as an on-rung charge-transfer structure [140]. This assignment was partly based on intensity arguments, which noted that the excitation in α'-NaV_2O_5 is significantly stronger than that expected for a symmetry forbidden process (as in $CuGeO_3$). From another point of view, the 1 eV feature was attributed to a $d_{xy} \rightarrow d_{yz}$ transition within the V d manifold, consistent with the polarized band structure in Fig. 12 [137]. Further, high-field optical experiments show that the SP transition has essentially

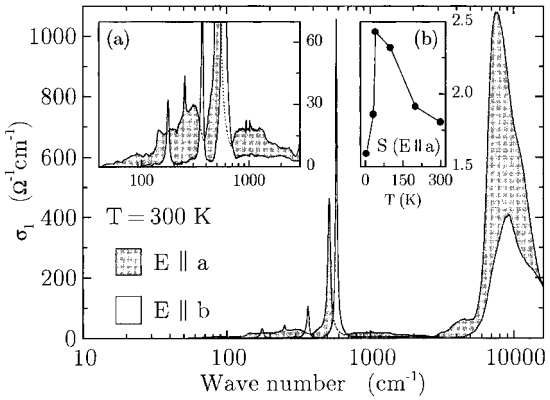

Fig. 12. Room temperature far-infrared reflectance spectra of α'-NaV_2O_5. Open circles represent experimental data. Solid lines are fit results. Reprinted with permission from Ref. [144], Copyright 1998 by the American Institute of Physics.

the same electronic structure changes at 28 T as at zero magnetic field, although the transition temperature is shifted slightly downward.

Popova et al. presented an elegant study of the lattice vibrations in α'-NaV_2O_5 at room temperature using infrared and Raman spectroscopic techniques to discriminate between the aforementioned centrosymmetric (Pmmm) and noncentrosymmetric ($P2_1mn$) structures [141]. Their polarized infrared reflectance data are shown in Fig. 13. On the basis of the number of experimentally observed modes and lattice dynamical calculations the authors concluded that the 300 K phase of α'-NaV_2O_5 is most consistent with the centrosymmetric structure. Interest has also focused on the temperature dependence of the vibrational modes through the 35 K SP transition in α'-NaV_2O_5. This is because the stronger magnetoelastic coupling in α'-NaV_2O_5 compared with $CuGeO_3$ suggests that such analysis will be highly profitable. Both infrared and Raman scattering data provided early information on the lattice distortion at T_c [115,139]. More recently, Smirnov et al. have presented a detailed investigation of the 718 cm^{-1} feature in the infrared, which has strong and systematic variation with temperature on passing through T_c [142]. Attributing an order-parameter-like behavior, the authors fit the oscillator strength of the feature to the form $(1 - T/T_{sp})^{2\beta}$, extracting a critical exponent, β, of ≈ 0.25. The temperature dependencies of this and other modes highlight the importance of pretransitional fluctuations, in line with the aforementioned ultrasound measurements. Another important aspect of the infrared spectra of α'-NaV_2O_5 is the continuum signal observed along the a direction (Fig. 12). On the basis of the overall low-energy of the continuum, several authors have speculated that some type of spin excitation along the rungs of the ladder might be responsible for this effect. Damascelli et al. explain the data in terms of two-magnon processes where spin flips on the rungs of the ladders can create local electric dipole moments [143,144]. While present over the full temperature range, the oscillator strength of the continuum increases upon approach to T_c from above and decreases sharply below 35 K. This increase has been attributed to enhanced short-range antiferromagnetic correlations of the chains upon approach to T_c, whereas the decrease corresponds to the suppression of these interactions below 35 K.

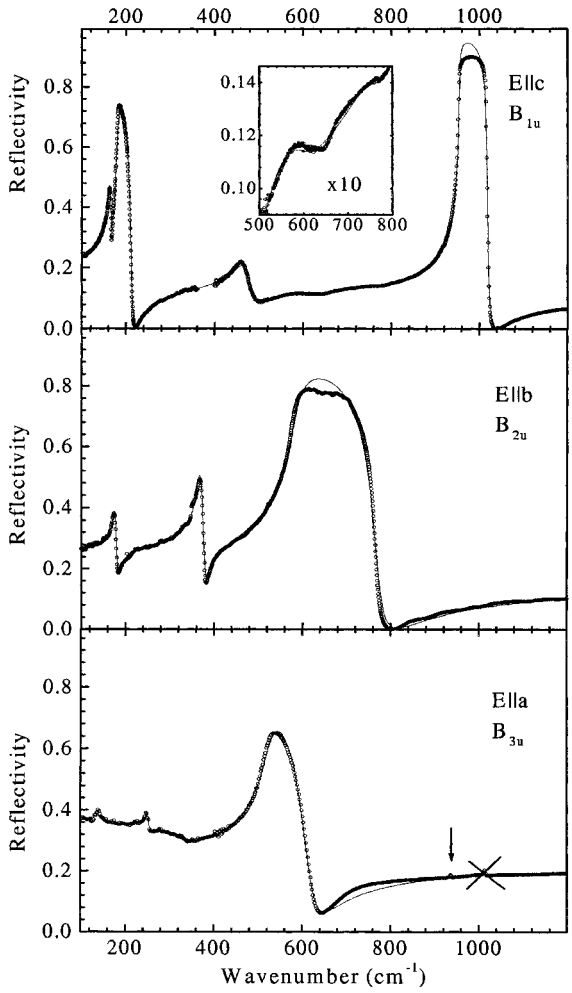

Fig. 13. Optical conductivity of α'-NaV_2O_5 at 300 K for *a* (shaded) and *b* (unshaded) polarizations. Inset *a*: enlarged view of $\sigma_1(\omega)$ from 40–3000 cm^{-1}. Inset *b*: plot of oscillator strength of electronic continuum along a against temperature. Reproduced with permission from Ref. [141], Copyright 1998 by the American Physical Society.

3.2.4 Doping in the α'-NaV_2O_5 System

From the chemical formula of the stoichiometric compound, it is easy to see that α'-NaV_2O_5 must have one spin per formula unit. To "move away" from the stoichiometric situation, doping is required [8]. To this end, sodium deficiencies in α'-NaV_2O_5 single crystals have been incorporated and controlled with success [145]. A rather wide range of both deficiency and excess is available. The main effect of creating a Na deficiency is to introduce nonmagnetic holes (V^{5+} ions) into the magnetic V^{4+} sites, thus creating "breaks" in the $S = 1/2$ spin chains.

The concentration-temperature phase diagram, has been mapped out by susceptibility and thermal conductivity techniques for α'-$Na_{1-x}V_2O_5$ [133]. The SP phase transition itself vanishes slightly above $x = 0.03$. Thermal conductivity suggests that

Table 1. Organic SP materials-summary of critical properties.

Material	T_c (K)	H_c (T)
(TTF)CuBDT	12	11.5
(TTF)AuBDT	2	2.25
(TTF)CuBDSe	6	–
$MEM(TCNQ)_2$	18	19.5
DAP(TCNQ)	160	–
$(TMTTF)_2PF_6$	20	19.1
$(BCPTTF)_2PF_6$	36	–
$(BCPTTF)_2AsF_6$	32.5	–
$Per_2[M(mnt)_2]$, M = Pt, Pd, Ni	8, 28, 25	–
α'-$(ET)_2Ag(CN)_2$	5.8	6.5
β'-$(ET)_2SF_5CF_2SO_3$	45	–
ζ-$(ET)PF_6$	40	–

this is because the spin gap fills with magnetic excitations upon departure from perfect stoichiometry. Currently, no additional low-temperature magnetic phases have been reported, in contrast to Zn-doped $CuGeO_3$. The lack of additional structure in the concentration-temperature phase diagram has been attributed to the strong one-dimensionality and lack of inter-chain interactions in the α'-$Na_{1-x}V_2O_5$ system. Excess Na doping has also been reported to reduce T_c [115].

The properties of a number of solid mixtures with α'-NaV_2O_5 are also under investigation. For instance, combining CaV_2O_5, which is a half-filled spin ladder system, with α'-NaV_2O_5 creates solid solutions of a spin-Peierls–spin gap material. Small Ca substitution suppresses the SP transition, analogous to Na deficiency [146]

3.3 Organic SP Materials

Organic molecular solids continue to remain prototype materials for the study of unusual magnetically driven phase transitions and magnetic ground states. To date, several systems have been identified which have an SP transition (Table 1), although the complete "list" of all organic SP materials remains fairly limited. That the SP ground state is not more common has been attributed to the predominance of long-range ordered phases driven by electron–electron interactions over those with low-energy magnetoelastic coupling; such mechanisms are particularly important in the organic solids and conspire to stabilize Neél and density-wave ground states. Nevertheless, organic molecular solids remain important fixtures in the SP field. The chemical structures of the organic building block molecules, which form the basis for the SP molecular solids, are shown in Fig. 14. Note the central importance of the TTF architecture here.

Considering the comprehensive article on the SP transition previously written by Bray et al. in the early 1980s [1], the goal in this review is to highlight the im-

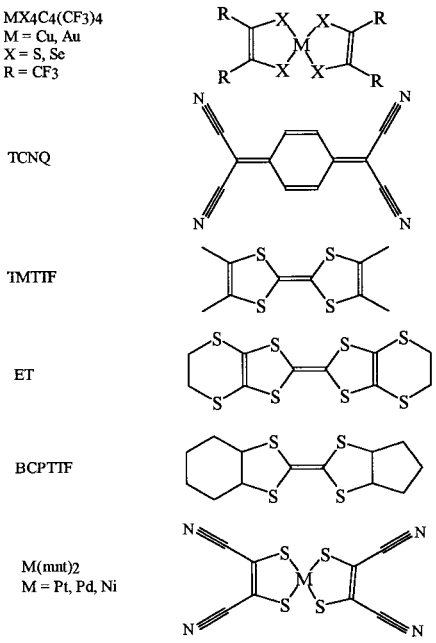

Fig. 14. Chemical structures of "building block molecules" for organic SP materials. (TTF)MBDT, bisethylenedithiolene; TCNQ, tetracyanoquinodimethane; TMTTF, tetramethyltetrathiofulvalene; ET, bisethylenedithiotetrathiafulvalene; BCPTTF, benzocyclopentyltetrathiafulvalene; $M(mnt)_2$, bismaleonitriledithiolate.

portant *new* developments with regard to these materials subsequent to 1983. In addition to results on traditional organic molecular solids (such as $MEM(TCNQ)_2$ and (TTF)CuBDT)), we also discuss modern donor systems based on TMTTF, BCPTTF, ET, and $M(mnt)_2$. Whereas most solids in Table 1 are low-dimensional, α'-$(ET)_2Ag(CN)_2$ and β'-$(ET)_2SF_5CF_2SO_3$ are especially curious as a result of important two-dimensional interactions. We begin our survey with the latest results on (TTF)CuBDT, the system developed at General Electric in which the SP transition was first observed.

3.3.1 (TTF)M(BDT): M = Cu, Au

To investigate the structural effects which are so central to the coupling of a low-dimensional quantum spin system and the lattice, Kiryukhin and coworkers made high-resolution X-ray diffraction measurements on single crystal samples of (TTF)CuBDT in an applied magnetic field to determine the structure in the high-field phase of (TTF)CuBDT [28]. As expected in this system, new Bragg reflections were observed in the low-temperature SP phase compared with the high-temperature paramagnetic phase; however, the same superlattice reflections decreased in intensity with applied field in the dimerized regime of the phase diagram. That the superlattice reflections go to zero at H_c is indicative of a nonexistent single–triplet gap at this point, in agreement with previous theoretical work. After a narrow co-existence regime, two satellite reflections develop at positions incommensurate with the underlying lattice, and the strength of the incommensurate reflection grows with the

applied field.This observation suggests that the lattice modulation wave vector becomes a continuous function of the applied magnetic field, as predicted in previous theoretical work. At the same time, the marked hysterisis effects and the two-phase coexistence implies that the commensurate → incommensurate transition is first-order in (TTF)CuBDT.

(TTF)AuBDT has also been the subject of proton and fluorine NMR studies in an effort to characterize the nature of the incommensurate phase [147]. Only a very moderate field is required here, because $H_c = 2.25\,\mathrm{T}$, making the "high-field phase" substantially more accessible than in (TTF)CuBDT, for instance. Hijmans et al. show that the shape and width of the spin echo is highly sensitive to the SP → incommensurate phase boundary, with the echo shape being well-described in terms of a soliton–lattice model by Nakano and Fukuyama [27]. ESR experiments have indirectly probed the magnetic nature and incommensurate structure of the high-field phase in TTF(AuBDT) also [148].

Bonner et al. have conducted detailed specific heat measurements on (TTF)AuBDT, with special interest in the SP → incommensurate phase boundary [10]. In addition to mapping the H–T phase diagram, the hysteresis in the high-field phase boundary and the validity of a soliton picture were assessed. The authors stress that the thermodynamic data does not reflect the characteristic features of soliton excitations, although they note that the pronounced mean-field character of the SP transition might obscure such signatures.

3.3.2 MEM(TCNQ)$_2$

As with the aforementioned (TTF)CuBDT system, accurate structural investigation of MEM(TCNQ)$_2$ has been one of the major achievements since the previous review of SP materials by Bray et al. [1]. This work has, however, concentrated on the details of molecular packing, both in the high-temperature and SP phases, and high-field structural studies are still lacking. For instance, the neutron scattering data of Visser et al. shows clear evidence for the dimer → tetramer transition along the TCNQ stack as the temperature is reduced below T_c, in agreement with previous data of van Bodegom et al. [149]. The interchain lattice fluctuations give rise to a transverse structural shift of every second dimer in the stack, according to $\Delta\vec{\nu} = 0.17L + 0.10M$. Note that this inter-dimer vector is parallel to the TCNQ molecular planes. Calculations of transfer integrals and probabilities are presented for both the normal and SP phases, and although these changes are small, modifications of the t and U bands are visible via optical spectroscopy [150]. Here U is the Coulomb repulsion energy and t is the transfer integral. In contrast to results on other organic SP materials, critical fluctuation effects in MEM(TCNQ)$_2$ are observed only about 20 K above T_c [151]. Further, these fluctuations have been shown to have a three-dimensional nature, which is fairly unconventional. The limited range of lattice fluctuations is thought to be responsible for the close fit of the Bonner–Fischer expression to the susceptibility of MEM(TCNQ)$_2$.

The theoretical work of Ung et al. concentrated on the nature of $2k_F$ and $4k_F$ bond-order wave and charge-density wave patterns for quarter-filled organic solid

under various correlation conditions [152]. It is found that Coulomb interactions add an increasing $4k_F$ component. The bond distortion and charge modulation for MEM(TCNQ)$_2$ below the $2k_F$ distortion is found to be a combination of period 4 and period 2 patterns.

The central role of the lattice in the magnetoelastic SP transition has led to several far-infrared investigations of MEM(TCNQ)$_2$ [153,154]. In particular, a soft mode has been identified at 8.5 cm^{-1}. This mode, which is polarized almost entirely in the TCNQ plane, contains the static shift associated with the SP transition. The 8.5 cm^{-1} structure appears only below T_c, red-shifting and broadening with increasing temperature. Such a soft mode is thought to facilitate spin–phonon ordering. To explore changes in the low-energy elastic response of MEM (TCNQ)2 through the SP $\rightarrow$ incommensurate phase boundary, Li et al. [63] performed far-infrared transmission measurements as a function of applied magnetic field (to 30 T) in the range 20–600 cm^{-1}. That neither the electron–phonon coupling modes nor the low-energy lattice modes of MEM(TCNQ)$_2$ were found to be sensitive to the high-field phase boundary was attributed to the molecular nature of the sample combined with the extent of spin localization. There have been no magnetospectroscopic studies to follow the aforementioned 8.5 cm^{-1} soft mode as a function of magnetic field.

The μsr studies of Blundell et al. have added another twist to the MEM(TCNQ)$_2$ story [155]. Passing through T_c, a crossover from a Gaussian relaxation (where the fluctuations are to fast for μsr to follow) to an exponential relaxation (indicating local fluctuations) is observed. A similar crossover is observed in the inorganic prototype, $CuGeO_3$, and might thus be a general feature of the SP transition. The authors associate the slowing down of the electronic spin-fluctuations with the opening of the gap in the magnetic excitation spectrum.

3.3.3 DAP(TCNQ)

1,6-Pyrenediamine (DAP) tetracyanoquniodimethane (TCNQ) has been investigated as a model SP system [156]. X-ray, susceptibility, infrared, and optical spectroscopies have characterized the 160 K transition. As expected, the lattice dimerization is along the chain direction. That the transition temperature is much higher than normally observed is attributed to the small U/t ratio. The most intriguing aspect of the DAP(TCNQ) system is that the band-filling deviates slightly from half-filling, which gives rise to $S = 0$ soliton formation. A midgap band in the optical spectra is associated with this spinless domain wall.

3.3.4 (TMTTF)$_2$PF$_6$

(TMTTF)$_2$PF$_6$ is the sulfur analog of the well-known (TMTSF)$_2$PF$_6$, widely recognized as the first organic superconductor and model spin-density wave compound. Within the generalized T–P phase diagram for the (TM)$_2$X system, widely popularized by Jérome, (TMTTF)$_2$PF$_6$ sits squarely on the left-hand side, where the internal

pressure (because of the nature of the anion) is fairly small [157]. Note also that at temperatures above T_c, spin–charge decoupling has been observed, with a charge gap developing in this region. Structural fluctuations seem to extend considerably into this charge gap regime directly above T_c. Changes in temperature and pressure can modulate the properties of $(TMTTF)_2PF_6$ considerably, tuning them from the SP state all the way through to the characteristic ground states of the selenide series. Indeed, it is the chemical and physical tunability of this internal pressure which links the various complexes on the T–P phase diagram. Electron correlation effects are extremely important over the full range of "internal pressures", and the relative size of the Hubbard parameters U and V seem to be one of the most important factors for exposing the differences between the TMTTF and TMTSF systems [152,158,159]. According to Seo and Fukuyama, the $(\uparrow, 0, \downarrow, 0)$ spin structure of $(TMTTF)_2Br$ requires a large V and concomitant charge disproportionation [159]. This generalized phase diagram is shown schematically in Fig. 15. Application of a magnetic field is an additional mechanism for modulating the dimensionality of the $(TMTTF)_2PF_6$ system. Indeed, the H–T diagram is in line with that expected for a SP material [160].

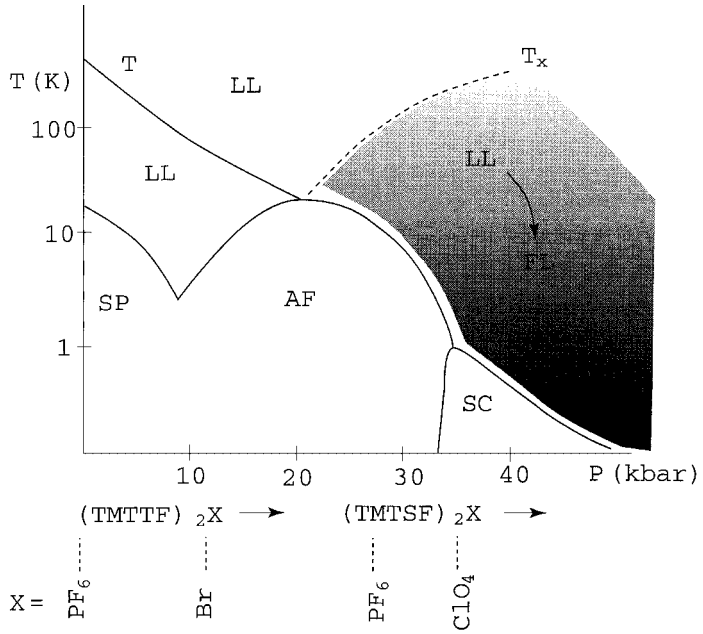

Fig. 15. Generalized temperature–pressure phase diagram for the Bechgaard salts $(TMTSF)_2X$ and their sulfur analog $(TMTTF)_2X$. On the left, the normal phase of the sulfur compounds is a Luttinger liquid (LL) that becomes gapped in the charge sector (LL_σ) below T_ρ and can develop either an SP or localized antiferromagnetic (AF) ordered state. Under pressure, the properties of the sulfur series evolve towards those of the selenides for which the normal state shows a progressive restoration of a Fermi liquid (FL) precursor to itinerant antiferromagnetism and superconductivity (SC). Reprinted with permission from Ref. [157], Copyright 1998 by the American Association for the Advancement of Science.

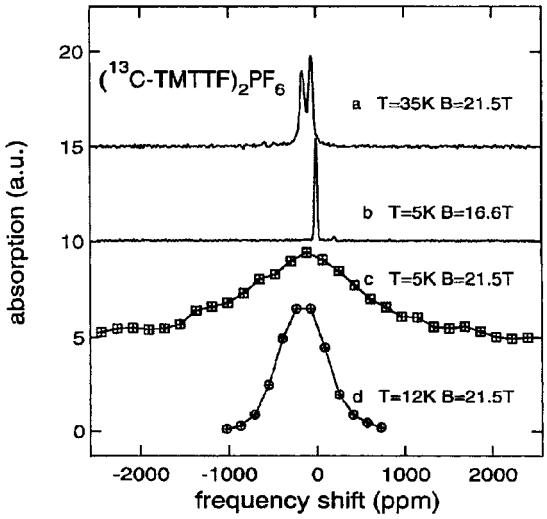

Fig. 16. ^{13}C NMR spectra of $(TMTTF)_2PF_6$ taken at different fields and temperatures. The relative shift from zero (in parts per million) arises from the hyperfine coupling. Reprinted with permission from Ref. [160], Copyright 1998 by the American Physical Society.

Perhaps the most striking example of the exotic physical phenomena in the TMTTF compound is the recent NMR measurements of Brown et al. [160]. Here, the authors investigate the lineshape of $(TMTTF)_2PF_6$ by ^{13}C NMR, using the temperature and applied field to move around the phase diagram. Typical data are shown in Fig. 16. In addition to establishing the H–T phase diagram of $(TMTTF)_2PF_6$ for the first time, the authors capture a fascinating view of dissipation mechanisms in this sample. In the incommensurate phase, the staggered component of the magnetization (or the characteristic spin–soliton wall width) in $(TMTTF)_2PF_6$ is quite large (small) compared with that the inorganic prototype $CuGeO_3$ and is attributed to strong intersite antiferromagnetic coupling. The authors also estimate the size of the singlet-triplet gap, Δ_s, as 50 K. Recently, NMR data of $(TMTTF)_2PF_6$ under pressure have also been reported [161].

3.3.5 $(BCPTTF)_2X$

Interest in the BCPTTF-based organic molecular solid stems from the unfortunate fact that accurate studies of structural fluctuations in the $(TMTTF)_2PF_6$ system can not be performed because of the sensitivity of the TMTSF material to irradiation damage by probing X-rays. Thus, the more robust $(BCPTTF)_2AsF_6$ (and $(BCPTTF)_2PF_6$) serve as useful model compounds for investigation of pretransitional fluctuations in TTF-based SP materials. That the crystal structure is fairly close to that observed in $(TMTTF)_2PF_6$, with short S–S contacts between neighboring chains and similar transfer integral ratios, adds credibility to this effort [151,162].

The asymmetrical BCPTTF compounds have low conductivity at 300 K, and strong activated behavior at reduced temperature [162]. This localization is actually a major

difference between the BCPTTF-based systems and related TMTTF compounds. As shown in Table 1, SP ordering sets in somewhat above 30 K. This relatively high transition temperature (even compared with $(TMTTF)_2PF_6$) has been attributed to enhanced one-dimensionality. The magnetic susceptibility of the PF_6 and AsF_6 compounds both deviate strongly from Bonner-Fischer behavior upon approach to T_c. In addition to the sharp drop of the susceptibility at T_c, superlattice reflections are also observed below the transition [151].

To probe the pretransitional fluctuations in $(BCPTTF)_2AsF_6$, X-ray diffraction measurements have been conducted at low temperature by Liu et al. [151]; the long-range order resulting from the transition to the SP state is clearly evident. Above 60 K, fluctuations are quasi-one dimensional, and they persist up to 120 K with a fairly substantial correlation length, establishing the one-dimensional nature of the driving force for the SP transition in $(BCPTTF)_2AsF_6$. Further, deviations from the Bonner–Fischer law upon approach to T_c are interpreted as arising from local pairing of the spins, because of the critical lattice fluctuations, therefore linking these two quantities. This provides a natural explanation for the deviation of χ below 120 K in $(BCPTTF)_2AsF_6$.

As a model system for investigation of structural effects to supplant those of $(TMTTF)_2PF_6$, the BCPTTF-type materials are highly successful. Unfortunately, these compounds have not been the subject of intense physical property characterization subsequent to these structural studies. High-field NMR measurements, which might compliment the aforementioned studies on $(TMTTF)_2PF_6$, would be most helpful here.

3.3.6 α′-$(ET)_2Ag(CN)_2$

The organic SP system α'-$(ET)_2Ag(CN)_2$ has been the subject of several wide-ranging investigations. The α' morphology consists of donor stacks of twisted ET dimers in an overall quasi-one-dimensional chain structure [163]. Despite the strong twist angle, which gives rise to the semiconducting character, some interchain interactions are established, because of the well-known S–S contacts of the ET molecules. That the $Ag(CN)_2$ salt has an SP ground state, while structurally similar $AuBr_2^-$ and $CuCl_2^-$ analogs do not, is attributed to structural differences and a possible soft mode of the lattice [163].

Susceptibility data of α'-$(ET)_2Ag(CN)_2$ are well described by a Bonner–Fisher model for a linear chain ferromagnet, although the exchange constant ($J = 59$ K) is somewhat smaller than that observed in other prototype organic SP materials [163,164]. The field dependence of the uniform $\rightarrow$ dimerized phase boundary line has been explored up to 5 T, and decreases with applied field, as expected [164].

Infrared and optical spectra support strong electron–phonon coupling and a large-U model, where electron correlation effects are very important [165]. Whereas the low-energy optical transition near 0.45 eV is attributed to intra-dimer charge transfer, the optical feature near 1.3 eV is likely associated with the on-site Coulomb repulsion, U–V.

3.3.7 β′-$(ET)_2SF_5CF_2SO_3$

A new strategy for the preparation of ET-based superconductors has recently been pursued on the basis of the design of large discrete counterions to enhance two-dimensional interactions in the solid state [166]. In the $(ET)_2SF_5RSO_3$ system, small chemical modifications of the anion template can result in the stabilization of a variety of different ground states, including SP, semiconducting, metallic, or superconducting types [166,167]. It is β'-$(ET)_2SF_5CF_2SO_3$, the newly discovered SP material with $T_c = 45$ K, which is of interest here.

The crystal structure of β'-$(ET)_2SF_5CF_2SO_3$ has the low-dimensional architecture typical of many β-type molecular conductors, with two-dimensional conducting planes separated by a charge storage layer [166,167]. Although strong ET dimers are formed in both stacks, interaction between dimers is not strong, leading the dimeric units in β'-$(ET)_2SF_5CF_2SO_3$ to act as spin centers. For this complex, no disorder is observed either in the cation or anion layers. The short contacts between the anions and the ET donors are not the same in the two stacks, however. Molecular charges are not identical either, favoring electron localization. A recent overview of synthetic efforts is provided in Refs. [166–168], and numerous investigations of physical properties are in progress.

3.3.8 Perylene

$Per_2[M(mnt)_2]$ (M = metal) is a two-chain organic solid [169]. Here M is Ni, Pt, Au, Co, Fe, Cu, or Pd. The solid comprises a "free carrier perylene stack" (where highly mobile carriers are responsible for the conductivity properties) and a chain of localized electrons on the bismaleonitriledithiolate ($M(mnt)_2$), which are responsible for the magnetic properties. There is non-negligible coupling between the conducting and magnetic chains. Thus, the $Per_2[M(mnt)_2]$ complexes enable study of the interaction between the conduction electrons and the localized spins at a molecular level.

The Au and Pt-based $Per_2[M(mnt)_2]$ systems have attracted special attention recently, because these two compounds are isostructural with similar metal → insulator transition temperatures [170–173]. However, the $S = 0$ Au system forms diamagnetic chains, whereas magnetic interactions are possible in the $S = 1/2$ Pt complex. In each case, the materials have an electronic Peierls transition at low temperature, the main driving force being electron–phonon interactions in the perylene chains. The Au system offers an opportunity to examine field effects on the electronic Peierls transition in isolation. For the Pt system, however, the density wave distortion forces a transition on the spin chains, leading to formation of a dimer in a singlet (SP) state [171]. In other words, the $4k_F$ distortion on the perylene chain equals the $2k_F$ distortion on the dithiolate stack. That magnetic ordering occurs at the same temperature as the metal → insulator transition is confirmed both by heat capacity measurements and by the field dependence of the transition temperatures for both the Au and Pt complexes.

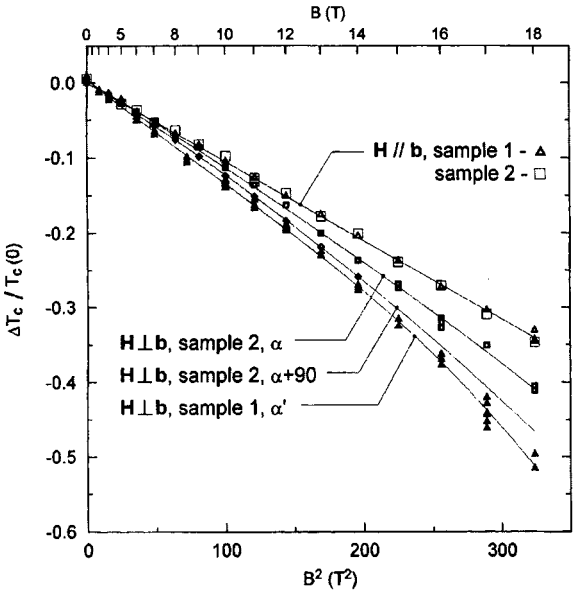

Fig. 17. Transition temperature shift, $\Delta T/T_c = [T_c(B) - T_c(0)]/T_c(0)$, as plotted as a function of B^2 for different $(Per)_2Pt(mnt)_2$ samples and configurations. For sample 2 in the perpendicular field direction, two sets of measurements with a 90° rotation of the sample holder around the b axis are shown. The lines guide the eye. Reprinted with permission from Ref. [173], Copyright 1996 by the American Physical Society.

The DC resistivity investigations of $Per_2[Pt(mnt)_2]$ and $Per_2[Au(mnt)_2]$ up to 18 T, performed by Matos et al. to assess the field dependence of the transition temperatures compared with mean field theoretical predictions, are particularly interesting [173]. The most striking result is the anisotropy reported in the Pt complex, the transition temperature for which decreases as H_2 for the field applied along the chain direction and for which the field fall-off is somewhat faster when H is applied perpendicular to the chains (Fig. 17). That no anisotropy in the transport or magnetic response is observed in the isostructural Au complex suggests that the anisotropy is a signature of the coupled perylene and $Pt(mnt)_2$ chains. The authors note that, in addition to being unable to account for fluctuation effects, the mean field model cannot explain the anisotropy found for the Pt compound.

Microwave dielectric measurements at 16 GHz have also been used to enable understanding of the effect of an applied field on the concomitant transitions in the Pt compound [174]. Here, the major effect of the field on ε_1 is to displace the peak to lower temperature, which is essentially a mean field modification of the gap as:

$$\Delta T_p(H)/T_p(H) = (T_p(H) - T_p(0))/T_p(0) = -\alpha(\mu_B H/k_B T_p(0))^2 . \qquad (9)$$

In contrast with the aforementioned resistivity measurements, no anisotropy is observed in the 16 GHz microwave dielectric measurements up to 14 T. Alloying

$Per_2[Pt(mnt)_2]$ with 2% Au reduces the transition temperature because of electron–hole pair-breaking effects.

3.3.9 ζ-(ET)PF_6

ζ-(ET)PF_6 is another organic molecular solid that displays a SP transition (40 K) [175]; it is particularly novel due to the 1 : 1 ratio of donor to acceptor. This material has been the subject of an extensive structural, magnetic, and optical investigation. The exact value of the critical field is unknown.

3.4 Summary

I have reviewed the new developments in the field of SP materials, and it is apparent that this area has experienced a renaissance in recent years, certainly since the very comprehensive review article of Bray et al. in 1982. This intense activity has been fueled by the discovery of new materials and by hardware developments in high magnetic field research and computing. Several major challenges still present themselves to researchers in the field of SP solids. New materials development certainly takes center stage. The explosion of interest since the 1993 discovery of the first inorganic SP system speaks for itself, and comparisons between the new inorganic SP crystals and the organic prototypes have been very useful. At the same time, the small size of organic crystals has severely limited the physical methods which can be used to probe the various ground states. If larger, high-quality single crystals could be grown, neutron-scattering measurements would be of particular interest. Second, the role of impurities and defects in modulating the properties of SP solids is still not well understood, and this is especially important given the suppression of T_c with Zn substitution in the copper oxide superconductors [175,176]. On-going theoretical work should resolve the nature of the competing ground states in these doped systems. While doping in $CuGeO_3$ and α'-NaV_2O_5 have already received enormous attention, solid solutions of the organics, pursued for a time on Cu and Au BDT systems, have not fared as well. Third, the role of pretransitional fluctuations and interchain coupling is of great interest. The low temperature structure of α'-NaV_2O_5 and the possible transverse spin pairing or modulated low temperature ground state is of central importance here. Two-dimensional SP systems are also of current concern [178–180], and the role of frustration in going from one $\rightarrow$ two dimensions is still unclear [181]. Finally, efforts to exploit the magnetic characteristics of SP compounds for useful devices should be expanded. Many fundamental materials properties of these compounds (such as high Curie temperature, the electromagnetic response, or very narrow ESR line-widths) could be exploited for various applications. New geometries, such as those recently discovered in fullerene and charge density wave materials, might also yield important new properties. Thus, it is the hope of this author that device engineers interested in thin-film formation, Langmuir–Blodgett

layers, wires, magnetic sensors, nonlinear optical solids, and magnetic storage devices might some day find the opportunity that lies with these prototype materials. Processing and interface issues will probably present the most important challenge here. Incorporation of organic and inorganic SP compounds in hybrid composites may also prove of value.

Fagot-Revurat et al. recently reported ^{23}Na and ^{51}V NMR evidence for a charge order driven spin Peierls transition in α'-NaV_2O_5 [182]. Nakao et al. also reported x-ray scattering evidence of the fully charged zigzag-type ordered state below 34 K in α'-NaV_2O_5 [183].

Acknowledgments

The author gratefully acknowledges financial support for this project from the Division of Materials Research at the National Science Foundation (Grant No. 9623221) and the the Division of Materials, Basic Energy Sciences, U.S. Department of Energy (Grant No. DE-FG02-99ER45741). She especially wishes to thank the authors whose figures she has reproduced in this article. She also thanks Professor J.W. Brill for his careful reading of this manuscript. Technical assistance was provided by A. Garlach, B.R. Jones, Z. Zhu, and I. Olejniczak.

References

[1] J.W. Bray, L.V. Interrante, I.S. Jacobs, and J.C. Bonner in *Extended Linear Chain Compounds*, Vol. 3, J.S. Miller (Ed.), Plenum, New York, **1983**.
[2] M.C. Cross, *Phys. Rev. B.*, **1979**, *20*, 4606–4611.
[3] M.C. Cross and D.S. Fischer, *Phys. Rev. B.*, **1979**, *19*, 402–419.
[4] M. Hase, I. Terasaki, and K. Uchinokura, *Phys. Rev. Lett.*, **1993**, *70*, 3651–3654.
[5] M. Hase, I. Terasaki, K. Uchinokura, M. Tokunaga, N. Miura, and H. Obara, *Phys. Rev. B.*, **1993**, *48*, 9616–9619.
[6] M. Hase, I. Terasaki, Y. Sasago, K. Uchinokura, and H. Obara, *Phys. Rev. Lett.*, **1993**, *71*, 4059–4062.
[7] M. Isobe and Y. Ueda, *J. Phys. Soc. Jpn*, **1996**, *65*, 1178–1181.
[8] Y. Ueda, *Chem. Mater.*, **1998**, *10*, 2653–2664.
[9] J.P. Boucher and L.P. Regnault, *J. Phys. I France*, **1996**, *6*, 1939–1966.
[10] J.C. Bonner, J.A. Northby, I.S. Jacobs, and L.V. Interrante, *Phys. Rev. B.*, **1987**, *35*, 1791–1798.
[11] I. Harada and A. Kotani, *J. Phys. Soc. Jpn*, **1982**, *51*, 1731–1744.
[12] W.A.C. Erkelens, L.P. Regnault, J. Laugrer, J. Rossat-Mignod, and L.J. de Jongh, *Solid State Commun.*, **1985**, *55*, 209–213.
[13] I.S. Jacobs, J.W. Bray, H.R. Hart, Jr., L.V. Interrante, J.S. Kasper, G.D. Watkins, D.E. Prober, and J.C. Bonner, *Phys. Rev. B.*, **1976**, *14*, 3036–3051.

[14] M.J. Rice, V.M. Yartsev, and C.S. Jacobsen, *Phys. Rev. B.*, **1980**, *21*, 3437–3446.
[15] M. Nishi, O. Fujita, and J. Akimitsu, *Phys. Rev. B.*, **1994**, *50*, 6508–6511.
[16] G.S. Uhrig, *Phys. Rev. Lett.*, **1997**, *79*, 163–166.
[17] J. Riera and A. Dobry, *Phys. Rev. B.*, **1995**, *51*, 16098–16102.
[18] G. Li, J.S. Lee, V.C. Long, J.L. Musfeldt, Y.J. Wang, M. Almeida, A. Revcolevschi, and G. Dhalenne, *Chem. Mater.* **1998**, *10*, 1115–1119.
[19] G. Castilla, S. Charkravarty, and V.J. Emery, *Phys. Rev. Lett.*, **1995**, *75*, 1823–1826.
[20] M. Azzouz and C. Bourbonnais, *Phys. Rev. B.*, **1996**, *53*, 5090–5093.
[21] J. Zang, A.R. Bishop, and D. Schmeltzer, *Phys. Rev. B.*, **1995**, *52*, 6233–6728.
[22] A.W. Sandvik, R.R.P. Singh, and D.K. Campbell, *Phys. Rev. B.*, **1997**, *56*, 14510–14528.
[23] A.W. Sandvik and D.K. Campbell, *Phys. Rev. Lett.*, **1999**, *83*, 195–198.
[24] R.J. Bursill, R.H. McKenzie, and C.J. Hamer, *Phys. Rev. Lett.*, **1999**, *83*, 408–411.
[25] M. Poirier, M. Castonguay, A. Revcolevschi, and G. Dhalenne, *Phys. Rev. B.*, **1995**, *51*, R6147–6150.
[26] L.N. Bulaevskii, A.I. Buzdin, and D.I. Khomskii, *Solid State Commun.*, **1978**, *27*, 5–12.
[27] T. Nakano and H. Fukuyama, *J. Phys. Soc. Jpn*, **1980**, *49*, 1679–1685.
[28] V. Kiryukhin, B. Keimern, and D.E. Moncton, *Phys. Rev. Lett.*, **1995**, *74*, 1669–1672.
[29] V. Kiryukhin and B. Keimer, *Phys. Rev. B.*, **1995**, *52*, R704–707.
[30] H. Völlenkle, A. Wittmann, and H. Nowotny, *Monatsch. Chem.*, **1967**, *98*, 1352–1357.
[31] M. Braden, G. Wilkendorf, J. Lorenzana, M. Aïn, G.J. McIntyre, M. Behruzi, G. Heger, G. Dhalenne, and A. Revcolevschi, *Phys. Rev. B.*, **1996**, *54*, 1105–1116.
[32] O. Kamimura, M. Terauchi, M. Tanaka, O. Fujita, and J. Arkimitsu, *J. Phys. Soc. Jpn*, **1994**, *63*, 2467–2471.
[33] H. Winkelmann, E. Gamper, B. Büchner, M. Braden, A. Revcolevschi, and G. Dhalenne, *Phys. Rev. B.*, **1995**, *51*, 12884–12887.
[34] K. Hirota, D.E. Cox, J.E. Lorenzo, G. Shirane, J.M. Tranquada, M. Hase, K. Uchinokura, H. Kojima, Y. Shibuya, and I. Tanaka, *Phys. Rev. Lett.*, **1994**, *73*, 736–739.
[35] J.P. Pouget, L.P. Regnault, M. Ain, B. Hennion, J.P. Renard, P. Veillet, G. Dhalenne, and A. Revcolevschi, *Phys. Rev. Lett.*, **1994**, *72*, 4037–4040.
[36] Q.J. Harris, Q. Feng, R.J. Birgeneau, K. Hirota, K. Kakurai, J.E. Lorenzo, G. Shirane, M. Hase, K. Uchinokura, H. Kojima, I. Tanaka, Y. Shibuya, *Phys. Rev. B.*, **1994**, *50*, 12606–12610.
[37] H. Kuroe, J.I. Sasaki, T. Sekine, N. Koide, Y. Sasago, K. Uchinokura, M. Hase, *Phys. Rev. B.*, **1997**, *54*, 409–415.
[38] L.P. Regnault, M. Aïn, B. Hennion, G. Dhalenne, and A. Revcolevschi, *Phys. Rev. B.*, **1996**, 53, 5579–5597.
[39] M. Arai, M. Fujita, M. Motokawa, J. Akimitsu, and S.M. Bennington, *Phys. Rev. Lett.*, **1996**, *77*, 3649–3652.
[40] M. Aïn, J.E. Lorenzo, L.P. Regnault, G. Dhalenne, A. Revcolevschi, B. Hennion, and Th. Jolicoeur, *Phys. Rev. Lett.*, **1997**, *78*, 1560–1563.
[41] M. Aïn, L.P. Regnault, G. Dhalenne, A. Revcolevschi, L.E. Lorenzo, and Th. Jolicoeur, *J. Appl. Phys.*, **1997**, *81*, 4393–4395.
[42] J.E. Lorenzo, L.P. Regnault, B. Hennion, M. Aïn, F. Bourdarot, J. Kulda, G. Dhalenne, and A. Revcolevschi, *J. Phys.: Condens. Matter*, **1997**, *9*, L211–L217.
[43] M. Braden, E. Ressouche, B. Büchner, R. Kebler, G. Heger, G. Dhalenne, and A. Revcolevschi, *Phys. Rev. B.*, **1998**, *57*, 11497–11503.
[44] M. Braden, B. Hennion, W. Reichardt, G. Dhalenne, and A. Revcolevschi, *Phys. Rev. Lett.*, **1998**, *80*, 3634–3637.
[45] M.C. Martin, G. Shirane, Y. Fujii, M. Nishi, O. Fujita, J. Akimitsu, M. Hase, and K. Uchinokura, *Phys. Rev. B.*, **1996**, *53*, R14713–14716.

[46] G. Els, P.H.M. van Loosdrecht, P. Lemmens, H. Vonberg, G. Güntherodt, G.S. Uhrig, O. Fujita, J. Akimitsu, G. Dhalenne, and A. Revcolevschi, *Phys. Rev. Lett.*, **1997**, *79*, 5138–5141.
[47] Y. Fagot-Revurat, M. Horvatic, C. Bertier, P. Ségransan, G. Dhalenne, and A. Revcolevschi, *Phys. Rev. Lett.*, **1996**, *77*, 1861–1864.
[48] M. Horvatic, Y. Fagot-Revurat, C. Bertier, P. Ségransan, G. Dhalenne, and A. Revcolevschi, *Phys. Rev. Lett.*, **1999**, *83*, 420–423.
[49] U. Ammerahl, T. Lorenz, B. Büchner, A. Revcolevschi, and G. Dhalenne, *Z. Phys. B.*, **1997**, *102*, 71–82.
[50] M. Nishi, O. Fujita, J. Akimitsu, K. Kakurai, and Y. Fujii, *Phys. Rev. B.*, **1995**, *52*, R6959–6962.
[51] Y.-K. Kuo, E. Figueroa, and J.W. Brill, *Solid State Commun.*, **1995**, *94*, 385–389.
[52] J.C. Lasjaunias, P. Monceau, G. Reményi, S. Ahling, G. Dhalenne, and A. Revcolevschi, *Solid State Commun.*, **1997**, *101*, 667–680.
[53] R.J. Birgeneau, V. Kiryukhin, and Y.J. Wang, submitted, *Phys. Rev. B.*
[54] T. Lorenz, U. Ammerahl, R. Ziemes, B. Büchner, A. Revcolevschi, and G. Dhalenne, *Phys. Rev. B.*, **1996**, *54*, R15610–15613.
[55] Y. Yamamoto, H. Ohta, M. Motokawa, O. Fujita, and J. Akimitsu, *J. Phys. Soc. Jpn*, **1977**, *66*, 1115–1123.
[56] M. Honda, T. Shibata, K. Kindo, and S. Sugai, *J. Phys. Soc. Jpn*, **1996**, *65*, 691–694.
[57] M. Itoh, M. Sugahara, T. Yamauchi, and Y. Ueda, *Phys. Rev. B.*, **1996**, *53*, 11606–11612.
[58] T.M. Brill, J.P. Boucher, J. Voiron, G. Dhalenne, and A. Revcolevschi, and J.P. Renard, *Phys. Rev. Lett.*, **1994**, *73*, 1545–1548.
[59] Z.V. Popovic, S.D. Devic, V.N. Popov, G. Dhalenne, and A. Revcolevschi, *Phys. Rev. B.*, **1995**, *52*, 4185–4190.
[60] M.N. Popova, A.B. Sushkov, S.A. Golibchik, A.N. Vasil'ev, and L.I. Leonyuk, *Phys. Rev. B.*, **1998**, *57*, 5040–5043.
[61] A. Damascelli, D. van derMarel, F. Parmigiani, G. Dhalenne, and A. Revcolevschi, *Phys. Rev. B.*, **1997**, *56*, R11373–11376.
[62] A. Damascelli, D. van der Marel, F. Parmigiani, G. Dhalenne, and A. Revcolevschi, *Physica B.*, **1998**, *244*, 114–120.
[63] G. Li, J.L. Musfeldt, Y.J. Wang, S. Jandl, M. Poirier, A. Revcolevschi, and G. Dhalenne, *Phys. Rev. B.*, **1996**, *54*, R15633–15636.
[64] P.H.M. Loosdretcht, S. Huant, G. Martinez, G. Dhalenne, and A. Revcolevschi, *Phys. Rev. B.*, **1996**, *54*, R3730–3733.
[65] K. Takehana, T. Takamasu, M. Hase, G. Kido, K. Uchinokura, *Phys. Rev. B.*, **2000**, *62*, 5191–5198.
[66] I. Terasaki, R. Itti, N. Koshizuka, M. Hase, I. Tsukada, and K. Uchinokura, *Phys. Rev. B.*, **1995**, *52*, 295–298.
[67] M. Bassi, P. Camagni, G. Samoggia, F. Parmigiani, G. Dhalenne, and A. Revcolevschi, *Phys. Rev. B.*, **1996**, *54*, R11030–11033.
[68] S.D. Devic, Z.V. Popovic, A. Breitschwerdt, G. Dhalenne, and A. Revcolevschi, *Phys. Stat. Sol. (B)*, **1997**, *203*, 579–583.
[69] M.N. Popova, A.B. Sushkov, S.A. Golubchik, A.N. Vasil'ev, and L.I. Leonyuk, *JETP*, **1996**, *83*, 1227–1230.
[70] F. Parmigiani, L. Sangaletti, A. Goldoni, U. del Pennino, C. Kim, and Z.-X. Shen, *Phys. Rev. B.*, **1997**, *55* 1459–1468.
[71] V.C. Long, J.L. Musfeldt, T. Schmeidel, G. Dhalenne, and A. Revcolevschi, *Phys. Rev. B.*, **1997**, *56*, R14263–14266.

[72] J. Zeman, G. Martinez, P.H.M. van Loosdretscht, G. Dhalenne, and A. Revcolevschi, *Phys. Rev. Lett.*, **1999**, *83*, 2648–2651.
[73] L.F. Mattheiss, *Phys. Rev. B.*, **1994**, *49*, 14050–14053.
[74] H. Wu, M.-C. Qian, and Q.-Q. Zheng, *J. Phys.: Condens. Matter*, **1999**, *11*, 209–219.
[75] Z.V. Sljivancanin, Z.S. Popovic, and F.R. Vukajlovic, *Phys. Rev. B.*, **1997**, *56*, 4432–4438.
[76] S. Zagoulaev and I.I. Tupitsyn, *Phys. Rev. B.*, **1997**, *55*, 13528–13541.
[77] Z.S. Popovic, F.R. Vukajlovic, and Z.V. Sljivancanin, *J. Phys.: Condens. Matter*, **1995**, *7*, 4549–4559.
[78] S. Inagaki and H. Fukuyama, *J. Phys. Soc. Jpn*, **1983**, *52*, 3620–3629.
[79] S. Inagaki and H. Fukuyama, *J. Phys. Soc. Jpn*, **1984**, *53*, 4386–4392.
[80] P.H.M. van Loosdretch, J.P. Boucher, S. Huant, G. Martinez, G. Dhalenne, and A. Revcolevschi, *Physica B.*, **1997**, *230–232*, 1017–1020.
[81] P.H.M. van Loosdrecht, J.P. Boucher, G. Martinez, G. Dhalenne, and A. Revcolevschi, *Phys. Rev. Lett.*, **1996**, *76*, 311–315.
[82] T. Lorenz, B. Büchner, P.H.M. van Loosdrecht, F. Schönfeld, G. Chouteau, A. Revcolevschi, and G. Dhalenne, *Phys. Rev. Lett.*, **1998**, *81*, 148–151.
[83] M. Saint-Paul, G. Reményi, N. Hegman, P. Monceau, G. Dhalenne, and A. Revcolevschi, *Phys. Rev. B.*, **1997**, *55*, R6121–6124.
[84] P.H.M. van Loosdretch, J.P. Boucher, G. Martinez, G. Dhalenne, and A. Revcolevschi, *J. Appl. Phys.*, **1996**, *79*, 5395–5397.
[85] P.H.M. van Loosdrecht, J. Zeman, G. Martinez, G. Dhalenne, and A. Revcolevschi, *Phys. Rev. Lett.*, **1997**, *78*, 487–490.
[86] G. Dhalenne, A. Revcolevschi, J.C. Rouchaud, and M. Fedoroff, *Mater. Res. Bull.*, **1997**, *32*, 939–946.
[87] Y. Sasago, N. Koide, K. Uchinokura, M.C. Martin, M. Hase, K. Hirota, and G. Shirane, *Phys. Rev. B.*, **1996**, *54*, R6835–6838.
[88] B. Grenier, J.-P. Renard, P. Veillet, C. Pailsen, g. Dhalenne, and A. Revcolevschi, *Phys. Rev. B.*, **1998**, *58*, 8202–8205.
[89] H. Fukiyama, T. Tanimoto, and M. Saito, *J. Phys. Soc. Jpn*, **1996**, *65*, 1182–1185.
[90] R. Kadono, *J. Phys. Soc. Jpn*, **1997**, *66*, 505–506.
[91] K.M. Kojima, Y. Fudamoto, M. Larkin, G.M. Luke, J. Merrin, B. Nachumi, Y.J. Uemura, M. Hase, Y. Sasago, K. Uchinokura, Y. Ajiro, A. Revcolevschi, and J.-P. Renard, *Phys. Rev. Lett.*, **1997**, *79*, 503–506.
[92] B. Büchner, T. Lorenz, R. Walter, H. Kierspel, A. Revcolevschi, and G. Dhalenne, *Phys. Rev. B.*, **1999**, *59*, 6886–6907.
[93] Y. Ajiro, T. Asano, F. Masui, M. Metata, H. Aruga-Katori, T. Goto, and H. Kikichi, *Phys. Rev. B.*, **1995**, *51*, R9399–9402.
[94] Y.J. Wang, V. Kiryukhin, R.J. Birgeneau, T. Masuda, I. Tsukada, and K. Uchinokura, *Phys. Rev. Lett.*, **1999**, *83*, 1676–1679.
[95] J.-P. Renard, K. Le Dang, P. Veillet, G. Dhalenne, A. Revcolevschi, and L.-P. Regnault, *Europhys. Lett.*, **1995**, *30*, 475–584.
[96] L.P. Regnault, J.P. Renard, G. Dhalenne, and A. Revcolevschi, *Europhys. Lett.*, **1995**, *32*, 579–584.
[97] M. Poirier, R. Beaudry, M. Castonguay, M.L. Plummer, G. Quirion, F.S. Razavi, A. Revcolevschi, and G. Dhalenne, *Phys. Rev. B.*, **1995**, *52*, R6971–6974.
[98] P. Fronzes, M. Poirier, A. Revcolevschi, and G. Dhalenne, *Phys. Rev. B.*, **1997**, *55*, 8324–8329.
[99] H. Nojiri, T. Hamamoto, Z.J. Wang, S. Mitsudo, M. Motokawa, S. Kimura, H. Ohta, A. Ogiwara, O. Fujita, and J. Akimitsu, *J. Phys.: Cond. Matt.*, **1997**, *9*, 1331–1338.

[100] T. Masuda, I. Tsukada, K. Uchinokura, Y.J. Wang, V. Jiryukhin, and R.J. Birgeneau, *Phys. Rev. B.*, **2000**, *61*, 4103–4108.
[101] S.V. Demishev, L. Weckhuysen, J. Vanacken, L. Trappeniers, F. Herlach, Y. Bruynseraede, V. V. Moshchalkov, A.A. Pronin, N.E. Sluchanko, N.A. Samarin, J. Meersschaut, and L.I. Leonyuk, *Phys. Rev. B.*, **1998**, *58*, 6321–6329.
[102] M. Fabrizio, R. Mélin, and J. Souletie, *Euro. Phys. J. B.*, **1999**, *10*, 607–621.
[103] M.C. Martin, M. Hase, K. Hirota, G. Shirane, Y. Sasago, N. Koide, and K. Uchinokura, *Phys. Rev. B.*, **1997**, *56*, 3171–3180.
[104] B. Grenier, L.P. Regnault, J.E. Lorenzo, J. Voiron, J. Bossy, J.P. Renard, G. Dhalenne, and A. Revcolevschi, *EuroPhys. Lett.*, **1998**, *44*, 511–517.
[105] J. Takeya, I. Tsukada, Y. Ando, T. Masuda, K. Uchinokura, *Phys. Rev. B.*, **2000**, *62*, R9260–9263.
[106] V. Kiryukhin and B. Keimer, J.P. Hill, S.M. Coad, and D. McK. Paul, *Phys. Rev. B.*, **1996**, *54*, 7269–7278.
[107] M. Hase, K.M.S. Etheredge, S.J. Hwu, K. Hirota, and G. Shirane, *Phys. Rev. B.*, **1997**, *56*, 3231–3238.
[108] P. Fronzes, M. Poirier, A. Revcolevschi, and G. Dhalenne, *Phys. Rev. B.*, **1997**, *56*, 7827–7830.
[109] A.K. Hassan, L.A. Pardi, G.B. Martins, G. Cao, and L.-C. Brunel, *Phys. Rev. Lett.*, **1998**, *80*, 1984–1987.
[110] H. Nojiri, H. Ohta, S. Okubo, W. Fujita, J. Akimitsu, and M. Motokawa, *J. Phys. Soc. Jpn.*, **1999**, *68*, 3417–3423.
[111] G. Balster Martins, E. Dagotto, and J.A. Riera, *Phys. Rev. B.*, **1996**, *54*, 16032–16038.
[112] J.J. McGuire, T. Room, T.E. Mason, T. Timusk, H. Dabkowska, S.M. Coad, and D. McK. Paul, *Phys. Rev. B.*, **1999**, *59*, 1157–1161.
[113] A. Damascelli, D. van der Marel, G. Dhalenne, and A. Revcolevschi, *Phys. Rev. B.*, **2000**, *61*, 12063–12074.
[114] B.R. Jones, a.B. Sushkov, J.L. Musfeldt, Y.J. Wang, G. Dhalenne, A. Revcolevschi, *Phys. Rev. B.* accepted.
[115] M. Weiden, R. Hauptmann, C. Geibel, F. Steglich, M. Fischer, P. Lemmens, and G. Güntherodt, *Z. Phys. B.*, **1997**, *103*, 1–3.
[116] D. Augier and D. Poilblanc, *Eur. Phys. J. B.*, **1998**, *1*, 19–28.
[117] D. Augier, D. Poilblanc, S. Haas, A. Delia, and E. Dagotto, *Phys. Rev. B.*, **1997**, *56*, R5732–5735.
[118] H.G. von Schnering, Y. Grin, M. Kaupp, M. Somer, R.K. Kre,er, O. Jepsen, T. Chatterji, and M. Weiden, *Z. Kristallogr.*, **1998**, *213*, 246–246.
[119] A. Meetsma, J.L. de Boer, A. Damascelli, J. Jegoudez, A. Revcolevschi, and T.T.M. Palstra, *Acta Crystallogr. Sect. C.*, **1998**, *54*, 1558–1561.
[120] H. Smolinski, C. Gros, W. Weber, U. Peuchert, G. Roth, M. Weiden, and C. Geibel, *Phys. Rev. Lett.*, **1998**, *80*, 5164–5167.
[121] T. Ohama, M. Isobe, H. Yasouka, and Y. Ueda, *J. Phys. Soc. Jpn*, **1997**, *66*, 545–547.
[122] T. Ohama, H. Yasouka, M. Isobe, and Y. Ueda, *J. Phys. Soc. Jpn*, **1997**, *66*, 3008–3011.
[123] Y. Fujii, H. Nakao, T. Yoshihama, M. Nishi, K. Nakajima, K. Kakurai, M. Isobe, Y. Ueda, and H. Sawa, *J. Phys. Soc. Jpn*, **1997**, *66*, 326–329.
[124] P. Thalmeier and P. Fulde, *Europhys. Lett.*, **1998**, *44*, 242–248.
[125] H. Seo and H. Fukuyama, *J. Phys. Soc. Jpn*, **1998**, *67*, 2602–2605.
[126] H.-J. Koo and M.-H. Whangbo, *Solid State Commun.*, **1999**, *111*, 353–360.
[127] A.I. Smirnov, M.N. Popova, A.B. Sushkov, S.A. Gulubchik, D.I. Khomskii, M.V. Mostovoy, A.N. Vasil'ev, M. Isobe, and Y. Ueda, *Phys. Rev. B.*, **1999**, *59*, 14546–14551.
[128] J. Lüdecke, A. Jobst, and S. van Smaalen, *Phys. Rev. Lett.*, **1999**, *82*, 3633–3636.

[129] A.N. Vasil'ev, A.I. Smirnov, M. Isobe, and Y. Ueda, *Phys. Rev. B.*, **1997**, *56*, 5065–5068.
[130] P. Fertey, M. Poirier, M. Castonguay, J. Jegoudez, and A. Revcolevschi, *Phys. Rev. B.*, **1998**, *57*, 13698–13701.
[131] D.K. Powell, J.W. Brill, Z. Zeng, and M. Greenblatt, *Phys. Rev. B. Rapid Commun.*, **1998**, *58*, R2937–2940.
[132] J.W. Brill et al., unpublished results.
[133] A.N. Vasil'ev, V.V. Pryadun, D.I. Khomskii, G. Dhalenne, A. Revcolevschi, M. Isobe, and Y. Udea, *Phys. Rev. Lett.*, **1998**, *81*, 1949–1952.
[134] H. Schwenk, S. Zherlitsyn, B. Lühi, E. Morre, and C. Geibel, *Phys. Rev. B.*, **1999**, *60*, 9194–9197.
[135] H. Wu and Q. Zheng, *Phys. Rev. B.*, **1999**, *59*, 15027–15032.
[136] S. Nishimoto and Y. Ohta, *J. Phys. Soc. Jpn*, **1998**, *67*, 3679–3682.
[137] V.C. Long, J.L. Musfeldt, X. Wei, H.-J. Koo, M.-H. Whangbo, Jegoudez, and A. Revcolevschi, *Phys. Rev. B.*, **1999**, *60*, 15721–15727.
[138] M. Cuoco, P. Hotsch, and F. Mack, *Phys. Rev. B.*, **1999**, *60*, R8438–8441.
[139] S.A. Golubchik, M. Isobe, A.N. Ivlev, B.N. Mavrin, M.N. Popova, A.B. Sushkov, Y. Ueda, and A.N. Vasil'ev, *J. Phys. Soc. Jpn*, **1997**, *66*, 4042–4046; Errata: *J. Phys. Soc. Jpn*, **1999**, *68*, 318.
[140] A. Damascelli, C. Presura, D. van der Marel, J. Jegoudez, and A. Revcolevschi, *Phys. Rev. B.*, **2000**, *61*, 2535–2551.
[141] M.N. Popova, A.B. Sushkov, S.A. Golubchik, B.N. Mavrin, V.N. Denisov, B.Z. Malkin, A.I. Iskhakova, M. Isobe, and Y. Ueda, *JETP*, **1999**, *88*, 1186–1197.
[142] D. Smirnov, P. Millet, J. Leotin, D. Poilblanc, J. Riera, D. Augier, and P. Hasen, *Phys. Rev. B.*, **1998**, *57*, R11035–11038.
[143] A. Damascelli, D. van der Marel, J. Jegoudez, G. Dhalenne, and A. Revcolevschi, *Physica B.*, **1999**, *259–261*, 978–980.
[144] A. Damascelli, D. van der Marel, M. Grüninger, C. Presura, T.T.M. Palstra, J. Jegoudez, and A. Revcolevschi, *Phys. Rev. Lett.*, **1998**, *81*, 918–921.
[145] M. Isobe and Y. Ueda, *J. Magnet. Mag. Mater.*, **1998**, *177–181*, 671–672.
[146] P.N. Rogers and R.N. Shelton, unpublished results.
[147] T.W. Hijmans, H.B. Brom, and L.J. de Jongh, *Phys. Rev. Lett.*, **1985**, *54*, 1714–1717.
[148] T.W. Hijmans and W.P. Beyermann, *Phys. Rev. Lett.*, **1987**, *58*, 2351–2354.
[149] R.J.J. Visser, S. Oostra, C. Vettier, J. Voiron, *Phys. Rev. B.*, **983**, *28*, 2074–2077.
[150] K.E. Swanson, V.C. Long, J.L. Musfeldt, and V. Zelenzny, unpublished results.
[151] Q. Liu, S. Ravy, J.P. Pouget, C. Coulon, and C. Bourbonnais, *Synth. Met.*, **1993**, *55–57*, 1840–1845.
[152] K.C. Ung, S. Mazumdar, and D. Toussaint, *Phys. Rev. Lett.*, **1994**, *73*, 2603–2606.
[153] Y. Tanaka, N. Satoh, and K. Nagasaka, *J. Phys. Soc. Jpn*, **1990**, *59*, 319–325.
[154] Y. Tanaka, N. Satoh, and K. Nagasaka, *Synth. Met.*, **1991**, *41–43*, 2503–2506.
[155] S.J. Blundell, FL. Pratt, P.A. Pattenden, M. Kurmoo, K.H. Chow, S. Takagi, Th. Jestädt, and W. Haynes, *J. Phys.: Condens. Matter*, **1997**, *9*, L119–L124.
[156] T. Sekikawa, H. Okamoto, T. Mitani, T. Inabe, and T. Kobayashi, *Phys. Rev. B.*, **1997**, *55*, 4182–4190.
[157] C. Bourbonnais and D. Jérome, *Science*, **1998**, *281*, 1155–1156.
[158] S. Mazumdar, S. Ramasesha, R. Torsten Clay, and D.K. Campbell, *Phys. Rev. Lett.*, **1999**, *82*, 1522–1525.
[159] H. Seo and H. Fukuyama, *J. Phys. Soc. Jpn*, **1997**, *66*, 1249–1252.
[160] S.E. Brown, W.G. Clark, F. Zamborszky, B.J. Klemme, G. Kriza, B. Alavi, and C. Merlic, *Phys. Rev. Lett.*, **1998**, *80*, 5429–5432.

[161] D.S. Chow, P. Wzietek, D. Fogliatti, B. Alavi, D.J. Tantillo, C.A. Merlic, and S.E. Brown, *Phys. Rev. Lett.*, **1998**, *81*, 3984–3987.
[162] L. Ducasse, C. Coulon, D. Chasseau, R. Yagbasan, J.M. Fabre, and A.K. Gouasmia, *Synth. Met.*, **1988**, *27*, B543–B548
[163] S.D. Obertelli, R.H. Friend, D.R. Talham, M. Kurmoo, and P. Day, *J. Phys.: Condens. Matter*, **1989**, *1*, 5671–5680.
[164] M. Kurmoo, M.A. Green, P. Day, C. Bellitto, G. Staulo, F.L. Pratt, and W. Haynes, *Synth. Met.*, **1993**, *55–57*, 2380–2385.
[165] I.D. Parker, R.H. Friend, M. Kurmoo, and P. Day, *J. Phys.: Condens. Matter*, **1989**, *1*, 5681–5688.
[166] J.A. Schlueter, B.H. Ward, U. Geiser, H.H. Wang, A.M. Kini, J. Parakka, E. Morales, H.-J. Koom M.-H. Whangbo, P.G. Nixon, R.W. Winter, and G.L. Gard, submitted, *Chem. Mater.*
[167] B.H. Ward, J.A. Schlueter, U. Geiser, H.H. Wang, E. Morales, J. Parakka, S.Y. Thomas, J.M. Williams, P.G. Nixon, R.W. Winter, G.L. Gard, H.-J. Koo, and M. -H. Whangbo, *Chem. Mater.*, **2000**, *12*, 343–351.
[168] J. Dong, J.L. Musfeldt, J.A. Schlueter, J.M. Williams, P.G. Nixon, R.W. Winter, and G.L. Gard, *Phys. Rev. B.*, **1999**, *60*, 4342–4350.
[169] L. Alcácer, Magnetic, ESR, and NMR Properties, in *Organic Conductors: Fundamentals and Applications*, J.P. Farges, Ed., Marcel Dekker, New York, **1994**.
[170] G. Bonfait, M.J. Matos, R.T. Henriques, and M. Almeida, *Physica*, **1995**, *B221*, 297–299.
[171] G. Bonfait and M. Almeida, *EuroPhys. Lett.*, **1996**, *36*, 477–479.
[172] G. Bonfait, M.J. Matos, R.T. Henriques, and M. Almeida, *J. Phys. IV Coll. C2*, **1993**, *3*, 251–254.
[173] M. Matos, G. Bonfait, R.T. Henriques, and M. ALmeida, *Phys. Rev. B.*, **1996**, *54*, 15307–15313.
[174] K. Monch, M. Poirier, C. Bourbonnais, M.J. Matos, and R.T. Henriques, *Synth. Met.*, **1999**, *103*, 2228–2231
[175] H.L. Liu, L.K. Chou, K.A. Abboud, B.H. Ward, G.E. Fanucci, G.E. Granroth, E. Canadell, M.W. Meisel, D.R. Talham, and D.B. Tanner, *Chem. Mater.*, **1997**, *9*, 1865–1877.
[176] C. Bernhard, J.L. Tallon, C. Bucci, R. De Renzi, G. Guidi, G.V.M. Williams, and Ch. Niedermayer, *Phys. Rev. Lett.*, **1996**, *77*, 2304–2307.
[177] C. Pepin and P.A. Lee, *Phys. Rev. Lett.*, **1998**, *81*, 2779–2782.
[178] M.P. Gelfand, Z. Weihong, R.R.P. Singh, J. Oitmaa, and C.J. Hamer, *Phys. Rev. Lett.*, **1996**, *77*, 2794–2797.
[179] A. Dobry, P. Hasen, J. Riera, D. Augier, and D. Poilblanc, *Phys. Rev. B.*, **1999**, *60*, 4065–4069.
[180] E. Dagotto and T.M. Rice, *Science*, **1996**, *271*, 618–623.
[181] Z. Weihong, R.H. McKenzie, R.R.P. Singh, *Phys. Rev. B.*, **1999**, *59*, 14367–14375.
[182] Y. Fagot-Revurat, M. Mehring, and R.K. Kremer, *Phys. Rev. Lett.*, **2000**, *84*, 4176–4179.
[183] H. Nakao, K. Ohwada, N. Takesue, Y. Fujii, M. Isobe, Y. Ueda, M. v. Zimmermann, J.P. Hill, D. Gibbs, J.C. Woicik, I. Koyama, and Y. Murakami, *Phys. Rev. Lett.*, **2000**, *85*, 4349–4352.

Magnetism: Molecules to Materials I: Models and Experiments.
Edited by Joel S. Miller and Marc Drillon

ISBNs: 3-527-29772-3 (Hardback); 3-527-60084-1 (Electronic)

4 Magnetic Measurements at the Atomic Scale in Molecular Magnetic and Paramagnetic Compounds

Philippe Sainctavit, Christophe Cartier dit Moulin, and Marie A. Arrio

4.1 X-Ray Absorption Spectroscopy (XAS) and X-Ray Magnetic Circular Dichroism (XMCD)

4.1.1 X-Ray Absorption Spectroscopy

X-ray absorption is very similar to optical absorption. In both, a sample is irradiated by photons and an absorption coefficient, given by the Beer–Lambert's law, is measured [1,2]. XAS has received new interest in the late 70s with the development of X-ray sources from synchrotron radiation. Synchrotron radiation is emitted by relativistic electrons or positrons accelerated by bending magnets or insertion devices in storage rings. The sources are high-intensity polychromatic sources with a usually well defined polarization state. More information about synchrotron radiation can be found elsewhere [2–5].The X-ray absorption spectrum corresponds to the variation of the absorption coefficient with the energy of the photons. The absorption edge is the drastic variation of the absorption coefficient for a photon energy close to the energy of a core level electron. It corresponds to the transition of deep core level electrons of a selected atom to empty levels above the Fermi energy.

The absorption cross-section $\sigma(\omega)$ is the ratio between the absorbed energy and the incident photon flux. It is given by the summation over all the possible final states, f, of squared matrix elements related to the transition probability from the initial state $|i\rangle$ towards the final states $|f\rangle$. In the electric dipole approximation, $\sigma(\omega)$ reads:

$$\sigma(\omega) = 4p^{2\alpha}h^{\nu}\sum_{f}|\langle f|\vec{\varepsilon}_{\mathrm{r}}\cdot\vec{r}|i\rangle|^{2\delta}(h^{\nu}-E_f+E_i) \tag{1}$$

where α is the fine structure constant (1/137), $\vec{\varepsilon}_{\mathrm{r}}\cdot\vec{r}$ the electric dipole interaction Hamiltonian and δ, the Dirac distribution, ensures energy conservation.

The chemical selectivity is the major interest of this spectroscopy. Tuning the X-ray photon energy enables selection of each element of the material and collection of experimental data element by element. In a one-electron approach, the electric dipole selection rules state that $\Delta l = \pm 1$. At K and L_1 edges a 1s or 2s electron ($l = 0$) is excited to p symmetry empty levels ($\Delta l = +1$). In the electric dipole approximation, the transitions to d levels are forbidden ($\Delta l = +2$). At the $L_{2,3}$ edges, a 2p electron ($l = 1$, $j = 3/2$ for L_3 and $j = 1/2$ for L_2) is excited to empty d levels

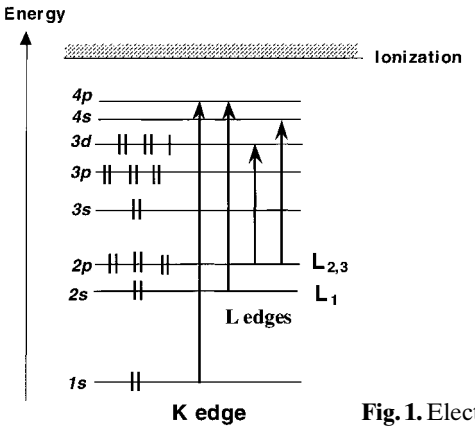

Fig. 1. Electron excitation by absorption of a X-ray photon.

($\Delta l = +1$) with a large transition probability and to vacant s levels ($\Delta l = -1$) with a much weaker transition probability. X-ray absorption spectroscopy is a selective probe of the angular momentum of empty levels on a specific atom (Fig. 1).

For 3d transition elements, the analysis of the K and $L_{2,3}$ edges are completely different. Interpretation for K edges uses monoelectronic models such as band structure or multiple scattering calculations [6,7]. The K edge is described as the transition from a 1s level to the p continuum states. The excited p electron is fully delocalized and submitted to a mean electronic potential that takes into account electronic repulsion resulting from all the other electrons of the ion. Multiple scattering theory solves the real space Schrödinger or Dirac equation for a definite cluster. In this approach, the photoelectron wave function results from the scattering by all the neighboring potentials of the cluster. These neighboring potentials impose boundary conditions on the site of the absorbing atom. The potentials are usually defined in the muffin-tin approximation. In the building of the potential there are some critical points:

- the cluster size. This step necessitates knowledge of the atomic crystallographic positions and the convergence of the calculation with the sizes of the cluster has to be checked.
- the exchange and correlation potentials are defined in various models: exchange potentials in the X–α or the Dirac-Hara formulations, exchange and correlation potentials such as the Hedin-Lundquist complex optical potential.
- self consistency can be required in either muffin-tin or nonmuffin-tin schemes.

$L_{2,3}$ edges for 3d transition elements cannot be reproduced accurately by one-electron theories (multiple scattering and band-structure calculations), because of the localized excited states of the photoelectron (3d level) and the strong interelectronic interaction between the 2p hole and the 3d shell. For the $L_{2,3}$ edges of 3d transition elements, the appropriate theoretical method is the ligand field multiplet (LFM) theory. The ligand field multiplet principle resides in the calculation of the atomic multiplets elements for atoms submitted to crystal-field and configuration interaction [8–10]. The theory relies on a multielectronic approach, where all the

electrons are taken into account. The L2,3 edges are described as transitions from the initial configuration $2p^6 3d^n$ to the excited one $2p^5 3d^{n+1}$ – a 2p electron is excited to the localized 3d orbitals. Electronic repulsion between 3d electrons and between 3d electrons and the 2p core hole are considered and both spin–orbit couplings in the 2p and 3d orbitals are computed (2p spin–orbit coupling is much larger than 3d). The crystal field is computed as an electrostatic Hamiltonian with the effective symmetry of the absorbing atom. In this approach, hybridization of the chemical bond such as covalence or charge-transfer can be taken into account through configuration interaction [11].

This model derives from the multiplet method that has long been used to interpret optical spectra. At the difference of optical spectroscopy that measures intra shell transitions, XAS measures inter-shell transitions. From this difference results the presence of insolite parameters such as those involving the 2p core hole (ζ_{2p} or inter-shell exchange integrals).

K edges contain essentially structural information while $L_{2,3}$ edges contain more electronic or magnetic information. Both measurements enable characterization of the ground state of the metallic ion in the compound – local symmetry, oxidation and spin states, spin–orbit coupling in the 2p and 3d orbitals, crystal field, covalence, and charge transfer [11,12].

4.1.2 X-Ray Magnetic Circular Dichroism

In the last ten years the advent of intense polarized synchrotron sources has given impulse to the use of X-rays to address the magnetic properties of condensed matter. X-ray magnetic circular dichroism (XMCD) in core level photoabsorption has been shown to be a unique element-selective magnetic probe [13]. The origin of XMCD is a local anisotropy of the absorbing atom as a result of a local magnetic field. The magnetic field breaks the local symmetry of the absorber and lifts the degeneracy of the Zeeman energy levels. The photoelectron transitions depend on the helicity of the photon polarization. The XMCD signal is the difference between cross-sections with left versus right polarization. To record XMCD signals, circularly polarized X-rays are absolutely essential. At the difference of circular dichroism in the visible range, XMCD receives its theoretical interpretation in the electric dipole approximation.

If circularly polarized photons are used to perform the absorption experiment, an extra selection rule takes into account the helicity of the photon: $\Delta m = \pm 1$, where m is the magnetic orbital quantum number. $\Delta m = +1$ for left-handed polarization and $\Delta m = -1$ for right-handed polarization. In a magnetic compound the levels with $|m|$ and $-|m|$ quantum are unequally populated. XMCD originates from this difference.

It has been proved theoretically and checked experimentally that reversing the magnetic field or the circular polarization yields the same results [13]. This is only exactly true when the interaction Hamiltonian is reduced to the electric dipole term. Because it is often experimentally easier to reverse the magnetic field than the polarization, most XMCD experiments are performed at constant helicity with a magnetic field parallel or antiparallel to the X-ray beam.

During an XMCD experiment, a first spectrum, labeled $\sigma_{\uparrow\uparrow}$, is recorded with the magnetic field parallel to the propagation vector of the photons. A second spectrum, labeled $\sigma_{\uparrow\downarrow}$, is then recorded with the magnetic field anti-parallel to the propagation vector of the photons. The XMCD signal is the difference $(\sigma_{\uparrow\uparrow} - \sigma_{\uparrow\downarrow})$ between the two spectra.

XMCD is sensitive to the local magnetic moment of the absorber atom on one specific level. The experimental spectra are analyzed in two different ways: sum rules can be applied or LFM calculations can be performed to reproduce the spectra. Sum rules enable direct extraction of the orbital and spin contributions to the local magnetic moment. The sum rules are detailed in Section 2. Multiplet calculations give a precise account of the ground state of the absorbing atom from which various parameters such as the exchange field can be deduced.

4.2 Sum Rules for XMCD

Optical sum rules are commonly found in atomic physics. In X-ray absorption spectroscopy two nonmagnetic sum rules were first suggested by Theo Thole. One relates the integrated absorption to the ground state expectation value of the number of holes in the final level of the transition. Another, that can be applied to core hole split edges, states that the branching ratio is proportional to the average value of the angular part of the spin–orbit coupling operator. With the development of XMCD, several magnetic sum rules were derived by Thole, Carra and Altarelli. Among these sum rules, two are widely used by XMCD experimentalists: these are the orbital and spin-sum rules.

The orbital sum rule states that the integrated dichroic signal is proportional to the ground state expectation value of the operator L_Z (z component of the orbital operator) acting on the shell that receives the photoelectron in the final state. The spin-sum rule relates a linear combination of dichroic signals at core hole split edges to the average value of two operators (S_Z, z component of the spin operator; T_Z, z component of the magnetic dipole operator) acting on the shell that receives the photoelectron in the final state.

The strength of the sum rules resides in the fact that the experimenter can obtain valuable information such as $\langle L_Z \rangle$ or $\langle S_Z \rangle$ by the simple numerical integration of experimental signals. There is no need to develop the complicated theories of the LFM model or the semi-relativistic multiple scattering method. The validity of the information extracted from the sum rules resides in a correct understanding of the various theoretical and experimental approximations present in their derivation.

4.2.1 The Magnetic Sum Rules

The two magnetic sum rules have been derived for transitions in the electric dipole approximation. The general formulation for the sum rules can be found elsewhere

[13]. Because this chapter is essentially devoted to $L_{2,3}$ edges, only the expression for the sum rules at these edges is given. If the channel from 2p to 3d is the main channel, the orbital sum rules at $L_{2,3}$ edges says:

$$\frac{I_{2,3}^{+} - I_{2,3}^{-}}{I_{2,3}^{+} + I_{2,3}^{-} + I_{2,3}^{0}} = -\frac{\langle \phi_i | L_z | \phi_i \rangle}{2(10-n)} \tag{2}$$

where ϕ_i is the ground state and n is the occupation number of the 3d shell. The precise definition of the I quantities can be found in the review chapter by Brouder, *Magnetic Circular Dichroism in X-ray Absorption Spectroscopy* [13]. The I values are related to the cross-section by the expression $4\pi^2 \alpha h\nu I = \sigma$. I_2^{+} is the integrated intensity over the L_2 edge of the XAS signal with left polarized light, I_2^{-} with right polarized light, I_2^{0} with linear polarized light parallel to the magnetic field. $I_{2,3}$ is the integrated signal over L_2 and L_3 and the other symbols have their conventional meanings.

At $L_{2,3}$ edges the spin–orbit coupling acting on the core-hole splits the final state into two groups of transition. If the energy separation between the two groups is large enough to enable integration over separate energy range it is found that:

$$\frac{(I_3^{+} - I_3^{-}) - 2(I_2^{+} - I_2^{-})}{I_{2,3}^{+} + I_{2,3}^{-} + I_{2,3}^{0}} = -\frac{2}{3(10-n)} \left[\langle \phi_i | S_Z | \phi_i \rangle + \frac{7}{2} \langle \phi_i | T_z | \phi_i \rangle \right] \tag{3}$$

Here solely the transition from 2p to 3d has been considered.

4.2.2 Validity of the Sum Rules

The two magnetic sum rules are based on several theoretical approximations. A first remark concerns the fact that we are dealing with normalized I that are proportional to the cross-section divided by the photon energy. If the range of integration is large the confusion between I and σ can yield incorrect results. When the measurement is performed in total electron yield, the proportionality constant between the measurement and the actual cross-section varies linearly with the energy [14,15]. Saturation effects are known to modify the application of the sum rules [16,17]. One must also consider carefully the possible variation of the circular polarization rate in case of double crystal monochromators [18].

The derivation of the magnetic sum rules has been performed for pure atomic configuration without configuration interaction. In doing so one considers that the other shells do not relax under the influence of the core hole. Thole has proposed arguments why the magnetic sum rules are still valid in the presence of configuration interaction but the question remains open. The denominator in the magnetic sum rules are there to remove the radial integrals. This procedure is correct if the radial integrals are independent of the energy and the spin. Wu et al. have shown that this is not true for metallic nickel at $L_{2,3}$ edges. This does not conflict with the application of the orbital sum rule but does with the spin-sum rule [19]. It has been shown that

radial matrix elements at the $L_{2,3}$ edges of rare earths are different for spin up or spin down [20]. A combination of ligand field multiplet calculations with one-electron band-structure calculations is usually necessary to clarify this point.

The spin-sum rule supposes that the core split edges can be well separated so that integration between the two energy ranges for L_2 and L_3 can be performed. There is often strong intermixing between the two edges and this partially impairs the application of the spin-sum rule. This has been shown for $L_{2,3}$ edges of manganese by Teramura [21] and $M_{4,5}$ edges of cerium by Brouder [22]. When intermixing is small, the choice of the integration limits is still arbitrary, as can be found by comparing the papers by D. Arvanitis et al. and C. Chen et al. [16,23].

4.2.3 The Contribution from the Magnetic Dipole Operator

In the spin-sum rule, the averaged value $\langle T\,Z\rangle$ is present. When the ground state is a pure J state, where crystal field acts only on the different $(2J+1)M_J$, an analytical expression can be derived for $\langle T_Z\rangle$. This is the case for the $M_{4,5}$ edges of rare earths. When the crystal field is large and couples various J in the ground state, there is no simple expression for $\langle T_Z\rangle$. In intermetallic compounds, one considers that $\langle T_Z\rangle = \langle S_Z\rangle\langle Q_{ZZ}\rangle$ where Q_{ZZ} is a quadrupolar operator with a vanishing trace [24]. If the crystallographic environment around the absorbing atom is cubic, then $\langle Q_{ZZ}\rangle = 0$ and $\langle T_Z\rangle = 0$. When it is not cubic, a linear combination of well selected experimental dichroic signals should ensure cancellation of the $\langle T_Z\rangle$ contribution [24]. In the general case of ionic ions, the cubic symmetry does not ensure the nullity of $\langle T_Z\rangle$. This has been shown for $L_{2,3}$ edges of Cu^{2+} in an octahedral environment where the contribution from $\langle T_Z\rangle$ is always twice larger than the contribution from $\langle S_Z\rangle$ in the spin-sum rules [25].

4.2.4 Checking the Theory with the Theory

The sum rules have been applied to calculated XMCD signals and compared with the theoretical averaged values of the appropriate operators. When the theory has been checked with the theory it has been found that when the spectra are well reproduced in the framework of the ligand-field multiplets ($L_{2,3}$ edges of "ionic" 3d transition elements and $M_{4,5}$ edges of rare earths), the sum rules are valid. When delocalized one-electron theories such as band structure or multiple scattering are the appropriate method ($L_{2,3}$ edges in metallic Fe, Co or Ni, $L_{2,3}$ edges of rare earths), the disagreement can be as large as several tens percent, especially on the spin-sum rule [26]. The disagreement is rooted in the neglect of the spin dependence of the radial matrix elements, the failure of the sum rule for the number of holes and also configuration mixing [15,19]. Following Wu et al. it is suggested that the experimental determination of the ratio $\langle L_Z\rangle/\langle S_Z\rangle$ should be more accurate [16,19,23,27]. This is the major conclusion concerning the sum rules.

4.3 Chemical Bond and Magnetism Explored by XMCD in Prussian Blue Analogs

Transition metal $L_{2,3}$ edges absorption spectroscopy gives information about the 3d levels which are directly involved in the magnetic exchange interaction. Analysis of the $L_{2,3}$ absorption spectrum of transition metals provides information about the oxidation state, spin state, site symmetry, and crystal field splitting of the absorbing transition metal ion [9,10].

4.3.1 Chemical Bond in $Cs^{I}[Ni^{II}Cr^{III}(CN)_6] \cdot 2H_2O$

The main purpose of this chapter is to demonstrate that isotropic $L_{2,3}$ edges yield much information about complex materials such as insulating magnets. The $Cs^{I}[Ni^{II}Cr^{III}(CN)_6] \cdot 2H_2O$ magnet belongs to the Prussian blue family that has been described by Verdaguer and Girolami in this book.

To extract quantitative information from $L_{2,3}$ edges, it is necessary to simulate the spectra in the LFM approach. This approach takes into account all the electronic Coulomb interactions, the spin–orbit coupling on every shell, and treats the geometrical environment of the absorbing atom in terms of a crystal field potential. In the simplest formulation, a pure $3d^n$ configuration is attributed to the 3d transition ions in the ground state and transitions between $2p^6 3d^n$ ground state and $2p^5 3d^{n+1}$ excited states are calculated. The interelectronic repulsions are introduced through Slater integrals F^2_{dd} and F^4_{dd} for the initial state and F^2_{dd}, F^4_{dd}, F^2_{pd}, G^1_{pd} and G^3_{pd} for the final state. The Slater integrals are calculated through an atomic Hartree–Fock model and are scaled down by a reduction factor κ which reflects the electronic delocalization. The κ factor is comparable with the factor $\beta = B/B_0$ used in optical spectroscopy for ordering the nephelauxetic series, where B_0 and B are, respectively, the free ion and the chemically bonded Racah parameters ($B_0 = (1/49)F^2_{dd} - (5/441)F^4_{dd}$). The atomic spin–orbit coupling parameters ζ_{3d} and ζ_{2p} are first calculated through the monoelectronic potential around the free ion. They are slightly adjusted to take into account modifications of the electronic potential by solid state effects. The octahedral surroundings of the metal ion are represented by an octahedral crystal-field potential whose strength is parametrized by $10Dq$. At this point hybridization is only present through the reduction parameter κ and it is impossible to take into account the ligand–metal charge-transfer. To model this effect it is necessary to perform the calculation with initial and final states that are mixtures of two or three appropriate configurations. The initial state $|\phi_i\rangle$ of a $3d^n$ divalent ion is taken to be a linear combination of two configurations: $|\phi_i\rangle = \alpha\,|d^n\rangle + \beta\,|d^{n+1}\underline{L}\rangle$, where d^{n+1} stands for an extra d-electron coming from the ligands and $\underline{L}$ for the corresponding hole on a ligand orbital. In the same way the final state levels $|\phi_f\rangle$ are $|\phi_f\rangle = \alpha'\,|2p^5 d^{n+1}\rangle + \beta'\,|2p^5 d^{n+2}\underline{L}\rangle$. The charge-transfer energy for the ground state is defined as $\Delta = E(3d^{n+1}\underline{L}\rangle) - E(3d^n)$, where $E(3d^{n+1}\underline{L}$ and $E(3d^n)$ are the average energies of, respectively, the $3d^{n+1}\underline{L}$ and $3d^n$ configurations. For the final

state the charge-transfer energy is defined as $\Delta' = E(2p^5 3d^{n+2}\underline{L}) - E(2p^5 3d^{n+1})$, where $E(2p^5 3d^{n+2}\underline{L})$ and $E(2|p^5 3d^{n+1})$ are the average energies of, respectively, the $2p^5 3d^{n+2}\underline{L}$ and $2p^5 3d^{n+1}$ configurations. Δ' can be expressed as a function of Δ by $\Delta' = \Delta + U_{dd} - U_{dp}$, where U_{dd} and U_{dp} are the average Coulomb interaction energies of dd and dp electron pairs. The strength of the charge-transfer hybridization is represented in octahedral symmetry by the two ligand-metal charge-transfer integrals $V_{t_{2g}}$ and V_{eg} with $V = \langle 3d^n | H | 3d^{n+1}\underline{L} \rangle$.

4.3.1.1 Ni^{II} $L_{2,3}$ edges: Ni^{II}-NC Bond

The experimental and the calculated Ni $L_{2,3}$ edges absorption spectra are presented in Fig. 2.

The calculations have been performed in the LFM model with hybridization by using two configurations in the initial state and in the final state, in octahedral symmetry and at 300 K. Good agreement is obtained between experiment and calculation. The ground state is defined by the O_h symmetry irreducible representation, the spin orbit parameters for 3d shell (ζ_{3d}) and 2p shell (ζ_{2p}), the crystal field strength ($10Dq$) and Slater integrals reduction factor (κ). These parameters are the same for the initial and the final states and are given in Table 1. The Slater integrals used in the calculation are listed in Table 2.

When the calculation is performed without configuration interaction, the value of the crystal field parameter is in agreement with optical spectroscopy measurements

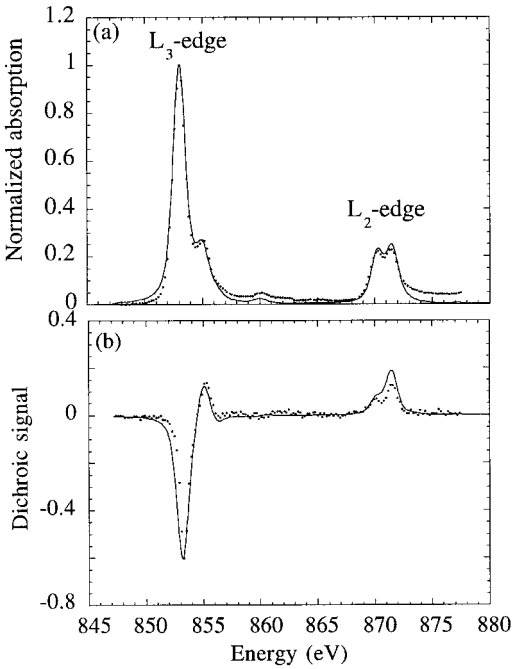

Fig. 2. Isotropic and dichroic $L_{2,3}$ edges of Ni^{II} in $Cs^{I}[Ni^{II}Cr^{III}(CN)_6]2H_2O$. Experiments: dots; calculations: continuous line.

Table 1. Spin-orbit coupling, Slater reduction factor, and crystal field parameter used for $L_{2,3}$ edges multiplet calculations.

	ζ_{2p} (eV)	ζ_{3d} (eV)	κ (%)	$10Dq$ (eV)
Ni^{2+}	11.45	0.10	90	0.9
Cr^{3+}	5.67	0.035	50	3.5

Table 2. Slater integrals for initial and final state configurations, used for $L_{2,3}$ edges multiplet calculations (after (reduction).

	F^2_{dd} (eV)	F^4_{dd} (eV)	F^2_{dd} (eV)	F^4_{dd} (eV)	F^2_{pd} (eV)	G^1_{pd} (eV)	G^3_{pd} (eV)
Ni^{2+}	12.5	7.8	–	–	7.9	6.0	3.4
Cr^{3+}	9.7	6.1	10.4	6.5	5.9	4.3	2.4

and comparable with $10Dq$ for complexes with similar ligands [28,29]. The reduction factor κ of the Slater integrals is 90%, confirming the weak covalent character of the Ni^{II}–NC bond. Configuration interaction is only required to reproduce the small intensity satellites in between the edges at 860 eV [28]. The weak charge transfer is at the origin of this small satellite [28,30]. The Ni^{II} ground state is made of approximately 90% $|3d^n\rangle$ and 10% $|3d^{n+1}\underline{L}\rangle$. This clearly indicates that the Ni^{II}–N bond experiences a very small ligand–metal charge-transfer.

To summarize the information that can be gained from comparison of calculations with experiments, one can say that the Ni^{II}–N bond is only faintly modified by covalence ($\kappa = 90 \pm 5\%$) and charge transfer (the ground state is an almost pure $|3d^n\rangle$ configuration with only 10% $|3d^{n+1}\underline{L}\rangle$ configuration). The effective electron number on the 3d shell of Ni^{II} in the series of bimetallic cyanides is 8.1.

4.3.1.2 Cr^{II} $L_{2,3}$ Edges: Cr^{II}-CN Bond

The experimental Cr^{III} $L_{2,3}$ edges in $Cs^{I}Ni^{II}[Cr^{III}(CN)_6]\cdot 2H_2O$ are reported in Fig. 3. They are much different from the $L_{2,3}$ edges spectra published for Cr^{III} in oxides [31,32]. The cyano bond through carbon atoms is strongly covalent and is associated with a large crystal field. From optical spectroscopy measurements on the molecular based magnets, one knows that $10Dq = 3.5$ eV for the crystal field parameter related to chromium ions. For the Cr^{III}-CN bond, κ must be small to take into account covalence as can be expected from the nephelauxetic series and charge transfer has to be introduced through configuration interaction [29,30].

In one-configuration calculation with $10Dq = 3.5$ eV and $\kappa = 0.5$, the theoretical spectrum has many fewer features than that obtained experimentally (Fig. 3c). Polarized neutron diffraction experiments on $K_3[Cr^{III}(CN)_6]$ have shown that the Cr^{III} ions have less than three electrons in the 3d shell [33,34]. To mimic this result, the bond is modeled by a metal-to-ligand charge transfer by mixing $|3d^3\rangle$ and $|3d^2L^1\rangle$ configurations. In such a scheme one 3d electron is partly delocalized on the lig-

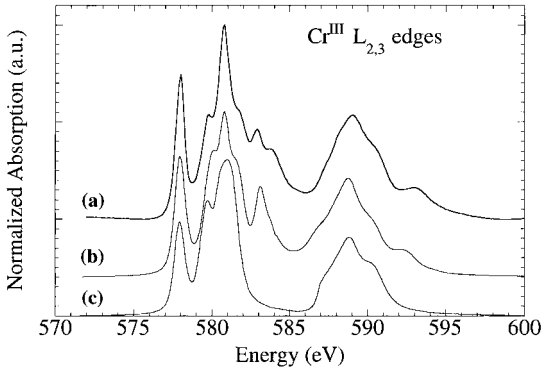

Fig. 3. Isotropic $L_{2,3}$ edges of Cr^{III} in $Cs^{I}[Ni^{II}Cr^{III}(CN)_6]2H_2O$. (a) experiment, (b) calculation with configuration interaction, (c) calculation without configuration interaction.

and orbitals $|L\rangle$ [30,35,36]. The existence of a large π back-bonding implies that the charge-transfer integrals related to the π bond should be larger than those related to the σ bond. From the previous discussion, the calculated spectrum is reported in Fig. 3. Good agreement is obtained between calculation and experiment. From this calculation we obtain insight about the precise ground state description of Cr^{III} and also about some Cr^{III}–CN bond characteristics-the ground state is made up of 80% $|3d^3\rangle$ and 20% $|3d^2L^1\rangle$. The effective electron number on the 3d shell of Cr^{III} in the series of bimetallic cyanides is 2.8.

Transition metal $L_{2,3}$ edges X-ray absorption spectroscopy can be used to study local electronic structure and chemical bond in molecular-based magnets from the Prussian blue family. By comparison with LFM calculations we can extract quantitative information on the ground state of the 3d ions and the chemical bonds [31]. Quantities such as the effective occupations of the 3d shell are essential in these magnetic compounds for the application of the sum rules.

4.3.2 Local Magnetic Moments by XMCD in $Cs^{I}[Ni^{II}Cr^{III}(CN)_6] \cdot 2H_2O$

XMCD experimental and calculated signals obtained at the nickel $L_{2,3}$ edges are plotted in Fig. 2. The sign of the experimental XMCD signal proves that nickel(II) ions are indeed coupled ferromagnetically to chromium(III) ions [28]. The application of the sum rules to experimental spectra gives the value for $\langle L_Z\rangle/\langle S_Z\rangle = 0.26 \pm 0.05$ and the theoretical value extracted from LFM calculation is around 0.29 ± 0.05.

There is some controversy concerning the use of XMCD to yield absolute magnetic moments. This debate has been well illustrated in papers by Arvanitis et al. and Chakarian et al. [16,17]. The conclusion is that total electron yield measurements are not exempt from saturation effects that tend to reduce the accuracy of magnetic moment determination. Even in the best cases (fully magnetized thin metallic foil), spurious effects as large as 10% of the XMCD signal lead to incorrect estimation of the orbital or spin magnetic moments. In our measurements, the samples are thick powder pellets and the face of the powder crystallites are oriented at random relative

to the incoming X-rays. Following Chakarian one can estimate that the combined effect of thickness and misorientation impairs by at least 10 or 20% any attempt to extract precise absolute magnetic moments. Despite this severe drawback of the method, there is still much qualitative information to be obtained from XMCD (spin orientation, orbital polarization, magnetic moment on one specific shell). In our opinion the only quantitative information lies in the determination of $\langle L_Z \rangle / \langle S_Z \rangle$. XMCD remains the only magnetic technique measuring orbitally selective signals localized on a specific ion.

4.3.3 Magnetic Anisotropy in $Cs^{I}[Ni^{II}Cr^{III}(CN)_6] \cdot 2H_2O$

The sample is a powder of crystallites with cubic crystallographic symmetry. In the absence of a magnetic field the cross-sections in the electric dipole approximation are isotropic for any crystallites. When a magnetic field is applied, the net magnetization of the sample breaks the cubic symmetry in each crystallite. Because of magnetic anisotropy the break of cubic symmetry depends on the orientation of the magnetic field relative to the crystallographic axes of the crystallites. To take this effect into account the powder spectrum must be calculated by averaging the cross-sections for all possible directions of magnetization relative to the symmetry axes of the crystallites. It is known that the powder cross-section can be obtained to a good approximation by a well-balanced average of cross-sections calculated with particular directions of the magnetic field. In the case of cubic symmetry, the powder spectrum is given by [28]:

$$\sigma_{\text{powder}} = \frac{176}{385}\sigma(B//C_2) + \frac{99}{385}\sigma(B//C_3) + \frac{110}{385}\sigma(B//C_4) \tag{4}$$

where $\sigma(B//C_2)$, $\sigma(B//C_3)$, and $\sigma(B//C_4)$ are the cross-sections corresponding to the magnetic field B parallel to the following directions: [110] or C_2, [111] or C_3 and [001] or C_4. The LFM isotropic spectra calculated for any of the three directions are very similar; this might be expected, because the Zeeman Hamiltonian is a small perturbation that cannot be resolved by the experimental resolution. On the contrary, when linear or circular dichroism is calculated some interesting differences are present, because of different degeneracy lifting and different dipole-allowed transitions. Large differences can be observed between the average spectra $1/2(\sigma_+ + \sigma_-)$ for $\sigma(B//C_2)$, $\sigma(B//C_3)$, and $\sigma(B//C_4)$. This proves that a well balanced averaging procedure is essential to enable extraction of physical quantities from the comparison of experimental and calculated $1/2(\sigma_+ + \sigma_-)$ spectra. X-ray magnetic circular and linear dichroism should, moreover, give much information on the magnetic anisotropy, although the impossibility of growing suffficiently large single crystals did not enable experimental solution of the question for this compound. For the three magnetic orientations, the circular dichroic signals $\sigma_- - \sigma_+$ only differ by 3% which means that the shape of XMCD at nickel $L_{2,3}$ edges is almost insensitive to the magnetic anisotropy.

4.3.4 Application of One-electron Theory to XMCD

XMCD at chromium, manganese, and nickel K edges has been measured in the ferrimagnet $Cs^{I}[Mn^{II}Cr^{III}(CN)_6] \cdot 2H_2O$ and the ferromagnet $Cs^{I}[Ni^{II}Cr^{III}(CN)_6] \cdot 2H_2O$. In the monoelectronic framework, the K edge corresponds to transitions from the 1s initial state towards p final states above the Fermi level. In contrast with the $L_{2,3}$ edges, for which XMCD signals can be as large as 60%, the XMCD signals at K edges is never larger than a few tenths of 1% of the atomic cross-section. There are two reasons for this: firstly, at K edges, there is no spin–orbit coupling acting on the monoelectronic initial state and XMCD finds its origin on the spin–orbit coupling acting on the p levels of the continuum; secondly the p levels are much less spin-polarized than the 3d levels which leads to a smaller contribution to XMCD, as can be inferred from recent magnetic sum rules.

The field applied to the sample was larger than 0.5 T and the temperature was 30 K, ensuring complete saturation of the magnetic moment of the magnets. The XMCD signals at the three edges in the two compounds are plotted in Fig. 4. The maximum of the isotropic cross-section is the reference energy for the three edges.

The nature of the magnetic coupling between the chromium ions and the divalent ions can be directly deduced from the analysis of the sign of the XMCD signals. In $Cs^{I}[Ni^{II}Cr^{III}(CN)_6] \cdot 2H_2O$ the shape of the XMCD signal $(-+)$ is the same at the two edges. This confirms the ferromagnetic coupling between the two ions. In $Cs^{I}[Mn^{II}Cr^{III}(CN)_6] \cdot 2H_2O$, the shape of the Mn XMCD signal is the same as in the previous magnet, indicating that the Mn magnetic moments are parallel to the applied magnetic field. The reversed sign of the Cr XMCD signal indicates the antiferromagnetic coupling between Cr and Mn.

The method used to interpret the XMCD structures at K edges derives from the real space multiple scattering theory applied to XAS. One starts from building a cluster of atoms surrounding the absorbing atom. The potential is built in the

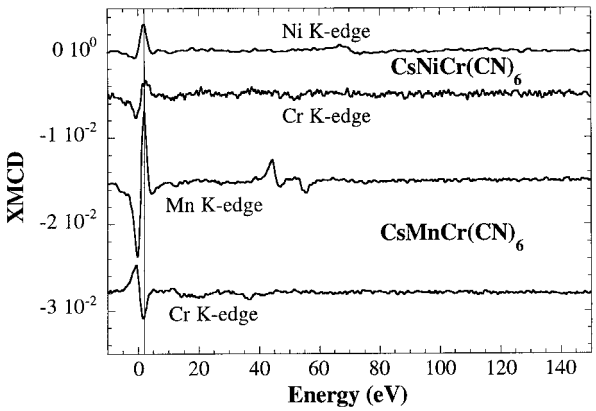

Fig. 4. Experimental XMCD spectra of $Cs^{I}[Ni^{II}Cr^{III}(CN)_6] \cdot 2H_2O$ and $Cs^{I}[Mn^{II}Cr^{III}(CN)_6] \cdot 2H_2O$.

muffin-tin approximation with a constant potential in the interstitial region. One calculates the Dirac Green function associated to the potential in a semi relativistic development where spin–orbit coupling that is responsible for XMCD is present [37]. From this formalism, one ends up with a concise form of the XMCD signal that can in turn be split into three different contributions. Each contribution is the difference between spin up and spin down of rather lengthy expressions that are not given here. The contributions are labeled σ_{1a}, σ_{1l}, and σ_{1n}. σ_{1a} is an atomic only contribution (Fano effect), σ_{1l} is roughly proportional to the difference between spin up and spin down density of empty states and σ_{1n} comes mainly from the spin orbit scattering of the photoelectron by the magnetic neighboring sites with also part scattering by the potential of the absorbing atom.

The muffin-tin potential around each atom in the unit cell has been calculated in the framework of the local-spin-density approximation using the ASW method and the convergence of the basis set has been fully checked. The calculations of XMCD signals performed at nickel and chromium K edges in $Cs^{I}[Ni^{II}Cr^{III}(CN)_6] \cdot 2H_2O$ are plotted in Fig. 5. The derivative-like signal at the Cr K edge and the one lobe signal at the Ni K edge are well reproduced by the calculations. The difference between the shapes of the two signals can be attributed to the position of the Fermi level relative to the magnetic states. If one calculates the XMCD signal at Ni K edge corresponding to "virtual" transitions below the Fermi level, one finds a large negative XMCD lobe as in the Cr signal. The derivative-like feature is characteristic of the XMCD signal for such compounds, as is shown at the Manganese K edge (Fig. 4).

As mentioned above, one advantage of the method is to enable decomposition of the different contributions to the total XMCD signal. The theoretical XMCD signals for chromium have been plotted in Fig. 6. The XMCD signal is dominated by σ_{1n}; there is also a rather large contribution from σ_{1l}. This situation is different from that encountered in metallic iron, where the contribution from σ_{1n} was largely the dominant term close to the edge [37]. This is because the first neighbors of the chromium ions are nitrogen and carbon atoms of the cyano bridge. Although they are spin polarized, they cannot be considered as magnetic neighbors and then only faintly contribute to σ_{1n}. The closest magnetic neighbors are nickel ions 5 Å from chromium ions.

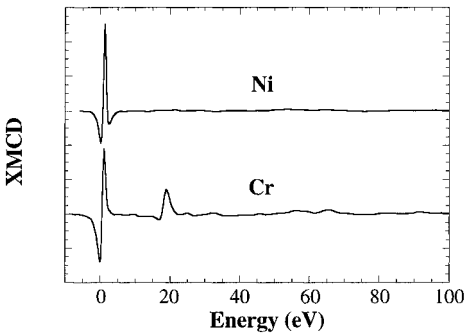

Fig. 5. Calculated XMCD spectra for $Cs^{I}[Ni^{II}Cr^{III}(CN)_6]2H_2O$.

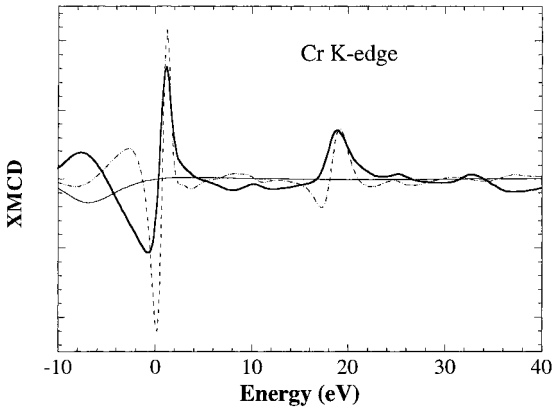

Fig. 6. Contribution to XMCD. σ_{1a} = thin continuous line; σ_{1l} = thick continuous line; σ_{1n} = broken line.

On the other hand, in the energy range far from the edge the XMCD signal is mainly dominated by σ_{1l} and the XMCD signal is found in phase with the total density of empty states. σ_{1a} is the smallest contribution. It has almost no structures and oscillates softly around zero.

Pure atomic effects contribute only slightly to XMCD in the whole energy range. Close to the edge, the spin orbit scattering dominates over spin polarized density of states; the opposite is true for magnetic EXAFS.

4.4 Local Magnetic Structure in Room-temperature Molecule-based Magnets

Most vanadium-chromium compounds of general formula $A^{I}_{y}V[Cr^{III}(CN)_6]_z \cdot nH_2O$ are room-temperature ferrimagnets with T_C varying between 295 K and 376 K. The synthesis and macroscopic magnetic properties of this family of compounds are reported in the chapter *Prussian Blue Structured Magnets* of this book by Verdaguer and Girolami. XMCD can be used to understand better the relationship between the magnetic properties of these systems and their synthetic conditions, particularly with the stoichiometry and the oxidation state of the vanadium ions.

By varying the stoichiometry by addition of cationic species in the tetrahedral holes of the Prussian blue structure, two bimetallic chromium-vanadium ferrimagnets have been synthesized [38]: **1** [in the absence of Cs(I)]: $\{V^{II}_{0.45}V^{III}_{0.53}(V^{IV}O)_{0.02}[Cr(CN)_6]_{0.69}\ (SO^{2-}_4)_{0.23}\ (K_2SO_4)_{0.02}\} \cdot 3H_2O$; and **2** [in the presence of Cs(I)]: $\{Cs^{I}_{0.82}V^{II}_{0.66}(V^{IV}O)_{0.34}\ [Cr(CN)_6]_{0.92}\ (SO^{2-}_4)_{0.20}\} \cdot 3.6H_2O$. The macroscopic magnetic properties of the two systems are very similar (magnetization at the saturation: $0.36\,N_A\beta$ for **1** and $0.40\,N_A\beta$ for **2**). In both compounds the vanadium sublattice is coupled antiferromagnetically to that of chromium. The antiparallel alignment of the neighboring spins in the magnetically ordered phases leads to a resulting total magnetization M_T which is the difference between the magne-

tization arising from the subset of chromium ions M_{Cr} and that from the subset of vanadium ions, M_V:

$$M_T = |M_{Cr} - M_V| \tag{5}$$

Two situations can arise, one when the larger magnetic moments are borne by the chromium ions and are aligned parallel to an external applied field ($M_{Cr} > M_V$), the other when $M_V > M_{Cr}$. In the later case, the sign of the quantity ($M_{Cr} - M_V$) is reversed and the magnetic moments of vanadium ions lie parallel to the field.

The spin values of these compounds can be expressed as a function of the Cr^{III}/V and V^{II}/V ratios [38]. For example, for analogs of compound **1**, $(C_y^I V^{II}{}_\alpha V^{III}_{1-\alpha}[Cr^{III}(CN)_6]_z \cdot nH_2O)$, the expression for M_T is:

$$M_T = -(3z - \alpha - 2) \tag{6}$$

The spin values of these compounds can be represented in a three-dimensional space, vs α, varying between 0 and 1, and vs z, varying between 2/3 and 1. The spin values are described by the diagram presented in Fig. 7 for analogs of **1**.

The calculated M_T value is positive for **1** ($M_T = +0.36N_A\beta$) and negative for **2** ($M_T = -0.42N_a\beta$). The crucial difference between the two compounds is the sign of M_T, depending on the balance between the values of Cr^{III}/V ratio and the V^{II}/V ratio. Conventional magnetization measurements give the absolute value of the macroscopic magnetization but not the local magnetization. The results of XMCD experiments at the K edges of vanadium and chromium are reported in Fig. 8. In **1**, at the chromium K edge, the dichroic signal is first positive and then negative (+ −) whereas at the vanadium K edge, it behaves in the opposite manner (− +). The 4p

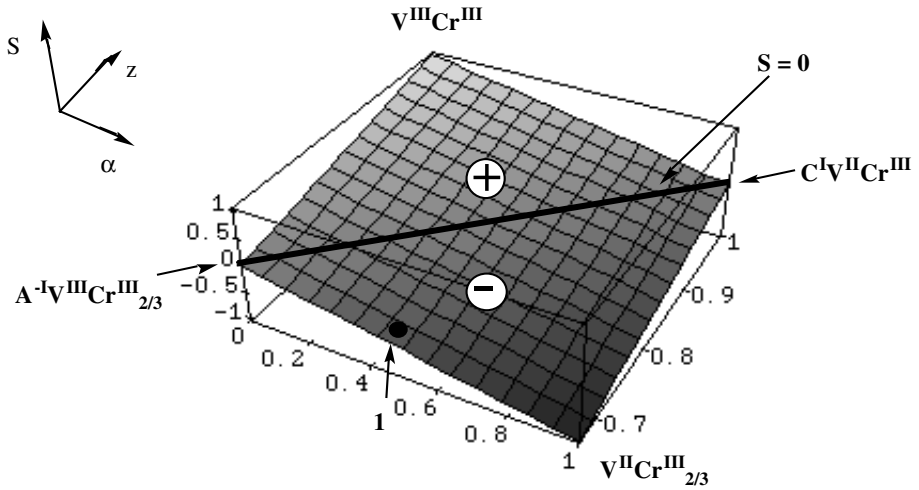

Fig. 7. Variation of the spin values S versus z and α parameters for analogs of **1**. **1** is in the part of the plane where the total spin has the same direction as the vanadium spins.

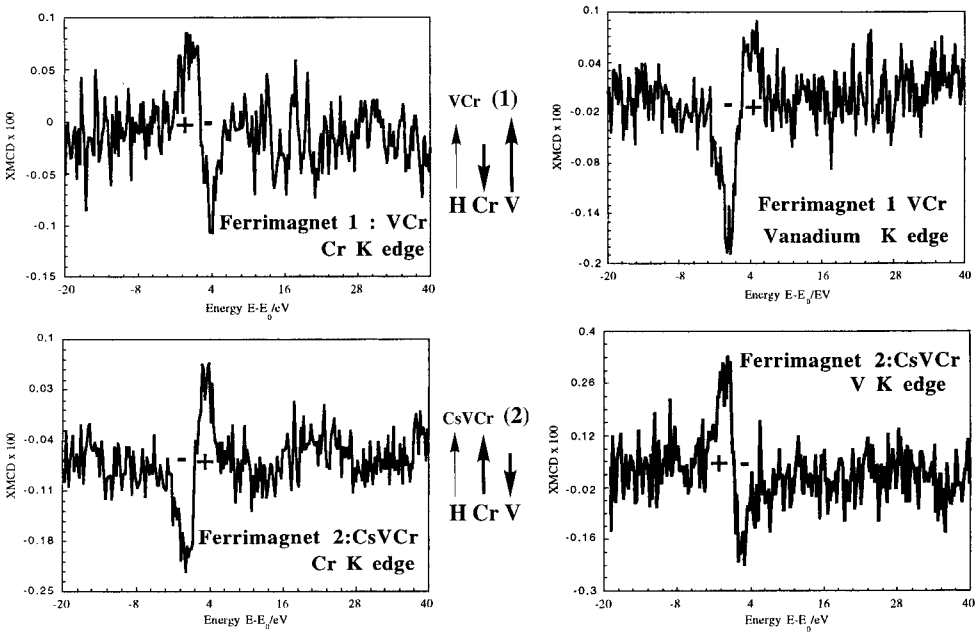

Fig. 8. XMCD signals at the chromium and vanadium K edges for compounds **1** and **2**.

orbitals are empty and the surroundings of the two metallic ions are quasioctahedral, so that the sign of the spin orbit constant should be the same in the chromium and vanadium 4p orbitals. The inversion of the dichroic signal, $(+-)$ in chromium compared with $(-+)$ in vanadium, is therefore a clear local demonstration of the antiferromagnetic coupling of V and Cr in ferrimagnet **1**. In **2**, one reaches exactly the same conclusion, because the dichroic signal is once more reversed in the chromium $(-+)$ compared with the vanadium $(+-)$ K edges. The new fact is that, for a given edge, the shape of the dichroic signal is exactly the opposite for compounds **1** and **2**. This is the experimental proof that the larger magnetic moment, aligned with the magnetic field, is borne in one compound by the vanadium ions and in the other one by the chromium ions. The change in the stoichiometry is followed by a slight change in the macroscopic magnetization, but, above all, by the change in the nature of the metallic species bearing the larger magnetic moment.

The absolute orientation of the magnetic moments proposed in Fig. 8 results from a complementary XMCD experiment on the ferromagnetic $CsNi[Cr(CN)_6]$ where all the magnetic moments are aligned parallel to the applied field with a dichroic signal for chromium similar to that of **2** [39].

Among the two techniques able to determine directly the orientation of the spins on local metallic centers, spin-polarized neutron diffraction and XMCD, the first was nonapplicable, because the compounds were microcrystalline powders, whereas XMCD is able to give the qualitative answer. This study shows the usefulness and the capacity of XMCD to determine the spin orientation on each metal ion in bimetallic ferri- or ferromagnets.

4.5 Paramagnetic Complexes

In the former part of this chapter, XMCD has been measured at the $L_{2,3}$ and K edges in molecular-based magnets. These compounds have net magnetization below the Curie temperature. Compounds with paramagnetic ions for which no three-dimensional magnetic order has ever been detected can also be studied by XMCD. To address this class of compounds, the sample must be cooled to a temperature sufficiently low that net magnetization exists in the presence of a reasonable magnetic field. This has been achieved in two recent experimental setups that cool the sample to ca 100 mK and in which a magnetic field as large as 7 T can be applied. Very few results concerning XMCD in paramagnetic compounds have been published and we focus here on two classes of molecular compound: high-spin molecules and biological metallic clusters belonging to proteins.

4.5.1 Instrumentation

The essential requirement to perform XMCD measurements in paramagnetic compounds lies in cooling the sample to a low enough temperature. This can be done in several ways. A tank of ^{4}He can be pumped to cool down a sample down to $\approx$1 K [40]. When the tank is filled with ^{3}He instead of ^{4}He, lower temperatures are obtained (ca 0.3 K), although the operation is usually not continuous and lasts until the ^{3}He tank is empty. To reach even lower temperature in a continuous mode, dilution refrigerators have been built [41,42]. Temperatures in the range of 100 mK are currently accessible.

The magnetic fields are usually produced by slip superconducting coils that can reach 7 T. The environment of the sample is ultra high vacuum, or at least good secondary vacuum, so that the cooled sample is not polluted by the residual gas. Detection can be performed in two modes – either fluorescence detection or total electron yield. In total electron yield one difficulty lies in the efficient cooling of a sample that is electrically insulated.

The magnetization of a paramagnetic impurity ion follows a Brillouin curve. In such a case reducing the temperature is theoretically identical to increasing the magnetic field. Because experimentally increasing the magnetic field is difficult beyond ca 10 T and induces large nonlinearities on the detection instrumentation, lowering the temperature is preferred. When the paramagnetic entities are coupled paramagnetic ions, reducing the temperature and increasing the magnetic field are not the same. Indeed for coupled paramagnetic ions, one can force the system into its ground state by reducing the temperature; this cannot be achieved merely by increasing the magnetic field.

4.5.2 High-spin Paramagnetic Heptanuclear Chromicyanides

Two heptanuclear high-spin molecules have been studied: $[Cr\{(CN)Ni(tetren)\}_6](ClO_4)_9$ (tetren = tetraethylenepentamine) labeled $CrNi_6$ with intramolecular ferromagnetic coupling ($J = +16.8\,cm^{-1}$) and $[Cr\{(CN)Mn(TrispicMeen)\}_6](ClO_4)_9 \cdot 3THF$ (TrispicMeen = N,N,N′-(tris(2-pyridylmethyl)-N′-methylethan)-1,2-diamine) labeled $CrMn_6$ with intramolecular antiferromagnetic coupling ($J = -8\,cm^{-1}$). Below the temperature of the coupling constant the molecule is in its ground state with a coupled spin $S = 15/2$ for $CrNi_6$ and $S = 27/2$ for $CrMn_6$. By registering isotropic and dichroic XAS signals, one can obtain the same kind of results as those obtained on the Prussian blue magnet presented in Section 3 – crystal field strength, spin–orbit coupling constants, orbital and spin magnetization [43]. In Fig. 3, the chromium $L_{2,3}$ edges of the Prussian blue magnet have been reproduced by careful choice of parameters. We have used the same set of parameters to calculate the XMCD signal in $CrMn_6$ (Fig. 9). The good agreement between calculation and experiment confirms that the LFM parameters indeed give a correct description of the chromium ground state.

Beyond this information, XMCD in paramagnetic molecules yields completely new physical and chemical insight into the local magnetic behavior of each atomic species. In a heptanuclear molecule with ferromagnetic intramolecular coupling, the ground state is obtained by the sum of the largest spin on each atomic species. In $CrNi_6$ the molecular ground state is $S = 15/2$ and it is built from the chromium spin $S = 3/2$ and the six nickel spin $S = 1$. The ground state is 16-fold degenerated with wave functions $|S = 15/2, M\rangle$. When a magnetic field is applied the lowest-lying wave-vector is $|S = 15/2, M = -15/2\rangle = |S_{6Ni} = 6, M_{6Ni} = -6\rangle \otimes |S_{Cr} = 3/2, M_{Cr} = -3/2\rangle$. In a heptanuclear molecule with antiferromagnetic intramolecular coupling, the ground state results from a difference between the spins

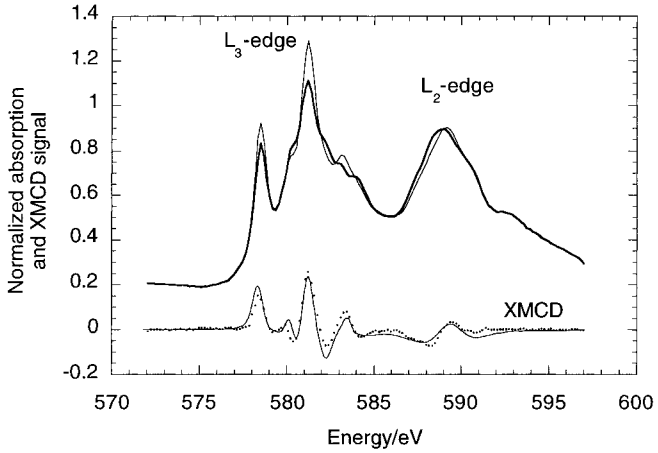

Fig. 9. Cr $L_{2,3}$ edges in $CrMn_6$. Upper panel. $\sigma_{\uparrow\downarrow}$ and $\sigma_{\uparrow\uparrow}$. Lower panel. dots: experimental XMCD signal; continuous line: calculated XMCD signal.

of the two different ion species. In $CrMn_6$ the molecular ground state is $S = 27/2$. The 28-fold wave functions $|S = 27/2, M\rangle$ are built from linear combinations such that the lowest lying state in a magnetic field is $|S = 27/2, M = -27/2\rangle$. In contrast with the ferromagnetic case, the magnetic ground state for $CrMn_6$ is a linear combination of four terms built from the products:

$$\begin{aligned}
&|S_{6\mathrm{Mn}} = 30/2, M_{6\mathrm{Mn}} = -30/2\rangle \otimes |S_{\mathrm{Cr}} = 3/2, M_{\mathrm{Cr}} = +3/2\rangle \\
&|S_{6\mathrm{Mn}} = 30/2, M_{6\mathrm{Mn}} = -28/2\rangle \otimes |S_{\mathrm{Cr}} = 3/2, M_{\mathrm{Cr}} = +1/2\rangle \\
&|S_{6\mathrm{Mn}} = 30/2, M_{6\mathrm{Mn}} = -26/2\rangle \otimes |S_{\mathrm{Cr}} = 3/2, M_{\mathrm{Cr}} = -1/2\rangle \\
&|S_{6\mathrm{Mn}} = 30/2, M_{6\mathrm{Mn}} = -24/2\rangle \otimes |S_{\mathrm{Cr}} = 3/2, M_{\mathrm{Cr}} = -3/2\rangle
\end{aligned} \tag{7}$$

with coefficients given by the related Clebsch–Gordan coefficients. Analysis of the theoretical magnetization of the ground state shows that when the magnetization of the $CrMn_6$ paramagnetic molecule is fully saturated the local magnetic moment of the manganese ions is 99% saturated, although the local magnetic moment of the chromium ions reaches only ca 90% of the saturation of an isolated chromium ion (Fig. 10). This effect is a direct consequence of the finite size of the heptanuclear high spin molecule [43]. In contrast with any macroscopic magnetic measurement, XMCD is the only experimental technique that can measure such a quantum-sized effect.

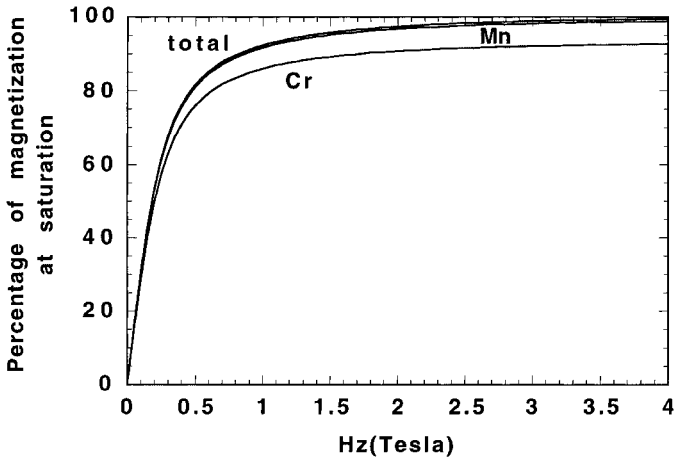

Fig. 10. Ratio of the actual magnetization at saturation in the molecule with the magnetization at saturation in the ion. ($T = 2\,\mathrm{K}$)

4.5.3 XMCD in Metal Clusters of Metalloproteins

S.P. Cramer and his team have performed pioneering work in the field of XAS applied to metallic sites in proteins. Their more recent efforts have been directed towards paramagnetic centers cooled to low temperature (below 1 K) to register XMCD. There is a twofold target concerning the metal clusters that are the active sites of the metalloproteins-determination of the oxidation state of the various 3d elements and understanding of the magnetic coupling inside the metallic clusters.

The first XMCD results ever published concern the copper site of the plastocyanin. This is a test case, because the electronic structure of copper in this protein is well understood from a variety of experimental and theoretical approaches [41]. The Cu^{II} $L_{2,3}$ edges have been measured at 400 mK in a $+/-$ 2 T magnetic field. From the dependence of the XMCD on the magnetic field, it has been found that the magnetization of the copper center followed a Brillouin curve. They have, moreover, explained that at saturation the observed magnetic moment per copper ion was reduced to 50% of the expected value. This effect is because of the random orientation of the molecules [44]. The authors suggested that the XMCD measurement of paramagnetic Cu^{II} in well characterized compounds might be used as an internal thermometer [45].

One strong potential of XMCD lies in the study of local spin orientations in coupled paramagnetic metal clusters. In human ferredoxin the metal cluster contain two tetrahedral Fe sites bridged by two inorganic sulfide residues. One expects that the two iron ions are Fe^{III} and Fe^{II} high spin states coupled antiferromagnetically, yielding a net $S = 1/2$ coupled ground state. This idea has been tested by measuring the XMCD signals from the metal cluster at Fe $L_{2,3}$ edges in ferredoxin and XMCD signals where only Fe^{III} or Fe^{II} was present in similar metal clusters. The Fe^{III} signal is from oxidized *Pyrococcus furiosus* rubredoxin and the Fe^{II} signal from reduced oxidized *Pyrococcus furiosus* rubredoxin. A large XMCD signal at Fe $L_{2,3}$ edges has been measured in both rubredoxin [45,46]. It is found that the dichroic signal at Fe $L_{2,3}$ edges in ferredoxin is different from the expected linear combination of XMCD signals in the rubredoxins. There have been several attempts to explain this puzzling XMCD behavior [46,47]. None has been completely successful, indicating that the electronic structure of human ferrodoxin might be more complex than was originally assumed.

4.6 Conclusion

XMCD and spin-polarized neutron diffraction are often compared. Spin polarized neutron diffraction measurements require single crystals that are always difficult to obtain in the field of molecular chemistry. When feasible, this type of measurement yields useful information enabling understanding of magnetic structure and interaction in such compounds. In antiferromagnets it can determine the three-dimensional antiferromagnetic structure among the many possible structures. XMCD can only be

applied to compounds which have a net macroscopic magnetic moment – ferromagnets, ferrimagnets, paramagnetic ions or molecules at low temperature, spin glasses in large magnetic field, or even antiferromagnetic nanoparticles. XMCD does not require single crystals. It is also well suited to the study of magnetic surfaces with few layers. XMCD cannot determine the three dimensional magnetic structure of compounds whose crystallographic and magnetic structures are completely unknown. The power of XMCD lies in its very high sensitivity to electronic structure, which enables refinement of the electronic structure determined by other spectroscopic methods.

New techniques using synchrotron radiation have been developed to characterize the magnetic and electronic structure of transition metal complexes. By performing high-resolution fluorescence experiments the chemical sensitivity of $K\beta$ emission spectra can be used to identify chemical states and the spin polarized near edge structure provides a measure of the spin density (site and spin selectivity) [48]. Recent experiments on metalloproteins [49], biological systems [50] and transition metal complexes [51] have been performed to characterize metal–ligand bonds and transition metal oxidation states in these complex systems. From analysis of the fluorescence decay it is also possible to discriminate between XAS signals coming from the same atom in various oxidation state [49]. De Groot has also shown that the cross-section of minority spin versus majority spin can also be separated by analysis of fluorescence decay [49]. Instead of measuring the $K\beta$ decay, one can register the optical luminescence consecutive to X-ray absorption. This powerful tool has been applied in chiral europium complexes, for which circular dichroic signals have been observed [52]. This method is also chemically selective for the oxidation states.

XMCD is a sensitive tool for determining local magnetic structure in magnetic and paramagnetic compounds. It has essentially been applied to the field of solid state physics and chemistry in intermetallic compounds. We hope that we have shown that the technique is also of interest for other compounds such as molecular-based magnets, paramagnetic molecular entities, or metal clusters in proteins. XMCD sum rules enable extraction of spin and orbit contributions to the local magnetic moment with the unique chemical and orbital selectivities of XAS. Although absolute magnetic moments remain difficult to measure, much information can be gained from this method:

- it is a powerful tool for determining accurate values of the $\langle L_Z \rangle / \langle S_Z \rangle$ ratio; and
- it enables cross checking of the validity of essential LFM parameters such as valence state, crystal field strength, spin–orbit coupling constants, charge transfer, and the covalence of the metal-ligand bond.

Acknowledgment

We are glad to thank Jean-Paul Kappler for many instrumental developments on the beam-lines, Elysabeth Dartyge and François Baudelet for K edges XMCD measurements and Michel Verdaguer for his constant support. Christian Brouder is deeply thanked for his computing assistance.

References

[1] *X-ray absorption. Principles and applications: techniques of EXAFS, SEXAFS and XANES, Chemical Analysis Vol. 92* (Eds.: D. C. Koningsberger, R. Prins), Wiley, **1988**.
[2] *Synchrotron radiation: techniques and applications, Topics in current physics* (Ed.: C. Kunz), Springer, **1979**.
[3] *Handbook on Synchrotron Radiation*, (Ed.: C. Koch) North Holland Pub. Corp., Vol. Ia and Ib **1983**, Vol. II **1987**.
[4] *Synchrotron radiation research*, (Eds.: H. Winick, S. Doniach), Plenum, **1980**.
[5] *Neutron and synchrotron radiation for condensed matter studies, Vol. 1* (Eds.: J. Baruchel, J.L. Hodeau, M.S. Lehmann, J.R. Regnard, C. Schlenker), Springer, Les éditions de physique, **1993**, pp. 323–361.
[6] C.R. Natoli, D.K. Misemer, S. Doniach, F.W. Kutzler, *Phys. Rev. A* **1980**, *22*, 1104.
[7] C.R. Natoli, *EXAFS and Near edge structure III*, Springer Proc. Phys., Vol. 2, **1984**, p. 38.
[8] R.D. Cowan, *The theory of Atomic Structure and Spectra*, University of California Press, Berkeley, **1981**.
[9] F.M.F. de Groot, J.C. Fuggle, B.T. Thole, G.A. Sawatzky, *Phys. Rev. B*, **1990**, *41*, 928.
[10] F.M.F. de Groot, J.C. Fuggle, B.T. Thole, G.A. Sawatzky, *Phys. Rev. B*, **1990**, *42*, 5459.
[11] G.A. Sawatzky, *Core Level Spectroscopy in Condensed Systems*, Springer, Kashikojima, **1987**, pp. 99–133.
[12] A. Okada, K. Kotani, Technical report of ISSP **1992**, Ser. A, 2541.
[13] *Magnetism and synchrotron radiation*, (Eds.: E. Beaurepaire, B. Carrière, J.P. Kappler), Les éditions de physique, Les Ulis, France, **1997**.
[14] W. O'Brien, B.L. Tonner, *Phys. Rev. B* **1994**, *50*, 12672.
[15] J.H. Dunn, D. Arvanitis, M. Materson, M. Tischer, F. May, M. Russo, K. Baberschke, *J. Phys.: Condens. Matter*, **1995**, *7*, 1111.
[16] D. Arvanitis, M. Tischer, J.H. Dunn, F. May, N. Martensson and K. Baberschke, *Spin orbit influenced spectroscopies of magnetic solids*, (Eds.: H. Ebert, G. Schütz), Springer, Berlin, **1996**.
[17] V. Chakarian, Y.U. Idzerda, C.T. Chen, *Phys. Rev. B*, **1998**, *57*, 5312.
[18] D. Lefebvre, Ph. Sainctavit, C. Malgrange, *Review of Scientific Instrumentation* **1994**, *65*, 2556.
[19] R.Q. Wu, A.J. Freeman, *Phys. Rev. Lett.*, **1994**, *73*, 1994.
[20] X. Wang, T.C. Leung, B.N. Harmon, P. Carra, *Phys. Rev. B*, **1993**, *47*, 9087.
[21] Y. Teramura, *J. Phys. Soc. Japan*, **1996**, *65*, 1053.
[22] J.-Ph. Schillé, F. Bertran, M. Finazzi, Ch. Brouder, J.-P. Kappler, G. Krill, *Phys. Rev. B*, **1994**, *50*, 2895.
[23] C.T. Chen, Y.U. Idzerda, H.J. Lin, N.V. Smith, G. Meigs, E. Chaban, G.H. Ho, E. Pellegrin, F. Sette, *Phys. Rev. Lett.* **1994**, *75*, 152.
[24] J. Stöhr, H. König, *Phys. Rev. Lett.*, **1995**, *75*, 3748.
[25] Ph. Sainctavit, M.-A. Arrio, Ch. Brouder, *Phys. Rev. B*, **1995**, *52*, 12766.
[26] D.S. Wang, R.Q. Wu, L.P. Zhong, A.J. Freeman, *J. Magn. Magn. Mater.* **1995**, *140–144*, 643.
[27] A.J. Freeman, O.N. Mryassov, D.S. Wang, R.Q. Wu, Matter. *Science and Engi. B*, **1995**, *31*, 225.
[28] M.-A. Arrio, Ph. Sainctavit, Ch. Cartier dit Moulin, Ch. Brouder, F.M.F. de Groot, T. Mallah, M. Verdaguer, *J. Phys. Chem.*, **1996**, *100*, 4679.

[29] A.B.P. Lever, *Inorganic electronic spectroscopy*; (2nd edition), Amsterdam: Elsevier, **1984**.
[30] G. van der Laan, J. Zaanen, G.A. Sawatzky, R. Karnatak, J.-M. Esteva, *Phys. Rev. B*, **1986**, *33*, 4253.
[31] M.-A. Arrio, Ph. Sainctavit, Ch. Cartier dit Moulin, T. Mallah, M. Verdaguer, E. Pellegrin, C.T. Chen, *J. Am. Chem. Soc.*, **1996**, *118*, 6422.
[32] D.W. Fisher, *J. Phys. Chem. Solids*, **1971**, *32*, 2455.
[33] B.N. Figgis, J.B. Forsyth, P.A. Reynolds, *Inorg. Chem.*, **1987**, *26*, 101.
[34] B.N. Figgis, E.S. Kucharski, M. Vrtis, *J. Am. Chem. Soc.*, **1993**, *115*, 176.
[35] A. Kotani, K. Okada, Technical Report of ISSP **1992**, Ser. A, no. 2562.
[36] a) J. Zaanen, C. Westra, G.A. Sawatzky, *Phys. Rev. B*, **1986**, *33*, 8060; b) F.M.F. de Groot, *Electron. Spectrosc. Relat. Phenom.*, **1994**, *67*, 529.
[37] Ch. Brouder, M. Alouani, K.H. Bennemann, *Phys. Rev. B*, **1996**, *54*, 7334.
[38] E. Dujardin, S. Ferlay, X. Phan, Ch. Cartier dit Moulin, Ph. Sainctavit, F. Baudelet, E. Dartyge, P. Veillet, M. Verdaguer, *J. Am. Chem. Soc.*, **1998**, *120*, 11347.
[39] M. Verdaguer, T. Mallah, C. Helary, F. L'Hermite, P. Sainctavit, M.A. Arrio, D. Babel, F. Baudelet, E. Dartyge, A. Fontaine, *Physica B*, **1995**, *208–209*, 765.
[40] S.P. Cramer, G. Peng, J. Christiansen, J. Chen, J. van Elp, S.J. George, A.T. Young. *J. Electron Spectr. Relat. Phen.*, **1996**, *78*, 225.
[41] H. Wang, C. Bryant, D.W. Randall, L.B. LaCroix, E.I. Solomon, M. LeGros, S.P. Cramer. *J. Phys. Chem.*, **1998**, *102*, 8347.
[42] A new experimental setup developed by J.-P. Kappler and Ph. Sainctavit is actually under test at LURE. It has already reached the temperature of 130 mK.
[43] M.-A. Arrio, A. Scuiller, Ph. Sainctavit, Ch. Cartier dit Moulin, T. Mallah, M. Verdaguer. *J. Am. Chem. Soc.*, **1999**, *121*, 6414.
[44] J. van Elp, B.G. Searle, *J. Electron Spectrosc. Relat. Phenom.*, **1997**, *86*, 93.
[45] S.P. Cramer, C.Y. Ralston, H. Wang, C. Bryant, *J. Electron Spectr. Relat. Phen.*, **1997**, *86*, 175.
[46] J. van Elp, G. Peng, Z.H. Zhou, S. Mukund, M.W.W. Adams, *Phys. Rev.*, **1996**, *B53*, 2523.
[47] S.W. Lovesey, P. Allenspach, *Physica Scripta*, **1998**, *57*, 657.
[48] X. Wang, F.M.F. de Groot, S.P. Cramer, *Phys. Rev. B*, **1997**, *56*, 4553.
[49] X. Wang, M.M. Grush, A.G. Froeschner, S.P. Cramer, *J. Synchrotron Rad.*, **1997**, *4*, 236.
[50] U. Bergmann, M.M. Grush, C.R. Horne, P. DeMarois, J.E. Penner-Hahn, C.F. Yocum, D.W. Wright, C.E. Dubé, W.H. Amstrong, G. Christou, H.J. Eppley, S.P. Cramer, *J. Phys. B*, **1998**, *102*, 8350.
[51] U. Bergmann, C.R. Horne, T.J. Collins, J.M. Workman, S.P. Cramer, *Chem. Phys. Lett.*, **1999**, *302*, 119.
[52] C. Gauthier, I. Ascone, J. Goulon, R. Cortes, J.M. Barbe, R. Guilard, *Chem. Phys.*, **1990**, *147*, 165.

Magnetism: Molecules to Materials I: Models and Experiments.
Edited by Joel S. Miller and Marc Drillon

ISBNs: 3-527-29772-3 (Hardback); 3-527-60084-1 (Electronic)

5 Magnetic Properties of Mixed-valence Clusters: Theoretical Approaches and Applications

Juan J. Borrás-Almenar, Juan M. Clemente-Juan, Eugenio Coronado, Andrew Palii, and Boris S. Tsukerblat

5.1 Introduction

The interplay between electron delocalization and magnetic interactions plays a key role in areas as diverse as solid-state chemistry (bulk magnetic materials, superconductors, ...) [1] and biology (iron–sulfur proteins, manganese-oxo clusters, ...) [2]. In molecular inorganic chemistry these two electronic processes have been traditionally studied independently. Thus, the electron dynamics of mixed-valence dimers, as exemplified by the Creutz–Taube complex $[(NH_3)_5Ru^{II}(\text{pyrazine})Ru^{III}(NH_3)_5]$, has been extensively investigated [3]. In this kind of molecular complex one extra electron is delocalized over two diamagnetic metal sites. Therefore, they constitute model systems for the study of the electron transfer. Their simplicity also enables treatment of the coupling of electronic and nuclear movements (vibronic interactions) at the molecular scale; this is an inherent problem for mixed valence (MV) systems because the itinerant electron causes severe deformation of the coordination sphere of the metal site [4]. The vibronic theory of MV dimers (focused mainly only on the phenomenon of intervalence optical absorption) has been formulated by Piepho, Krausz, and Schatz and referred to as PKS model [5]. Piepho later developed a new vibronic model [6,7].

In their turn, magnetic exchange interactions were initially investigated in exchange-coupled dimers as exemplified by copper acetate. The explanation of the *anomalous* magnetic behavior of this coordination complex by Bleaney and Bowers [8] in the fifties constituted the starting point of modern magnetochemistry. Since then many other exchange-coupled compounds have been prepared with increasing nuclearities, topologies, and dimensionalities, and with combinations of different magnetic metal ions and/or organic radicals in the same lattice [9]. In all these systems the spin carriers are completely localized on the magnetic sites.

As a further degree of complexity it is possible to think in terms of introducing some electron delocalization into these exchange-coupled molecular systems – in other words, to prepare mixed-valence exchange-coupled magnetic systems in which itinerant electrons and localized magnetic moments can coexist and interact. One of the main interests of these systems in molecular magnetism comes from the possibility of stabilizing strong ferromagnetic coupling between the magnetic centers through the itinerant electrons via a double-exchange mechanism. These molecular systems

can serve as models of extended MV magnetic systems, which are of current interest in solid state chemistry.

In this review we focus on the magnetic properties of mixed-valence magnetic clusters. We show how in these systems the energies of the spin states depend on the interplay between electronic interactions (double-exchange, Heisenberg exchange and Coulomb repulsions) and vibronic interactions. We consider the role of the electronic interactions in MV dimers, trimers, tetramers and higher nuclearity magnetic clusters, paying particular attention to the double-exchange concept. We also discuss the influence of the vibronic interactions in connection with both electron localization and magnetic properties.

5.2 Double-exchange Mechanisms

Double-exchange interaction involves the coupling of two localized magnetic moments, having spin cores S_o, through an itinerant *extra* electron that can travel forth and back between the two magnetic centers. Because the itinerant electron keeps the orientation of its spin during transfer, double-exchange results in a strong spin polarization effect which favors ferromagnetic spin-alignment in the system. This mechanism of electron-spin interaction was first suggested by Zener [10] to explain the ferromagnetism observed in the mixed valence (MV) manganites of perovskite structure, such as $(La_xCa_{1-x})(Mn^{III}Mn^{IV}_{1-x})O_3$. Notice that these MV oxides are an active focus of research in solid state chemistry, because they exhibit colossal magnetoresistance, a property that has been attributed to double-exchange [11]. Anderson and Hasegawa [12] suggested a solution of the double-exchange for a MV dimer deducing the spin-dependence of the double-exchange parameter.

Let us start with the simplest case of one d-electron moving between two spinless transition metal sites A and B in the molecule (d^1–d^0 problem). The sites are supposed to be symmetrically equivalent. We also assume that, because of the crystal field effect, the ground state of the electron trapped on each of these sites is orbitally nondegenerate; the corresponding orbitals will be denoted a and b, and the associated energies E_a and E_b are equal. When these two orbitals are allowed to interact, the trapped state of the electron is unstable. In fact, its kinetic energy and the attraction to the *alien* site promote the transfer process with the rate t which can be associated with the transfer integrals $t_{a\to b} = t_{b\to a}$. The transfer integral for a one-electron MV dimer is defined as a matrix element of the monoelectronic part $\hat{h}$ of the Hamiltonian $t = \langle a|\hat{h}|b\rangle$. The sign of t is usually opposite to that of the overlap integral $\langle a|b\rangle$. The transfer processes split the energy level as shown in Scheme 1 for

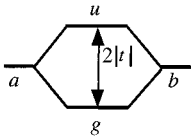

Scheme 1.

$t < 0$ (the bonding orbital is ψ_g). The two resulting delocalized functions are:

$$\psi_g = (1/\sqrt{2})(a + b) \text{ and } \psi_u = (1/\sqrt{2})(\text{a} - \text{b}) \tag{1}$$

where g (even) and u (odd) refer to the parity of the molecular orbitals.

If the metal ions are separated by a ligand, electron transfer must occur through the orbitals of the bridging atoms, giving rise to effective contact between the metal orbitals. The first idea of this indirect transfer was suggested by Zener on the basis of the exchange mechanism. In this scheme the two localized states of the d^1–d^0 system (shown in Scheme 2) are connected by the matrix element given in Eq. (2).

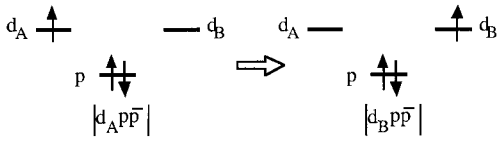

Scheme 2.

$$\left\langle d_{\mathrm{B}}(1)\,p(2)\left|\frac{1}{r_{12}}\right|d_{\mathrm{A}}(2)\,p(1)\right\rangle \tag{2}$$

This transfer integral resembles an exchange integral describing the following two-step exchange process (Scheme 3): 1) electron 1 virtually jumps from the p orbital to the empty place, d_{B}, keeping its spin orientation; then 2) electron 2 occupying the d_{A} orbital jumps into the p orbital, restoring thus the closed p^2 configuration.

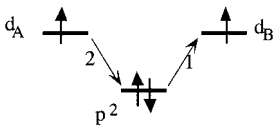

Scheme 3.

For practical purposes, instead of involving pure d-metal and p-ligand orbitals in the indirect transfer process, it is more convenient to consider as starting functions molecular orbitals essentially localized on the metal centers but that include a small admixture with the orbitals of the bridging atoms. This idea, introduced by Anderson and Hasegawa [12], enables us to use the same model for both direct and indirect transfer processes, as in direct exchange and superexchange. Thus, the indirect transfer from A to B can be taken into account by use of an effective transfer parameter t_{ab} which is of the order of $(t_{\mathrm{dp}})^2/\Delta E_{\mathrm{dp}}$ where t_{dp} and ΔE_{dp} are the transfer integral and the energy gap between d-metal and p-ligand orbitals, respectively.

5.3 Classical Spin Model for the Double Exchange

Let us now consider the general case of a MV dimer d^n–d^{n+1}. The first problem in question is how the magnetic moment of the metal ions affect the electron transfer. It happens that, in this case, electron transfer is spin-dependent. The main features of the phenomenon can be understood in the framework of the classical spin model developed by Anderson and Hasegawa [12]. As distinguished from a quantum spin, which can be oriented in the space in $2S+1$ directions, a classical spin represents the infinite spin limit for which all the directions in the space are allowed (Scheme 4).

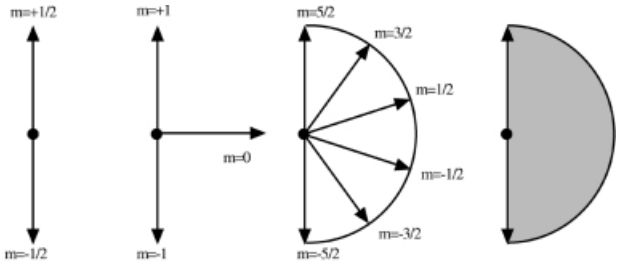

Scheme 4.

Let us consider a high-spin state (Hund's configuration) for the d^{n+1} ions. From the classical point of view, that means that the extra electron lines up its spin, $\boldsymbol{s}$, parallel to the spin core $\boldsymbol{S}_0$ (Scheme 5), taking thus the gain in energy from the ferromagnetic intraatomic exchange.

Scheme 5.

For the MV dimer, the full spin of the system can take $2S+1$ values with S between $S_{\max} = 2S_0 + 1/2$ and $S_{\min} = 1/2$. In the classical limit, $S_0 \gg 1/2$, so that $S_{\max} \approx 2S_0$ and $S_{\min} \approx 0$. These two extremes correspond to parallel and antiparallel orientations of the spin cores (Scheme 6), while the intermediate spin values are to be correlated with intermediate angles between the spin cores.

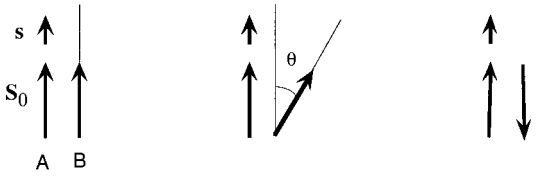

Scheme 6.

Let us consider the dependence of the electron transfer on the angle θ. From Scheme 6 it is clear that the transfer is most efficient when both spin cores are parallel ($\theta = 0^\circ$), whereas it is zero when they are antiparallel ($\theta = 180^\circ$), because then the moving electron must reverse its spin to be parallel to $\boldsymbol{S}_\mathrm{B}$. The maximum value of the transfer will be denoted as t. In the general case where the angle between the spin cores $\boldsymbol{S}_\mathrm{A}$ and $\boldsymbol{S}_\mathrm{B}$ is θ, the spin $\boldsymbol{s}$ associated with the electron moving from A to B must adopt a direction parallel to $\boldsymbol{S}_\mathrm{B}$ to form a high-spin B ion. For that, $\boldsymbol{s}$ must be rotated by an angle θ. This is easy to do by use of the well known transformation of spin functions ($s = 1/2$) under rotation:

$$\alpha' = \cos(\theta/2)\alpha - \sin(\theta/2)\beta \quad \text{and} \quad \beta' = \sin(\theta/2)\alpha + \cos(\theta/2)\beta \tag{3}$$

where α (α') and β (β') denote the two spin-functions referred to the direction $\boldsymbol{S}_\mathrm{A}$ ($\boldsymbol{S}_\mathrm{B}$).

The electron transfer, $a \rightarrow b$, between two spin cores, $\boldsymbol{S}_\mathrm{A}$ and $\boldsymbol{S}_\mathrm{B}$, bent at the angle θ can be then written as:

$$t(\theta) = (d_\mathrm{B}\alpha'|\hat{H}|d_\mathrm{A}\alpha\rangle = t\ \cos(\theta/2) \tag{4}$$

which is maximum (and equal to t) when $\theta = 0^\circ$ and zero when $\theta = \pi$.

Now the problem is how to evaluate the classical angle θ in terms of S_0 and the full spin of the system, S. Considering $\boldsymbol{S}_\mathrm{A}$ and $\boldsymbol{S}_\mathrm{B}$ as classical vectors (Scheme 7) one can express the full spin as $\boldsymbol{S} = \boldsymbol{S}_\mathrm{A} + \boldsymbol{S}_\mathrm{B}$, where $S_\mathrm{A} = S_\mathrm{B} = S_0$, because in the classical limit $s = 1/2$ is negligible. From Scheme 7 we find:

$$\cos(\theta/2) = S/(2S_0) \tag{5}$$

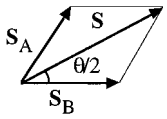

Scheme 7.

Combining Eqs. (4) and (5) one can express t in terms of both S_0 and S:

$$t(S) = tS/2S_0 \tag{6}$$

This expression confirms that the rate of transfer is spin-dependent and increases as the full spin, S, is increased. Thus, for parallel $\boldsymbol{S}_\mathrm{A}$ and $\boldsymbol{S}_\mathrm{B}$, $S = S_\mathrm{max} \approx 2S_0$ and the rate of transfer achieves its maximum value t, whereas in the antiparallel case $S = S_\mathrm{min} = 0$ and the transfer rate vanishes because only a non-Hund state (that is high in energy) can be formed when the moving electron retains its spin direction in the course of the transfer.

Taking into account that the transfer matrix has the form:

$$\begin{array}{l|cc|} \langle SM, S_\mathrm{A}^*, S_\mathrm{B}| & 0 & t(S) \\ \langle SM, S_\mathrm{A}, S_\mathrm{B}^*| & t(S) & 0 \end{array} \tag{7}$$

where the star indicates the location of the extra electron, the energy spectrum of the MV dimer is:

$$E_{\pm} = \pm t(S) = \pm tS/2S_0 \tag{8}$$

Because in the classical spin model $S_{\max} \approx 2S_0$, the above expression enables deduction that the energy levels of a dimer form a continuous band of width $2t$ in which each sublevel corresponds to a definite angle between classical spins $\boldsymbol{S}_{\mathrm{A}}$ and $\boldsymbol{S}_{\mathrm{B}}$. It is important to note that the ground state has the maximum spin value so that the double exchange gives rise to a strong ferromagnetic effect.

5.4 Mixed-valence Dimers

5.4.1 Electronic Interactions

5.4.1.1 Double Exchange: Quantum-mechanical Considerations

The transfer process from site A to B (or from B to A) involves two localized configurations, A*B and AB*, as depicted in Scheme 8 for the simplest case of the d^1–d^2 dimer. The star indicates the location of the extra electron and the two sites A and B are assumed to be identical. Electrons of spin cores occupy orbitals a_1 and b_1. The extra electron can move over the orbitals a and b.

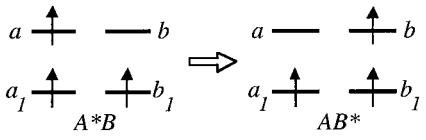

Scheme 8.

Two configurations A*B and AB* are coupled by the transfer Hamiltonian:

$$\hat{H}_t = \sum_{\sigma} t\left(C^{+}_{b\sigma}C_{a\sigma} + C^{+}_{a\sigma}C_{b\sigma}\right) \tag{9}$$

where $C_{a\sigma}$ annihilates the electron with spin projection σ at orbital a, and $C^{+}_{b\sigma}$ creates an electron with spin projection σ at orbital b; t is the transfer or resonance integral and takes into account mixing of the A*B and AB* configurations.

According to Hund's rule, electrons will be parallel within each site, so for the a^*b configuration we have $S_{\mathrm{A}} = 1$, $S_{\mathrm{B}} = 1/2$, and for the ab^* configuration we have $S_{\mathrm{A}} = 1/2$, $S_{\mathrm{B}} = 1$. The available spin states for the pair will then be $S = 1/2$ and $3/2$, and each spin state will occur twice (one for each configuration). Therefore, the delocalization doubles the number of low-lying states. These states will be split as a result of electron transfer which is facilitated when the two spin cores are parallel, thus favoring the state of highest spin ($S = 3/2$) as the ground state. In fact, the

solution of the above Hamiltonian (Eq. 9) demonstrates that this splitting is spin-dependent and is $t(S + 1/2)$, giving the energy spectrum depicted in Fig. 1. Two main points should be noticed: 1) the components of the split levels are disposed symmetrically ($\pm t$ and $\pm t/2$ for $S = 3/2$ and $S = 1/2$, respectively); 2) The labels g and u refer to the parity (even or odd) of the delocalized functions. Quantum mechanical calculation [13] shows that the orders resulting from the double-exchange splitting of the two spin states ($S = 1/2$ and $3/2$) are reversed. With regard to the magnetic properties this feature is irrelevant, but they might be important when discussing spectroscopic properties.

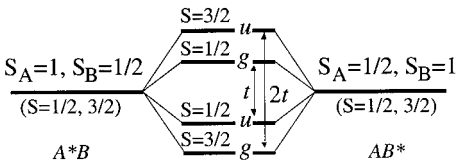

Fig. 1. Energy levels of the delocalized MV dimer d^1–d^2. Influence of the double-exchange

These results can easily be generalized to the dinuclear dimers d^n–d^{n+1} with a fully delocalized extra particle (electron or hole) [12]. The energy levels can be expressed as:

$$E(S) = \pm t(S + 1/2)/(2S_0 + 1) \tag{10}$$

where S_0 is the value of the spin core and t is the one-electron transfer parameter associated with the jumps of the *extra* particle over the orbitals a and b.

Comparison of Eqs. (8) and (10) reveals that the quantum-mechanical expression for the double-exchange splitting can be obtained from the classical expression by simple substitution $S \to S + 1/2$; $S_0 \to S_0 + 1/2$.

Because now $S_{max} = 2S_0 + 1$, the double-exchange spin levels for all d^n–d^{n+1} dimers are arranged in the gap $2t$, as in the classical limit (Scheme 9).

One can see that the double-exchange splitting is spin-dependent, and increases linearly as the full spin, S, is increased. The value $t/(2S_0 + 1)$ plays the role of multielectron transfer parameter and the splittings of the S-multiplets are directly proportional to $(S + 1/2)$. Because of the spin-dependence of the double-exchange splitting, the level with $S = S_{max}$ proves to be the ground state and we arrive to the general conclusion that *in dimeric MV clusters double-exchange always results*

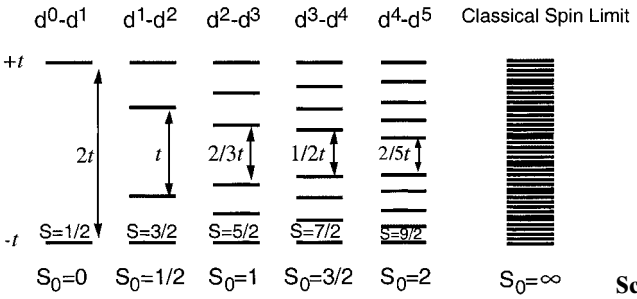

Scheme 9.

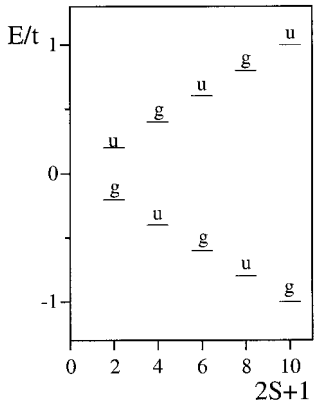

Fig. 2. Energy spectrum of a d^5–d^6 MV dimer ($t > 0$) as a function of the spin multiplicity ($2S + 1$). Influence of the double-exchange

in the ferromagnetic spin alignment irrespective of the sign of the double-exchange parameter t. Quantum-mechanical consideration shows that the sign of t determines only the order of even and odd levels in the spectrum. This order also depends on the nature of the delocalized extra particle. As an illustration let us consider the energy spectrum of a d^5–d^6 system, which can correspond to an MV dimer Fe^{III}–Fe^{II} with high-spin local states (Fig. 2). In this dimer one extra hole is delocalized over two paramagnetic sites with an $S_0 = 2$ spin core. Energetically this dimer is equivalent to the d^5–d^4 system. Accordingly, double-exchange splitting is the same in both dimers. We observe a symmetric splitting of the spin states, with the highest spin state, $S = 9/2$, being the ground state. The only noticeable difference between these two cases is the reversal of the parity of the spin states. Thus, while in the d^5–d^6 system a positive value of t stabilizes the even ferromagnetic state, in the d^5–d^4 system it stabilizes the odd ferromagnetic state. Magnetically such a difference is irrelevant, owing to the symmetric splitting of the spin states, but it will become important in higher-nuclearity MV clusters in which an unsymmetric spectrum is observed, as we will see hereinafter.

5.4.1.2 Combined Effect of Double Exchange and Magnetic Exchange

Because the two sites contain unpaired electrons, the magnetic exchange interaction will be superimposed on the double-exchange interaction. The expression for the isotropic exchange (Heisenberg) Hamiltonian is:

$$\boldsymbol{H} = -2J\boldsymbol{S}_\mathrm{A}\boldsymbol{S}_\mathrm{B} \tag{11}$$

where $\boldsymbol{S}_\mathrm{A}$ and $\boldsymbol{S}_\mathrm{B}$ are the full spins of ions A and B, and J is the many-electron exchange parameter. As distinguished from the transfer Hamiltonian, the exchange Hamiltonian is operative in the localized configurations A*B and AB*. In each, the exchange splitting is identical and is given by the well known expression:

$$E(S) = -J[S(S+1) - S_\mathrm{A}(S_\mathrm{A}+1) - S_\mathrm{B}(S_\mathrm{B}+1) \tag{12}$$

Omitting in Eq. (12) the last two additive terms (independent of S) and combining this with Eq. (10) we obtain the energies for a MV dimer in presence of both electron delocalization and magnetic exchange:

$$E_{\pm}(S) = -JS(S+1) \pm t(S+1/2)/(2S_0+1) \tag{13}$$

We observe that whereas the splitting of the spin states as a result of Heisenberg exchange is quadratic in S (proportional to $S(S+1)$), the splitting arising from the double-exchange is linear in S. Therefore, the energy spectrum of a MV dimer is expected to be different from that of a fully localized spin dimer.

Let us use Eq. (13) to obtain the energy levels of the d^5–d^6 dimer. In the presence of antiferromagnetic exchange ($J < 0$) that tends to stabilize the states of lower S values, the ground spin state will be the result of competition between the two interactions (exchange and double-exchange). This effect can be seen in the so-called correlation diagram $E/|J|$ vs $t/|J|$ (Fig. 3). When double-exchange is weak enough ($t/|J| < 15$) the exchange dominates and the antiferromagnetic spin state $S = 1/2$ is the ground state. When the ratio $t/|J|$ increases, the ground state becomes successively $S = 3/2, 5/2, 7/2$, and, finally, $9/2$ in the strong double-exchange limit. This example shows that the magnetic properties of MV dimeric systems are the result of the interplay between Heisenberg and double-exchange interactions. For the dimeric systems the last effect always provides a ferromagnetic contribution which, usually, should exceed the antiferromagnetic exchange interaction. In fact, double-exchange is a first-order effect (proportional to t) involving the ground state configuration of the fully delocalized MV system, whereas magnetic exchange is a second-order effect involving mixing with the excited states (and proportional to t^2/U, where U is one center Coulomb repulsion).

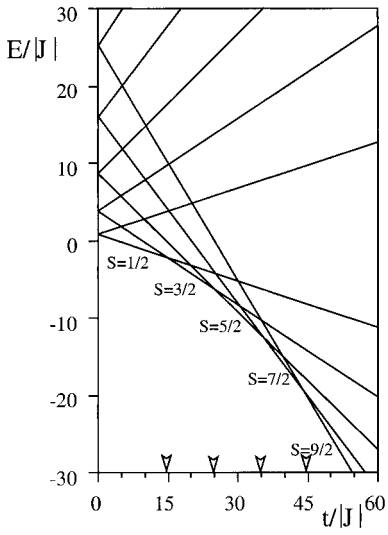

Fig. 3. Correlation diagram of a d^5–d^6 dimer showing the combined effect of double-exchange t and antiferromagnetic Heisenberg exchange J

For real systems, however, this is not the general rule, because other effects, for example vibronic interactions or distortions of the sites, can dramatically reduce the electron delocalization [14,15]. We will examine this problem in detail below.

5.4.1.3 Effect of the Asymmetry

In actual systems the extra electron might be trapped because of effects different from the vibronic interaction, for example the asymmetry in the dimer (the sites A and B are no longer identical). Such electron trapping strongly reduces the double-exchange effect and then the antiferromagnetic exchange might become the dominant effect [16].

The effect of the asymmetry can be taken into account through the difference in energy between the two configurations A^*B and AB^*, which are no longer degenerate. $\Delta = E_A - E_B$ will then define a trapping parameter. Then the energies of the d^n–d^{n+1} dimers are given by:

$$E_{\pm}(S) = -JS(S+1) \pm \sqrt{\Delta^2 + \frac{t^2(S+1/2)^2}{(2S_0+1)^2}} \tag{14}$$

where the isotropic exchange, J, is also taken into account.

One observes that the distortion of the system restores the antiferromagnetic ground state, specific for the localized system with $J < 0$ (Fig. 4). Physically the distortion leads to localization of the extra electron on the lower energy site, so isotropic exchange plays a predominant role in a strongly distorted system. At the same time,

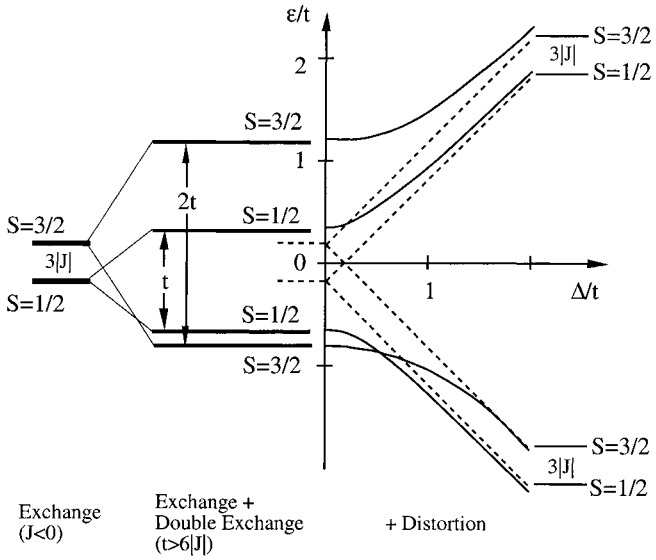

Fig. 4. Influence of asymmetry in the d^1–d^2 MV dimer

the excited levels ($E_+(1/2)$ and $E_+(3/2)$) are very high in the limit of strong distortion, whereas the low-lying levels ($E_-(1/2)$ and $E_-(3/2)$) are split with a gap $3|J|$ just as in the localized exchange-coupled dimer. The distortion thus eliminates the double-exchange effect restoring the Heisenberg-type pattern of spin levels when Δ is large compared with t.

More careful consideration shows that the second-order effect of the double exchange contributes to the isotropic exchange with the parameter $J' = t^2/[2\Delta(2S_0 + 1)] > 0$. In the limit of strong distortions the energy levels can be approximately expressed as:

$$E_{\pm}(S) = (-J \pm J')S(S+1) \pm (\Delta + \Delta_0)$$

where $\Delta_0 = t^2/[8\Delta(2S_0 + 1)]$. One can see that the gap $3|J|$ is slightly reduced for the low-lying levels and increased for the upper pair of levels.

5.4.1.4 Effect of the Orbital Degeneracy [17]

The model so far considered is based on the assumption that the one-electron orbitals and the terms associated with the sites A and B are orbitally nondegenerate and thus only full spin S characterize the sates of the systems. One ion or both can, however, have orbitally degenerate ground terms. The last case occurs in a bioctahedral d^1–d^2 dimer where we meet the ${}^2T_2(t_2)$–${}^3T_1(t_2^2)$ MV problem with the extra electron occupying t_2-orbitals. As an example we give briefly the results for the edge-shared system in which the most efficient transfer pathway $(xy)_A \leftrightarrow (xy)_B$ is taken into account (Fig. 5). Because of the T–P analogy, orbital parts of ${}^3T_1$ and ${}^2T_2$ terms can be associated with the orbital angular momenta, $L_A = L_B = 1$, so the full states of the system in the pseudoangular momentum representation belong to $L = 0, 1, 2$ and $S = 1/2, 3/2$. These states $|\pm; SM_S; LM_L\rangle$ (Z is the quantization axis for both L and S) are specified also by the symbol of the parity ($+$ and $-$). The energy pattern for this MV system is shown in Fig. 6 (M_s is omitted from the labels).

Two points should be mentioned: 1) The ground state proves to be high-spin, so the conclusion about ferromagnetic spin-coupling produced by the double exchange is valid also for the orbitally degenerate system. This result is shown to be common for all MV dimers [17] At the same time, the energy pattern is much more complicated and, at E = 0, contains the level corresponding to the mixture of $S = 1/2$ and

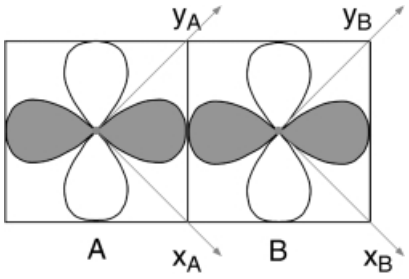

Fig. 5. $(xy)_A \rightarrow (xy)_B$ overlap in the edge-shared D_{2h} system. The molecular frame XYZ coincides with the local ones

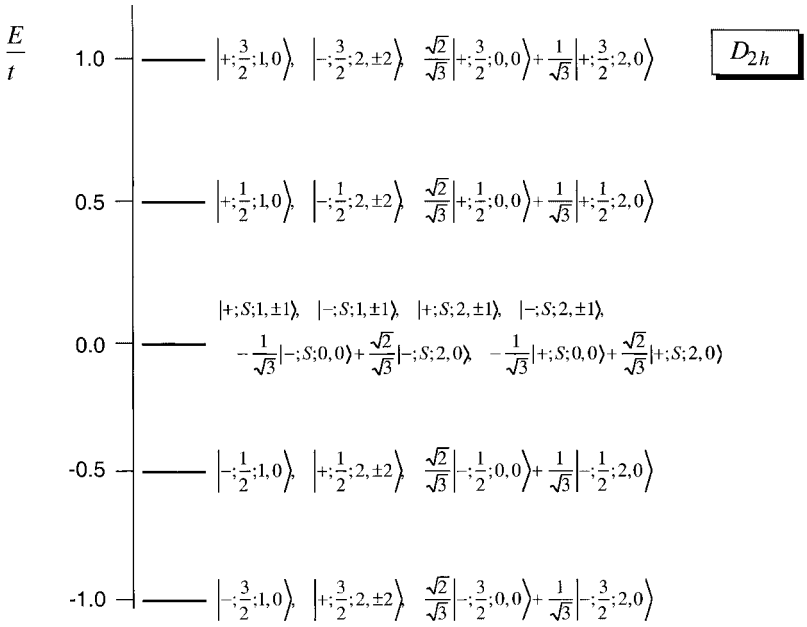

Fig. 6. Energy diagram for an edge-shared binuclear d^1–d^2 MV dimer

$S = 3/2$. 2) As distinguished from the case of spin-systems (nondegenerate ions), the degeneracy of metal sites brings a magnetic anisotropy of orbital nature to the whole system. In fact, the ground state $|3/2; 2 \pm 2\rangle$ has a strong orbital magnetic contribution when the field is applied along the Z axis and proves to be nonmagnetic when it is applied in the perpendicular directions (along X or Y). The system is fully anisotropic in the sense that $\chi_{\parallel}$ comes from a first order contribution whereas $\chi_{\perp}$ comes from a second order contribution (van Vleck paramagnetism). Through this example we can see that for degeneracy the double exchange can be referred to as an anisotropic magnetic interaction (for this reason we have proposed the term *anisotropic* double exchange [17]). More precise consideration shows that both the double-exchange splittings and the sign of anisotropy, $\chi_{\parallel} - \chi_{\perp}$, are specific for each kind of MV pair, being closely related to the ground terms (singlet–triplet, triplet–triplet) of the constituent ions, overall symmetry, and transfer pathways. In particular, a corner-shared (D_{4h}) dimer has orbital van Vleck paramagnetism and the sign of the magnetic anisotropy is opposite ($\chi_{\perp} > \chi_{\parallel}$).

5.4.2 Vibronic Interactions in Dimers

The background for the consideration of vibronic effects in MV systems is represented by the PKS model [5]. Being very efficient and, at the same time, relatively simple, the PKS model takes into account the most important features of the phenomenon without consideration of details.

During ten years the PKS model remained the only theoretical tool for consideration of vibronic effects in MV compounds. Later Piepho [6,7] suggested a new vibronic model. In this section we consider both models in the dimeric systems and the magnetic manifestations of vibronic coupling.

5.4.2.1 PKS Model

The main idea of PKS model can be illustrated taking as an example two coupled octahedral centers containing a unique unpaired electron (d^1–d^0 system). Denoting their full-symmetric vibrational coordinates as q_A and q_B (*breathing* modes), two new collective coordinates can be constructed which refer to the *in-phase* (q_+) and *out-of-phase* (q_-) vibrations of the two moieties

$$q_+ = (1/\sqrt{2})(q_A + q_B), \quad q_- = (1/\sqrt{2})(q_A - q_B) \equiv q$$

Nuclear displacements corresponding to the q_+ vibration (the two coordination spheres are expanded or compressed simultaneously) decrease or increase the potential energy of the system independently of the site of localization. Interaction of the moving electron with this in-phase vibration can be eliminated by shifting in the q_+ space. That means that only the reference size of the dimer is modified by the extra electron. In contrast, the out-of-phase vibration, q_-, proves to be a mode relevant to the electron-transfer processes. Thus, when $q < 0$ the coordination sphere on A is compressed whereas that on B is expanded. It should be noted that the intercenter distance R_{AB} remains constant in course of nuclear motion. This nuclear movement increases the energy of the electron located on A, thus promoting the electron transfer A $\rightarrow$ B (Fig. 7). In a similar way the opposite phase ($q > 0$) promotes the jumping back of the extra electron (B $\rightarrow$ A transfer).

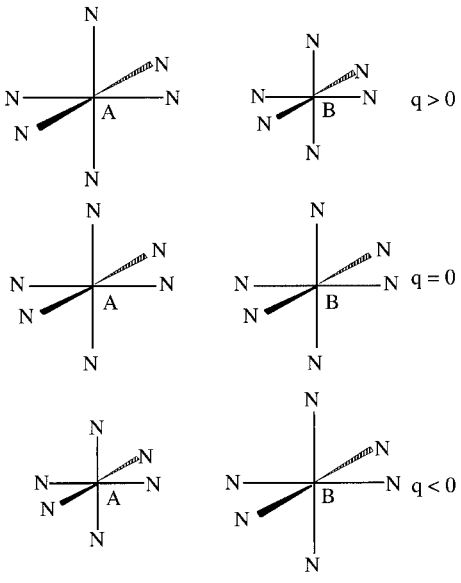

Fig. 7. Pictorial representation of the out-of-phase vibrational mode for two octahedral moieties

In the semiclassical adiabatic approximation (very slow nuclear motion), the full energy of the system can be associated with the potential energy only. Such energy includes the nuclear potential energy $\omega q^2/2$ (ω is the vibrational frequency, q is the dimensionless normal coordinate, $\hbar = 1$) and the mean value of the vibronic interaction energy $E(q)$.

To find $E(q)$ we should know that the vibronic interaction mixes two states of opposite parity (ψ_g and ψ_u). Taking into account also the transfer energy, we find the full adiabatic Hamiltonian for the d^1–d^0 problem in the matrix form as follows:

$$\frac{\omega}{2}q^2\mathbf{I} + \begin{array}{c} \begin{array}{cc} \psi_u & \psi_g \end{array} \\ \left| \begin{array}{cc} -t & \upsilon q \\ \upsilon q & t \end{array} \right| \end{array} \tag{15}$$

where υ is the vibronic coupling parameter and $\mathbf{I}$ is $[2 \times 2]$ unit matrix in the basis ψ_g and ψ_u. The full energy in the adiabatic approximation can be finally expressed as an adiabatic potential $U(q)$:

$$U_{\pm}(q) = \frac{\omega}{2}q^2 \pm \sqrt{t^2 + \upsilon^2 q^2} \tag{16}$$

Let us discuss briefly the shape of the adiabatic potential in view of the Robin and Day scheme that classifies MV compounds according to the degree of delocalization of the extra electron over the metal sites. The original form of this classification, proposed in 1967 [18], was based on the parameter W which is the difference in energy between the two localized configurations, A*B and AB*, in an unsymmetric MV dimer (Section 5.4.1.3). Piepho, Krausz, and Schatz [19] later realized to its full extent the crucial role of the vibronic interaction in the description of MV compounds in connection with the problem of localization–delocalization, especially for the spectroscopic manifestations of the mixed valence. In the symmetric MV dimers (equivalent sites, $W = 0$) the vibronic coupling proves to be the only physical interaction that is able to localize the *extra* electron (like W-energy in an unsymmetric system).

The adiabatic potential (Eq. 16) comprises two branches U_+ and U_-. If there is no electron interaction between the A and B sites, we obtain two independent potential energy curves associated with the A*B and AB* configurations (Fig. 8a). In this case, the electron transfer is not allowed ($t = 0$) and the system will be fully localized (Class I in Robin and Day classification) [5]. When the vibronic interaction is strong compared with the electron interaction ($\upsilon^2/\omega > |t|$), we obtain a double well potential curve $U_-(q)$ and an energy barrier with the top at $q = 0$ increasing as the vibronic interaction increases (Fig. 8b). The electron transfer process is then possible but requires an activation energy for the electron hopping or can occur as the tunneling through the barrier (Class II systems). Finally, in the case of weak vibronic interaction ($\upsilon^2/\omega < |t|$) both branches have a minimum at $q = 0$ (Fig. 8c) and the electron is fully delocalized. In this case the system belongs to Class III in Robin and Day classification. Therefore, the vibronic interaction plays a role of a localizing factor being in competition with the transfer processes which promote delocalization. The main spectroscopic consequence of the combined action of electron transfer and vibronic interaction is the occurrence of the so-called electron transfer optical

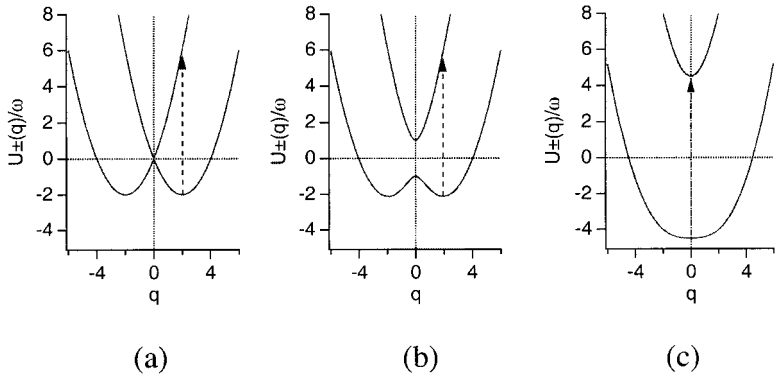

Fig. 8. The adiabatic potential for a one-electron MV dimer: (a) $t = 0$, $\upsilon = 2\omega$, (b) $t = \omega$, $\upsilon = 2\omega$, (c) $t = 4.5\omega$, $\upsilon = 2\omega$. Franck–Condon considerations are indicated by dotted arrows

absorption (intervalence band) arising from $U_-(q) \rightarrow U_+(q)$ transitions (dotted lines in Fig. 8)

The shape and intensity of the intervalence band in the PKS model is defined by the ratio $|t|/\upsilon^2/\omega$. In weak transfer (Fig. 8a) the vertical (Franck–Condon) transitions are almost forbidden since the matrix element of the dipole moment $\langle\varphi_A|d|\varphi_B\rangle$ vanishes due to the parity rule; at the same time, the Stokes shift can be significant. For these reasons the MV dimers of Class I are expected to exhibit weak and wide intervalence bands. On the contrary, in the Class III compounds (Fig. 8c) the Franck–Condon transition is allowed (the matrix element $\langle\psi_u|d|\psi_g\rangle \neq 0$) and the Stokes shift is zero. For this reason intervalence optical bands in delocalized MV dimers are strong and narrow.

5.4.2.2 Piepho Model

Piepho suggested a vibronic model [6,7] that takes into account multicenter vibrations (P-vibrations) that allow metal–metal distances to change. The electron–vibrational coupling appears as a result of the modulation of the transfer integral due to changes in the intermetallic distances $R \equiv R_{AB}$ (Fig. 9). $Q = (R - R_0)$ plays the role of the vibrational coordinate. As distinguished from the PKS model, the interacting moieties maintain their sizes in course of vibration.

The transfer integral can be expanded in the series:

$$t(R) = t(R - R_0) + \left(\frac{\partial t(R)}{\partial R}\right)_{R=R_0} (R - R_0) + \cdots \tag{17}$$

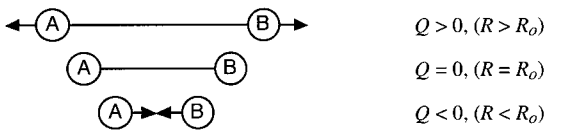

Fig. 9. Pictorial representation of the P-vibration for a MV dimer

where $\lambda = -(\partial t(R)/\partial R)_{R=R_0}$, is the vibronic interaction parameter, and $t(R = R_0)$ is just the transfer parameter. The matrix of the adiabatic potential in the delocalized MO-basis, ψ_u and ψ_g, can be presented as:

$$U = \frac{\Omega Q^2}{2} \begin{vmatrix} t - \lambda Q & 0 \\ 0 & -t + \lambda Q \end{vmatrix} \tag{18}$$

where Ω is the vibrational frequency and Q is now the dimensionless vibrational coordinate $Q = (R - R_0)/(\hbar/M\Omega)^{1/2}$; $\lambda = (\partial t(R)/\partial R)_{R=R_0}(\hbar/M\Omega)^{1/2}$ is the vibronic coupling parameter (M is the effective mass associated with the P-vibration).

The adiabatic potential has two branches:

$$U_{\pm} = \frac{\Omega^2}{2}(Q \mp Q_0)^2 \pm t - \frac{\lambda^2}{2\Omega} \tag{19}$$

as shown in Fig. 10. Both states (with the initial energies $+t$ and $-t$) are stabilized by the term $-\lambda^2/(2\Omega)$ and minima at $\pm Q_0$ ($Q_0 = \lambda/\Omega$) appear that correspond to two delocalized states ψ_u and ψ_g.

In the bonding state, ψ_g, the transfer is effectively increased $2|t(R_0 - Q_0)| = 2|t| + 2\lambda^2/\Omega$, meanwhile in the antibonding state, ψ_u, the transfer is decreased $2|t(R_0 + Q_0)| = 2|t| - 2\lambda^2/\Omega$. One can see that the main effect of the P-vibration is to produce a strong detrapping effect, i. e. to stabilize delocalized states. This effect is in a sharp contrast to that produced by the PKS-vibrations that localize the extra electron on the sites.

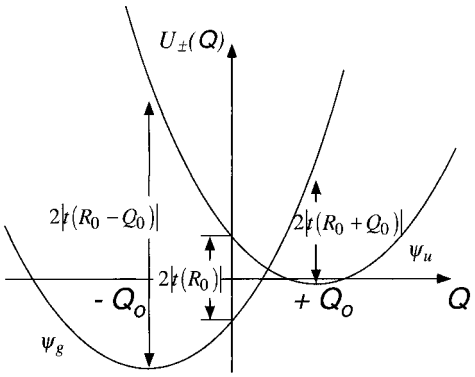

Fig. 10. Adiabatic potential of the d^1–d^0 system in the Q-space for ($t < 0$)

5.4.2.3 Localization vs Delocalization in the Generalized Vibronic Model [20]

Because PKS and P-vibrations lead to competitive effects, we consider now the generalized vibronic model that takes simultaneously into account both types of vibronic interactions. From Eqs. (16) and (18) one can find the following expression for the adiabatic surface of the d^1–d^0 system in the qQ-space:

$$U_{\pm}(q, Q) = 1/2(\omega q^2 + \Omega Q^2) \pm \sqrt{(t - \lambda Q) + \upsilon^2 q^2} \tag{20}$$

where the signs "−" and "+" relate to the lower and upper branches, respectively.

Because the physical results are independent of the sign of the parameters, for the sake of simplicity, we assume that υ and λ are both positive. Depending on the relative values of the key parameters, several qualitatively different types of adiabatic surfaces should be distinguished. The lower sheets of these surfaces are shown in Fig. 20.

5.4.2.3.1 Case 1 – PKS-coupling Exceeds P-coupling ($\upsilon^2/\omega > \lambda^2/\Omega$)
In this case, depending on the value of the transfer parameters, there are two physically different situations: **1a**, *comparatively weak transfer*, $|t| < \upsilon^2/\omega - \lambda^2/\Omega$, and **1b**, *comparatively strong transfer*, $|t| \geq \upsilon^2/\omega - \lambda^2/\Omega$.

In **1a** the lower sheet, $U_-(q, Q)$, has two equivalent minima that are symmetric in the q-subspace (Fig. 11a,b). The minima are separated by two saddles when $|t| < \lambda^2/\Omega$ (Fig. 11a), or by one saddle when $|t| > \lambda^2/\Omega$ (Fig. 11b). Calculations of the degrees of localization, ρ_A and ρ_B, in the adiabatic approximation show that P-vibration decreases ρ_A and ρ_B when compared with PKS-vibration lowering, at the same time, the barrier separating the minima. When the transfer is increased, the two minima move toward the deeper saddle point, while the barrier between the minima decreases and the system becomes more and more delocalized. In this way, we arrive to the situation **1b** (Fig. 11c), wherein the system is fully delocalized so that U_- presents a single minimum.

5.4.2.3.2 Case 1 – P-coupling Exceeds PKS-coupling ($\upsilon^2/\omega < \lambda^2/\Omega$)
As in the previous case, two different situations should be considered, namely **2a**, *weak transfer*: $|t| < \lambda^2/\Omega - \upsilon^2/\omega$, and **2b**, *strong transfer*: $|t| \geq \lambda^2/\Omega - \upsilon^2/\omega$.

Providing weak transfer, the adiabatic surface $U_-(q, Q)$ has two minima with different energies. These minima are then in the same positions where the saddle points were in the previous case (Figs. 11d,e). The adiabatic wave-functions in the minima points are ψ_g (deepest minimum) and ψ_u (shallow minimum) so that, under the condition of the relatively strong P-coupling and weak transfer (case **2a**), the system proves to be always fully delocalized. The localized states correspond now to the saddle points and so they are unstable. Increase of $|t|$ leads to the transformation of the adiabatic surface in such a way that the saddle points move toward the shallow minimum until it disappears when the transfer is strong enough (case **2b**) (Figs. 11d–f). It should be stressed that, independently of the key parameters defining the position of the minima and that of the saddle points (as well as the heights of the barriers), the system remains fully delocalized in the case **2**.

Let us consider now the Robin and Day classification scheme from the point of view of the generalized vibronic model. In the case **1** ($\upsilon^2/\omega > \lambda^2/\Omega$), depending on the magnitude of the electron transfer parameter, MV compounds can belong to Classes I, II or III. So, when $|t| \ll \upsilon^2/\omega - \lambda^2/\Omega$ the system is strongly localized and belongs to Class I. For $|t| < \upsilon^2/\omega - \lambda^2/\Omega$, the system can be assigned to Class II. Finally, for $|t| \geq \upsilon^2/\omega - \lambda^2/\Omega$ we arrive at the fully delocalized system (Class III). These conditions are formally similar to those describe in the PKS-model (Section 5.4.2.1). However, there is an essential difference between these two criteria: in the generalized model, instead of pure PKS vibronic contribution υ^2/ω, we are dealing with the combined parameter $\upsilon^2/\omega - \lambda^2/\Omega$. Hence, the vibronic localiza-

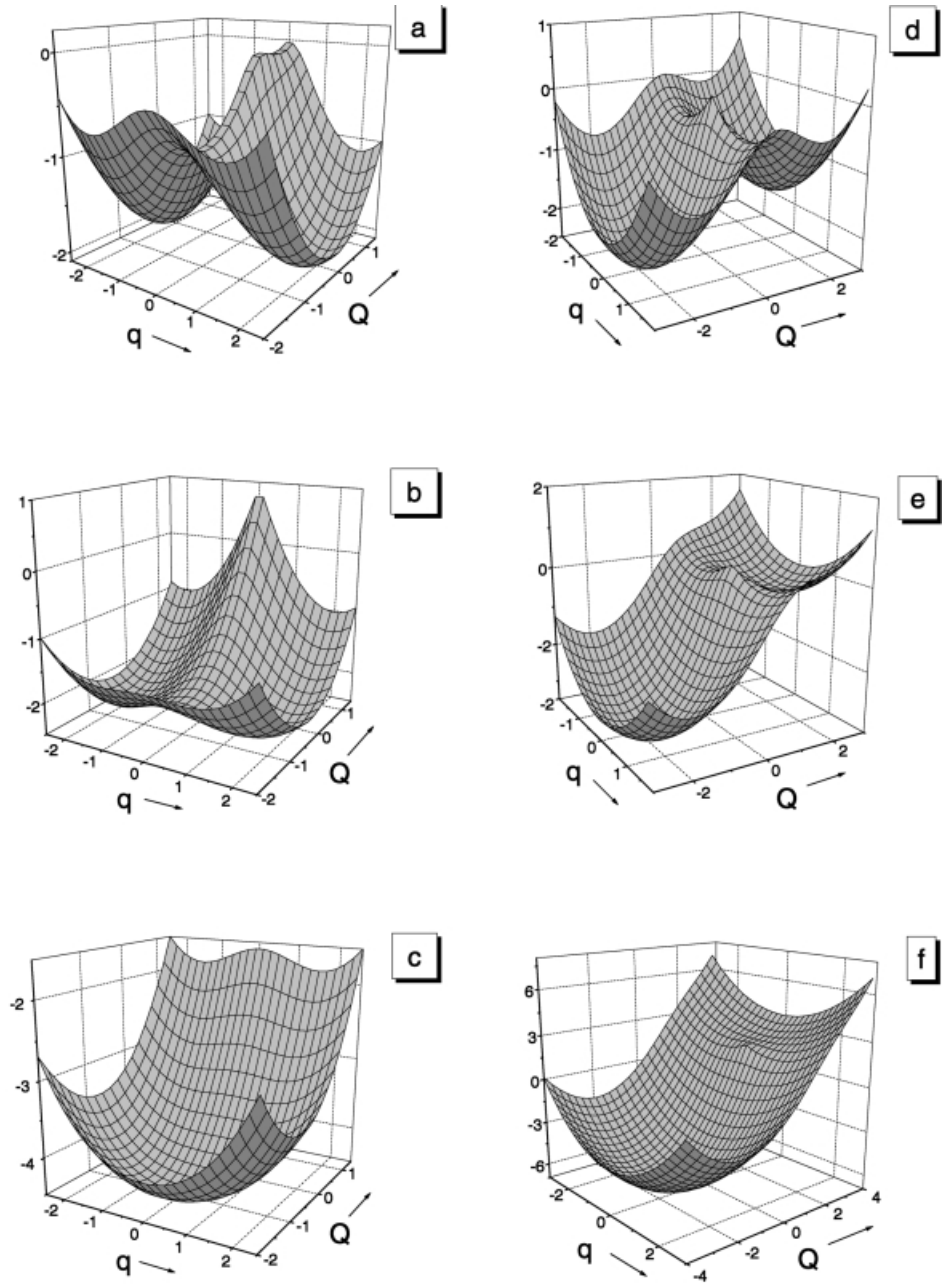

Fig. 11. The lower sheet $U_{-}(q, Q)$ of the adiabatic potential for the d^1–d^0 dimer ($\omega = \Omega$): a) $|t| = 0.4\omega$, $\upsilon = 2\omega$, $\lambda = \omega$; b) $|t| = 1.5\omega$, $\upsilon = 2\omega$, $\lambda = \omega$; c) $|t| = 4\omega$, $\upsilon = 2\omega$, $\lambda = \omega$; d) $|t| = 0.4\omega$, $\upsilon = \omega$, $\lambda = 2\omega$; e) $|t| = 1.5\omega$, $\upsilon = \omega$, $\lambda = 2\omega$; f) $|t| = 4\omega$, $\upsilon = \omega$, $\lambda = 2\omega$

tion effect is reduced because the P-coupling promotes delocalization. In fact, the tunneling of the system between the two minima is expected to occur through the saddle point (that is shifted along Q) rather than along the q axis, where the barrier is higher (Figs. 11a,b). This can be illustrated by the contour plot of the adiabatic surface represented in Fig. 12. Two vertical sections of the adiabatic potential are shown also: one along the q axis that crosses the minima point, and the other along Q. The most efficient way of tunneling or thermally activated transition is through the saddle point (this transfer pathway is indicated in Fig. 12a). So, the MV system can belong to Classes II or III, even providing weak electron transfer (or strong PKS coupling). On the other hand, strong localization (Class I) is achieved only for weak transfer and/or weak P-coupling.

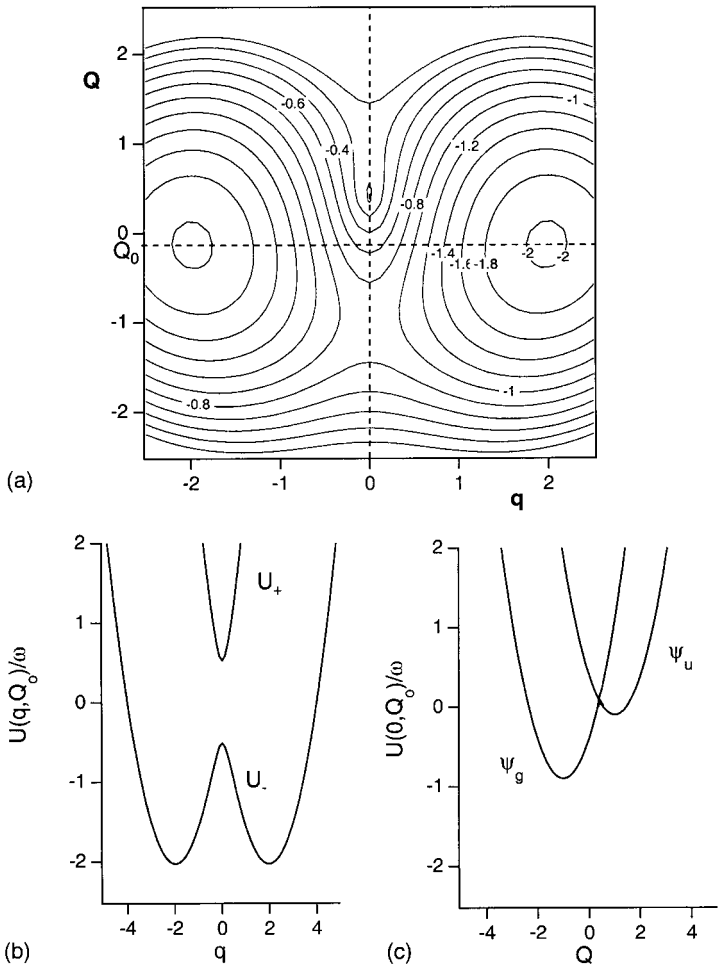

Fig. 12. Contour plot of the lower sheet of the adiabatic surface $U_{-}(q, Q)$ (a). Two vertical sections: along q (b) and along Q (c); $|t| = 0.4\omega$, $\upsilon = 2\omega$, $\lambda = \omega$

Let us pass now to the case **2**, $\upsilon^2/\omega < \lambda^2/\Omega$. As was shown above, within this case the system is fully delocalized independently of the relative values of $|t|$ and υ^2/ω. This means that a system with dominating P-interaction always belongs to Class III, even providing very small $|t|$. This result is in striking contradiction with the prediction of the PKS model in which the degree of the delocalization in the symmetric MV dimers is determined only by the interplay between the electron transfer and the PKS vibronic coupling. Fig. 13 illustrates a contour plot (a) and two sections of the adiabatic potential (b) and (c) in the case of strong P-coupling

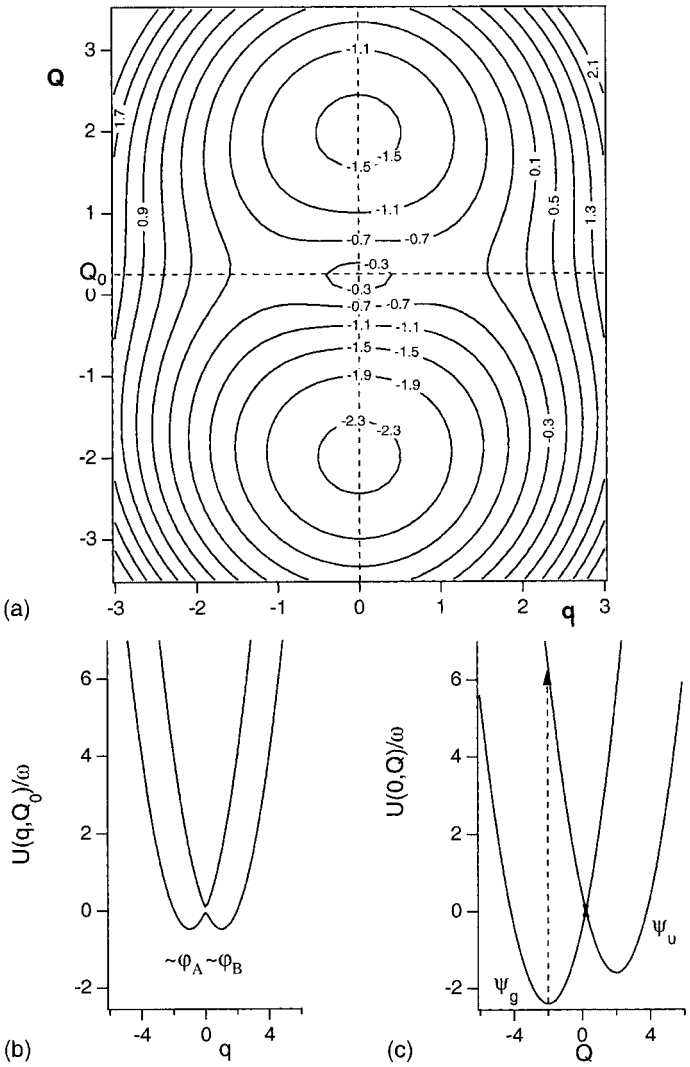

Fig. 13. Contour plot of the lower sheet of the adiabatic surface $U_{-}(q, Q)$ (a). Two vertical sections: along q, (b), and along Q, (c); $|t| = 0.4\omega$, $\upsilon = 2\omega$, $\lambda = 2\omega$

(Fig. 11d). Fig. 13b shows that, within the PKS model, the system can be referred as belonging to Class I or II, since it shows two minima. However, as a matter of fact, these minima are saddle points in the two-dimensional Q–q space and the true minima (Fig. 13c) correspond to delocalized states (Class III).

In view of these curves, the correlation between degree of localization and parameters of the intervalence bands (width, position and intensity) established in the PKS model is to be reconsidered. Particularly, in the contrast to the conclusion based on the PKS model, a fully delocalized system (Class III) can now exhibit a strong and broad (instead of narrow) intervalence band, if the P-coupling is dominant. In fact, as it is clear from Fig. 12b, the Franck–Condon transition is intense (allowed $\psi_u \rightarrow \psi_g$ transition) and the band has a large Stokes shift, $2Q_0$, giving rise to a broad band.

5.4.2.4 Magnetic Manifestations of the Vibronic Coupling

Let us return to the MV dimeric clusters with magnetic cores, starting with the case of PKS model. In the general case d^n–d^{n+1} we find an independent vibronic problem for each full spin-value of the system, S, of the system with the effective spin-dependent transfer parameter $t(S) = t(S + 1/2)/(2S_0 + 1)$. So the adiabatic potentials are now:

$$U_{\pm}^{(S)}(q) = -JS(S+1) + \frac{\omega}{2}q^2 \pm \sqrt{t^2\frac{(S+1/2)^2}{(2S_0+1)} + \upsilon^2 q^2} \tag{21}$$

Because t increases with the increase of S, the condition for localization will be more favorable for the states with the lower spin values, whereas delocalization will be favored for the high-spin states.

The main consequence of the vibronic interaction in these dimers can be illustrated taking as an example the d^1–d^2 system and neglecting isotropic exchange. Fig. 14 shows the variation of the potential curves of the system with the increase of vibronic interaction. The vibronic interaction clearly gives an antiferromagnetic contribution to the adiabatic energy pattern due to the preference in stabilizing more the $S = 1/2$ levels in the region of moderate vibronic coupling. Providing strong vibronic coupling the wells of the adiabatic potential are very deep and the barriers separating these wells are very high constraining the tunneling between the two localized states. The electron proves to be strongly trapped into one of the two wells wherein the $S = 1/2$ and $S = 3/2$ energies coincide (encircled in Fig. 14) giving thus a paramagnetic mixture of the initial $S_A = 1/2$, $S_B = 1$ and $S_A = 1$, $S_B = 1/2$ states. In the strong coupling limit the ferromagnetic effect of the double-exchange is therefore eliminated in the ground manifold, whereas the excited states are very high in energy and can not be populated at reasonable temperatures. This really means that the double-exchange effect is reduced by the vibronic coupling and the system will exhibit the magnetic behavior specific for the valence-localized d^1–d^2 system.

If the isotropic (Heisenberg-type) exchange is then included this is the only interaction effectively operating. Indeed, in the strong vibronic coupling limit, the Heisenberg scheme of levels proves to be restored (in this limit, the minima of the

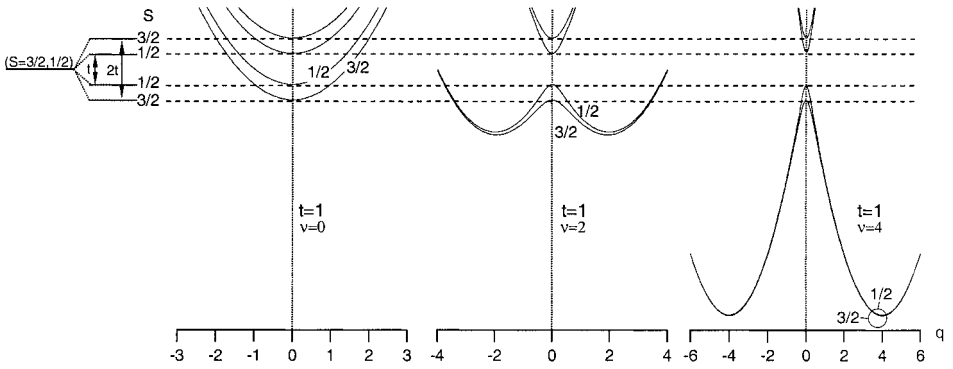

Fig. 14. Vibronic localization in the d^1–d^2 MV dimer (t and υ in $\hbar\omega$ units)

lower sheets of the adiabatic potential corresponding to the two different spin states will be separated by an energy gap of $3|J|$, the same as for the Heisenberg exchange splitting). This result is general and valid for all d^n–d^{n+1} dimers. We should mention that the restoration of the Heisenberg-type energy pattern can be achieved *only* in the limit of strong vibronic interaction. In this limit *the Heisenberg Hamiltonian can be used again to find the energies of the low-lying levels*.

In the case of intermediate vibronic coupling, the energy levels can be obtained by numerical diagonalization of the vibronic matrix for each pair of states (even and odd) belonging to a specific spin-value. Fig. 15a shows the temperature dependence of the magnetic moment for a MV d^3–d^4 dimer with strong double-exchange and AF exchange. It illustrates the effect of suppression of the double-exchange by the presence of a vibronic coupling. We observe that for relatively weak vibronic coupling ($\upsilon = 2.0$ and 2.6 in $\hbar\omega$ units) the system is ferromagnetic ($S_{gr} = 7/2$) since double-exchange dominates over AF exchange and vibronic coupling, while for $\upsilon = 3.0$ the system is antiferromagnetic ($S_{gr} = 1/2$) due to the antiferromagnetic exchange interaction. What is surprising in this behavior is that the ground spin state of the system passes directly from $S_{\max}$ to $S_{\min}$ but not through the intermediate spin states 3/2 and 5/2, when the vibronic coupling increases. This example shows that *the effective reduction of the double-exchange due to the vibronic coupling cannot be simply represented as an effective decrease in the transfer parameter*. In terms of the static correlation diagram (Fig. 15b) one can imagine that, passing from the right side (strong double-exchange) to the left side (weak double-exchange), we miss the domain of $S_{gr} = 5/2$ and $3/2$.

Let us now discuss the magnetic manifestations of the P-coupling. As it follows from the definition of the P-coupling parameter (Eq. 17), λ, for multielectron ions λ proves to be spin dependent and has the same spin-dependence as the double-exchange parameter, t:

$$\lambda(S) = [\lambda/(2S_0 + 1)](S + 1/2) \tag{22}$$

so that the adiabatic potentials are now:

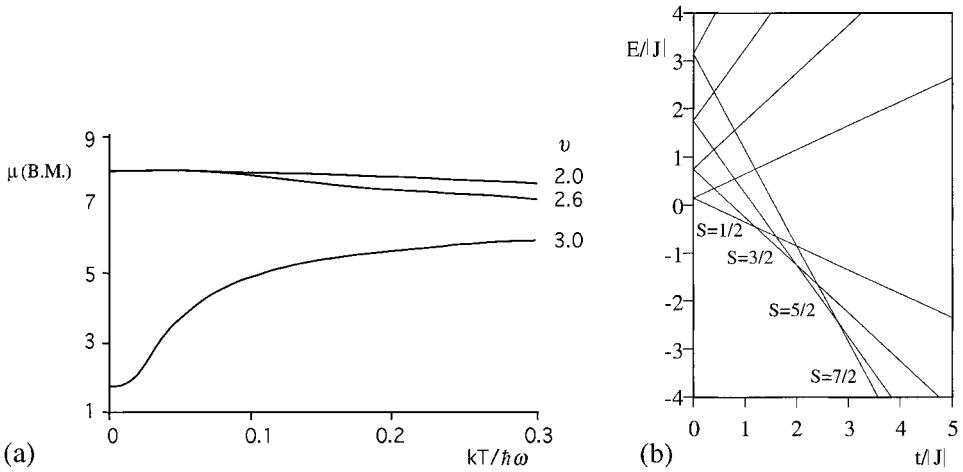

Fig. 15. (a) Magnetic behavior of a d^3–d^4 MV dimer ($t/\omega = 3.5$) and Heisenberg exchange ($J/\omega = -0.2$). Effect of the vibronic coupling. (b) Correlation energy diagram of the d^3–d^4 dimer in presence of double-exchange

$$U_{\pm}^{(S)}(Q) = -JS(S+1) \pm \frac{t}{2S_0+1}(S+1/2) + \frac{\Omega}{2}(Q \mp Q_S^0)^2 - \frac{\lambda^2(S+1/2)^2}{2\Omega(2S_0+1)^2} \tag{23}$$

where the positions of the minima $\mp Q_S^0 = \pm\lambda(S)/\Omega$ and the energies of stabilization, the last term in Eq. (23), are spin-dependent (Fig. 16).

For strong P-coupling the energy levels of the system can be roughly identified with the energies $U_{\min}(S)$ of the minima of the adiabatic potentials, where the system spends the most part of the time. Substituting the positions of the minima $\mp Q_S^0$ in $U^{(S)}(Q)$, one find the energies of minima:

$$U_{\min}^{(S)}(Q) = -J_{\text{eff}}S(S+1) \mp t\frac{S+1/2}{2S_0+1} \tag{24}$$

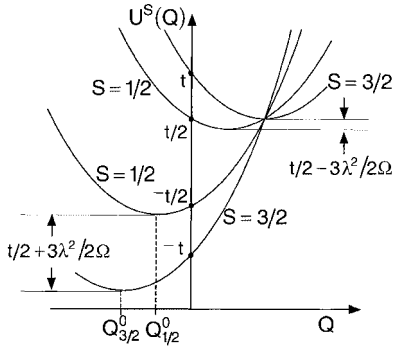

Fig. 16. Adiabatic potentials of d^1–d^2 MV dimer in the Piepho model ($J = 0$)

The energy pattern of the minima (Eq. 24) is formally similar to that produced by the combined action of the isotropic exchange and double-exchange (Eq. 13). The essential difference is that now we are dealing with the effective exchange parameter:

$$J_{\text{eff}} = J + \lambda^2/2\Omega \tag{25}$$

containing strong ferromagnetic contribution $\lambda^2/2\Omega$. Figure 16 shows that this ferromagnetic contribution increases the gap between the low-lying levels (with the initial energies $-t$ and $-t/2$) and decreases the gap between excited levels (t, $t/2$).

Figure 17a illustrates the magnetic effect of P-vibronic coupling for the simplest d^1–d^2 MV dimer ($S_0 = 1/2$, $S = 1/2, 3/2$) in the case of relatively small double-exchange (compared with the antiferromagnetic isotropic exchange $t < 6|J|$). When $\lambda = 0$, the competition between the isotropic exchange and the double-exchange gives the antiferromagnetic ($S_{gr} = 1/2$) ground state. As λ is increased the magnetic moments increase, so that the double-exchange proves to be effectively enhanced. Providing $\lambda/\omega = 2$, the ground state remains antiferromagnetic while for $\lambda/\omega = 3$ it changes to ferromagnetic ($S_{gr} = 2$).

Figure 17b illustrates the combined effect of the two types of vibronic coupling (P and PKS) in the case of relatively strong double-exchange ($|t| = 10|J|$). In absence of any vibronic coupling ($\upsilon = 0$, $\lambda = 0$), the ground spin state is ferromagnetic due to the double-exchange. Inclusion of the PKS interaction ($\upsilon/\omega = 2$) reduces the magnetic moment and gives $S_{gr} = 1/2$. When the P-coupling is considered it competes with the PKS coupling so that for $\lambda/\upsilon \geq 1$ the ferromagnetic $S = 3/2$ state becomes the ground state. This conclusion is also in agreement with the fact that a delocalization of the extra electron produces a ferromagnetic effect due to the polarization of the spin cores. In this sense, double-exchange and vibronic P-coupling produce similar effects.

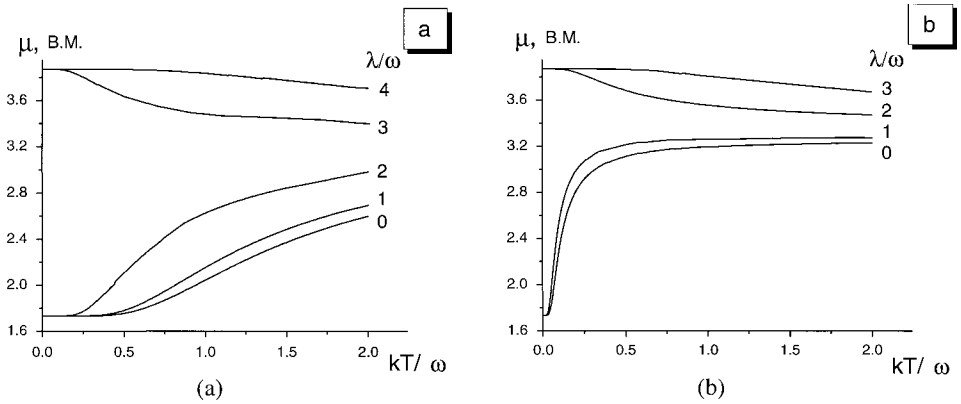

Fig. 17. Magnetic moments of d^1–d^2 MV dimer. Effect of the P-coupling: (a) $|t|/\omega = 0.5$, $J/\omega = -1$, $\upsilon/\omega = 0$; (b) $|t|/\omega = 1$, $J/\omega = 0.1$, $\upsilon/\omega = 2$

5.4.3 Examples

A lot of examples of MV dimers are known in inorganic chemistry but the observation in these of ferromagnetic ground spin states due to electron delocalization is still unusual. Often the vibronic coupling (dominated by the PKS-mode) leads to a valence trapping that strongly reduces the double-exchange effect compared to the antiferromagnetic exchange effect. Let us mention two representative examples in which double-exchange is the dominant effect.

The first one concerns the fully delocalized $Fe^{II}Fe^{III}$ dimer $[L_2Fe_2(\mu\text{-}OH)_3](ClO_4)_2 \cdot 2CH_3OH \cdot 2H_2O$, where L is the tridentate ligand *N*,*N*′,*N*″-trimethyl-1,4,7-triazacyclononane, isolated by the Wieghardt's group (Fig. 18) [21,22]. This compound has an $S = 9/2$ ground spin state resulting from the ferromagnetic coupling between $S_{Fe(II)} = 2$ and $S_{Fe(III)} = 5/2$ local spins. A strong intervalence band is observed at $13\,200\,cm^{-1}$ which should correspond to the gap between the two $S = 9/2$ spin states (of different parity). Since this gap is equal to $2t$ (Fig. 2), an absolute value for the double-exchange parameter of $6600\,cm^{-1}$ may be estimated, as well as an energy gap as large as $1300\,cm^{-1}$ between the ground state, $S = 9/2$, and the first excited state $S = 7/2$. This gap may be reduced by the antiferromagnetic interaction but, in any case, it is to be larger than $300\,cm^{-1}$, since up to room temperature, the $S = 9/2$ state is the only thermally populated.

The second example concerns the fully delocalized $Ni^{I}Ni^{II}$ dimer $[Ni_2(napy)_4Br_2](BPh_4)$, where napy is the bidentate ligand naphthyridine, reported by Gatteschi et al. [23] (Fig. 19). In this compound the two nickel atoms have identical square pyramidal surroundings with the apical positions occupied by Br^- ions and a short

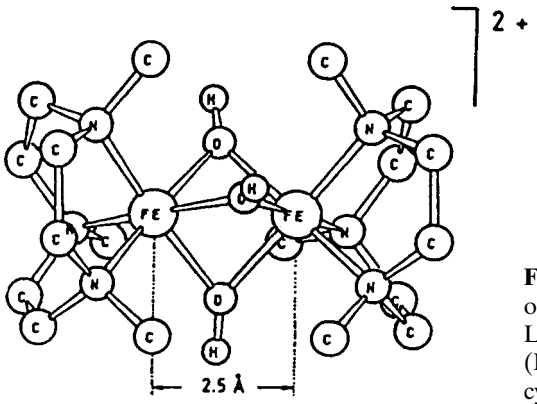

Fig. 18. Schematic structure of the MV iron dimer $L_2Fe_2(\mu\text{-}OH)_3](ClO_4)_2.2CH_3OH.2H_2O$ (L = *N*,*N*′,*N*″-trimethyl-1,4,7-triazacyclononane)

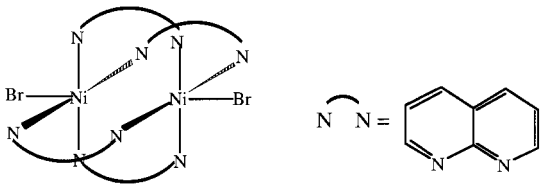

Fig. 19. Schematic structure of the MV nickel dimer $[Ni_2(napy)_4Br_2]^+$ (napy = naphthyridine)

Ni–Ni distance of 2.41 Å which favors a large transfer integral between the two metal orbitals containing the moving electron (of z^2-type). In fact, the ferromagnetic $S = 3/2$ state resulting from the coupling between $S_{Ni(I)} = 1/2$ and $S_{Ni(III)} = 1$ local spins, has been found to be the ground state. Moreover, only this state is thermally populated up to room temperature indicating a large energy gap between this ground state and the antiferromagnetic one $S = 1/2$.

5.5 Mixed Valence Trimers

5.5.1 Electronic Interactions

The effects of the electron delocalization in MV systems with nuclearities >2 are, in several aspects, different from those found in the MV dimers. In trimers the most clear differences are seen in the energy splittings caused by double-exchange, and in the appearance of other electronic processes, as for example the presence of three-site interactions (exchange–transfer).

5.5.1.1 Double-exchange [24–26]

As distinguished from the dimeric systems, in trimers (and in higher nuclearities systems) the sign of transfer integral t is of crucial importance for the energy pattern and character of the vibronic coupling. Fig. 20 shows two possible overlaps of the localized orbitals implying negative (a) and positive (b) sign for t.

In a triangular cluster with a unique unpaired electron in the spin core of each site and one extra electron fully delocalized over the three sites (d^1–d^1–d^2 system),

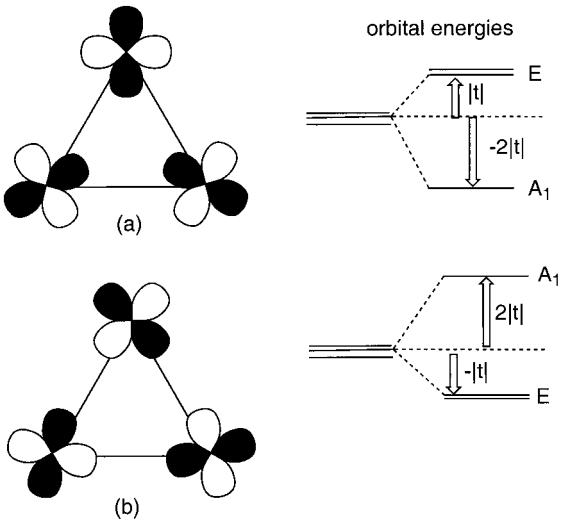

Fig. 20. Illustration for different signs of the transfer integrals in a MV trimer

one observes that double-exchange leads to an unsymmetric splitting of the spin levels with respect to the sign reversal of t (Fig. 21a). Thus, for positive t the ground state is accidentally degenerate being formed by an admixture of states with spin values comprised between $S_{min} = 0$ and $S_{max} = 2$, while the most excited state is the ferromagnetic one. For negative t the spectrum is reversed and the ferromagnetic spin state becomes the ground state. This unexpected result is in clear contradiction with the simple idea that *double-exchange always leads to a strong stabilization of the ferromagnetic state*. It calls for the following two important remarks:

1. The degenerate ground state found in these MV systems is probably the most clear illustration of the concept of *spin frustration* in molecular magnetism. It emphasizes that in a cluster not only the presence of competing magnetic interactions can lead to an accidentally degenerate ground state. Double-exchange can also do that. In this respect, double-exchange is expected to be much more efficient than the magnetic exchange interactions since it can lead to a fully degenerate ground state formed by an extensive mixture of spin-states, independently of the magnitude of t, whereas, in case of magnetic interactions, the frustrated state arises only if these antiferromagnetic interactions have the right relative magnitude. We have proposed to coin this effect as *transfer frustration* [24]. In such situations other electronic effects of smaller magnitude (as for example the magnetic exchange interactions, local spin-anisotropies, or exchange–transfers [25–27]) will determine the nature of the ground state of the cluster as well as the structure of the low-lying levels.

2. The unsymmetric splitting of the spin-states is a characteristic feature of the triangular geometry. For a different topology, as for example for a linear trimer, the double-exchange splitting is symmetrical, as for a dimer, and results in the stabilization of the ferromagnetic spin state, irrespective of the sign of t (Fig. 21b). However, in a linear trimer the magnetic exchange is expected to be the leading parameter since for this topology the local symmetry of the central site is different from that of the terminal sites, and therefore the electron must be trapped, reducing thus the double-exchange effect.

The above features are also observed in the general case d^n–d^n–d^{n+1} containing high-spin metal sites with single occupied d-orbitals ($n \leq 4$) and one extra electron (*electron-type clusters*) and also in triangular clusters of the type (d^{n+1}–d^{n+1}–d^n) containing high-spin metal sites with single occupied d-orbitals and one extra hole (*hole-type clusters*). One can notice however two significant peculiarities in the energy levels of these clusters: 1) The ferromagnetic spin state becomes the ground state when t is positive (while for the electron-type clusters that occurs for negative t values); 2) the accidentally degenerate level does not contain the state with $S = S_{max}$ that has a slightly different energy value. These features are exemplified by the d^2–d^2–d^1 system (Fig. 21c).

For electron-type clusters containing double occupied d-orbitals ($n > 4$) the energy spectra are identical to those derived for hole-type clusters with $n \leq 4$ and the same spin values, but reversed in energy. The same holds for hole-type clusters. Thus, the energy spectrum for the d^5–d^5–d^6 triangle (an electron-type cluster with $S_A = S_B = 5/2$ and $S_C = 2$) is identical to that obtained for the d^5–d^5–d^4 triangle (a hole-type cluster), but reversed (Fig. 22). The same holds for d^6–d^6–d^5 and d^4–d^4–d^5 systems (Fig. 23).

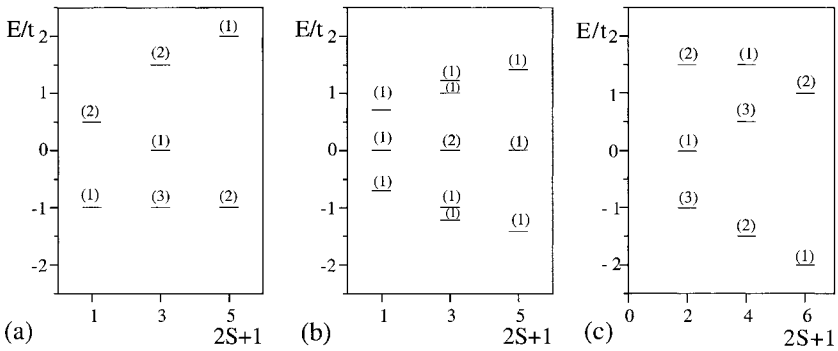

Fig. 21. Energy levels for MV trimers: (a) The triangular d^1–d^1–d^2 cluster; (b) The linear d^1–d^1–d^2 cluster; (c) The triangular hole-type cluster d^2–d^2–d^1. The numbers in brackets indicate the number of spin states

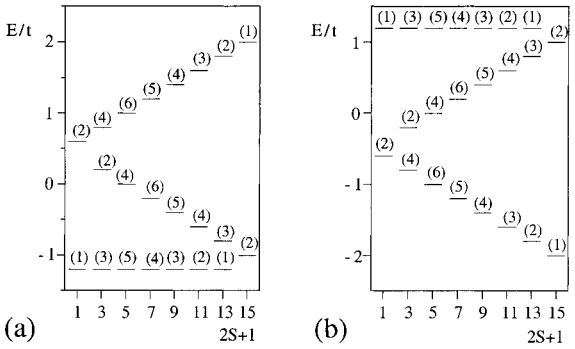

Fig. 22. Energy levels for MV triangular clusters. Double-exchange splitting in d^5–d^5–d^6 (a), and d^5–d^5–d^4 clusters (b)

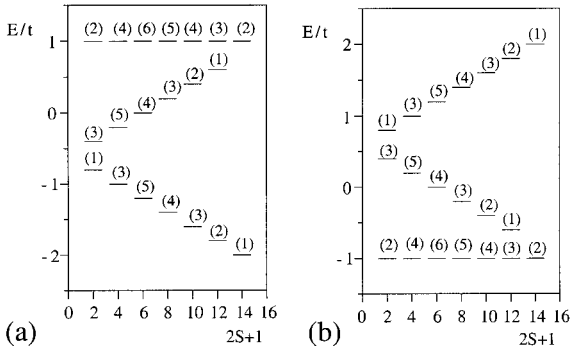

Fig. 23. Energy levels for MV triangular clusters. (a) Double-exchange splitting in d^6–d^6–d^5, and (b) d^4–d^4–d^5 clusters

The important conclusion obtained from the above considerations is that in *contrast to the initial concept, double-exchange in MV clusters with nuclearities larger than 2 not always results in a ferromagnetic effect*, but gives rise to a much more complicated picture of the energy levels which, for triangular clusters, depends on the sign of t.

5.5.1.2 Exchange–Transfer

A second important difference between dimers and trimers concerns the possibility of having three-site interactions. Double-exchange and magnetic exchange are two electronic interactions that respectively involve first and second order electron-transfer processes between two metal sites. In systems with more than two metal sites a two-step transfer process that involves the interaction between three sites, can also be operative. Such a mechanism has been firstly introduced in solid state physics in the study of nonphonon induced superconductivity [28] and referred to as exchange–transfer by Girerd et al. in the context of the MV clusters [29,30]. Fig. 24 illustrates how exchange–transfer mechanism operates in the simple case of a d^1–d^1–d^2 triangle with single-occupied φ-orbitals of spin cores and ψ-orbitals available for the extra electron. The extra electron initially localized on the high-spin ion k jumps on the ion i forming a non-Hund excited state. At the second stage the extra electron moves toward the ion m, restoring the high-spin state. This two-step process gives rise to the effective transfer from site k to site m via the low-spin excited state of the intermediate site i. Since exchange-transfer occurs through an excited non-Hund state with the energy J_0 (intra-atomic exchange), this term will be then of the order of $\Lambda = t^2/J_0$ and represents a second order process in the framework of the perturbation theory. Therefore, exchange transfer is expected to be of the same order of magnitude as the kinetic part of the magnetic exchange, and should be included for the correct calculation of the low-lying energy levels of trimers and higher nuclearity clusters.

The exchange transfer mechanism so far discussed is similar to the Anderson's mechanism of the magnetic kinetic exchange. In fact, the exchange transfer arises from the monoelectronic part of the Hamiltonian (mainly, kinetic energy) and appears as a second order effect. For the reason we have named this kind of interactions as *kinetic exchange transfer* [26,27]. The two-electronic part of the Hamiltonian (interelectronic interaction) contributes to the energies of trimers and higher-nuclearity systems. The parameter accounting for this type of contribution can be expressed by

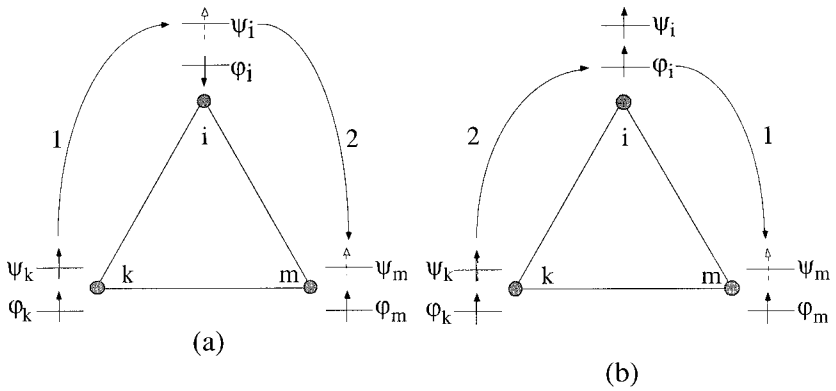

Fig. 24. Illustration of the exchange-transfer mechanism: (a) d^1–d^1–d^2 triangle; (b) d^2–d^2–d^1 triangle

integrals of the type $\langle \psi_m \psi_i | g | \psi_m \psi_i \rangle$. This interaction (mentioned elsewhere [31,32]) operates within the ground manifold and leads to an effective one-step jump. The underlying physical processes as well as its magnitude are similar to the magnetic potential exchange are quite similar. For this reason we have referred this kind of transfer to as *potential exchange–transfer*.

In our papers [25] we have reported a general solution of the exchange transfer problem for high nuclearity clusters and its main manifestations for the trimeric systems. One general point should be stressed. As distinguished from the magnetic exchange, the kinetic and potential contributions to the exchange–transfer act independently and their parameters can not be in general combined to give a joint parameter of exchange–transfer. The above consideration will be of particular relevance in triangular MV clusters where, as we have seen, the ground state can contain an extensive mixture of different spin states, even when double-exchange interaction is large. In these cases, Heisenberg exchange, J, and exchange-transfer, Λ, will play a key role in the splitting of the lower-lying levels of the cluster, thus determining the nature of the ground state and the magnetic properties. Under these conditions, Heisenberg exchange will lead to the same splitting pattern in both localized and delocalized clusters. However, in a delocalized MV cluster the influence of the exchange-transfer can substantially modify the order of levels. In Fig. 25 one can see the effect of the kinetic exchange-transfer in the fully delocalized d^1–d^1–d^2 triangle [27].

This process destabilizes the states with intermediate ($S = 1$) or minimum spin ($S = 0$) belonging to the degenerate ground state, while the state with S_{max} (^5E) stays constant. In turn, the excited states $^3A_1$ and ^1E undergo a stabilization that is stronger for the intermediate spin state. In this way, we observe that the ground state of the cluster is the ferromagnetic one in the range $0 < \Lambda/|J| < 0.3$, whereas for stronger Λ values, the intermediate spin state, $^3A_1$, becomes the ground state. What is important to notice is that, in this kind of clusters (electron-type clusters),

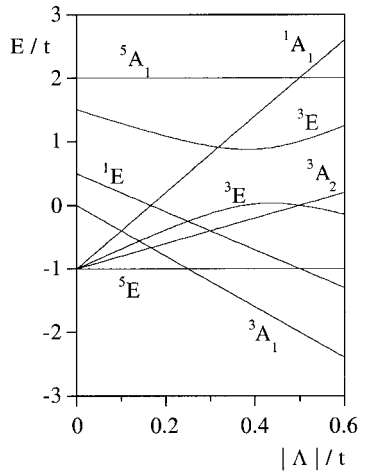

Fig. 25. Energy levels for the d^1–d^1–d^2 triangle. Combined effect of positive double-exchange and exchange transfer

the exchange transfer is unable to stabilize the ferromagnetic states of the cluster since this process occurs via an excited state that can not have the maximum spin (according with the Hund rule). However, in the hole-type clusters this second order transfer process involves Hund excited states of the intermediate ion (Fig. 24b) and therefore a different effect on the energy of the spin states of the cluster can be anticipated. In fact, it has been found that now the effect of Λ depends on the sign of t stabilizing either antiferromagnetic as well as ferromagnetic spin states [27].

5.5.2 Vibronic Interactions in Trimers

The vibronic problem for MV trimers is much more complicated that for dimers and has only been treated within the PKS-model. In fact, besides the in-phase full symmetrical a_1-vibration, which is irrelevant to the electron transfer process, two PKS-vibrations are now involved forming the double degenerate mode labeled as e-vibration in C_{3v} symmetry. The corresponding ligand displacements are shown schematically in Fig. 26.

As distinguished from the dimeric systems, even in the simplest case d^1–d^0–d^0, the two electronic levels E and A resulting from double-exchange (Fig. 20) are mixed through the e-vibrations. Thus, the vibronic interaction operates within the E-doublet (*Jahn–Teller effect*), and mixes E and A states (*pseudo-JT effect*). If the orbital singlet is the ground state ($t < 0$), the system is completely delocalized providing relatively weak vibronic coupling (in this case the potential surface possesses one minimum at q_{e_x} and $q_{e_y} = 0$), but can be localized on one of the three sites if pseudo-JT coupling is strong enough (three minima in the potential surface), (Fig. 27a). Providing the intermediate vibronic coupling, one can also find four minima in the potential surface. The shallow central minimum corresponds to a fully delocalized state, while the other three minima correspond to the localized states. Thus, we have in this case the coexistence of localized and delocalized states [33].

In the case of positive t the ground state is the orbital doublet. In the limit of strong transfer the lower sheet of the adiabatic surface represents the *Mexican Hat*

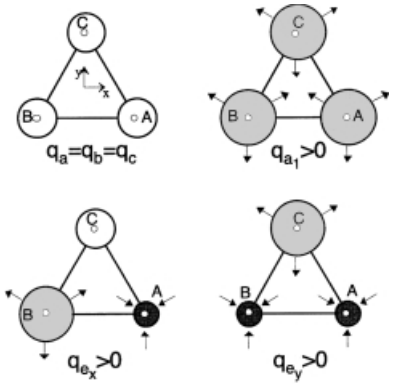

Fig. 26. PKS-vibrations of a triangular cluster: a_1, full symmetrical coordinate; e, double degenerate vibration; q_{e_x} and q_{e_y} coordinates are transformed like x and y under the operations of C_{3v}

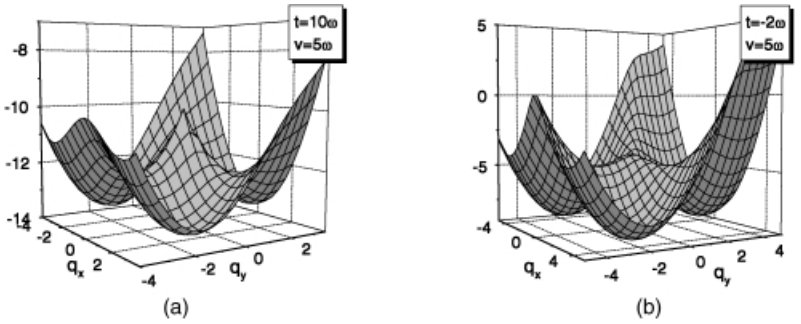

Fig. 27. PKS model for a trimer: lower sheet of the potential surface for $t > 0$, (a), and $t < 0$, (b); t and υ are in $\hbar\omega$ units, $\hbar = 1$, ω is the frequency of the PKS vibration

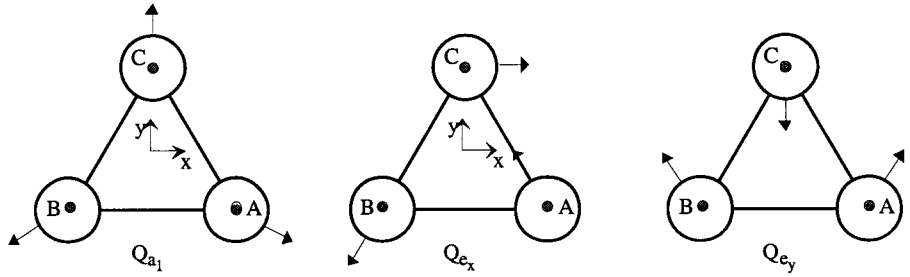

Fig. 28. P-vibrations of a triangular cluster

($(E \otimes e)$ JT problem [34]). As a result, the electronic distribution is dynamically averaged so that the system looks like fully delocalized. Decrease of transfer or/and increase of the vibronic coupling results in the appearance of three minima in which the extra electron is mostly localized on the sites. In the strong coupling limit (that is equivalent to *accidental* ($A_1 + E$) degeneracy) the system becomes fully localized on the sites A, B, or C (Fig. 27b)

In triangular clusters with more than one electron, several orbital multiplets for each full spin S are mixed leading to combined Jahn–Teller and pseudo-Jahn–Teller problems [35,36]. In these cases vibronic coupling effects can also result in the stabilization of other types of electron distributions, as for example the electron delocalization over a pair of sites in an equilateral triangle [37,38]. Such a pair-delocalization has been experimentally found in the reduced form of the triangular Fe_3S_4 cluster contained in the ferredoxin II.

In [39] we have considered electron delocalization in an unsymmetric d^1–d^0–d^0 trimer. The effect of second-order vibronic coupling on the adiabatic potential energy surfaces is studied by Riley et al. [40]. Adiabatic vibronic problem for the d^1–d^0–d^0 trimer in Piepho model was considered in [41]. Three displacements ΔR_{ij} form the basis ($a_1 + e$) of P-vibrations as schematically shown in Fig. 28.

Since the gap between the electronic levels A_1 and E (Fig. 20) depends on the transfer parameter $3|t|$, the full-symmetric displacement affects this gap creating

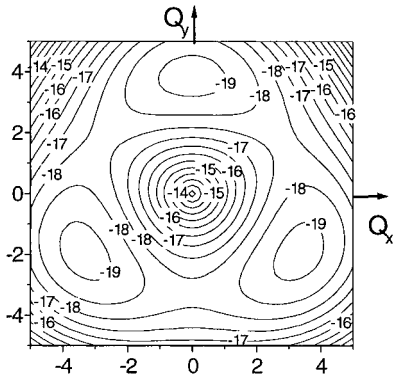

Fig. 29. Piepho model for a trimer: contour plot for the lower sheet of the potential surface ($t > 0$), $t = 10\Omega$, $\lambda = 4\Omega$, $Q_{A_1} = -2.15$; Ω is the frequency of the P-vibrations

thus a vibronic coupling with the a_1-mode. For this reason the a_1-vibration can not be eliminated (as in the PKS model) and we are dealing with a more complicated $(A_1 + E) \otimes (a_1 + e)$ pseudo Jahn–Teller vibronic problem (three-dimensional vibrational space).

Assuming strong transfer ($t > 0$, ground doublet) we arrive at the dynamically electronic distribution that is peculiar to the JT ($E \otimes e$) problem. Increase of P-coupling shifts Q_{A_1} so that the triangle is compressed taking gain of the energy of transfer. At the same time three minima in Q_x–Q_y space appear at the bottom of the ring. The system in these three minima is distorted. For example, for the minimum at Q_y axis, the AB-side is elongated meanwhile AC and BC-sides are compressed. In the minima the system proves to be partially localized. The maximum degree of localization corresponds approximately to the following electronic functions at the bottom of the surface (Fig. 29):

$$\Phi_A = (1/\sqrt{6})(2\varphi_A - \varphi_B - \varphi_C)$$
$$\Phi_B = (1/\sqrt{6})(2\varphi_B - \varphi_A - \varphi_C)$$
$$\Phi_C = (1/\sqrt{6})(2\varphi_C - \varphi_A - \varphi_B)$$

The degrees of localization in minima can be represented (approximately) by the vector:

$$(\rho_A, \rho_B, \rho_C) = (4, 1, 1), (1, 4, 1), (1, 1, 4)$$

Providing strong P-coupling and/or weak transfer, the electronic functions at the bottom of the minima are:

$$\phi_A = (1/\sqrt{3})(\varphi_A - \varphi_B - \varphi_C)$$
$$\phi_B = (1/\sqrt{3})(\varphi_B - \varphi_A - \varphi_C)$$
$$\phi_C = (1/\sqrt{3})(\varphi_C - \varphi_A - \varphi_B)$$

Being nonfull-symmetric, these functions ensure uniform distribution of the electronic density, i. e. the system is fully delocalized in each minimum. This unusual type

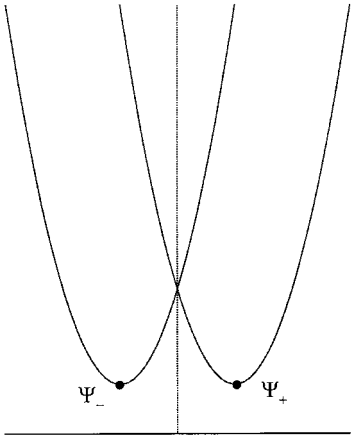

Fig. 30. Accidental degeneracy of the adiabatic potentials in the Q-space

of electronic density in the distorted system is reached providing accidental $(A_1 + E)$ degeneracy. This curious observation can be understood considering a dimer. In the limit of $t = 0$ (accidental degeneracy of odd and even states) a schematic view of the adiabatic potentials in Q-space are shown in Fig. 30 (compare with Fig. 13).

Both minima are energetically equivalent and correspond to delocalized distributions in a distorted system (compressed and elongated). In the case of a trimer the distortions lower the symmetry but also possess a delocalized electronic distribution in the minima. For $t < 0$ (A-ground state) the surface shows one minimum in the ground state with fully delocalized distribution.

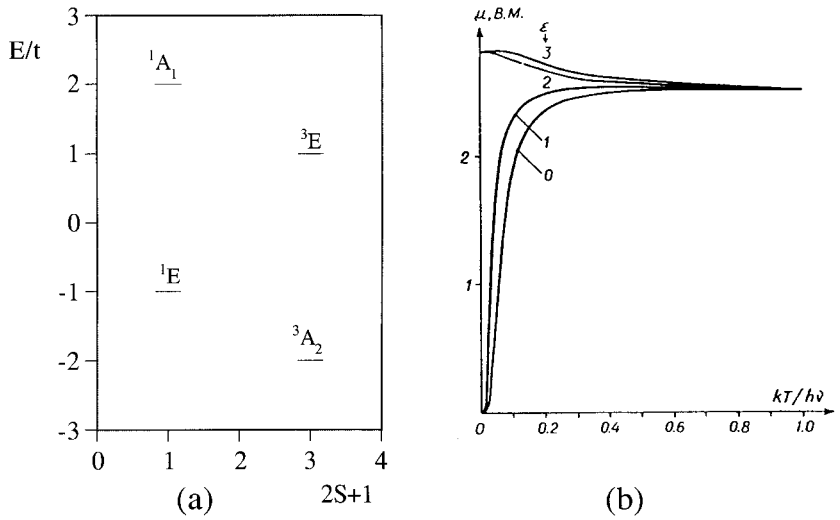

Fig. 31. d^1–d^1–d^0 MV trimer: (a) Double-exchange electronic energy levels; (b) Influence of the vibronic interaction on the magnetic behavior ($t = 0.5$, $J = -0.15$, in $\hbar\omega$ units)

As far as the magnetic properties are concerned we observe that, in the same way as for dimers, the vibronic PKS-interactions play the role of a localizing factor reducing the double-exchange with respect to the Heisenberg exchange. This is illustrated in Fig. 31b which shows the influence of the vibronic interaction on the magnetic moment for the d^1–d^1–d^0 MV trimer. In the case under consideration $t/|J| = 3.33$ and the ground state of the system is ferromagnetic ($^3A_2$) (Fig. 31a).

When the vibronic coupling increases from $\upsilon = 0$ to 1 (in $\hbar\omega$ units), the magnetic moment decreases but the low-temperature limit corresponds to a ground spin state $S = 1$. A further increase in υ ($\sim$2, 3) leads to an antiferromagnetic behavior due to the stabilization of the singlet spin state (^1E) which becomes the ground state of the system.

5.5.3 Examples

The most representative examples of MV trimers concern the tri-μ-oxo metal acetate complexes $M_3O(RCO_2)_6L_3$ where M_3 is either $Fe_2^{III}Fe^{II}$ or $Mn_2^{III}Mn^{II}$ and L = pyridine, H_2O. In this kind of MV clusters the metals are connected by a central oxo ligand and by six peripheral carboxylate ligands (Fig. 32a). Accordingly, two different transfer pathways (though the central oxo group and through the carboxylates) are available for the moving electrons. There are considerable experimental data for this complexes that indicate a thermally activated intramolecular electron hopping promoting a rapid valence delocalization at high temperatures but a valence trapping at low temperatures due to vibronic and solid-state (solvate molecules, packing arrangements) effects [42]. However, even if double-exchange is expected to occur in these systems, the magnetic properties have always shown the presence of antiferromagnetic pairwise interactions. This result is in agreement with the above theoretical expectations that indicate that in triangular clusters double-exchange can be unable to stabilize the highest spin state due to the transfer frustration. Thus, in this case the structure of the low-lying energy levels can be reproduced from a Heisenberg exchange Hamiltonian.

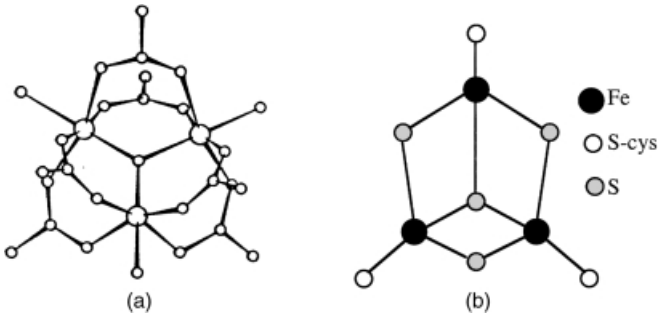

Fig. 32. Schematic structure of triangular MV clusters (a) $M_3O(RCO_2)_6L_3$ (L = pyridine, H_2O; M = Fe, Mn); (b) three iron site $[Fe_3S_4]$ in oxidized ferredoxin II

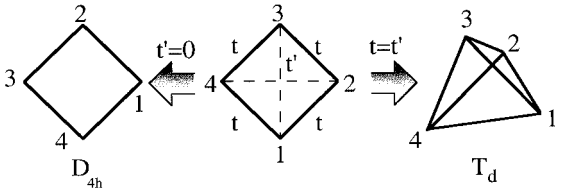

Fig. 33. D_{4h} and T_d topologies arising from a tetramer

The situation is somewhat different in the triangular Fe_3S_4 cluster contained in the ferredoxin II (Fig. 32b). As it has been pointed out above, in this Fe^{II}–Fe^{II}–Fe^{III} system the vibronic coupling results in a strong distortion of the triangle restricting the electron delocalization to a pair. The ground state of the cluster has been found to be $S = 2$. This intermediate spin state may be viewed as the result of the antiferromagnetic coupling between the local spin $S = 5/2$ of Fe^{III} and the spin $S = 9/2$ associated to the delocalized Fe^{II}–Fe^{III} pair.

5.6 Mixed Valence Tetramers

5.6.1 Electronic Interactions

As far as the electronic interactions are concerned, the fact of increasing the nuclearity from 3 to 4 introduces two additional effects that should be taken into account by the models. The first one deals with the topology. In fact, as distinguished from trimers, tetrameric MV clusters formed by four *equivalent* sites can exhibit different topologies for the pairwise electronic interactions (double-exchange and Heisenberg exchange). Thus, starting from the case in which two different transfer pathways are present ($t \neq t'$) (D_{2d} symmetry), we can pass from a tetrahedral T_d structure ($t = t'$) to a square planar D_{4h} structure ($t' = 0$) (Fig. 33).

The second important difference concerns the possibility of having two delocalized extra electrons (or holes) in the cluster. Thus, when different intermetallic distances are present in the cluster, different Coulomb repulsions between these two electrons need to be considered. For example, in the square planar geometry two different distributions for the electron pair are possible, depending on whether the pair occupies adjacent (1, 2) or nonadjacent (1, 3) metal sites. The difference in energy between these two configurations defines the interelectronic Coulomb parameter $U = U_{12} - U_{13}$.

In the following we will present the influence of the above two effects on the energy levels of a tetranuclear cluster. This problem will be examined in tetrameric Fe^{II}–Fe^{III} clusters that constitute an important class of MV systems of relevance in biology (iron–sulfur proteins with cubane-like structures). Depending on the number of delocalized electrons three different cases can be considered namely $1Fe^{II}$–$3Fe^{III}$ (d^6–d^5–d^5–d^5), $2Fe^{II}$–$2Fe^{III}$ (d^6–d^6–d^5–d^5) and $3Fe^{II}$–$1Fe^{III}$ (d^6–d^6–d^6–d^5). We assume that due to crystal field effects the metal ions have orbitally nondegenerate ground states.

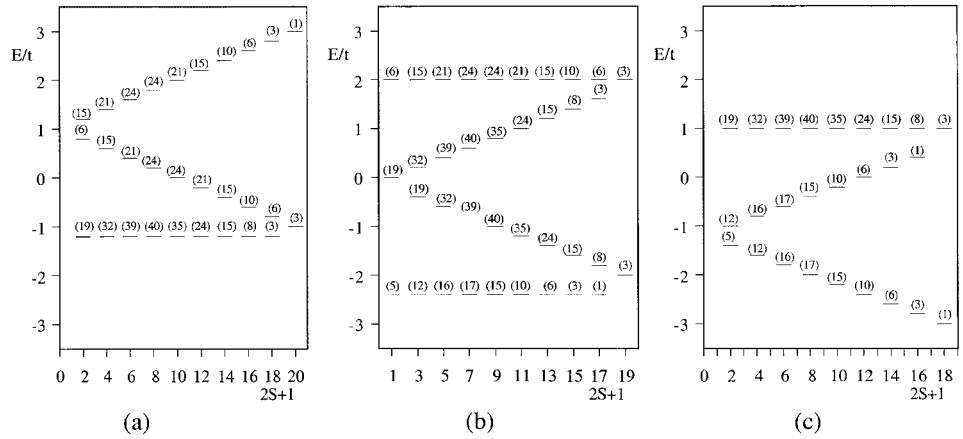

Fig. 34. Influence of the transfer on the energy spectrum of the cluster as a function of the spin multiplicity in the T_d case ($t'/t = 1$). (a), (b), and (c) corresponds to the systems d^6–d^5–d^5–d^5, d^6–d^6–d^5–d^5, and d^6–d^6–d^6–d^5, respectively

5.6.1.1 Double-exchange and Effect of the Topology

For the tetrahedral geometry unsymmetrical arrangements of levels are observed in the three considered cases (Fig. 34), so as the ground spin state depends on the sign of the transfer parameter and on the number of moving electrons. Thus, in the case with one *extra* electron (d^6–d^5–d^5–d^5), double-exchange stabilizes the ferromagnetic spin state ($S_{max} = 19/2$) when t is negative. For positive t the ground level is a degenerate one that comprises spin states between $S_{min} = 1/2$ and $S = 17/2$; the ferromagnetic spin state is slightly excited (by $0.2t$). For the d^6–d^6–d^6–d^5 system the energy spectrum is quite similar to the previous case, but is reversed with respect to the sign of t. A second difference is that now the degenerate level comprises spin states between S_{min} and S_{max}. Such differences where already found in triangular clusters (Section 5.5.1.1) and are to be attributed to the fact that now a hole, instead of an electron, is migrating. They are general for all the tetrahedral clusters having one migrating particle. Finally, the intermediate d^6–d^6–d^5–d^5 system shows an unexpected *quasi* symmetrical energy spectrum in which degenerate ground states are observed both for positive and for negative t values (for $t > 0$ the ground level comprises spin states between $S_{min} = 1/2$ and $S = 17/2$, while for $t < 0$ this comprises spin states between S_{min} and S_{max}). This is a very important result that indicates that in this case double-exchange is completely unable to stabilize a particular spin configuration. In a certain sense, the energy spectrum of this cluster can be seen as the result of the combination of two energy spectra: that of the cluster having one extra electron (which exhibits a degenerate ground spin state for $t > 0$), and that of the cluster having one extra hole (which exhibits a degenerate ground spin state for $t < 0$).

Let us examine now the MV clusters with D_{4h} symmetry (Fig. 35). In contrast to the T_d symmetry, a symmetrical energy diagram with respect to the sign reverse of the transfer parameter is obtained in the three cases, and furthermore the energy levels exhibit a large dispersion forming energy bands. However, the energy spectra

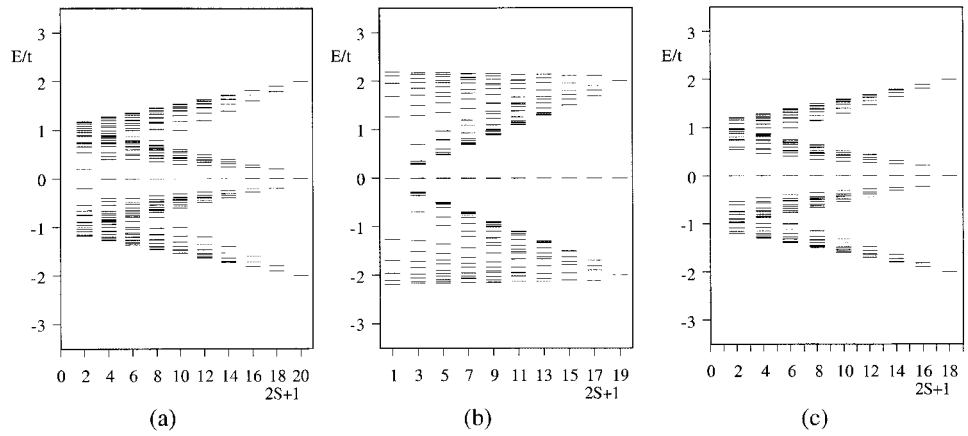

Fig. 35. Influence of the transfer on the energy spectrum of the cluster as a function of the spin multiplicity in the D_{4h} case ($t'/t = 0$). (a), (b) and (c) corresponds to d^6–d^5–d^5–d^5, d^6–d^6–d^5–d^5 and d^6–d^6–d^6–d^5 systems, respectively

of systems involving one *extra* electron (or hole) are significantly different from that observed when two *extra* electrons are involved. Thus, in the d^6–d^5–d^5–d^5 and d^6–d^6–d^6–d^5 systems the stabilization of the spin states increases with the spin multiplicity, so as the ground spin state is always the ferromagnetic one. Conversely, in the d^6–d^6–d^5–d^5 system a *quasi* degenerate ground state formed by a mixture of the different spin states with $S < S_{max}$ is observed; actually, the ground state corresponds to the antiferromagnetic one, but the differences in energy with the lower lying levels of other spin multiplicities are quite small (for the first excited state this energy is $0.02\,t$).

We have also studied the influence of trigonal distortions on the energy pattern of the d^6–d^6–d^6–d^5 and d^5–d^5–d^5–d^6 tetramers [43,44]. Both types of trigonal distortions (stretching and compression) lead to an unsymmetric picture of the energy pattern. Since the trigonally distorted system retains triangular faces, this conclusion is in agreement with the line of the concept of transfer frustration.

5.6.1.2 Influence of the Coulomb Repulsion

In the d^6–d^6–d^5–d^5 system, the presence of two moving electrons forces us to consider, besides the transfer energies, the difference in energy between the configuration having close electronic pairs from that having distant pairs. This Coulomb repulsion effect will be encountered in the square planar geometry, and when the tetrahedron is distorted. In Fig. 36 we show the influence of this parameter in the D_{4h} case. As we can see, U produces a small asymmetry in the energy spectrum, leading to a shift by U of the upper energy band and of the spin states situated at $E = 0$. However, the structure of the two energy bands remains unchanged, so as the relative energies of the low lying levels, and in particular the nature of the ground state, are not affected in a significant manner by the electron repulsion.

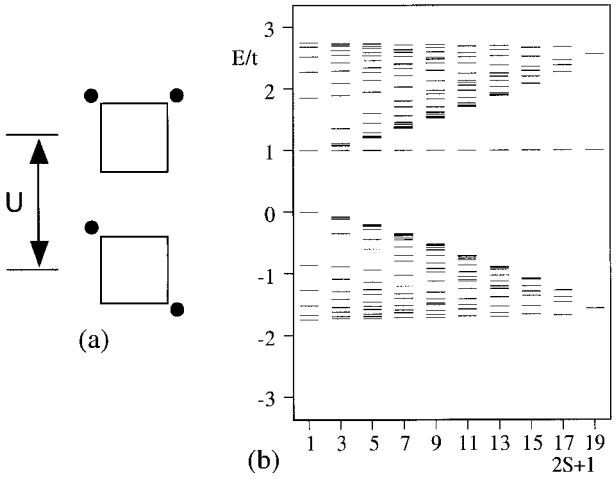

Fig. 36. (a) Electronic configurations in a D_{4h}-cluster with two moving electrons. (b) Influence of the Coulomb repulsion on the energy spectrum of the d^6–d^6–d^5–d^5 D_{4h} cluster as a function of the spin multiplicity, $U = t > 0$

Some concluding remarks concerning the energy pattern for tetrameric systems should be emphasized:

1. We have observed that both the topology of the cluster and the sign of t play a key role in the energy spectrum of the cluster. Thus, while for a D_{4h} symmetry the spin state structure is symmetrical with respect to the sign reversal of t, for a T_d cluster having a unique extra particle, an unsymmetrical spectrum is predicted by the model. In these cases, the asymmetry in the spectrum as well as the type of splitting for the spin states closely resembles that calculated for the triangular clusters which exhibit a highly degenerate (*frustrated*) ground state for a given sign of t, and a progressive stabilization of the low-lying states as S is increased, for the opposite sign of t. This observation allows us to point out a general conclusion: *The asymmetry in the spectrum as well as the transfer frustration are the characteristic features of clusters having triangular faces* (or, in general, faces formed by an odd number of interacting sites). In these clusters only if the sign of t is the appropriate, double-exchange will be able to stabilize a ferromagnetic ground state; for the opposite sign of t, the ground state of the cluster will be largely frustrated and therefore, the structure of the low lying levels and the magnetic properties will be largely independent of the magnitude of t; other electronic effects will become then the leading ones (magnetic exchange and exchange-transfer interactions, distortions of the cluster, local anisotropy of the magnetic ions, etc.).

2. The type of energy spectrum also depends on the number of extra electrons (or holes) in the cluster. For example, double-exchange splitting in a T_d cluster having two extra electrons is quasi-symmetrical, in contrast with the results obtained on trinuclear and tetranuclear clusters having one extra electron. Furthermore, an additional term arising from the Coulomb repulsion between the two electrons needs to be taken into account when two or more extra electrons are delocalized. This last term will restrict the electron delocalization in the cluster favoring those configurations in which the electrons are as separated as possible.

These models may account for the wide variety of ground spin states experimentally found in the iron–sulfur tetrameric clusters.

5.6.2 Vibronic Interactions in Tetramers

Increase in the nuclearity leads to a further complication of the vibronic problem due to the increase in the dimensionality of the vibrational space and of the electronic basis. Thus, in the vibrational space we pass from a doubly-degenerate PKS e-vibration in trimers, to a triply degenerate t_2-vibration in tetramers. Marks and Prassides [45] considered vibronic effects in the simplest case: one-electron four-center tetrahedral MV system (d^1–d^0–d^0–d^0). In this system the triply-degenerate (t_2) PKS-vibration is operative in a four-dimensional electronic basis (A_1 and T_2 levels separated by a gap $3t$). The role of the vibronic coupling on the electron distribution is similar to that reported above in the MV trimer (d^1–d^0–d^0). Thus, for $t < 0$ the orbital singlet A_1 is the ground state; the adiabatic surface in the space of the three t_2-coordinates (Q_x, Q_y, Q_z) has one minimum at $Q = 0$ when the pseudo JT effect mixing A_1 and T_2 states is weak; this corresponds to a fully delocalized electronic state. If pseudo-JT mixing is strong enough, the electron can be localized on one of the four centers. As for trimers the coexistence of localized and delocalized states is also possible for the intermediate pseudo-JT interaction. For $t > 0$ the orbital triplet T_2 is the ground state; a JT effect occurs within this ground state favoring localized states of trigonal symmetry.

Adiabatic surfaces of the tetrameric (T_d) one-electron system in the limit of strong multicenter coupling was studied in [41]. Six P-vibrations form the $a_1 + e + t_2$ basis (as in trimers, a_1 can be eliminated), so we are dealing with the complicated combined Jahn–Teller and pseudo-Jahn–Teller problem. In the case of strong transfer $t > 0$ we arrive at a classical $T_2 \otimes (e + t_2)$ problem. The system was shown to possess three tetragonal minima (and four trigonal saddle points) in which the extra electron is fully delocalized. The same points in Q-space remain the minima when the gap, $\varepsilon(A_1) - \varepsilon(T_2) = 4|t|$, is small enough. In this case however, the potential surface possesses also four excited trigonal minima corresponding also to full delocalization, and one additional minimum in which only Q_{a_1} is shifted. In the limit $t = 0$, all eight minima are degenerate and the extra electron is delocalized, the system being, at the same time, distorted.

Electron distributions of tetrameric clusters with more than one electron have also been calculated using the PKS-model. For example, in the iron–sulfur tetrameric clusters of the type $[Fe_4S_4]^{3+}$ (d^5–d^5–d^5–d^6 problem) we have pointed out above that double-exchange leads to an orbitally nondegenerate ferromagnetic ground state $S = 19/2$ when t is negative (Fig. 35a). In such a situation the extra electron should be uniformly distributed over the four sites if the pseudo-JT mixing is assumed to be small. However for positive t, the ground state is the accidentally degenerate one. Thus, JT-effect operates in this basis set giving rise to minima corresponding to pair-delocalized states [38]. In fact, there are experimental evidences on MV model compounds containing the $[Fe_4S_4]^{3+}$ core which indicate that delocalization occurs only within a pair Fe^{II}–Fe^{III} [46].

With respect to the magnetic properties it is important to underline the enormous difficulties encountered when we try to calculate the energy levels, that actually are vibronic levels. In principle, this problem requires a dynamic approach that takes into account the kinetic energy of the nuclear motion (this term has been neglected

in the calculation of the adiabatic potentials). For many-electron clusters we find an independent vibronic problem for each full spin value, S, of the system. As basis set, the dynamic approach uses the wave-functions of noninteracting electronic and vibronic subsystems (i. e. products of electronic and vibrational wave-functions). As a result, the vibronic problem requires the diagonalization of a matrix that has a dimension much higher than that associated to the electronic double-exchange problem. This dimension is the product of the electronic wave functions times the vibrational wave functions, and since the number of vibrational states is infinite, this basis set must always be truncated. The number of involved vibrational states providing reasonably accurate calculations is high even in relatively simple cases. This explains why for a tetranuclear MV cluster the only multielectronic problem solved so far from the dynamic approach is the d^1–d^1–d^1–d^2 tetramer with T_d symmetry [47]. In this particular case, the initial basis set has high dimensionality due to the high degree of degeneracy of vibrational levels of the three dimensional oscillator (t_2-vibrations). The dimension of the vibronic matrix for a given total spin S is $N_S = ms(n+1)(n+2)(n+3)/6$, where $m = 4$ is the number of electronic states ($A+T_2$), s is the number of intermediate spin combinations for this total spin ($s = 1, 4, 5$ for $S = 5/2, 3/2, 1/2$, respectively), and n is the maximum number of vibrational quanta that need to be considered. We can imagine that, even for a moderate vibronic coupling, the size of the vibronic matrix is very high. Thus, in the calculation of the vibronic levels of the d^1–d^1–d^1–d^2 tetramer the vibrational basis has been restricted to $n = 25$, and then the full dimension of the vibronic matrix is $4 \times 5 \times 26 \times 27 \times 28/6 = 65520$ for $S = 1/2$.

To overcome the difficulties encountered to solve the dynamic vibronic problem, a semiclassical adiabatic approach has recently been proposed for consideration of the magnetic properties of MV clusters [48,49]. Let us briefly describe this approach.

To calculate the magnetic behavior of a system we must substitute the energy levels $E(S)$ into the van Vleck equation:

$$\mu^2(T) = g^2\mu_B^2 \frac{\sum_S S(S+1)(2S+1)\ \exp[-E(S)/kT]}{\sum_S (2S+1)\ \exp[-E(S)/kT]} \tag{26}$$

In the dynamic approach, $E(S)$ are the vibronic levels of the system that depend on the quantum number v enumerating the vibrational states; thus, a summation over these states should be introduced in Eq. (27). In the framework of the semiclassical adiabatic approach, the adiabatic potentials $U^S(q)$ play the role of full energies of the system and the summation over the quantum vibronic states in Eq. (27) can be replaced by the integration over the nuclear coordinate q of the active vibration:

$$\mu^2(T) = g^2\mu_B^2 \frac{\sum_S S(S+1)(2S+1) \sum_i \int_{-\infty}^{+\infty} \exp[-U_i(S)/kT]\, dq}{\sum_S (2S+1) \sum_i \int_{-\infty}^{+\infty} \exp[-U_i(q)/kT]\, dq} \tag{27}$$

where symbol i enumerates the branches of the adiabatic potential for each spin state of the system ($i = +,-$). In this way, the movement of the nuclei and the corresponding changes in the energy scheme during this motion are taken into account.

The magnetic properties predicted by this simple approach have been compared with those calculated from the exact dynamic approach. The agreement between the two approaches is remarkable. Thus, for those systems in which a dynamic approach is feasible, the semiclassical results allows to adequately describe, qualitatively and quantitatively, the temperature dependence of the magnetic moments. The accuracy is better than 0.01% in the overall temperature range as illustrated in Fig. 37. Therefore, this approach proves to be a very powerful and efficient tool to properly describe the magnetic properties of MV clusters of different nuclearities, whatever the values of the electronic and vibronic parameters.

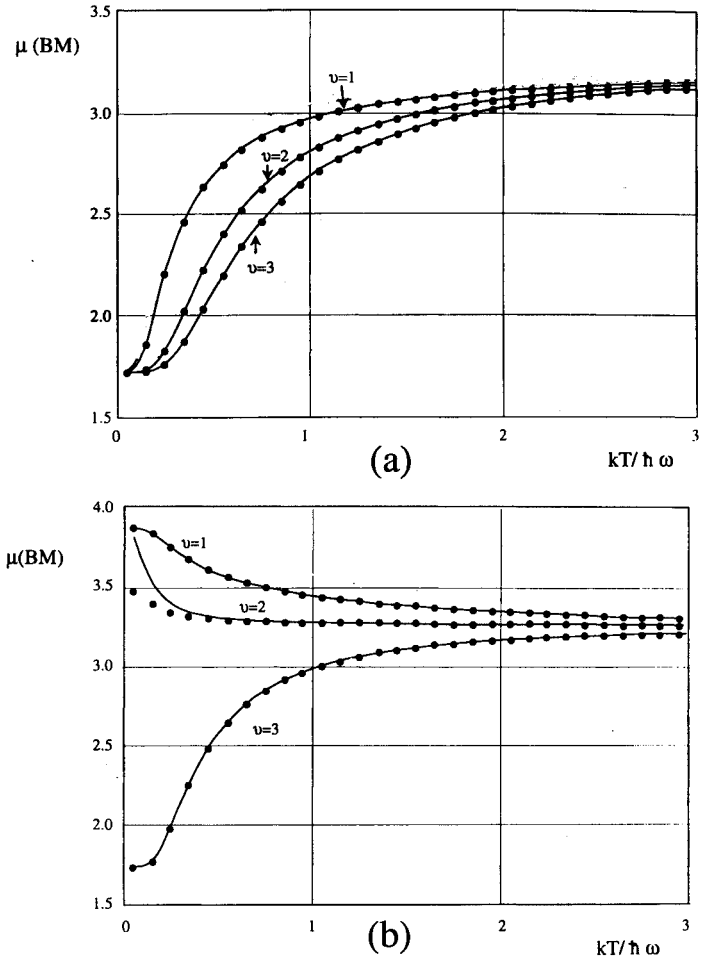

Fig. 37. Temperature dependencies of the magnetic moments for a MV d^1–d^2 dimer, (–) dynamic model, (•) semiclassical results, (a) $J = -0.5, t = 2$ (antiferromagnetic region in the static model), (b) $J = -0.5, t = 4$ (ferromagnetic region in the static model). J and t are in $\hbar\omega$ units

5.7 Higher Nuclearity Mixed Valence Clusters

In recent years many MV molecular systems containing large clusters have been reported and their magnetic properties investigated. An important class of compounds of this kind is the so-called polyoxometalates [50,51]. These inorganic complexes present discrete cluster-like structures of definite sizes and shapes formed by closed and highly symmetrical networks of MO_x polyhedra (usually octahedra and tetrahedra; M = V, Mo, W), which resemble discrete fragments of metal oxide structures [52–54]. From the electronic point of view, these molecular metal oxides have a remarkable electron storage capacity which have attracted considerable interest in catalysis and other interrelated areas, including applications in materials and solid-state chemistry and biomedical applications.

The structures of some representative examples are depicted in Fig. 38. At the top two polyoxovanadates are shown: $[H_3KV_{12}As_3O_{39}(AsO_4)]^{6-}$ containing three localized vanadium(IV) centers (sites 10, 11 12) and one vanadium (IV) delocalized over three sites (1, 2, 3), and $[V_{12}As_8O_{40}(HCO_2)]^{3-,5-}$, comprising four localized and two or four delocalized vanadium(IV) ions, respectively [55–57]. At the bottom of the Fig. 38 two typical structures of polyoxotungstate and polyoxomolybdate anions are shown, namely the Keggin and Wells–Dawson structures. These anions can be reversibly reduced to mixed-valence species (*heteropoly blues* and *browns*) by addition of various specific numbers of electrons, which are delocalized over a significantly large number of atoms of the heteropoly framework yielding to multinuclear mixed valence species of Class II. The additional possibility of accommodation into these structures of paramagnetic metal atoms, which contain localized magnetic moments, yields to MV clusters in which localized and itinerant electrons can coexist and interact [58].

In the theory of mixed valence these polyoxometalate complexes are very suitable as model systems to study electron delocalization and magnetic interactions in high-nuclearity clusters. Thus, although the topologies exhibited by these clusters are much more complex than those previously examined, their high symmetries allow us to exploit the group theoretical approach. This facilitates the development of analytical solutions for the electronic energy levels and magnetic properties of the cluster, providing at the same time a clear picture of the role of the different types of electronic processes involved.

Still, in a high nuclearity MV cluster, the problem can become very complex and a computational approach need to be developed. Such a procedure has been worked out [59] in the most general case: a cluster of N magnetic sites containing an arbitrary number of delocalized electrons P (Fig. 39). The developed approach is based on the successive (chain-like) spin-coupling scheme and takes full advantage from the quantum angular momentum theory. In the framework of this approach, analytical expressions are deduced for the matrix elements of the double-exchange interaction, two electron transfer, and three-center interactions. The matrix elements of all these interactions are expressed in terms of all relevant spin quantum numbers and 6j-symbols and do not contain higher order recoupling coefficients.

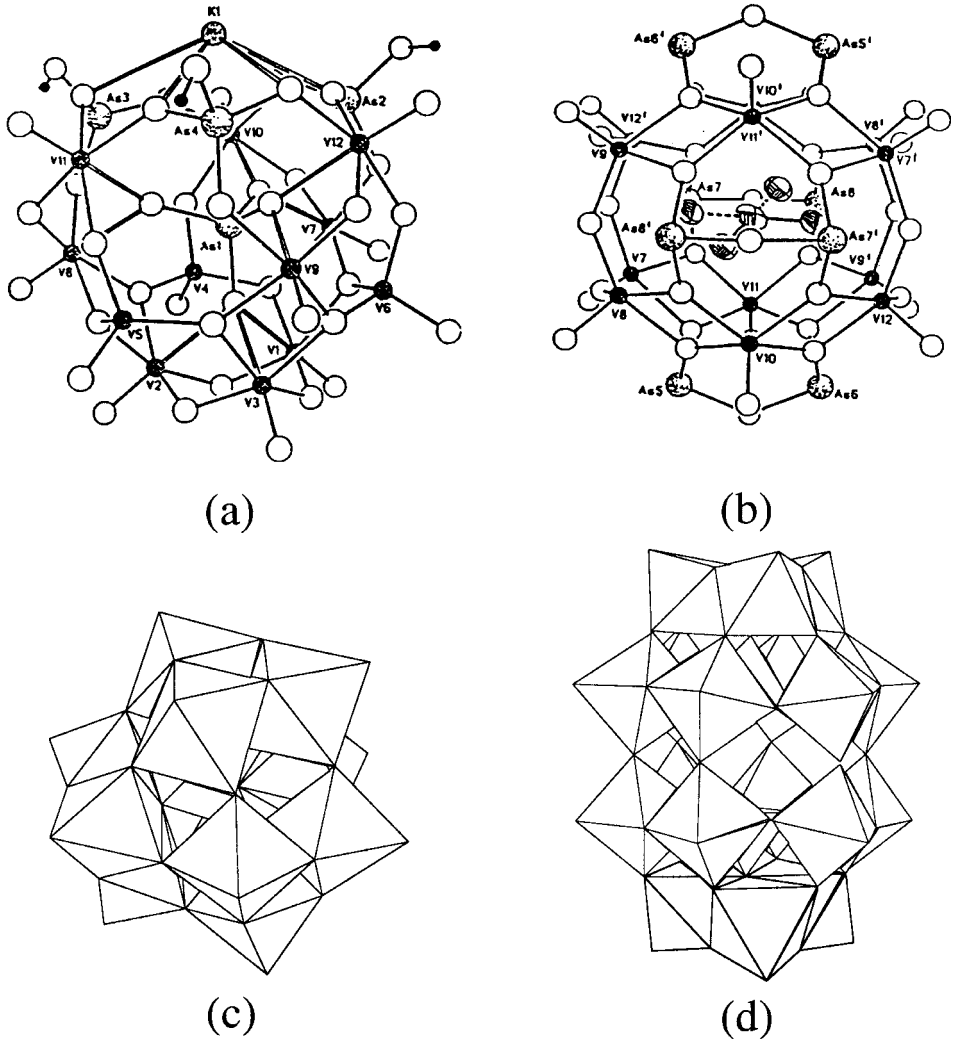

Fig. 38. (a) Sketch of the structure of $[H_3KV_{12}As_3O_{39}(AsO_4)]^{6-}$. (b) Sketch of the structure of $[V_{12}As_8O_{40}(HCO_2)]^{n-}$ ($n = 3, 5$). (c) Keggin structure of a $[XM_{12}O_{40}]$ cluster (M = Mo, W; X = B^{III}, Si^{IV}, P^{V}, Co^{II}, Co^{III}, Fe^{III}, Cu^{II}, etc.) (d) Wells–Dawson structure of a $[X_2M_8O_{62}]$ cluster (X = P^{V}, As^{V}; M = Mo, W)

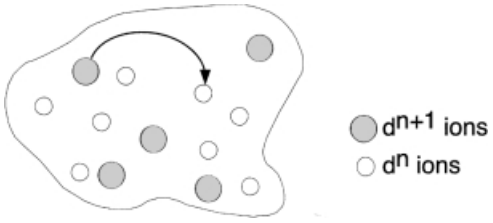

Fig. 39. Representation of a high-nuclearity MV system showing one of the $N!/[P!(N - P)!]$ electronic distributions

5.7.1 Electronic Interactions in Polyoxometalates

To illustrate the role of both electronic and vibronic interactions in these clusters we focus on the problem of delocalization of two electrons in the Keggin and Wells–Dawson structures [36]. We will elucidate the conditions accounting for the complete pairing of the spins of two delocalized electrons observed experimentally, even at room temperature.

Let us first describe the main features of both structures (Fig. 38c, d). In the Keggin anion the idealized structure consists of four edge-sharing triads of MO_6 octahedra arranged around the central atom X by sharing corners, in such a way that the resulting species has a tetrahedral symmetry. A view of this anion along one of the C_3 axes allows to describe the structure in terms of one M_6 hexagonal belt, with MO_6 sites alternatively sharing edges and corners, in between two triangles M_3; in one of these triangles the MO_6 sites are sharing edges while in the another they are sharing corners. In a similar way, the Wells–Dawson anion may be viewed as formed by two M_6 hexagonal belts joined by corners, in between two edge-sharing triangles M_3. Spectroscopic experiments indicate that in the Keggin anions the two extra electrons are delocalized over the twelve metal sites, while for the Wells-Dawson anion such electron delocalization is restricted to the two internal hexagonal belts [60].

A site symmetry approach has been developed to calculate the electronic structure of these MV clusters. This makes possible a group theoretical classification of the delocalized pair states, according to the irreducible representations, thus favoring an easier calculation of the transfer matrices. The details of this new approach are reported in refs. [61–63]. We restrict our discussion to present the role played by the relevant electronic terms on the pattern of the low-lying energy levels. These terms are the following: 1) the Coulomb interactions between the two delocalized electrons that tend to keep the electrons on fairly widely separated metal atoms; 2) the single and double electron transfer processes that occur through the corners or through the edges of neighboring octahedral metal sites, promoting the electron delocalization. For single transfers one of the two electrons jumps from one site to a neighboring one. For double transfers the two electrons jump simultaneously; and 3) the superexchange interactions that occur when the two electrons are occupying neighboring metal sites.

In view of the different intermetallic distances shown by the above structures, different interelectronic Coulomb repulsions for the electron pairs are expected to occur. Thus, in the Keggin structure up to five different intermetallic distances are possible, that should lead to five different types of electron pair configurations having different energies in such a way that the ground configuration is separated from the first excited one by about $2500\,cm^{-1}$ (Fig. 40). The ground configuration corresponds to the situation in which the two electrons are in nonadjacent MO_6 sites, occupying opposite positions in the structure. In the Wells-Dawson structure up to seven different types of electron pairs can be distinguished, but now the first two excited configurations (denoted II and III in the figure) are very close in energy (around 1600 and $1900\,cm^{-1}$).

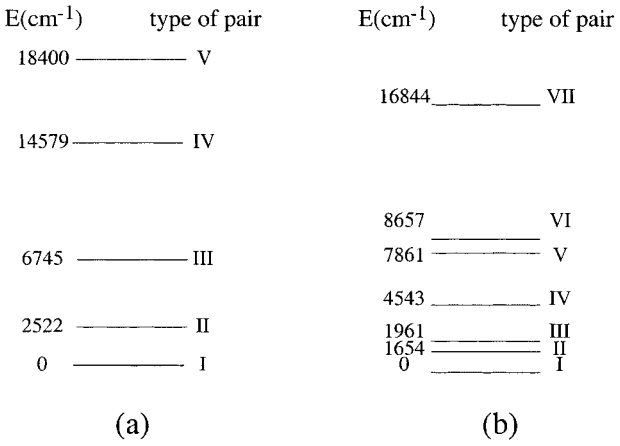

Fig. 40. Effect of the interelectronic Coulomb repulsions in Keggin (a) and Wells–Dawson (b) structures

Both electron transfer and magnetic exchange processes will split each one of these energy levels, but since the energy gap between the ground configuration and the lower excited ones is large, the pattern of the low-lying levels of the cluster is expected to come from the splitting of the states belonging to the ground configuration. Then, if we restrict our discussion to this configuration, only the transfer processes will be operative since the two moving electrons are widely separated, making completely irrelevant the possibility of a magnetic exchange coupling. The influence of the electron delocalization on the energies of the group of states that form the ground configuration is depicted in Figs. 41 and 42 in the case of the Keggin anion. We see that both single and double transfer processes split the ground level into four different levels that can be either a spin singlet $^1A_1$, or a mixture of a singlet and a triplet spin

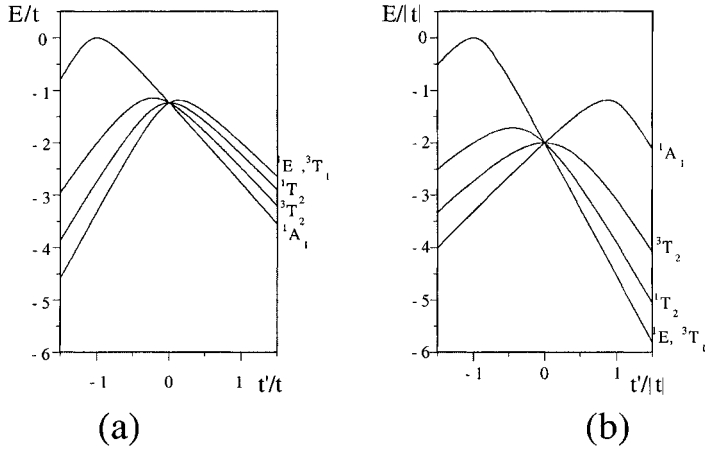

Fig. 41. Keggin structure. Influence of the single transfer processes on the ground configuration; t and t' refer to the two types of transfers (through edges and corners of the octahedra). (a) $t > 0$, (b) $t < 0$

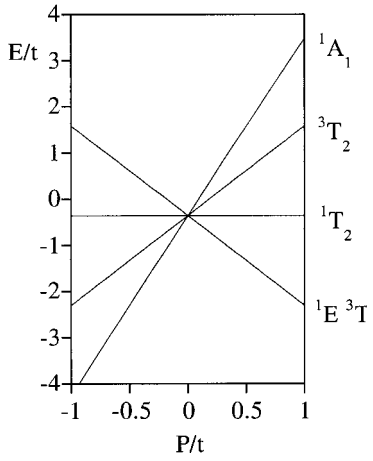

Fig. 42. Keggin structure. Influence of the double transfer process on the ground configuration

states (^{1}E and $^3T_1$). The splitting is unsymmetric with respect to the sign reversal of the involved transfer parameters, as in the simple MV clusters formed by triangular metal units. What is important to notice is that for certain values of these parameters the electron delocalization leads to a stabilization of the singlet spin state, allowing thus to explain the spin pairing observed in this kind of high-nuclearity mixed valence clusters. The results are similar for the Wells–Dawson cluster. In the general framework of the double-exchange theory, these results emphasize once again that in MV clusters with nuclearities larger than 2 this mechanism can also result in an antiferromagnetic spin coupling between the interacting electrons.

5.7.2 Vibronic Interactions in Polyoxometalates

As we have already mentioned the vibronic problem in the high-nuclearity systems is very complicated. Here we will briefly discuss the vibronic approach developed for the bielectronic problem in the twelve-site Keggin structure [62]. Because of the high nuclearity of the system, only the static case, i. e. the adiabatic potentials, has been examined. This provides a basic picture of the different ways of electron delocalization in this kind of clusters.

The vibronic problem involves a considerable number of electronic states and twelve vibrational PKS coordinates. This problem can be simplified if the electronic basis set is restricted to the wavefunctions of the most distant electron pairs (of type I in the above notations), neglecting the mixing of these low-lying group of levels with those belonging to other kinds of pair configurations (excited levels). Accordingly, the electronic structure of the system consists of two spin triplets $^3T_1$ and $^3T_2$, and three spin singlets $^1A_1$, ^{1}E and $^1T_2$ which are split by the effect of the double transfer processes (Fig. 42). As far as the vibrational states are concerned, it is reasonable to employ the *pair-vibrational* basis set:

$$q_{ab}^{\pm} = \frac{1}{\sqrt{2}}(q(a_2) \pm q(b_2))$$

where a_2b_2 is one of the six distant positions of the electron pair in the Keggin structure. This basis involves symmetric and antisymmetric combinations of local PKS coordinates, linked only with the sites occupied by the distant electron pair. As distinguished from the case of one itinerant electron, only *in phase* (symmetric) PKS mode changes simultaneously the potential energy of both electrons. In turn, antisymmetric (out-of-phase) displacement does not change the common potential energy of the electron pair since it has the effect of increasing the energy of one electron (compressed site), while the energy of the second electron decreases (expanded site). For this reason only the six symmetric vibrational coordinates are involved in the transfer processes. From these coordinates one can obtain the six symmetry adapted vibrational coordinates in the T_d group of the cluster. These are of the type a, e and t_2, but only the e and t_2 vibrational modes have been proved to be relevant in the vibronic problem under consideration. Therefore, this vibronic problem will finally involve the coupling of these two modes with the two electronic spin subsets: i. e., the Jahn–Teller and pseudo-Jahn–Teller problems $({}^3T_1 + {}^3T_2) \otimes (e + t_2)$ and $({}^1A_1 + {}^1E + {}^1T_2) \otimes (e + t_2)$.

Several kinds of spatial electronic distributions have been found corresponding to stable points of the energy surfaces. Thus, for spin-triplet states, weak vibronic coupling in the space of e-modes restricts electron delocalization to two of the three metal sites of each M_3O_{12} triad in such a way that each electron moves over a tetrameric unit in which the metal sites are alternatively sharing edges and corners (shaded octahedra of Fig. 43a); in the limit of strong coupling, the electron delocalization is restricted to one of the three metal octahedra (Fig. 43b), but since these four sites are not connected through oxygen bridges the system is expected to be fully localized. In the space of t_2-modes the electronic pair can be either delocalized

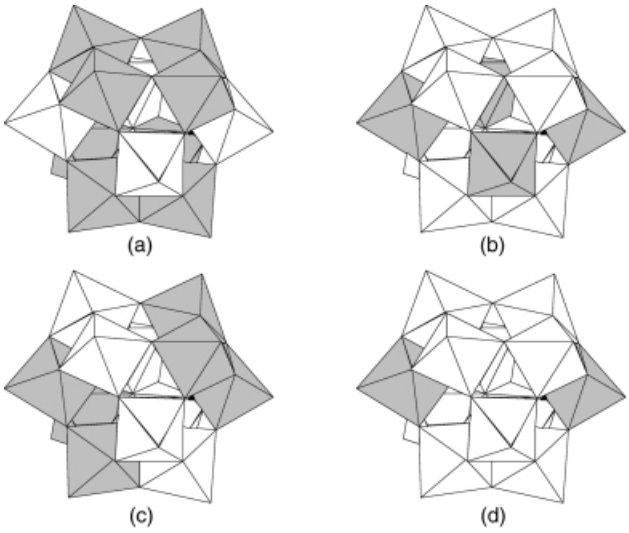

Fig. 43. Possible types of delocalization of the electron pair in the Keggin structure

over two opposite M_3O_{12} triads (case of weak vibronic coupling; Fig. 43c), or be completely localized (case of strong vibronic coupling; Fig. 43d). Notice that in all these cases the vibronic coupling leads always to a partial delocalization, or even to a full localization of the electron pair. By no means one can obtain from the coupling with the spin-triplet states a full delocalization of the electron pair over the twelve metal sites. This is possible only when the vibronic coupling with the spin-singlet states is considered. Thus, it has been found that, for both positive and negative values of the transfer parameter and weak enough vibronic coupling, the system possesses a stable point in the high-symmetrical nuclear configuration, corresponding to a uniform electronic distribution of the electron pair in the Keggin cluster. Difficulties in solving the vibronic problems progressively increase in more extended systems due to the increase of electronic basis and number of active modes. In this context the 12-site Keggin structure seems to be the largest vibronic system considered till now in the static (adiabatic) approach.

5.7.3 Other High Nuclearity Mixed-valence Systems

In the previous section we have seen how the delocalization of two electrons over the polyoxometalate clusters can result in an antiferromagnetic spin coupling which stabilize the $S = 0$ ground spin state. This problem has been recently extended to model higher nuclearity spin clusters. An example is provided by the fulleride anion C_{60}^{2-} which contains two electrons delocalized over 60 equivalent carbon sites (Fig. 54) [64]. In this case two electronic interactions have been considered: the Coulomb interactions between the two delocalized electrons, and two types of electron transfer integrals associated to both types of connectivity between neighbor carbons, t and t'. The delocalization of these two extra electrons over the fullerene molecule results in an effective antiferromagnetic coupling between the two spins and the magnitude of the singlet-triplet energy gap ($\sim 10^3\,\mathrm{cm}^{-1}$) is mainly determined by the electron transfer parameters, being almost independent on the Coulomb repulsions.

The last example we consider here represents a chain consisting of equivalent exchange coupled MV dimers [65]. We denote the sites of dimers as A_1B_1, A_2B_2, $\ldots A_nB_n$, where $n = N/2$ is the number of dimers in the chain (N is the number of sites). Each MV dimer is supposed to have one moving electron delocalized over two

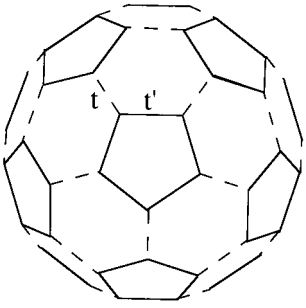

Fig. 44. Figures of the two kinds of C-C bonds present in the C_{60} molecule and the associated electron transfer parameters, t and t'

spin-less cores A_iB_i. Each site is assumed to have only one nondegenerate orbital. The states with two electrons in the dimeric unit are expected to be inaccessible due to the strong intracluster Coulomb repulsion. This system may be viewed as a model of diphthalocyanine chains $[YPc_2] \cdot CH_2Cl_2$ and $[ScPc_2] \cdot CH_2Cl_2$ [66,67]. The extra electron of each MV pair is delocalized over two sites of the macrocyclic unit and we arrive at the problem of an infinite chain of MV dimeric units.

The following three types of interactions are relevant in the system under consideration:

1. The electron delocalization inside each dimeric unit is described by the intracluster transfer parameter $t_{A_iB_i} \equiv t$.

2. A ferromagnetic exchange interaction between the electrons occupying adjacent sites of the neighboring dimers (the associated parameter is denoted as $J_{B_iA_{i+1}} \equiv J$).

3. Inter-dimer Coulomb interaction described by the parameter $U_{B_iA_{i+1}} \equiv U$ (as for the exchange, only the shortest distance Coulomb interaction seems to be important).

Using the general computing approach described above [59], the magnetic properties of a finite chain formed by six MV dimers (twelve sites) have been calculated. With the aim of better approach the properties of the infinite chain, the closed chain has been considered.

Let us briefly examine the role of the electron transfer on the magnetic properties of this MV system. Depending on the relative values of the parameters J and U we can have two limiting cases which will be referred to as strong exchange interaction limit and strong Coulomb interaction limit.

Provided no electron transfer ($t = 0$) one can see that in the strong exchange limit, the chain adopts an antiferroelectric charge-ordered distribution (the electric dipole moments of neighboring MV dimers are antiparallel) in which the electrons of two neighboring MV pairs are located in adjacent sites in order to take advantage of the exchange interaction (Fig. 45a). In this case the magnetic properties will exhibit at low

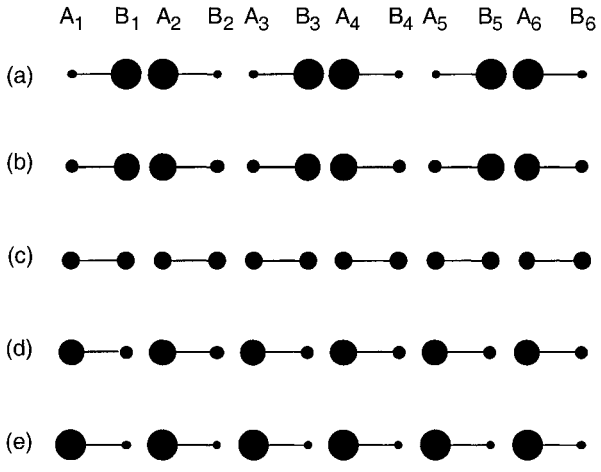

Fig. 45. Electron density distributions in a MV chain

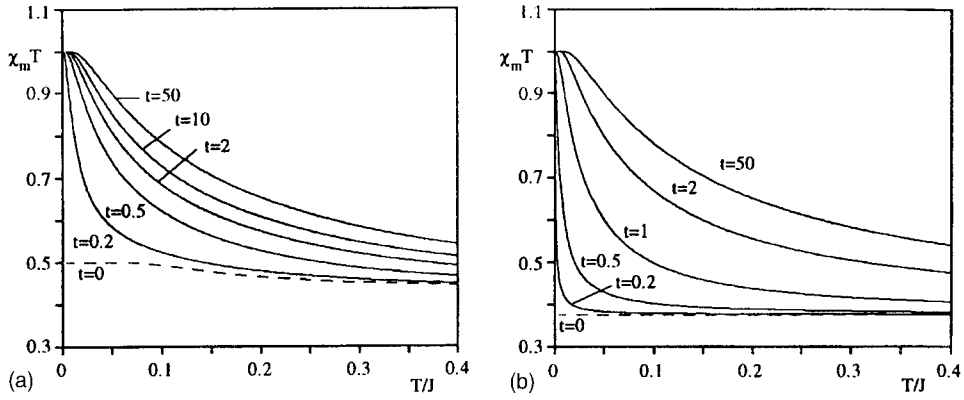

Fig. 46. Magnetic susceptibility for a 6-dimer closed chain: (a) strong exchange interaction ($U/J = 0$), (b) strong Coulomb interaction ($U/J = 5$). (t is in J units)

temperatures ($kT \ll 1$) the behavior corresponding to the sum of $n/2$ ferromagnetic dimers with $S = 1$; that is, the behavior of a paramagnet formed by $n/2$ spins $S = 1$ (dashed line in Fig. 46a).

In the another limit (strong Coulomb interaction), the electrons tend to be as separated as possible (Fig. 45e) stabilizing thus a ferroelectric charge ordered distribution (all the dipole moments are parallel). In such a situation the electrons can not be magnetically coupled and hence the chain will behave at low temperatures ($kT \ll U$) as a paramagnet formed by n spins $S = 1/2$ (dashed line in Fig. 46b). To summarize we can say that these two limiting cases keep the electrons fully localized on one of the two sites of the MV dimer preventing thus the occurrence of long range spin correlations.

When the electron transfer is taken into account, the above situation changes since the delocalization within the dimer leads to an electron density different from zero on both sites (Figs. 45b, d). This results in the stabilization of a parallel alignment of all the spins of the chain due to the ferromagnetic exchange interaction between nearest dimers, leading thus to a one-dimensional ferromagnetic behavior (Fig. 46). This finding is in agreement with the magnetic behavior exhibited by $[YPc_2]$ and $[ScPc_2]$ chains. We can see in the Fig. 46 that the increase of t leads to an increase in the ferromagnetic coupling between spins (the magnetic curves are shifted towards higher T). In the limit of very strong electron transfer this effective ferromagnetic coupling between delocalized electrons will reach its maximum value, since the electron density will be equally averaged over all the sites (Fig. 45c). It can be easily demonstrated that this value is $J/4$.

The electron delocalization account also for the low temperature minimum on the magnetic curve observed for a $[ScPc_2]$ chain. As one can see in Fig. 47, in the strong Coulomb interaction limit this minimum appears providing weak electron transfer. Indeed, in this case in the low temperature region $\chi_m T$ decreases abruptly with the increase of T from its ferromagnetic low temperature limit towards the limit corresponding to a paramagnet containing n spins $S = 1/2$. This is because the exchange pathways are broken by Coulomb repulsion and the electron transfer

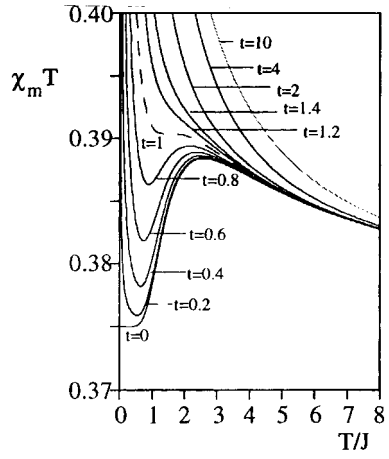

Fig. 47. Low-temperature minima in the case of strong Coulomb ($U/J = 5$) interaction. (t is in J units)

is too weak to promote visible one-dimensional ferromagnetism. Thus the system being formally ferromagnetic, exhibits the paramagnetic behavior inherent to n spins $S = 1/2$. The further increase of the temperature leads to the population of the excited states corresponding to the electronic distributions with partially restored exchange pathways. Therefore, the ferromagnetic coupling becomes more efficient leading thus to the increase of $\chi_m T$. In the case of strong electron transfer the exchange pathways are restored even for very low temperatures and we observe the monotonic ferromagnetic behavior.

5.8 Final Remarks

In this contribution we have examined the interplay between electron delocalization, magnetic exchange interactions and vibronic interactions in magnetic MV clusters and low-dimensional MV chains materials. We have focussed our attention on this kind of molecular systems since they constitute the simplest species on which the role played by the different physical processes in the electronic and magnetic properties of *mixed-valence magnetic materials* can be studied in a quantitative manner.

To take into account the electron delocalization in these MV magnetic systems is not an easy theoretical task since the dimension of the matrices to be diagonalized are much larger than that encountered in localized systems. The number of parameters also increases significantly. Thus, for example in a MV triangular cluster, the electronic problems involved besides the exchange interaction are both the two-site electron transfer (or double-exchange interaction) and the three-site electron transfer (exchange–transfer interaction). Moreover, we should also consider the vibronic coupling interaction which is an inherent problem for the MV systems. This feature strongly limits the correct analysis of the experimental data since the electronic and magnetic properties of MV systems will be the result of an intricate combination of parameters. Furthermore, it underlines the need of using several kinds of techniques

in order to get independent information on these parameters. This includes the use of molecular orbital techniques in order to evaluate the magnitude and sign of the transfer parameters.

Keeping in mind these remarks, it should be still useful to summarize the influence of the above parameters on the magnetic properties of the mixed valence systems:

5.8.1 Role of the Electron Transfer

This process results in a *spin-dependent electron delocalization* through the so-called double-exchange mechanism. In fully delocalized MV dimers, this process always leads to a symmetric splitting of the spin states, which is larger as the spin increases; therefore, a strong stabilization of the ferromagnetic spin state is predicted, independently of the sign of the double-exchange parameter t.

In contrast, in clusters of higher nuclearity the type of energy splitting for the spin states caused by electron transfer depends on the *topology* of the cluster. In many cases this splitting is unsymmetric with respect to the sign of t, so that the nature of the ground spin state depends on the sign of t. It follows that the electron delocalization can favor other spin states different from the ferromagnetic one. Hence, not always double-exchange favors a ferromagnetic spin coupling.

5.8.2 Role of the Second-order Electronic Processes

Electron transfer represents a first order process in the framework of the perturbation theory. Apart from this term, other two-site electronic interaction terms can also contribute to the splitting of the low-lying levels. The most important of these terms is the magnetic exchange which represents a second order electron-transfer process; therefore, the associated parameter J is expected to be of smaller magnitude than the double-exchange parameter. It follows that, in a delocalized MV dimer, the double-exchange will be the leading parameter. Indeed, the ferromagnetic contribution arising from double-exchange should exceed the antiferromagnetic exchange contribution, and a ferromagnetic ground state should be expected in this kind of systems.

The situation is different in clusters of nuclearity > 2 for two reasons. First, because other second order processes that may be of the same order of magnitude as the magnetic exchange can occur; these involve three-site (exchange–transfer) or/and four-site interactions (double-transfer). Second, because the splitting of the energy levels caused by electron delocalization is different. Thus, in trimers and higher nuclearity clusters double-exchange can give rise to a degenerate ground state formed by an extensive mixture of different spin states. In such situations these second order terms will be the leading parameters in determining the nature of the ground state as well as the type of splitting of the lower excited states, while double-exchange will play a minor role; for these systems a large variability in the spin of the ground state is to be expected, with a stabilization of the lower spin states even in presence of strong double-exchange.

5.8.3 Role of the Vibronic Coupling

The fully delocalized situation is rarely achieved in mixed-valence systems due to the coupling of electronic and nuclear movements. In all the above reported cases this vibronic interaction represents a trapping effect that tend to localize the extra electron. As intuitively expected this term leads to an effective reduction of the transfer parameter. In dimers for example the presence of a strong vibronic coupling restores the Heisenberg type energy pattern and therefore the antiferromagnetic spin state becomes the ground state.

It should be stressed however that *not always vibronic coupling has a localization effect*. This conclusion is valid in the framework of the PKS model that takes into account the nuclear motion of ligands coordinated to the central metal ions, neglecting the motion of the metals. However, other types of vibrational modes in which the intermetallic distances are allowed to vary can also be considered. The resulting vibronic coupling arises then from the modulation of the transfer integral t by the nuclear motion of the metals, and can promote the electron delocalization. This leads to a strong ferromagnetic contribution and delocalized electron states. Such a kind of vibronic coupling can be of outmost importance in the case of organic mixed valence systems as the interatomic C–C distances strongly vary with the molecular vibrations.

Acknowledgments

Financial support by the Ministerio de Educación y Cultura (Grant PB96-0862) and Generalitat Valenciana (Grand GVDOC00-01-02) are acknowledged. B.S.T. thanks the Universidad de Valencia for a visiting professor grant. J.M.C-J. thanks the Ministerio de Education for a postdoctoral grant.

References

[1] J. B. Goodenough, Prog. *Solid State Chem.* **1971**, *5*, 145.
[2] G. Blondin, J. J. Girerd, *Chem. Rev.* **1989**, *90*, 1359.
[3] (a) *Mixed Valence Compounds*, (Ed.: D. B. Brown), NATO ASI Series D, Riedel Publ. Comp., Dordrecht, **1979**; (b) L. Noodleman, D. Case, *Adv. in Inorg. Chem.*, **1982**, *38*, 423; (c) L. Noodleman, E.J. Baerends, *J. Am. Chem. Soc.*, **1984**, *106*, 2316; (d) J.M. Mouesca, J.L. Chen, L. Noodleman, D. Bashford, D.A. Case, *J. Am. Chem. Soc.*, **1994**, *116*, 11898; (f) J. Jorcanov, E.K.H. Roth, P.H. Fries, L. Noodleman, *Inorg. Chem.*, **1990**, *29*, 4228.
[4] *Mixed Valence Systems: Applications in Chemistry, Physics and Biology*, (Ed.: K. Prassides), NATO ASI Series C, *Vol. 343*, Kluwer Academic Publishers, Dordrecht, **1991**.
[5] K. Y. Wong, P. N. Schatz, *Prog. Inorg. Chem.* **1981**, *28*, 369.
[6] S. B. Piepho, *J. Am. Chem. Soc.* **1988**, *110*, 6319.
[7] S. B. Piepho, *J. Am. Chem. Soc.* **1990**, *112*, 4197.
[8] B. Bleaney, K. D. Bowers, *Proc. Roy. Soc. (London) Ser. A* **1952**, *214*, 451.
[9] *Magnetic Molecular Materials*, (Eds.: D. Gatteschi, O. Kahn, J. S. Miller, F. Palacio), NATO ASI Series E, *Vol. 198*, Kluwer Academic Publishers, Dordrecht, **1991**.

[10] C. Zener, *Phys. Rev.* **1951**, *82*, 403.
[11] C. N. R. Rao, *Chem. Eur. J.* **1996**, *2*, 1499.
[12] P. W. Anderson, H. Hasegawa, *Phys. Rev.* **1955**, *100*, 675.
[13] B. S. Tsukerblat, M. I. Belinskii, V. E. Fainzilberg, in Soviet *Sci. Rev. B., Vol. 9* (Ed.: M.E.Vol'pin), Harwood Acad. Pub., New York, **1987**, p. 337.
[14] E. Coronado, B. S. Tsukerblat, R. Georges, in *Molecular Magnetism: From Molecular Assemblies to the Devices*, NATO ASI Series E, *Vol. 321* (Eds.: E. Coronado, P. Delhaes, D. Gatteschi, J. S. Miller), Kluwer Academic Publishers, Dordrecht, **1995**, p. 65.
[15] J. J. Borrás-Almenar, E. Coronado, B. S. Tsukerblat, R. Georges, in *Molecular Magnetism: From Molecular Assemblies to the Devices*, NATO ASI Series E, *Vol. 321* (Eds.: E. Coronado, P. Delhaes, D. Gatteschi, J. S. Miller), Kluwer Academic Publishers, Dordrecht, **1995**, p. 105.
[16] B. S. Tsukerblat, A. V. Palii, V. Y. Gamurar, B. A. S., H. M. Kishinevskii, *Phys. Let. A* **1991**, *158*, 341.
[17] J. J. Borrás-Almenar, J. M. Clemente-Juan, E. Coronado, A. V. Palii, B. S. Tsukerblat, *Chem. Phys.*, **2000**, *254*, 275.
[18] M. V. Robin, P. Day, *Adv. Inorg. Radiochem.* **1967**, *10*, 247.
[19] S. B. Piepho, E. R. Krausz, P. N. Shatz, *J. Am. Chem. Soc.* **1978**, *100*, 2996.
[20] J. J. Borrás-Almenar, E. Coronado, S. M. Ovstrosvsky, A. V. Palii, B. S. Tsukerblat, *Chem. Phys.* **1999**, *240*, 149.
[21] S. Drüeke, P. Chaudhuri, K. Pohl, K. Wieghardt, X. Q. Ding, E. Bill, A. Sawaryn, A. X. Trautwein, H. Winkler, S. J. Gurman, *J. Chem. Soc. Chem. Commun.* **1989**, *59*.
[22] X. Q. Ding, E. L. Bominaar, B. E.Winkler, A. X. H. Trautwein, S. Drüeke, P. Chaudhuri, K. Wieghardt, *J. Chem. Phys.* **1990**, *92*, 178.
[23] A. Bencini, D. Gatteschi, L. Sacconi, *Inorg. Chem.* **1978**, *17*, 2670.
[24] (a) C.J. Gómez-García, E. Coronado, R. Georges, P.G., *Physica B* **1992**, *182*, 18; (b) G. Pourroy, E. Coronado, M. Dullon, R. Georges, *Chem.Phys.*, **1986**, *104*, 73; (c) M.J. Belinskii, *Sovret Phys.Solid.State*, **1985**, *27*, 1761; (d) M.J. Belinskii, *Mol. Phys.*, **1987**, *60*, 793.
[25] J. J. Borrás-Almenar, E. Coronado, A. V. Palii, B. S. Tsukerblat, R. Georges, *Chem. Phys.* **1998**, *226*, 231.
[26] J. J. Borrás-Almenar, E. Coronado, R. Georges, A. V. Palii, B. S. Tsukerblat, *Phys. Lett. A* **1996**, *220*, 342.
[27] J. J. Borrás-Almenar, E. Coronado, R. Georges, A. V. Palii, B. S. Tsukerblat, *Chem. Phys. Lett.* **1996**, *249*, 7.
[28] J. E. Hirsch, *Phys. Rev. Lett.* **1985**, *54*, 1317.
[29] J. J. Girerd, V. Papaefthymiou, K. K. Surerus, E. Münck, Pure *Appl. Chem.* **1989**, *61*, 805.
[30] G. Blondin, S. Borshch, J. J. Girerd, *Comments Inorg. Chem.* **1992**, *12*, 315.
[31] M.I. Belinskii, B.S. Tsukerblat, S.A. Zaitsev, I.S. Belinskaya, *New J. Chem.* **1992**, *16*, 791.
[32] A. V. Palii, S. M. Ostrovsky, B. S. Tsukerblat, *New J. Chem.* **1992**, *16*, 943.
[33] I. B. Bersuker, S. A. Borshch, in *Adv. in Chem. Phys., Vol. 81* (Eds.: Prigogine, S. A. Rice), **1992**, p. 703.
[34] I. B. Bersuker, *The Jahn–Teller effect and vibronic interactions in modern chemistry*, Plenum, New York, **1984**.
[35] S. I. Boldirev, V. Y. Gamurar, B. S. Tsukerblat, A. V. Palii, *Mol. Phys.* **1994**, *81*, 621.
[36] J. J. Borrás-Almenar, J. M. Clemente-Juan, E. Coronado, R. Georges, B. S. Tsukerblat, *J. Magn. Magn. Mater.* **1995**, *140–144*, 197.
[37] S. A. Borshch, L. F. Chibotaru, *Chem. Phys.* **1989**, *135*, 375.
[38] E. L. Bominar, S. A. Borshch, G. Blondin, J. J. Girerd, *J. Am. Chem. Soc.* **1994**, *116*, 5362.
[39] A. V. Babich, J. J. Borrás-Almenar, E. Coronado, A. V. Palii, B. S. Tsukerblat, *J. of Struct. Chem. (Engl. Transl.)* **1995**, *36*, 593.

[40] M. I. Riley, H. U. Güdel, A. Norton, *Chem. Phys.* **1992**, *166*, 19.
[41] J. J. Borrás-Almenar, J. M. Clemente-Juan, E. Coronado, S. M. Ostrovsky, A. V. Palii, B. S. Tsukerblat, Proceedings of *XIV International Symposium of Electron-Phonon Dynamics and Jahn–Teller Effect*, Vibronic interactions in mixed-valence clusters: General overview and applications, (Ed.: G. Bevilacqua, L. Martinelli, N. Terzi), World Scientific (Singapore), 1999, p. 302.
[42] Hendrickson, Cannon, in *Mixed Valence Systems: Applications in Chemistry, Physics and Biology*, NATO ASI series C, *Vol. 343* (Ed.: K. Prassides), Kluwer Academic Publishers, **1991**.
[43] J. J. Borrás-Almenar, R. Georges, S. I. Klokishner, E. Coronado, S. M. Ostrovskii, A. V. Palii, B. S. Tsukerblat, *J. of Struct. Chem. (Eng. Transl.)* **1996**, *37*, 699.
[44] J. J. Borrás-Almenar, R. Georges, S. I. Klokishner, E. Coronado, S. M. Ostrovskii, A. V. Palii, B. S. Tsukerblat, *J. of Struct. Chem. (Eng. Transl.)* **1996**, *37*, 689.
[45] A. Marks, K. Prassides, *New. J. Chem.* **1993**, *17*, 59.
[46] J. Jordanov, E. K. H. Roth, P. H. Fries, L. Noodelman, *Inorg. Chem.* **1990**, *29*, 4288.
[47] A. Marks, K. Prassides, *Chem. Phys.* **1994**, *179*, 93.
[48] J. J. Borrás-Almenar, E. Coronado, H. M. Kishinevskii, B. S. Tsukerblat, *Chem. Phys. Lett.* **1994**, *217*, 525.
[49] J. J. Borrás-Almenar, J. M. Clemente-Juan, E. Coronado, R. Georges, R. Kishinevskii, S. I. Klokishner, S. M. Ostrovskii, A. V. Palii, B. S. Tsukerblat, *J. Magn. Magn. Mat.* **1995**, *140–144*, 1807.
[50] J. M. Clemente-Juan, E. Coronado, *Coord. Chem. Rev.* **1999**, *193–195*, 361.
[51] A. Müller, F. Peters, M. T. Pope, D. Gatteschi, *Chem. Rev.* **1998**, *98*, 239.
[52] M. T. Pope, *Heteropoly and Isopoly Oxometalates*, Springer, Berlin, **1983**
[53] M. T. Pope, A. Müller, *Angew. Chem. Int. Ed. Eng.* **1991**, *30*, 34.
[54] *Polyoxometalates: from Platonic Solids to Anti-retroviral Activity*, (Eds.: M. T. Pope, A. Müller), Kluwer Academic Publishers, Dordrecht, **1994**.
[55] A. L. Barra, D. Gatteschi, B. S. Tsukerblat, J. Doring, A. Müller, L. C. Brunel, *Inorg. Chem.* **1992**, *31*, 5132.
[56] D. Gatteschi, B. S. Tsukerblat, *Mol. Phys.* **1993**, *79*, 121.
[57] D. Gatteschi, B. S. Tsukerblat, A. L. Barra, L. C. Brunel, A. Müller, J. Doring, *Inorg. Chem.* **1993**, *32*, 2114.
[58] N. Casañ-Pastor, L. C. W. Baker, *J. Am. Chem. Soc.* **1992**, *114*, 10384.
[59] J. J. Borrás-Almenar, J. M. Clemente, E. Coronado, A. V. Palii, B. S. Tsukerblat, R. Georges, *J. Chem. Phys.* **1996**, *105*, 6892.
[60] M. Kozik, C. F. Hammer, L. C. W. Baker, *J. Am. Chem. Soc.* **1986**, *108*, 2748.
[61] J. J. Borrás-Almenar, J. M. Clemente, E. Coronado, B. S. Tsukerblat, *Chem. Phys.* **1995**, *195*, 1.
[62] J. J. Borrás-Almenar, J. M. Clemente, E. Coronado, B. S. Tsukerblat, *Chem. Phys.* **1995**, *195*, 16.
[63] J. J. Borrás-Almenar, J. M. Clemente, E. Coronado, B. S. Tsukerblat, *Chem. Phys.* **1995**, *195*, 29.
[64] J. J. Borrás-Almenar, J. M. Clemente-Juan, E. Coronado, B. S. Tsukerblat, *Chem. Phys. Lett.* **1998**, 283, 363.
[65] J. J. Borrás-Almenar, J. M. Clemente, E. Coronado, A. V. Palii, B. S. Tsukerblat, *Mol. Cryst. Liq. Cryst.* **1997**, *306*, 209.
[66] J. L. Paillaud, M. Drillon, A. De Cian, J. Fischer, R. Weiss, G. Villeneuve, *Phys. Rev. Lett.* **1991**, *67*, 244.
[67] J. L. Paillaud, Doctoral Dissertation, *Université L. Pasteur*, **1991**.

Magnetism: Molecules to Materials I: Models and Experiments.
Edited by Joel S. Miller and Marc Drillon

ISBNs: 3-527-29772-3 (Hardback); 3-527-60084-1 (Electronic)

6 Magnetocrystalline Anisotropy of Transition Metals: Recent Achievements in X-ray Absorption Spectroscopy

Wilfried Grange, Jean Paul Kappler, and Mireille Maret

6.1 Introduction

This chapter provides an introduction to X-ray magnetic circular dichroism. It discusses the use of this technique for probing the microscopic origin of magnetocrystalline anisotropy in transition metal thin films. By use of an appropriate illustrative example we attempt to present an up-to-date account of this research field.

After the considerable improvement of X-ray synchrotron radiation sources (i. e. high brilliance, tuneable polarization of the light), new techniques have been developed to investigate the magnetic properties of thin films. These techniques (X-ray magnetic scattering, Compton scattering with circularly polarized light, X-ray magnetic circular dichroism ...) have grown into a major research branch of almost unlimited potential. This interest is closely connected to: 1) the elemental and orbital selectivity of X-ray absorption spectroscopy; and 2) the strong interaction of X-rays with matter (i. e. sensitivity down to the monolayer range).

In this chapter we have chosen to outline the main strengths of X-ray Magnetic Circular Dichroism (XMCD) and we will demonstrate that its use can greatly alter our basic understanding of the magnetocrystalline anisotropy (MCA) of transition metal thin films.

The text itself comprises two largely self-contained parts. Part 1 provides an introduction to the XMCD technique. Part 2 considers a second-order perturbation theory for the MCA energy; then emphasizes the importance of XMCD measurements for probing the microscopic origin of the MCA in transition metals. Finally, Part 3 illustrates the main ideas introduced in Parts 1 and 2.

6.2 The X-ray Magnetic Circular Dichroism Technique

This part is organized as follows. Section 2.1 is a brief historical introduction to magnetic dichroism effects, caused by the interplay of spin-polarization and spin-orbit coupling (Section 2.2). In Section 2.3, we introduce the XMCD sum rules that enable one to obtain reliable information on the micro-magnetism (the evaluation

and the separation of the spin and orbital magnetic moments on a specific shell and site). We assume throughout that the reader has a firm grasp of basic X-ray absorption.

6.2.1 An Historical Survey

It has long been known that chiral molecules present an optical activity at visible wavelengths. For achiral systems, an optical activity call also be induced by an external magnetic or electric field. The first magneto-optic effect has been discovered more than 150 years ago by Faraday who observed a rotation of the plane of polarization of radiation passing though glass in the direction of an applied magnetic field. In the visible range, the Kerr effect (the rotation of the plane of polarization and the change in ellipticity) is a similar effect to the Faraday effect; and is currently used in most laboratories to characterize the macroscopic magnetic properties of compounds. Microscopically the change in ellipticity arises because of a difference in absorption for right- and left-handed circularly polarized light. In other words, it is a magnetic circular dichroism effect at visible wavelengths.

Because the electronic transitions at these wavelengths are difficult to describe, it is still a challenge to investigate the Kerr effect theoretically (the first Kerr spectrum was calculated in 1992 by Oppeneer [1]). The situation is, however, much more simple at X-ray wavelengths, because the latter involve electronic excitations from a well defined core-hole initial state. In this respect, Erskine and Stern [2] succeeded in calculating the XMCD at the $L_{2,3}$ edges of nickel in 1975. They realized that it would also be possible to probe experimentally the local magnetic properties of ferromagnetic compounds. Ten years later, Thole [3] performed calculations at the $M_{4,5}$ edges of rare earth metals predicting a strong X-ray Magnetic Linear Dichroism (XMLD) effect, i. e. depending on the relative orientation of the electrical field and the magnetization. Because of the considerable development of brilliant X-ray synchrotron radiation sources, van der Laan [4] measured a XMLD signal at the $M_{4,5}$ edges of terbium and confirmed Thole's theoretical predictions. Finally, the first XMCD spectrum was measured in 1987 by the team of Materlik [5] at the Fe K edge.

XMLD and XMCD are two powerful and appealing techniques that enable investigation of previously inaccessible magnetic properties. Until recently, less attention has been paid to the XMLD technique, because it measures the expectation value of the square of the magnetization $\langle M^2 \rangle$ (on a specific shell and site). This limitation is overcome by the use of XMCD from which the orbital and spin contributions to the magnetic moment (on a specific shell and site) are obtained.

6.2.2 Theoretical Background

XMCD is defined as the difference between the absorption of right- and left-handed circularly polarized light when the applied magnetic field (that determines the direction of the magnetization) is parallel to the incident X-ray wave-vector. (Although

there have been some fluctuations in the conventions used for XMCD in the past, an XMCD measurement performed at the $L_{2,3}$ edges of Co-hcp single crystal should yield negative and positive signs, respectively, at the L_3 and L_2 edges.) According to Schütz [6], the mechanisms involved in the XMCD at the $L_{2,3}$ edges of 3d metals can, to some extent, be understood in a simple two-step model. In a first step, core-hole electrons are spin-polarized by X-ray circularly polarized photons; in a second step, the valence band acts as a spin detector (Fig. 1). These two steps are assumed to be independent. In the absence of spin-orbit interaction, incident X-rays transfer their angular momentum to the orbital part, $\vec{l}$, of the excited photoelectrons, only. When the 2p level is split by the spin–orbit interaction into well defined $2p_{1/2}$ (L_2 edge) and $2p_{3/2}$ (L_3 edge) sub-levels, however, the electronic states are no longer pure spin states. Left-handed circularly polarized photons have their angular momentum σ^* parallel to the direction of the incoming beam and favor the excitation of spin-up photoelectrons at the L_3 edge. (The quantization axis is determined by the direction of the magnetic field.) Indeed, the probability of exciting a photoelectron with spin-up is maximum, because $\vec{l}$, $\vec{s}$, and $\vec{\sigma}^*$ are parallel. (Using standard notation, we define $\vec{l}$ and $\vec{s}$, respectively, as the one-electron orbital and spin angular momentum.) At the L_2 edge, $\vec{\sigma}^*$ and $\vec{s}$ are anti-parallel. Hence, left-handed circularly polarized photons will excite more spin-down photoelectrons. Right-handed circularly polarized photons have their angular momentum anti-parallel to the direction of the incoming beam and will excite spin polarized photoelectrons in reverse proportions. As suggested previously, the valence band acts as a spin-detector if it carries a nonzero magnetic moment. In other words, if there is a difference in the spin-up and spin-down populations.

At first glance, the two-step model seems to be a crude and simple approximation of the physical mechanisms that govern XMCD. ("Pronounced" XMCD spectra have been measured for the K edge ($l = 0$) of 3d transition metals, [5]. Thus the spin–orbit coupling of the final states also contributes to the XMCD. Its interpretation is rather difficult and multiple scattering theory must be used to reproduce the experimental spectra [8].) It states however correctly that XMCD is primarily governed by: 1) the

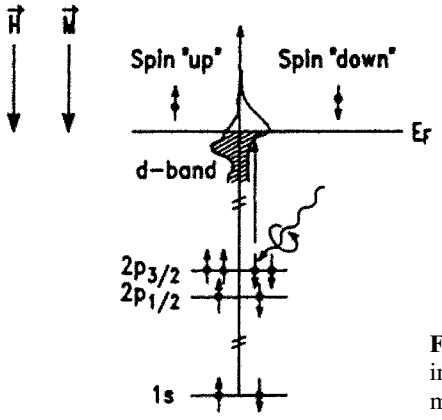

Fig. 1. A two-step model illustrating the mechanisms involved in XMCD at the $L_{2,3}$ edges of 3d transition metals [7]

spin–orbit coupling of the core-hole states: 2) the exchange splitting in the valence band.

6.2.3 The Sum Rules

We shall now introduce the optical sum rules and briefly discuss their limitations. A critical and exhaustive discussion of the sum rules can be found elsewhere [9].

For clarity, we define I_{L_2} and I_{L_3} as the dichroic intensities involving electronic excitation from the $2p_{1/2}$ and $2p_{3/2}$ sub-levels, respectively. As outlined in the previous section, $\vec{l}$ and $\vec{s}$ are parallel in the $2p_{3/2}$ sub-level, anti-parallel in the $2p_{1/2}$ sub-level. We could therefore expect that the combination $(I_{L_3} + I_{L_2})$ would account for orbital polarization, only. Alternatively, the combination $(I_{L_3} - I_{L_2})$ would be a direct measure of the spin-polarization.

We realize now that a proper linear combination of the dichroic intensities measured oil two core-hole absorption edges $c + (1/2)$ and $c - (1/2)$ might provide quantitative information on both the orbital (orbital sum rule [10]) and spin (spin sum rule [11]) magnetic moments in the valence band.

For a transition from a core hole absorption edge c towards a valence band state l and assuming that the $c + 1$ absorption channel is the main absorption channel, the two sum rules can be written as (for simplicity, we assume that the incident wave-vector $\vec{k}$ and the applied magnetic field $\vec{H}_{\text{ext}}$ are parallel to the z direction):

$$\frac{\int_{j^+ + j^-}(I^{-1} - I^{+1})}{\int_{j^+ + j^-}(I^1 + I^0 + I^{-1})} = \frac{\langle L_z \rangle}{l \cdot n_h} \tag{1}$$

$$\frac{\int (I^{-1} - I^1) - \dfrac{l}{l-1}\displaystyle\int_{j^-}(I^{-1} - I^1)}{\int_{j^+ + j^-}(I^1 + I^0 + I^{-1})} = \frac{2}{3n_h}\left[\langle S_z \rangle + \frac{2l+3}{l}\langle T_z \rangle\right] \tag{2}$$

$j^{\pm} = c(\pm)1/2$, the I^q terms denote the normalized absorption cross-section (the usual absorption cross-section σ divided by the energy) obtained for left-handed circularly polarized light ($q = -1$), right-handed circularly polarized light ($q = -1$), and linear polarization parallel to the magnetic field ($q = 0$), respectively. $\langle L_z \rangle$ ($\langle S_z \rangle$) is the expectation value of the orbital (spin) magnetic moment. Finally, $\langle T_z \rangle$ denotes the expectation value of the magnetic dipole term, which describes the nonsphericity of the spin–charge distribution:

$$\langle T_z \rangle = \sum_{i,\alpha} \langle Q_{iz\alpha} \rangle \langle s_{i\alpha} \rangle = \sum_i \langle Q_{izz} \rangle \langle s_{iz} \rangle \tag{3}$$

where $r_{i\alpha}$ ($s_{i\alpha}$) denotes the projection of the position (spin) operator of an electron i on to the direction α, and Q is the quadripolar moment operator of the electronic charge distribution. (The relationships between the expected values of momentum operators and the corresponding magnetic moments are: $m_{\text{orb}} = -(\mu_B)\langle L_z \rangle$ for the

orbital magnetic moment, $m_{\text{spin}} = -(2\mu_{\text{B}})\langle L_z\rangle$ for the spin magnetic moment, and $m_{\text{dip}} = +(\mu_{\text{B}})\langle T_z\rangle$ for the magnetic dipole term.)

We shall outline that the derivation of the XMCD sum rules is based on several important assumptions; however, numerous experimental and theoretical studies have shown that they are sufficiently "robust" to be applied when the latter assumptions are a priori not fulfilled [12–15].

6.2.3.1 The Magnetic Dipole Term

The magnetic dipole term arises from the anisotropy of the spin density within the Wigner-Seitz cell [11]. It can therefore represent a significant contribution to the effective spin magnetic moment, $m_{\text{spin}}^{\text{eff}}$ [$m_{\text{spin}}^{\text{eff}} = m_{\text{spin}} - (4l + 6)m_{\text{dip}}/l$), i. e. the quantity directly determined using Eq. (2)] for a low-symmetry crystal environment or a high spin–orbit coupling.

For instance, Wu and Freeman [16] have shown that the use of the spin sum rule could result in an error up to 50% for the (001) surface of Ni. Note, however, that the m_{dip} contribution can be safety neglected when the spin–orbit coupling amplitude, ξ, is small relative to the crystal-field parameters Δ_{cf}. Then Eq. (3) becomes:

$$\langle T_z\rangle = \sum_{i,\alpha}\langle Q_{iz\alpha}\rangle\langle s_{i\alpha}\rangle = \sum_{i}\langle Q_{izz}\rangle\langle s_{iz}\rangle \tag{4}$$

(Equation (4) is obtained by separating the spin and position variables, i. e. writing $\langle s_{i\alpha}\rangle = \langle s_i\rangle$ for any α direction. In perturbation theory, the induced spin–orbit coupling corrections to the magnetic dipole term are only ca 10% [17].) In this relationship it is assumed that the spin magnetic moment re-orients along the direction of the external magnetic field (z direction). Because $\sum_\alpha\langle Q_{\alpha\alpha}\rangle = 0$ in a Cartesian frame, the contribution of m_{dip} vanishes when three independent XMCD measurements are performed along three orthogonal directions. Similarly, $m_{\text{spin}}^{\text{eff}} = m_{\text{spin}}$ for a polycrystalline sample ($\xi \ll \Delta_{\text{cf}}$). (For itinerant 4d (5d) electrons it is generally assumed that the m_{dip} contribution is rather small [14,18].)

6.2.4 Conclusion

XMCD is a local probe of magnetism that enables separate determination of both the orbital and spin magnetic moments on a specific shell and site. In the last decade, XMCD has become a powerful and valuable technique for investigation of some magnetic properties that had not previously been accessible. We shall now mention some of the most significant XMCD results.

In Fe/Cu/Co magnetic multilayers, Chen [19] has determined separately the Fe and Co magnetic hysteresis and has studied the magnetic coupling mechanisms. Because the interaction of X-rays with matter is very strong at the $L_{2,3}$ edges of transition metals, XMCD is capable of determining the magnetic properties at surfaces or interfaces in such systems. For instance, XMCD measurements have confirmed the results

of ab initio calculations that predicted enhancement of the Co-3d orbital magnetic moment in Co/Pd multilayers [20,21]. XMCD spectroscopy in conjunction with photoelectron emission microscopy enables the recording of magnetic domain images with lateral resolution comparable with that obtained in magnetic force microscope experiments [22]. Finally, XMCD has revealed the microscopic origin of the MCA in transition metal thin films [23,24]. This will be discussed in detail in Section 3.

6.3 The Anisotropy of the Orbital Magnetic Moment: A Relevant Parameter for the Anisotropy Energy

In a ferromagnetic system, the direction of the net magnetization is determined by the anisotropy energy E_{MAE}, which is the difference in free energy when the direction of the magnetization is rotated from an easy to an hard direction of magnetization. The microscopic origin of E_{MAE} cannot be explained by the exchange interaction since this latter is invariant when the spin direction is changed. There are therefore other interactions that couple the spin magnetic moment to the lattice. Dipole–dipole interactions only contribute to a less extend to this coupling and are responsible for the so-called shape anisotropy energy.

6.3.1 Probing the Magnetocrystalline Anisotropy Energy

In 1937, van Vleck [25] suggested that the coupling between the magnetization and the lattice could be explained by the following relevant physical quantities: 1) the orbital magnetic moment, 2) the crystal field; and 3) the spin–orbit coupling. According to van Vleck, the electronic charge distribution, i. e. the orbital moment, is coupled to the lattice via the electrical field arising from the surrounding ions. Because of spin–orbit coupling, the spin magnetic moment (which is the main contribution to the magnetic moment for 3d transition metals) is only slightly affected by the crystal symmetry. This contribution is called the MCA energy E_{MCA}.

From the pioneer work of van Vleck to the late eighties, experimenters have concentrated mainly on explaining the origin of the MCA in this way (i. e. qualitatively) and have characterized E_{MCA} in terms of phenomenological anisotropy energy constants. These constants can be determined from macroscopic magnetic measurements, e. g. torque magnetometry, ferromagnetic resonance, and magnetization measurements. They can, moreover, be easily compared with those obtained from calculations (which consist in computing the difference in total energy for two principal crystallographic directions). Because the MCA is relatively small in bulk 3d cubic transition metals ($E_{\mathrm{MCA}} \sim \mu$eV per atom), such calculations are still a real "tour de force". For instance, calculations based on the local spin density approximation fail to reproduce the correct easy axis of magnetization for Ni metal [26]. For reduced dimensionality structures (thin-film sandwiches, multilayers, dots), the

results of such ab initio approaches also overestimate the MCA. It might, furthermore, be difficult for experimenters to recognize the relevant physical parameters that govern the MCA.

One consistent trend in magnetism, however, has been the progression towards increasingly quantitative methods. This trend has been accelerated over the past decade because of the considerable interest in magnetic or magneto-optic information technology. In 1989, an effective and appropriate relation between the MCA, the anisotropy of the orbital magnetic moment $m_{\mathrm{orb}}^{\mathrm{A}}$ and the spin–orbit coupling ξ (i. e. the different parameters outlined by van Vleck) has been derived by Bruno [27,28]:

$$E_{\mathrm{MCA}} \approx -\xi m_{\mathrm{orb}}^{\mathrm{A}} \tag{5}$$

where, using standard notation, we have defined ξ as the integrated value of the radial part $\xi(r)$ of the spin–orbit coupling interaction.

The advantage of Bruno's relation is the direct explanation of the enhancement of the MCA in thin films. At the surface, the breaking of symmetry leads to a large difference in the bandwidth for the in-plane and out-of-plane orbitals. This yields strongly anisotropic orbital magnetic moments and therefore a large MCA. In principle, various technique are capable of measuring an anisotropy of the orbital magnetic moment:

- In a Co-hcp single crystal, macroscopic magnetization measurements have provided evidence for an anisotropy in the total magnetization (which results entirely from the anisotropy of the orbital magnetic moment since the spin magnetic moment is a priori an isotropic quantity) [29].
- Polarized neutron diffraction measurements enable separate determination of the spin and orbital magnetic moments in single crystals.
- Also, ferromagnetic resonance measures the g factor that is proportional to the $m_{\mathrm{orb}}/m_{\mathrm{spin}}$ ratio [30].

These techniques are however hardly feasible in thin films or bulk systems because $m_{\mathrm{orb}} \approx 0.1\,\mu_{\mathrm{B}}$. Owing to its sensitivity and element-specificity (Section 2.4), we feel that XMCD is the most appropriate and valuable technique to provide experimental support for Bruno's approach.

6.3.2 A Perturbation Approach

In this section, we present in details the perturbation approach of the MCA proposed by Bruno and discuss its limitations.

6.3.2.1 The Anisotropy of the Magnetization

From the early sixties, numerous theoretical and experimental studies have outlined the possible connection between the anisotropy of the orbital magnetic moment and

the anisotropy energy. An exhaustive bibliography of these studies can be found elsewhere [31]. In 1960, Callen [32] suggested that the anisotropy of macroscopic magnetization should be large in materials having a large MCA. According to Callen the MCA tends to align the individual spin magnetic moments along an easy axis of magnetization (and therefore tends to increase the magnitude of the magnetization), whereas it favors the dispersion of the individual spin magnetic moments along the hard axis (and therefore tends to reduce the magnitude of the magnetization). On the basis of this work, Aubert measured the anisotropy of the total magnetization of ca $0.1\,\mathrm{emu\,cm^{-3}}$ ($T = 4.2\,\mathrm{K}$) in a single crystal of nickel [33]. Unfortunately, this behavior was not reproduced satisfactorily by theory – for example, the model proposed by Callen predicts vanishing anisotropy at $T = 0$. In tackling these problems, Aubert proposed a new approach and suggested that the anisotropy of the magnetization resulted entirely from anisotropy of the orbital magnetic moment. Five years later, electronic band structure calculations corroborated this suggestion [34]. Finally, in 1989 Bruno derived the first linear relation between the MCA and the relevant physical parameters that govern this quantity.

6.3.2.2 Theoretical Background

The theory presented in this section is applicable to 3d transition metals only; that for rare earth metals is discussed elsewhere [35].

For 3d metals development in second-order perturbation theory is justified, because the integrated value of the spin–orbit coupling amplitude $\xi(r)$ is small relative to the electronic bandwidth. The lowest-order contribution to the spin–orbit coupling change in the total energy becomes second-order (because of time-reversal symmetry, the spin–orbit coupling contribution vanishes in first-order perturbation theory.):

$$\delta E = \sum_{\mathrm{ex}} \frac{\langle gr|\boldsymbol{H}_{\mathrm{so}}|ex\rangle\langle ex|\boldsymbol{H}_{\mathrm{so}}|gr\rangle}{E_{\mathrm{gr}} - E_{\mathrm{ex}}} \tag{6}$$

Similarly, the expectation value of the orbital moment operator is written (in first-order perturbation theory) as:

$$\langle \vec{L}_v \rangle = \sum_{\mathrm{ex}} \langle gr|\vec{L}_v|ex\rangle \frac{\langle ex|\boldsymbol{H}_{\mathrm{so}}|gr\rangle}{E_{\mathrm{gr}} - E_{\mathrm{ex}}} \tag{7}$$

In Eqs. (6) and (7) $\boldsymbol{H}_{\mathrm{so}}$ is the spin–orbit coupling Hamiltonian ($\boldsymbol{H}_{\mathrm{so}} = \xi(r)\vec{L}\cdot\vec{S}$), $|gr\rangle$ ($|ex\rangle$) denotes a nonperturbed (excited) state, and E_{gr} (E_{ex}) are the corresponding one-electron energies. The only excitations that have to be considered are those that involve an electronic transition from an occupied state to an unoccupied state above the Fermi level ($E_{\mathrm{gr}} < E_{\mathrm{f}} < E_{\mathrm{ex}}$). If we further assume that the exchange coupling, Δ_{exc}, is large relative to the crystal-field parameters, Δ_{cf}, we can: 1) neglect the coupling between the spin-up (majority spin band) and spin-down (minority spin band) states; and 2) assume that the majority spin band is completely filled. With these assumptions, the tight-binding approach proposed by Bruno yields [27,28]:

$$\delta E \approx -\frac{1}{4}\xi \hat{S} \cdot \vec{m}_{\mathrm{orb}}^{\downarrow} \tag{8}$$

where $\hat{S}$ denotes a unit-vector along the direction of the spin magnetic moment (along the direction of the magnetic field) and $\vec{m}_{\mathrm{orb}}^{\downarrow}$ denotes the orbital magnetic moment in the minority spin band. Hence, the MCA energy, i. e. the difference between the total energy for two principal crystallographic directions (say z and x) is (assuming that the majority spin band is completely filled):

$$E_{\mathrm{MCA}} \approx -\frac{1}{4}\xi (m_{\mathrm{orb}}^{z} - m_{\mathrm{orb}}^{x})^{\downarrow} \tag{9}$$

for uniaxial symmetry, and assuming $\Delta_{\mathrm{exc}} \gg \Delta_{\mathrm{cf}}$. (We use the same notation as elsewhere [27] – $E_{\mathrm{MCA}} = \delta E_z - \delta E_x = -K_1^{\mathrm{MC}}$, where K_1^{MC} denotes the second-order anisotropy constant.) The MCA anisotropy can therefore be computed directly, without taking into account the energy of the nonperturbed states. In general, we cannot neglect the coupling between spin-up and spin-down states, neither assume that the majority spin band is filled. In this case Eq. (9) reads (taking into account holes in the spin majority band) [36]:

$$\begin{aligned} E_{\mathrm{MCA}} \approx & -\frac{1}{4}\xi \left[(m_{\mathrm{orb}}^{z} - m_{\mathrm{orb}}^{x})^{\downarrow} - (m_{\mathrm{orb}}^{z} - m_{\mathrm{orb}}^{x})^{\uparrow} \right] \\ & + \frac{21\xi^2}{2\Delta_{\mathrm{exc}}} (m_{\mathrm{dip}}^{z} - m_{\mathrm{dip}}^{x}) \end{aligned} \tag{10}$$

In the limit of strong exchange coupling (3d metals), the last term of Eq. (10) can be safely neglected because it scales as $\xi^2/\Delta_{\mathrm{exc}}$ [36,37]. Eq. (10) states also that the MCA is no longer proportional to the anisotropy of the orbital magnetic moment but to the difference between orbital magnetic moment of the spin-up and spin-down contributions. For nonsaturated ferromagnets such as Fe metal, the latter contribution cannot be ignored (to do so can lead to pronounced errors because XMCD measures $m_{\mathrm{orb}}^{\downarrow} + m_{\mathrm{orb}}^{\uparrow}$) .

As far as we are aware, the angle-dependent XMCD measurements of Weller et al. [23] first succeeded in demonstrating the validity of Bruno's relationship. For four Co monolayers, this study found evidence for anisotropy in the orbital magnetic moment of ca 0.14 μ_{B}, in good agreement with Bruno's theoretical predictions. Unfortunately, the observed anisotropy of the orbital magnetic moment had to be scaled down to match the experimental MCA values obtained from conventional macroscopic magnetization measurements. This can be attributed to two assumptions:

- the change in the Fermi surface because of the spin–orbit coupling is neglected (and we should introduce a correcting factor of the opposite sign [27]); and
- the exchange splitting is assumed to be larger than the bandwidth (while W $\approx$ 5 eV and $\Delta_{\mathrm{exc}} \approx 1$ eV in 3d transition metals).

We also point out that:

- Eqs. (9) and (10) are valid at $T = 0$, only; and
- ab initio calculations have shown that there is no simple linear relationship between $m_{\mathrm{orb}}^{\mathrm{A}}$ and E_{MCA} [38,39].

The previous discussion emphasizes that it is certainly difficult to obtain a quantitative value of the MCA energy from XMCD. For this reason, the anisotropy is generally discussed only qualitatively in terms of the anisotropy of the orbital magnetic moment. We should, however, state that the main advantage of XMCD over conventional techniques such as torque measurements is that XMCD is element-specific.

6.3.3 XMCD Measurements in Collinear and Transverse Geometries

In this section, we demonstrate that the anisotropy of both the orbital and effective spin magnetic moments can be easily obtained from XMCD measurements performed in a collinear ($\vec{H}_{\text{ext}} \parallel \vec{k}$) or a transverse ($\vec{H}_{\text{ext}} \perp \vec{k}$) experimental arrangement.

6.3.3.1 Collinear Geometry

As mentioned in Section 2.3, the XMCD sum rules (Eqs. 1 and 2) relate the integrated XMCD signal to the orbital and effective spin magnetic moments. These relations can be re-written as (for the $L_{2,3}$ edges of transition metals):

$$\vec{m}_{\text{orb}} \cdot \hat{P} = -\frac{2Q^{\gamma}(10-n)}{3A} \tag{11}$$

$$(\vec{m}_{\text{spin}} - 7\vec{m}_{\text{dip}}) \cdot \hat{P} = -\frac{(3P^{\gamma} - 2Q^{\gamma})(10-n)}{A} \tag{12}$$

As seen in Section 2, the I_{q} terms denote normalized absorption cross-sections. To save space, however, we implicitly assume that the integration is carefully performed. In Eqs. (11) and (12) $\hat{P}$ denotes a unit-vector along the direction of the incident X-ray photons (parallel to the direction of the external magnetic field in a collinear set-up), γ is the angle between the direction of the incident photons and a reference direction (e. g. parallel to the normal to the surface, Fig. 2), Q^{γ} denotes the integrated XMCD signal over the L_2 and L_3 edges (corrected for the finite rate of circular polarization (CP)), P^{γ} denotes the integrated XMCD signal (corrected for CP) over the L_3 edge, A is the integrated isotropic absorption cross-section involving transitions towards

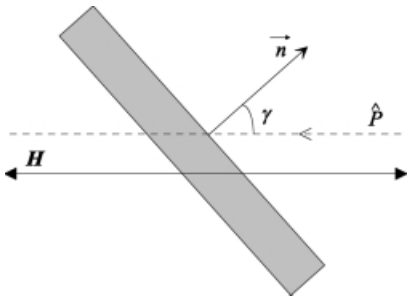

Fig. 2. The angle γ, defined as the angle between the direction $\hat{P}$ of the incident wave-vector and a reference direction, e. g. the normal to the surface

the different nd states (n = 3 for 3d transition metals), and n is the number of electrons in the d shell under study.

Equation (7) shows that the orbital magnetic moment can be expressed in terms of the $\langle ex|\boldsymbol{H}_{so}|gr\rangle$ angular matrix elements. This gives [36]:

$$\vec{m}_{orb} = R\vec{S} \tag{13}$$

where R is a second-rank Cartesian tensor (diagonal in an appropriate referential). For uniaxial symmetry and a 3d transition metal, the angular dependence of $\vec{m}_{orb}$ is [27,36,40]:

$$m^{\gamma}_{orb} = R_{zz} + (R_{xx} - R_{zz}) \sin^2 \gamma \tag{14}$$

where z is the uniaxial direction (in the xy plane all directions are equivalent, thus $R_{xx} = R_{yy}$) and m^{γ}_{orb} denotes the projection of $\vec{m}_{orb}$ on to the direction of $\vec{S}$ (γ is the angle between the z direction and the direction of the spin magnetic moment) Because R_{zz} and R_{xx} have different values in an anisotropic compound, we realize that the orbital magnetic moment cannot be collinear with the spin magnetic moment when the latter lies along a nonprincipal crystallographic direction (Fig. 3). We shall return to this point later.

Similarly, the angular dependence of the magnetic dipole term can be determined. Because, for a 3d transition metal, the magnetic dipole term only describes a quadripolar term in the spin charge distribution around the nucleus, Eq. (4) takes the form:

$$\vec{m}_{dip} = Q^* \hat{S} \tag{15}$$

where Q^* is a second-rank tensor with vanishing trace. Because the angular dependence of m_{dip} and m_{orb} is constrained by the crystal field only:

$$m^{\gamma}_{dip} = Q^*_{zz} + (Q^*_{xx} - Q^*_{zz}) \sin^2 \gamma \tag{16}$$

In a collinear geometry and for a 3d transition metal with uniaxial symmetry, the XMCD sum rules read (assuming the magnetic field is large enough to align the spin magnetic moment along the direction of the incident photons, i. e. $\hat{P} \parallel \vec{m}_{spin}$):

$$m^{\gamma}_{orb} = (R_{zz} \cos^2 \gamma + R_{xx} \sin^2 \gamma) = \Omega^{\gamma}_{exp} \tag{17}$$

$$m^{\mathrm{eff},\gamma}_{spin} = m_{spin} - 7(Q^*_{zz} \cos^2 \gamma + Q^*_{xx} \sin^2 \gamma) = \Lambda^{\gamma}_{exp} \tag{18}$$

In Eqs. (17) and (18), Ω^{γ}_{exp} and Λ^{γ}_{exp} are the experimental XMCD values which appear on the right-hand sides of Eqs. (11) and (12), respectively. (In Eq. (18), it is assumed the spin magnetic moment is an isotropic quantity. In second-order perturbation theory, the induced spin–orbit corrections are ca $(\xi/\Delta_{exc})^2$ i. e. 1% for a 3d transition metal [17].) Although, in practice, it is a difficult task to measure absorption spectra at grazing incidence, the anisotropy of the orbital magnetic moment

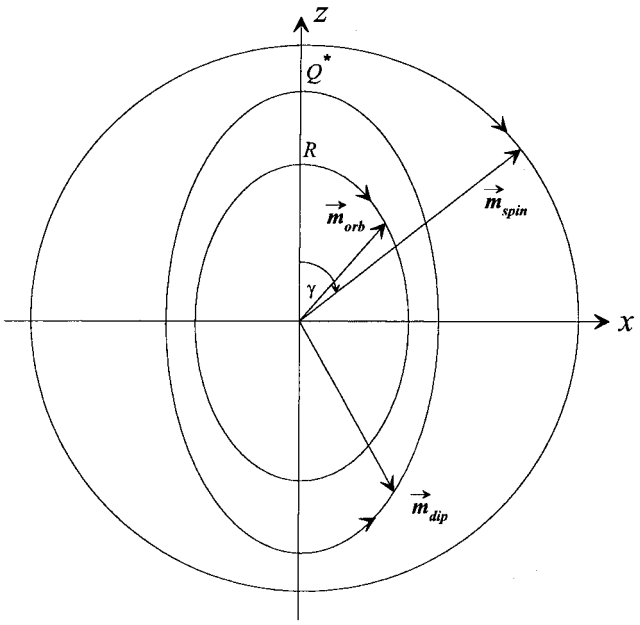

Fig. 3. The angular dependence of the ground state magnetic moments for a 3d transition metal and uniaxial symmetry (in second-order perturbation theory). We assume that the R and Q^* Cartesian tensors have their principal axis along the x and z axes. (denotes the angle between the direction of the spin magnetic moment (the direction of the applied magnetic field) and the z direction (Fig. 2) [41]

$m_{\mathrm{orb}}^{\mathrm{A}} = R_{zz} - R_{xx}$) can be estimated from its angular dependence (Eq. 14). Similarly, two angle-dependent XMCD measurements enable separation of the spin magnetic moment and the magnetic dipole term (Eq. 16). (Because the effective spin magnetic moment is the sum of an anisotropic and isotropic term, the latter demonstration also holds for nonuniaxial symmetry and a 4d (5d) transition metal.)

6.3.3.2 Transverse Geometry

A transverse XMCD measurement is an appealing means of determining directly the anisotropy of both the orbital and effective spin magnetic moments. As outlined in the previous section, m_{orb} and m_{dip} are no longer collinear with the spin magnetic moment if the magnetic field is applied along a direction other than a crystallographic axis (Fig. 3; Eqs. 13 and 15). (The angle between m_{dip} (m_{orb}) and m_{spin} is determined by the relative magnitude of the crystal field and the spin–orbit coupling. Because ξ is small relative to Δ_{cf} for 3d transition metals, the crystal field (which tends to re-align the magnetic moments along principal crystallographic directions) causes

noncollinear alignment of m_{dip} (m_{orb}) and m_{spin}. The situation might be different for actinides where $\xi \gg \Delta_{\mathrm{cf}}$.) It is therefore possible to obtain a nonvanishing XMCD signal for this particular geometry, which is in principle forbidden [24,36]. In the transverse geometry, we have (for uniaxial symmetry and a 3d transition metal and assuming that the magnetic field is strong enough to align the spin magnetic moment along the above defined direction):

$$(R_{zz} - R_{xx}) \cos\gamma \sin\gamma = \Omega^{\gamma}_{\mathrm{exp},t} \tag{19}$$

$$7(Q^{*}_{zz} - Q^{*}_{xx}) \cos\gamma \sin\gamma = \Lambda^{\gamma}_{\mathrm{exp},t} \tag{20}$$

where γ denotes, as previously, the angle between the direction of the incident X-ray photons and the z axis. The subscript t is relative to XMCD measurements performed in a transverse experimental arrangement. For $\gamma = \pi/4$, Eqs. (19) and (20) become:

$$(m^{z}_{\mathrm{orb}} - m^{x}_{\mathrm{orb}}) = 2\Omega^{\pi/4}_{\mathrm{exp},t} \tag{21}$$

$$(m^{z}_{\mathrm{dip}} - m^{x}_{\mathrm{dip}}) = \frac{2}{7}\Lambda^{\gamma/\pi 4}_{\mathrm{exp},t} \tag{22}$$

which are valuable relationships for determining the anisotropy of the orbital and effective spin magnetic moments.

6.3.3.3 A "Magic" Geometry

A collinear XMCD measurement performed at $\gamma = (\arccos(-1/3)/2) \approx 54.7^{\circ}$ gives:

- the isotropic part, m^{*}_{orb}, of the orbital magnetic moment ($m^{*}_{\mathrm{orb}} = (m^{z}_{\mathrm{orb}} + 2m^{x}_{\mathrm{orb}})/3$); Eq. 17); and
- the spin magnetic moment, i. e. the isotropic part of the effective spin magnetic moment (Eq. (18).

In other words, there is a peculiar angle, known as the "magic" angle, for which $m_{\mathrm{dip}} \perp m_{\mathrm{spin}}$. The physical reason for this behavior is that because Q^{*} is a tensor with vanishing trace ($m^{z}_{\mathrm{dip}} + 2m^{x}_{\mathrm{dip}} = 0$), the magnetic dipole term should be anti-parallel to the spin magnetic moment along the z or x axis. There should, therefore be an angle for which the projection of m_{dip} along m_{spin} vanishes [42].

Finally, we remark that Eqs. (17) and (18) are the main relationships that will be used in the forthcoming sections. It should be remembered that these relations rely on the approximations:

- the spin–orbit coupling is assumed to be small with respect to the crystal field parameters (when a second-order perturbation holds); and
- the symmetry is assumed to be uniaxial.

For convenience, we also define the isotropic (I) and anisotropic (A) variables:

$$
\begin{aligned}
m_{\mathrm{orb}}^{I} &= \frac{1}{3}Tr(R) = \frac{1}{3}(R_{zz} + 2R_{xx}) \\
m_{\mathrm{orb}}^{A} &= R_{zz} - R_{xx} \\
m_{\mathrm{spin}}^{\mathrm{eff},I} &= m_{\mathrm{spin}} \\
m_{\mathrm{spin}}^{\mathrm{eff},A} &= -7(Q_{zz}^{*} - Q_{xx}^{*}) = -\frac{21}{2}Q_{zz}^{*}
\end{aligned}
$$

6.4 Magnetocrystalline Anistropy of Co_xPt_{1-x} Thin Film Alloys

In the preceding sections, the relationship between the MCA energy and the electronic structure was investigated. We have also outlined that XMCD, which is element specific and has surface sensitivity, is a valuable technique for probing the microscopic origin of MCA. To clarify these ideas, we shall present XMCD measurements performed at both the Co and Pt $L_{2,3}$ edges in two epitaxial $CoPt_3$ thin film alloys (grown at 690 and 800 K, respectively).

Section 4.1 gives some experimental details on the molecular-beam epitaxy (MBE) growth of the two samples and the XMCD experimental arrangement. In Sections 4.2 and 4.4, the results of the angle-dependent XMCD measurements are presented. Finally, the role of both the Co and Pt atoms in the appearance of the MCA will be discussed.

6.4.1 Experimental

6.4.1.1 Sample Preparation and Characterization

The two 50-nm $CoPt_3$ (111) thin film alloys were co-deposited under UHV conditions on a mica (0001) substrate, after the growth of a 15-nm Ru (0001) buffer layer [43]. As evidenced from X-ray absorption fine structure measurements, there are anisotropic local-order effects (i. e. the formation of small Co in-plane 2D clusters embedded in Pt) in the $CoPt_3$ thin film grown at 690 K [44,45]. In contrast, the $CoPt_3$ thin film grown at 800 K has an isotropic $L1_2$-type crystal structure.

It is expected that such a difference in chemical local ordering will dramatically affect the magnetic properties [43,46,47]. For instance, SQUID measurements provide evidence for strong perpendicular magnetocrystalline anisotropy (PMA) in the film grown at 690 K ($K_1^{\mathrm{MC}} \sim +6 \times 10^6\,\mathrm{erg\,cm^{-3}}$ ($E_{\mathrm{MCA}} = -0.2\,\mathrm{meV}$ per unit cell; $1\,\mathrm{eV} = 1.602 \times 10^{-12}\,\mathrm{erg}$), $T = 300\,\mathrm{K}$) whereas almost isotropic magnetic behavior is found in the film grown at 800 K ($K_1^{\mathrm{MC}} \sim +0.4 \times 10^6\,\mathrm{erg\,cm^{-3}}$ ($E_{\mathrm{MCA}} = -0.02\,\mathrm{meV}$ per unit cell), $T = 300\,\mathrm{K}$) [43].

6.4.1.2 XMCD Measurements

XMCD measurements were performed in collinear geometry at the European Synchrotron Radiation Facility on the ID12B (Co $L_{2,3}$ edges) and ID12A (Pt $L_{2,3}$ edges) beam-lines, respectively [48,49]. The X-ray absorption spectra were monitored at room temperature in the total electron yield detection mode (Co $L_{2,3}$ edges) and in the total fluorescence detection mode (Pt $L_{2,3}$ edges); for these XMCD measurements, both these methods give a correct measure of the absorption cross-section. We found that a 4-T applied magnetic field was large enough to saturate the samples magnetically.

6.4.2 XMCD at the Co $L_{2,3}$ Edges

Figure 4 shows the results of the XMCD measurements performed in the two $CoPt_3$ thin film alloys under study. For each sample, the incident angle, γ, the angle between the direction of the incident X-rays (the direction of the applied magnetic field in a collinear experimental set-up) and the normal to the surface (the [111] crystallographic direction) (Fig. 2) was varied from 0 to 60°. For the thin film grown at 690 K, we observed a strong variation in the integrated XMCD signal (leading to angular dependence of the orbital magnetic moment (Eq. 11)) when the spin magnetic moments are forced out of the [111] direction by the applied magnetic field. As outlined in Section 3.2, such anisotropy in the orbital magnetic moment indicates that the thin film grown at 690 K has strong MCA [27]. In contrast, only small angle-dependence of the orbital magnetic moment was found in the thin film grown at 800 K.

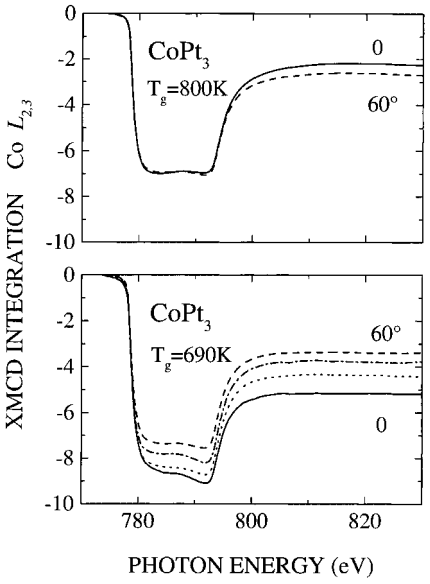

Fig. 4. Integrated XMCD signal (corrected for incomplete polarization of the X-rays) at the Co $L_{2,3}$ edges measured for different values of γ in the two $CoPt_3$ thin films ($H = 4$ T, $T = 300$ K). Upper panel: thin film grown at 800 K ($\gamma = 0°$, solid line; $\gamma = 60°$, dashed line). Lower panel: thin film grown at 690 K ($\gamma = 0°$, solid line; $\gamma = 150°$, dots; $\gamma = 450°$, short dashed line; $\gamma = 60°$, dashed line)

As we shall demonstrate below, analysis based on the magnitude and anisotropy of the orbital magnetic moment provides valuable insights into the understanding of the microscopic origin of the MCA. Because cobalt is an hard ferromagnet, we can safely assume that the easy axis of magnetization lies along the direction of the maximum orbital magnetic moment (Eq. 8). In agreement with macroscopic magnetization measurements, we found that the thin film grown at 690 K has a PMA (Fig. 4). This result is also consistent with the difference in the structural properties. As shown by Maret [43], the MBE process leads to the formation of preferential Co-Pt pairs along the growth direction (the [111] direction) in the film grown at 690 K. We therefore expect that the out-of-plane 3d bandwidth will be larger than the in-plane 3d bandwidth. (The Pt-5d electrons are strongly delocalized. Hence, we realize that an anisotropic 5d/3d hybridization will cause a large difference in the bandwidth for the in-plane and out-of-plane Co-3d orbitals.) As suggested by Stöhr [7], this yields larger out-of-plane orbital magnetic moments and therefore a PMA.

Because the absorption coefficient cannot be measured at grazing incidence (Section 3.3), it is difficult to determine directly the anisotropy of the orbital magnetic moment (the difference between the values of the orbital magnetic moment measured along and perpendicular to the surface normal). We have, however, previously emphasized that the angle-dependence of the orbital magnetic moment can be accurately determined once the crystal symmetry is known. Because the structural order effects are preferentially oriented along the growth direction, we can safety assume that the film grown at 690 K has an uniaxial crystal symmetry. (The MCA in the (111) plane is at least one order of magnitude smaller.) This gives (Eq. 14):

$$m_{\mathrm{orb}}^{\gamma} = R_{\perp} + (R_{\parallel} - R_{\perp}) \sin^2 \gamma \tag{23}$$

where $R_{\perp}$ ($R_{\parallel}$) denotes the value of the orbital magnetic moment measured along the [111] direction (in the (111) plane), respectively (Fig. 5). Assuming that the number of Co-3d holes is 2.25 [50], we can deduce from the application of the sum rules:

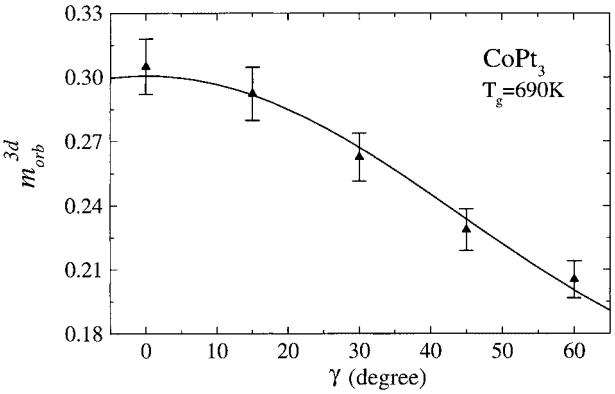

Fig. 5. Co-3d orbital magnetic moment (in units of μ_B/atom), measured in the (111) $CoPt_3$ thin film grown at 690 K, as a function of the photon incident angle γ ($H = 4$ T, $T = 300$ K). The solid curve is a fit assuming that the angular dependence of m_{orb} is given by Eq. (23)

– the magnitude of the 3d orbital magnetic moment along the easy axis of magnetization ($m_{\rm orb}^{3d,\perp} = 0.30 \pm 0.02\,\mu_{\rm B}$ per Co atom);
– the anisotropy of the 3d orbital magnetic moment ($m_{\rm orb}^{3d,A} = m_{\rm orb}^{3d,\perp} - m_{\rm orb}^{3d,\parallel} = 0.13 \pm 0.02\,\mu_{\rm B}$ per Co atom; at the magic angle we have (Section 3.3.3) $m_{\rm orb}^{3d,\gamma(*)} = m_{\rm orb}^{3d,I} = 0.21 \pm 0.02\,\mu_{\rm B}$ per Co atom.). In comparison, the orbital magnetic moment is almost isotropic in the film grown at 800 K ($m_{\rm orb}^{3d,A} = 0.02 \pm 0.02\,\mu_{\rm B}$ per Co atom) (Because the alloy grown at 800 K has a $L1_2$-type crystal structure, the anisotropy of $m_{\rm orb}$ has been estimated from the difference between the values obtained at $\gamma = 0$ and 60°.)

We now demonstrate that the enhancement of the 3d orbital magnetic moment along the [111] direction in the film grown at 690 K (Table 1) does not all result from enhancement of the 3d spin magnetic moment. Instead, such an enhancement would result from:

– the hybridization between the Co-3d and Pt-5d orbitals; and
– crystal field effects (i. e. from local changes in the density of states). (In perturbation theory, the orbital magnetic moment is proportional to $\sum_{\rm ex}\langle ex|\boldsymbol{H}_{\rm so}|gr\rangle/(E_{\rm gr} - E_{\rm ex})$ (Eq. 7). Hence, the magnitude of the 3d orbital magnetic moment depends on the symmetry of the electronic states located above and below the Fermi level and their separation in energy. Enhancement of the spin and orbital magnetic moments has the same origin (e. g. reduced dimensionality, tailored structures), but the enhancement of $m_{\rm orb}$ is a priori not correlated with the enhancement of $m_{\rm spin}$ [51].)

Table 1. The results of the XMCD measurements performed at the Co $L_{2,3}$ edges in the two alloys under study

	$m_{\rm orb}^{\rm A,3d}$	$m_{\rm orb}^{\perp,3d}$	$m_{\rm spin}^{{\rm eff}I,3d}$	$m_{\rm spin}^{{\rm eff}A,3d}$
$T_{\rm g} = 690$ K	0.13 ± 0.02	0.30 ± 0.02	1.44 ± 0.10	0.20 ± 0.05
$T_{\rm g} = 800$ K	-0.02 ± 0.02	0.15 ± 0.02	1.60 ± 0.10	~ 0

$m_{\rm orb}^{\rm A,3d}$ is the difference between the orbital magnetic moment measured along and perpendicular to the [111] direction (the normal to the surface), $m_{\rm orb}^{\perp,3d}$ is the orbital magnetic moment along the [111] direction, $m_{\rm spin}^{{\rm eff}I,3d}$ is the spin magnetic moment, and $m_{\rm spin}^{{\rm eff}A,3d}$ is the anisotropic part of the effective spin magnetic moment. Values are in $\mu_{\rm B}$/atom. $T_{\rm g}$ denotes the growth temperature.

Although the quantity determined from the spin-sum rule is an effective spin magnetic moment (Eq. 12), we have shown previously (Section 3.3) that the spin and dipole magnetic contributions can be obtained independently. Assuming uniaxial symmetry, the angle-dependent spin-sum rule takes the form:

$$m_{\rm spin}^{{\rm eff},\gamma} = \lambda + \beta\,\sin^2\gamma = \Lambda_{\rm exp}^{\gamma} \tag{24}$$

with $\lambda = (m_{\text{spin}} - 7Q_{\perp}^{*})$, $\beta = (21/2)Q_{\perp}^{*}$, and $Q_{\perp}^{*} = 2Q_{\parallel}^{*}$ (Section 3.3). (It is assumed that the applied magnetic field is large enough to align the spin magnetic moment along a nonprincipal crystallographic direction.) λ and β can be determined from the angle-dependence of the spin magnetic moment itself (Fig. 6). We found a spin magnetic moment of $1.44 \pm 0.10\,\mu_B$ (per Co atom) and dipole magnetic moments of $-0.019 \pm 0.003\,\mu_B$ and $0.009 \pm 0.002\,\mu_B$ for the out-of-plane and in-plane orientations, respectively. (At the magic angle we found $m_{\text{spin}}^{\text{eff},\gamma(*)} = m_{\text{spin}} = 1.42 \pm 0.05\,\mu_B$ per Co atom (Fig. 6).) Note that the magnetic dipole term can be safety neglected for cubic symmetry [14,15]. Thus, for the film grown at 800 K with a $L1_2$-type long-range chemical ordering, we have $m_{\text{spin}}^{\text{eff},\gamma} \sim m_{\text{spin}} = 1.60 \pm 0.10\,\mu_B$ (per Co atom). While the orbital magnetic moment is enhanced by a factor of approximately 2 in the film grown at 690 K (Table 1), there is no significant variation of the spin magnetic moment for the two samples, which indicates that the spin magnetic moment, which is almost saturated in Co-based systems is less sensitive to changes in atomic environment [52].

We now demonstrate that the enhancement of the out-of-plane effective spin magnetic moment in the film grown at 690 K is also well correlated with the local atomic ordering. In 3d transition metals, the effective spin magnetic moment takes the form (Eq. 4):

$$m_{\text{spin}}^{\text{eff},\alpha} = m_{\text{spin}} - 7m_{\text{dip}}^{\alpha} = -2\sum_{i}\langle s_i\rangle\left[1 + \frac{7}{2}\langle Q_{i\alpha\alpha}\rangle\right] \tag{25}$$

where α denotes a principal crystallographic direction of the xyz Cartesian frame. An XMCD measurement along two principal crystallographic directions (say x and z) yields [7]:

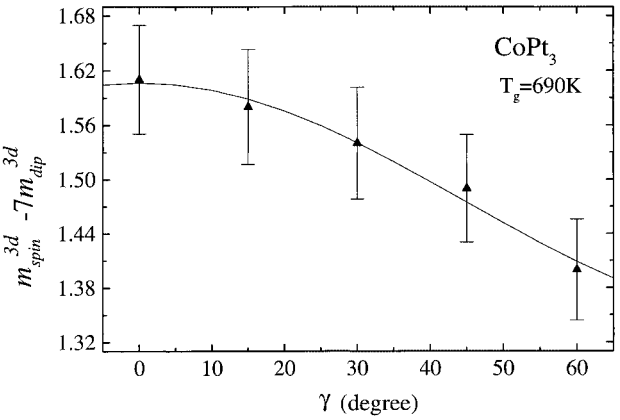

Fig. 6. Co-3d effective spin magnetic moment (in units of μ_B/atom), measured in the (111) $CoPt_3$ thin film grown at 690 K, as a function of the photon incident angle γ ($H = 4$ T, $T = 300$ K). The solid line is a fit assuming that the angular dependence of $m_{\text{spin}}^{\text{eff}}$ is given by Eq. (24)

$$\vec{k} \parallel x : m_{\text{spin}}^{\text{eff},x} = -2\left\{3\langle s_{yz}\rangle + 2\langle s_{3z^2-r^2}\rangle\right\} \approx 5m_{\text{spin}}^{\perp} \tag{26}$$

$$\vec{k} \parallel z : m_{\text{spin}}^{\text{eff},z} = -2\left\{-\langle s_{3z^2-r^2}\rangle + 3\langle s_{xy}\rangle + 3\langle s_{x^2-y^2}\rangle\right\} \approx 6m_{\text{spin}}^{\parallel} - m_{\text{spin}}^{\perp} \tag{27}$$

where $m_{\text{spin}}^{\perp(\parallel)}$ denotes the spin magnetic moment per 3d out-of-plane (in-plane) orbital, respectively. For simplicity, we assume:

- that the z principal crystallographic direction lies along the surface normal; and
- that an electron in the $d_{3z^2-r^2}$, d_{xz}, or d_{yz} out-of-plane orbital has a spin magnetic moment $m_{\text{spin}}^{\perp}$. Eqs. (26) and (27) show that a decrease in the in-plane bandwidth (i. e. the spin magnetic moment of the $d_{x^2-y^2}$ and d_{xy} states increases for nonsaturated ferromagnets) causes enhancement of the effective spin magnetic moment along the z direction. Because the hybridization between the Co-3d and Pt-5d orbitals is strongly anisotropic in the film grown at 690 K, out-of-plane 3d orbitals have a larger bonding. This yields $m_{\text{spin}}^{\text{eff},\perp} \geq m_{\text{spin}}^{\text{eff},\parallel}$ ($m_{\text{dip}}^{\parallel} \geq m_{\text{dip}}^{\perp}$), as observed.

6.4.3 MCA in 3d/5d Systems

As mentioned in the previous section, the anisotropic hybridization between the Co-3d and Pt-5d orbitals favors a PMA in the film grown at 690 K. Because the orbital magnetic moment is almost identical for the two samples under study (Table 1), we may consider that the combined role of the crystal field and the hybridization is certainly to locate, below and above the Fermi level, relevant electronic states (with d_{xy} and $d_{x^2-y^2}$ character) that tend to increase the out-of-plane orbital magnetic moment (the PMA) in the film grown at 690 K (Eqs. 6 and 7) [53].

Because second-order perturbation theory states that the MCA is proportional to the square of the spin–orbit interaction (Eqs. 7 and 8), it might be expected that the 5d electronic states themselves have an important role to play in the MCA of 3d/5d-based systems. For Co/Pd multilayers, ab initio calculations provide evidence for a strong decrease of the PMA when the 4d spin–orbit coupling is artificially neglected [54]. Daalderop attributed this effect to the presence of 3d electronic states at the Fermi level which have primarily d_{xy} and $d_{x^2-y^2}$ character and which are hybridized with Pd-4d electronic states. These states make an important contribution to the MCA, because they have, on average, a large spin–orbit coupling. If this theoretical approach may improve the understanding of the PMA in epitaxial transition metal alloys (the smaller MCA found in Co–Ag multilayers is attributed to greater filling of the 3d band and weaker 3d/4d hybridization [54]) it is primarily concerned with the analysis of the fine structure of the density of states. (In second-order perturbation theory, the magnetocrystalline anisotropy energy scales inversely with the energy separation of the d_i and d_j states. Note that the $\langle d_{xy}|\boldsymbol{H}_{\text{so}}|d_{x^2-y^2}\rangle$ and $\langle d_{yz}|\boldsymbol{H}_{\text{so}}|d_{xz}\rangle$ matrix elements contribute to the out-of-plane magnetic moment and consequently to the PMA (assuming that the isotropic orbital magnetic moment is constant). Hence, theorists mainly concentrate on analyzing the symmetry of the electronic states located above and below the Fermi level.) A simpler, and meaningful, approach

is based on Bruno's arguments: owing to their strong spin–orbit coupling ($\xi_{so}^{Pt} \approx \xi_{so}^{Co}$), the 5d (4d) electrons can acquire a sizeable anisotropic orbital polarization (once spin polarization is induced by the 3d/5d hybridization) and might therefore represent a significant contribution to the MCA. In a naive picture, the 3d electrons would play a minor role in the MCA, acting as a "source of magnetism", only [55].

6.4.4 XMCD at the Pt $L_{2,3}$ Edges

Figure 7 shows the angular dependence of the XMCD signal recorded at the $L_{2,3}$ edges of Pt in the alloy grown at 690 K. A decrease in the Pt-XMCD signal is clearly visible when the 5d spin magnetic moments are forced out the surface normal by the applied magnetic field. This variation should be attributed to a decrease of the 5d orbital magnetic moment (Eq. 11). This result thus provides experimental proof for the role played by the 5d electrons themselves in the appearance of a strong PMA. Although the variation of the 5d orbital magnetic moment is weak (approximately one order of magnitude smaller than the one measured at the $L_{2,3}$ edges of Co – Tables 1 and 2), it is substantially enhanced by the strong 5d spin–orbit coupling (Eq. 8). We shall recall that there is no point in using Bruno's relation for relativistic electrons (Section 3.2.2). However, Bruno's approach reflects the experimental trends. For instance, the 5d orbital magnetic moment does not show any significant variation in the film grown at 800 K.

As outlined previously, the orbital magnetic moment (the effective spin magnetic moment) anisotropy m_{orb}^{A} ($m_{spin}^{eff,A}$) is determined from the angular dependence of the ground state moments. This angular dependence is obtained from the $\langle gr|\boldsymbol{H}_{so}|ex\rangle$ matrix elements and the crystal symmetry (Eq. 7) [40]. For relativistic electrons (e. g. 5d electrons), some additional terms (e. g. $\sin^4\gamma$ terms for an uniaxial symme-

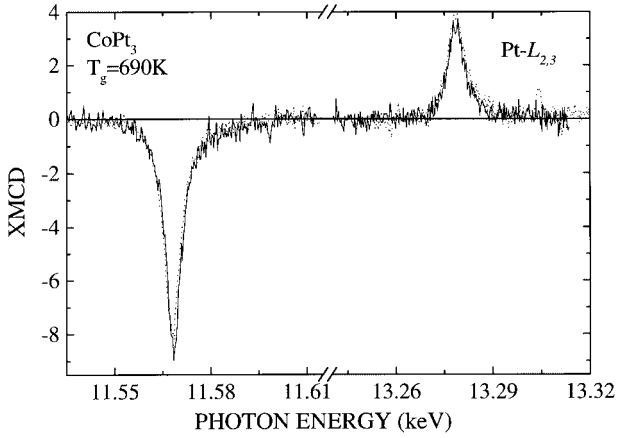

Fig. 7. The angular dependence of the XMCD signal at the $L_{2,3}$ edges of Pt in the (111) $CoPt_3$ thin film grown at 690 K. Solid line, $\gamma = 10°$; dashed line, $\gamma = 45°$. The XMCD signal is corrected for the incomplete polarization of the X-rays

Table 2. The Pt orbital and spin magnetic moments (in (B/atom) measured in the two studied (111) $CoPt_3$ thin films. The ratio $m_{orb}^{5d}/m_{spin}^{5d}$ is also given for more accurate analysis. It is assumed that the contribution of the magnetic dipole term to the effective spin magnetic moment is negligible

$CoPt_3$ ($T_g = 690$ K)			
γ	m_{orb}^{5d} (± 0.004)	m_{spin}^{5d} (± 0.02)	$m_{orb}^{5d}/m_{spin}^{5d}$ (± 0.02)
10	0.058	0.22	0.26
30	0.052	0.23	0.22
45	0.049	0.22	0.22
60	0.044	0.24	0.18
$CoPt_3$ ($T_g = 800$ K)			
γ	m_{orb}^{5d} (± 0.005)	m_{spin}^{5d} (± 0.03)	$m_{orb}^{5d}/m_{spin}^{5d}$ (± 0.03)
30	0.053	0.23	0.23
80	0.057	0.24	0.24

try) could represent an important contribution. For this reason, it seems difficult to determine accurately the magnitude of the in-plane 5d orbital magnetic moment. Finally, we point out that the 5d dipole magnetic term is negligible. This assumption is to some extent justified because of the finding of an isotropic 5d effective spin magnetic moment, which should be attributed to the strong delocalization of the 5d electrons [18].

6.4.5 Discussion

This partly analyzes of the role played by the 3d and 5d electrons in the appearance of a strong PMA in transition metals thin films. In addition, the benefits and drawbacks of a perturbation theory are briefly discussed.

6.4.5.1 3d Anisotropy

As mentioned in Section 4.2, the large anisotropy of the 3d orbital magnetic moment found in a $CoPt_3$ alloy grown at 690 K should be related to a difference in the Co–Pt coordination numbers for the out-of-plane and in-plane orientations, respectively. According to Bruno, this gives a strong MCA. This findings corroborate the ideas developed by Mel [56] some fifty years ago, which suggested that modulation of the chemical composition dramatically affects the MCA. Note, however, that Mel does not discuss the sign of the anisotropy in his original paper. In contrast, Bruno's relation states that the easy axis of magnetization lies along the maximum orbital magnetic moment for a hard ferromagnet (e. g. cobalt or nickel metal).

We recall that Bruno's relationship is based on several drastic assumptions (Section 3.2.2). The observed m_{orb}^{A} values must, therefore, be scaled down to match the

experimental macroscopic results (obtained from torque, ferromagnetic resonance, or magnetization measurements).

6.4.5.2 5d Anisotropy

The element specificity of XMCD has provided new opportunities to understand MCA. Assuming that MCA is related to both the spin–orbit coupling and the anisotropy of the orbital magnetic moment, we have shown that the 5d electrons play an important, if not crucial, role in PMA. This hypothesis is corroborated by: 1) the enhancement of MCA with increasing the 5d orbital magnetic moment anisotropy; and 2) the fact that MCA in Co/Au multilayers is small compared with that in Co/Pt multilayers whereas Au-5d spin–orbit coupling is slightly larger [57]. Because noble metals (Cu, Ag, and Au) alloyed with 3d elements have their d band almost filled, their spin (orbital) polarization is almost negligible. In consequence, their strong spin–orbit coupling interaction will play only a minor role in the MCA.

For the reasons discussed above, it is difficult to estimate the contribution of the Pt-5d electrons to the MCA. In comparison, state-of-the art calculations do not emphasize the physically relevant factors that govern the MCA and also overestimate the phenomenological anisotropy constants.

6.5 Conclusion

In this chapter we have shown that XMCD, which is element- and orbital-sensitive, is a valuable technique for investigating the microscopic origin of the MCA in transition metal thin films. When the symmetry is reduced (either by anisotropy in the chemical bonding or intrinsic structural anisotropy), the orbital magnetic moment has different values for the in-plane and out-of plane orientations. As suggested theoretically [27,56], this gives rise to a large MCA. Present achievements (e. g. spin re-orientation at surfaces [58], element-specific anisotropy [59]) are remarkable, considering that most of the work spans only the last five years and that the origin of the MCA has been debated since the late thirties [25]. We do not need to stress that this research field is still of great interest with relevant applications in magnetic and magneto-optic information storage technology [60,61].

New experimental and theoretical developments [62] make the use of X-ray absorption spectroscopy a very promising tool for completing the gaps in our understanding of the MCA in reduced dimensionality artificial structures.

Acknowledgments

We are grateful to A. Fontaine, G. Krill, and A. Rogalev for their interest in this work. Ph. Sainctavit and M. Kurmoo are acknowledged for critically reading the manuscript.

Finally, we wish to thank the staff of the ESRF in Grenoble for efficient assistance during the experiments. This work is part of the Ph.D. thesis of W. Grange (available on line at http://www.multimania.fr/wgrange) from which it is deeply inspired.

References

[1] P. M. Oppeneer, T. Maurer, J. Sticht, and J. Kübler, *Phys. Rev. B* **1992**, *45*, 10924–33.
[2] J. L. Erskine and E. A. Stern. *Phys. Rev. B* **1975**, *12*, 5016–24.
[3] B. T. Thole, G. van der Laan, and G. A. Sawatzky. *Phys. Rev. Lett.* **1985**, *55*, 2086–8.
[4] G. van der Laan, B. T. Thole, G. A. Sawatzky, J. B. Goedkoop, J. C. Fuggle, J.-M. Esteva, R. Karnatak, J. P. Remeika, and H. A. Dabkowska. *Phys. Rev. B* **1986**, *34*, 6529–31.
[5] G. Schütz, W. Wagner, W. Wilhelm, P. Kienle, R. Zeller, R. Frahm, and G. Materlik. *Phys. Rev. Lett.* **1987**, *58*, 737–40.
[6] G. Schütz, M. Knülle, R. Wienke, W. Wilhelm, W. Wagner, P. Kienle, and R. Frahm. *Z. Phys. B Cond. Matt.* **1988**, *73*, 67–75.
[7] J. Stöhr., *J. Electron Spectrosc. Relat. Phenom.* **1995**, *75*, 253–72.
[8] Ch. Brouder, M. Alouani, and K. H. Bennemann, *Phys. Rev. B* **1996**, *54*, 7334–49.
[9] M. Altarelli and Ph. Sainctavit in: Magnetism and Synchrotron Radiation: Sum Rules for XMCD (Eds E. Beaurepaire, B. Carrière, J.-P. Kappler), Les Editions de Physique, Les Ulis, 1997, Chap. 5.
[10] B. T. Thole, P. Carra, F. Sette, and G. van der Laan. *Phys. Rev. Lett.* **1992**, *68*, 1943–6.
[11] P. Carra, B. T. Thole, M. Altarelli, and X. Wang. *Phys. Rev. Lett.* **1993**, *70*, 694–7.
[12] R. Wu, D. Wang, and A. J. Freeman. *Phys. Rev. Lett.* **1993**, *71*, 3581–4.
[13] P. Strange. *J. Phys. Cond. Matt.* **1994**, *6*, L491–5.
[14] C. T. Chen, Y. U. Idzerda, H.-J. Lin, N. V. Smith, G. Meigs, E. Chaban, G. H. Ho, E. Pellegrin, and F. Sette. *Phys. Rev. Lett.* **1995**, *75*, 152–5.
[15] G. Y. Guo. *Phys. Rev. B* **1998**, *57*, 10295–8.
[16] R. Wu and A. J. Freeman. *Phys. Rev. Lett.* **1994**, *73*, 1994–7.
[17] J. Stöhr and H. König. *Phys. Rev. Lett.* **1995**, *75*, 3748–51.
[18] J. Vogel, A. Fontaine, V. Cros, F. Petroff, J.-P. Kappler, G. Krill, A. Rogalev, and J. Goulon. *Phys. Rev. B* **1997**, *55*, 3663–9.
[19] C. T. Chen, Y. U. Idzerda, H.-J. Lin, G. Meigs, A. Chaiken, G. A. Prinz, and G. H. Guo. *Phys. Rev. B* **1993**, *48*, 642–5.
[20] G. H. O. Daalderop, P. J. Kelly, and M. F. H. Schuurmans. *Phys. Rev. B.* **1991**, *44*, 12054–7.
[21] Y. Wu, J. Stöhr, B. D. Hermsmeier, M. G. Samant, and D. Weller. *Phys. Rev. Lett.* **1992**, *69*, 2307–10.
[22] J. Stöhr, H. A. Padmore, S. Anders, T. Stammler, and M. R. Scheinfein. *Surf. Rev. Lett.* **1998**, *5*, 1297–308.
[23] D. Weller, J. Stöhr, R. Nakajima, A. Carl, M. G. Samant, C. Chappert, R. Mégy, P. Beauvillain, P. Veillet, and G. A. Held. *Phys. Rev. Lett.* **1995**, *75*, 3752–5.
[24] H. A. Dürr, G. Y. Guo, G. van der Laan, J. Lee, G. Lahoff, and J. A. C. Bland. *Science* **1997**, *277*, 213–5.
[25] J. H. van Vleck. *Phys. Rev.* **1937**, *52*, 1178–98.
[26] J. Trygg, B. Johansson, O. Eriksson, and J. M. Wills. *Phys. Rev. Lett.* **1995**, *75*, 2871–4.
[27] P. Bruno. *Phys. Rev. B* **1989**, *39*, R865–8.
[28] P. Bruno. PhD Thesis, Paris-Sud University, France, **1989**.

[29] R. Pauthenet. *J. Appl. Phys.* **1982**, *53*, 8187–92.
[30] A. N. Anisimov, M. Farle, P. Poulopoulos, W. Platow, K. Baberschke, P. Isberg, R. Wäppling, A. M. N. Niklasson, and O. Eriksson. *Phys. Rev. Lett.* **1999**, *82*, 2390–3.
[31] P. Escudier, PhD Thesis, Grenoble University, France, **1973**; *Ann. Phys.* **1975**, *9*, 125–73.
[32] E. R. Callen and H. B. Callen. *J. Phys. Chem. Solids* **1960**, *16*, 310–28.
[33] G. Aubert. *J. Appl. Phys.* **1968**, *39*, 504–10.
[34] E. I. Kondorskii and E. Straube. *Soviet Physics JETP* **1973**, *36*, 188–93.
[35] K. H. J. Buschow in *Ferromagnetic Materials*, Vol. 1 (Ed. E. P. Wohlfarth), North–Holland, Amsterdam, **1980**, Chap. 4.
[36] G. van der Laan. *J. Phys. Cond. Matt.* **1998**, *10*, 3239–53.
[37] D.-S. Wang, R. Wu, and A. J. Freeman. *Phys. Rev. B* **1993**, *47*, 14932–47.
[38] B. Újfalussy, L. Szunyogh, P. Bruno, and P. Weinberger. *Phys. Rev. Lett.* **1996**, *77*, 1805–8.
[39] O. Hjortstam, K. Baberschke, J. M. Wills, B. Johansson, and O. Eriksson. *Phys. Rev. B* **1997**, *55*, 15026–32.
[40] E. Abate and M. Asdente. *Phys. Rev.* **1965**, *140*, A1303–8.
[41] H. A. Dürr and G. van der Laan. *Phys. Rev. B* **1996**, *54*, R760–3.
[42] G. van der Lann. *Phys. Rev. B* **1998**, *57*, 5250–8.
[43] M. Maret, M. C. Cadeville, R. Poinsot, A. Herr, E. Beaurepaire, and C. Monier. *J. Magn. Magn. Mater.* **1997**, *166*, 45–52.
[44] C. Meneghini, M. Maret, M. C. Cadeville, and J. L. Hazemann. *J. Phys. IV France* **1997**, *7*, C21115–7.
[45] C. Meneghini, M. Maret, V. Parasote, M. C. Cadeville, J. L. Hazemann, R. Cortes, and S. Colonna. *Eur. Phys. J. B* **1999**, *7*, 347–57.
[46] P. W. Rooney, A. L. Shapiro, M. Q. Tran, and F. Hellman. *Phys. Rev. Lett.* **1995**, *75*, 1843–6.
[47] T. A. Tyson, S. D. Conradson, R. F. C. Farrow, and B. A. Jones. *Phys. Rev.* **1996**, *54*, R3702–5.
[48] N. Drescher, G. Snell, U. Kleineberg, H.J. Stock, N. Müller, U. Heinzmann, and N. B. Brookes. *Rev. Sci. Instrum.* **1997**, *68*, 1939–44.
[49] L. Varga, C. Giles, C. Neumann, A. Rogalev, C. Malgrange, J. Goulon, and F. de Bergevin. *J. Phys IV France* **1997**, *7*, C2309–13.
[50] D. Stoeffler, personal communication, **1997**.
[51] R. Wu, D. Wang, and A. J. Freeman. *J. Magn. Magn. Mater.* **1994**, *132*, 103–23.
[52] J. L. Rodriguez-López, J. Dorantes-Dávila, and G. M. Pastor. *Phys. Rev. B* **1998**, *57*, 1040–5.
[53] N. Nakajima, T. Koide, T. Shidara, H. Miyauchi, H. Fukutani, A. Fujimori, K. Lio, T. Katayama, N. Nyvlt, and Y. Suzuki. *Phys. Rev. Lett.* **1998**, *81*, 5229–32.
[54] G. H. O. Daalderop, P. J. Kelly, and M. F. H. Schuurmans. *Phys. Rev. B.* **1994**, *50*, 9989–10003.
[55] I. V. Solovyev, P. H. Dederichs, and I. Mertig. *Phys. Rev. B* **1995**, *52*, 13419–28.
[56] L. Néel. *J. Phys. Rad.* **1954**, *4*, 225–39.
[57] P. Beauvillain, A. Bounouh, C. Chappert, R. Mégy, S. Ould-Mahfoud, J.-P. Renard, P. Veillet, D. Weller, and J. Corno. *J. Appl. Phys.* **1994**, *76*, 6078–80.
[58] M. Arend, W. Felsch, G. Krill, A. Delobbe, F. Baudelet, E. Dartyge, J.-P. Kappler, M. Finazzi, A. San Miguel-Fuster, S. Pizzini and A. Fontaine. *Phys. Rev. B* **1999**, *59*, 3707–21.
[59] W. Grange, M. Maret, J.-P. Kappler, J. Vogel, A. Fontaine, F. Petroff, G. Krill, A. Rogalev, J. Goulon, M. Finazzi, and N. B. Brookes. *Phys. Rev. B* **1998**, *58*, 6298–303.
[60] http://www.almaden.ibm.com/sst.
[61] http://www.quinta.com.
[62] G. van der Laan. *Phys. Rev. Lett.* **1999**, *82*, 640–3.

Magnetism: Molecules to Materials I: Models and Experiments.
Edited by Joel S. Miller and Marc Drillon

ISBNs: 3-527-29772-3 (Hardback); 3-527-60084-1 (Electronic)

7 Muon-spin Rotation Studies of Molecule-based Magnets

Stephen J. Blundell

7.1 Introduction

The crucial experiment to characterize the behavior of any organic or molecular magnetic material is a measurement of the magnetization. Only when a material shows some long-range ferromagnetic order, even if it is only a canted moment superimposed upon an antiferromagnetic background, will the magnetization be nonzero when there is no applied magnetic field. A magnetization experiment using a conventional magnetometer is essentially a measurement of $\langle M \rangle$, the magnetic moment per unit volume, averaged over the bulk of a sample. However this provides no information about the magnetization at a local level. To be able to measure $\mathbf{M}(\mathbf{r})$ at a particular atomic position $\mathbf{r}$ would give a new view of the magnetism from a local level and would provide complementary information. To achieve this one would need a probe which could pass unobtrusively into a sample, come to a complete rest at an atomic position deep within it (not just at the surface where the sample quality could be less good), record information about the local magnetic field, transmit that information, and then disappear without a trace. It turns out that a radioactive particle called a muon fulfills all of these conditions and can be used as just such a probe.

The muon is a spin-1/2 particle which has a short lifetime of only 2.2 μs. The mass of the muon is intermediate between that of the electron and the proton, and thus so are its magnetic moment and gyromagnetic ratio. It comes in either charge state, although it is the positive muon, μ^+, which is of particular use in experiments on molecular magnets. As a small, positively charged particle, it is attracted by areas of large electron density and stops in interstitial sites or bonds to organic molecules. By contrast the negative muon, μ^-, implants close to an atomic nucleus and is generally much less sensitive to magnetic properties. The muon is found in nature as the dominant constituent of the cosmic rays arriving at sea-level. For research work it is necessary to use the more intense beams of muons available at synchrotrons and cyclotrons. It is important to realize that in sharp contrast to neutron and X-ray techniques, scattering is not involved; muons are implanted into a sample of interest and reside there for the rest of their short lives, never to emerge again. It is the positrons into which they decay that are released from the sample and yield information about the muons from which they came.

It turns out that this experimental technique, usually referred to as muon-spin rotation (μSR), is extremely useful for studying various magnetic and superconducting

systems (for reviews of the technique, see Refs. [1–6]. As will be described in more detail below, this is because the frequency of the spin-precession of the implanted muon (as measured by the time-dependence of the spatial asymmetry in the decay positron emission) is directly related to the magnetic field at the muon site; hence the muon can be used as a "microscopic magnetometer". Muons have been found to be effective probes of various types of condensed matter physics phenomena and their use has been aided by the development of a number of accelerator facilities, most notably TRIUMF (Vancouver), PSI (Villigen, near Zürich), ISIS (Rutherford Appleton Laboratory, Oxfordshire, UK) and KEK (Tsukuba). The technique requires the use of bulk samples because the incident muons are formed with energy 4 MeV and penetrate a few hundred micrometers into any sample. Even with the use of degraders, surface studies have so far not been possible. However surface studies may be performed in the future with the development of "slow muon" beams in which the energy of the muon beam is reduced down to ~1–10 eV. This is achieved by either moderation in thin layers of rare gas solid [7] or by resonant ionization of thermal muonium (μ^+e^- produced from the surface of a hot tungsten foil placed in a pulsed proton beam) by a pulsed laser source [8] although the efficiency of both of these processes is currently rather low.

μSR has been extensively used in the study of various organic materials [9], including conducting polymers [10–12] and organic superconductors [13,14]. The technique has its most obvious application in the study of magnetic systems [4,15] and thus is ideally suited to studies of molecular magnetism. As a general probe of magnetic materials the muon can be very helpful because:

- it is a *local* probe of internal fields;
- it can be used to follow an order parameter as a function of temperature;
- it works very well at milli-Kelvin temperatures (the incident muons easily pass through the dilution refrigerator windows);
- it provides information on antiferromagnets, spin-gap systems and spin glasses as well as on ferromagnets;
- if there are a range of muon sites it can provide information about internal magnetic field distributions; and
- it provides information about magnetic fluctuations and spin dynamics, even above the magnetic transition temperature.

The muon has been a particularly sensitive probe of the very weak magnetism sometimes found in heavy fermion systems [16] and therefore is demonstrably suitable for studying low-moment magnetism. In the next section I will describe the principles of the experimental technique and in the subsequent section I will review recent μSR experiments on various organic and molecular magnetic systems.

7.2 The Principles of the Experimental Technique

At a number of locations in the world (see above), intense beams of muons are prepared artificially for research in condensed matter physics. These beams are made by colliding a high energy proton beam with a suitable target which produces pions. The pions decay very quickly into muons; if one selects the muons arising from pions which have stopped in the target, the muon beam emerges completely spin-polarized.

The muons can then be implanted into a sample but their energy is large, at least 4 MeV. After implantation they lose energy very quickly (in 0.1–1 ns) to a few keV by ionization of atoms and scattering with electrons. A muon then begins to undergo a series of successive electron capture and loss reactions which reduce the energy to a few hundred eV in ca a picosecond. If muonium is ultimately formed then electron capture ultimately wins and the last few eV are lost by inelastic collisions between the muonium atom and the host atoms. All of these effects are very fast so that the muon (or muonium) is thermalized very rapidly. Moreover the effects are all Coulombic in origin and do not interact with the muon-spin so that the muon is thermalized in matter without appreciable depolarization. This is a crucial feature for muon-spin rotation experiments. One may be concerned that the muon may only measure a region of sample which has been subjected to radiation damage by the energetic incoming muon. This does not seem to be a problem because there is a threshold energy for vacancy production, which means that only the initial part of the muon path suffers much damage. Beyond this point of damage the muon still has sufficient energy to propagate through the sample a further distance, thought to be ca 1 μm, leaving it well away from any induced vacancies [17]. The thickness of sample needed to stop the muons can be predicted from a range curve, the exact form of which depends on the sample material but as a first approximation the position of the peak of the range curve depends only on the density of the material and the muon momentum. This peak range is ca 110 mg cm^2 for the muon beam-lines at ISIS (this corresponds to 1 mm of water, or a few hundred microns of typical metals). Samples should be thicker than the calculated range otherwise some extra material must be placed in front of the sample to bring the peak of the range curve well inside the sample. The peak of the range curve is, however, quite broad so that muons stop in sample at significantly smaller and greater depths than the peak range. These constraints make experiments on very small samples, such as those on BEDT-TTF superconductors [13], particularly challenging though not impossible.

The muon decays with a mean lifetime of 2.2 μs as follows:

$$\mu^+ \rightarrow e^+ + \nu_e + \bar{\nu}_\mu$$

The decay involves the weak interaction, which does not conserve parity, and this leads to a propensity for the emitted positron to emerge predominantly along the direction of the muon-spin when it decayed. The angular distribution of emitted positrons is shown in Fig. 1a for the most energetically emitted positrons. In fact positrons over a range of energies are emitted so that the net effect is something not quite as pronounced, but this phenomenon nevertheless enables one to follow the

polarization of an ensemble of precessing muons with arbitrary accuracy, providing one is willing to take data for long enough.

A schematic diagram of the experiment is shown in Fig. 1b. A muon, with its polarization aligned antiparallel to its momentum, is implanted in a sample. (It is antiparallel because of the way that it was formed, see above, so the muon enters the sample with its spin pointing along the direction from which it came.) If the muon is unlucky enough to decay immediately, it will not have time to precess and a positron will be emitted preferentially into the backward detector. If it lives a little longer it will have time to precess so that if it lives for half a revolution the resulting positron will be preferentially emitted into the forward detector. Thus the positron beam from an ensemble of precessing muons can be likened to the beam of light from a lighthouse. The time evolution of the number of positrons detected in the forward and backward detector is described by the functions $N_F(t)$ and $N_B(t)$ respectively and these are shown in Fig. 1c. Because the muon decay is a radioactive process these two terms sum to an exponential decay. Thus the time evolution of the muon polarization can be obtained by examining the normalized difference of these two functions via the asymmetry function $A(t)$, given by:

$$A(t) = \frac{N_B(t) - N_F(t)}{N_B(t) + N_F(t)} \tag{1}$$

and is shown in Fig. 1d. This experimentally obtained asymmetry function has a calculable maximum value, A_{max}, for a particular experimental configuration which depends on the initial beam polarization (usually very close to 1), the intrinsic asymmetry of the weak decay, and the efficiency of the detectors for positrons of different

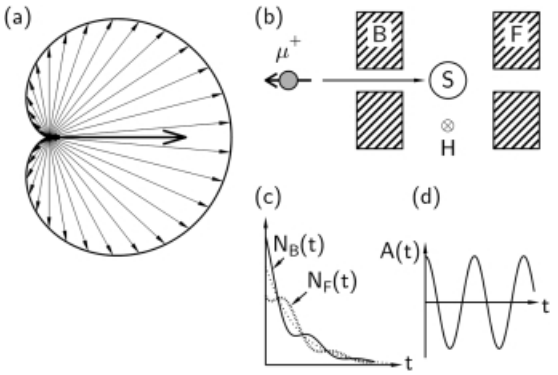

Fig. 1. (a) The angular distribution of emitted positrons relative to the initial muon-spin direction. The expected distribution for the most energetically emitted positrons is shown. (b) Schematic illustration of a μSR experiment. A spin-polarized beam of muons is implanted in a sample S. After decay, positrons are detected in either a forward detector F or a backward detector B. If a transverse magnetic field, H, is applied to the sample as shown then the muons will precess. (c) The number of positrons detected in the forward (dashed-line) and backward (solid-line) detectors. The dotted line shows the average of the two signals. (d) The asymmetry function

energies, and usually turns out to be around $A_{\max} \sim 0.25$. The function can be normalized to 1, in which case it expresses the spin autocorrelation function of the muon, $G(t) = A(t)/A_{\max}$, which represents the time-dependent spin polarization of the ensemble of muons.

Fig. 2 shows a drawing of a muon spectrometer used at the ISIS pulsed muon facility. Two banks of detectors are arranged on either side of the sample and the grouped signals from each bank constitute the forward and backward detectors of Fig. 1b. Each detector consists of a piece of scintillator light guide connected to a photomultiplier tube. The spectrometer is equipped with a variety of possible sample environments, including a furnace, a dilution refrigerator, a He^4 cryostat and a closed cycle refrigerator, with magnetic fields up to 0.2 T in the transverse or longitudinal directions.

We will now recall the principles of Larmor precession. Consider a magnetic moment $\mathbf{m}$ in a magnetic field $\mathbf{B}$. The energy E of the magnetic moment is given by $E = -\mathbf{m} \cdot \mathbf{B}$, so that the energy is minimized when the magnetic moment lies along the magnetic field. There will be a torque $\mathbf{G}$ on the magnetic moment given by $\mathbf{G} = \mathbf{m} \times \mathbf{B}$, which will tend to turn the magnetic moment until it rotates around and lies along the magnetic field. However, because the magnetic moment is associated with the angular momentum $\mathbf{L}$ by the equation $\mathbf{m} = \gamma \mathbf{L}$ where γ is the gyromagnetic ratio, and because $\mathbf{G} = \mathrm{d}\mathbf{L}/\mathrm{d}t$, our expression for the torque can be rewritten as:

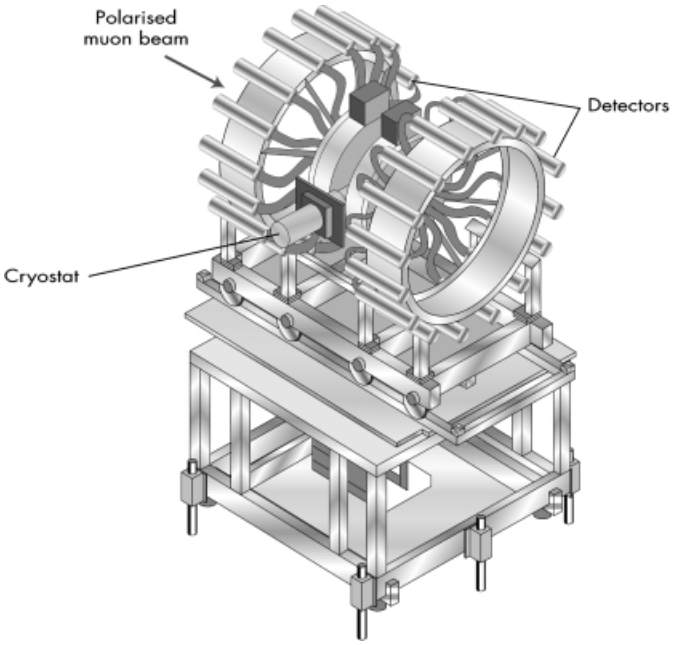

Fig. 2. The spectrometer on the MUSR beam-line at ISIS, the Rutherford Appleton Laboratory, Oxfordshire, UK. (Courtesy ISIS Pulsed Muon Facility.)

$$\frac{\mathrm{d}\mathbf{m}}{\mathrm{d}t} = \gamma \mathbf{m} \times \mathbf{B} \tag{2}$$

which implies that $|\mathbf{m}|$ is time-independent, but that the direction of $\mathbf{m}$ precesses around $\mathbf{B}$. To see this more clearly, let us consider the case in which $\mathbf{B}$ is along the z-direction and $\mathbf{m}$ is initially at an angle of θ to $\mathbf{B}$ and in the xz plane (see Fig. 3). Then:

$$\begin{aligned} \dot{m}_x &= \gamma B m_y \\ \dot{m}_y &= -\gamma B m_x \\ \dot{m}_z &= 0 \end{aligned} \tag{3}$$

so that m_z is constant with time and m_x and m_y both oscillate. Solving the differential equations leads to:

$$\begin{aligned} m_x(t) &= |\mathbf{m}| \sin\theta \cos(\omega_L t) \\ m_y(t) &= |\mathbf{m}| \sin\theta \sin(\omega_L t) \\ m_z(t) &= |\mathbf{m}| \cos\theta \end{aligned} \tag{4}$$

where

$$\omega_L = \gamma B \tag{5}$$

is known as the Larmor precession frequency. Note that the gyromagnetic ratio γ is the constant of proportionality which connects both the angular momentum with the magnetic moment (through $\mathbf{m} = \gamma \mathbf{L}$) and the precession frequency with the magnetic field (through Eq. 5).

Hence in a magnetic field B the muon-spin precesses with angular frequency ω_μ given by $\omega_\mu = \gamma_\mu \mathrm{B}$ where $\gamma_\mu = ge/2m_\mu$ is the gyromagnetic ratio for the muon and m_μ and g are the muon mass and g-factor, respectively. The field-dependent precession frequencies for the muon, electron and proton are shown in Fig. 4. The highest frequencies are associated with the lightest particle, the electron, and the lowest with the proton. Hence for usual laboratory magnetic fields ESR (electron-spin resonance) is typically performed at microwave frequencies while NMR (nuclear magnetic resonance) uses radio-frequencies. In both of these techniques resonance occurs when the precession frequency matches the resonance frequency. Muon-spin rotation (μSR) is associated with frequencies intermediate between NMR and ESR but unlike those resonance techniques, no electromagnetic field is necessary since the precessing muon can be followed directly. (Muon-spin *resonance* experiments

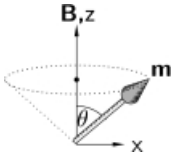

Fig. 3. A magnetic moment $\mathbf{m}$ in a magnetic field $\mathbf{B}$ precesses around the magnetic field at the Larmor precession frequency, γB. The magnetic field $\mathbf{B}$ lies along the z-axis and the magnetic moment is initially in the xz-plane at an angle θ to $\mathbf{B}$. It precesses around a cone of semi-angle θ

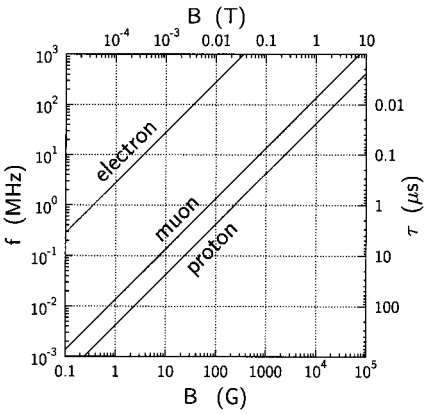

Fig. 4. The Larmor precession frequency, f, in MHz (and the corresponding period $\tau = 1/f$) for the electron, muon, and proton as a function of applied magnetic field B

can however be performed [3,18] but a discussion of this is outside the scope of this chapter.)

Very often magnetic fields are applied to the sample either perpendicular or parallel to the initial muon-spin direction. The perpendicular (or transverse) case causes the muon to precess in the applied magnetic field and any dephasing in the observed oscillations is evidence for either an inhomogeneous internal field distribution or spin–spin (T_2 in the language of NMR) relaxation. The parallel (or longitudinal) case does not lead to spin precession, but spin relaxation. This can be because of inhomogeneous field distributions or spin–lattice (T_1) relaxation processes. In magnetic systems the experiment can be performed in zero applied magnetic field because the muons will then precess in the internal field of the magnet. This will also be the case in antiferromagnets because the muons measure a local dipolar field [19], not the net magnetization.

Muon experiments can be performed in two different ways depending on the time structure of the muon beam. If the muon beam is continuous (CW, or continuous wave), then muons arrive at the sample intermittently. When the muon enters the experiment it must itself be detected to start a clock. When the positron is detected in either the forward or backward detectors, the clock is stopped. If a second muon arrives before the first one has decayed then one has no way of knowing whether a subsequently emitted positron came from the first or second muon, so this event must be disregarded. Sophisticated high-speed electronics and a low incident muon arrival rate are needed. Alternatively one can use an electrostatic deflector triggered by the detectors to ensure no muons enter the experiment until the current implanted muon decays.

These complications are circumvented with a pulsed muon beam. In this case a large number of muons arrives in a very intense pulse so there is no need to detect when each muon arrives. The detection of positrons is then made and each event is timed with respect to the arrival of the pulse. A typical data-set contains several million detected positrons so that an appreciable number of muons (the fraction is given by $e^{-20/2.2} \sim 0.01\%$) live for 20 μs or longer. Long-lived muons are difficult to measure with CW beams; the arrival of the next muon tends to interrupt the first

muon which has outstayed its welcome. Nevertheless the long-lived muons can be accurately detected at a pulsed source. Unfortunately this method also suffers from a drawback which is that the muon pulse has a finite width, τ_w, which results in a slight ambiguity in all of the timing measurements and leads to an upper limit on precession frequencies which can be measured. CW muon beams are operated at the Paul Scherrer Institute in Switzerland and at TRIUMF in Canada. Pulsed muon beams are used at KEK in Japan and at ISIS (the spallation source at the Rutherford Appleton Laboratory) in the UK.

To understand the ability of the muon to study randomness and dynamics in magnetism it is helpful to consider further some aspects of spin precession. If the local magnetic field at the muon-site is at an angle of θ to the initial muon spin-direction at the moment of implantation, the muon-spin will subsequently precess around the end of a cone of semi-angle θ about the magnetic field (Fig. 3). We now require our coordinates to be rotated so that we measure directions with respect to the initial muon-spin direction. Hence by using Eq. (3) and rotating the coordinates by an angle θ it is straightforward to show that the normalized decay positron asymmetry will be given by:

$$G(t) = \cos^2\theta + \sin^2\cos(\gamma_\mu BT) \tag{6}$$

If the direction of the local magnetic field is entirely random then averaging over all directions would yield:

$$G(t) = \frac{1}{3} + \frac{2}{3}\cos(\gamma_\mu Bt) \tag{7}$$

If the strength of the local magnetic field is taken from a Gaussian distribution of width Δ/γ_μ centered around zero, then a straightforward averaging over this distribution gives:

$$G(t) = \frac{1}{3} + \frac{2}{3}e^{-\Delta^2 t^2/2}(1 - \Delta^2 t^2) \tag{8}$$

a result which was first obtained by Kubo and Toyabe [20]. This relaxation function is illustrated in Fig. 5a and is a weighted sum of oscillatory terms, each following Eq. (7) but with a different value of the internal field B. Initially all of the contributions behave similarly (i. e. they all fall from 1 to a minimum value and then increase) but after a short time they dephase with respect to each other. Hence their average, the Kubo–Toyabe relaxation function, would be expected to fall from unity to a minimum and then recover to an average value, in this case to one-third. If the form of the distribution of internal fields was different this would affect the form of the observed muon-spin time evolution. For example, in a material with a spin-density wave which is incommensurate with the crystal lattice, there will be a sinusoidal modulation of the internal field which the muons will randomly sample. In this case one finds that the muon-spin relaxation follows a Bessel function [16,21]. Such an effect has been observed in chromium [21] and also in an organic system, $(TMTSF)_2PF_6$, which has a spin-density wave ground state [22].

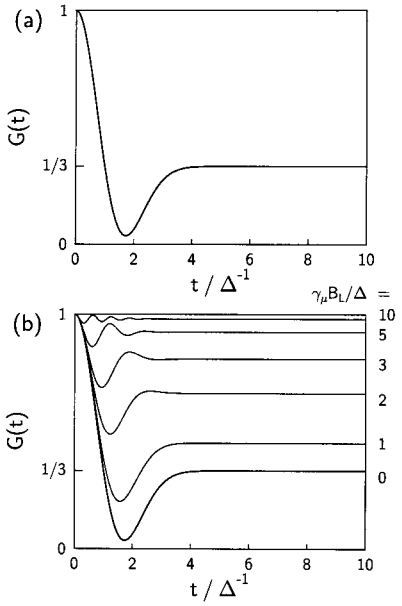

Fig. 5. (a) The time evolution of the muon-spin polarization according to the Kubo–Toyabe relaxation function (Eq. 8) with its characteristic dip and recovery to a value of 1/3. (b) The effect of a longitudinal magnetic field B_{L}. The time is measured in units of Δ^{-1} and the longitudinal field values shown are in units of Δ/γ_{μ}

If there is an almost uniform static internal field in the sample, but there is a slight variation from site to site, different muons will precess at slightly different frequencies and become progressively dephased so that the oscillations in the data will be damped. If the field varies a great deal the damping could be so large that no oscillations can be observed. This effect could, however, also be caused by fluctuations either of the internal field, because of some intrinsic property of the sample, of the muon's position, or because of muon diffusion. One method of distinguishing between these possibilities is to apply a magnetic field in the longitudinal direction, parallel to the initial muon-spin direction. For example, this modifies the Kubo–Toyabe relaxation function as shown in Fig. 5b, causing the "1/3-tail" to increase, because in this case the muons precess in both the internal field and the applied field. Since the magnetic field B_{L} is applied along the initial muon-spin direction then in the limit of large B_{L} the muon-spin is held constant and does not relax from a value near unity. This technique is useful to distinguish the effects of inhomogeneous line broadening (a distribution of static internal fields as considered above) and fluctuations because the two have very different types of behavior in a longitudinal field [23].

The effects of muon hopping on the relaxation are shown in Fig. 6. The different traces are for different hopping rates ν. When $\nu = 0$ we recover the zero-field Kubo–Toyabe curve of Eq. (8). For fast hopping the relaxation of the muon-spin becomes dominated by the hopping process and the relaxation is exponential. The relaxation rate goes down as the dynamics get faster. This effect is known as motional narrowing because it is essentially identical to the effect of the same name in NMR spectroscopy. Motional effects narrow NMR linewidths which are measured in the frequency domain; consequently in the time domain (in which data from μSR

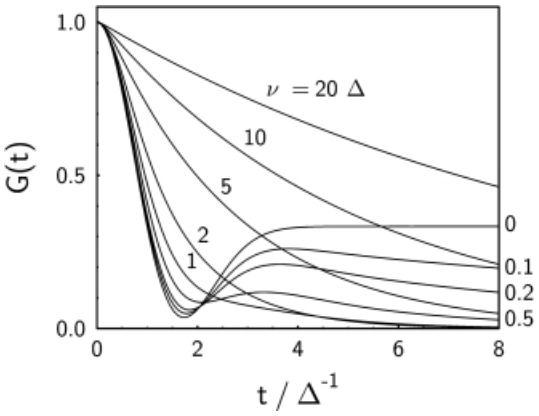

Fig. 6. The relaxation function for a muon hopping at rate ν. After each hop the value of the internal field is taken from a Gaussian distribution about zero with width Δ/γ_μ. The curve for $\nu = 0$ corresponds to the zero-field Kubo–Toyabe relaxation function of Eq. (8)

experiments are usually considered) this corresponds to a motional widening and a reduction in relaxation. For slow hopping, very little effect is observed at very short times but a large sensitivity to weak hopping is observed in the 1/3-tail which is observed at longer times. This sensitivity to slow dynamics via the behavior of the tail of the relaxation function observed at long times enables measurement of dynamics over a very large range of time-scale. If a longitudinal magnetic field is applied it has a large effect on the muon relaxation if the dynamics are weak but much less of an effect if the dynamics are fast. Thus by a careful combination of zero-field and longitudinal-field experiments the nature of the internal field distribution can be extracted. Muon hopping (also known as muon diffusion) is observed in many inorganic systems at high temperatures. Other types of dynamics (in which the muon may be at rest but its environment fluctuates) can be treated in similar ways.

An interesting case where the need to understand dynamics is of crucial importance is that of the dilute alloy spin glass prepared by dissolving small concentrations of Mn in a Cu matrix. In this system dilute magnetic impurities couple via an RKKY exchange interaction which alternates in sign as a function of distance. Because the magnetic impurities are present at random, these materials cannot show long-range order but have built-in frustration. When cooled one observes a slowing down of spin fluctuations and a divergence in the correlation time between Mn spin fluctuations at the spin glass temperature. Below this temperature a static component of the local field is observed with muons, corresponding to some degree of spin freezing, with each Mn spin having its own preferred orientation, although fluctuating around this [24]. Above the spin glass temperature muon-spin relaxation measurements have been used to follow the spin glass dynamics and to extract directly the form of the autocorrelation function of the spins [25,26].

Depending on its chemical environment, the muon can thermalize and pick up an electron and form a neutral atomic state called muonium (abbreviated $\mathrm{Mu} = \mu^+ e^-$) which is an analog of atomic hydrogen. In muonium the electronic spin and the muon-spin are coupled by a hyperfine interaction which we will initially assume is isotropic. This leads to two energy levels, a lower triplet state and a higher singlet state. Muonium states can be formed in many chemical systems and these enable

a unique form of radical spectroscopy [27]. Muonium adds to unsaturated bonds to form muonated free radicals. For example, addition to benzene (C_6H_6) leads to the muonated cyclohexadienyl radical (C_6H_6Mu). The advantage here is that one can work with concentrations down to just one muonated radical at a time in an entire sample. In contrast ESR detection needs $\sim 10^{12}$ radicals in a cavity, forbidding measurements at high temperatures where the radicals become mobile and terminate by combination. The technique has been applied to radicals in different environments [27] including those absorbed on surfaces [28]. The muonium can always be studied by measuring precession signals in an applied magnetic field, or by using a technique known as repolarization. In this latter method a longitudinal magnetic field is applied to the sample, along the initial muon-spin direction, and as the strength of the magnetic field increases, the muon and electron spins are progressively decoupled from the hyperfine field. For isotropic muonium, half of the initial polarization of implanted muons is lost because of the hyperfine coupling, but this is recovered in a sufficiently large applied field, enabling estimation of the strength of the hyperfine field. If the hyperfine coupling is anisotropic, this affects the form of the repolarization curve, enabling further information to be extracted [29].

An extreme case where the muon plays a strongly active role is found in conducting polymers [11]. The reaction between muonium and *trans*-polyacetylene [30,31] produces a diamagnetic, neutral muon defect and a highly mobile unpaired spin. This soliton diffuses up and down the chain but cannot cross the muon defect which acts as a barrier. Every time the soliton briefly revisits the muon, the muon-electron hyperfine coupling is turned on and then off, so that successive visits progressively relax the muon polarization. Measurement of the field-dependence of this relaxation yields the spectral density function associated with the defect random walk and can be used to infer the dimensionality of the soliton diffusion [12]. This occurs because the relaxation rate is connected with the noise power, $J(\omega_\mu)$, in the fluctuating magnetic field at the muon Larmor frequency, ω_μ, associated with that particular magnetic field. Sweeping the magnetic field enables extraction of the frequency distribution of the fluctuations. In other polymers, such as polyaniline, the muon-induced defect is a negatively charged polaron. Muons are uniquely sensitive to the motion of this defect in undoped materials [10] and in contrast to transport studies, which are inevitably dominated by the slowest component of the transport process, can provide information on the intrinsic transport processes governing the mobility of an electronic excitation along a chain.

The muon technique is sensitive to spin dynamics, and this can be formalized by expressing the connection with the response function $S(\mathbf{q}, \omega)$ which is measured in neutron scattering through the differential cross-section. This can be expressed, via the fluctuation-dissipation theorem, as:

$$S(q, \omega) = \frac{k_B T}{\pi} \chi(\mathbf{q}) \frac{\Gamma(\mathbf{q})}{\omega^2 + \Gamma(\mathbf{q})^2} \tag{9}$$

where $\chi(\mathbf{q})$ and $\Gamma(\mathbf{q})$ are the wave-vector dependent susceptibility and inverse lifetime, respectively, for excitations with wave vector $\mathbf{q}$. The measured longitudinal

relaxation rate is proportional to a sum over all modes **q** of the response function (because one is using a point probe) and because one is usually dealing with the low-frequency limit ($\omega \ll \Gamma$):

$$\frac{1}{T_1} \propto k_B T \sum_{\mathbf{q}} \frac{\chi(\mathbf{q})}{\Gamma(\mathbf{q})} \tag{10}$$

This expression is useful in understanding both critical and paramagnetic relaxation [4,5,32]. We simply note here that for uncorrelated fluctuations (where γ and χ have no **q**-dependence and $\chi \propto 1/T$) this leads to a temperature independent $1/T_1$.

7.3 Experimental Results

The field of molecular magnetism has recently produced many advances, surprises and revolutions, not to mention a multitude of new families of materials with extraordinary properties [33]. We now have fully organic magnets, containing only the elements carbon, hydrogen, oxygen, and nitrogen (with sadly very low Curie temperatures) but also molecular magnets based on transition metal ions with much higher transition temperatures, large coercivities and intriguing optical properties. In the last seven or eight years, μSR has begun to be applied to this field and in this section I will review the recent studies which have been made using muons.

7.3.1 Nitronyl Nitroxides

Many organic radicals exist which have unpaired spins, but few are stable enough to be assembled into crystalline structures. Moreover, even when that is possible *aligning* these spins ferromagnetically is usually impossible. Ferromagnets are rather rare even among the elements and are exclusively found in the d- or f-block. Thus the discovery of ferromagnetism, albeit at rather low temperatures, in certain nitronyl nitroxide molecular crystals was particularly remarkable. The first material of this sort to be found was *para*-nitrophenyl nitronyl nitroxide (*p*-NPNN) which showed ferromagnetism up to $T_C \sim 0.65\,\mathrm{K}$ in one of its crystal phases only [34]. Nitronyl nitroxides contain only the elements C, H, N, and O and are therefore fully organic. On each nitronyl nitroxide molecule there is an unpaired spin associated with the two N–O groups. Small chemical changes to the rest of the molecule lead to significant changes in crystal structure, thereby altering the intermolecular overlaps and thus the magnetic interactions between unpaired spins on neighboring molecules. Thus, different compounds have very different magnetic ground states. Muon studies of this and related materials began soon after the initial discovery [35–39].

Following muon implantation it is thought that muonium ($\mathrm{Mu} = \mu^+ e^-$), with a single electronic spin, attaches to a particular nitronyl nitroxide and combines with the unpaired spin on the nitronyl nitroxide. As shown in Fig. 7, the resulting

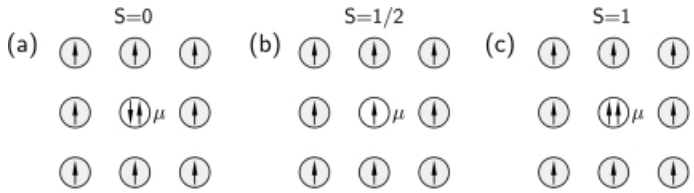

Fig. 7. Electronic spin states after muon implantation in a nitronyl nitroxide system. In each case the (a) singlet, (b) doublet and (c) triplet states are surrounded by nearest neighbors each with an unpaired spin. (a) and (c) are formed by Mu = μ^+e^- addition. (b) is formed by μ^+ addition. The muon spin is not shown in each case (after [38])

electronic spin-state of the muonated radical can be a singlet ($S = 0$, leading to a diamagnetic state) or a triplet ($S = 1$, leading to a paramagnetic state) [38]. Both states are found in experiments. In a diamagnetic state the muon-spin precesses at a frequency $\nu_\mu = \gamma_\mu B = 0.1355\,\text{MHz/mT} \times B$ so the frequency of the precession signal directly yields the local field B at the muon-site. (γ_μ is the muon gyromagnetic ratio.) In a paramagnetic state the muon-spin precesses at very high frequency in the hyperfine field and the presence of this state can be detected via a loss of muon polarization at $t = 0$.

In Fig. 8 the time evolution of the muon polarization in polycrystalline p-NPNN is plotted as a function of temperature [38]. This is an example of an experiment with zero applied magnetic field (in fact a small magnetic field was applied to compensate the effect of the Earth's field). At ~0.67 K there is a clear change between the high-temperature paramagnetic state, in which there are no oscillations, and the low temperature ordered state, in which clear oscillations can be seen. As the sample is warmed, the frequency of oscillations decreases as the internal field decreases until it is above the Curie temperature and no oscillations can be observed, only a weak spin relaxation arising from spin fluctuations. The temperature dependence of the precession frequency ($\nu_\mu(T)$) of these oscillations is shown in Fig. 9 together with the calculated local internal field. This is fitted to a functional form $\nu_\mu(T) = (1 - (T/T_C)^\alpha)^\beta$ yielding $\alpha = 1.7 \pm 0.4$ and $\beta = 0.36 \pm 0.05$. This is consistent with three-dimensional long range magnetic order. Near T_C the critical exponent is as expected for a three-dimensional Heisenberg model (one expects $\beta \approx 0.36$ in this

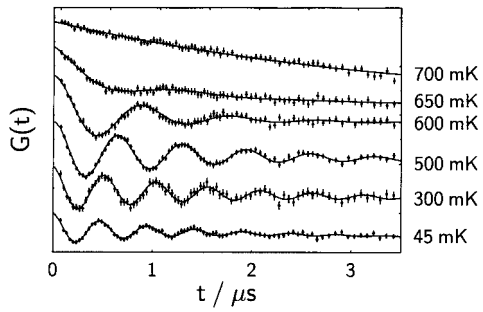

Fig. 8. Zero-field muon spin rotation frequency in the organic ferromagnet p-NPNN [38]. The data for different temperatures are offset vertically for clarity

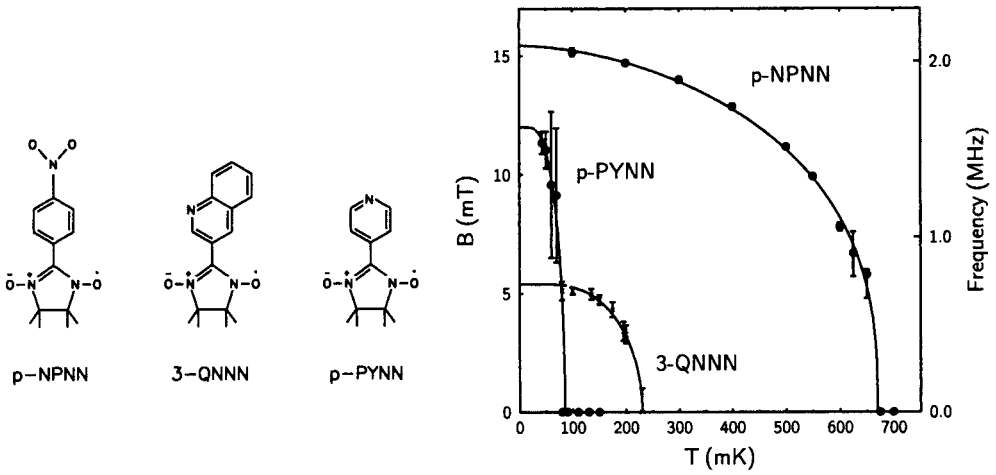

Fig. 9. Temperature-dependence of the zero-field muon spin rotation frequency in *p*-NPNN, 3-QNNN, and *p*-PYNN [37–39]. The fitted curve for *p*-NPNN is as described in the text. For 3-QNNN and *p*-PYNN the fitted curve assumes a mean-field dependence. The molecular structure of each compound is also shown

case). At low temperatures the reduction in local field is consistent with a Bloch-$T^{3/2}$ law, indicative of three-dimensional spin waves [38].

Although for *p*-NPNN the magnetic properties had been first determined by use of conventional magnetic measurements [34], the ease of combining μSR with very low temperatures led to ordered states being discovered using muons. In 3-quinolyl nitronyl nitroxide (3-QNNN) μSR oscillations have been observed below 210 mK and a lower local field at the muon site. The reduced local field is consistent with a canted magnetic structure [35,39,40]. The crystal structure of *para*-pyridyl nitronyl nitroxide, *p*-PYNN, is very different and consists of one-dimensional chains in which molecules are arranged side-by-side and head-to-tail [37]. This favors ferromagnetic interactions along the chain but the inter-chain interactions are thought to be antiferromagnetic. Weak μSR oscillations below ~90 mK are observed superimposed on a large background [37], reflecting this more complicated magnetic structure. The temperature dependence of the precession frequencies of these three compounds together with their molecular structures are shown in Fig. 9.

The dependence of the magnetic ground state on the molecular shape is well illustrated by the chemical isomers 1-NAPNN and 2-NAPNN (NAPNN is naphthyl nitronyl nitroxide) whose different molecular shapes leads to different crystal packing and consequently different magnetic properties and hence μSR behavior [41] (1-NAPNN has a magnetic transition, 2-NAPNN does not). For the isomers 2-HOPNN and 4-HOPNN (HOPNN is hydroxyphenyl nitronyl nitroxide), the former give oscillatory μSR data characteristic of three-dimensional ordering below ~0.5 K but the latter has only low frequency oscillations below ~0.7 K with evidence of a dimensional magnetic crossover at 0.1 K [42]. A magnetic transition has also been found in *p*-CNPNN (CNPNN is cyanophenyl nitronyl nitroxide, see [43]). The

overlaps in all these materials which favor ferromagnetism seem to agree with the McConnell mechanism – as a result of spin-polarization effects, positive and negative spin-density can exist on different parts of each molecule; intermolecular exchange interactions tend to be antiferromagnetic, so if the dominant overlaps are between positive (majority) spin-density on one molecule and negative (minority) spin density on another molecule, the overall intermolecular interaction can be ferromagnetic. Although the mechanism for ferromagnetism is electronic, the low values of T_C imply that the dipolar interactions will play an additional role in contributing to the precise value of T_C and determining the easy magnetization axis. This also depends on the crystal structure which in turn depends on the molecular shape [44,45]. Calculations of the muon-site can be performed for nitronyl nitroxide systems although these tend to produce a range of possible sites [46].

7.3.2 Other Molecular Magnets

A variety of other organic magnetic materials exists and has been studied by use of μSR, but the nitronyl nitroxides remain to date the main source of purely organic bulk ferromagnets (recently magnets based on TEMPO radicals have been discovered and a μSR study has been reported [47]). Tanol suberate is a biradical with formula $(C_{13}H_{23}O_2NO)_2$. The susceptibility follows a Curie–Weiss law with a positive Curie temperature (+0.7 K) The specific heat has a λ anomaly [48] at 0.38 K and is found to be an antiferromagnet, but in a field of 6 mT undergoes a metamagnetic transition [49,50]. μSR experiments yield clear spin precession oscillations [51] (Fig. 10). The temperature-dependence of the precession frequency follows an equation $\nu_\mu(T) = \nu_\mu(0)(1 - T/T_C)^\beta$, where $\beta = 0.22$. This critical exponent is consistent with a two-dimensional XY magnet [52] and also with the temperature dependence of the magnetic susceptibility [51]. The relaxation rate of the oscillations rises to a maximum at the transition temperature and then falls dramatically.

The transition temperature of organic radicals with long range magnetic order has been typically very low. This situation has changed recently with the discovery of spontaneous magnetization below 35 K associated with noncollinear antiferromagnetism in the β crystal phase of the dithia-diazolyl molecular radical p-$NC(C_6F_4)(CNSSN)$ [53]. Zero field μSR has been used to study the internal field in this system [54]. Two distinct frequencies are resolved in the zero field muon spin rotation signal; these have been assigned to muon states bonded at two different sites on the CNSSN ring. The muon data show that the easy direction for the spin structure is along the b axis. Muon spin relaxation below the transition follows the power law expected for two-magnon scattering and also has a distinct anti-resonance feature just below the magnetic transition; this has been assigned to an interaction between magnons and low-frequency intermolecular phonons [54].

Some of the most technologically promising materials are molecular magnets in which a transition metal ion provides the localized moment and organic bridges act as exchange pathways. Progress has been achieved using materials with unpaired electrons on both the metal ions and the organic molecules, as in (DMeFc)TCNE [55] (where DMeFc = $[Fe((CH_3)_5C_5)_2]$ is a donor and TCNE is an acceptor). This

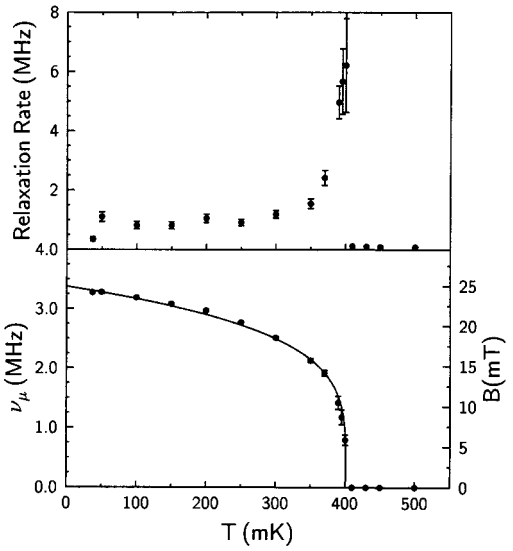

Fig. 10. μSR data measured on tanol suberate, showing the temperature dependence of the relaxation rate and frequency of the muon-spin oscillations [51]

material has a chain structure but shows bulk ferromagnetic order below 4.8 K. Muons have been used to measure the development of short-range spin correlations above this temperature which are very slow in this quasi-1D material [56]. Molecular magnets can also be made using the dicyanamide ligand; in particular $Ni(N(CN)_2)_2$ and $Co(N(CN)_2)_2$ have been prepared and show long-range ferromagnetic order below 21 K and 9 K, respectively [57–59]. μSR experiments on these materials detect the magnetic order by a loss of muon polarization below T_C and have a highly damped precession signal suggestive of a broad internal field distribution. Significant spin relaxation is observed in the paramagnetic state, which persists well above T_C [60].

μSR can also be useful for studying gapped systems. One such organic example is $MEM(TCNQ)_2$ which undergoes a spin-Peierls (SP) transition at low temperature. This is an intrinsic lattice instability in spin-1/2 antiferromagnetic Heisenberg chains. Above the transition temperature T_{SP}, there is a uniform antiferromagnetic next-neighbor exchange in each chain; below T_{SP} there is an elastic distortion resulting in dimerization and hence two, unequal, alternating exchange constants. The alternating chain has an energy gap between the singlet ground state and the lowest lying band of triplet excited states which closes up above T_{SP}. μSR studies indicate a slowing down of the electronic fluctuations resulting from the opening of a gap in the magnetic excitation spectrum as the temperature is lowered below T_{SP} [61,62]. At the very lowest temperatures the electronic spin fluctuations freeze out and the muon-spin depolarization is dominated by persistent slow fluctuations which can be ascribed to a defect-spin system [63]. The muon may not necessarily be regarded merely as a passive probe in this case, because it seems that the muon-spin itself playas a role in locally creating a spin defect by breaking a singlet pair. This could give rise to the relaxation ascribed to defect spins and which is only revealed when the other sources of relaxation have frozen out (Fig. 11) [63].

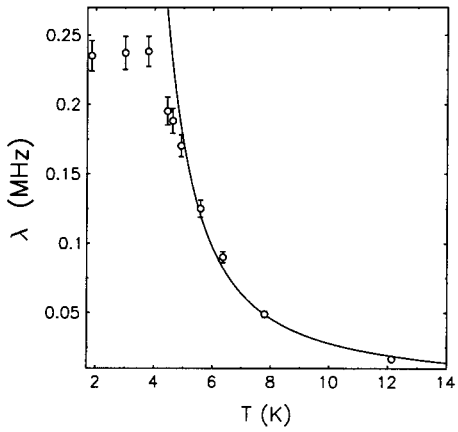

Fig. 11. The low temperature relaxation rate for $MEM(TCNQ)_2$. This is used to extract an energy gap equal to ~17 K extrapolated to zero temperature. At low temperatures, the relaxation saturates to a constant value, 0.235 MHz, which is determined by the (temperature-independent) defect spin concentration (after [63])

An interesting muon-spin-relaxation study of the ground state of the two dimensional S = 1 kagomé antiferromagnet [2-(3-*N*-methylpyridium)-4,4,5,5-tetramethyl-4,5-dihydro-1*H*-imidazol-1-oxyl-3-*N*-oxide]BF_4 (*m*-MPYNN.BF_4) has also been reported [64]. In this material there are magnetic layers containing the nitronyl nitroxide cation allyl radical with $S = 1/2$. Two *m*-MPYNN molecules make a dimer state via an intra-dimer ferromagnetic interaction $2J_0$. An implanted muon is expected to make a hydrogen-bonding state with F^- ions in this crystal [65]. Muon-spin depolarization by a dynamically fluctuating component of an internal field was still observed at 30 mK with no sign of a development of static magnetic order. It is suggested that the fluctuating component is caused by an intra-dimer ferromagnetic interaction of $2J_0/k_B = 23.3$ K between radicals. The absence of clear long-range static magnetic ordering of the dimer spins suggests that the ground state of *m*-MPYNN.BF_4 is indeed nonmagnetic [64].

7.3.3 Organic Salts

A variety of charge-transfer salts of the organic molecules TMTSF and BEDT-TTF are found to be very good metals and some have interesting magnetic properties. The properties of these salts can be chemically tuned by small variations of the anion (for example $(BEDT\text{-}TTF)_2NH_4Hg(SCN)_4$ is a superconductor with $T_C = 1$ K whereas the isostructural $(BEDT\text{-}TTF)_2KHg(SCN)_4$ is not). In several of these metallic charge-transfer salts it is found that there is a competition between a spin-density wave (SDW) ground state and a superconducting ground state. Thus the SDW state is of great interest to study, because its presence precludes superconductivity. If the muon occupies one site per unit cell and the SDW is commensurate with the crystal lattice, several distinct muon-spin precession frequencies would be expected to be measured. If the SDW is incommensurate, a Bessel function relaxation [22] is predicted if the field at the muon site varies sinusoidally; this is easily recognized, because the maxima and minima seem shifted by a $\pi/4$ phase. The SDW state in $(TMTSF)_2X$, where X = PF_6, NO_3, or ClO_4, has been detected by use of μSR; the

amplitude is similar for all three compounds [22]. The observed oscillations are consistent with an incommensurate SDW. In $(BEDT\text{-}TTF)_2KHg(SCN)_4$ a very weak SDW (of estimated amplitude $3 \times 10^{-3}\ \mu_B$) has been detected [66] below 12 K. Too small to be seen by NMR, this SDW state was suspected on the basis of susceptibility and Fermi surface experiments, but appeared in μSR data as a small change in zero-field spin relaxation.

High-conductivity molecular metals can be made from Cu salts of R_1,R_2-DCNQI, a flat molecule with large electron-affinity (a good acceptor). The salts consist of face to face stacks of R_1,R_2-DCNQI molecules next to chains of Cu ions. By changing the groups R_1 and R_2, by applying pressure or by selective deuteration, large changes in the electrical and magnetic properties can be induced, including metal–insulator transitions and charge and spin ordering. A zero-field muon spin-precession signal has been observed in a salt with $R_1 = CD_3$, $R_2 = D$ below 7 K associated with 3D magnetic ordering of the Cu spins [67]. Enhancement of the muon-spin relaxation rate is observed near and below the metal-insulator transition at 80 K, reflecting the localization of spins along the Cu columns (in which a threefold-sequence Cu^{2+}, Cu^{+}, Cu^{+} develops below the transition with a full spin only on every third Cu). The muon-site in this material has been determined by use of quadrupolar level crossing resonances between the muon and the imine nitrogen [67,68].

Another initially promising candidate for high-temperature organic magnetism is a electron-transfer salt comprising the organic donor TDAE and C_{60} [69]. The resulting material, TDAE-C_{60}, is electrically conducting and has a ferromagnetic-like transition at 16.1 K. It is, however, not metallic [70] and a μSR experiment [71] shows a broad distribution of internal fields at the muon site which could be consistent with incommensurate magnetic order resulting from density-wave formation.

The problem of understanding how muons stop in fullerenes is itself fascinating. In the case of pure C_{60}, muonium can implant inside the buckyball cage (this state is called endohedral muonium). The unpaired electron part of the muonium greatly enhances the sensitivity to scattering from conduction electrons so that this state is extremely useful for studying alkali-fulleride superconductors [72]. It is also possible to form a muonium radical by external addition, essentially muonium attacking the outside of a buckyball, breaking a double bond and ending up covalently bonded to a single saturated carbon atom. This center is very sensitive to the molecular dynamics of the local environment and has been used to extract the correlation time for molecular reorientation [73]. In metallic samples the muon's positive charge is screened by conduction electrons which form a cloud around the muon, of size given by a Bohr radius. Thus μ^+, rather than muonium, is the appropriate particle to consider in a metal. (The endohedral muonium found in alkali fulleride superconductors is the only known example of a muonium state in a metal.) In insulators and semiconductors screening cannot occur so that the muon is often observed in these systems either as muonium or is found to be chemically bound to one of the constituents, particularly to oxygen if it is present. Isotropic muonium states are found in many semiconducting and insulating systems. The value of the hyperfine coupling strength is close to that for vacuum (free) muonium if the band gap is large. For materials with smaller band gap the hyperfine coupling is lower reflecting the greater delocalization of the electron spin density on to neighboring atoms [1].

7.3.4 Nanomagnets

Large magnetic molecules have recently been employed in studies of mesoscopic magnetism which attempt to bridge the gap between the microscopic world of quantum-mechanical atomic magnets and the macroscopic world of classical magnets [74]. This field has grown rapidly, because of interest in phenomena such as macroscopic quantum tunneling of magnetization [75]. One system which has been much studied is the molecule $[Mn_{12}O_{12}(CH_3COO)_{16}(H_2O)_4]$, $Mn_{12}O_{12}$ acetate for short, which contains a cluster of 12 Mn ions, four inner Mn^{4+} are parallel to each other (yielding a spin of $4 \times 3/2 = 6$) and the remaining eight Mn^{3+} ions are also parallel (yielding a spin of $8 \times 2 = 16$) with the two groups antiparallel (thus the next spin is $S = 10$). An $S = 10$ cluster has 21 energy levels and μSR and proton NMR have been used to study the interplay between thermal fluctuations and tunneling between different states [76,77]. These clusters provide attractive and well-defined model systems for testing theories of relaxation and dynamics. The μSR experiments described above are, therefore, likely to be extended to the many other magnetic molecular clusters which have recently been discovered. Superparamagnetism has already been effectively studied using muons in inorganic systems [78] and an extension of this technique to organic materials would be quite natural.

7.4 Conclusions

Though a relatively new technique, μSR has already been found to be a useful addition to the armory of experimental probes available to physicists and chemists interested in organic and molecular systems. Unlike most neutron methods, μSR experiments do not require samples to be deuterated, and, because organic materials usually contain much hydrogen, this is an obvious advantage. Muons detect impurities only as a relative volume fraction, so one is not as easily fooled into believing the magnetism of a nonmagnetic sample with a magnetic impurity as would be the case when performing a bulk susceptibility measurement. μSR is therefore an ideal complement to traditional magnetic measurements. Although the technique requires the use of some large-scale, expensive, apparatus, muon beam-lines can be cheaply added on to accelerators designed to produce neutrons with no extra demands on the original accelerator. Such facilities are available for user access and scientists working in this field can therefore make good use of them. Determining the muon-site remains a complication that can sometimes hinder straightforward interpretation of the data, but with the increasing experience being gained in many types of sample together with the use of simulations of muon-sites, many of these difficulties can be circumvented. Thus as the field of molecular magnetism continues to grow, the muon technique looks likely to continue to grow with it.

My own work in μSR over several years, some of which is described above, is supported by the EPSRC, UK. It is a pleasure to acknowledge the collaboration of Rob Bewley, Kim Chow, Bill Hayes, Anke Husmann, Thomas Jestädt, Brendon

Lovett, Mohammedally Kurmoo, Ishbel Marshall, Paul Pattenden, Francis Pratt, Tadashi Sugano, and Renela Valladares and the assistance and support of the staff of the ISIS Pulsed Muon Facility and the Paul Scherrer Institute Muon Group.

References

[1] S. F. J. Cox, *J. Phys. C* **1987**, *20*, 3187–3319.
[2] A. Schenck, *Muon Spin Rotation Spectroscopy*, Adam Hilger, **1985**.
[3] J. H. Brewer in *Encyclopaedia of Applied Physics*, VCH, **1994**, *11*, pp. 23–53.
[4] A. Schenck, F. N. Gygax in *Handbook of Magnetic Materials*, volume 9, edited by Buschow, K. H. J., (Elsevier), **1995**, pp. 57–302.
[5] P. Dalmas deReotier, A. Yaouanc, *J. Phys.: Condens. Matter* **1997**, *9*, 9113–9166.
[6] S. J. Blundell, *Contemp. Phys.* **1999**, *40*, 175–192.
[7] E. Morenzoni, F. Kottmann, D. Maden, B. Matthias, M. Meyberg, T. Prokscha, T. Wutzke, U. Zimmermann, *Phys. Rev. Lett.* **1994**, *72*, 2793–2796.
[8] K. Nagamine, Y. Miyake, K. Shimomura, P. Birrer, M. Iwasaki, P. Strasser, T. Kuga, *Phys. Rev. Lett.* **1995**, *74*, 4811–4814.
[9] S. J. Blundell, *Appl. Mag. Res.* **1997**, *13*, 155–164.
[10] F. L. Pratt, S. J. Blundell, W. Hayes, K. Nagamine, K. Ishida, A. P. Monkman, *Phys. Rev. Lett.* **1997**, *79*, 2855–2858.
[11] F. L. Pratt, W. Hayes, G. R. Mitchell, B. Rossi, M. S. Kiani, B. D. Malhotra, S. S. Pandey, A. Milton, A. P. Monkman, *Synth. Met.* **1993**, *55*, 677–684.
[12] F. L. Pratt, S. J. Blundell, P. A. Pattenden, W. Hayes, K. H. Chow, A. P. Monkman, T. Ishiguro, K. Ishida, K. Nagamine, *Hyp. Int.* **1997**, *106*, 33–38.
[13] S. L. Lee, F. L. Pratt, S. J. Blundell, C. M. Aegerter, P. A. Pattenden, K. H. Chow, E. M. Forgan, T. Sasaki, W. Hayes, H. Keller, *Phys. Rev. Lett.* **1997**, *79*, 1563–1566.
[14] S. J. Blundell, S. L. Lee, F. L. Pratt, C. M. Aegerter, T. Jestadt, B. W. Lovett, C. Ager, T. Sasaki, V. N. Laukhin, E. Laukhina, E. M. Forgan, W. Hayes, *Synth. Met.* **1999**, *103*, 1925–1928.
[15] A. B. Denison, H. Graf, W. Kündig, P. F. Meier, *Helv. Phys. Acta* **1979**, *52*, 460–517.
[16] A. Amato, *Rev. Mod. Phys.* **1997**, *69*, 1119–1179.
[17] J. Chappert in *Muons and Pions in Materials Research* ed. J. Chappert and R. I. Grynszpan, Elsevier, **1984**, pp. 35–62.
[18] S. R. Kreitzman, D. L. Williams, N. Kaplan, J. R. Kempton, J. H. Brewer, *Phys. Rev. Lett.* **1988**, *61*, 2890–2894.
[19] Th. Jestädt, K. H. Chow, S. J. Blundell, W. Hayes, F. L. Pratt, B. W. Lovett, M. A. Green, J. E. Millburn, M. J. Rosseinsky, *Phys. Rev. B* **1999**, *59*, 3775–3782.
[20] R. Kubo, T. Toyabe, in *Magnetic Resonance and Relaxation*, ed. R. Blinc, **1967**, pp. 810–823 North-Holland, Amsterdam.
[21] J. Major, J. Mundy, M. Schmolz, A. Seeger, K. P. Döring, K. Fürderer, M. Gladisch, D. Herlach, G. Majer, *Hyp. Int.* **1986**, *31*, 259–264.
[22] L. P. Le, A. Keren, G. M. Luke, B. J. Sternlieb, W. D. Wu, Y. J. Uemura, J. H. Brewer, T. M. Riseman, R. V. Upasani, L. Y. Chiang, W. Kang, P. M. Chaikin, T. Csiba, G. Grüner, *Phys. Rev. B* **1993**, *48*, 7284–7296.
[23] R. S. Hayano, Y. J. Uemura, J. Imazato, N. Nishida, T. Yamazaki, R. Kubo, *Phys. Rev. B* **1979**, *20*, 850–859.

[24] Y. J. Uemura, T. Yamazaki, D. R. Harshman, M. Senba, E. J. Ansaldo, *Phys. Rev. B* **1985**, *31*, 546–563.
[25] I. A. Campbell, A. Amato, F. N. Gygax, D. Herlach, A. Schenck, R. Cywinski, S. H. Kilcoyne, *Phys. Rev. Lett.* **1994**, *72*, 1291–1294.
[26] A. Keren, P. Mendels, I. A. Campbell, J. Lord, *Phys. Rev. Lett.* **1996**, *77*, 1386–1389.
[27] E. Roduner, *Chem. Rev.* **1993**, *22*, 337–346.
[28] I. D. Reid, T. Azuma, E. Roduner, *Nature* **1990**, *345*, 328–330.
[29] F. L. Pratt, *Phil. Mag. Lett.* **1997**, *75*, 371–379.
[30] K. Nagamine, K. Ishida, T. Matsuzaki, K. Nishiyama, Y. Kuno, T. Yamazaki, *Phys. Rev. Lett.* **1984**, *53*, 1763–1766.
[31] W. Hayes, *Phil. Trans. R. Soc. Lond. A*, **1995**, *350*, 249–263.
[32] A. Yaouanc, P. D. Dereotier, E. Frey, *Phys. Rev. B* **1993**, *47*, 796–809.
[33] O. Kahn, *Molecular Magnetism*, **1993**, VCH.
[34] M. Tamura, Y. Nakazawa, D. Shiomi, K. Nozawa, Y. Hosokoshi, M. Ishikawa, M. Takahashi, M. Kinoshita, *Chem. Phys. Lett.* **1991**, *186*, 401–404.
[35] F. L. Pratt, R. Valladares, J. Caulfield, I. Deckers, J. Singleton, A. J. Fisher, W. Hayes, M. Kurmoo, P. Day, T. Sugano, *Synth. Met.* **1993**, *61*, 171–175.
[36] L. P. Le, A. Keren, G. M. Luke, W. D. Wu, Y. J. Uemura, M. Tamura, M. Ishikawa, M. Kinoshita, *Chem. Phys. Lett.* **1993**, *206*, 405–408.
[37] S. J. Blundell, P. A. Pattenden, R. M. Valladares, F. L. Pratt, T. Sugano, W. Hayes, *Sol. Stat. Commun.* **1994**, *92*, 569–572.
[38] S. J. Blundell, P. A. Pattenden, F. L. Pratt, R. M. Valladares, T. Sugano, W. Hayes, *Europhys. Lett.* **1995**, *31*, 573–578.
[39] S. J. Blundell, P. A. Pattenden, F. L. Pratt, K. H. Chow, W. Hayes, T. Sugano, *Hyp. Int.* **1997**, *104*, 251–256.
[40] P. A. Pattenden, R. M. Valladares, F. L. Pratt, S. J. Blundell, A. J. Fisher, W. Hayes, T. Sugano, *Synth. Met.* **1995**, *71*, 1823–1824.
[41] S. J. Blundell, T. Sugano, P. A. Pattenden, F. L. Pratt, R. M. Valladares, K. H. Chow, H. Uekusa, Y. Ohashi, W. Hayes, *J. Phys.: Condens. Matter* **1996**, *8*, L1–L6.
[42] J. L. Garçia-Muñoz, J. Cirujeda, J. Veciana, S. F. J. Cox, *Chem. Phys. Lett.* **1998**, *293*, 160–166.
[43] S. J. Blundell, P. A. Pattenden, K. H. Chow, F. L. Pratt, T. Sugano, W. Hayes, *Synth. Met.* **1997**, *85*, 1745–1746.
[44] T. Sugano, F. L. Pratt, M. Kurmoo, N. Takeda, M. Ishikawa, S. J. Blundell, P. A. Pattenden, R. M. Valladares, W. Hayes, P. Day, *Synth. Met.* **1995**, *71*, 1827–1828.
[45] T. Sugano, M. Kurmoo, P. Day, F. L. Pratt, S. J. Blundell, W. Hayes, M. Ishikawa, M. Kinoshita, Y. Ohashi, *Mol. Cryst. Liq. Cryst.* **1995**, *271*, 107–114.
[46] R. M. Valladares, A. J. Fisher, S. J. Blundell, W. Hayes, *J. Phys.: Condens. Matter* **1998**, *10*, 10701–10713.
[47] R. Imachi, T. Ishida, T. Nogami, S. Ohira, K. Nishiyama, K. Nagamine, *Chem. Lett.* **1997**, *235*, 233–234.
[48] M. Saint Paul, C. Veyret, *Phys. Lett.* **1973**, *45A*, 362–364.
[49] A. Benoit, J. Flouquet, B. Gillon, J. Schweizer, *J. Magn. Magn. Mat.* **1983**, *31–34*, 1155–1156.
[50] G. Chouteau, Cl. Veyret-Jeandey, *J. Physique* **1981**, *42*, 1441–1444.
[51] T. Sugano, S. J. Blundell, F. L. Pratt, T. Jestadt, B. W. Lovett, W. Hayes, P. Day, *Mol. Liq. Cryst.* in press.
[52] S. T. Bramwell, P. C. W. Holdsworth, *J. Phys.: Condens. Matter* **1993**, *5*, L53–L59.
[53] F. Palacio, G. Antorrena, M. Castro, R. Burriel, J. Rawson, J. N. B. Smith, N. Bricklebank, J. Novoa, C. Ritter, *Phys. Rev. Lett.* **1997**, *79*, 2336–2339.

[54] F. L. Pratt, A. E. Goeta, F. Palacio, J. M. Rawson, J. N. B. Smith, *Physica B* in press.
[55] S. Chittipeddi, K. R. Cromack, J. S. Miller, A. J. Epstein, *Phys. Rev. Lett.* **1997**, *58*, 2695–2698.
[56] Y. J. Uemura, A. Keren, L. P. Le, G. M. Luke, B. J. Sternlieb, W. D. Wu, *Hyp. Int.* **1994**, *85*, 133–144.
[57] M. Kurmoo, C. J. Kepert, *New J. Chem.* **1998**, *22*, 1515–1524.
[58] J. L. Manson, C. R. Kmety, Q. Z. Huang, J. W. Lynn, G. M. Bendele, S. Pagola, P. W. Stephens, L. M. LiableSands, A. L. Rheingold, A. J. Epstein, J. S. Miller, *Chem. Mater.* **1998**, *10*, 2552–2560.
[59] S. R. Batten, P. Jensen, B. Moubaraki, K. S. Murray, R. Robson, *Chem. Comm.* **1998**, *10*, 439–440.
[60] Th. Jestädt, M. Kurmoo, S. J. Blundell, B. W. Lovett, F. L. Pratt, M. Hayes, *Synth. Met.* **1999**, *103*, 2325–2326.
[61] S. J. Blundell, F. L. Pratt, P. A. Pattenden, M. Kurmoo, K. H. Chow, S. Takagi, T. Jestadt, W. Hayes, *J. Phys.: Condens. Matter* **1997**, *9*, L119–L124.
[62] B. W. Lovett, S. J. Blundell, T. Jestadt, F. L. Pratt, M. Kurmoo, S. Tagaki, W. Hayes, *Synth. Met.* **1999**, *103*, 2034–2037.
[63] B. W. Lovett, S. J. Blundell, T. Jestadt, F. L. Pratt, M. Kurmoo, S. Tagaki, W. Hayes, *Phys. Rev. B* **2000**, *61*, 12241–12248.
[64] I. Watanabe, N. Wada, H. Yano, T. Okuno, K. Awaga, S. Ohira, K. Nishiyama, K. Nagamine, *Phys. Rev. B* **1998**, *58*, 2438–2441.
[65] J. H. Brewer, S. R. Kreitzman, D. R. Noakes, E. J. Ansaldo, D. R. Harshman, R. Keitel, *Phys. Rev. B* **1986**, *33*, 7813–7816.
[66] F. L. Pratt, T. Sasaki, N. Toyota, K. Nagamine, *Phys. Rev. Lett.* **1995**, *74*, 3892–3895.
[67] F. L. Pratt, P. A. Pattenden, S. J. Blundell, T. Jestadt, K. H. Chow, W. Hayes, R. Kato, M. Tamura, H. Sawa, S. Aonuma, *Hyp. Int.* **1997**, *104*, 357–362.
[68] F. L. Pratt, P. A. Pattenden, S. J. Blundell, K. H. Chow, T. Jestädt, W. Hayes, R. Kato, M. Tamura, H. Sawa, Y. Kashimura, *Synth. Met.* **1997**, *85*, 1747–1748.
[69] P.-M. Allemand, K. C. Khemani, A. Koch, F. Wudl, K. Holczer, S. Donovan, G. Grüner, J. D. Thompson, *Science*, **1991**, *253*, 301–303.
[70] A. Omerzu, D. Mihailovic, S. Tomic, O. Milat, N. Biskup, *Phys. Rev. Lett.* **1996**, *77*, 2045–2048.
[71] A. Lappas, K. Prassides, K. Vavekis, D. Arcon, R. Blinc, P. Cevc, A. Amato, R. Feyerherm, F. N. Gygax and A. Schenck, *Science* **1995**, *267*, 1799–1802.
[72] W. A. MacFarlane, R. F. Kiefl, S. Dunsiger, J. E. Sonier, J. Chakhalian, J. E. Fischer, T. Yildirim, K. H. Chow, *Phys. Rev. B* **1998**, *58*, 1004–1024.
[73] R. F. Kiefl, J. W. Schneider, A. MacFarlane, K. Chow, T. L. Duty, T. L. Estle, B. Hitti, R. L. Lichti, E. J. Ansaldo, C. Schwab, P. W. Percival, G. Wei, S. Wlodek, K. Kojima, W. J. Romanow, J. P. McCauley, N. Coustel, J. E. Fischer, A. B. Smith, *Phys. Rev. Lett.* **1992**, *68*, 2708–2712.
[74] D. Gatteschi, A. Caneschi, L. Pardi, R. Sessoli, *Science* **1994**, *265*, 1054–1058.
[75] L. Thomas, F. Lionti, R. Ballou, D. Gatteschi, R. Sessoli, B. Barbara, *Nature* **1996**, *383*, 145–147.
[76] A. Lascialfari, D. Gatteschi, F. Borsa, A. Shastri, Z. H. Jang, P. Carretta, *Phys. Rev. B* **1998**, *57*, 514–520.
[77] A. Lascialfari, Z. H. Jang, F. Borsa, P. Carretta, D. Gatteschi, *Phys. Rev. Lett.* **1998**, *81*, 3773–3776.
[78] R. I. Bewley, R. Cywinski, *Phys. Rev. B* **1998**, *58*, 11544–11551.

Magnetism: Molecules to Materials I: Models and Experiments.
Edited by Joel S. Miller and Marc Drillon

ISBNs: 3-527-29772-3 (Hardback); 3-527-60084-1 (Electronic)

8 Photomagnetic Properties of Some Inorganic Solids

François Varret, Marc Nogues, and Antoine Goujon

8.1 Introduction

Photomagnetism is a fascinating field which covers all changes in magnetic properties induced by the application of light [1,2]: photoelectrons in semiconductors, optical electron transfers in insulators, photo-induced defects and excitons of short lifetime, photoexcited states of long lifetime. Both irreversible and reversible effects can be observed. The first examples were provided by insulators, Si^{4+} doped YIG [3–5], spinels and ferrites [6–8], aluminosilicate glasses [9] and amorphous materials [10] ..., as well as magnetic and semimagnetic semiconductors [11–13].

Some of these systems contain structural disorder and exhibit subtle aging effects, with kinetics sensitive to the presence of light. The so-called "magnetic after effect" (MAE), which consists in a slow variation of the magnetization after the system has been submitted to a rapid change of magnetic field or temperature, has its kinetics changed transiently or permanently by the presence of light. We describe here the first example of photo-stimulated MAE in an inorganic solid, $Cs_{0.83}Cr_{2.10}(CN)_6$, $3.9H_2O$ [14]. The effect is reversible, i. e. only transient, and we shall focus on the novel access, by optical means, to the aging properties of the disordered system.

Further promising effects appeared with the discovery of the light-induced excited spin state trapping (LIESST) in spin crossover systems [15,16]. The major aspects of LIESST are described by P. Gütlich in the future volume. Using different wavelengths, the low spin/high spin (LS/HS) transformation was shown to be reversible [16], an appealing property for optical information storage. Accordingly, the system was denoted "photo-switchable". See also [17,18] for review papers and applications. The long lifetime of the photoexcited state is ensured by the energy barrier associated with the structural relaxation involved in the spin state change. As a matter of fact, the working temperature of photo-controlled devices based on spin crossover materials does not seem to exceed ~70 to 80 K. A more severe drawback is the low efficiency of the photoexcitation process: up to recently, it was admitted that one photon might switch no more than a single spin-crossover molecule. Presently, efforts are under way in several groups in order to produce multi-site photoexcitation processes, since recent experiments obtained the first evidence for these collective effects, either in a binuclear solid [19], or using an intense pulse of laser light [20]. The collective photoexcitation process, or "photo-induced phase transition" (PIPT) was introduced as the "Domino effect", for a neutral to ionic transition [21]. Such a collective photoexcitation, although actively researched in the field of photomagnetism, does not appear in the examples reported here.

The magnetic properties of the spin-crossover systems are those of paramagnets, eventually diamagnets in the Fe^{II} low-spin state, and usually photoexcitation does not result in spectacular changes in the magnetic properties: the value of the effective magnetic moment somewhat increases following the LS $\rightarrow$ HS conversion. Application of a magnetic field during illumination does not seem (to our knowledge) to affect the photoexcitation process, presumably because the magnetic energy is extremely small compared to the photon energy. Some interesting effects, however, are obtained in binuclear solids, since a HS–HS molecule which involves an antiferromagnetic interaction exhibits a magnetization smaller than a HS–LS molecule. This was the criterion for deciding that photoexcitation proceeds by pairs in the binuclear system reported elsewhere [19]. We shall describe here the spin crossover systems with the purpose of illustrating some general features of photoexcitation in inorganic systems, because they are the most documented photo-switchable inorganic systems, and they are both thermochromic, photochromic and piezochromic, because of the structural relaxation which follows the optical electron transfer [15,16]. These properties provide various ways for investigating the photoexcitation effects.

Further examples of photo-switchable systems are also provided by inorganic solids involving a spin crossover. However, in principle, other mechanisms might provide the energy barrier needed to ensure long-lifetime photoexcited states. For example photoisomerizable ligands, such as styrene, should be suitable; however the design of 3D solids liable to accept the geometrical changes due to the conformational isomerization seems to be a real challenge. The first results of this research came from the Orsay Group [22], who succeeded in synthesizing a solid where the spin-crossover is triggered by ligand photoisomerization. Also, photomagnetic properties have been reported for the Ni-nitroprusside system [23], but does not seem to be consistent with the structural [24] and Mössbauer [25] data of the related compound Na-nitroprusside, so we think the problem remains open.

The recent examples of photomagnetic inorganic solids involving a spin crossover are those of the Prussian Blue (PB) analog, Cobalt hexacyanoferrate $CoFe(CN)_6$ [26–29] and of the valence tautomeric system Co-semiquinone (Co-sq) [30]. Both involve an interatomic optical electron transfer, associated with a spin change of the photo-induced Co^{II} state, from LS ($S = 1/2$) to HS ($S = 3/2$). This mechanism is precisely the valence tautomerism previously introduced by Hendrickson et al [31] to explain the temperature-induced phase transition they observed in Co-sq, with the (spontaneous) electron transfer associated with the Co^{II} spin change. While the investigations of the photomagnetic properties of Co-sq yet are at their very beginning, the PB analog derivatives are already better documented, at least from the photoexcitation viewpoint [29], with the specific features of photo-induced ferrimagnetism and magnetic metastability [28,29]. One application of the photo-induced ferrimagnetism is the design of a "photo-induced magnetic pole inversion" [32]. The novel aspects involved in the "magnetic metastability" of the photoexcited state have been investigated quite recently [53]. Some other perspectives offered by these "tunable magnets" will be discussed.

A further family of photomagnetic inorganic solids is linked with the charge transfer salts, following the discovery of a photo-induced spin-flop in MnTEtOPP-TCNE, thus realizing a "soft–hard tunable magnet" [33]. Obviously, tune all magnetic prop-

erties by applying light will probably be realized in the next few years, and the further challenge will be to obtain photoexcited states with long lifetimes at reasonably high temperatures, and with a reasonably high efficiency. Practical applications will concern information storage and data processing. Also, a light-induced magnetic phase transition was recently evidenced in a Pr–La manganite [34], thus promising a novel access to hot subject of colossal magnetoresistance.

We describe here recent work of the Versailles group on several systems, spin transition solids, PB analog, valence tautomeric solid. We include general features of photoexcitation and cooperative relaxation, together with technical aspects, such as the simultaneous detection by magnetization and reflectivity [35]. A first review of photomagnetic inorganic solids was given three years ago in [28], and comparison with the present report illustrates the rapid progress in this field.

8.2 Technical and Practical Aspects

The magnetization curves are recorded using a SQUID magnetometer (Quantum Device MPMS5) operating in the alternative mode, equipped with an Y-shaped optical fiber, made of multiwire silica, for light irradiation and reflectivity measurement in the visible – near IR range. The flexible end with a larger number of wires is used for excitation and is connected to a broadband source of light (tungsten halogen lamp, 100 W), through interferential filters (100 nm bandwidth). A cut-off filter $\lambda > 665$ nm provided, with the source and fibers, a large intensity in the range 600–1000 nm, up to $\sim$100 mW cm^{-2}. The light filtered with the cut-off filter is denoted here "filtered red light". The other flexible end is used when thermo- or photochromic properties are studied and is connected to a photodiode at the input of the reflectivity recording system. The first reflectivity device using a Y-shaped optical fiber for monitoring the spin transition through the color change of the compounds was reported in [36]. Our reflectivity device [35] uses photodiodes as detectors for both incident and reflected light, connected to a 3-channel "intelligent" temperature controller (Oxford Instruments ITC4 or ITC 502). The device is fitted to the magnetometer. A coupled magnetization/reflectivity experiment is carried out as follows: the sample is placed in the SQUID magnetometer, which controls the temperature, measures the magnetization and the time. Independently, the reflectivity device is driven by an other computer (IBM PC) which also measures the time and dialogs with the 3-channel temperature controller. Post-synchronization of the data is made using home-made software. The optical fiber is housed in a stainless steel tube, $\sim$4 mm in outer diameter, which also holds the sample cell in the SQUID, as sketched in Fig. 1.

We have reduced as much as possible the distance between the end of the optical fibers and the sample, down to $\sim$1 mm, despite of the large magnetic contributions of the stainless steel tube. To keep the end of the tube far enough from the pick-up coils of the SQUID, we have inserted a pair of short rods of silica (optical fibers), each approximately 10 cm long, on either side of the sample cell. The best choice was a silica light-guide, whose transmittance is not disturbed by the unavoidable

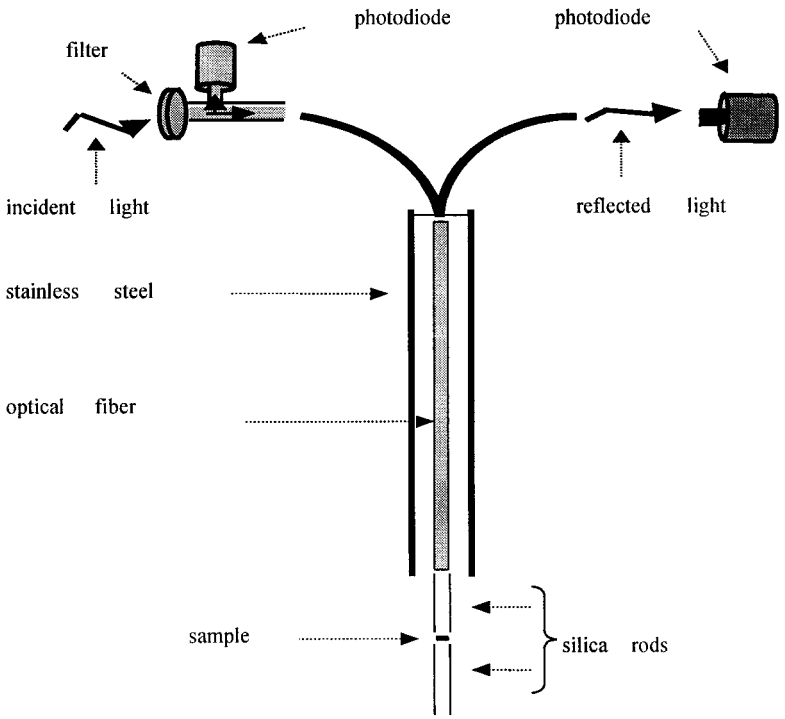

Fig. 1. The Y-shaped optical fiber used for photoexcitation and reflectivity in the SQUID. Such a device allows the investigation of both surface and volume properties of photoexcitable compounds

condensation of gases at low temperature, previously reported in [28]. However, the magnetic contribution of the empty system (cell + silica rods) is far from negligible in some cases, and we systematically subtract this parasitic contribution, in all situations of temperature and field. The needed calibrations of light intensity were made using a home made bolometer, prior to the experiments.

8.2.1 Magnetic and Reflectivity Measurements: Twofold Access to the Behavior under Photoexcitation

We briefly discuss here the agreement and complementary aspects of the two techniques, following [28,35]. The optical and magnetic data, simultaneously measured, are compared at best on the example of spin transition solids. The case of Fe(II) spin crossover compounds is quite well documented (review papers in [17]): most of crystals are transparent at high temperatures, i. e. in the high-spin (HS) state, and dark purple in the low-temperature, low-spin (LS) state, with absorption bands in the red (~800 nm) and in the green (~550 nm) respectively. A high contrast is thus obtained for reflectivity, by using any of these bands. In some cases, the high-spin fractions

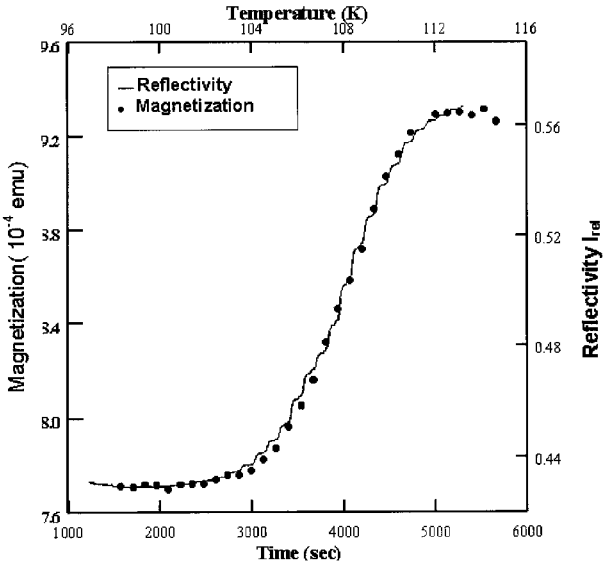

Fig. 2. Magnetization and reflectivity data at the thermal spin transition of $[Fe_{0.50}Co_{0.50}(btr)_2(NCS)_2].H_2O$, in the heating mode. $H = 1000$ Oe, $\lambda = 550$ nm (after [35b]). The excellent agreement between the two sets of data has been obtained through magnetization and reflectivity adapted scales. A detailed inspection of the reflectivity curve reveals the step-wise character of the temperature sweep governed by the SQUID magnetometer

derived from the two techniques differ a little, and this is attributed to the surface character of reflectivity, which probes the material only down to the penetration depth of the radiation. We present in Fig. 2 the data, simultaneously recorded for the thermal spin transition of $Fe_{0.64}Co_{0.36}(btr)_2(NCS)_2].H_2O$, in the heating mode. An excellent agreement is obtained.

In Fig. 3 we have reported the data for the direct LIESST of the same material. The reflectivity data show a rapid transformation of the surface, up to saturation, while magnetization data reveal a slower transformation of the bulk. This is due to bulk absorption of light, which sizably reduces the intensity with respect to the incoming intensity. Another feature of Fig. 3 deserves to be discussed: the increase in the reflectivity signal. Such an increase seems to be the rule for spin-crossover compounds upon light-induced transformations, and is explained as merely due to the progressive removal of the absorbing centers, in other words to a bleaching process. The bleaching process works as well for the reverse LIESST, with another radiation, as shown in Fig. 4.

The case of the PB analog, Cobalt hexacyanoferrate, is shown in Fig. 5. The photodarkening effect is presumably due to a light-induced shift of the charge-transfer bands which are very intense. The complete understanding of the photodarkening effect requires a spectral study, which is in progress. The effect of bulk absorption of light is quite large in this deep blue compound.

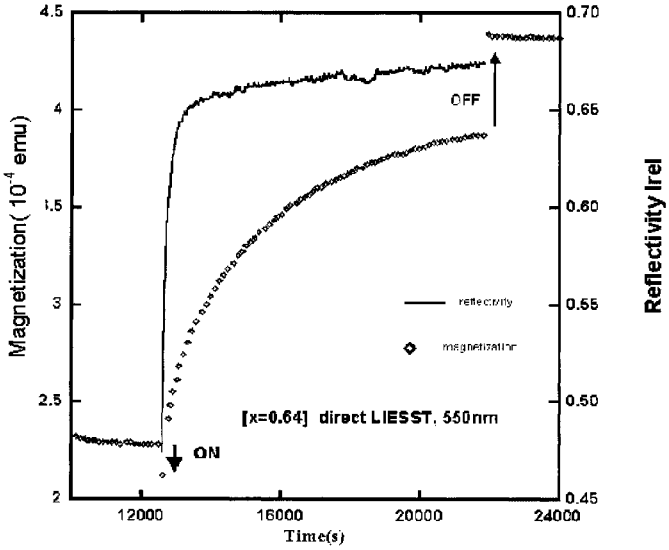

Fig. 3. Direct LIESST of $[Fe_{0.64}Co_{0.36}(btr)_2(NCS)_2].H_2O$, at 8 K, 50 Oe, 550 nm, 25 mW cm^{-2} (after [35b]). The magnetization increases due to the light-induced population of the HS state. The reflectivity increases, thus indicating a bleaching process. The reflectivity signal, given by the surface of the sample, saturates rapidly. The magnetization signal increases slowly, because absorption of light reduces the intensity of light in the bulk. Also notice the jumps due to the thermal effect of light (developed in Fig. 6)

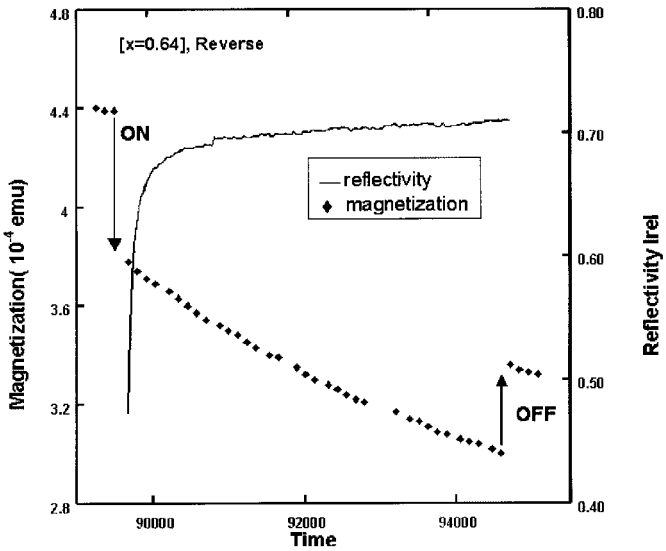

Fig. 4. Reverse LIESST of $[Fe_{0.64}Co_{0.36}(btr)_2(NCS)_2].H_2O$, at 8 K, 50 Oe, 800 nm, 25 mW cm^{-2}, after photoexcitation shown in Fig. 3 (after [35b]). The magnetization decreases due to the light-induced depopulation of the HS state. Bleaching, bulk absorption of light and thermal effects are again evidenced

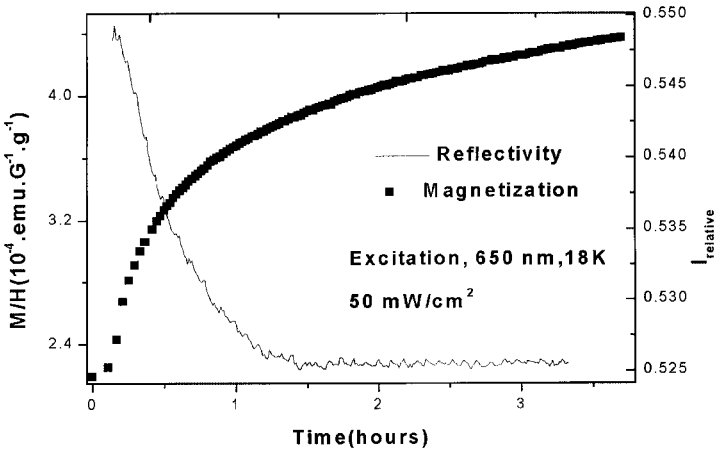

Fig. 5. Simultaneous measurement of reflectivity and magnetization of the PB analog $Rb_{0.52}Co[Fe(CN)_6]_{0.84}.2.31H_2O$, at 18 K, 1000 Oe, 750 nm, 50 mW cm^{-2} (after [29a]).The decrease in reflectivity indicates photodarkening of the sample

8.2.2 An Unavoidable Side-effect: Heating of the Sample

We first discuss an inherent effect of irradiation, which is the heating of the sample. Indeed, under permanent energy flow, the sample temperature may sizably rise above the controlled temperature of the heat exchanger. This heating effect is easily evidenced by chopped light experiments, as shown in Fig. 6. The sample is warmer when light is on, yielding to a quasi-immediate decrease in magnetization. The ther-

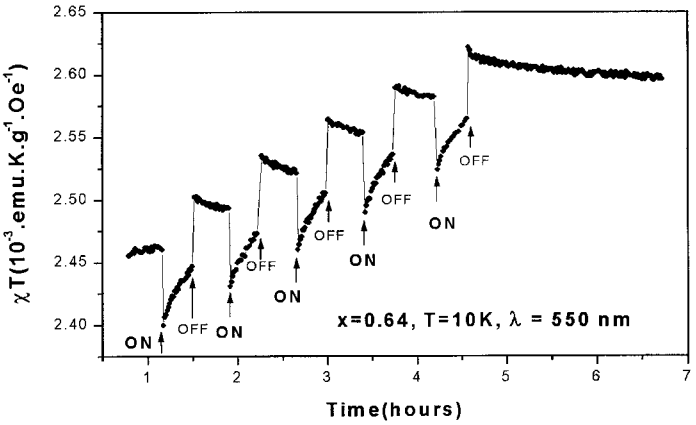

Fig. 6. Chopped light experiments on $[Fe_{0.64}Co_{0.36}(btr)_2(NCS)_2].H_2O$, at 10 K, 500 Oe, 550 nm, 25 mW cm^{-2}. The reversible jumps when light is switched on and off evidence the thermal effect of light

mal shift can be estimated for this paramagnetic sample, through the Curie law, as ≅ 0.25 K.

Another feature in Fig. 6 can be discussed: during the light-off stages, the magnetization decays a little, according to a stretched exponential, which is better seen on the right hand part of the curve. The complete explanation combines the bulk attenuation of light, previously discussed, the concept of cooperative relaxation, to be developed in the next section, and a "frontal propagation mode" of light in the sample, previously introduced by A. Hauser [16]. In a frontal mode, light enters progressively, bleaching the sample layer after layer. Cooperative relaxation is such that layers having reached the higher (weaker) excitation have the longer (shorter) lifetime. The chopped experiment is thus described as follows: during the light-on stages, a weakly excited layer is formed, at the penetration depth of light; this "frontier" layer decays rapidly during each light-off stage and can be created again during the next light-on stage. The stretched exponential decay is associated with the inhomogeneous excitation state of the sample, the detailed explanation of which will be given later.

8.2.3 The Problem of Bulk Absorption of Light

Optical absorption plays an ambiguous role in photoexcitation, since the photo process is based on a given absorption band, d–d or metal-to-ligand transfer, which, it is hoped, is intense, while strong bulk absorption prevents the light from penetrating in the bulk. It will be shown in the next section that cooperative effects may lead to an intensity threshold effect, making intensity problems crucial for a successful photoexcitation. Therefore, very often, in the most absorbing solids, photoexcitation is restricted to the vicinity of the surface of the sample. Reflectivity may be an elegant way to by-pass this difficulty, and may be encouraging towards applications, by optical means. However, it is not directly useful for magnetic purposes, and the recourse to thin films may be necessary. The recent success in photoexciting Langmuir-Blodgett films [37,38] is a real progress in this field.

8.3 Cooperative Effects (after Ref. [39])

A preliminary review of cooperative effects in photoswitchable systems is useful for understanding some of the features of the photomagnetic experiments in the solid state. We focus here on the relaxation effects which depopulate the photoexcited state, i. e. the decay which competes with the photoexcitation process during irradiation experiments, and therefore leads to a "photostationary state", or "steady state" of the system under permanent irradiation. We recently observed that the so-called "cooperative relaxation", previously analyzed by the Mainz and Bern groups [40], could induce an instability of the steady state, and hence lead to light-induced hys-

tereses: as a function of temperature, LITH = light-induced thermal hysteresis [41], of light intensity, LIOH = light-induced optical hysteresis, or of pressure, LIPH = light-induced pressure hysteresis. LIPH was predicted in [42] and partially observed in [43]. Examples so far reported are those of the spin transition solids, but this is not exclusive and such effects should be observed as well with other photoswitchable cooperative systems. The properties of spin-crossover solids [17] at low temperature are summarized as follows:

Spin-crossover solids usually have a low spin (LS) ground state. The optical switching is performed at low temperatures, by the so-called direct or inverse LIESST effect, using different wavelengths for the back and forth processes (blue/green and red light respectively). At higher temperatures (after photoexcitation) the metastable high spin (HS) state decays through a radiationless process [15,16], i. e. HS $\rightarrow$ LS relaxation occurs. Experimentally, the HS fraction, i. e. the relative amount of spin-crossover molecular units in the high-spin state, denoted n_{HS}, is measured as a function of time, via magnetic or optical measurements.

Cooperative relaxation [40] is characterized by a post-LIESST relaxation curve, $n_{\mathrm{HS}}(t)$ of sigmoidal shape, see Fig. 7. The relaxation rate $k_{\mathrm{HL}} = -\mathrm{d}n_{\mathrm{HS}}(t)/n_{\mathrm{HS}}(t)\mathrm{d}t$ is an increasing function of time, such that the effect is also denoted "self-accelerated relaxation". Detailed investigations of the former examples, in terms of thermally activated process showed a quasi linear dependence of the activation energy on the high-spin fraction, so that the relaxation rate could be expressed as:

$$\begin{aligned} k_{\mathrm{HL}}(T, n_{\mathrm{HS}}) &= k_{\infty} \exp\left(-\frac{Ea(n_{\mathrm{HS}})}{kT}\right) \\ &= k_{\infty} \exp\left(-\frac{Ea(0)}{kT}\right) \exp(-\alpha(T) n_{\mathrm{HS}}) \end{aligned} \tag{1}$$

where the self-acceleration factor α is proportional to the inverse temperature, the strength of interactions and the atomic concentration x in the active element. The linear dependence $E_a(n_{\mathrm{HS}})$ is correlated to a linear variation of the electronic energy gap $\Delta(n_{\mathrm{HS}})$ in the mean-field approach. The "moving" configurational diagram is shown in Fig. 8. A similar expression holds in the tunneling regime [40b].

Besides of the sigmoidal decay curves, cooperative relaxation results in a typical feature, already displayed in Fig. 6, in the case of inhomogeneous photoexcitation, a stretched exponential decay due to the distribution of relaxation times: the weakly excited layers of the sample (the deeper layers) decay faster that the more saturated layers (closer to the sample surface). In any relaxation experiment, after photoexcitation, as soon as the light is switched off, the weakly excited layers rapidly decay, and only the saturated layers remain excited, with a long lifetime; then the sigmoidal decay can be properly observed, at a long time scale.

Irradiation competes with the thermal HS $\rightarrow$ LS relaxation, and the balance between the HS $\rightarrow$ LS and LS $\rightarrow$ HS processes determines the evolution and the steady state of the system. In this balance, the spontaneous LS $\rightarrow$ HS relaxation is negligible at low temperatures, as shown by the detailed balance equation:

$$k_{\mathrm{HL}} n_{\mathrm{HS}}^{\mathrm{equil.}} = k_{\mathrm{LH}} n_{\mathrm{LS}}^{\mathrm{equil.}}, \quad \text{with} \quad n_{\mathrm{HS}}^{\mathrm{equil.}} \ll n_{\mathrm{LS}}^{\mathrm{equil.}}$$

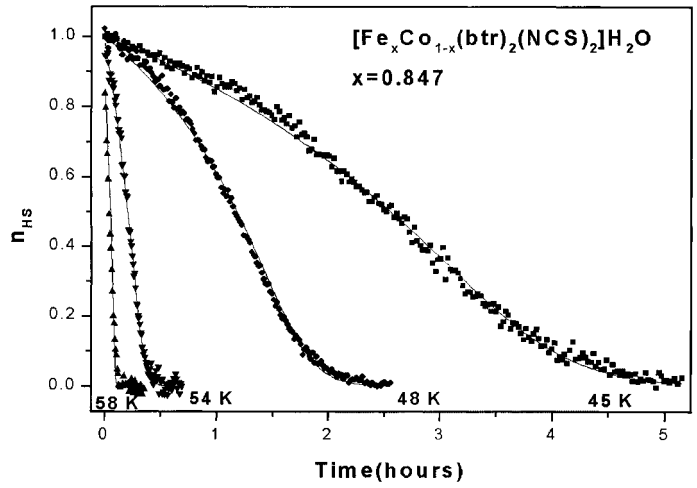

Fig. 7. Relaxation curve, i. e. HS → LS decay in the dark after photoexcitation, of $[Fe_{0.85}Co_{0.15}(btr)_2(NCS)_2].H_2O$, at several temperatures, $H = 1000$ Oe (after [46]). The sigmoidal shape, i. e. that of a self-accelerated decay, is typical for the so-called "cooperative relaxation" (see text)

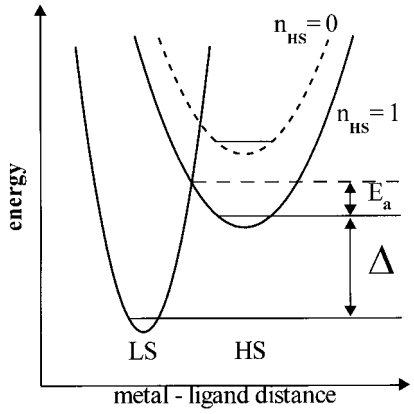

Fig. 8. Configurational diagram for spin-crossover, adapted from [39]. Cooperativity makes Δ a decreasing function of n_{HS}. In general terms, cooperativity correlates population and stability: increasing the population of a state increases its stability, both statically (lower energy) and dynamically (higher energy barrier)

Then, the master equation (evolution equation) of the system becomes:

$$\frac{dn_{HS}}{dt} = \Phi_{up} - \Phi_{down}$$
$$= I_0\sigma(1 - n_{HS}) - n_{HS}k_\infty \exp\left(-\frac{Ea(0)}{kT}\right) \exp(-\alpha(T, x)n_{HS}) \qquad (2)$$

where Φ_{up}, Φ_{down} are the flows up and down, $I_0\sigma$ the transition rate for a molecular unit to switch LS → HS, with I_0 the beam intensity and σ the atomic absorption cross-section.

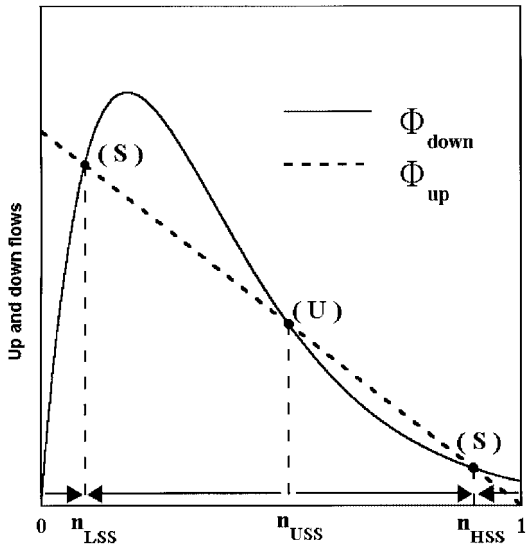

Fig. 9. Graphical resolution of Eq. (3) computed with $\alpha = 5.83$ (after [39]). "up" and "down" stand for LS $\rightarrow$ HS and HS $\rightarrow$ LS, respectively. The steady state values are given by the intersects of the curve (Φ_{down}) and the straight line (Φ_{up}). The slope of the straight line is proportional to I_0. $n_{\text{LSS}}, n_{\text{USS}}, n_{\text{HSS}}$, respectively stand for LS-rich, unstable, HS-rich steady states

The steady state of the system (dynamical equilibrium) occurs when Φ_{up}, Φ_{down} are set equal, leading to the nonlinear state equation:

$$n_{\text{HS}} k_\infty \exp\left(-\frac{E_a(0)}{kT}\right) \exp(-\alpha(T, x) n_{\text{HS}}) = I_0 \sigma (1 - n_{\text{HS}}) \tag{3}$$

Equation (3) has previously been proposed by Prigogine [44] for adsorption problems and may have up to 3 solutions for $\alpha > \alpha_c = 4$. The 3-solution situation is treated graphically in Fig. 9, which shows the number of solutions depends on the slope of the straight line, i. e. on the value of I_0.

The stability character of the steady states is shown in Fig. 10, through the time dependence of the system for various initial states. Such time dependencies have been indeed observed and modeled (see [45] Fig. 6).

The relaxation rates depend on temperature and pressure [40b,c], so that the steady states are controlled by intensity, temperature, and pressure. Therefore, thermal (constant I_0, p), optical (constant T, p) or pressure (constant T, I_0) hystereses, could be expected. We focus here on the optical hysteresis (LIOH), see Fig. 11.

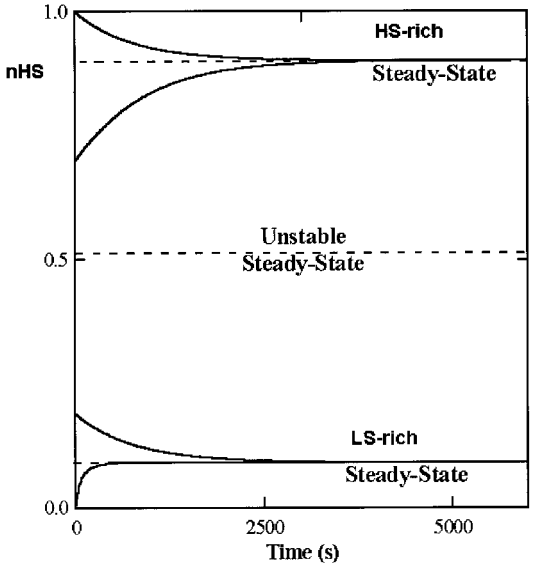

Fig. 10. Computed time dependence of the population of the photoexcited state under continuous excitation, using Eq. (2), for different initial states, with parameter values of Fig. 9 (after [39])

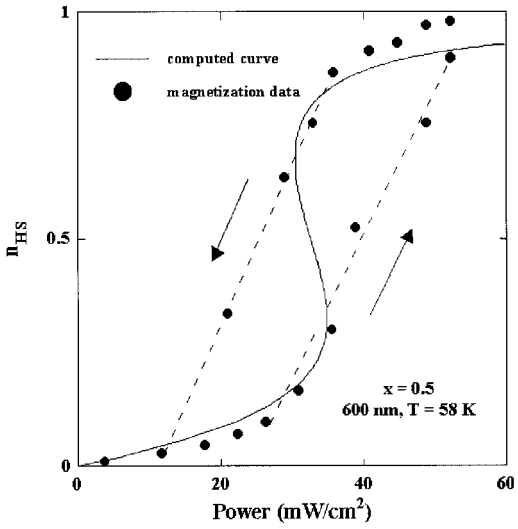

Fig. 11. Light Induced Optical Hysteresis loop, obtained with $[Fe_{0.50}Co_{0.50}(btr)_2(NCS)_2].H_2O$ at 58 K, 600 nm, and computed curve using Eq. (3) (after [39])

8.3.1 The Intensity Threshold Effect

Because the goal of quantitative LIESST is to reach the HS-rich steady state, it is clear that light-induced optical hysteresis has the effect of an intensity threshold. Of major importance is the fact that the threshold value dramatically increases on increasing the cooperativity parameter. This is illustrated in Fig. 12.

Strongly cooperative materials may even miss the initial energy barrier needed to provide the excited state a sufficient lifetime; the barrier has to be induced by the

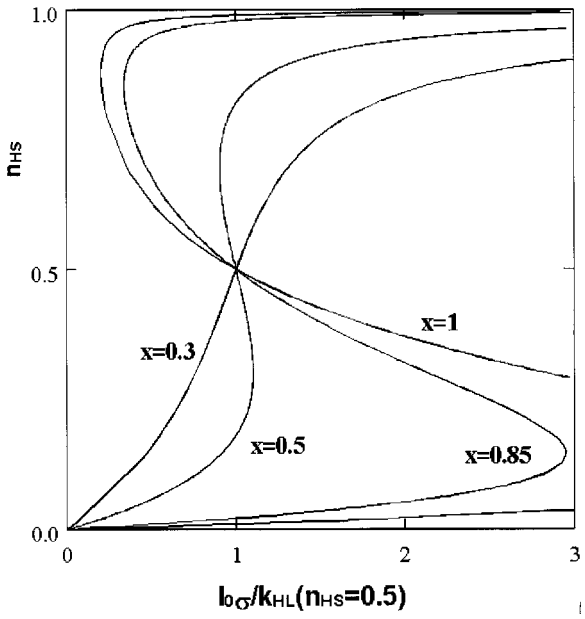

Fig. 12. Computed curves for the intensity threshold effect, using Eq. (3), plotted as a function of $I_0\sigma/k_{\mathrm{HL}}(n_{\mathrm{HS}} = 1/2)$, with x the atomic proportion of the spin-crossover element, and $\alpha(x = 0.5) = 4.7$ (after [39]). In a ideal case, $E_{\mathrm{a}}(n_{\mathrm{HS}} = 1/2)$ and consequently $k_{\mathrm{HL}}(n_{\mathrm{HS}} = 1/2)$ can be considered as independent of x, making the horizontal scale a true intensity scale. It is observed that the intensity needed for reaching the HS-rich steady state increases very rapidly with increasing cooperativity

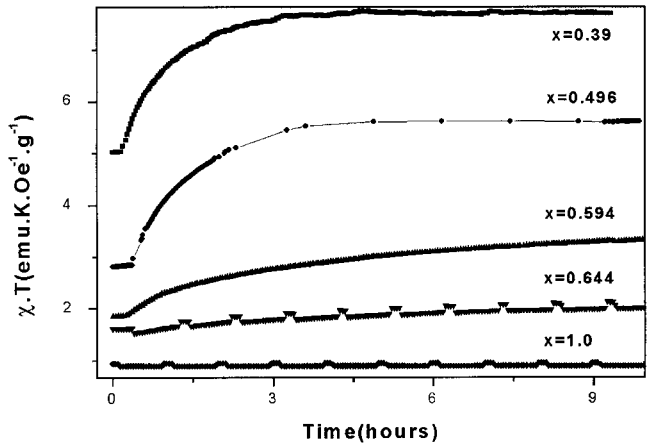

Fig. 13. Photoexcitation of $[Fe_xCo_{1-x}(btr)_2(NCS)_2].H_2O$ for different values of x, under identical conditions: $P \approx 5\,\mathrm{mW\,cm^{-2}}$, unfiltered white light, $H = 1000\,\mathrm{Oe}$ (after [46]). The most diluted compounds reach the larger magnetization because of the weaker cooperativity (see text)

population of the excited state. This explains, at least qualitatively, why the LIESST is almost inefficient for the pure $[Fe(btr)_2(NCS)_2]H_2O$ solid, while the light excitation is relatively easy for the diluted case. Illustrative data are reported in Fig. 13.

As a further consequence of light-induced instabilities, the onset of patterns, spin-domain like, can be predicted. Optical microscopy studies should be carried out on

single crystals under permanent irradiation. Both steady-state and transient patterns are expected, with possible periodic and chaotic behaviors. Transient patterns in single crystals [47] and "spurious" transient behaviors in powders [39a] have each been reported once and deserve more systematic studies.

8.4 Magnetic Properties of Prussian Blue Analogs

Bimetallic transition metal hexacyanides form 3D structures isotypic of the Prussian Blue (PB) $KFe^{III}[Fe^{II}(CN)_6]$. The ideal so-called 1:1 structure $K^IA^{III}[B^{II}(CN)_6]$ is cubic, as sketched in Fig. 14.

Chemical synthesis can be performed in aqueous solution, enabling the control of the nature of the metal in each site [48]. However, sizeable departures from ideal stoichiometry may occur with K^I or $B^{II}(CN)_6$ vacancies, partially filled by water molecules. Also some of the CN ligands may be reversed by irradiation with short wavelengths. This reversal did not seem to occur during our investigations. Recent attention has been drawn to these systems for two main reasons:

High-T_C ferrimagnets (T_C above room temperature [49]) have been prepared, thanks to a suited choice of transition metals [50].

Spectacular photo-induced magnetic effects have been observed [26] in the Cobalt hexacyanoferrate $K_{0.2}Co_{1.4}[Fe^{II}(CN)_6]$ ($T_C = 16\,K$). Irradiation at low temperature with red light induces a long lasting increase in both the magnetization and the Curie temperature (T_C from 16 to 20 K), see Fig. 15. By consecutive irradiation with blue

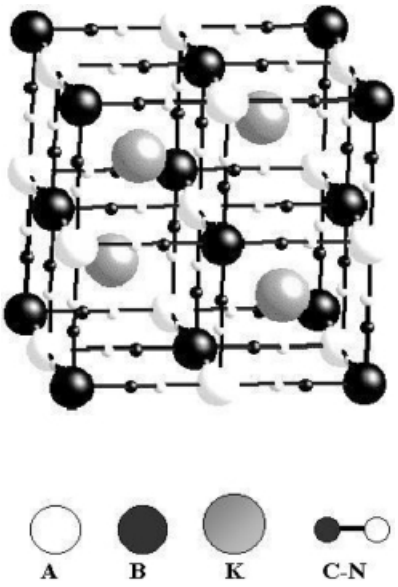

Fig. 14. The ideal Prussian Blue structure, formulated $K^IA^{III}[B^{II}(CN)_6]$.It contains tetrahedral sites for alkaline cations K, weak ligand-field octahedral sites, with N as first neighbors, for transition metal A, strong ligand-field octahedral sites, with C as first neighbors, for transition metal B

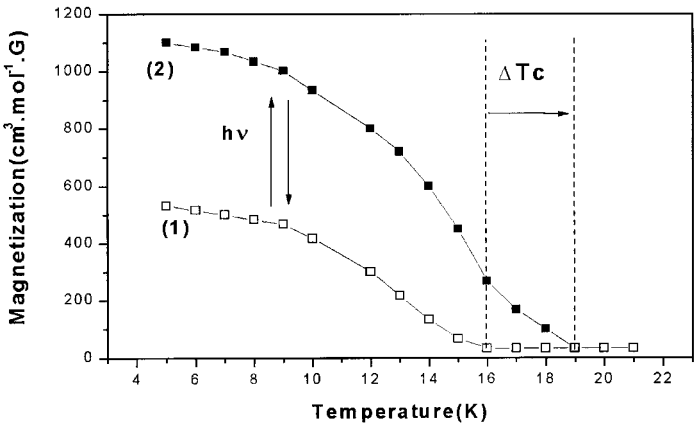

Fig. 15. Field cooled magnetization curves of $K_{0.2}Co_{1.4}[Fe^{II}(CN)_6]$ at $H = 5$G before (1) and after (2) red light irradiation. The magnetization enhanced by illumination can be removed by thermal annealing above 150 K (after [26])

light the sample (almost) recovers its initial magnetic properties. This is explained as due to an optical electron transfer from Fe to Co (red light) or from Co to Fe (blue light), according to:

$$\begin{array}{cccccc} Co^{III}(LS) & + & Fe^{II}(LS) & \rightarrow & Co^{II}(HS) & + & Fe^{III}(LS) \\ S(A) = 0 & & S(B) = 0 & & S(A) = 3/2 & & S(B) = 1/2 \end{array} \tag{4}$$

The evidence for the electron transfer was provided by Mössbauer spectroscopy [27]. In this reference, it was also shown that for a chosen stoichiometry, the material initially is (approximately) a diamagnet, and the ferrimagnetic state is entirely created by application of light. Thus the concept of "photo-tunable magnet" was created for which recent work was presented in [53], and further applications were researched, e. g. "photo-induced magnetic pole inversion" [32]. The best evidence for Co^{II} spin conversion consecutive to the electron transfer was provided quite recently by XANES experiments [51] on the analogous Cobalt hexacyanoferrate series $Rb_xCo\,[Fe^{II}(CN)_6]_y \cdot zH_2O$.

It was tempting to undertake photoexcitation experiments on high-T_C ferrimagnets. Compositions such as $Cr^{II}_{1.5}[Cr^{III}(CN)_6] \cdot 5H_2O$ and $Cs_{0.83}Cr^{II}_{1.10}[Cr^{III}(CN)_6]_3 \cdot 9H_2O$ were available in Prof. M. Verdaguer's group [52], with $T_C = 240$ and 170 K respectively, see Fig. 16. Indeed, the absorption spectrum of these compounds contains an intervalence band in the near IR, so that optical electron transfers were expected, according to:

$$\begin{array}{cccccc} Cr^{III} & + & Cr^{II}(LS) & \leftrightarrow & Cr^{II}(HS) & + & Cr^{III} \\ S(A) = 3/2 & & S(B) = 1 & & S(A) = 2 & & S(B) = 3/2 \end{array} \tag{5}$$

Because of the antiferromagnetic coupling between A and B sites, only the difference between the A and B sublattices is considered for the net magnetization,

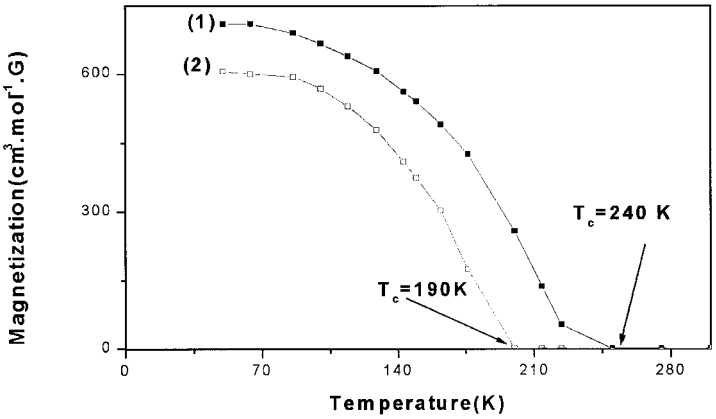

Fig. 16. Field-cooled magnetization curves at $H = 5$G, for (1) $Cr^{II}_{1.5}[Cr^{III}(CN)_6] \cdot 5H_2O$ and (2) $Cs_{0.83}Cr^{II}_{1.10}[Cr^{III}(CN)_6] \cdot 3.9H_2O$ (extracted from [49])

and it was therefore expected to be little sensitive to the light. On the contrary, the light-induced increase in the atomic moments, in presence of large interactions, was expected to sizably shift the Curie temperature upwards.

We performed photomagnetic experiments on these compounds, and found totally different behaviors. The stoichiometric compound $Cr^{II}_{1.5}[Cr^{III}(CN)_6] \cdot 5H_2O$ was not photomagnetic. The nonstoichiometric compound $Cs_{0.83}Cr^{II}_{1.10}[Cr^{III}CN)_6] \cdot 3.9H_2O$ showed photomagnetic effects, but nonpermanent, even at low temperature, and we evidenced [14a] an optical stimulation of the Magnetic After Effect (MAE). This is, to our knowledge, the first example of light-stimulated MAE in an inorganic solid. A detailed report will be given in the next section. The occurrence of MAE results from a structural disorder which is linked to the nonstoichiometry.

We also understood that the long lifetime (at low temperature) of the photoexcited state in the Co-hexacyanoferrates was because of the occurrence of the Co^{II} spin state conversion, which creates the needed energy barrier. We then started investigating, again in collaboration with Prof. M. Verdaguer's group, other Co-hexacyanoferrates series, with alkaline cation Rb [28] or Cs [53] instead of K. All these compounds have basically similar photomagnetic properties, and we mainly report here on the novel aspects inherent to the photo-induced character of the magnetic properties.

While developing extensive studies of these materials, we came to the conclusion [29,51] that structural relaxation accompanying the spin conversion might be sterically hindered in the crystal. It appears that the proximity of vacancies is needed to allow the occurrence of the spin conversion, so that the photo-switching properties are closely related to the amount and distribution of vacancies in the crystalline structure. Thus, the effect of composition could be cleared up in the Cs Co-hexacyanoferrate series [53], and the crucial effect of the details of preparation (washing conditions of the sample, for instance) on the photomagnetic performances of the samples could be qualitatively understood.

8.4.1 Light-stimulated MAE of $Cs_{0.83}Cr_{2.10}(CN)_6 \cdot 3.9H_2O$

At the time of the measurements, the SQUID magnetometer (MPMS5) was equipped with a thin optical fiber made of plastic, 1.5 mm in diameter, guiding the light down to 1.5 cm from the sample. With the filtered red light (cut-off filter $\lambda \geq 665$ nm), the power received by the sample was typically $\sim 2\,\mathrm{mW\,cm^{-2}}$. The sample was made of ~ 3 mg of microcrystalline powder spread over a 4 mm inner diameter plexiglass cell. Preliminary experiments without the filter or with a green filter showed that the efficient wavelength range was in the near IR, which corresponds to a charge-transfer optical band. It was also shown that the light-induced changes mainly affected the MAEs and we focussed on the isothermal remanent magnetization IRM(t), i. e. the magnetization measured versus time after applying the field on a demagnetized state. Other magnetic characteristics, such as the FC and ZFC curves, or the M–H loops at low temperatures, only showed minor changes under the effect of irradiation.

To record the IRM(t) curves, the magnetization was measured in the dark, after the sample was annealed at 200 K and zero-field cooled down to 10 K. We controlled the reproducibility of the measurements, after renewed thermal annealing at 200 K and ZF cooling, and we tested the role of the parameters which define the initial state of the system. We observed that the only crucial parameter for "preparing" the system was the actual value of the magnetic field during cooling. Other parameters such as applying or not the light while cooling, or waiting for long or short times before applying the magnetic field, under light or in the dark, did not sizably affect the initial magnetization and the kinetics of the MAE in the dark. These experiments also showed the absence of irreversible effects of light in the Cr^{II}–Cr^{III} system, at variance from the Co–Fe system. The main experimental problem was the remanent field of the superconductive magnet, which we could not perfectly control, thus resulting in a small scatter of the initial magnetization values. However, the main features of the MAE which are reported here (IRM logarithmic slope, photo-induced acceleration, reversible jumps of thermal origin ...) remained very reproducible during the whole year needed by the experimental work.

A typical IRM(t) curve obtained at 10 K and 50 Oe is shown in Fig. 17. The occurrence of MAE is usually related to a structural disorder, e. g. in spin-glasses or semi spin-glasses. Indeed, the saturation magnetization value, corresponds to a noncollinear ferrimagnetic structure [49], presumably due to the nonstoichiometric character of the compound. As usual for a first approach of the MAE, we fitted the IRM(t) by a logarithmic dependence $M(t) = M_0 + p \ln(t + t_i)$. This empirical law well describes, for a finite time interval, over several decades of time, the evolution of a system which possesses a broad distribution of relaxation times. M_0 and t_i are constants governed by the evolution of the system before the first measurement (at $t = 0$), usually fitted to the experimental data for obtaining the best linear plot in logarithmic scale. We show in Fig. 18 the logarithmic plot of the data presented in Fig. 17.

The effect of light is first illustrated in Fig. 19, where we show the striking effect of switching on the light some time after the magnetic field. The MAE effect is obviously speeded up by light. In agreement with this test experiment, further experiments

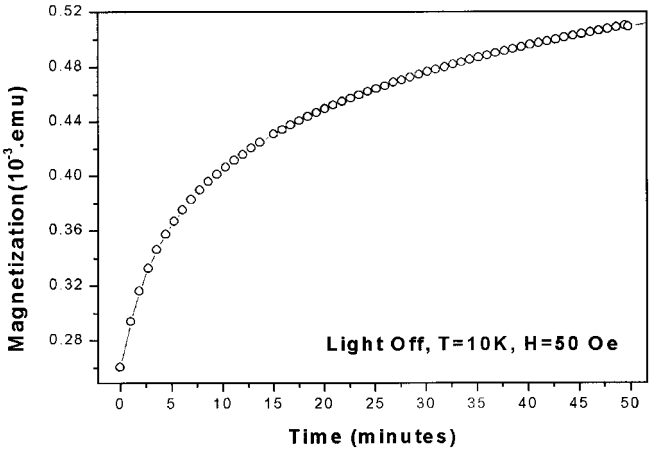

Fig. 17. Magnetic after effect of $Cs_{0.83}Cr^{II}_{1.10}[Cr^{III}(CN)_6]\cdot 3.9H_2O$: IRM($t$) in the dark, at 10 K, 50 Oe

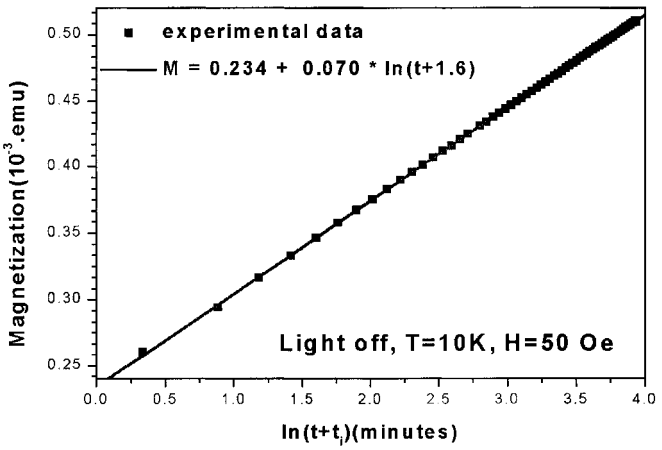

Fig. 18. The previous IRM(t) curve plotted on a logarithmic scale and fitted to a law $M(t) = M_0 + p\ \ln(t+t_i)$, with $M_0 = 0.234$ emu g^{-1}, $p = 0.0070$ emu g^{-1}, t in minutes and $t_i = 1.60$ min

where the light was switched on before the field was applied gave an increased value of the logarithmic slope, and confirmed the photomagnetic properties of the system. But, however, the role of the thermal effect of light had to be cleared up before establishing the presence of a purely optical mechanism in the photomagnetic process.

The most straightforward way to control the thermal effect consisted in repeating the experiment at several different temperatures. We report in Fig. 20 the logarithmic slope data obtained at various temperatures and light intensities. Simple inspection of the figure shows that the effect of light cannot be assimilated to a pure thermal effect,

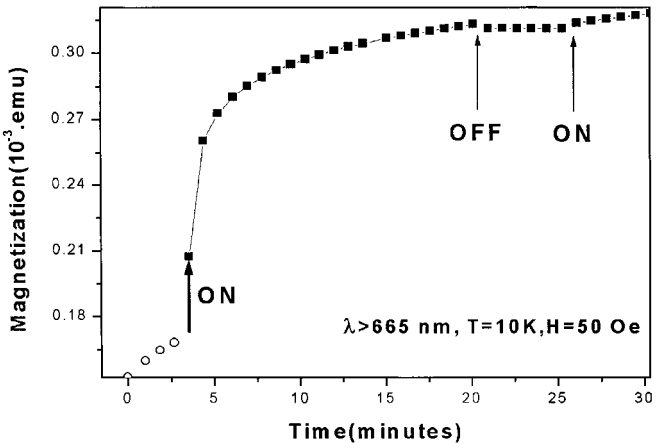

Fig. 19. The effect of light on the previous IRM(t) curve, with filtered red light ($\lambda > 665$ nm), 2 mW cm^{-2}. Light speeds up the MAE. Reversible thermal effects are observed when the light is switched off and on (see Fig. 22)

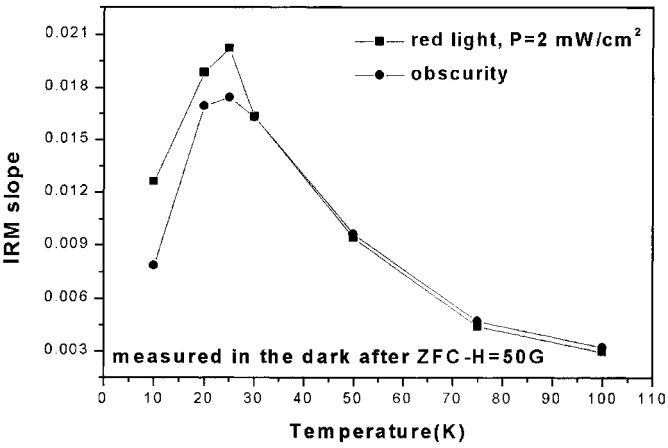

Fig. 20. The logarithmic slope data obtained at various temperatures and intensities for $Cs_{0.83}Cr^{II}_{1.10}[Cr^{III}(CN)_6] \cdot 3.9H_2O$, at 50 Oe, filtered red light, 2 mW cm^{-2}. Notice that a pure thermal effect would only shift the curve along the temperature axis

i. e. a simple temperature shift of the curve. These data provided the evidence for a light-stimulated effect, i. e. for the reality of an optical process. We also determined the initial parameters t_i and M_0, which were found to be almost light-insensitive, but strongly temperature-dependent. The temperature dependence of M_0 is reported in Fig. 21.

It is worth discussing further the test-experiment reported in Fig. 19. To obtain linear plots of both parts of the curve in logarithmic scale, it was necessary to use

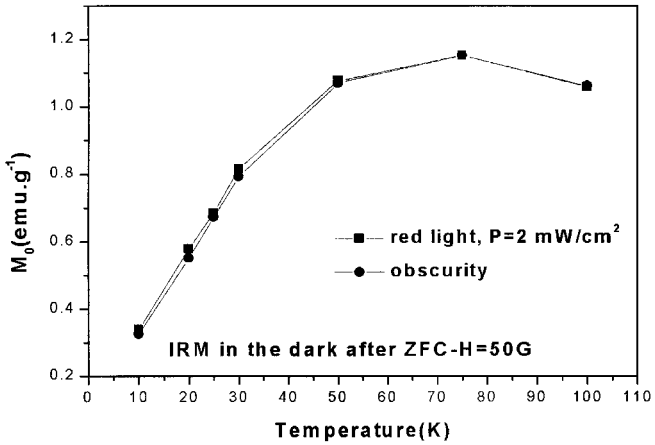

Fig. 21. The M_0 data obtained at various temperatures and light intensities for $Cs_{0.83}Cr^{II}_{1.10}[Cr^{III}(CN)_6] \cdot 3.9H_2O$, derived from the same experiments than the logarithmic slope data in Fig. 20. Notice the M_0 values are little sensitive to the effect of light

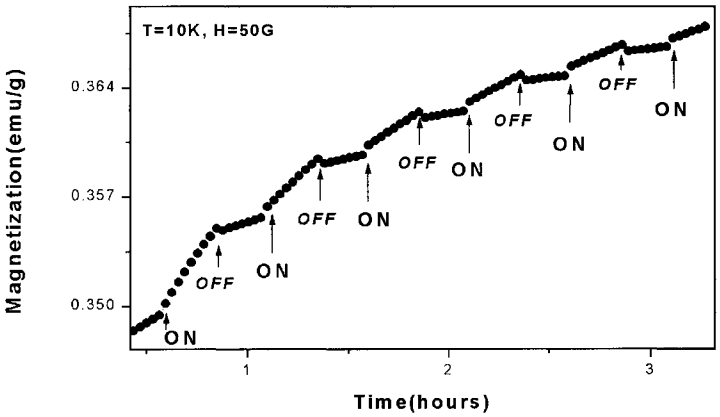

Fig. 22. The chopped light experiments, continued after Fig. 19. The light-induced temperature variations result in reversible magnetization jumps the amplitude of which remains constant all over the experiment: switching *on* (*off*) the light leads to an increase (decrease) in temperature and magnetization

different values of the initial time when the white light was used, but a unique value was sufficient when the red filter was used. This observation will be correlated to the fact that illumination with the unfiltered light source results in a much larger heating of the sample, such that the t_i and M_0 values are sizably modified, instantaneously. The thermal effect has been specifically investigated by combining chopped light (Fig. 22) and "alternate temperature" experiments in the dark (Fig. 23).

For the needs of the discussion below, we have given in Fig. 24 the FC and ZFC curves of the sample under the same field 50 Oe. In Figs 22, 23, we first analyze

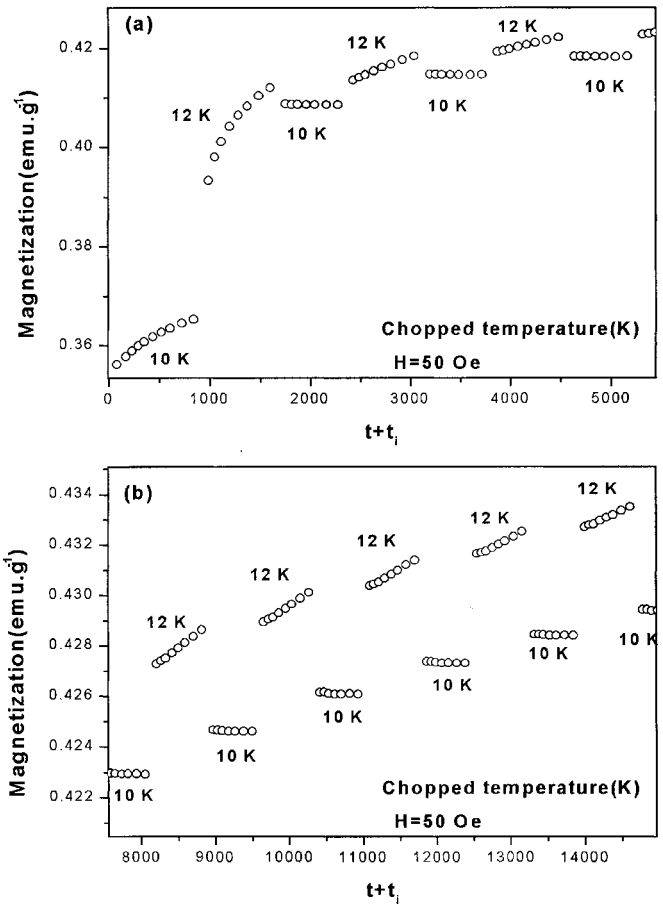

Fig. 23. A typical "alternate temperature" experiment, for $Cs_{0.83}Cr^{II}_{1.10}[Cr^{III}(CN)_6] \cdot 3.9H_2O$, $T = 10$ or 12 K, $H = 50$ Oe, filtered red light, 2 mW cm^{-2}, (a) from the beginning, (b) at longer times. The first jump is large and not entirely reversible, the following ones are reversible, with a constant amplitude during the whole experiment. The reversible variations in magnetization have been reported in Fig. 24 for further discussion

the reversible jumps which are associated with the switching on and off, of light or temperature. Switching on the light or increasing the temperature leads to an increase in magnetization, switching off the light or decreasing the temperature leads to a decrease in magnetization. This agrees qualitatively with the positive slopes of both the FC and ZFC curves at the same temperature and field (Fig. 24). It is worth noting the reversible character of the magnetization jumps which all exhibit the same amplitude along the $M(t)$ curve, the first jump excepted, of course.

The reversible effects of temperature variations have been schematically reported in Fig. 24 as straight segments, with slopes that are remarkably equal and close to the slope of the FC magnetization curve in the same temperature range. In addition

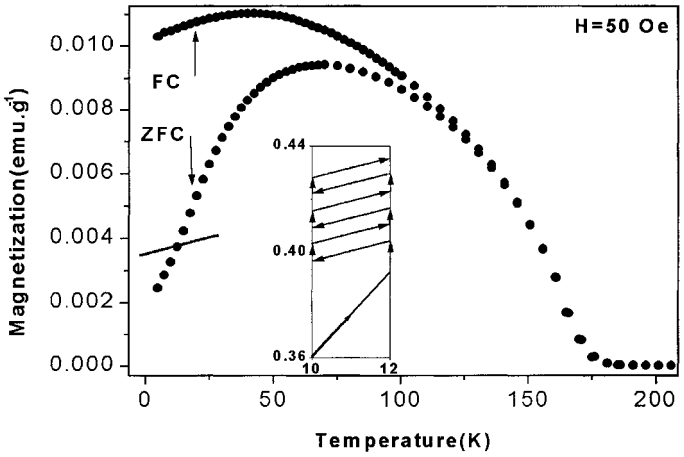

Fig. 24. Field cooled and zero field cooled curves of $Cs_{0.83}Cr^{II}_{1.10}[Cr^{III}CN)_6] \cdot 3.9H_2O$, at $H = 50$ Oe. Notice the initial positive slope of both curves. The MAE data with alternate temperatures of the previous figure are shown in the insert; the common slope of the reversible jumps is figured as a thick straight line in the main figure. Notice this "reversible" line is grossly parallel to the FC branch

– which is the more useful here – these data enable us to calibrate the thermal effect of light: linear interpolation of the reversible temperature effect ($\Delta M \cong 4 \times 10^{-3}$ emu g^{-1} for $\Delta T = 2$ K) leads to estimate the temperature increase due to light, as: +0.25 K for filtered red light at 10 K. Now, using the data of Fig. 20, it can be concluded that the thermal effect at low temperatures only weakly contributes to the observed increase in the logarithmic slope: at 10 K with filtered red light it contributes only ~+8%, while the total measured increase was ~+60%. For a similar experiment performed without filter, at 10 K, the thermal effect ($\Delta T = 3$ K) was responsible for ~ one half of the total increase.

Thus, the optical mechanism of the photomagnetic process has been established. It presumably involves the optical electron transfer described by Eq. (5). One might imagine that this transfer results in a small drift of the valence equilibrium in the system. However, the similarity between light and temperature effects rather suggests that the valence equilibrium of the system (little temperature dependent) should not be sizably light sensitive. Indeed, due to the usually fast electronic relaxation in mixed valence systems, and the low fluence of the photon flux, the drift of the valence equilibrium is expected to be extremely small. The situation is to be compared to that of a spin-crossover system at room temperature or above, where clearly photoexcitation cannot compensate the short lifetime of the photoexcited state. Under these conditions, the photomagnetic effect essentially remains a kinetic effect, which provides an additional channel for the relaxation of the magnetic system. The exact nature of this channel remains to be elucidated. The creation of photo-induced defects may be suggested, as resulting in a de-pinning of the domain walls, or more generally, as producing local fluctuations liable to de-trap the system from a local

free-energy minimum. A more extensive study of the system, e. g. as a function of the applied magnetic field, should be necessary to try to elucidate the microscopic mechanisms involved in the photomagnetic effect.

This example opens attractive perspectives for the study of aging effects in disordered systems. An appealing property of photostimulated MAE is the flexibility of the optical parameter, which can be controlled within very short times, which is not the case for the temperature (see for example [54]). We could observe in Fig. 22 that the system can be optically driven to the quasi-equilibrium value of the magnetization in the dark: during the light-on stages, magnetization increases, far from reaching saturation, i. e. the FC value; during the light-off stages, magnetization no longer increases. This is shown again in Fig. 25, on a "cumulative" logarithmic time scale. A linear plot, common to all data of the light-on stages, can be obtained provided that the time data of the light-off stages are not accounted for. This plot shows that during the light-off stages the system no longer ages, i. e. it has reached a quasi-equilibrium state. In further experiments, with unfiltered radiation, we even observed that magnetization might decrease during the light-off stages: the quasi-equilibrium value was passed. A tentative description of these metastable properties is the following: the photo-induced fluctuations enable the system to reach a quasi-equilibrium state which is closer to the FC stable state than the quasi-equilibrium state reachable by the thermal fluctuations alone. This way, the photostimulated MAE might offer a novel way for investigating the hierarchy of the free-energy valleys [55] of the system, in addition to temperature, magnetic field and (for dielectrics) electric field [54].

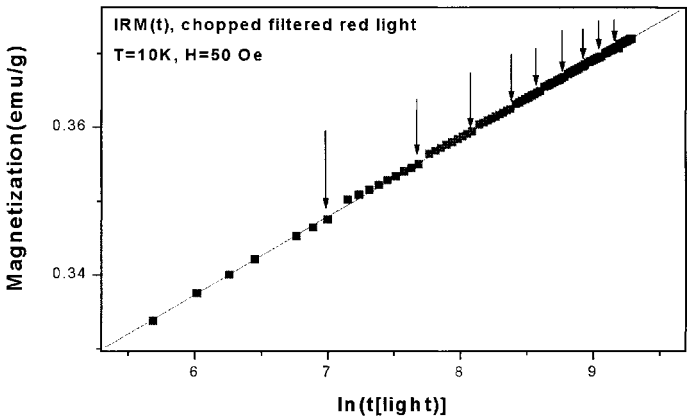

Fig. 25. Chopped light data of Figs. 19 and 22, plotted in a "*cumulative*" logarithmic scale, only accounting for the light-on stages. The light-off stages are indicated by vertical arrows. In the upper part of the figure, the light-on data follow a single straight line. Thus, the system remains frozen during the light-off stages, i. e. it has reached a light-off quasi-equilibrium state

8.4.2 The Photo-induced Ferrimagnetic State of $Rb_{0.52}Co[Fe(CN)_6]_{0.84} \cdot 2.31H_2O$

The synthesis and physicochemical analysis of the Co-hexacyanoferrate $Rb_{0.52}Co[Fe(CN)_6]_{0.84} \cdot 2.31\ H_2O$ are described in [51]. We briefly summarize the photoexcitation properties of the system, already reported in [29], before dealing with the (mostly novel) properties of the photo-induced ferrimagnet. A typical photoexcitation curve, obtained with the multi-wire optical fiber, is reported in Fig. 26.

The initial part of the magnetization curve, shown in the insert, displays a nonlinear increase obviously attributable to the simultaneous onset of the magnetic moments and interactions. On the contrary, similar experiments above the Curie temperature display a linear initial variation, which is consistent with the presumed linear increase in the number of magnetic moments (no evidence for a DOMINO effect [21]). Also, photo-experiments with different optical filters showed a maximum efficiency in the range 650–800 nm [29].

We observed the decay of the excited electronic state, at ~110 K, by warming the sample up to 150 K, at the temperature sweeping rate $\sim 0.5\ K\ min^{-1}$. This is shown in Fig. 27 for the magnetization recorded in the dark. This value enabled us to determine the systematic de-excitation treatment needed for further photoexcitation experiments: a systematic thermal annealing at 150 K during 10 min.

After renewed photoexcitation, we investigated the kinetics of the thermal relaxation, in the dark, at the constant temperature of 95 K. The curve is plotted in Fig. 28. The major part of the curve follows a nonexponential law, with a sigmoidal shape typical for a self-accelerated process, already analyzed (in Section 3) as due to cooperative effects on the energy barrier. The presence of cooperative relaxation is confirmed by chopped light experiments (reported in [29]), similar to those shown in Fig. 6, and also giving evidence for a frontal propagation mode of the photoexcited state, despite the darkening effect.

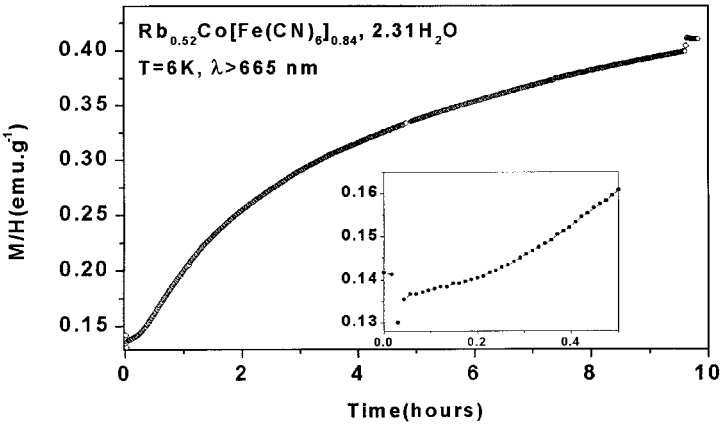

Fig. 26. $Rb_{0.52}Co[Fe(CN)_6]_{0.84} \cdot 2.31H_2O$, photoexcitation at 10 K, filtered red light, $60\ mW\ cm^{-2}$, 150 Oe. Insert: zoom of the nonlinear beginning of the curve (after [29])

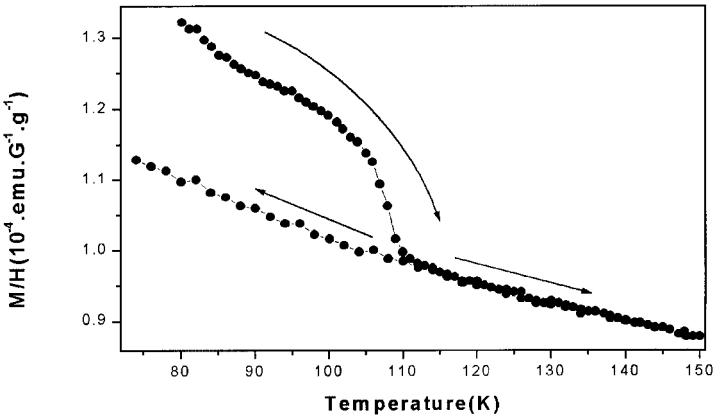

Fig. 27. Photoexcited $Rb_{0.52}Co[Fe(CN)_6]_{0.84} \cdot 2.31H_2O$, decay of the excited electronic state in the dark. Above 110 K, the system recovers its initial electronic state. Typical temperature sweeping rate is 0.5 K/min (after [29])

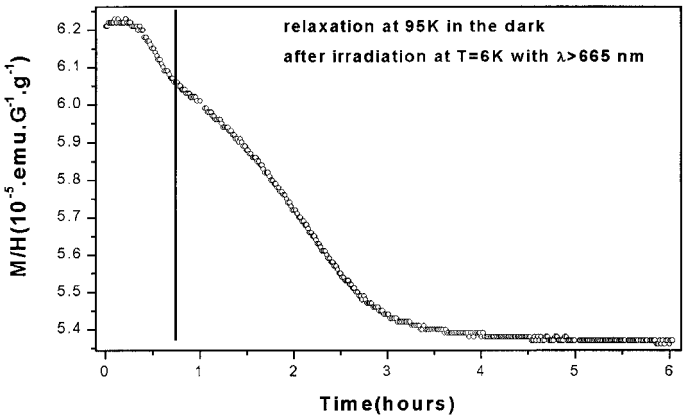

Fig. 28. Photoexcited $Rb_{0.52}Co[Fe(CN)_6]_{0.84} \cdot 2.31H_2O$, decay of the excited electronic state at 95 K. The first part of the curve is presumably due to chemical inhomogeneity of the sample. The main part of the decay curve displays a sigmoidal shape typical for a cooperative process (after [29])

The cooperative effect on the energy barrier plays a crucial role at the very beginning of the photoexcitation process: the first excited Co-Fe pairs have a very short lifetime. Consequently, the photoexcitation process has to be fast enough to provide a sufficient population of the excited state, which ensures the raising up of the energy barrier. Then, only the saturated parts of the sample have a long lifetime and therefore remain populated at higher temperatures, until the thermal decay is observed as in Fig. 28. Also, due to the presence of cooperativity, a light-induced instability may be expected at low temperatures, according to the general phase diagram pub-

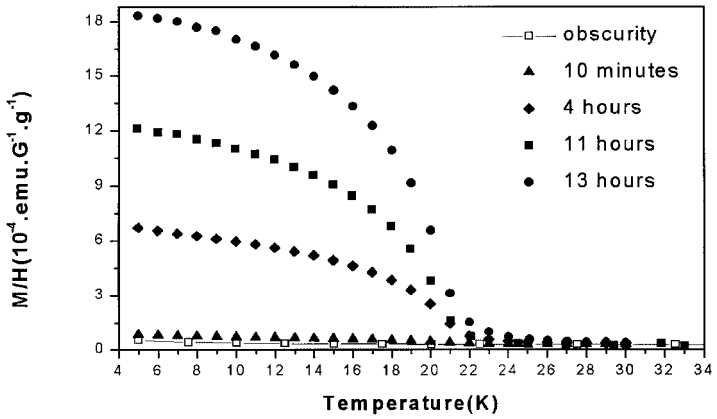

Fig. 29. $Rb_{0.52}Co[Fe(CN)_6]_{0.84} \cdot 2.31H_2O$, Field Cooled (FC) magnetization data recorded in the dark, before and after illumination at 10 K, 50 Oe, red filtered light, 50 mW cm^{-2} for different illumination times. (after [29])

lished in [39b], and reflectivity experiments are in progress to detect such an effect in this very absorbing material. The comparison to the spin-crossover compounds also suggests the eventuality of a phase transition, entropy-driven. The transition temperature is expected at $T_{equil} = \Delta / \ln(g_H/g_L)$, where Δ is the energy gap and $g_{H,L}$ the degeneracies of the two states ([56] and references included). The expected transition was not observed, on warming up to room temperature. It presumably is too high, but direct measurements of the thermodynamic parameters Δ, $\ln g$, are desirable to clarify this point. On the Cs-system studied later [53], such a thermal transition has been indeed observed at ~250 K.

We show in Fig. 29 the field-cooled (FC) magnetization data recorded in the dark, before and after illumination. Before illumination, i. e. in the nonexcited state, the magnetization is small, due to few Co^{II} ions, diluted in a diamagnetic matrix. After illumination the FC procedure was carried out in the dark. During the whole experiment (excitation + magnetic annealing at 30 K + measurement) the field was kept constant. The FC curves are shown for different illumination times, and beyond a short illumination time, ~10 min, all the curves indicate the same value for the magnetic ordering temperature ~21 K. According to the antiferromagnetic nature of the A–B interactions [49,50], this is a Curie temperature, T_C, and the photo-induced state is ferrimagnetic. Further experiments show that this photo-induced T_C does not sizably depend on the value of the magnetic field applied during the illumination of the sample. The quasi-constant value of this photo-induced T_C confirms the frontal process, with a photo-induced saturated state, which progressively propagates through the sample as a function of the illumination time.

Repeated experiments on a given sample, after the thermal annealing which returns the sample to its nonexcited state, always gave reproducible T_C values. Also, the T_C data for different polycrystalline samples were in the range 20–21 K. In [29] we argued that the T_C value enabled us to conclude there was a rather complete transformation of the material according to Eq. (4), by comparison to the well-documented

case of Co_3Fe_2, representative of the ideal ferrimagnet with 3:2 structure, and for which $T_C = 15\,K$.

Quantitative estimates of the (totally) transformed fraction of the material are interesting since they reveal the efficiency of the various photoexcitation devices. In Mössbauer experiments [28,29], no more than ~20 at.% were transformed. In the SQUID experiments, due to the large parasitic contributions of the optical device, we had to estimate this fraction from the decrease in magnetization during the thermal decay (shown in Fig. 27); assuming a Curie law, the fraction was estimated to be $\sim 14 \pm 3\%$ in the best case.

8.4.3 The Magnetic Properties of the Photo-induced State

We now focus on the magnetic properties of the photoexcited state, and start with the M–H loops obtained after different photoexcitation experimental conditions (temperature, field, magnetization). Typical M–H loops are reported in Fig. 30, giving evidence for a ferrimagnetic state. All loops at the same temperature (10 K) have the same coercive field ~1000 Oe and similar shape.

We have systematically determined the saturation magnetization values M_S, i. e. the magnetization values extrapolated to $H = 0$ from the saturated branches of the $M(H)$ curves. The data are reported in Fig. 31, as a function of the illumination time, and all of them define a single plot, except for temperatures above ~60 K, and save for a sizable scatter of the data, presumably due to the uncontrolled condensation of gases on the sample holder.

From Fig. 31 it is apparent that the photoexcitation yield does not sizably depend on field and temperature (below 60 K). The time dependence of the magnetization

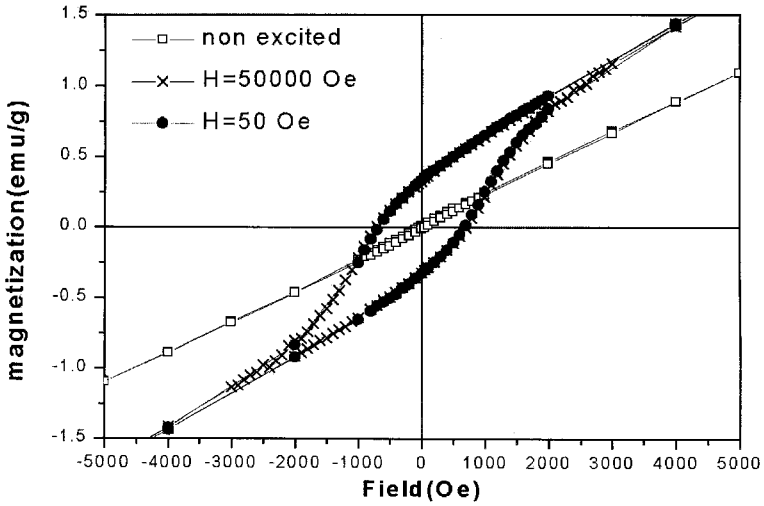

Fig. 30. Photoexcited $Rb_{0.52}Co[Fe(CN)_6]_{0.84} \cdot 2.31H_2O$, M–H loops obtained after different experimental excitation conditions. The linear extrapolation which provides the saturation spontaneous magnetization ($H = 0$) is shown

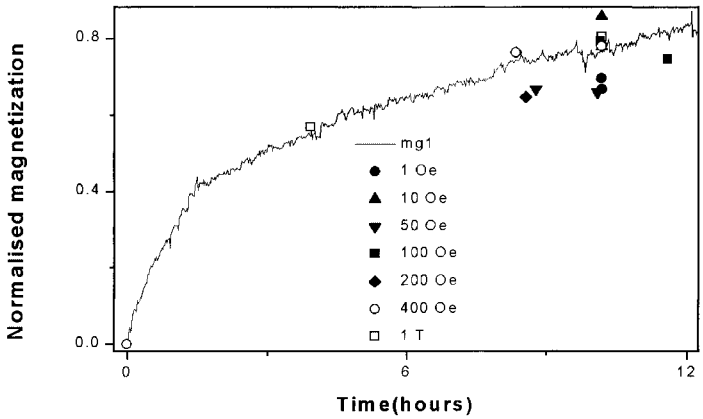

Fig. 31. Photoexcited $Rb_{0.52}Co[Fe(CN)_6]_{0.84}\cdot 2.31H_2O$, saturation spontaneous magnetization data, $H = 50\,\text{Oe}$, $T = 10\,\text{K}$, for various experimental condition during photoexcitation, plotted as a function of excitation time. The full line is taken from Fig. 26

grossly has the shape of a stretched exponential, in agreement with the previous Fig. 26. The lack of sensitivity to the magnetic field can be explained by the weakness of the magnetic energy with respect to the optical transition energy. The process is expected to be temperature-independent, as long as the lifetime of the excited state remains long.

However, the magnetic field applied during photoexcitation governs some subtle and unexpected features of the magnetic properties. For example, when the photoexcitation process is performed at low temperature (e. g. 10 K), under weak magnetic field (e. g. 50 Oe) and moderate light intensity (few mW cm^{-2}), so as to avoid a large heating effect, the resulting magnetic state reveals a metastable character, with a thermal magnetization curve between the field-cooled (FC) and zero-field cooled (ZFC) curves, see Fig. 32.

The FC and ZFC curves could be repeated several times, at will. On the contrary, the metastable magnetic state was lost as soon as the sample was heated above T_C. The state provided by the photoexcitation process is denoted here the raw photoinduced state (RPI). When temperature is raised for the first time, under the same field, the system follows the RPI curve; after annealing at T_C, it reversibly follows the FC curve. This establishes the metastable character of the RPI state, inherent to any low-temperature process which builds up a magnetic structure below its ordering temperature. Systematic investigation of the conditions which influence the RPI state will be reported below. We first follow, in Fig. 33, the irreversible evolution of the RPI state upon thermal annealing. The magnetization curve, under constant field, progressively shifts towards the FC curve, during a set of successive annealing at higher and higher temperatures. It must be observed that the annealing effect begins close to T_C, and continues well above, presumably due to the kinetics of magnetic domain relaxation. Further experiments at different temperature sweep rates are needed for reaching a definitive conclusion with respect to the range of magnetic correlations which are involved in the RPI domain structure.

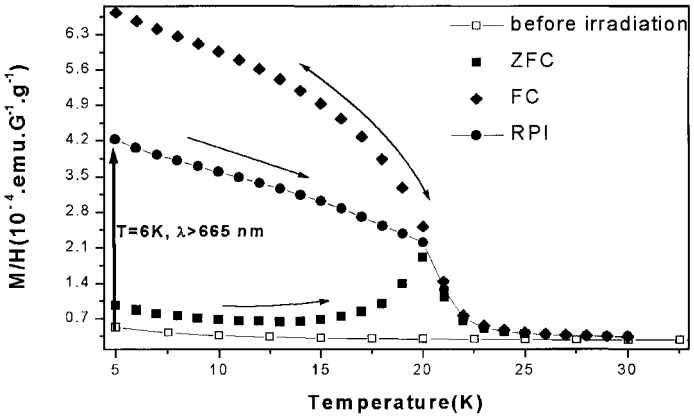

Fig. 32. Magnetic metastability of photoexcited $Rb_{0.52}Co[Fe(CN)_6]_{0.84} \cdot 2.31H_2O$, after illumination at 5 K, 50 Oe, red filtered light, 3 mW cm^{-2}, 12 h. The four magnetization curves have been recorded in the dark, at constant field, with the following sequence: the *nonexcited state* (bottom curve); the up-going curve of the metastable *raw photo-induced state* (RPI) obtained just after illumination; the reversible *field-cooled* (FC) curve, obtained after annealing at 30 K. For comparison the corresponding *zero-field cooled* (ZFC) curve has been recorded

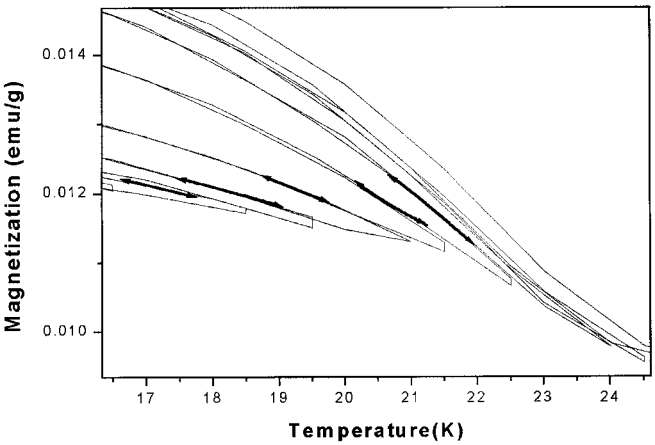

Fig. 33. Magnetic metastability of the RPI state of $Rb_{0.52}Co[Fe(CN)_6]_{0.84} \cdot 2.31H_2O$, after photoexcitation at 10 K, 50 Oe, 10 h, filtered red, P = 3 mW cm^{-2}: the irreversible evolution of the RPI state towards the FC state is shown upon successive annealing stages, with increasing maximum temperatures: [5 → 17 K → 5 K]; [5 → 19 *K* → 5 *K*]; [5 → 21 *K* → 5 *K*]; [5 → 22 *K* → 5 *K*]; [5 → 23 *K* → 5 *K*], [5 → 25 *K* → 5 *K*], [5 → 30 *K* → 5 *K*], [5 → 40 *K* → 5 *K*]; typical temperature sweep rate is 0.5 K/min. The top curve is FC (annealed at 40 K). Sizable annealing effects start close to T_C, and extend far above

In the following experiments, we have investigated the value of the *genuine magnetization of the RPI state*, i. e. the magnetization measured at the end of the photoexcitation process. For various experimental conditions, we have compared the genuine RPI magnetization and the corresponding FC value, i. e. the magnetization values obtained in the same field before and after thermal annealing above T_C (at 30 K, 10 min, systematically). To allow for the different irradiation times, we have normalized all these values to the corresponding value on the M-H loop. The so-reduced data are displayed in Fig. 34, as a function of the magnetic field value. It is shown that both RPI and FC values have a linear initial increase, and then saturate, i. e. they remain inside the M–H loop. Also, the RPI value always remains smaller than the FC value (for the same field). These data are consistent with the simple picture [29] that the specificity of the RPI state merely lies in a *nonrelaxed domain structure*.

In further experiments, we carefully compared the M–H loops obtained before and after thermal annealing, and found them identical within a high accuracy. This means that the RPI state is destroyed by application of a large field which saturates the magnetization and obviously wipes out the genuine nonrelaxed domain structure. In a quite recent paper [61] we described the RPI state as resulting from a hybrid process, schematized by a simple combination of FC and ZFC states.

Quite recently, we also started investigating the coercivity of the nonrelaxed magnetic structure, i. e. in the genuine RPI state and, for comparison, in the FC state obtained by thermal annealing under the same field. For this, after photoexcitation at 10 K, 200 Oe, we have performed the minor hysteresis loops reported in Fig. 35.

According to Fig. 35, the RPI state is "softer" than the FC state, with (pseudo) coercive field values of ~650 and ~700 Oe, respectively. Another obvious difference lies in the shape of the minor loop, which is wider for the RPI state than for the FC state. This presumably is due to kinetic effects, which are faster in the RPI state, as revealed by the successive measurements at −700 Oe. Thus, a magnetic after-effect

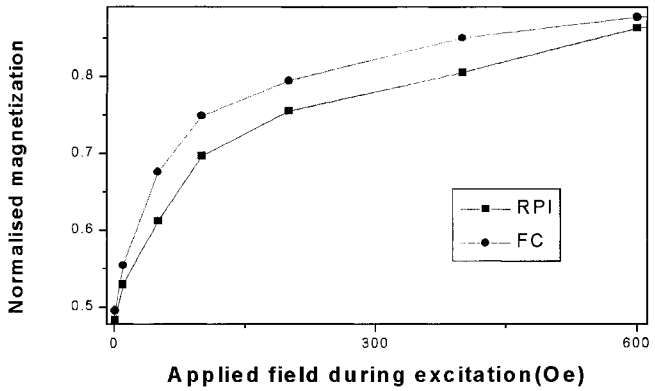

Fig. 34. Photoexcited $Rb_{0.52}Co[Fe(CN)_6]_{0.84} \cdot 2.31H_2O$, collected data of FC and genuine RPI magnetization, as a function of the applied field during irradiation. To allow for the different irradiation times, we have normalized all values to the corresponding value on the M–H loop

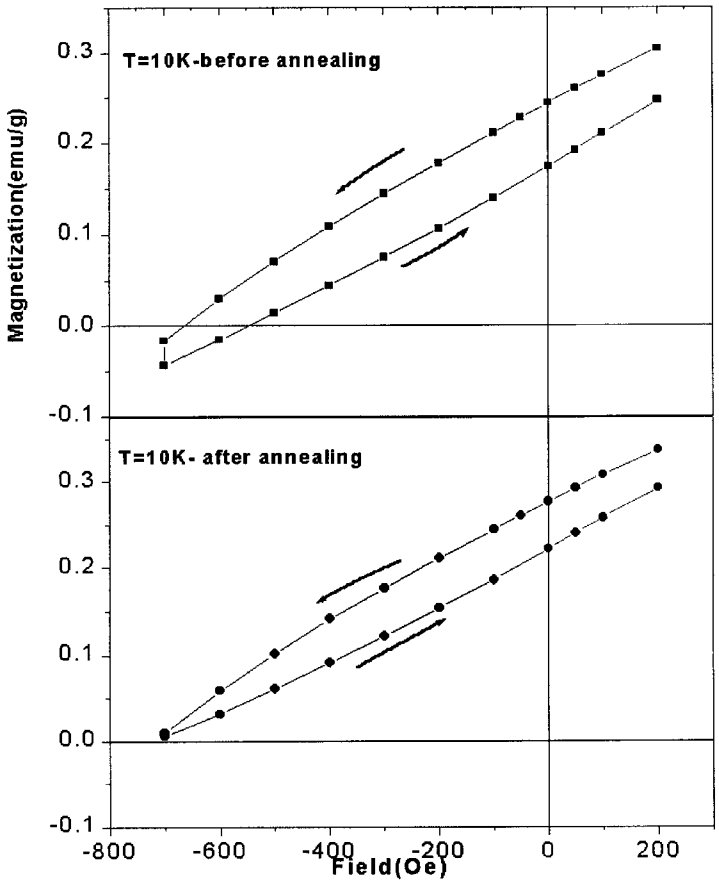

Fig. 35. Photoexcited $Rb_{0.52}Co[Fe(CN)_6]_{0.84} \cdot 2.31H_2O$, minor hysteresis loops in the RPI state (top) and FC state (bottom) recorded with the same sequence of magnetic fields

is evidenced in the RPI state and should be related to nonrelaxed character of the genuine light-induced domain structure. An extensive study of the MAE is obviously worth being done for following the evolution of the domain structure properties, in the genuine state, after magnetic saturation, and after thermal annealing. The lifetime of the RPI state is under study, and a general comprehension of the aging properties of the light-induced domain structure might emerge.

8.5 The Valence Tautomeric Solid Co-semiquinone

The valence tautomeric solids [Co-(phen)(3,5-DTBSQ)$_2$]-L where L is an organic ligand were first studied by Hendrickson et al. [31]. The valence tautomerism consists of a metal to ligand (or vice-versa) electron transfer associated with a spin change of the transition metal, according to the following reaction equation (where cat = catecholate is the reduced form of sq$^\bullet$ = semiquinone):

$$\begin{array}{ccccccccc} \mathrm{Co^{III}(LS)} & + & \mathrm{sq^\bullet} & + & \mathrm{cat} & \leftrightarrow & \mathrm{Co^{II}(HS)} & + & \mathrm{sq^\bullet} & + & \mathrm{sq^\bullet} \\ S=0 & & S=1/2 & & S=0 & \leftrightarrow & S=3/2 & & S=1/2 & & S=1/2 \end{array} \quad (6)$$

With the appropriate aromatic ligand L = C_6H_5–CH_3, at the solid state, a phase transition has been observed, see Fig. 36.

It is worth considering the thermodynamic parameters which are associated with the reaction Eq. (6), namely the changes in molar enthalpy and entropy, ΔH and ΔS. These quantities have not been obtained directly, by the usual calorimetric methods. They have been derived from the thermal dependence of the equilibrium constant, in solution [31c]. ΔS and ΔH are obviously related to the equilibrium temperature ($\Delta H = T_{\mathrm{equil}} \times \Delta S$), and we focus on the measured ΔS value, ca. 118 J K^{-1} mol^{-1}, which indicates, as for the spin transitions [57], a contribution in large excess of the expected electronic contribution, calculated through the spin and orbital contributions $\Delta S = \Sigma R \ln(2S+1)_{\mathrm{HS}} - R \ln 2(2S+1)_{\mathrm{LS}}$ where two-fold orbital degeneracy of the (sq$^\bullet$)(cat) mixed-valence pair has been accounted for. The electronic contribution is thus [31c]: $R \ln(16/4) = 11.5\,\mathrm{J\,K^{-1}\,mol^{-1}}$. The presence of a large vibrational contribution is consistent with a large change in the elastic properties of the solid, upon the Co$^{\mathrm{II}}$ spin conversion. We have introduced these

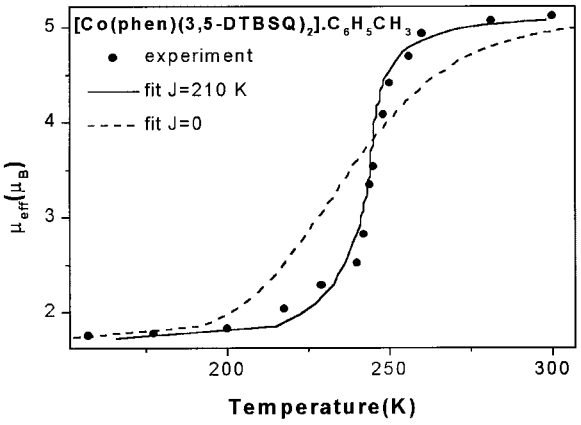

Fig. 36. The valence tautomeric transition of [Co(phen)(3,5-DTBSQ)$_2$] · $C_6H_5CH_3$: from Co(sq$^\bullet$)(cat) (low temperature) to Co(sq$^\bullet$)$_2$ (high temperature) (adapted from [31]). The full line is the best fit using a Ising-like model (see text): $\Delta = \Delta H/\mathrm{Na} = 3300\,\mathrm{K}$, $\ln(g_{\mathrm{H}}/g_{\mathrm{L}}) = \Delta S/R = 14.2$, $J = 210\,\mathrm{K}$

data for reproducing the experimental curve of Fig. 36, i. e. those of the system at the solid state. A good agreement is obtained by introducing an interaction term, in the mean-field Ising-like formalism currently used for the spin transition solids [56]. Thus, the obvious cooperativity of the system is quantified; the value of the interaction parameter is a little smaller than the threshold value $J_{\text{threshold}} = k_B T_{\text{equil}}$ associated with the occurrence of the first-order transition.

Following the example of spin transition compounds [58], application of pressure was expected to induce the $Co^{II}(HS)(sq^{\bullet})_2 \rightarrow Co^{III}(LS)(sq^{\bullet})(cat)$ transformation, due to the smaller Co-ligand distances in the LS state. The pressure-induced transition was indeed evidenced by Verdaguer's group, using EXAFS measurements [59], see Fig. 37. We have also reproduced the data, using the two-level model completed by the pressure contribution to the energy gap + $p\Delta V$ (pressure $\times$ increase in the molar volume). The curve was reasonably fitted with the parameter values already determined and $\Delta V = 1980\,\text{K GPa}^{-1}\,\text{mol}^{-1} = 27\,\text{Å}^3$/molecule. This value compares well with typical values for the spin-crossover solids: $\Delta V = 22$–$26\,\text{Å}^3$/molecule [60].

Following further the striking analogy to spin crossover systems, we tried to carry out the light-induced trapping of the high-temperature form, i. e. the low-temperature photo-induced transformation $Co^{III}(LS)$-$(sq^{\bullet})(cat) \rightarrow Co^{II}$ (HS)-$(sq^{\bullet})_2$. Previous experiments by Hendrickson et al. [31b,c] at higher temperature, showed that transient photoexcitation was possible using visible light. We report here, in Figs. 38 and 39, some of the preliminary results we obtained with a sample of [Co-(phen)(3,5-DTBSQ)$_2$]-C_6H_5-CH_3.

In Fig. 38 is shown the photoexcitation at 10 K, with the most efficient radiation for the present device. The photoexcitation features are rather similar to those of the PB analog Co-hexacyanoferrate, typical for a material with strong bulk absorption. The weakness of the magnetization increase, compared to the PB analog, may be

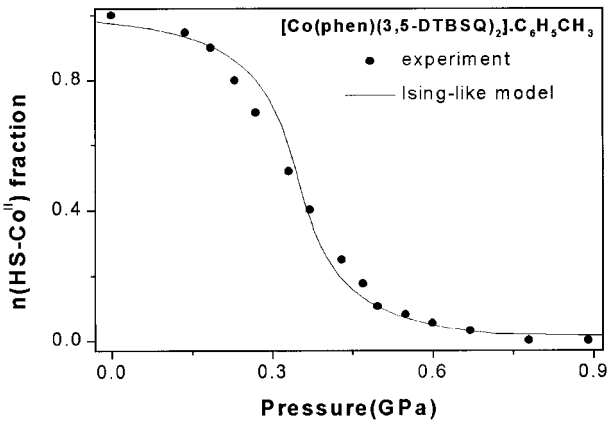

Fig. 37. [Co(phen)(3,5-DTBSQ)$_2$]·$C_6H_5CH_3$, the application of pressure at room temperature induces the transformation: high-temperature form $\rightarrow$ low-temperature form (after [59]). The full line is a computed curve with a Ising-like model (see text): $\Delta = \Delta H/\text{Na} = 3300\,\text{K}$, $\ln(g_H/g_L) = \Delta S/R = 14.2$, $J = 210\,\text{K}$, $\Delta V = 1980\,\text{K GPa}^{-1}$

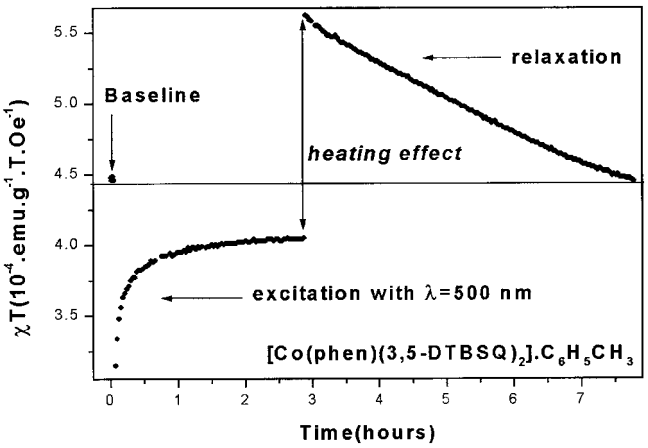

Fig. 38. $[Co(phen)(3,5\text{-}DTBSQ)_2] \cdot C_6H_5CH_3$, photoexcitation at 10 K, 550 nm, 20 mW cm^{-2}. The expected features of photoexcitation in an absorbing cooperative solid are observed: relatively large thermal effect, small increase in magnetization which rapidly saturates, non-exponential decay. The lifetime of the photoexcited state is short, compared to all other examples reported here

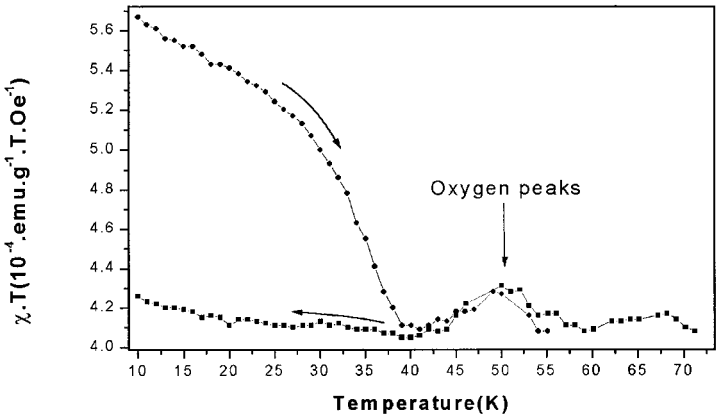

Fig. 39. $[Co(phen)(3,5\text{-}DTBSQ)_2] \cdot C_6H_5CH_3$: Thermal decay of the photoexcited state Co^{II}-$(sq^{\bullet})_2 \rightarrow Co^{III}$-$(sq^{\bullet})$(cat) for temperature sweep rate 0.5 K/min

due to the presumably paramagnetic state of the solid in the $Co^{II}(HS)(sq^{\bullet})_2$ excited state, which misses the strong magnetic interactions of the PB analog. The relaxation exhibits a nonexponential shape. Indeed, the high-temperature transition indicates a strong cooperativity, and the relaxation curve presumably combines the sigmoidal behavior and the stretched exponential previously discussed. There are some indications that the rapid character of the low-temperature relaxation may be due to the rather weak light-induced population of the photoexcited state, as a consequence of

the strong threshold effect described in Section 3. Therefore, we are now preparing experiments with a stronger source of light, and if a rapid decay was to be observed in the case of a saturated population of the excited state, we would conclude it is the effect of a tunneling mechanism, for which the cooperative relaxation equations of Section 3 would be adapted as well [39a].

In Fig. 39, we show the thermal decay of the photoexcited state, which occurred at ~40 K, i. e. sizably lower than for the spin transition systems (~60–70 K) and the Co-hexacyanoferrate (~110 K). This is consistent with the observation of a short lifetime at 10 K.

8.6 Conclusion and Perspectives

The photomagnetism of inorganic solids is based on optical electron transfers, either intra-atomic (spin crossover compounds), or inter-atomic (valence tautomeric systems and PB analogs). The consequences of the photosensitivity of the compound considerably differ according to the lifetime of the photoexcited state which is governed by the eventual existence of an energy barrier created by the structural relaxation which may follow the photon absorption.

The photoexcitation processes which involve a change in the spin state of the transition metal have an excited state with a long lifetime, and the compound may be switched reversibly by the use of suited wavelengths. These compounds form a *novel class of magnetic materials*, where the concentration of magnetic ions can be controlled reversibly by light, an external parameter easy to tune and to switch. There is no doubt that these systems will provide diluted systems in novel experimental conditions, of basic interest for the magnetism of disordered and spin-glass like systems.

On the other hand, the photosensitive compounds which do not possess the energy barrier only undergo transient photomagnetic effects, the most spectacular being the light-stimulated magnetic after effects. Then, photoexcitation provides a *novel optical channel to the aging processes*. Precisely, the optical excitations of the system, due to their higher energy, may be much more efficient than the thermal fluctuations for driving the system above the multiple energy barriers associated with the underlying structural disorder.

A specific character of the light-induced magnetic structures is *metastability*. Indeed the raw photo-induced (RPI) state results from a peculiar building process of the magnetic system, the magnetic moments and interactions of which have been created at low temperature, e. g. below T_C. At such low temperatures a nonrelaxed domain structure is obtained, which combines the FC and ZFC characters. It can be destroyed by either thermal annealing or by isothermal magnetic saturation.

The practical applications of the photomagnetic properties of inorganic solids remain, at the moment, quite hypothetical. Among drawbacks for eventual devices, e. g. the low yield of the photoexcitation process, we focus the discussion on the working temperatures. These are obviously limited by both the magnetic ordering

temperatures and the decay temperature of the photoexcited state. Much effort is presently devoted to increasing the decay temperatures up to room temperature, and in this respect the use of novel photoswitchable ligands seems to be promising. In all cases, however, the devices have to face the crucial problem of the optical density. Thin layer samples, or the recourse to optical and magneto–optical measuring devices might solve the problem. For all these reasons, we speculate that optical applications such as erasable optical memories emerge out first, and specific magnetic applications might appear later.

Acknowledgments

We are deeply indebted to Prof. Michel Verdaguer [52] and his group for providing interesting materials, problems and discussions, to Drs E. Vincent and M. Guyot for enlightening discussions on the remanence properties, to Prof. S. Klokishner for help in understanding the photoexcitation processes. We thank A. Wack and Dr. E. Codjovi for valued work in designing and testing the photomagnetic device. This work was supported by Center National de la Recherche Scientifique (LMOV is Unité Mixte UMR 8634), and by European Communities for a TMR program (Contract TOSS, ERB-FMRX-CT98-0199) and for a COST Action (no. 518). The special budget (BQR-1999) of Université de Versailles Saint-Quentin is acknowledged.

References

[1] V. F. Kovalenko and E. L. Nagaev, *Sov. Phys. Usp.* **29** (1986) 297–321.
[2] E. L. Nagaev and A. I. Podel'shchikov, *Sov. Phys. JETP* **63** (1986).
[3] R. W. Teale and D. W. Temple, *Phys. Rev. Lett.* **19** (1967) 904.
[4] U. Enz and H. van der Heide, *Solid State Commun.* **2** (1968) 347.
[5] E. M. Gyorgy, J. F. Dillon and J. P. Remeika, *J. Appl. Phys.* **42** (1971) 1454.
[6] H. D. Jonker, *J. Solid State Chem.* **10** (1974) 116.
[7] W. Lems, P. J. Rijnierse, P. F. Bongers and U. Enz, *Phys. Rev. Lett.* **21** (1968) 1643.
[8] P. Berstein and T. Merceron, *Phys. Stat. Sol. (a)* **40** (1977) 159.
[9] M. Ayadi and J. Ferré, *J. Mag. Mag. Mat.* **91** (1986) 54; *Phys. Rev. Letters* **50** (1983) 274, *J. Appl. Phys.* **55** (1984) 1720.
[10] B. Wu, L. Ren, C. J. O'Connor, J. Tang, J. S. Jung, J. Ferré and J. P. Jamet, *J. Mater. Res.* **9** (1994) 909.
[11] H. Krenn, W. Zawadski and G. Bauer, *Phys. Rev. Lett.* **55** (1985) 1510.
[12] D. D. Awschalom, J. Warnock and S. von Molnar, *Phys. Rev. Lett.* **58** (1987) 812.
[13] K. A. Khachaturyan, D. D. Awschalom, J. R. Rosen and E. R. Weber, *Phys. Rev. Lett.* **63** (1989) 1311.
[14] F. Varret, *VIth Polish-French seminar (Rydzyna, Poland, 1996), Biuletyn Inst. Chem. Fiz. Teor. Polit. Wroclaw.* **5** (1997) 177–182.

[15] S. Decurtins, P. Gütlich, H. Spiering and A. Hauser, *Inorg. Chem.* **24** (1985) 2174; P. Gütlich, A. Hauser and H. Spiering, *Angew. Chem. Int. Ed. Engl.* **33** (1994) 2024; A. Hauser, *Comments Inorg. Chem* **17** (1995) 17.
[16] A. Hauser, *Chem. Phys. Letters* **124** (1986) 543.
[17] P. Gütlich, *Struct. Bonding* (Berlin) **44** (1981) 83; H. Toftlund, *Coord. Chem. Rev* **94** (1989) 67; E. König, Struct. *Bonding* (Berlin) **76** (1991) 51; O. Kahn, *Molecular Magnetism* (VCH, New York 1993).
[18] O. Kahn, J. Kröber and C. Jay, *Advanced Materials* **4** (1992) 718; see also T. Woike, W. Kirchner, G. Schetter, T. Barthel, H. Kim, S. Haussuhl, *Opt. Commun.* **106** (1994) 6.
[19] J. F. Létard, J. A. Real, N. Moliner, A. B. Gaspar, L. Capes, O. Cador and O. Kahn, *J. Amer. Chem. Soc.*, **121** (1999) 10630–10631; V. Ksenofantov, P. Gütlich and H. Spierung, 5th Meeting of the European Spin Grossover Family (Leiden, April 2000).
[20] S. Koshihara, Y. Takahashi, H. Sakai, Y. Tokura and T. Luty, *J. Phys. Chem. B* **103** (1999) 2592.
[21] *Relaxation of Excited States and Photo-Induced Structural Phase Transitions*, K. Nasu, Ed., *Springer Series in Solid State Sciences*, **124** (Springer:1997).
[22] C. Roux, J. Zarembowitch, B. Gallois, T. Granier, R. Claude, *Inorg. Chem.* **33** (1994) 2273; M. L. Boillot, C. Roux, J. P. Audière, A. Dausse and J. Zarembowitch, *Inorg. Chem.* **35** (1996) 3975; M. L. Boillot and H. Soyer, *New J. Chem.* **21** (1997) 889; M. L. Boillot, S. Chantraine, J. Zarembowitch, J.-Y. Lallemand and J. Prunet. *New J. Chem.* **2** (1999) 179; A. Sour, M. L. Boillot, E. Rivière and P. Lesot, *Eur. J. Inorg. Chem.*, (1999), p. 2117.
[23] Z. Z. Gu, T. Iyoda, K. Hashimoto and A. Fujishima, *J. Phys. Chem. Letters* **100** (1996) 18289.
[24] M. D. Carducci, M. R. Pressprich and P. Coppens, *J. Am. Chem. Soc.* **119** (1997) 2669.
[25] U. Hauser, V. Oestreich and H. D. Rohrweck, *Z. Phys. A* **280** (1977), 17 and 125, A 284 (1978) 9; T. Woike, W. Kirchner, H. Kim, S. Haussuhl, V. Rusanov, V. Angelov, S. Ormandjiev, T. Bonchev, and A. N. F. Schroeder, *Hyperf. Inter.* **7** (1993), 265.
[26] O. Sato, T. Iyoda, A. Fujishima and K. Hashimoto, *Science*, **272** (1996) 704.
[27] O. Sato, T. Iyoda, A. Fujishima and K. Hashimoto, *J. Electrochem. Soc.*, **144** (1997) L11.
[28] F. Varret, H. Constant-Machado, J. L. Dormann, A. Goujon, J. Jeftic, M. Noguès, A. Bousseksou, S. Klokishner, A. Dolbecq and M. Verdaguer, *Invited lecture at ICAME'97, proceedings published in Hyperf. Inter.* **113** (1998) 37–46.
[29] A. Goujon, O. Roubeau, F. Varret, A. Dolbecq, A. Bleuzen and M. Verdaguer, *Eur. Phys. J. B* (1999), **14** (2000) 115; A. Bleuzen, C. Lomenech, v. Escax, F. Villain, F. Varret, C. Cartier and M. Verdaguez, *J. Amer. Chem. Soc.*, **122** (2000) 6648; C. Cartier; F. Villain, A. Bleuzen, M.A. Arrio, P. Sainctavit, C. Lomenech, V. Escax, F. Baudelet, E. Dartyge, J.J. Gallet and M. Verdaguer, *J. Amer. Chem. Soc.*, **122** (2000) 6653.
[30] A. Goujon, F. Varret and D. Hendrickson, work in progress.
[31] D. M. Adams, A. Dei, A. L. Rheingold, and D. N. Hendrickson, *J. Am. Chem. Soc.* **115** (1993) 8221; D. M. Adams, Bulang Li, J. D. Simon, and D. N. Hendrickson, *Angew. Chem. Int. Ed. Engl.* **34** (1995) 1481; D. M. Adams and D. N. Hendrickson, *J. Am. Chem. Soc.* **118** (1996) 11515.
[32] S. Ohkoshi, S. Yorozu, O. Sato, T. Iyoda, A. Fujishima and K. Hashimoto, *Appl. Phys. Lett.* **70** (1997) 1040.
[33] K. Nagai, T. Iyoda, A. Fujishima and K. Hashimoto, *Solid State Commun*, **102** (1997) 809.
[34] M. Baran, S. L. Gnatchenko, O. Y. Gorbenko, A. R. Paul, R. Szymczak and H. Szymczak, *Phys. Rev. B* **60** (1999) 9244.
[35] W. Morscheidt, E. Codjovi, J. Jeftic, J. Linarès, A. Bousseksou, H. Constant-Machado and F. Varret, *Meas. Sci. Techn.* **9** (1998) 1311; E. Codjovi, W. Morscheidt, J. Jeftic, J. Linares,

M. Nogues, A. Goujon, O. Roubeau, H. Constant-Machado, A. Desaix, A. Bousseksou, M. Verdaguer and F. Varret, *ICMM'98, Proceedings in J. Mol. Cryst. Liq. Cryst.*, **335** (1999) 1295.

[36] O. Kahn and E. Codjovi, Phil. Trans. *R. Soc. London A* **354** (1996) 359; E. Codjovi, L. Sommier, O. Kahn, C. Jay, *New J. Chem.* **20** (1996) 503.

[37] H. Soyer, C. Mingotaud, M. L. Boillot and P. Delhaès, *Langmuir*, **14** (1998) 5890 and *Thin Solid Films*, **32** (1998) 329..

[38] J. F. Létard, O. Nguyen, H. Soyer, C. Mingotaud, P. Delhaès and O. Kahn, *Inorg. Chem.* **38** (1999) 3020.

[39] A. Desaix, O. Roubeau, J. Jeftic, J. G. Haasnoot, K. Boukheddaden, E. Codjovi, J. Linarès, M. Nogues and F. Varret, *Eur. Phys. J. B* **6** (1998) 183; F. Varret, K. Boukheddaden, J. Jeftic and O. Roubeau, *ICMM'98 (Seignosse), Proceedings in J. Mol. Cryst. Liq. Cryst.*, **335** (1999) 1273

[40] H. Spiering, E. Meissner, H. Köppen, E. W. Müller and P. Gütlich, *Chem. Phys.*, **68** (1982) 65; A. Hauser, *J. Chem. Phys.*, **94** (1991) 2741; J. Jeftic and A. Hauser, *J. Phys. Chem. B*, **101** (1997) 10262; A. Hauser, Comments on Inorg. Chem., **17** (1995) 17.

[41] J. F. Letard, P. Guionneau, L. Rabardel, J. A. K. Howard, A. E. Goeta, D. Chasseau, and O. Kahn., *Inorg. Chem.* **37** (1998) 4432.

[42] K. Boukheddaden, *personal communication*.

[43] N. Menendez, E. Codjovi and F. Varret, 4th Sprin Crossover Family Meeting, (Seeheim, April 1999).

[44] I. Prigogine, R. Lefever, J. S. Turner and J. W. Turner, *Phys. Lett. A* **51** (1975) 317.

[45] O. Roubeau, J. G. Haasnoot, J. Linarès and F. Varret, *ICMM'98 (Seignosse), Proceedings in J. Mol. Cryst. Liq. Cryst.*, **335** (1999) 1253.

[46] Hector Constant-Machado, *Thèse de Doctorat, Université Pierre et Marie Curie (Paris, 1997)*.

[47] J. Jeftic, J. Jeftic, H. Romstedt, F. Varret, A. Hauser, O. Roubeau, M. Matsarski and J. P. Rivera, *ICMM'98 (Seignosse), Proceedings in J. Mol. Cryst. Liq. Cryst.*, **335** (1999) 1223.

[48] T. Mallah, S. Thiébaut, M. Verdaguer and P. Veillet, *Science* **262** (1993) 1154.

[49] S. Ferlay, T. Mallah, R. Ouahès, P. Veillet and M. Verdaguer, *Nature*, **378** (1995) 701.

[50] M. Verdaguer, *Science*, **272** (1996) 698.

[51] A. Bleuzen, C. Lomenech, A. Dolbecq, F. Villain, A. Goujon, O. Roubeau, M. Noguès, F. Varret, F. Baudelet, E. Dartyge, C. Giorgetti, J. Gallet, C. Cartier and M. Verdaguer, *ICMM'98 (Seignosse), Proceedings in J. Mol. Cryst. Liq. Cryst.*, **335** (1999) 965.

[52] Laboratoire de Chimie des Métaux de Transition, CNRS-Université Pierre et Marie Curie, 4 place Jussieu, 75252 Paris cedex 05, France.

[53] A. Goujon, F. Varret, V. Escax, A. Bleuzen and M. Verdaguer, Int. Conf. Molecul. Magnetism (ISMM '2000, San-Antonio, Texas, Sept. 2000), Proceedings to appear in Polyhedron.

[54] P. Doussineau, A. Levelut and S. Ziolkiewicz, *Europhysics Letters*, **33** (1996) 391 and 539; F. Alberici, P. Doussineau and A. Levelut, *Europhysics Letters*, **39** (1997) 329; F. Alberici-Kious, J. P. Bouchaud, L. F. Cigliandolo, P. Doussineau and A. Levelut, *Phys. Rev. Lett.* **81** (1998) 4987.

[55] E. Vincent, J. Hamman and M. Ocio, in *Recent Progress in Random Magnets*, D. H. Ryan ed, Word Scientific Publishing Co. Pte. Ltd., (Singapore 1992); P. Doussineau, A. Levelut and S. Ziolkiewicz, *Europhysics Letters*, **33** (1996) 391; K. Jonason, E. Vincent, J. Hamman, J. P. Bouchaud and P. Nordblat, *Phys. Rev. Lett.* **81** (1998) 3243; E. Vincent, V. Dupuis, M. Alba, J. Hamman and J. P. Bouchaud, *Europhys. Lett.*, **29** (1999), in press.

[56] A. Bousseksou, J. Nasser, J. Linares, K. Boukheddaden, and F. Varret, *J. Phys. I France* **2** (1992) 1381; *J. Mol. Cryst. Liq. Cryst.* **234** (1993) 269.

[57] M. Sorai and S. Seki, *J. Phys. Chem. Solids* **35** (1974) 555; A. Bousseksou, H. Constant-Machado, F. Varret, *J. Phys. I France* **5** (1995) 747; A. Bousseksou, JG. McGarvey, F. Varret, JP. Tuchagues, AC. Dennis, ML. Boillot, *Chem. Phys. Lett.*, **318** (2000) 409.
[58] E. König, G. Ritter, S. K. Kulshreshtha, J. Waigel and H. A. Goodwin, *Inorg. Chem.* **23** (1984) 1896; J. Zarembowitch, C. Roux, M. L. Boillot, R. Claude, J. P. Itié, A. Polian and M. Bolte, *Mol. Cryst. Liq. Cryst.*, **234** (1993) 247; J. Jeftic, N. Menéndez, A. Wack, E. Codjovi, J. Linarès, A. Goujon, G. Hamel, S. Klotz, G. Syfosse and F. Varret, *Meas. Sci. Techn.*, in press, and references included..
[59] C. Roux, D. M. Adams, J. P. Itié, A. Polian, D. N. Hendrickson, M. Verdaguer, *Inorg. Chem.* **35** (1996) 2846.
[60] J. Jeftic and A. Hauser, *Chem. Phys. Letters* **248** (1996) 458; *J. Phys. Chem. B* **101** (1997) 10262; S. Schenker, A. Hauser, W. Wang and I. Y. Chan, *J. Chem. Phys.* **109** (1998) 9870.
[61] F. Varret, A. Goujon, Latino-American Conf. App. Mössbauer Effect (LACAME '00, Caracas, Venezuela, Nov. 2000), Proceedings to appear in Hyperf. Interactions.

Magnetism: Molecules to Materials I: Models and Experiments.
Edited by Joel S. Miller and Marc Drillon

ISBNs: 3-527-29772-3 (Hardback); 3-527-60084-1 (Electronic)

9 Colossal Magnetoresistance and Charge-ordering in Rare Earth Manganites

Bernard Raveau and Chintamani N. R. Rao

9.1 Abstract

Rare earth manganites of general formula $Ln_{1-x}A_xMnO_3$ (Ln = rare earth, A = alkaline earth) with the perovskite structure have become a subject of intense study in recent years, because of colossal magnetoresistance, charge-ordering, and their other fascinating properties. Structural and magnetotransport properties of these manganites are examined in this article in the light of recent findings. The extraordinary sensitivity of the properties of these materials to structure, composition, size of the cations, impurity substitution at the Mn site, and magnetic and electric fields is reviewed in some detail.

9.2 Introduction

Since the discovery of negative magnetoresistance in perovskite manganites of the type $Ln_{1-x}A_xMnO_3$ (Ln = rare earth, A = Ca, Sr, etc.) [1], extensive studies have been performed on these materials, which have very large resistance ratios, R_0/R_H, where R_0 and R_H are the values of the resistance in the presence and the absence of a magnetic field [2]. This effect has been called colossal magnetoresistance (CMR). Intense activity in this field [3] originates from the possible application of these materials in magnetic sensors and recording. The particular transport and magnetic properties of these materials mainly arise from the double-exchange mechanism between the Mn^{3+} and Mn^{4+} species [4], and are closely related to the crystallographic structure so that a structural transition often induces a magnetic and resistive transition. The double-exchange process gives rise to ferromagnetism and an insulator-metal (I–M) transition around the ferromagnetic T_C in these materials. In this review, we shall describe the main features which characterize the CMR manganites with respect to their crystal chemistry. Other important aspects such as charge- and orbital-ordering in the manganites will also be presented.

9.3 From Hole-doped to Electron-doped CMR Manganites

The manganites $Ln_{1-x}A_xMnO_3$ with the perovskite structure, where A is a divalent cation (e. g. Sr or Ca), can be subdivided into two groups depending on the x value. For $x < 1/2$, one obtains hole doped manganites which correspond to the introduction of Mn^{4+} species in the Mn^{3+} lattice of $LnMnO_3$, whereas for $x > 1/2$ the electron-doped manganites are formed, which correspond to the introduction of Mn^{3+} species in the Mn^{4+} lattice of $CaMnO_3$ (or $SrMnO_3$). The $Ln_{0.5}A_{0.5}MnO_3$ manganites which contain an equal number of Mn^{3+} and Mn^{4+} species ($x = 1/2$) are generally called half doped manganites.

In the hole-doped manganites, the CMR effect appears when the Mn^{4+} content is sufficiently large [1–3], the optimum value being around 30% (x 0.30). As illustrated for the manganite $Pr_{0.7}Ca_{0.25}Sr_{0.05}MnO_3$ (Fig. 1), the material exhibits an insulator

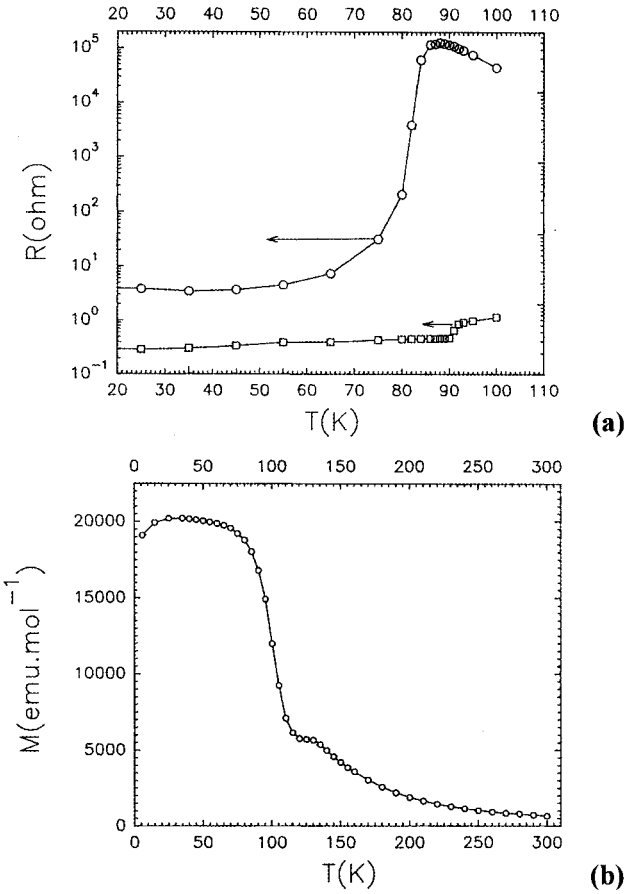

Fig. 1. $Pr_{0.7}Ca_{0.25}Sr_{0.05}MnO_3$: Temperature-dependence of (a) the resistance R under 0 T (○) and 5 T (◊) and (b) magnetization registered under 1.4 T

to metal transition (I → M) at a low temperature (Fig. 1a) which coincides with the Curie temperature T_C, corresponding to the paramagnetic (PM) to ferromagnetic (FM) transition (Fig. 1b). Application of a magnetic field of 5 T decreases the resistivity by several orders of magnitude around T_C (Fig. 1b).

In the electron-doped manganites, the CMR effect is observed for a rather small Mn^{3+} content around 15% ($x \sim 0.85$) [5]. More importantly, the behavior of the electron-doped materials is fundamentally different from the hole doped ones as illustrated for $Sm_{0.85}Ca_{0.15}MnO_3$ (Fig. 2). One indeed observes that, in contrast to hole doped manganites, the electron-doped phases, exhibit a metal (or semi-metal) to insulator (M → I) transition at decreasing temperature (Fig. 2a). Moreover, this electron-doped manganite is no more ferromagnetic at low temperature, but antiferromagnetic (AFM) and the $M(T)$ curve registered under 1.4 T registered shows a peak at the resistive transition temperature (Fig. 2b). In fact this $M(T)$ peak, which corresponds to a competition between FM and AFM is induced by the applied

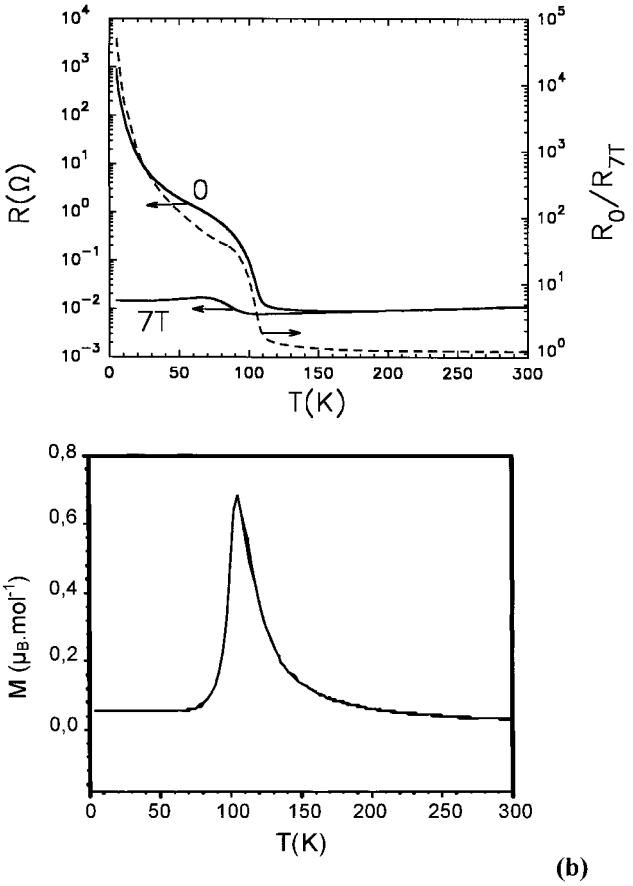

Fig. 2. $Sm_{0.85}Ca_{0.15}MnO_3$: Temperature-dependence of (a) the resistivity, ρ, under 0 and 7 T and (b) the magnetization registered under 1.4 T

magnetic field (its intensity is dramatically decreased under 100 G). Thus, the M–I transition in the electron-doped manganites coincides with a PM–AFM transition, instead of a PM–FM transition for the hole doped ones. For this optimum composition, the resistivity is decreased by two orders of magnitude at low temperature by application of a magnetic field of 7 T (Fig. 2a).

In the half-doped manganites, the CMR effect can also be observed as shown for instance for $Pr_{0.5}Sr_{0.5}MnO_3$ by Tomioka et al. [2]. In that case, two transitions are observed versus temperature as shown from the $\rho(T)$ curves (Fig. 3a) and $M(T)$ curves under 100 G (Fig. 3b). The first one around 250 K corresponds to a PMI $\rightarrow$ FMM transition like in the hole doped manganites, whereas the second one at 140 K involves a FMM $\rightarrow$ AFMI transition. The application of a magnetic field decreases also the resistivity, but much more importantly in the AFM region, i. e. by about 20 times, than in the FMM region (Fig. 3a).

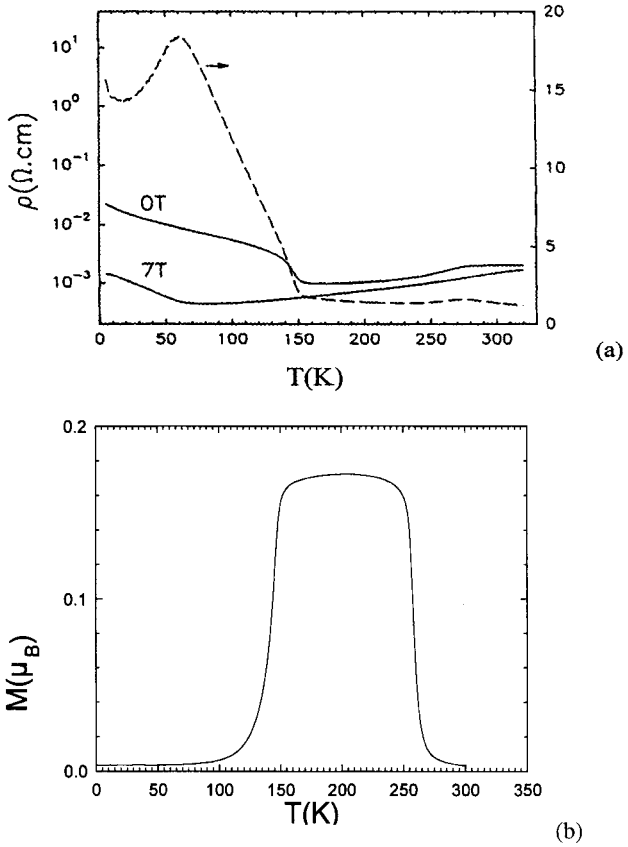

Fig. 3. $Pr_{0.5}Sr_{0.5}MnO_3$: Temperature-dependence of (a) the resistivity under 0 and 7 T and (b) the magnetization registered under 100 Gauss

9.4 Key Factors Controlling the CMR Properties-Magnetic Phase Diagrams

Like for most transition metal oxides, the transport and magnetic properties of the manganites are controlled by the carrier density and by the bandwidth which results from the overlapping of the Mn-3d and O-2p orbitals. The first one is determined by the amount of Mn^{4+} in the Mn^{3+} matrix of the hole doped system and vice-versa by the amount of Mn^{3+} in the Mn^{4+} matrix of the electron-doped oxides. The bandwidth depends on the Mn–Mn distance and more so on the Mn–O–Mn angle, and consequently can be modified by varying the size of the A-site cation. Besides the carrier concentration and size of the A site cation, there exists a third factor, the A site ion size mismatch, first introduced by Rodriguez-Martinez and Attfield [6]. These authors have shown that for the same average size $\langle r_A \rangle$, the T_C decreases as the cationic disorder because of the size difference between the A site cations increases. They have quantified this effect by the variance σ^2 of the A site cations radii distribution, $\sigma^2 = \sum y r_i^2 - \langle r_A \rangle^2$, where y_i are the fractional occupancies of the different i cation with r_i radius.

The effect of hole concentration and of the size of the A site cation upon the magnetoresistive properties of hole doped manganites was studied by several groups simultaneously [2a,7]. For a constant hole carrier concentration, T_C increases practically in a linear way with the average ionic radius of the interpolated cation, provided the size difference between the A cations be not too large. This is illustrated for the series $Pr_{0.7}Ca_{0.30-x}Sr_xMnO_3$ and $Pr_{0.7-x}La_xCa_{0.3}MnO_3$ and for the series $Pr_{0.66}Ca_{0.34-x}Sr_xMnO_3$ (Fig. 4). Thus, the large size of the A site cation seems to be the dominant factor responsible for the increase in T_C and, consequently, the CMR at higher temperature. The comparison of the "$Pr_{0.7}$" and "$Pr_{0.66}$" series shows also that the influence of the hole carrier density upon T_C is spectacular: for the same $\langle r_A \rangle$ value, each member of the series "$Pr_{0.66}$" exhibits a Curie temperature 50 K

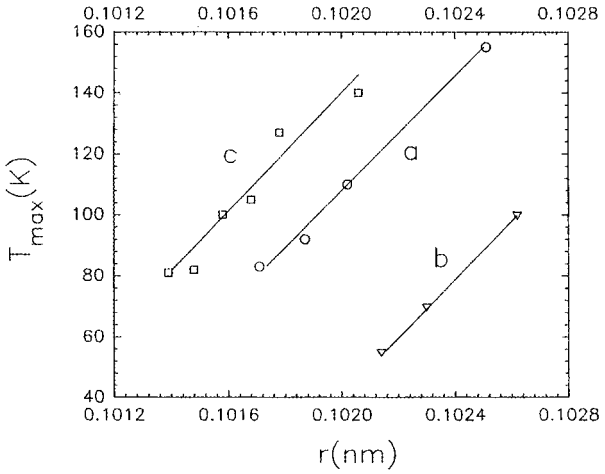

Fig. 4. Evolution of the dependence of T_C on $\langle r_A \rangle$ for the series (a) $Pr_{0.7}Ca_{0.30-x}Sr_xMnO_3$, (b) $Pr_{0.66}Ca_{0.34-x}Sr_xMnO_3$, (c) $Pr_{0.7-x}La_xCa_{0.3}MnO_3$

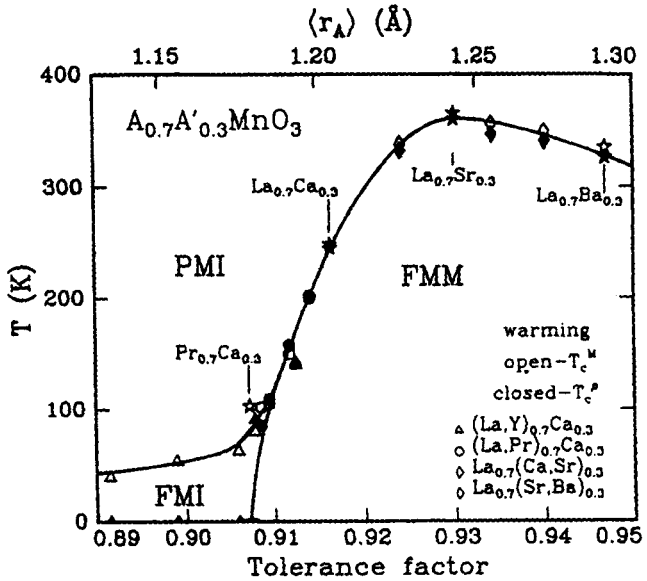

Fig. 5. Dependence of $\langle r_A \rangle$ (or tolerance factor) on T_C for $Ln_{0.7}A_{0-.3}MnO_3$ manganites (after H.Y. Hwang et al. [7a])

smaller than the oxide of the series "$Pr_{0.7}$". This demonstrates that T_C and CMR are both strongly reduced when the hole concentration deviates from the optimal hole concentration of 30% ($x \cong 0.30$). Nevertheless, CMR and the PMI–FMM transition can be obtained over a rather wide range of hole concentrations, provided the size of the A site cation is sufficiently large.

Taking into consideration the size effects, magnetic phase diagrams can be established as shown for the compounds $Ln_{0.7}A_{0.3}MnO_3$ (Fig. 5). This diagram shows clearly that the FMM state appears only above a certain critical $\langle r_A \rangle$ value, whereas below this $\langle r_A \rangle$ value ($\sim$1.18 Å), one observes only a FMI state at low temperatures. Thus, the PMI-FMM transition, and consequently the CMR properties require a minimum value of $\langle r_A \rangle$ of 1.18 Å (or of the tolerance factor) in the hole doped manganites, to appear. Such a decrease of the ferromagnetism with $\langle r_A \rangle$ is easily explained by the decrease of the Mn-O-Mn angle with $\langle r_A \rangle$, which creates a bandwidth narrowing [8]. Moreover, it can be seen from this diagram, that T_C first increases practically linearly with $\langle r_A \rangle$ in the region 1.18–1.22 Å, in agreement with the above statements. But then, for higher $\langle r_A \rangle$ value, T_C deviates from the linearity, becoming smaller than the expected value, goes through a maximum for $\langle r_A \rangle$ = 1.24 Å, and finally decreases as $\langle r_A \rangle$ increases. Such an evolution is easily explained by the A site size mismatch effect [6]. In order to continue to increase $\langle r_A \rangle$, one must indeed introduce strontium and then barium on the La site so that the size difference and consequently the mismatch effect are increased dramatically. As a result, the size mismatch which tends to decrease T_C, competes with the size effect which tends to increase T_C, and finally becomes predominant for $\langle r_A \rangle > 1.24$ Å.

In the electron-doped manganites, the CMR effect appears only for a small range of electron concentration, and in contrast to the hole-doped manganites requires a small size of the A-site cation. This is illustrated in Fig. 6 where the magnetic diagrams of the manganites $Pr_{1-x}Sr_xMnO_3$ and $Pr_{1-x}Ca_xMnO_3$ [9] are compared. The $Pr_{1-x}Sr_xMnO_3$ diagram (Fig. 6a), characterized by a large size of the A-site cation (Pr/Sr) displays a wide FMM domain and consequently CMR properties over a large range of composition ($0.25 \leq x \leq 0.54$) extending especially in the hole doped region, whereas in the electron-doped region close to $SrMnO_3$ ($x \sim 0.7$–

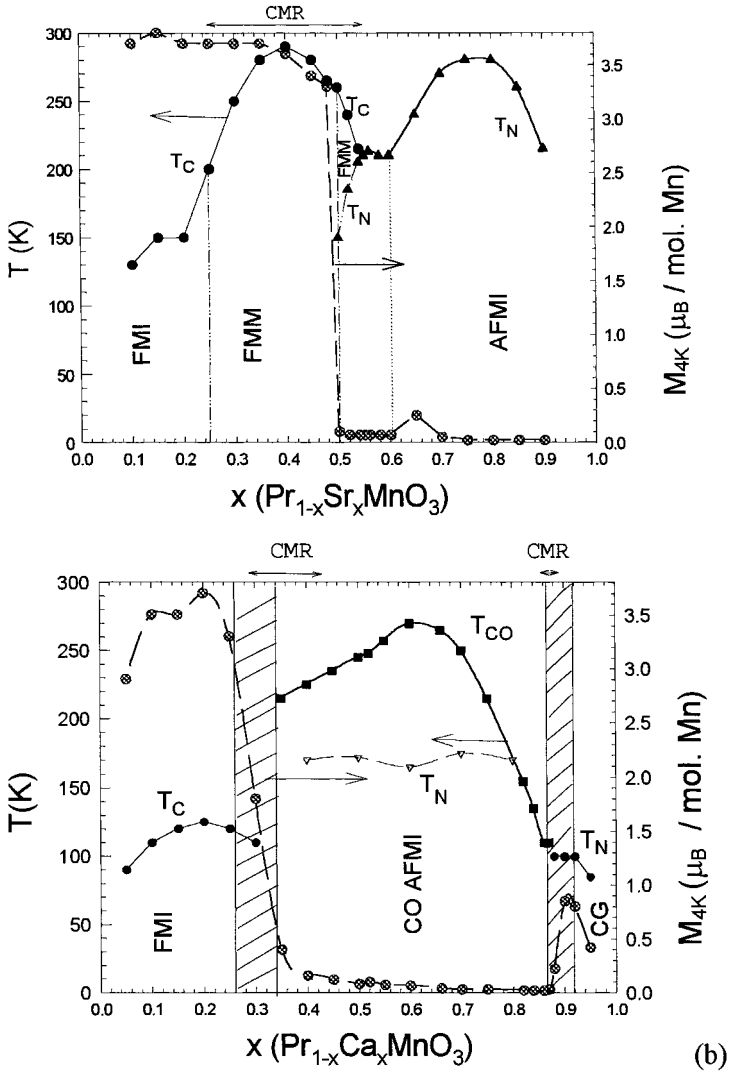

Fig. 6. Magnetic phase diagrams of (a) $Pr_{1-x}Sr_xMnO_3$ and (b) $Pr_{1-x}Ca_xMnO_3$

0.9) no CMR effect is observed. In contrast, the $Pr_{1-x}Ca_xMnO_3$ diagram (Fig. 6b), which corresponds to a smaller size of the A site (Pr/Ca), shows that the CMR domain in the hole-doped region has been considerably reduced ($0.3 \leq x \leq 0.45$), FMM properties being not detected in the diagram, but there exists a second CMR domain in the electron-doped region ($0.85 \leq x \leq 0.90$).

It is remarkable that the CMR domain in the electron-doped system is narrow and the situation is common to all the lanthanides from La to Ho in the $Ln_{1-x}Ca_xMnO_3$ system ($x = 0.80$–0.87) [5]. It is easy to determine the role of the electron concentration upon the magnetic and transport properties of these materials by plotting the temperature T_{peak} of their M(T) curve against $1 - x$ (Fig. 7), because it was shown that this peak corresponds to the maximum CMR effect [5a].

For most of the lanthanides T_{peak} appears for the same electron concentrations ($1 - x \cong 0.13$ to 0.20), whereas for cerium and thorium T_{peak} and consequently CMR appear for a much lower electron concentration ($1 - x \sim 0.07$ to 0.12). This difference comes from the tetravalent character of thorium or cerium which introduces an electron concentration per atom twice higher than that introduced by trivalent lanthanides. By plotting T_{peak} against $2(1 - x)$ or Th or Ce phases (dashed line Fig. 7), it can be seen that these oxides exhibit a similar behavior. These results demonstrate that the electron concentration is a predominant factor for the magnetic and transport and especially CMR properties of the electron-doped manganites. The transition temperature T_{peak} is also slightly affected by the size of the lanthanide. For a fixed electron concentration, the transition temperature T_{peak} decreases with

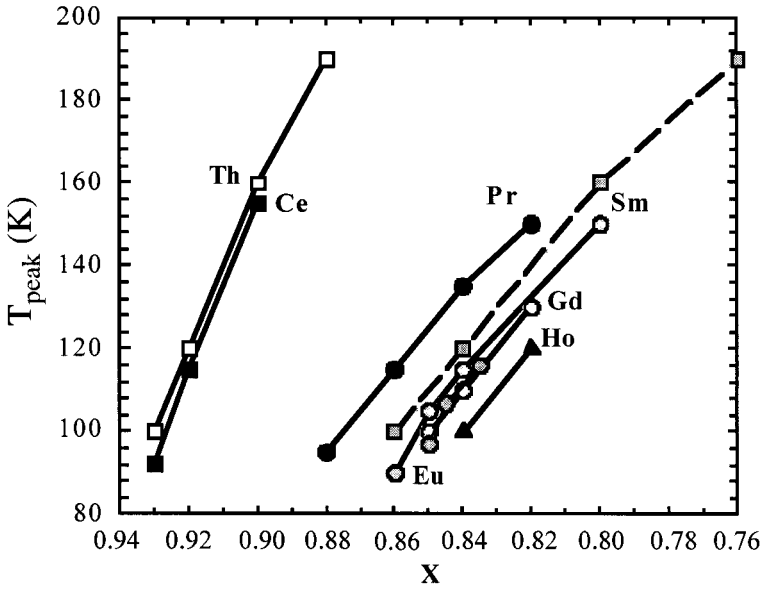

Fig. 7. Evolution of the dependence of Tpeak (or metal-insulator temperature transition) on electron concentration x for electron-doped manganites $Ln_{1-x}Ca_xMnO_3$. The dashed line corresponds to the $2(1 - x)$ electron concentration for Th and Ce

the lanthanide size. In other words, as the mean ionic radius $\langle r_A \rangle$ of the interpolated cation increases, a smaller electron concentration is necessary to replace the FMM state at the benefit of the AFMI state. Thus, in contrast to the hole-doped manganites, the stability of the FMM state increases as the size of the interpolated cation decreases. Note that the size of the A site cation also influences the optimal electron concentration, for the appearance of CMR, increasing slightly from 0.135 for Pr to 0.16 for Eu and remaining constant down to Ho. The size of the A-site cation and the electron concentration are not the only factors which influence the CMR properties of these materials; the size mismatch effect should also be considered, but the latter effect is too small in this series to be evaluated easily. Nevertheless in a recent study of the perovskites $Th_{0.35}AE_{0.65}MnO_3$ (AE = Ca, Sr, Ba), it has been shown that a transition from a FMM to a SPGI (spin glass insulator) state is induced as the A-site size mismatch is increased. Moreover, the magnetoresistance is strongly reduced for the spin glass insulators, demonstrating that the A-site cationic disorder is detrimental for the CMR properties in the electron-doped manganites.

The size of the A site cation plays also an important role in the magnetic and transport properties of the half doped manganites [10], as illustrated for the series $Pr_{0.5}Sr_{0.5-x}Ca_xMnO_3$ (Fig. 8a). In these oxides, T_N increases and T_C decreases as x increases i. e. as $\langle r_A \rangle$ decreases, showing that the AFMI and PMI states are favored at the expense of the FMM state by decreasing the size of the A site cation. Moreover, application of a magnetic field shows that the size of the A site cation also affects the amplitude of the CMR effect, giving a resistance ratio of 3000, a value higher than for $Pr_{0.5}Sr_{0.5}MnO_3$ ($\cong 20$). A similar magnetic phase diagram is observed for $(Ln, Ln')_{0.5}Sr_{0.5}MnO_3$ manganites [10] as shown in Fig. 8b. The two diagrams are not superimposable and the $\langle r_A \rangle$ dependence of T_C is more severe for the "$Sr_{0.5}$" phases (Fig. 8b) than for the "$Pr_{0.5}$" phases (Fig. 8a). Thus, T_N is nearly constant for "$Sr_{0.5}$" (Fig. 8b), whereas it decreases significantly as $\langle r_A \rangle$ increases for "$Pr_{0.5}$" (Fig. 8a). This difference between the two series is explained on the basis of the A site size mismatch.

It has been observed that σ^2 and $\langle r_A \rangle$ are not univocally related [11] making it necessary for a new magnetic phase diagram in the (σ^2, r_A) plane (Fig. 9) obtained by measuring T_N and T_C for the different members of the general formula $Ln_{0.5}A_{0.5}MnO_3$. Four regions can be distinguished: weak ferromagnetic (WFM), ferromagnetic (FM) and two charge-ordered (CO) regions. The first type of charge ordered phases (1.21–1.26 Å) exhibit two transitions, AFMI–FMM and FMM–PMI. For those compounds, the larger is $\langle r_A \rangle$, wider is σ^2, indicating that this CO-type becomes less sensitive to size mismatch when $\langle r_A \rangle$ increases. Nevertheless, the FMM–PMI transition (FM regions) is observed beyond a critical σ^2 value. In contrast, when $\langle r_A \rangle$ is small (<1.19 Å) and σ^2 is not too high (<0.002 Å^2), a second type of charge-ordered phase is obtained wherein a AFMI–PMI transition occurs. Note that whatever be the $\langle r_A \rangle$, whenever σ^2 is increased CO tends to disappear leading either to a FM or to WFM behavior. These results indicate the important role of both $\langle r_A \rangle$ and σ^2 on the magnetoresistive properties of these manganites.

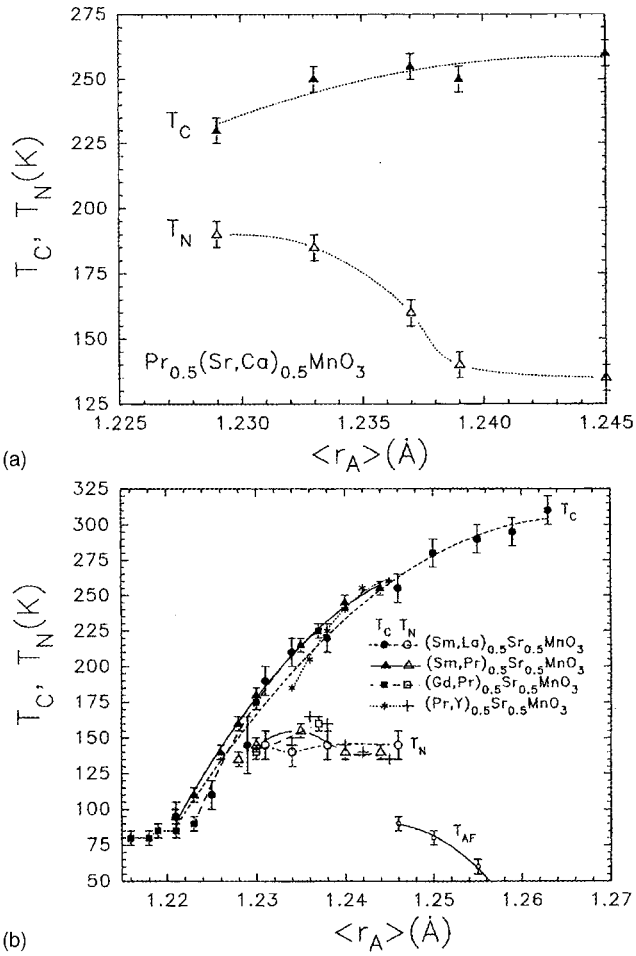

Fig. 8. Dependence of $\langle r_A \rangle$ on both T_C and T_N for (a) $Pr_{0.5}Sr_{0.5-x}Ca_xMnO_3$ and (b) for (Ln, Ln′)$_{0.5}Sr_{0.5}MnO_3$ manganites

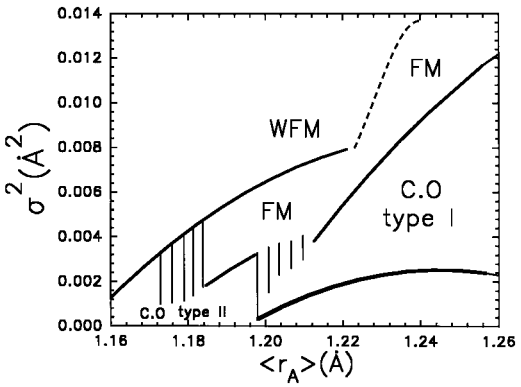

Fig. 9. Magnetic phase diagram in the σ^2-$\langle r_A \rangle$ plane of $Ln_{0.5}A_{0.5}MnO_3$ manganites

9.5 Structural Transitions

The magnetic and transport properties of the manganites are closely related to the crystallographic structure. It is indeed remarkable that most of the magnetic and transport transitions coincide with a structural transition. The evolution of the perovskite structure versus temperature (distortion of the MnO_6 octahedra, tilting of the octahedra, cationic displacements, ordering of the Mn^{3+} and Mn^{4+} species called charge-ordering) is one of the key points for the understanding of the magnetotransport transitions in those materials.

In the hole-doped CMR manganites, which show the PMI–FMM (I–M) transition, a significant contraction of the lattice, without any change of the symmetry is generally observed just below T_C in the FMM state [12]. This is illustrated by the evolution of the Mn–O distances versus temperature in the CMR manganite $Pr_{0.70}Ca_{0.20}Sr_{0.1}MnO_3$ (Fig. 10a), which has a T_C of 170 K. It can be seen that an abrupt variation of the Mn–O distances is observed at the transition. In the PMI state, the Jahn–Teller distortion increases as T decreases, whereas in the FMM state the Jahn–Teller distortion still exists but does not vary significantly at low temperatures. Clearly, T_C coincides exactly with the decrease in the Jahn-Teller distortion (Fig. 10b).

Although they correspond to a static effect, these correlations between Jahn–Teller distortion and magnetic ordering are in agreement with the theory of Millis et al. [8] which emphasizes the important role of the dynamic Jahn–Teller effect in the properties of these materials. For smaller size of the interpolated cation, the FMM domain is reduced and finally replaced by an AFM domain at low temperature as $\langle r_A \rangle$ decreases, as shown in $La_{1-x}Ca_xMnO_3$ [13], $Nd_{1-x}Ca_xMnO_3$ [14] and $Sm_{1-x}Ca_xMnO_3$ [15]. The PM $\rightarrow$ AFM transition which occurs at low temperatures in the latter manganites is related to the appearance of charge-ordering, i. e. to the ordering of the Mn^{3+} and Mn^{4+} species as the temperature decreases below the transition temperature. In the half-doped regime, this charge-ordering involves the

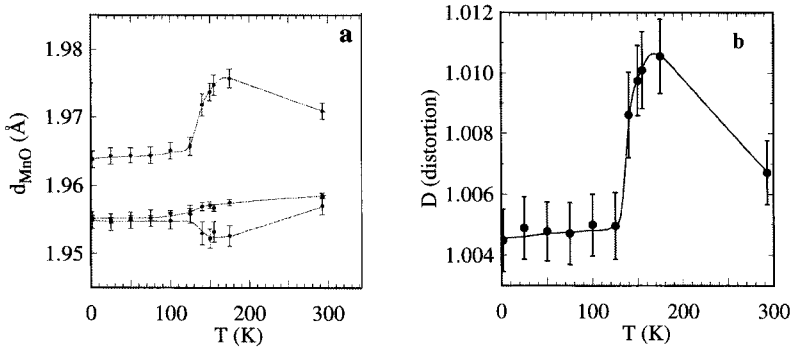

Fig. 10. Evolution of the Mn–O distances (a) and of the Jahn–Teller distortion dMn-Oapical/dMn-Oequatorial (b) for the hole doped manganite $Pr_{0.7}Ca_{0.2}Sr_{0.1}MnO_3$

doubling of one parameter of the orthorhombic cell at low temperature, in agreement with the 1:1 ordering of Mn^{3+} species with Mn^{3+}/Mn^{4+} mixed species type. This issue of charge-ordering will be discussed in detail in the next section. Nevertheless it is worth pointing out, that it is the charge-ordering phenomenon which hinders the appearance of the metallicity and consequently the FMM state in zero field. The application of a magnetic field can then melt the charge-order in large $\langle r_A \rangle$ systems and generate the FMM state, so that CMR properties can be obtained at high magnetic fields.

9.6 Charge-ordering

Charge-ordering is a phenomenon observed in solids wherein electrons become localized due to the ordering of cations of differing charges on specific lattice sites. Several of the rare earth manganites of the general composition $Ln_{1-x}A_xMnO_3$ (Ln = rare earth, A = alkaline earth) have fascinating properties and phenomena associated with charge-ordering [3,16]. Historically, the occurrence of charge-ordering in these manganates was first observed by Wollan and Koehler [17] and later examined by Jirak et al. [18]. Charge-ordering competes with double-exchange, and promotes insulating behavior and antiferromagnetism in the manganites. The charge-ordered phases in the manganites are manifestations arising from the interaction between the charge carriers and the phonons wherein the Jahn–Teller distortions play a significant role. Charge-ordering arises because the carriers get localized into specific sites below a certain temperature, T_{CO}, giving rise to long-range order throughout the crystal structure. Furthermore, the Mn^{3+} (e_g) orbitals ($3d_z^2$) and the associated lattice distortions (long Mn–O bonds) also develop long-range order, giving rise to orbital-ordering. Then, the magnetic exchange interactions between the Mn ions become anisotropic because the Mn–O–Mn superexchange interaction is ferromagnetic through a filled and an empty $3d_z^2$ orbital, but antiferromagnetic through two empty $3d_z^2$ orbitals. This gives rise to complex magnetic-ordering in these structures. Thus, at low temperatures, the rare earth manganites get antiferromagnetically ordered (AFM) with CE or A type ordering, but only the former occurs in the charge-ordered materials where the e_g electrons are localized. The CE-type spin-ordering is characterized by the ordering of Mn^{3+} and Mn^{4+} ions alternately. The spin-ordering in the *ab* plane is somewhat complex and it stacks antiferromagnetically along with *c* axis. In the A-type spin-ordering, the spins order ferromagnetically in the *ab* plane (with the moments pointing towards the *a* axis) and these planes stack antiferromagnetically along the *c* axis. In Fig. 11 we show the features of CE- and A-type ordering in half-doped manganites ($x = 0.5$). Orbital-ordering can occur in both A and CE-type AFM ordering, but they differ in detail. The CE type AFM state can be attained on cooling a ferromagnetic state or a charge-ordered paramagnetic state.

The basic features of charge-ordering in the perovskite rare earth manganites, $Ln_{1-x}A_xMnO_3$, can be understood by examining the properties of $Pr_{0.6}Ca_{0.4}MnO_3$ and $Nd_{0.5}Sr_{0.5}MnO_3$. These two manganites with different sizes of the A-site cations

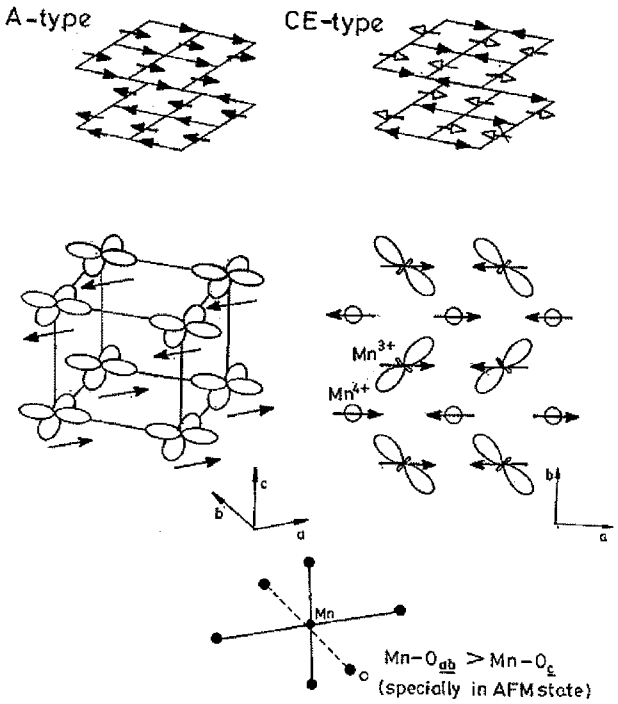

Fig. 11. A-type and CE-type antiferromagnetic (AFM) ordering in rare earth manganites, $Ln_{0.5}A_{0.5}MnO_3$. The figure shows spin-ordering (*ab* plane) and orbital-ordering ($d_{x^2-y^2}$ in A type, $d_{y^2-r^2}$ in CE type) in the two types. The $Mn^{3+}O_6$ octahedra have long Mn–O bonds in the ab plane, specially in the AFM state

(the average radius $\langle r_A \rangle$ being 1.17 and 1.24 Å respectively), exhibit significantly different properties $Pr_{0.6}Ca_{0.4}MnO_3$ is an insulator at all temperatures and becomes charge-ordered around 235 K. At this transition temperature, T_{CO}, anomalies are found in the magnetic susceptibility as well as the resistivity [19] (Fig. 12). In the charge-ordered (CO) state, the Mn^{3+} and Mn^{4+} ions are regularly arranged in the *ab* plane with the associated ordering of the $d_{x^2-y^2}$ and $d_{y^2-r^2}$ orbitals. On cooling, antiferromagnetic (AFM) ordering (CE type) occurs at 170 K (T_N). The CE-type spin structure contains ferromagnetically aligned chains along the *c*-axis. The ferromagnetic spin-ordering in $Pr_{0.6}Ca_{0.4}MnO_3$ is likely to be due to the extra electrons (arising from the deviation from $x = 1/2$) which hop in a manner that aligns the t_{2g} spins in the Mn^{4+} sites by the double-exchange mechanism. It must be noted $Pr_{0.5}Ca_{0.5}MnO_3$ is a CO material with an antiferromagnetic chain along the *c*-axis. Around 40 K, $Pr_{0.6}Ca_{0.4}MnO_3$ exhibits canted antiferromagnetic ordering. Application of an external magnetic field transforms the CO state to a ferromagnetic metallic (FMM) state as shown in Fig. 12. The transition is first-order and is associated with large hysteresis. The basic features the CO state in $Pr_{0.6}Ca_{0.4}MnO_3$ are exhibited by other rare earth manganites with relatively small A-size cations, in that the CO state

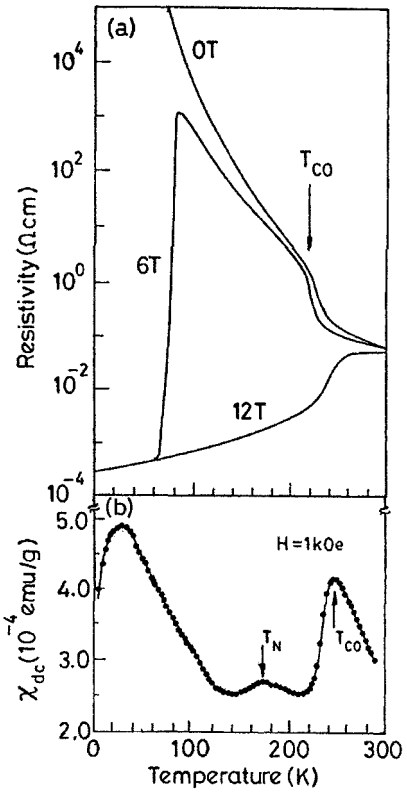

Fig. 12. Temperature-variation of (a) resistivity and (b) magnetic susceptibility of $Pr_{0.6}Ca_{0.4}MnO_3$ [19]

is the ground state. These materials do not become ferromagnetic in the absence of an external field. Thus, $Nd_{0.5}Ca_{0.5}MnO_3$ ($\langle r_A \rangle = 1.17$ Å) is a paramagnetic insulator with a charge-ordering transition around 240 K.

$Nd_{0.5}Sr_{0.5}MnO_3$ is a ferromagnetic metal with a T_C of ~250 K and transforms to an insulating CO state around 150 K [20] (Fig. 13). The FMM–CO transition is accompanied by spin- and orbital-ordering, and the CO insulator is antiferromagnetic (CE type). Application of a magnetic field of ~6T destroys the CO state, and the material becomes metallic. The transition is first-order showing hysteresis and is associated with changes in unit cell parameters. $Pr_{0.5}Sr_{0.5}MnO_3$ undergoes a transition from a FMM state to an AFM state (A type) at 140 K, but is not charge-ordered [21]. Note that there can be charge-ordering only in the CE-type AFM structure. Note that the CO states of both $Nd_{0.5}Sr_{0.5}MnO_3$ and $Pr_{0.6}Ca_{0.4}MnO_3$ could be transformed into the FMM state by the application of magnetic fields. The sensitivity of the CO state to magnetic fields depends on the average size of the A-site cations, $\langle r_A \rangle$.

A few decades ago, Goodenough [22] interpreted the CE-type antiferromagnetic structure of $La_{0.5}Ca_{0.5}MnO_3$ as evidence of charge-ordering and suggested a possible orbital-ordering pattern associated with it. The crystallographic superstructure arising from such ordering has been observed by electron diffraction and solved by neutron and X-ray diffraction. $La_{0.5}Ca_{0.5}MnO_3$ shows a ferromagnetic transition at

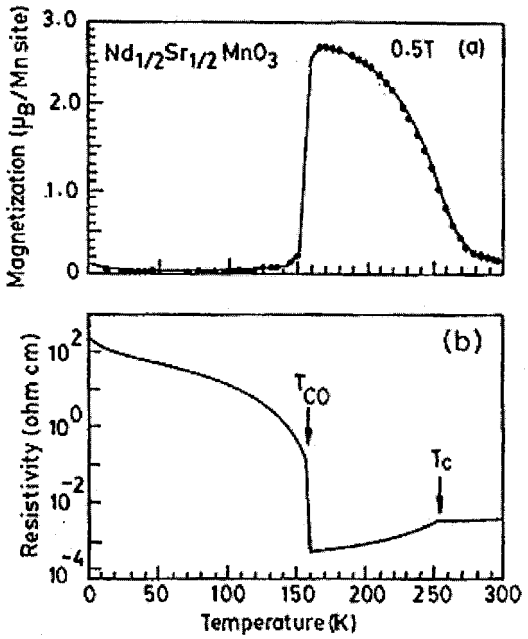

Fig. 13. Temperature-variation of (a) magnetization and (b) resistivity of $Nd_{0.5}Sr_{0.5}MnO_3$ [20]

225 K, followed by a first-order transition at 135 K to an AFM(CE) state. The latter transition coincides with a change from incommensurate to nearly commensurate charge-ordering. What is surprising, however, is the co-existence of ferromagnetism and charge-ordering in the narrow temperature range (220–135 K). This is apparently due to an inhomogeneous spatial mixture of the incommensurate CO and FM (charge-disordered) microdomains [23].

In $Pr_{1-x}Ca_xMnO_3$ ($0.35 \leq x \leq 0.5$), CE type charge-ordering occurs around 230 K (T_CO) and AFM ordering around 170 K. The paramagnetic state is characterized by ferromagnetic spin fluctuations with a small energy scale [24]. At T_{CO}, these fluctuations decrease and disappear at T_N. It appears that charge-ordering is incommensurate in the paramagnetic insulating state (180–260 K) of the $x = 0.5$ composition. At T_N, there is an incommensurate to commensurate CO transition. In the incommensurate CO structure, partial orbital-ordering is likely to be present. Similar charge, orbital and spin-ordering is found in the 0.3 composition as well. $Pr_{0.67}Ca_{0.33}MnO_3$ shows thermal relaxation effects from the metastable FMM state (produced by the application of a 10 T magnetic field) to the CO state [25]. An electron microscopic study of $La_{1-x-y}Pr_yCa_xMnO_3$ with $x = 3/8$ suggests this manganate to be electronically phase-separated into a sub-micrometer-scale mixture of CO insulating regions and metallic, ferromagnetic domains [26]. The balance between the two states is affected by changes in chemical substitution, magnetic field etc. Percolative transport between the two states could be responsible for the high CMR in such manganites with low T_C.

In $Nd_{0.5}Sr_{0.5}MnO_3$, which has a first order transition from the FMM state to the CO-AFM state, the Imma space group renders the Mn–O–Mn angle in the *ab* plane

to be closer to 180°, promoting the overlap of the Mn(e_g) and O(2p) orbitals. The e_g electrons are delocalized in the FMM state, but localized in the AFM (CE) state below T_CO. Vacuum tunneling measurements show that at the 150 K transition, a CO gap of 250 meV opens up [27]. The gap collapses on applying the magnetic field, suggesting that a gap in the density of states at E_F is necessary for the stability of the CO state. $Nd_{0.5}Sr_{0.5}MnO_3$ shows anomalous magnetostriction behavior, with a large positive magnetovolume effect due to the magnetic field-induced structural transition accompanying the CO–FMM transition [28]. It is to be noted that the unit cell volume of the FMM phase is higher than that of the CO phase. In $Pr_{0.7}Ca_{0.3}MnO_3$, the destruction of the CO state gives rise to a negative magneto volume effect. It appears that the magnetic field-induced structural transition occurs when the CO state is established in the FM state, as in $Nd_{0.5}Sr_{0.5}MnO_3$. The magnetovolume effect in $Nd_{0.5}Sr_{0.5}MnO_3$ is consistent with the existence of an electron phase segregation at low temperatures which is reversed by a magnetic field.

High-resolution X-ray and neutron diffraction investigations show that $Nd_{0.5}Sr_{0.5}MnO_3$ phase separates into three macroscopic phases at low temperatures. These are the FMM high-temperature phase (Imma), the orbitally ordered AFM (A-type) phase (Imma), and the charge and orbitally ordered AFM (CE type) low-temperature phase ($P2_1/m$) [29]. The A-type AFM phase starts manifesting itself around 220 K, while the CE type CO phase first appears at 150 K. In Fig. 14, we show the phase compositions at different temperatures. The presence of the high-temperature FMM phase, even at very low temperatures, is noteworthy. These results are of considerable significance in interpreting many properties of this manganite. The FMM phase has a larger volume than the average volume or the volume of the low-temperature CO phase. The phase segregation behavior of this system and the relative stabilities of the structures seem to depend crucially on the Mn^{4+}/Mn^{3+} ratio. Thus, $Mn^{4+}/Mn^{3+} > 1$ appears to stabilize the orbitally ordered AFM (A-type) phase.

In the hole-doped manganites exhibiting CMR, the ferromagnetic T_C increases with the average radius of the A-site cations, $\langle r_A \rangle$. Increasing $\langle r_A \rangle$, which is equivalent to increasing the hydrostatic pressure, increases the Mn–O–Mn angle and e_g band-

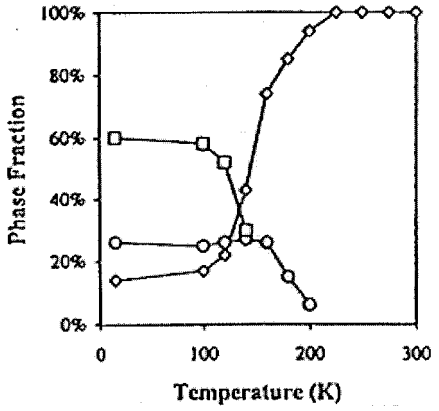

Fig. 14. Variation in the percentage of the different phases of $Nd_{0.5}Sr_{0.5}MnO_3$ with temperature: FMM phase (diamonds); orbitally ordered A-type AFM phase (squares); Charge-ordered CE-type AFM phase (circles) [29]

width. If there is considerable mismatch in the radii of the different A-site cations, however, the T_C does not increase with $\langle r_A \rangle$, an aspect that we will discuss later. The charge-ordering transition is also highly sensitive to $\langle r_A \rangle$ and the T_{CO} increases with decrease in $\langle r_A \rangle$. The sensitivity of T_{CO} to $\langle r_A \rangle$ has been discussed in some detail recently [16,30,31] and is generally attributed to an increased tilting of the MnO_6 octahedra as the $\langle r_A \rangle$ decreases. Careful structural investigations [30] show that the Mn–O(eq)–Mn and Mn–O(ax)–Mn bonds are identical in $Ln_{0.5}Ca_{0.5}MnO_3$ (except when Ln = La). For $Ln_{0.5}Ca_{0.5}MnO_3$ and all the $Ln_{0.5}Sr_{0.5}MnO_3$ compounds, the Mn–O(eq)–Mn angle is significantly larger (2–6°) than the Mn–O(ax)–Mn angle. While the $Ln_{0.5}Ca_{0.5}MnO_3$ manganites crystallize in Pnma symmetry, in the $Ln_{0.5}Sr_{0.5}MnO_3$ manganites, there is an evolution from Pnma to I_4/mcm through Imma with increase in $\langle r_A \rangle$. The changes in the octahedral tilt system have consequences on the low-temperature magnetic structure. This is seen in $Nd_{0.5}Sr_{0.5}MnO_3$ where the charge-ordering in the CE-type AFM state is associated with the Imma structure.

We noted earlier that the CO state of $Nd_{0.5}Sr_{0.5}MnO_3$ ($\langle r_A \rangle = 1.24$ Å) and $Pr_{0.6}Ca_{0.4}MnO_4$ ($\langle r_A \rangle = 1.17$ Å) are both destroyed by magnetic fields. The field required to melt the CO state varies with $\langle r_A \rangle$ and the manganites with very small $\langle r_A \rangle$ remain charge-ordered even on application of high magnetic fields. Thus, $Y_{0.5}Ca_{0.5}MnO_3$ ($\langle r_A \rangle = 1.13$ Å) has a very robust CO state which is not affected by high magnetic fields (>15T). We can thus distinguish three types of manganite by their sensitivity to magnetic fields [31]: (a) manganites that are ferromagnetic and become charge-ordered at low temperatures (e. g., $Nd_{0.5}Sr_{0.5}MnO_3$), with the CO state transforming to a FMM state on application of a magnetic field, (b) manganites that are charge-ordered in the paramagnetic state and do not exhibit an FMM state, but transform to a FMM state under a magnetic field (e. g. $Pr_{1-x}Ca_xMnO_3$) and (c) those which are charge-ordered in the paramagnetic state as in (b), but are not affected by magnetic fields up to ~6T (e. g. $Y_{0.5}Ca_{0.5}MnO_3$). Some of the manganites in category (c), such as $Nd_{0.5}Ca_{0.5}MnO_3$, show a CO → metal transition only on the application of very high fields (≥15T). The $x = 0.5$ manganites with $\langle r_A \rangle \leq 1.17$ Å seems to belong to category (c). The apparent one-electron bandwidths estimated on the basis of the experimental Mn–O–Mn angles and Mn–O distances in $Ln_{0.5}A0.5MnO_3$ do not vary significantly with $\langle r_A \rangle$, suggesting that other factors may be responsible for the sensitivity of the CO state to $\langle r_A \rangle$. One possibility is the competition between A- and B-site cations for covalent mixing with the O(2p) orbitals [31]. By increasing the size of the A-site cations, the CO state in the manganites can be transformed to a FMM state. Here also, increasing $\langle r_A \rangle$ has the same effect as increasing the external pressure.

While one employs $\langle r_A \rangle$ as a parameter to vary the eg bandwidth for purpose of convenience, it should be realized that there are no simple systematics in charge-ordering and magnetic behavior of $Ln_{0.5}A_{0.5}MnO_3$ compounds with $\langle r_A \rangle$. Considering that the rare earth manganites with large $\langle r_A \rangle$, as exemplified by $Nd_{0.5}Sr_{0.5}MnO_3$ ($\langle r_A \rangle = 1.24$ Å), and those with small $\langle r_A \rangle$, as exemplified by $Nd_{0.5}Ca_{0.5}MnO_3$ ($\langle r_A \rangle = 1.17$ Å), exhibit entirely different characteristics of the CO state, and that $\langle r_A \rangle = 1.17$ Å categorizes the manganites with respect to the effect of the magnetic fields, we would expect interesting and unusual properties in the intermediate range

of $\langle r_A \rangle$ of 1.20 ± 0.20 Å. In this regime, T_{CO} approaches T_C leading to a competition between charge-ordering and ferromagnetism.

$Nd_{0.25}La_{0.25}Ca_{0.5}MnO_3$ ($\langle r_A \rangle = 1.19$ Å) reveals an intriguing sequence of phase transitions [32]. On cooling, this manganite develops an incipient CO state below 220 K. The formation of this state is accompanied by an increase in electrical resistivity and the opening up of a gap in the density of states near E_F. The orthorhombic distortion also increases as a consequence of cooperative Jahn–Teller distortion of the lattice and short-range ordering of the Mn^{3+} and Mn^{4+} ions. Around 150 K, the incipient CO state becomes unstable and the material undergoes a re-entrant transition to a FMM state. The transition is characterized by a sharp decrease in resistivity, collapse of the CO gap (Fig. 15), development of FM ordering and an abrupt decrease in the orthorhombic distortion. There is a two phase coexistence region (150–220 K) around the CO-Fmm transition (see Fig. 15).

The effect of magnetic fields on the CO states of rare earth manganites was discussed earlier. In $Pr_{1-x}Ca_xMnO_3$ ($x \approx 0.4$), magnetic fields cause a CO–FMM transition. High electric fields and X-irradiation also give rise to such a transition. Irradiation with visible light at small electric fields is reported to delocalize the CO state, causing an insulator-metal transition. The light-induced insulator-metal transition in $Pr_{0.7}Ca_{0.3}MnO_3$ appears to generate a localized conduction path, although the bulk of the sample is insulating. A recent study of the electric-field induced effects in thin films of several charge-ordered rare earth manganites including $Nd_{0.5}Ca_{0.5}MnO_3$ and $Pr_{0.7}Ca_{0.3}MnO_3$, shows that very small dc currents (fields) destroy the CO state and give rise to insulator–metal transitions [33]. The current–voltage characteristics are nonohmic and show hysteresis. The I–M transition temperature decreases with increasing current (Fig. 16). The hysteretic I–M transition in Fig. 17 is specially noteworthy, in that there is a reproducible memory effect in the cooling and heating cycles. The current-induced I–M transition occurs even in $Y_{0.5}Ca_{0.5}MnO_3$, which is

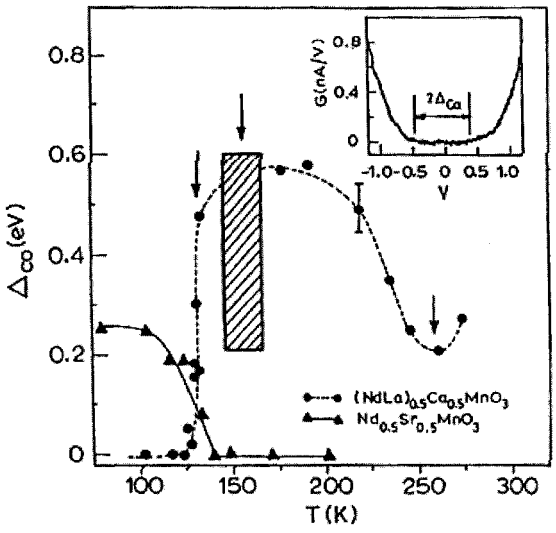

Fig. 15. Temperature variation of the CO gap in $Nd_{0.5}Sr_{0.5}MnO_3$ (Triangles) and in $Nd_{0.25}La_{0.25}Ca_{0.5}MnO_3$ (circles). Shaded area is the mixed phase (CO–FM) region where a first order transition occurs. Inset shows a typical conductance curve [32]

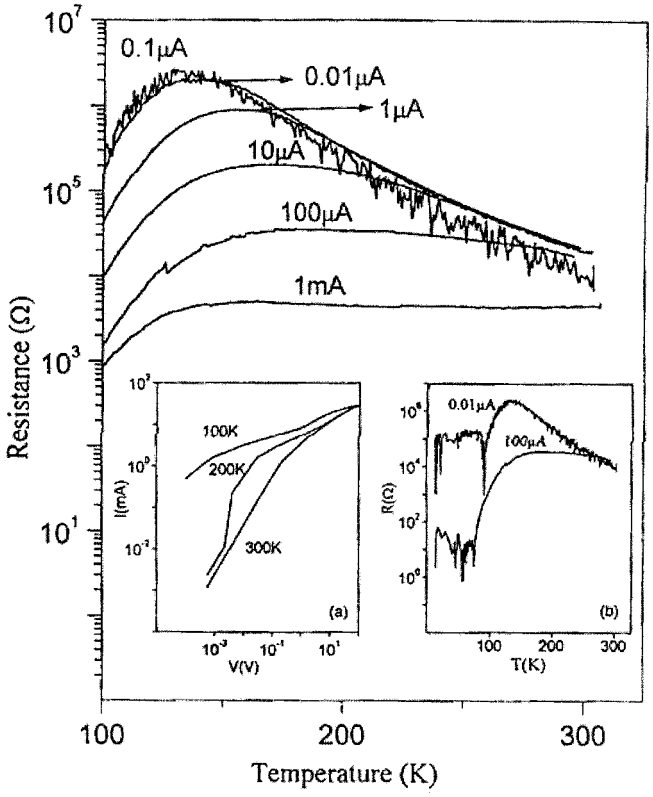

Fig. 16. Electric current-induced insulator-metal transition in $Pr_{0.7}Ca_{0.3}MnO_3$ films deposited on Si(100) at different values of the current. Inset (a) shows I–V curves at different temperatures. Inset (b) shows resistance oscillations at low temperatures (from Parashar et al., to be published)

not affected by large magnetic fields. Furthermore, there is no need for prior laser irradiation to observe the current-induced I–M transitions. It is proposed that electric fields cause depinning of the randomly pinned charge solid. There appears to be a threshold field in the CO regime beyond which nonlinear conduction sets in along with a large broad-band conductivity noise. Threshold-dependent conduction disappears around T_{CO} suggesting that the CO state gets depinned at the onset of nonlinear conduction. It is interesting that at small currents or low magnetic fields, resistance oscillations occur because of temporal fluctuations between resistive states. The role of possible inhomogeneities or phase segregation in these materials giving rise to percolative conduction has to be considered.

In the electron-doped manganites, the situation is different, close to $CaMnO_3$ or to $SrMnO_3$ [34]. As stated above, for large A site cation, the electron-doped manganites, close to $SrMnO_3$, do not exhibit any CMR properties, nor ferromagnetism. Nevertheless, a metal to insulator transition is observed at low temperatures. This

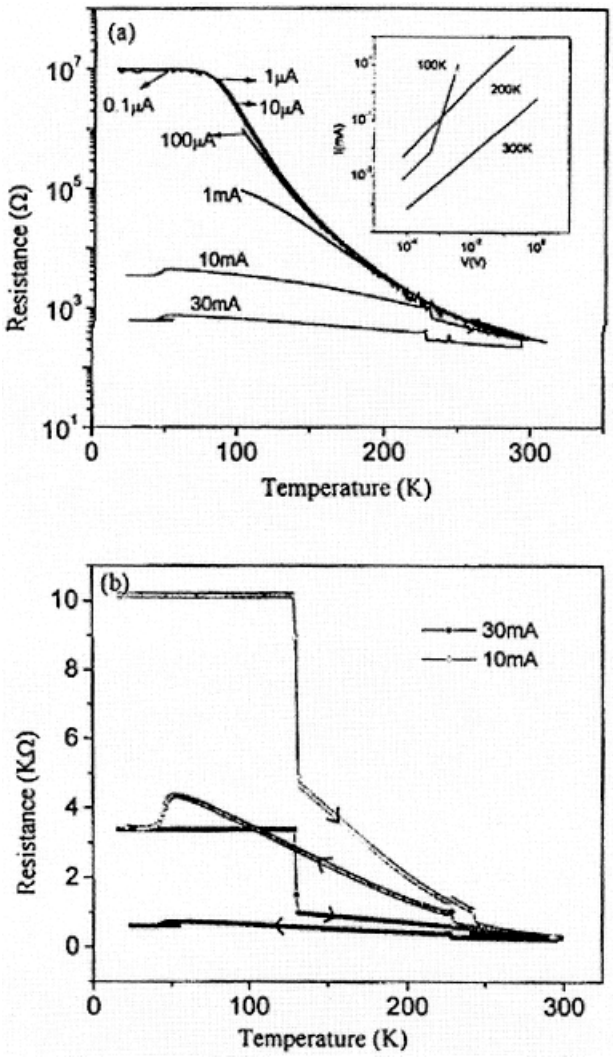

Fig. 17. (a) Temperature-variation of resistance of an oriented $Pr_{0.7}Ca_{0.3}MnO_3$ film deposited on $LaAlO_3(001)$ for different values of the current; (b) Resistance-temperature plots for two current values recorded over cooling and heating cycles showing memory effect. Inset in (a) show I–V curves at different temperatures (from Parashar et al., to be published)

is illustrated for $Sr_{0.85}Pr_{0.15}MnO_3$ (Fig. 18) which has an $R(T)$ curve similar to that observed for $Ca_{0.85}Sm_{0.15}MnO_3$ (Fig. 2a) but with a much higher transition temperature (260 K instead of 110 K). More importantly, this resistive transition is also correlated to a magnetic and structural transition. One indeed observes a transition from a cubic (Pm3m) symmetry ($a \sim a_p$) in the PMI state to the orthorhombic 14/mcm symmetry ($a \sim a_p\sqrt{2}$, $b \sim 2a_p$, $c \sim a_p\sqrt{2}$) in the C-type antiferromagnetic phase, as T decreases below 260 K.

For a smaller size of the A site cation, close to $CaMnO_3$, the appearance of CMR, i. e. the resistive transition close to 110 K and the magnetic peak at this temperature (Fig. 2), is related to a structural transition. This is shown for $Sm_{0.15}Ca_{0.85}MnO_3$ [34]

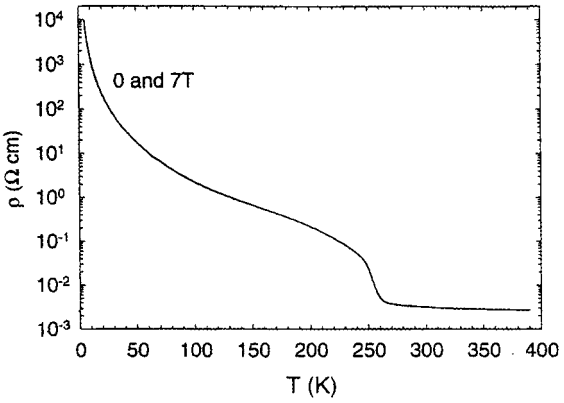

Fig. 18. Evolution of the dependence of resistivity on temperature for the electron-doped manganite $Sr_{0.85}Pr_{0.15}MnO_3$, under 0 and 7 T

for which a transition from the orthorhombic Pnma symmetry ($a\ a_p\sqrt{2}$, $b \sim 2a_p$, $c \sim a_p\sqrt{2}$) in the PM state to the monoclinic $P2_1/m$ symmetry with similar parameters in the C-type AFM state is observed at 110 K. Note that, although both, low temperature forms of "$Sr_{0.85}$" and "$Ca_{0.85}$" phases exhibit a C-type AFM behavior, they differ by the tilt arrangement of their octahedra (I4/mcm and $P2_1/m$ respectively). This is certainly correlated to their different magnetotransport properties, CMR being only obtained for $Ca_{0.85}Sm_{0.15}MnO_3$. In the small A cations system such as $Sm_{1-x}Ca_xMnO_3$ [35], it is remarkable that charge-ordering appears as x decreases. In the latter system, electron microscopy shows indeed the appearance of short range charge-ordering for $x = 0.80$. For lower x values, $0.80 \leq x \leq 0.75$, the low temperature ED patterns observed at 92 K show the presence of extra reflections with respect to the basic reflections of the room temperature Pnma structure. Charge-ordering phenomena take place along $\vec{a}$ leading to a supercell with the following parameters "$a \sim 1/q\ a_p\sqrt{2}$, $b \sim 2a_p$, $c \sim a_p\sqrt{2}$". In this supercell, q characterizes the commensurate or incommensurate nature of charge-ordering and is found roughly equal to the Mn^{3+} content, i. e. $q \sim 1 - x$. Thus, for $x = 3/4$, $2/3$ and $1/2$ the [010] patterns registered at 92 K (Fig. 19a, b, c) show a commensurate superstructure with a quadrupling ($q = 1/4$), a tripling ($q = 1/3$) and a doubling ($q = 1/2$) of the a parameter respectively. In contrast, for intermediate x values, the structure is incommensurate, as shown for instance for $x = 0.55$ (Fig. 20) for which $q \cong 0.43$ at 92 K. High resolution lattice images recorded at 92 K show a system of fringes spaced by 22 Å for $x = 0.75$ (Fig. 12a), 16.5 Å for $x = 0.66$ (Fig. 19b) and 11 Å for 0.50 (Fig. 19c), confirming the a parameter $4a_p\sqrt{2}$, $3a_p\sqrt{2}$, and $2a_p\sqrt{2}$ respectively. As for $La_{1-x}Ca_xMnO_3$ [18], these observations suggest that the various superstructures involve the alternation along $\vec{a}$ of one Mn^{3+} stripe with n Mn^{4+} stripes (Fig. 21), but does not bring the direct proof of the existence of such stripes, contrary to what is written in many papers. For intermediate x values, i. e. nonintegral $1/q$ values, the distribution of the stripes is then incommensurate. The evolution of the q value against T for each x composition (Fig. 22) clearly shows the rather abrupt transition from the Pnma room temperature structure to the charge-ordered one. It is remarkable that this structural transition coincides with the peak observed on the $M(T)$ curves of all these oxides.

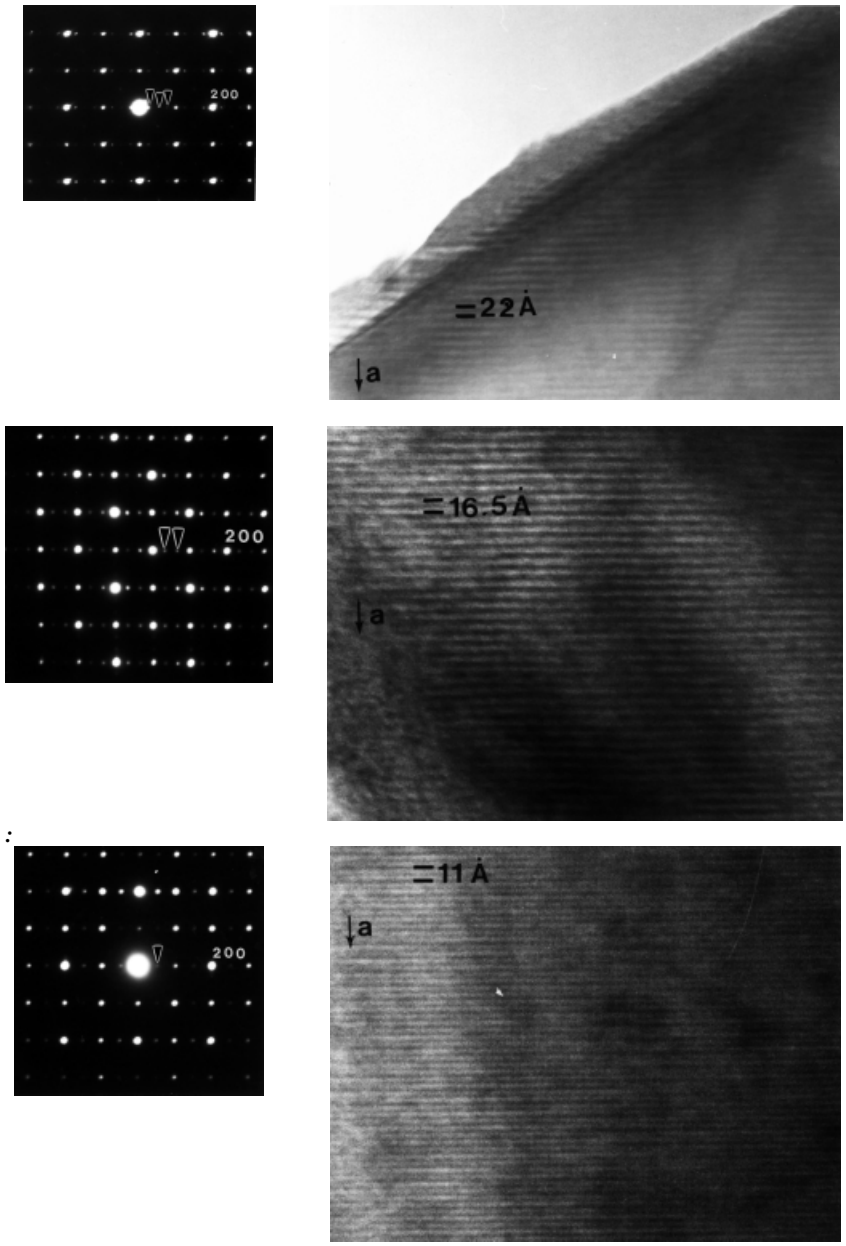

Fig. 19. [010] ED patterns and [010] lattice images recorded at 92 K for (a) $x = 0.75$ (b) $x = 0.66$ and (c) $x = 0.50$ of the $Sm_{1-x}Ca_xMnO_3$ manganites

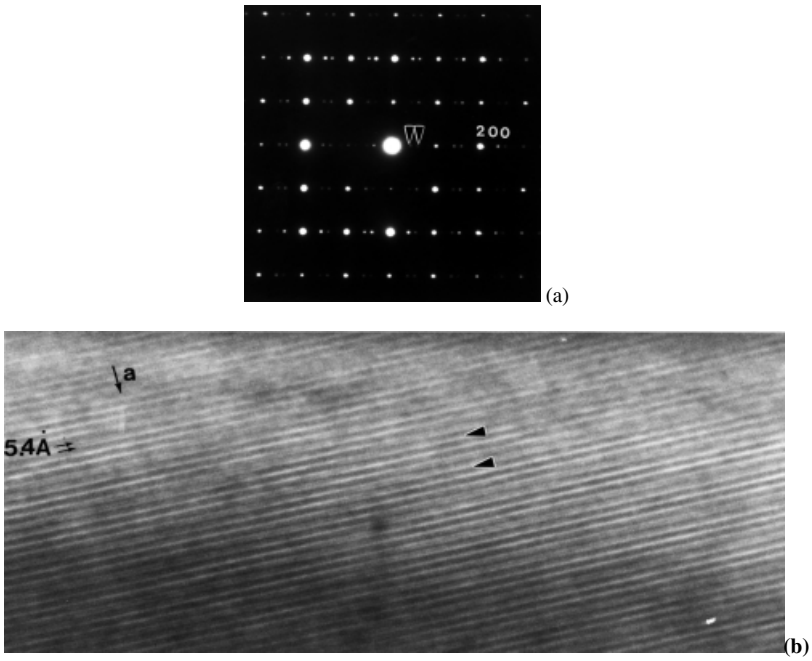

Fig. 20. [010] ED pattern (a) corresponding to long-range ordering (b) in $Sm_{0.45}Ca_{0.55}MnO_3$ ($x = 0.55$)

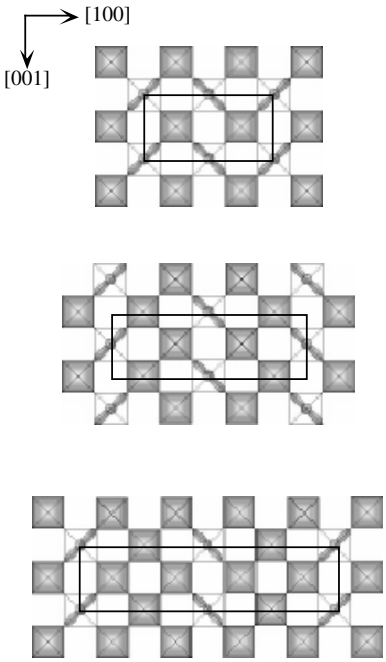

Fig. 21. Structural model showing the ordering between the Mn^{3+} octahedra (white) and the Mn^{4+} octahedra (gray) in the form of stripes parallel to [001]. From the top to the bottom 1:1, 1:2 and 1:3 Mn^{3+}:Mn^{4+} ordering

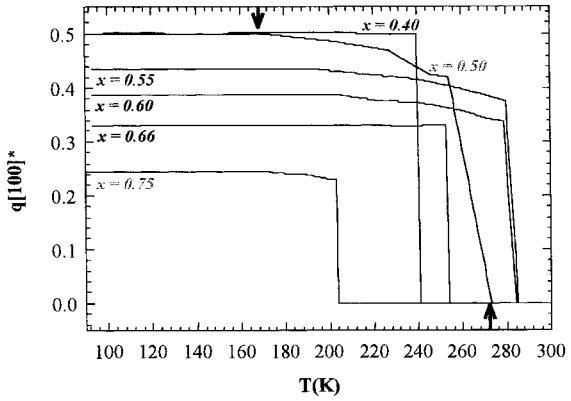

Fig. 22. Evolution of the dependence of the modulation vector q on T for $Sm_{1-x}Ca_xMnO_3$ manganites with $0.40 \leq x \leq 0.85$

The behavior of the half doped manganites discussed earlier is clearly more complex. For small A-site cations a transition to a charge-ordered state by decreasing temperature is generally observed for $Ln_{0.5}Ca_{0.5}MnO_3$ manganites. This is illustrated by $Nd_{0.5}Sr_{0.5}MnO_3$ and $Pr_{0.5}Sr_{0.5}MnO_3$. Both manganites exhibit similar PMI–FMM–AFMI transitions at decreasing temperature. Nevertheless these oxides exhibit significant differences in their structural transition. The AFMI low temperature phase of $Nd_{0.5}Sr_{0.5}MnO_3$ is charge-ordered and belongs to the CE-type whereas the AFMI phase of $Pr_{0.5}Sr_{0.5}MnO_3$ belongs to the A-type and no charge-ordering is observed.

9.7 Effect of Mn-site Doping

The substitution of divalent, trivalent or tetravalent elements for manganese (M = Al, Ga, In, Ti, Fe, Sn, Mg) in CMR hole doped manganites such as $Pr_{0.7}Ca_{0.2}Sr_{0.1}MnO_3$ [36] decreases T_C but increases significantly the magnetoresistance. In contrast, similar substitutions in $Pr_{0.5}Sr_{0.5}MnO_3$ do not enhance significantly the magnetoresistance. The most spectacular effect concerns the doping of the Mn sites with chromium, cobalt or nickel [37]. This is illustrated by the $R(T)$ curves (Fig. 23a) and $M(T)$ curves (Fig. 23b) of the series $Pr_{0.5}Ca_{0.5}Mn_{1-x}Cr_xO_3$ which show that chromium doping not only destroys charge-ordering but induces an insulator to metal transition and ferromagnetism as T decreases. This behavior is different from that observed for other doped manganites such as $Pr_{0.5}Ca_{0.5}Mn_{1-x}M_xO_3$ with M = Fe, Al, Ga, Ti, that remain insulator whatever M. Another remarkable feature concerns the transition temperature T_{IM} which increases with the chromium content (Fig. 23a). The similar effect is observed for Co- and Ni-doped manganites. This transition from an insulator to a ferromagnetic metal suggests that the so doped samples exhibit colossal magnetoresistance properties. The induced CMR effect is indeed spectacular with resistance ratio at 60 K ranging from 3×10^4 for Cr-doped phase to 3×10^6 for Co-doped manganites.

The possibility to induce MI transition in small A-site cation manganites by doping with Cr, Co, or Ni has been extended to different series of $Ln_{0.5}Ca_{0.5}Mn_{1-x}M_xO_3$.

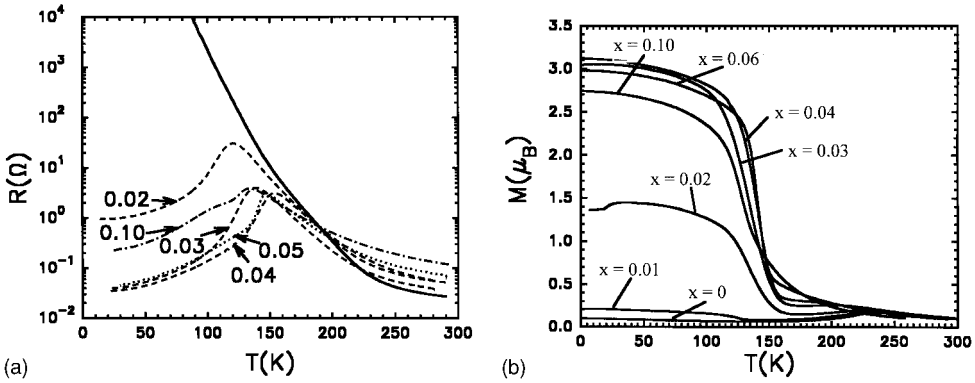

Fig. 23. Temperature-dependence of the resistance (a) and of the magnetization (b) for the chromium doped manganites $Pr_{0.5}Ca_{0.5}Mn_{1-x}Cr_xO_3$

Chromium has been found to be the most efficient cation to induce the MI transition. This is illustrated by comparing the saturated magnetization at 5 K for different doping elements (Fig. 24). It can be seen that the highest magnetization values are obtained for Cr-doping and moreover the chromium effect is not limited to a narrow composition range, in contrast to cobalt or nickel. Finally, the investigation of the A site size effect in the Cr-doped manganites $Ln_{0.5}Ca_{0.5}Mn_{1-x}Cr_xO_3$ shows that the doping with chromium pushes down the $\langle r_A \rangle$ limit for the appearance of the MI transition and consequently for the appearance of CMR properties. This is illustrated on the $T_{MI}(\langle r_A \rangle)$ diagram (Fig. 25) for these compounds: in the undoped materials the MI transition and consequently the CMR effect cannot be obtained for $\langle r_A \rangle$ smaller than 1.19 Å, whereas by Cr-doping these effects can be obtained for significantly smaller $\langle r_A \rangle$ values down to 1.15 Å. These results show that Cr not only destroys charge-ordering but certainly participates to double exchange mechanism, i. e. is ferromagnetically coupled to its manganese neighbors so that charge-delocalization occurs.

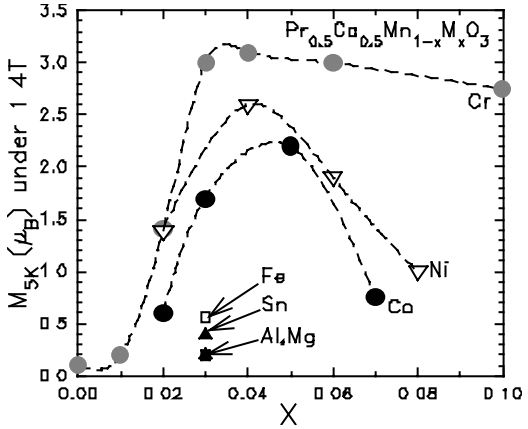

Fig. 24. Dependence of the magnetization at 5 K registered under 1.4 T on the doping level x for the series $Pr_{0.5}Ca_{0.5}Mn_{1-x}M_xO_3$ with M = Cr, Ni, Co, Fe, Sn, Al Mg

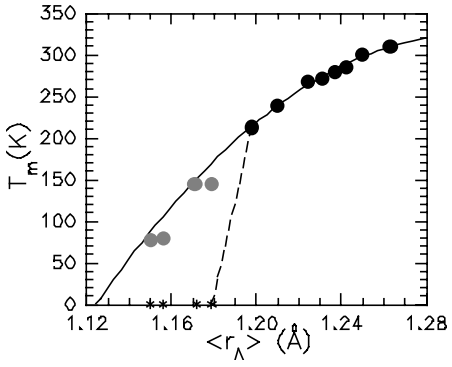

Fig. 25. Evolution of the dependence of the metal-insulator transition temperature TMI on $\langle r_A \rangle$ for the undoped $Ln_{0.5}Ca_{0.5}MnO_3$ manganites (full circles) and the chromium doped $Ln_{0.5}Ca_{0.5}Mn_{1-x}Cr_xMnO_3$ (open circles). Stars represent the undoped phases which are insulating

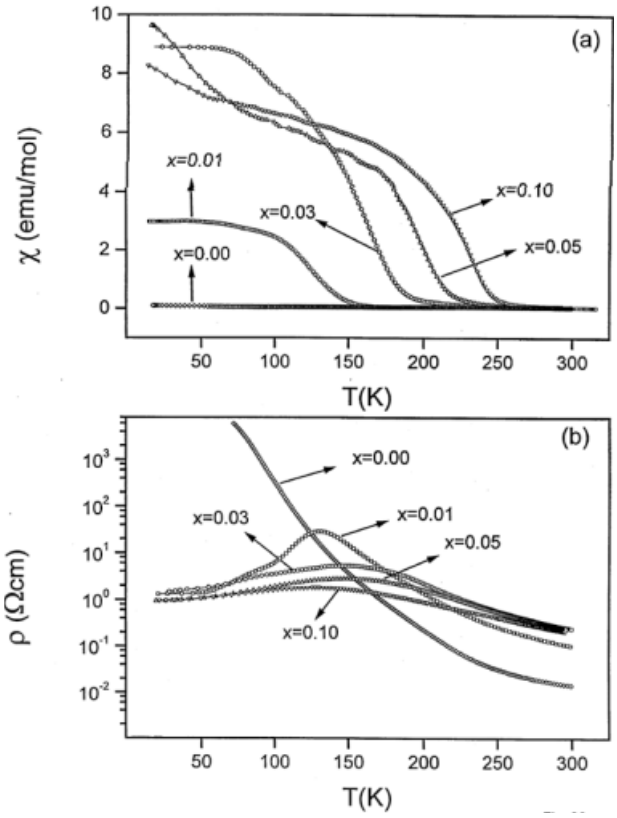

Fig. 26. Temperature variation of the (a) magnetic susceptibility and (b) resistivity of $Nd_{0.5}Ca_{0.5}Mn_{1-x}Ru_xO_3$

Besides those doping elements, a recent study of the substitution of Mn by Ru in $Nd_{0.5}Ca_{0.5}MnO_3$ [38] shows that ruthenium is very effective. Doping with this element not only destroys charge-ordering but also renders this material ferromagnetic with T_C increasing with Ru content; the material also shows an insulator-metal transition (Fig. 26). The effectiveness of Ru^{4+} (t_{2g}^4) is because it will be surrounded by Mn^{3+} ($t_{2g}^3 e_g^1$), promoting electron transfer.

References

[1] R.M. Kusters et al., *Physica B* **155**, *362* (**1989**).

[2] Some examples of early studies: S. Jin et al., *Science 264*, 413 (**1994**); K. Chahara et al., *Appl. Phys. Lett. 63* (**1993**); R. von Helmot, *Phys. Rev. Lett. 71*, 2331 (**1993**); M. Mc Cormack et al., *Appl. Phys. Lett. 64*, 3045 (**1994**); R. Mahendiran et al., *Solid State Commun. 94*, 515 (**1995**); R. Mahesha et al., *J. Solid State Chem. 114*, 297 (**1995**); ibid *120*, 204 (**1995**); J. Inone and S. Maekawa, *Phys. Rev. Lett. 74*, 3407 (**1995**); Y. Tokura et al., *J. Phys. Soc. Jap. 63*, 3931 (**1994**); H. Kuwaha et al., *Science 270*, 961 (**1995**); A. Urushibara et al., *Phys. Rev. B 51*, 14103 (**1995**); Y. Tomioka et al., *Phys. Rev. Lett. 74*, 5108 (**1995**); V. Caignaert et al. *Solid State Commun. 95*, 357 (**1995**); A. Maignana et al., *J. Mater Chem. 5*, 1089 (**1995**) and *Solid State Commun. 96*, 623 (**1995**); B. Raveaua et al., *J. Solid State Chem. 117*, 424 (**1995**); C.N.R. Rao et al., *Chem. Mater. 8*, 2421 (**1996**); C.N.R. Rao and A. Arulraj. *Curr. Opinion Solid State Mater Sci. 3*, 23 (**1998**).

[3] *Colossal and Magnetoresistance, Charge-ordering and Related Properties of Manganese Oxides*, C.N.R. Rao and B. Raveau (eds.) World Scientific 1998; Y. Tokura et al., *J. Appl. Phys. 79*, 5288 (**1996**).

[4] C. Zener, *Phys. Rev. 82*, 403 (**1951**); P.G. de Gennes, *Phys. Rev. 118*, 141 (**1960**); J.B. Goodenough, *Phys. Rev. 100*, 564 (**1995**).

[5] Murakami et al., *Phys. Rev. B 55*, 1 (**1997**); Troyanchuk et al., *J. Solid State Chem. 131*, 144 (**1997**); C. Martina et al., *J. Solid State Chem. 134*, 198 (**1997**); A. Maignana et al., *Chem. Mater. 10*, 950 (**1998**); B. Raveau et al., *Chem. Mater. 10*, 950 (**1998**); B. Raveau[a] et al., *J. Superconductivity 12* (**1999**).

[6] L.M. Rodriguez-Martinez and J.P. Attfield, *Phys. Rev. B 54*, R15622 (**1996**).

[7] A. Maignan et al., *Z. für Physik B 99*, 305 (**1996**); J. Hejtmanek et al., *Phys. Rev. B 54*, 11947 (**1996**); F. Millange et al., *Z. für Physik B 101*, 169 (**1996**); J. Fontcuberta et al., *Phys. Rev. Lett. 76*, 1122 (**1996**); P.G. Radaelli et al., *J. Solid State Chem. 122*, 444 (**1996**); H.Y. Hwang et al., *Phys. Rev. Lett. 75*, 914 (**1995**)a; R. Mahendiran et al., *Phys. Rev. B 53*, 12160 (**1996**); A. Maignan et al., *J. Appl. Phys. 79*, 7891 (**1996**); R. Mahesh et al., *J. Solid State Chem., 114*, 297 (**1995**).

[8] A.J. Millis et al., *Phys. Rev. Lett. 74*, 5144 (**1995**).

[9] C. Martin et al., *Phys. Rev. B*, *60*, 12191 (**1999**); A. Maignan et al., *Phys. Rev. B* **1999**, accepted.

[10] J. Wolfman et al., *J. Solid State Chem. 123*, 413 (**1996**) and *J. Magn. Magn. Mater. 159*, L299 (**1996**); F. Damay et al., *J. Appl. Phys. 81*, 1372 (**1997**).

[11] F. Damay et al., *J. Appl. Phys.*, *82*, 6181 (**1997**).

[12] V. Caignaert et al., C.R. *Acad. Sc. 321*, 515 (**1995**) and *J. Magn. Magn. Mater. 153*, L260 (**1996**); D.N. Argyriou et al., *Phys. Rev. Lett. 76*, 3826 (**1996**).

[13] P.G. Radaelli et al., *Phys. Rev. Lett. 75*, 4488 (**1995**); A.P. Ramirez et al., *Phys. Rev. B 76*, 3188 (**1996**); M.R. Ibarra et al., *Phys. Rev. B 56*, 8252 (**1997**).

[14] K. Liu et al., *Phys. Rev. B 54*, 3007 (**1996**); O. Richard et al., *Phys. Rev. B* accepted.

[15] Z. Jirak et al., *J. Magn. Magn. Mater. 15*, 519 (**1980**); ibid 53, 153 (**1985**).

[16] C.N.R. Rao et al., *Chem. Mater. 10*, 2714 (**1998**).

[17] E.O. Wollan and W.C. Koehler, *Phys. Rev. 100*, 545 (**1955**).

[18] Z. Jirak et al., *J. Magn. Magn. Mater. 53*, 153 (**1985**).

[19] Y. Tomioka et al., *Phys. Rev. B 53*, 1689 (**1996**); M.R. Lees et al., *Phys. Rev. B 52*, 14303 (**1995**).

[20] H. Kuwahara et al., *Phys. Rev. B 56*, 9386 (**1997**).

[21] H. Kawano et al., *Phys. Rev. Lett. 78*, 4253 (**1997**).

[22] J.B. Goodenough, *Phys. Rev. 100*, 564 (**1955**).
[23] S. Mori et al., *Phys. Rev. Lett. 81*, 3972 (**1998**).
[24] R. Kajimoto et al., *Phys. Rev. B 58*, R11837 (**1998**).
[25] A. Anane et al., *Phys. Rev. B 59*, 77 (**1999**).
[26] M. Uehara et al., *Nature 399*, 560 (**1999**).
[27] A. Biswas et al., *J. Phys: Condens. Matter 9*, L355 (**1997**).
[28] R. Mahendiran et al., *Phys. Rev. Lett. 82*, 2191 (**1999**).
[29] P.M. Woodward et al., *Chem. Mater. 11*, 3528 (**1999**).
[30] P.M. Woodward et al., *Chem. Mater. 10*, 3652 (**1998**).
[31] A. Arulraj et al., *J. Phys: Condens. Matter 10*, 8497 (**1998**).
[32] A. Arulraj et al., *Phys. Rev. B 57*, R8115 (**1998**).
[33] V. Ponnambalam et al., *Appl. Phys. Lett. 74*, 206 (**1999**); A. Guha et al., *Appl. Phys. Lett. 75*, 3391 (**1999**).
[34] C. Martin et al., *J. Magn. Magn. Mater.*, *205*, 184 (**1999**).
[35] M.Hervieu et al., *Eur. J. Phys. B*, *8*, 31 (**1999**).
[36] A. Maignan et al., *Z. Physik B 102*, 19 (**1997**); ibid 102, 209 (**1997**); C. Martin et al., *J. Mater. Chem. 6*, 1245 (**1996**); F. Damay et al., *J. Solid State Chem. 124*, 385 (**1996**); *J. Magn Magn. Mater.*, *183*, 143 (**1998**).
[37] B. Raveau et al., *J. Solid State Chem. 130*, 162 (**1997**); A Maignan et al., *Mater. Res. Bull. 32*, 965 (**1997**); P.V. Vanitha et al., *Solid State Commun. 109*, 135 (**1999**).
[38] P.V. Vanitha et al., *C.R. Acad. Sc.*, *2*, IIc, 595 (**1999**); B. Raveau et al., *J. Solid State Chem.*, *151*, 330 (**2000**).

Magnetism: Molecules to Materials I: Models and Experiments.
Edited by Joel S. Miller and Marc Drillon

ISBNs: 3-527-29772-3 (Hardback); 3-527-60084-1 (Electronic)

10 Neutron Scattering and Spin Densities in Free Radicals

Jacques Schweizer and Eric Ressouche

10.1 Introduction

Neutron scattering has progressed over the last fifty years to become an invaluable tool to probe experimentally condensed matter. As far as magnetism is concerned, this technique has been recognized from the early days as unique. The most widespread use of neutron diffraction is the determination of magnetic structures, that is the determination of the directions in which moments point in a magnetically ordered material. In such studies, the distribution of the magnetization density $\boldsymbol{M}(\boldsymbol{r})$ around magnetic atoms is usually taken from ab-initio calculations for free ions in the appropriate configuration. On a sub-atomic scale, neutron diffraction also permits to go beyond this simple approximation and to investigate the distributions themselves. These distributions of magnetization density contain precious information on the electronic structure of the sample. The nature of the magnetic orbitals, the interactions with neighboring molecules in the solid, effects such as chemical bonding, spin delocalization or spin polarization strongly affect this function and can thus be revealed experimentally. Furthermore, these distributions can be directly related to the wave functions calculated from first principles and can therefore provide a stringent test for theory.

Such studies require very precise measurements of the so-called magnetic structure factors, and therefore the use of polarized neutron diffraction (PND). This technique has been mostly used for systems in which the magnetization is due to d or f electrons in the unfilled shells of transition metals, rare earths or actinides. More recently, it has been successfully applied to molecular compounds, where the role played by 2p electrons is crucial. In this chapter, a review of the results obtained in this field is made after an introduction to the experimental technique, to the methods used for the data analysis and a presentation of the different types of theoretical calculations.

10.2 Measurement and Reconstruction of Magnetization Distributions

10.2.1 Experimental Technique

The classical polarized neutron diffraction technique is a very sensitive tool to probe magnetization distributions. This technique applies to single crystals which are mag-

netized by an external field and scatter a beam of polarized neutrons, the polarization of the beam being either parallel to the magnetic field or reversed. Neutrons interact in the sample both with nuclei and magnetic moments. When the periodicity of the magnetic and chemical structures are the same, magnetic and nuclear scattering occur at the same points in reciprocal space corresponding to the Bragg peaks and interfere. The intensity scattered in such a mixed reflection is:

$$I(\boldsymbol{K}) = |F_N(\boldsymbol{K})|^2 + \boldsymbol{P} \cdot \boldsymbol{Q}(\boldsymbol{K}) F_N^*(\boldsymbol{K}) + \boldsymbol{P} \cdot \boldsymbol{Q}^*(\boldsymbol{K}) F_N(\boldsymbol{K}) + |\boldsymbol{Q}(\boldsymbol{K})|^2 \tag{1}$$

In this equation, $\boldsymbol{P}$ is the polarization of the incident beam, $\boldsymbol{K}$ is the scattering vector, $F_N(\boldsymbol{K})$ is the nuclear structure factor and $\boldsymbol{Q}(\boldsymbol{K})$ is the magnetic interaction vector. This latter quantity, also written as $\boldsymbol{F}_M^{\perp}(\boldsymbol{K})$, is the projection of the magnetic structure factor $\boldsymbol{F_M}(\boldsymbol{K})$ on to the plane perpendicular to the scattering vector $\boldsymbol{K}$. It should be noted that both $\boldsymbol{Q}(\boldsymbol{K})$ and $\boldsymbol{F_M}(\boldsymbol{K})$ are complex vector quantities, whereas $F_N(\boldsymbol{K})$ is a scalar (also complex in the general case). All these quantities are real in the case of centric structures. The nuclear structure factor is defined for a scattering vector $\boldsymbol{K}$ through:

$$F_N(\boldsymbol{K}) = \sum_j b_j \, \mathrm{e}^{i\boldsymbol{K}\cdot\boldsymbol{r}_j} \, \mathrm{e}^{-W_j} \tag{2}$$

where the sum is performed over the j atoms contained in the unit cell, b_j being the nuclear scattering length characteristic of the chemical element j (expressed in 10^{-12} cm), r_j the position within the unit cell of the atom and W_j the thermal Debye–Waller factor.

Magnetic structure factors are the Fourier components of the magnetization density $\boldsymbol{M}(\boldsymbol{r})$ and are defined by:

$$\boldsymbol{F_M}(\boldsymbol{K}) = \int_{cell} \boldsymbol{M}(\boldsymbol{r}) \, \mathrm{e}^{i\boldsymbol{K}\cdot\boldsymbol{r}} \mathrm{d}^3\boldsymbol{r} \tag{3}$$

The interference term between nuclear and magnetic scattering in the expression of the intensity is at the origin of the high sensitivity of polarized neutrons to weak magnetic signal. In practice, the ratios, R, between the intensities for the two polarization states, + and −, of the incident beam are investigated systematically for a set of $\boldsymbol{K}$ vectors corresponding to Bragg reflections. These ratios, called "flipping ratios", are given by:

$$R(\boldsymbol{K}) = \frac{|F_N(\boldsymbol{K})|^2 + \boldsymbol{P} \cdot \boldsymbol{Q}(\boldsymbol{K}) F_N^*(\boldsymbol{K}) + \boldsymbol{P} \cdot \boldsymbol{Q}^*(\boldsymbol{K}) F_N(\boldsymbol{K}) + |\boldsymbol{Q}(\boldsymbol{K})|^2}{|F_N(\boldsymbol{K})|^2 - \boldsymbol{P} \cdot \boldsymbol{Q}(\boldsymbol{K}) F_N^*(\boldsymbol{K}) - \boldsymbol{P} \cdot \boldsymbol{Q}^*(\boldsymbol{K}) F_N(\boldsymbol{K}) + |\boldsymbol{Q}(\boldsymbol{K})|^2} \tag{4}$$

where $\boldsymbol{P}$ is the polarization of the incident beam. When all the quantities are real (centric structures) and if the magnetization in the sample is aligned along the vertical magnetic field that defines the quantization axis (z axis), this equation simplifies to:

$$R(\boldsymbol{K}) = \frac{1 + 2P\gamma \, \sin^2\alpha + \gamma^2 \, \sin^2\alpha}{1 - 2P\gamma \, \sin^2\alpha + \gamma^2 \, \sin^2\alpha} \tag{5}$$

where α is the angle between the vertical axis and the scattering vector $\boldsymbol{K}$, and with:

$$\gamma = \frac{F_{Mz}(\boldsymbol{K})}{F_N(\boldsymbol{K})} \tag{6}$$

For a weak magnetic signal ($\gamma \ll 1$), Eq. 5 can be approximated to $R \approx 1 + 4(P \sin^2 \alpha)\gamma$. R varies linearly with γ whereas for an unpolarized beam ($P = 0$) the magnetic signal contributes as γ^2. The improvement is thus substantial and induced magnetic moments as small as 10^{-3} μ_B can be detected routinely. Moreover, in such centric cases, the experiment gives access both to the modulus and to the sign of the Fourier components of the magnetization density.

10.2.2 Methods of Analysis

To determine the shape of the magnetization density in real space from the measured Fourier coefficients, the inverse Fourier problem has to be solved. Several approaches exist, and belong to two main families: direct (model free) methods and parametrized models. This latter class requires the system to be well enough understood for a model to be proposed. On the contrary, direct methods use nothing but the experimental data, and are therefore a necessary step before any attempt to refine a model.

10.2.2.1 Model-free Methods: Fourier Inversion

Because the experiment gives (at least in centrosymmetric cases) the Fourier components of the magnetization density, the first idea to relate the data to the density in real space is to use the Fourier inversion:

$$\boldsymbol{M}(\boldsymbol{r}) = \frac{1}{V} \sum_{\boldsymbol{K}} \boldsymbol{F_M}(\boldsymbol{K})\, \mathrm{e}^{-i\boldsymbol{K}\cdot\boldsymbol{r}} \tag{7}$$

where V is the unit cell volume. This technique is very simple to operate and has been widely used in the past. However, the number of measured reflections is limited and all the Fourier coefficient which are not measured are considered as being equal to zero. This default, combined to the fact that no use is made of standard deviations of the observations, results in spurious spatial correlations which do not represent reality. This problem is particularly acute for molecular compounds, in which large cells of low symmetry are often encountered, resulting in a set of independent reflections completely prohibitive to be measured completely. The quality of the reconstructions performed under these conditions is thus generally very poor. Moreover, this technique is restricted to the centric structures only.

10.2.2.2 Model-free Methods: The Maxent Solution

A major breakthrough in the way of treating polarized neutron diffraction data has been reached with the maximum of entropy (Maxent) solution. This method,

based on Bayesian statistical techniques, was first applied to radio astronomy [1] and has been transposed to magnetization reconstructions from polarized neutron diffraction data by Papoular [2]. It essentially provides the least informative map consistent with the observations, taking into account their standard deviations.

Actually, given the limited number of data points (measurements) and given the experimental error bars, an infinite number of maps consistent with the experiment exists. The Maxent approach defines a probability for all these possible maps. This probability, or *posterior probability*, is the product of two quantities, namely the *likelihood* and the *prior*. The *likelihood* is directly related to the usual χ^2, that is the agreement with the observed data. The *prior* represents the intrinsic probability of the map, and can be expressed in terms of Boltzmann entropy. The "best map" is chosen in a way to maximize this entropy under the constraint to keep a good agreement with the data. The considerable advantage of this method relies on the fact that no assumptions are necessary about nonobserved Fourier coefficients. The quality of the obtained reconstructions, especially in the case of molecular compounds, is incomparably improved compared to the classical Fourier inversion and therefore can be used at a quantitative level. Another advantage arises from the fact that this approach has been extended to acentric structures [3], and can thus operate directly from the experimental flipping ratios.

10.2.2.3 Parametrized Model: Wave-function Approach

In the two next approaches, the spin density is developed according to a parametrized model, and this model is refined to fit the experimental data: the magnetic structure factors $\boldsymbol{F_M}(\boldsymbol{K})$ for the centric structures or the flipping ratios $R(\boldsymbol{K})$ for the acentric ones. Here, in the wave function approach, the spin density is defined as the square of atomic wave functions. At each magnetic site j, a Hartree–Fock type magnetic wave function $|\psi_j\rangle$ is constructed from atomic orbitals $|\phi_k\rangle$ according to:

$$|\psi_j\rangle = \sum_k \alpha_{jk} |\phi_k\rangle \tag{8}$$

To allow for both positive and negative values, the magnetization density is obtained by first squaring the atomic wave functions and only then a linear combination is made:

$$\boldsymbol{M}(\boldsymbol{r}) = \sum_{\text{atoms}} S_j \langle \psi_j \mid \psi_j \rangle \tag{9}$$

The atomic orbitals $|\phi_k\rangle$ are standard orbitals, with a Slater radial part and a spherical part built with the spherical harmonics functions Y_{lm}. The parameters of the model are the spin populations, s_j, at each magnetic sites, the coefficients, α_j, and the radial exponents of the Slater orbitals, $|\phi_k\rangle$. They are obtained by least-squares fit to the measured data.

10.2.2.4 Parametrized Model: Multipole Expansion

In this second parametrized model, more flexibility is introduced as the spin density is directly projected on to a basis set of Slater-type functions for the radial parts and spherical harmonic functions centered at the atomic positions for the angular parts [4], according to:

$$\boldsymbol{M}(\boldsymbol{r}) = \sum_{\text{atoms}} \sum_{\ell} R_{\ell}(\boldsymbol{r}) \sum_{m=-\ell}^{m=+\ell} P_{\ell m} y_{\ell m}(\hat{\boldsymbol{r}}) \tag{10}$$

where the Y_{lm} are now the real spherical harmonics. The parameters of the model are the populations P_{lm} (populations of the harmonic functions) and the radial exponents of the Slater functions, the starting values coming from free atoms or ions ab-initio calculations. All these parameters are obtained by least-squares fit to the measured data.

We emphasize the fact that these two last methods apply to acentric as well as centric structures.

10.2.3 Ab-initio Calculations of the Spin Density

Theoretical calculations are very often carried out in parallel with PND determination of the spin density because the comparison between experimental and theoretical distributions is of the highest importance. On the one hand, contrarily to the charge density which corresponds to a sum, the spin density represents a difference between the charge distribution of the two spin states $\rho_{+}(r)$ and $\rho_{-}(r)$. Therefore, comparing the theoretical map with the experimental one is a very severe test to judge the validity of the calculation method. On the other hand, as it is in general possible to perform several calculations with modified configurations of the molecule, the comparison allows to test different possible assumptions to explain some unexpected feature which appears in the experimental results.

There are two main families of ab-initio calculations. The first family, based on the Hartree-Fock approximation, calculates the multicoordinate molecular wave functions, expressed as Slater determinants of single particle atomic wave functions. The Hamiltonian is a sum of single particle Hamiltonians including kinetic energy, Coulomb attraction by the nucleus and Coulomb repulsion by the other electrons. To express this last term, one assumes that the electrons are distributed over their wave function. The calculation is processed self consistently. Each molecular wave function is occupied by two electrons, one with spin + and one with spin −. The unpaired electron occupies the SOMO (single occupied molecular orbital). In the restricted Hartree–Fock method (RHF), the orbital part of the wave functions of electrons of spin + and − are the same. Therefore, the spin density obtained by this method is automatically positive. In the unrestricted Hartree-Fock method (UHF), the spatial part of the wave functions of electrons of spin + and − may be different. The spin density thus obtained may be negative in some parts of the molecule. To go beyond the Hartree–Fock approximation, that is to take into account the correlations which exist between the electrons (the electrons do not stay unperturbed over their

wave function when another electron passes by) one may develop the multiparticle molecular wave functions on the basis of the Hartree–Fock molecular wave functions and optimize the different coefficients. The method is time consuming. According to the complexity of the development one has the Moller-Plessey [5] methods (MP2, MP3) or the full configuration interaction (full CI) [6].

The second family of electronic calculations, called the Density Functional Theory (DFT), is based on the Hohenberg–Kohn theorem [7] which states that the energy of an ensemble of electrons is a functional of the charge density only and that the fundamental state is the state which minimizes this functional. The method calculates directly the electron density instead of the wave functions, which simplifies the problem very much. The functional contains a kinematic term, a Coulomb term and an exchange–correlation term. However, the analytical expression of this last term cannot be derived in the general case. A first approximation is the local density approximation (LDA) [8] which assumes that the exchange-correlation term for electrons in a crystal has the same expression as for an homogeneous interacting electron gas. This approximation has been extended to magnetic systems (local spin density approximation or LSD) [9,10] by introducing a functional of two electronic densities $\rho_+(r)$ and $\rho_-(r)$, where the exchange-correlation term is the same as for an homogeneous interacting and partly polarized electron gas (Vosko–Wilk–Nusair functional [11]). Other approaches have been proposed for the exchange-correlation term, to go beyond this local approximation. One of them is the gradient method [12].

10.3 Spin Densities in Isolated Radicals

In conventional insulating magnetic materials, the magnetization density is the sum of contributions due to individual magnetic atoms, each of them being characteristic of a particular configuration. The magnetic moments are well localized around the atoms or ions, and the shape of the density corresponds to one particular atomic orbital. A small part of the density on the metal can be transferred on the ligands, but this fraction is generally weak and does not affect strongly the nature of the magnetic orbital.

In the case of magnetic molecular compounds, the situation is completely different. In the framework of elementary molecular orbital theory, the magnetism of a free radical is attributed to an unpaired electron described by the SOMO. This molecular orbital is built up from the individual atomic orbitals of the atoms constituting the molecule. It can happen that orbitals on different atomic sites strongly contribute to this SOMO, resulting in one unpaired electron strongly delocalized over the complete molecule. The spin is no longer restricted to one particular atom, but is spread over the whole molecule or over a part of the molecule. This property is often referred in the literature as "*spin delocalization*". To understand the role of these free radicals as chemical and magnetic ligands, the knowledge of their electronic structure, in particular the nature of the SOMO, is essential.

10.3.1 The Spin Delocalization Effect

A particularly interesting illustration of the spin delocalization is met in the nitroxide free radicals, where the spin density is a priori located on a group of two atoms: N and O. One of the first cases which was investigated by PND is the tempone radical (4-oxo-2,2,6,6-tetramethyl-1-piperidinyloxy) [13] (Fig. 1a). In the solid state, this compound crystallizes under three different forms: triclinic, orthorhombic, and hexagonal. The orthorhombic phase (space group $Pca2_1$) has been investigated by polarized neutrons. Magnetically, this compound remains paramagnetic down to very low temperatures (0.05 K) [14], with very small interactions with neighboring molecules. It is therefore representative of a well isolated radical.

The spin density, as determined experimentally, is mainly localized on the NO bond, as shown in the left part of Fig. 2, in a π^*-antibonding orbital, mainly built from the $2p_z$ atomic orbitals of the oxygen and of the nitrogen atoms. It is equally shared between these two atoms (0.40(2) μ_B on N, 0.36(2) μ_B on O). However, a non-negligible delocalization (21% of the total spin) is observed on the alkyl backbone, and represents the contribution of these atoms to the total magnetic molecular orbital. This delocalization concerns mainly the α-dimethyl groups directly connected to the nitrogen atom.

Another nitroxide spin density investigation is that of the indolinonic nitroxide radical (1,2-dihydro-2-methyl-2-phenyl-3*H*-indole-3-oxo-1-oxyl) [15]. This free radical is a stable compound where the nitroxide function is involved in conjugative interactions through the adjacent fused benzene ring. It crystallizes in the monoclinic space group $P2_1/c$. In this radical, the spin delocalization effect has been found, using a multipolar expansion refinement, much larger than for the tempone, as shown in Fig. 3 which represents the projection of the reconstructed spin density on to the principal plane of the molecule. The spin transferred from NO to the other atoms amounts to 42% of the total spin, 24% being associated to the carboxide group. Positive and negative contributions are carried out by the carbon atoms of the benzene ring. In contrast to the case of tempone, and certainly resulting from

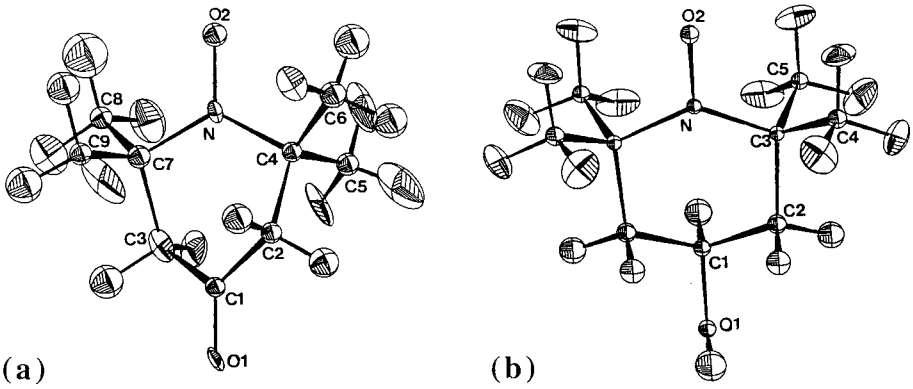

Fig. 1. View of the two closely related molecules (a) tempone and (b) tempol

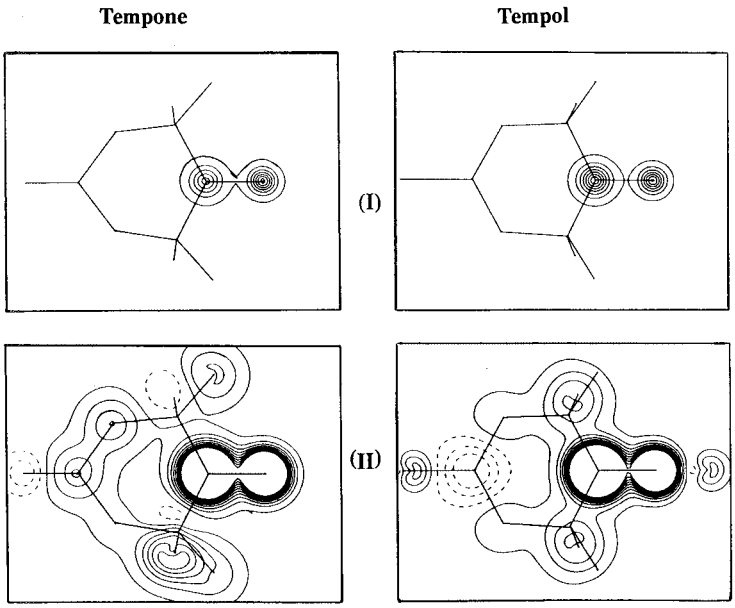

Fig. 2. Spin density projections along the π-direction for tempone and tempol. The spin densities have been normalized to 1 μ_B per molecule. Equidistance between the contours: high level plots (I) 0.20 μ_B Å^{-2}, low level plots (II) 0.01 μ_B Å^{-2}

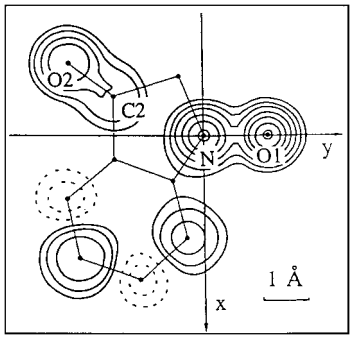

Fig. 3. Projection of the spin density on to the plane of the principal ring of indolinonic nitroxide. Equidistance of 0.005 μ_B Å^{-2} between the positive contours and 0.0025 μ_B Å^{-2} between the negative contours

this strong delocalization, the spin localized on the nitroxide function is not equally shared between the N and the O atoms, 59% of it being on the oxygen. The 2p orbitals on the nitrogen and oxygen atoms are almost perpendicular to the N–O bond as expected.

10.3.2 The Spin Polarization Effect

Spin delocalization is easily understood in terms of molecular orbitals. The SOMO may account for spin density over several atoms in the molecule. But, at the first level at least of the Hartree–Fock theory (RHF), this spin density should be positive everywhere, which means parallel to the applied field. A spin density with an opposed sign, when it exists, should relate to a further step in theory. Such a negative density is often encountered; it is called spin polarization.

The phenyl nitronyl nitroxide compound (NitPh; 2-phenyl-4,4,5,5-tetramethyl-4,5-dihydro-1*H*-imidazol-1-oxyl 3-oxide), is an interesting example to illustrate both the spin delocalization and the spin polarization effect. In the recent years, nitronyl nitroxide free radicals have played a key role in the engineering of molecular-based magnetic materials: they are stable, capable of being handled under ordinary conditions, and they carry a spin $S = 1/2$. The phenyl derivative crystallizes in the monoclinic space group $P2_1/c$ with two molecules per asymmetric unit, and remains paramagnetic down to very low temperature, with very little interactions between neighboring molecules. The knowledge of the ground state of this isolated radical was a necessary step to understand the properties of the interacting derivatives, that will be treated in the next section.

Fig. 4 shows the projection of the Maxent reconstructed spin density from polarized neutron diffraction data [16] on to the molecular O–N–C–N–O plane of one of the two molecules and Fig. 5 its projection on to the π plane. These two projections show that most of the spin density is carried out by the two nitrogen and the two oxygen atoms. They also confirm the equivalence of the two NO groups within the molecule and even suggest the π-shape of the magnetic molecular orbital (Fig. 5), despite the rather low experimental resolution available. It is indeed important to stress that such a Maxent reconstruction is model-free and does not include any assumption concerning the shape of the magnetic orbital. Maxent also shows that the spin density is evenly shared by the N and O atoms within each NO group. No spin density is detected on the carbon skeleton, but this cannot be considered as a definitive proof of the absence of such contributions, since the method is well known to smooth out small details that are just beside strong contributions, as long as this is permitted by the data.

To obtain individual spin populations and to extract some information on the spin density of the molecular skeleton (including the phenyl ring), a magnetic wave-

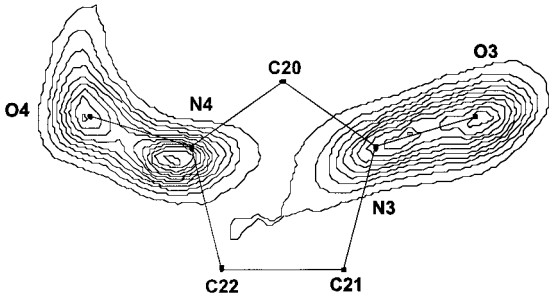

Fig. 4. Projection of the Maxent reconstructed spin density of NitPh on to the nitroxide mean plane. Contour step 0.02 μ_B Å^{-2}

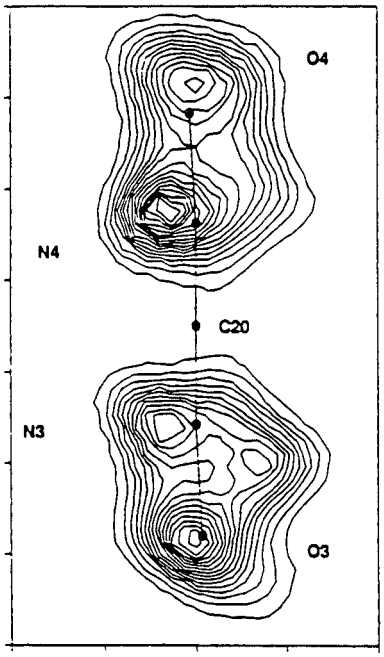

Fig. 5. Projection of the Maxent reconstructed spin density of NitPh on to the π plane of the nitroxide. Contour step 0.01 μ_B Å^{-2}

function refinement method has been used. The reconstructed spin density is represented on Fig. 6 as a projection on to the O–N–C–N–O plane. As expected from the Maxent result, the unpaired electron occupies a π^* antibonding molecular orbital mainly built from the $2p_z$ atomic orbitals of the two oxygen and the two nitrogen atoms. The magnetization density is equally shared between these four atoms. The fraction of spin delocalized on the rest of the molecule is rather small. One other feature deserves a special attention: there is a large negative contribution (roughly 1/3 of the other contributions) on the sp^2 bridging carbon atom C20. Such a spin polarization effect is conveniently explained in term of a triplet HOMO–LUMO excitation, induced by the unpaired spin of the SOMO. These frontier orbitals have a large contribution from the atomic orbital $2p_z$ on C20, which becomes polarized. The resulting density is negative since, as pointed out by Anderson, the positive spins on the frontier molecular orbitals are attracted by the positive spin on the SOMO, leaving behind the negative spins on the node of the SOMO, that is on the C20 site. The sign alternating spin densities found on the carbon atoms of the phenyl ring are also manifestations of this spin polarization effect.

At this stage, it is relevant to compare the experimental results with the spin densities calculated by the different ab-initio methods. This has been done for an optimized, planar and truncated molecule, where the phenyl and methyl groups were replaced by hydrogen atoms [16]. The theoretical spin populations on the oxygen, nitrogen and central carbon are reported in Table 1, together with the experimental values averaged and normalized to 1 μ_B/NitPh molecule. In the Hartree-Fock approach, no calculation has been made by the RHF method as it is clear that it would

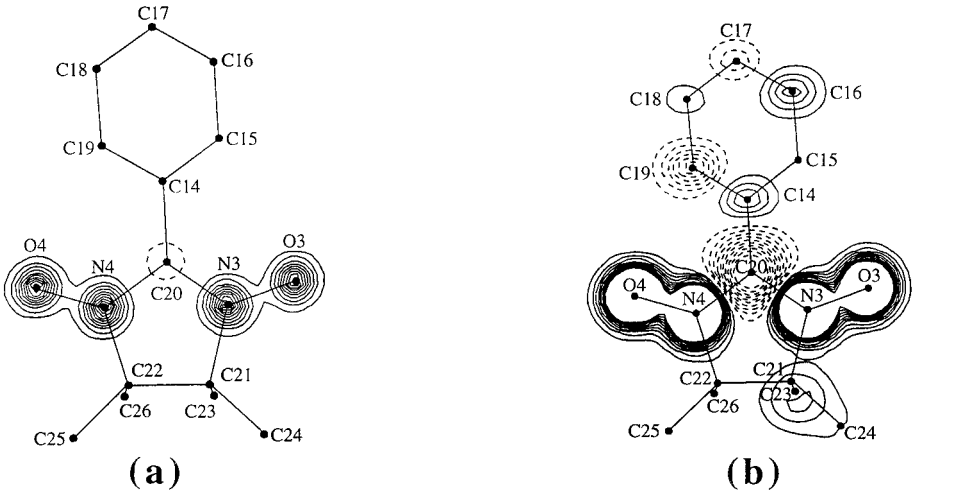

Fig. 6. Spin density of NitPh reconstructed by wave function modeling and projected on to the nitroxide mean plane: (a) high level contours (step 0.1 μ_B Å^{-2}), (b) low level contours (step 0.01 μ_B Å^{-2})

not find the negative density on the central carbon. We report here UHF results with two basis sets: the rather small 3-21G and the huge 6-311G**, the results of the MP2 method and the full CI. All these methods overestimate considerably the negative spin density on the central carbon. Another discrepancy, for all but MP2, is the ratio O/N. Surprisingly, full CI, which in principle is more elaborate than MP2, is farther from reality considering this ratio. We can then conclude than the methods based on Hartree-Fock do not account correctly for the spin density in free radicals. Furthermore, they are unstable: the results depend very much on which method is exactly used and which basis set has been taken for the calculation.

In Table 1 are also displayed the results obtained by the DFT approach: at the local approximation level (VWN functional), with DZVP and TZVP basis sets, and at the nonlocal level referred as B88VWN. There are two points which must be emphasized. On the one hand these calculations are stable: changing approximation or basis set changes very little the calculated spin populations. On the other hand, even if the observed ratio O/N is not exactly reproduced, the theoretical results are not very far from the experimental one. This substantial assertion which acknowledges that methods based on DFT are much more reliable than methods based on Hartree–Fock to calculate the spin densities in molecular compounds from first principles, is not new. It was already demonstrated by systematic calculations on nitroxide [17] and DPPH [18] radicals. Therefore, in the following sections, we shall restrict the comparison of experimental spin densities to DFT calculations only.

A complete calculation of the NitPh molecule in its crystal geometry, using the LSD approximation is reported in Table 2, together with the experimental spin

Table 1. Experimental and theoretical atomic spin populations for the ONCNO fragment of NitPh. DFT calculations were performed using the DGAUSS[(a)] [42] and DMOL[(b)] [43] programs

	Site		
	O	N	C(sp^2)
UHF 3-21G	0.50	0.27	−0.55
UHF 6-311G**	0.40	0.36	−0.52
MP2 3-21G	0.32	0.34	−0.31
CI 3-21G	0.39	0.23	−0.24
VWN[(a)] D-ZVP	0.32	0.21	−0.08
VWN[(a)] TZVP	0.30	0.22	−0.07
VWN[(b)] DNPP	0.29	0.20	−0.02
B88VWN[(b)] DNPP	0.29	0.21	−0.04
Experiment	0.27	0.27	−0.11

Table 2. Theoretical atomic spin populations of NitPh calculated by the DFT (DGAUSS) program for the experimental geometry of one of the two molecules, in comparison with the experimental values found for this molecule and scaled to 1 μ_B

Site	Experiment	DFT
O4	0.277(13)	0.319
N4	0.278(15)	0.238
C20	−0.121(17)	−0.065
N3	0.278(16)	0.210
O3	0.247(13)	0.288
C21	−0.025(16)	−0.004
C22	0.009(13)	−0.005
C23	0.055(12)	0.021
C24	0.009(13)	0.000
C25	−0.008(12)	0.001
C26	−0.005(13)	0.023
C15	0.000(13)	−0.009
C16	0.025(13)	0.002
C17	−0.016(12)	−0.009
C18	0.011(12)	0.002
C19	−0.037(13)	−0.009
C14	0.024(16)	0.004

populations normalized to 1 μ_B/NitPh molecule. As found experimentally, because of their environment, atoms O3 and O4 are no longer exactly equivalent. Furthermore, the sign alternation on the phenyl ring is very well reproduced, though the amplitudes are less than found experimentally.

10.3.3 The Shape of the Spin Density

In the previous section, we have seen through the example of the phenyl nitronyl nitroxide compound how polarized neutron diffraction combined with the Maxent method was able to reveal the shape of the magnetic distributions around magnetic atoms, in particular the 2p character of these distributions. The method also permits in particular cases to demonstrate the bonding or antibonding character of the molecular wave function.

The radical-based cyano-acceptor tetracyanoethylene TCNE has received considerable interest since the compound $V[TCNE]_x.yCH_2Cl_2$ [19] was discovered to magnetically order above room temperature. Another successful synthesis involving TCNE was that of $[Fe(C_5Me_5)_2]^{\bullet+}[TCNE]^{\bullet-}$, a ferromagnet with $T_C = 4.8\,K$ [20].

The spin density in $[TCNE]^{\bullet-}$ has been determined with polarized neutrons in a compound where $[TCNE]^{\bullet-}$ was crystallized together with the nonmagnetic counterion $[Bu_4N]^+$ [21]. Fig. 7 represents the Maxent projection of this spin density on to the molecular plane of TCNE. This projection confirms that the singly occupied orbital of $[TCNE]^{\bullet-}$ is the π^* antibonding molecular orbital consistent with molecular orbital predictions. A careful examination of this map reveals however that on each of the central carbons the spin density is not centered at the nuclei but is bent away from the midpoint of the bond between these two atoms. This bending has been carefully checked by a multipolar expansion analysis and by an extension of the Maxent method to include a non-uniform prior [22]. It came out from both analysis that this shape was not an artifact but the result of the antibonding character of the singly occupied molecular orbital containing the unpaired electron in this radical. It is well known indeed from molecular orbital theory that antibonding orbitals do not have their maximum electron density centered over the bond, but rather the density is bent away from the center of the bond due to the presence of a node. Polarized

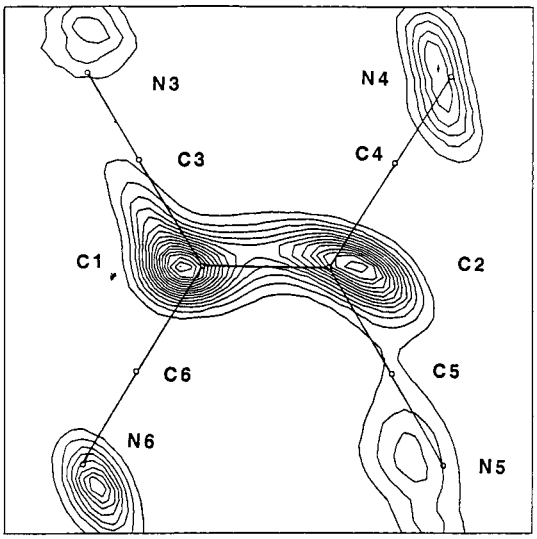

Fig. 7. Projection of the Maxent reconstructed spin density on to the plane of the $[TCNE]^{\bullet-}$ molecule. Step of the contours 0.01 μ_B Å^{-2}

neutron diffraction give access to such details, and is therefore presently the most powerful tool for determining the absolute spin density of a radical.

Such an effect was also observed in the more complex situation of imino nitroxides. In these free radicals, the unpaired electron is mainly located on the N–C–N–O fragment, but, on the contrary to what happens for nitronyl nitroxides, the carbon atom is no longer a node of the SOMO and participates to this magnetic molecular orbital. A polarized neutron investigation has been performed on the *meta*-nitrophenyl derivative (*m*-NPIM; 2-(3-nitrophenyl)-4,4,5,5-tetramethyl-4,5-dihydro-1*H*-imidazol-1-oxyl) [23]. This compound crystallizes in the monoclinic space group $P2_1/c$, with two different molecules A and B in the asymmetric unit, and presents from susceptibility measurements only very weak antiferromagnetic intermolecular interactions.

Figure 8 is the Maxent projection of this spin density on to the N–C–N–O planes of the two independent molecules. The majority of the spin resides in the two molecules on the N1, N2 and O1 atoms, and is equally shared between those sites. On the N1 and O1 atoms of both molecules the density is not centered on the nuclei but is slightly shifted away from the center of the NO bond, as already observed in the case of $[TCNE]^{\bullet -}$. This shifting is what one would expect from the antibonding nature of the SOMO, which has a node on this N1–O1 bond.

The central carbon atom C1 carries in each molecule a negative spin density which is shifted from the nucleus position in the N1–N2 direction. This density is in fact the

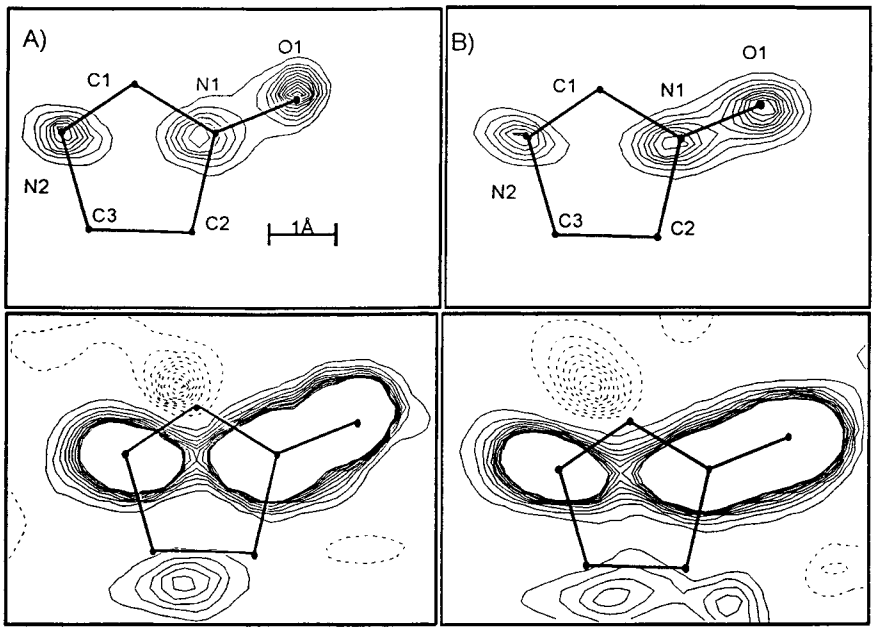

Fig. 8. Projection of the Maxent reconstructed spin density on to the NCNO plane of the two independent A and B *m*-NPIM molecules. Above: high level contours (step 0.05 μ_B Å^{-2}), below: low level contours (step 0.003 μ_B Å^{-2})

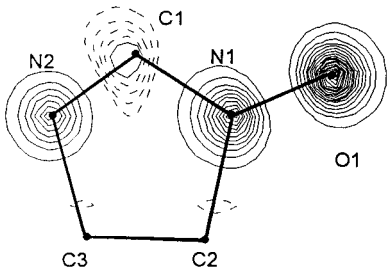

Fig. 9. DFT spin projection on to the NCNO plane of *m*-NPIM. Step for positive contours 0.02 μ_B Å^{-2}, for negative contours 0.002 μ_B Å^{-2}

sum of two competing contributions, namely the positive spin delocalization of the SOMO and the negative spin polarization. The SOMO has two nodes-one between N1 and O1 and one between C1 and N2. This orbital is thus antibonding on N1–O1, bonding on N1–C1 and antibonding on C1–N2. As a result, the positive contribution due to the spin delocalization effect on C1 is attracted in the direction of N1. The negative contribution arising from spin polarization is centered on the nucleus and larger in amplitude, and superimposed to the former one results in a small negative contribution shifted towards N2. This effect has been retrieved by DFT calculations performed on this molecule. The theoretical spin density, projected on to the O–N–C–N plane is represented in Fig. 9: the density on C1 is negative and clearly shifted from the C1 nucleus in the N1–N2 direction.

10.4 Spin Densities in Interacting Molecules

We shall consider now the rather frequent case where the free radicals are arranged in the crystal in such a way that it is no more possible to neglect the magnetic interactions which exist between them. On the macroscopic scale, the magnetic susceptibility does not follow a Curie law at low temperature, and the deviations from the Curie law inform on the nature and the dimension of the magnetic couplings.

Neutron diffraction (ND) is able, at least in principle, to see, in the absence of any external magnetic field, all kinds of ordering: magnetic clusters, magnetic chains, magnetic planes and magnetic structures. On the other hand, polarized neutron diffraction (PND) , though it is usually performed above the ordering temperature and despite the fact that it implies a large external field to align the magnetic moments, is perfectly suited to explore whether the magnetic interactions modify the spin distribution throughout the free radical. We shall examine such examples, going from the cases of weakly to more and more interacting molecules.

10.4.1 Positive Coupling Between Neighboring Molecules

The main aim of molecular magnetism is to obtain ferromagnets, which means the building of compounds with positive interactions between the constitutive molecules.

Such interactions should couple the spin densities of neighboring molecules, and one can expect that the investigation of these spin densities by PND illustrates the paths of the magnetic interactions, sheds some light on the interaction mechanisms and helps improving the performances of the expected magnets.

The first purely organic ferromagnet that was ever synthesized [24] is the β phase of the *para*-nitrophenyl nitronyl nitroxide (*p*-NPNN; 2-(4-nitro-phenyl)-4,4,5,5-tetramethyl-4,5-dihydro-1*H*-imidazol-1-oxyl 3-oxide), a derivative of the nitronyl nitroxide free radical, with a temperature $T_C = 0.6$ K. The arrangement of the molecules in the orthorhombic cell [25,26] is represented in Fig. 10: the nitrogen atom N2 of molecule I is just at the midpoint between the oxygen atoms O1 and O1′ of the two adjacent molecules II and III, at a distance of 3.22 Å. A PND experiment, performed at $T = 2$ K, in the paramagnetic state, revealed a spin density represented in Fig. 11. The atomic spin populations, scaled to 1 μ_B/molecule are reported in Table 3. As for NitPh, most of the spin density lies on the O–N–C–N–O group, with the shape of p orbitals and a negative density on the central carbon. But, contrarily to the NitPh, the sign alternating density on the phenyl ring does not exist anymore: the main feature here is the presence of a positive density on the nitrogen atom of the NO_2 group, also with a p orbital shape, but orthogonal to the orbitals on O1 and O1′. We have here an outlook over the ferromagnetic interaction mechanism between molecules I, II and III, in the frame of the theory proposed by Kahn et al. [27,28]. According to this theory, the interaction between two adjacent molecules is the sum of two terms: a Coulomb exchange term which is positive and an overlap term which is negative. The contacts between the spin density of molecules I, II and III concerns the spin densities on atoms N2, O1 and O1′. As the orbital on N2 is orthogonal to orbitals on O1 and O1′, the overlap term disappears and only remains the exchange term

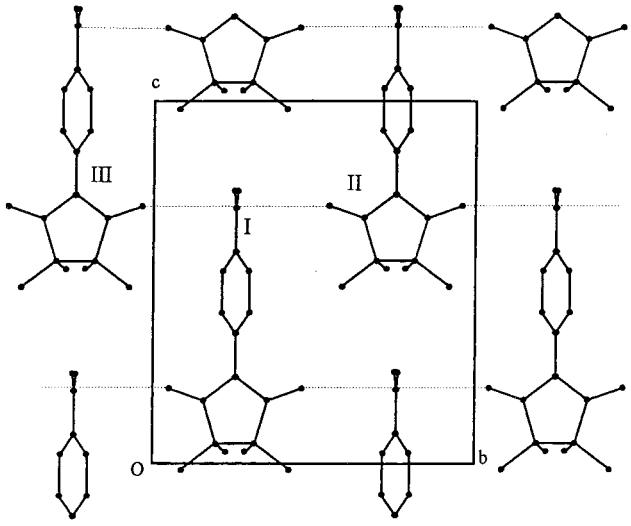

Fig. 10. Arrangement of the molecules in the orthorhombic β phase of *p*-NPNN

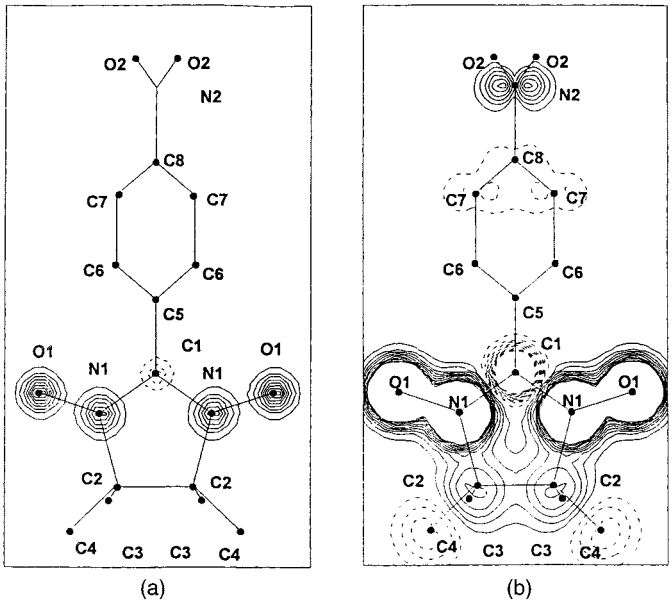

Fig. 11. Wave function refined spin density of *p*-NPNN projected on to the nitroxide mean plane: (a) high level contours (step 0.1 μ_B Å^{-2}), (b) low level contours (step 0.005 μ_B Å^{-2})

Table 3. Selected experimental atomic spin populations of p-NPNN, scaled to 1 μ_B/molecule, in comparison with the theoretical results calculated by the DFT (DMOL) method for one isolated molecule and for the crystal

Atom	Experiment	DFT (DMOL) one isolated molecule	DFT (DMOL) crystal
O1	0.283(7)	0.291	0.274
N1	0.257(7)	0.193	0.198
O2	−0.002(5)	−0.001	−0.001
N2	0.021(5)	−0.001	0.001

which, as the three densities are positive, ensures a ferromagnetic coupling between the three molecules (see Fig. 10).

To check theoretically the interconnection between spin density and magnetic interactions in β *p*-NPNN, we report in Table 3 the results based on the DFT method: calculations for an isolated molecule and calculations for a molecule surrounded by the other molecules of the crystal [44]. In this last case, compared to the former one, some positive density appears on the nitrogen of the nitro group, but it is smaller by one order of magnitude to that observed experimentally. Another trend is visible in this comparison: the interaction with neighboring molecules depletes the spin density on the oxygen atoms of the O–N–C–N–O group, and we shall see in the future that this feature is widespread.

Another example of path research for the magnetic interactions concerns Cl-tempo (4-(*p*-chlorobenzylideneamino)-2,2,6,6-tetramethylpiperidin-1-oxyl), a ferromagnetic tempo derivative, with a Curie temperature $T_C = 0.28$ K [29]. The difference with the magnetic behavior of the parent compound, tempone, described in the first sections and which remains paramagnetic down to very low temperatures, is related to the piling of molecules. In Cl-tempo, the NO sites, which are supposed to carry the unpaired electrons, are located on zigzag sheets, but far enough inside a sheet to prevent direct interactions. However, there are interacting methyl and methylene groups which can play the role of ferromagnetic exchange couplers.

The spin density, measured at 1.5 K, above the Curie temperature, is represented in Fig. 12 [30]. Beside the NO group, where most of the magnetization is located, some density appears on the rest of the molecule. In particular, among the possible exchange couplers, methyl hydrogens H61, H63, H72 and H93, at distances 2.37 Å, 3.40 Å, 2.62 Å and 2.49 Å of the oxygen atom, carry significant spin populations (0.038(12) μ_B, 0.038(12) μ_B, 0.056(14) μ_B, and 0.053(14) μ_B respectively). They certainly participate to the exchange process. A mechanism of ferromagnetic interactions inside the sheets had been proposed by Nogami et al. [31] between the oxygen atom and the N1 spin of one neighboring molecule through a path: O1–H93–C9–C4–N1 and between the same oxygen atom and the N1 spin of another neighboring molecule through another pass: O1–H61–C6–C3–N1. In this model, the signs of the spin populations on O, H, C, C and N should alternate, as a result of the hyperconjugation, with a negative sign on the hydrogen atoms. The experimental spin density does not show this sign alternation and, in particular, the difference of signs on C3 and C4, the two neighboring atoms of nitrogen N1, indicates that the coupling scheme is more complex than the model which has been proposed.

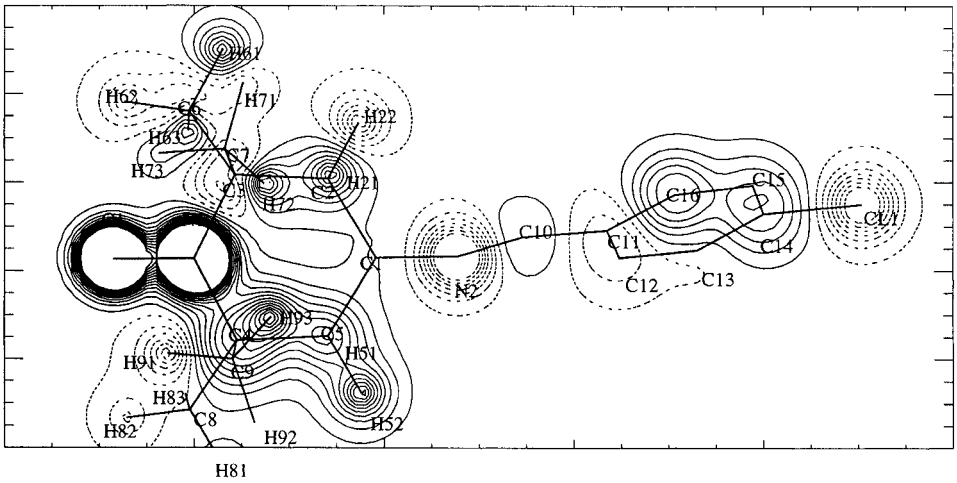

Fig. 12. Spin density of Cl-tempo reconstructed by wave function modeling and projected along the π direction of the nitroxide. Step between the contours 0.01 μ_B Å^{-2}

On the other hand, a surprising spin density has been found on the imino nitrogen N2 ($-0.069(14)\,\mu_B$) and on the terminal chlorine: $-0.059(13)\,\mu_B$. These densities have been interpreted [30] as spin polarizations resulting from the intramolecular interactions between atoms N1, N2 and Cl and followed by an intermolecular interaction between the N2 and Cl atoms of two adjacent molecules (distance N2-Cl: 3.77 Å), interaction which is weak, but enough at low temperature to couple zigzag sheets.

A last example of a purely organic ferromagnet is the nitronyl nitroxide free radical Nit(SMe)Ph (2-(4-thiomethylphenyl)-4,4,5,5-tetramethylimidazoline-1-oxyl-3-oxide), with a Curie temperature $T_C = 0.2\,K$ [32]. On the basis of spin diffusion observed by EPR, the magnetic interactions in this compound were attributed to an exchange pathway involving the NO group of one molecule with the SMe group of a neighboring molecule. In particular, it was assumed that the S atom, with its expanded electron cloud play a major role. To check this assumption, a PND experiment [33] was performed at low temperature, in the paramagnetic state ($T = 5.3\,K$). The spin density, thus obtained, and projected on to the nitronyl nitroxide plane, is represented in Fig. 13 for high contours and low contours. Besides the usual scheme of positive and negative density on the ONCNO group, the striking point is the absence of any density on the sulfur atom. Instead, the methyl carbon C14 carries a

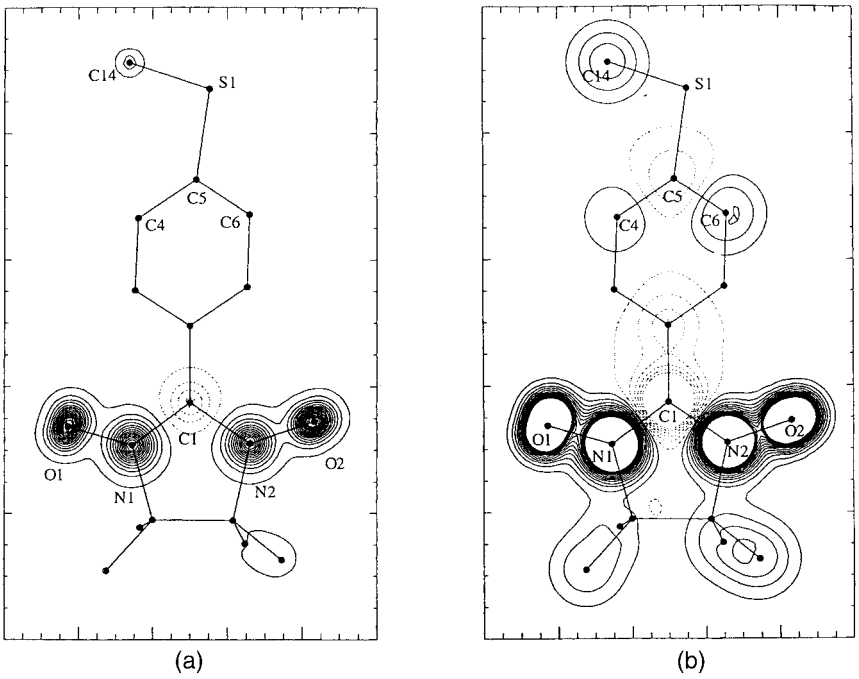

Fig. 13. Spin density of Nit(SMe)Ph reconstructed by wave function modeling and projected on to the nitroxide mean plane: (a) high level contours (step $0.02\,\mu_B\,Å^{-2}$), (b) low level contours (step $0.006\,\mu_B\,Å^{-2}$)

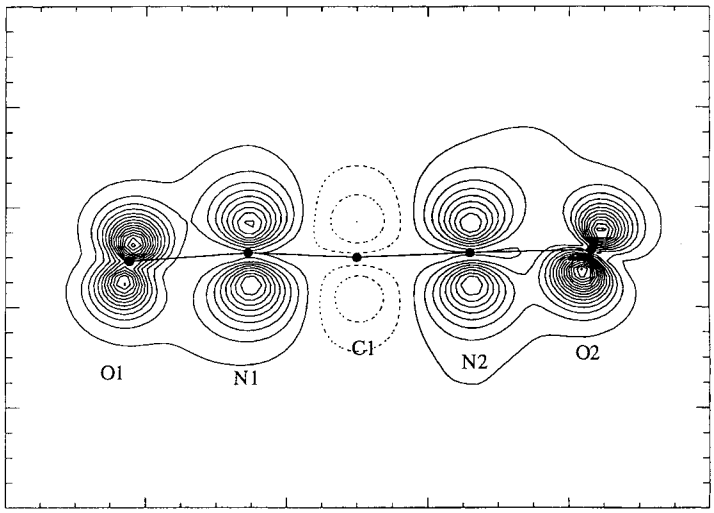

Fig. 14. Spin density of Nit(SMe)Ph reconstructed by wave function modeling and projected on to the π plane of the nitroxide. Step between the contours 0.03 μ_B Å^{-2}

positive spin population of 0.031(7) μ_B. On the phenyl ring, the density is significant on the three carbon atoms: C4, C5 and C6. Another projection of the spin density, perpendicular to the former one, is reported in Fig. 14. It shows that the orbitals carrying the spin density, particularly on oxygen atoms O1 and O2, are distorted. They are no more perpendicular to the nitronyl nitroxide plane and the two lobes of these p orbitals are no more equivalent: one is more inflated than the other. These deformations of the oxygen orbitals are not artifacts of the reconstruction, they have been carefully checked by the multipole expansion and the maximum entropy method. At the opposite, no significant distortion exists on the nitrogen orbitals [33].

The contacts between one molecule and its neighbors is represented in Fig. 15. On the one hand, oxygen O1 is at short distances of carbon atoms C4, C5 and C6 of the phenyl ring of one neighboring molecule, at distances 3.64 Å, 4.12 Å and 4.08 Å respectively. On the other hand, oxygen O2 is at 3.74 Å of the methyl carbon C14 of another neighboring molecule. The appearance of a significant spin density on these carbon atoms and the distortion of the oxygen orbitals are certainly signatures of the pathways of the magnetic interactions. In particular, the pathway which was assumed along the sulfur and the methyl carbon is confirmed, but the assumption that the sulfur atom should carry a spin density appears to be unfounded.

This contact between O2 and C14 has been investigated by an ab-initio DFT calculation [33] which compares the spin populations on one isolated molecule and on two molecules connected through this contact. The result is given in Table 4. The effect is there: the spin density is depleted on the interacting oxygen and some spin density appears on the corresponding carbon C14. But once more, the quantitative result is one order of magnitude smaller than experimentally observed.

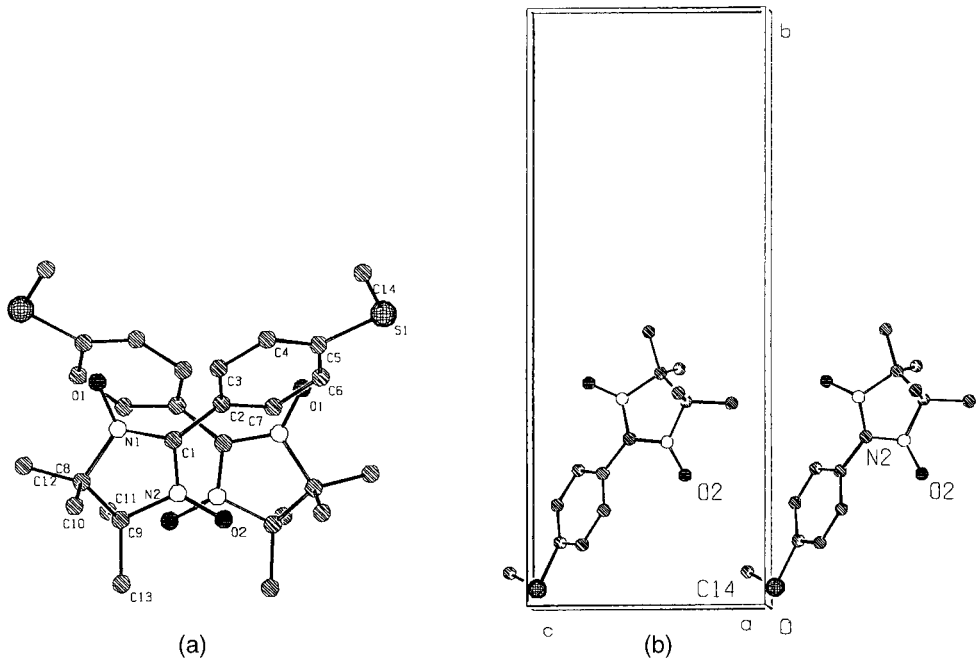

Fig. 15. Intermolecular contacts in Nit(SMe)Ph (a) between O1 and C4, C5, C6; (b) between O2 and C14

Table 4. Selected experimental atomic spin populations of Nit(SMe)Ph scaled to 1 μ_B/molecule, in comparison with the theoretical results calculated by the DFT (DGAUSS) method for one isolated and two interacting molecules

Atom	Experiment	DFT (DMOL) one isolated molecule	DFT (DMOL) crystal
O1	0.226(7)	0.304	0.307
N1	0.272(9)	0.221	0.221
C1	−0.099(8)	−0.063	−0.063
N2	0.247(9)	0.225	0.229
O2	0.226(8)	0.308	0.298
C14	0.031(7)	0.000	0.001

10.4.2 Hydrogen Bonds

Hydrogen bonds are often present in molecular magnetic materials. They couple most of the time the O–H group of one molecule to an oxygen atom belonging to the next molecule, to form a bond which is weak, but, nevertheless, able to bind neighboring molecules. Magnetic interactions can propagate through these hydrogen

bridges. These interactions are positive or negative, and are frequently at the origin of ferromagnetic or antiferromagnetic chains.

The first investigation of the effect of an hydrogen bond on the spin density distribution of a free radical was obtained in comparing the spin distribution of two alkyl nitroxides [13]: tempone, already described, and tempol (4-hydroxy-2,2,6,6-tetramethyl-1-piperidinyloxy). With their six-membered ring and their N–O group, the two molecules look very similar (Figs. 1a and 1b) and differ mainly by their chemical function: ketone for tempone and alcohol for tempone. In the first compound, the molecules are isolated and the magnetic susceptibility exhibits a Curie behavior. In the second compound, the hydrogen of the alcohol function induces a bridge between the H of the alcohol group of one molecule and the O of next molecule's NO group. As a result, tempol susceptibility departs from the Curie law: it reaches a maximum at $T = 5\,\mathrm{K}$ and drops at lower temperatures, as a result of antiferromagnetic intermolecular interactions.

The spin densities of the two compounds are represented in Fig. 2. They are localized mainly on the N–O groups in $2p_z$ orbitals centered on oxygen and nitrogen atoms. However, in the tempol case, the spin partitioning inside the N–O group is strongly affected by the coupling with the next molecule through the hydrogen bond. It changes from 53%(N)/47%(O) for the tempone to 61%(N)/39%(O) on the tempol. The density on the bonding oxygen is depleted and consequently the density on the nitrogen is reinforced. This feature has been encountered in all the nitroxide radicals affected by an hydrogen bond.

Furthermore, a small and negative spin density: $-0.012(12)\ \mu_B$ after normalization, at the limit of the detection threshold, is found on the hydrogen of the bridge. In spite of its small amplitude, this polarization seems also to be a signature of the magnetic interaction through the hydrogen bond.

The case of the nitronyl nitroxide radical 6-NitPy(C≡C-H) (2-(6-ethynyl-2-pyridyl)-4,4,5,5-tetramethylimidazoline-1-3-oxide) is of particular interest as the hydrogen bonds which connect adjacent molecules imply a carbon (C7) instead of an oxygen atom: C6≡C7-H16...O1. These bonds organize the molecules in zigzag chains, but, in contrast to tempol, the magnetic interactions along the chains are positive [34]: the χT product increases with decreasing temperature, down to 0.56 K where it reaches a sharp maximum; it decreases steadily below this temperature as a result of the negative interactions between adjacent chains.

The spin density, measured at 4.75 K by PND [35], is displayed in Fig. 16. As usual for the nitronyl nitroxide radicals, most of the density is concentrated on the O–N–C–N–O part of the molecule, positive on O, N, N and O and negative on the central carbon, but the striking points concern the hydrogen bond: first, a significant density exists on hydrogen H16 ($0.045(10)\ \mu_B$) and second, there is a difference between the spin populations on the two oxygen atoms of the nitronyl nitroxide group: O1 which participates to the bond is markedly depleted: $0.203(10)\ \mu_B$, compared with O2: $0.278(7)\ \mu_B$ while the two nitrogen atoms carry spin populations which are nearly equal: $0.242(12)\ \mu_B$ for N2 and $0.225(12)\ \mu_B$ for N3.

The spin populations, obtained by ab-initio calculations (DFT method) for the NitPy(C≡C-H) molecules, in their crystal geometry, (first: one isolated molecule, secondly: two molecules connected via the hydrogen bond and finally: the whole

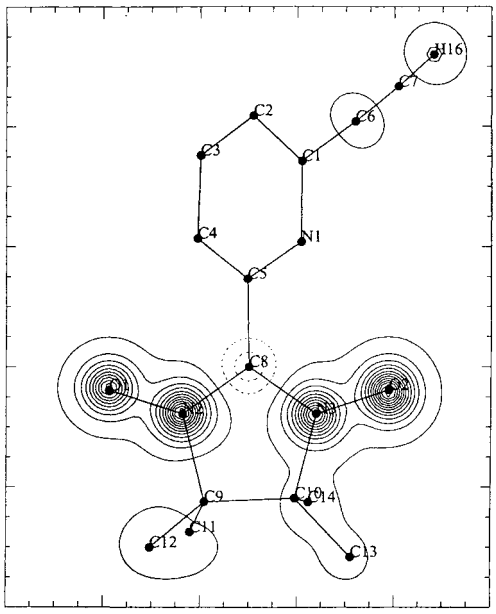

Fig. 16. Spin density of NitPy(C≡C-H) reconstructed by wave function modeling and projected on to the nitroxide mean plane. Step between the contours 0.1 μ_B Å^{-2}

crystal) are reported in Table 5 and compared to those found experimentally. As already seen for nitronyl nitroxide radicals, the DFT overestimates the spin density on the oxygen atoms of the O–N–C–N–O group and weakens it on the nitrogen ones. But here, the calculations made on the isolated molecule evidence some depletion on oxygen O1, which must originate from the asymmetry of the molecule itself: either the position of the ethynyl group C≡C-H or the presence of the nitrogen atom N1 in the pyridine cycle. Other DFT calculations have then been accomplished on one isolated molecule but with different geometries [35]. Attaching the ethynyl group to C3 instead of C1 does not modify practically the spin densities calculated on O1 and O2. But, inverting atoms N1 and C4 in the pyridine cycle reverses the balance, and the spin density becomes larger on O1 than on O2 for the isolated molecule

Table 5. Selected experimental atomic spin populations of NitPy(C≡C-H), scaled to 1 μ_B/molecule, in comparison with the theoretical results calculated by the DFT method for one isolated molecule, for two interacting molecules and for the crystal

Atom	Experiment	DFT Isolated molecule	DFT Two molecules connected	DFT Crystal
O1	0.203(10)	0.270	0.243	0.239
N2	0.242(12)	0.212	0.224	0.188
C8	−0.071(11)	−0.086	−0.084	−0.075
N3	0.225(12)	0.230	0.230	0.212
O2	0.278(7)	0.312	0.318	0.312
H16	0.045(10)	0.000	0.002	0.004

[35]. However, for the real geometry, the comparison between calculations for one isolated molecule with calculations either for two molecules in interaction via the hydrogen bond or for the whole crystal, shows that half the difference between O1 and O2 results from the intermolecular magnetic interactions which propagate along the chain and deplete the O1 site. The examination of Table 5 shows that, according to the DFT results, the magnetic interaction induces also a spin density on the hydrogen atom of the bond, but very small. The DFT method is unable to account for the 0.045(10) μ_B found experimentally. The agreement is only qualitative and not quantitative.

10.4.3 Strongly Interacting Spin Carriers

In their attempt to produce molecular materials with efficient properties, the magnet builders keep optimizing the magnetic interactions and also the number of magnetic carriers present in the synthesized compounds. Quite frequently, they prepare molecules which are themselves composed of two or more spin carrier entities. In these cases, the magnetic interactions between these entities will be stronger than formerly, as they are related to the chemical bonds inside the molecule instead of bonds between separate molecules. The spin density maps will show up these strong coupling and illustrate their mechanism.

A case of organic molecular compound, which clearly corresponds to a unique entity, but which includes different spin carriers is the ball-shaped DTDA, named also dupeyredioxyl (catena(μ-1,3-(2,4,4,5,5-pentamethyl-4,5-dihydro-1*H*-imidazolyl-1-oxyl 3-oxide)bis(hexafluoroacetylacetonato)copper(II)), and represented in Fig. 17. This molecule is a biradical, with two unpaired electrons which are expected to be localized on the two NO groups. The molecular backbone ensures orthogonal 2p orbitals for the nitrogen atoms of these two groups and therefore a positive interaction between the related moments. The magnetic susceptibility [36] corresponds indeed at higher temperatures to two independent spin 1/2, but indicates below 100 K that these two spins couple ferromagnetically. Furthermore, at $T_C = 1.48$ K, a three dimensional magnetic order occurs [37], representing the highest Curie temperature ever reported for a purely organic ferromagnet.

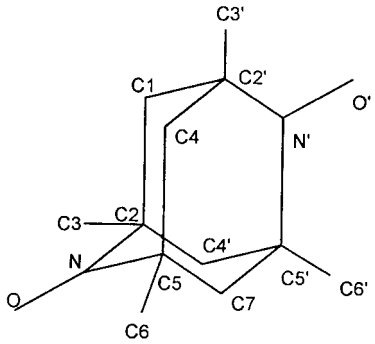

Fig. 17. The DTDA molecule

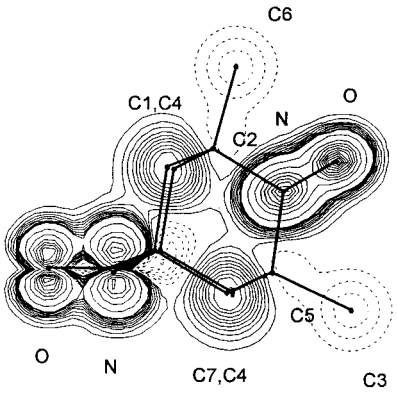

Fig. 18. Spin density of DTDA reconstructed by wave function modeling and projected on to the π plane of one of the two NO groups. Step between the high level contours 0.1 μ_B Å^{-2}, between the low level contours 0.005 μ_B Å^{-2}

A PND experiment was performed at $T = 2$ K, still in the paramagnetic state [38]. The spin density, projected on to the π plane of one NO group and along the direction of the other is represented in Fig. 18. The spin populations, scaled to 2 μ_B/molecule are presented in Table 6. The density is positive on the two NO groups and has, on each of these atoms, the shape of a 2p orbital. It is not absolutely evenly shared between the N and O sites: the former site carries approximately 15% more spin than the latter. Between the two radicals, the ferromagnetic exchange interaction is not direct but should pass through the polarized carbon skeleton of the molecule. This is supported by the experimental results, which confirm the alternating sign of the carbon spin populations along all the paths linking the two NO groups.

Two ab-initio DFT calculations of this molecule, in its crystal geometry, have been performed : the first one [39] using the deMon program and the second one [38] with the DMol program package. The results are also reported in Table 6. Both calculations produce very close results, confirming the good stability of the DFT method. Compared to experiment, the spin populations are not too far. On the NO part, the balance has been reversed, but on the carbon skeleton, the sign alternation is there. Furthermore, contrarily to the experimental data treatment where sites C1, C4,

Table 6. Experimental atomic spin populations of DTDA, scaled to 1 μ_B/molecule, in comparison with the theoretical results calculated by the DFT method by the DEMON and by the DMOL program

Atom	Experiment	DFT (DMON)	DFT (DMOL)
N	0.536(17)	0.451	0.441
O	0.469(14)	0.501	0.484
C1	0.057(9)	0.062	0.067
C2	−0.027(10)	−0.021	−0.040
C3	−0.033(8)	–	0.000
C4	0.057(=C1)	0.037	0.039
C5	−0.027(=C2)	−0.019	−0.010
C6	−0.033(=C3)	–	0.000
C7	0.057(=C1)	0.012	0.017

and C7 were incorrectly considered as equivalent, in the calculations, the nitroxide groups, because they are not planar, induce different spin densities on these carbon sites. These subtle results are the same in the two calculations. We can say that, inside this molecular entity, the exchange interactions are reproduced in a satisfactory way by the DFT method.

We shall now examine the spin densities of two complexes between copper (II) and nitronyl nitroxides [40] presenting different types of bond. In the first one, of axial coordination, $Cu(hfac)_2NitMe$ (catena(μ-1,3-(2,4,4,5,5-pentamethyl-4,5-dihydro-1*H*-imidazolyl-1-oxyl 3-oxide)bis(hexafluoroacetylacetonato)copper(II)), each Nit ligand bridges to two Cu atoms, Cu1 and Cu2, creating alternate chains. The Cu atoms are bonded to four oxygen atoms from the hfac parts (distance range from 1.86 Å to 2.01 Å), which nearly form a square. The axial positions are occupied by two O atoms from the NO groups of the Nit radical (distance 2.39 Å and 2.56 Å), giving an elongated octahedral environment to each Cu (see Fig. 19a). In such an axial coordination, the overlap between the Cu orbital (orbital $3d_{x^2-y^2}$) and the oxygen orbital is very reduced; one can expect nearly orthogonality and therefore a positive interaction between the copper spin ($S = 1/2$) and the Nit spin ($S = 1/2$). The temperature dependence of the magnetic susceptibility shows that there are actually ferromagnetic interactions inside the chains, but no three dimensional ordering.

The spin density was measured at 2.5 K by PND. Its projection on to the plane of the Nit radical is represented in Fig. 20 and the spin populations of the different atoms, normalized to 4 μ_B for 2 Cu and 2 Nit, are reported in Table 7. The first point to be noticed is that the spin density is delocalized around the copper atoms: O1, O2 around Cu1 and O3, O4 around Cu2. This leads to three different sub-units having the following moments: 1.093(20) μ_B around Cu1, 0.925(23) μ_B on the Nit and 1.058(20) μ_B around Cu2. The deviation from 1 μ_B per sub-unit shows that the molecular wave function is not limited to each sub-unit but includes all them along the chain. We can also note that the oxygen atoms of the Nit radical are seriously affected by the bond with the copper sub-units: on the one hand, they carry a spin population much lower than the nitrogen atoms (average 0.208(6) μ_B for O and 0.322(6) μ_B for N), a difference which is much larger than those observed previously, and in the other hand, as it can be observed on Fig. 20, their orbitals have still a p shape, but are no more perpendicular to the Nit plane as the N orbitals are: they have been rotated by the magnetic interactions. Unfortunately, up to now, no calculation has been performed on $Cu(hfac)_2NitMe$ to compare with the experiment.

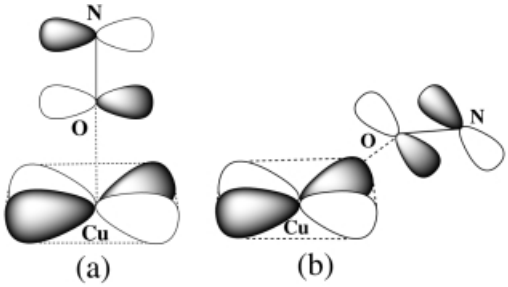

Fig. 19. Coordinations between Nit and Cu: (a) axial coordination, (b) equatorial coordination

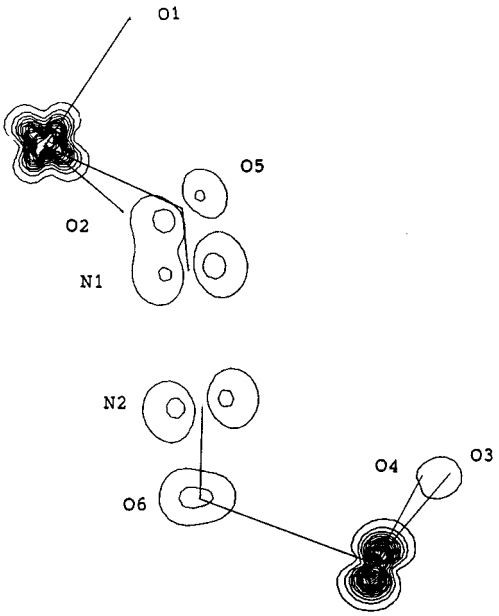

Fig. 20. Spin density of $Cu(hfac)_2NitMe$ reconstructed by wave function modeling and projected on to the π plane of the Nit. Step between the contours 0.2 μ_B $Å^{-2}$

Table 7. Experimental atomic spin populations of $Cu(hfac)_2NitMe$, scaled to 4 μ_B for 2 Cu and 2 Nit

Atom	Spin population	Spin per subunit
Cu1	0.905(9)	
O1	0.032(6)	1.093
O2	0.062(6)	
Cu2	0.796(8)	
O3	0.054(6)	1.058
O4	0.077(6)	
N1	0.328(8)	
O5	0.216(7)	
N2	0.316(8)	
O6	0.201(10)	0.925
C11	−0.106(9)	
C13	0.012(8)	
C16	−0.042(8)	

The second Cu complex, $CuCl_2(NitPh)_2$ (bis(2-phenyl-4,4,5,5-tetramethyl-4,5-dihydro-1*H*-imidazolyl-1-oxyl 3-oxide)copper(II)), corresponds to an equatorial coordination around the copper. There is only one Cu site in the compound, which is surrounded by a square: two Cl atoms (distances 2.19 Å) and the two O atoms (distances 1.98 Å) of two neighboring NitPh, to give a 3 sub-unit molecule. With this square environment (see Fig. 19b), one expects a large overlap between the $3d_{x^2-y^2}$ orbital of Cu and the oxygen orbitals and therefore a negative interaction between

the copper spin and each of the NitPh spin on both sides of the copper. Actually, the susceptibility measurements in the range 30–300 K [41] show a Curie law with $S = 1/2$ for the whole molecule, indicating that the negative coupling between the three spins 1/2 of each sub-unit is very strong. At lower temperature, the susceptibility presents a maximum and then decreases, as a result of the negative couplings existing between the molecules.

The spin density, measured by PND at $T = 13$ K, the temperature of the susceptibility maximum, is displayed in Fig. 21 and the spin populations, normalized to 1 μ_B per molecule, are reported in Table 8. The spin density is positive on most of the two NitPh atoms and negative on the copper. Actually, each NitPh sub-unit carries 0.70(11) μ_B and the sub-unit $CuCl_2$ carries $-0.40(11)$ μ_B. Considering the coupling of three spins 1/2, which may lead to one quadruplet ($S = 3/2$) and two doublets ($S = 1/2$) with two possible repartitions for the spin density: (0 μ_B, 1 μ_B, 0 μ_B) and (2/3 μ_B, $-1/3$ μ_B, 2/3 μ_B), the observed spin density corresponds clearly to this last case. However, one feature is particularly striking: there is no spin density on O1, the oxygen atom bonded to Cu, while the spin populations on the two nitrogen atoms and the other oxygen are nearly equal. We are here in an extreme case where the spin distribution has been completely upset by the magnetic interactions. We can say that oxygen O1 belongs both to the Nit sub-unit with a positive density and to the Cu sub-unit with a negative density and the result of this strategic position is the complete loss of its spin density.

A DFT calculation of the spin density has been performed on this molecule, with the geometry observed in the crystal [44]. The Mulliken spin populations are reported in Table 8 and compared to the experimental results. The moment found on the copper is much less than that measured. On the Nit fragment, the calculation yields 0.082 μ_B for the binding oxygen O1, that is a reduced value, but not a zero value as found experimentally. On the contrary, the population calculated on O2 is almost the double of those of N1 and N2. More globally, the DFT method finds a moment of 0.580 μ_B on the O–N–C–N–O fragment and -0.193 μ_B on the $CuCl_2$ group. We have now discrepancies with the Heitler-London (2/3 μ_B, $-1/3$ μ_B, 2/3 μ_B) distribution. The DFT method tends to fade out the partition in magnetic subunits, more than what the neutron experiment indicates.

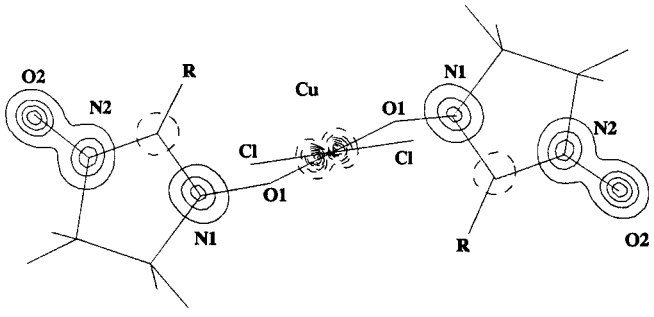

Fig. 21. Spin density of $CuCl_2(NitPh)_2$ reconstructed by wave function modeling and projected along the π direction of the Nit. Step between the contours 0.01 μ_B Å^{-2}

Table 8. Experimental atomic spin populations of $CuCl_2(NitPh)_2$, scaled to 1 μ_B/molecule, in comparison with the theoretical results calculated by the DFT (DMOL) method

Atom	Experiment	DFT (DMOL)
Cu	−0.36(4)	−0.123
Cl	−0.02(5)	−0.035
N1	0.32(4)	0.144
N2	0.35(4)	0.142
O1	−0.01(4)	0.082
O2	0.33(4)	0.263
C1	−0.19(4)	−0.042
C2	−0.06(4)	−0.004
C3	−0.04(4)	−0.005

10.5 Conclusions

Neutron scattering, a microscopic technique which measures the spin density on each point of the crystal, has brought a lot to the knowledge of magnetism in free radicals. It is the only way which allows to know this spin density on the different atoms of a molecular compound. Some of the results obtained by this method are rather unexpected since they are difficult to anticipate by theoretical considerations.

Concerning the ab initio calculations, the comparison with the experimental results have definitely shown that methods based on the Hartree–Fock approach are not reliable to provide correct spin density maps. On the contrary, for isolated molecules, calculations based on DFT can reproduce quite well, though not rigorously, the main features of the experimental maps. However, in the case of molecules in interaction, the coupling mechanisms cannot be correctly determined, even with the DFT approach. In these cases, some modifications brought to the spin density distribution by the magnetic couplings, do appear in the theoretical results, but their value is underestimated by almost one order of magnitude. Therefore, for the present time, the only way to approach the magnetic interactions and to know the related spin densities in interacting free radicals, is polarized neutron experiments.

Acknowledgments

We want to thank Dr Paul Rey (CEA-Grenoble), who opened for us the field of molecular magnetism and took part, together with us, in many investigations and Dr. Bernard Delley (PSI Zurich) who introduced the DFT method in spin density calculations for free radicals. We also want to express our acknowledgments to Dr. Andrey Zheludev (Brookhaven National Laboratory) and Dr. Yves Pontillon (ILL Grenoble) who participated actively to most of the experiments reviewed in this paper.

References

[1] S.F. Gull and G.J. Daniell, *Nature 272* (**1978**) 686.
[2] R.J. Papoular and B. Gillon, *Europhys. Lett. 13* (**1990**) 429.
[3] P. Schleger, A. Puig-Molina, E. Ressouche, O. Rutty, and J. Schweizer, *Acta Cryst. A53* (**1997**) 426.
[4] N.K. Hansen and P. Coppens, *Acta Cryst. A34* (**1978**) 909.
[5] C. Moller and M.S. Plessey, *Phys. Rev. 46* (**1934**) 618.
[6] Shavitt, *Methods of Configurational Interaction*, in *Modern Theoretical Chemistry*, H.F. Shaefer, Editor, Plenum Press, New York, (**1977**), 189.
[7] P. Hohenberg and W. Kohn, *Phys. Rev. 136* (**1964**) 864.
[8] W. Kohn and L.J. Sham, *Phys. Rev. A140* (**1965**) 1133.
[9] U. von Bart and L. Hedin, *J. Phys. C 5* (**1972**) 1629.
[10] A.K. Rajagopal and J. Callaway, *Phys. Rev. B7* (**1973**) 1912.
[11] S.H. Vosko, L. Wilk, and M. Nausair, *Can. J. Phys. 58* (**1988**) 1200.
[12] A.D. Becke, *Phys. Rev. A38* (**1988**) 3098.
[13] D. Bordeaux, J.X. Boucherle, B. Delley, B. Gillon, E. Ressouche, and J. Schweizer, *Z. Naturforsch. 48A* (**1993**) 120.
[14] Y. Karimov, *Sov. Phys. JETP 30* (**1970**) 1062.
[15] R. Caciuffo, et al., *Mol. Phys. 74* (**1991**) 905.
[16] A. Zheludev, et al., *J. Am. Chem. Soc. 116* (**1994**) 2019.
[17] B. Delley, P. Becker, and B. Gillon, *J. Chem. Phys. 80* (**1984**) 4286.
[18] E. Wimmer, A. Freeman, C.-L. Fu and B. Delley: *Computational Chemistry by Supercomputer: Steps toward Computer-aided Design of New Materials*. Cray Channels, pp. 2–9, **1986**.
[19] J.M. Manriquez, G.T. Yee, R.S. McLean, A.J. Epstein, and J.S. Miller, *Science 252* (**1991**) 1415.
[20] J.S. Miller, J.C. Calabrese, H. Rommelmann, S.R. Chittipeddi, J.H. Zhang, W.M. Reiff, and A.J. Epstein, *J. Am. Chem. Soc. 109* (**1987**) 769.
[21] A. Zheludev, A. Grand, E. Ressouche, J. Schweizer, B.G. Morin, A.J. Epstein, D.A. Dixon, J.S. Miller, *J. Am. Chem. Soc. 116* (**1994**) 7243.
[22] A. Zheludev, R.J. Papoular, E. Ressouche, and J. Schweizer, *Acta Cryst. A51* (**1995**) 450.
[23] A. Zheludev, M. Bonnet, B. Delley, A. Grand, D. Luneau, L. Ohrstrom, E. Ressouche, P. Rey, J. Schweizer, *J. Magn. Magn. Mater. 145* (**1995**) 293.
[24] P. Turek, K. Nozawa, D. Shiomi, K. Awaga, T. Inabe, Y. Maruyama, and M. Kinoshita, *Chem. Phys. Lett. 180* (**1991**) 327.
[25] K. Awaga, T. Inabe, U. Nagashima, and Y. Maruyama, *J. Chem. Soc., Chem. Commun.* (**1989**) 1617.
[26] K. Awaga, T. Inabe, U. Nagashima, and Y. Maruyama, *J. Chem. Soc., Chem. Commun.* (**1990**) 520.
[27] O. Kahn and B. Briat, *J. Chem. Soc., Faraday II 72* (**1976**) 268.
[28] O. Kahn and B. Briat, *J. Chem. Soc., Faraday II 72* (**1976**) 1441.
[29] R. Imachi, T. Ishida, T. Nogami, S. Ohira, K. Nishiyama, and K. Nagamine, *Chem. Lett.* (**1977**) 233.
[30] Y. Pontillon, A. Grand, T. Ishida, E. Lelièvre-Berna, T. Nogami, E. Ressouche, and J. Schweizer, to appear in *J. Am. Chem. Soc.*
[31] T. Nogami, T. Ishida, M. Yasui, F. Iwasaki, N. Takeda, M. Ishikawa, T. Kawakami, K. Yamagushi, *Bull. Chem. Soc. Japan 69* (**1996**) 1841.

[32] A. Caneschi, F. Ferraro, D. Gatteschi, A. Le Lirzin, and E. Rentschler, *Inor. Chem. Acta 217* (**1994**) 7.
[33] Y. Pontillon, A. Caneschi, D. Gatteschi, A. Grand, E. Ressouche, R. Sessoli, and J. Schweizer, to appear in *Chemistry European Journal.*
[34] F.M. Romero, R. Ziessel, A. De Cian, J. Fischer, P. Turek, *New J. Chem. 20* (**1996**) 919.
[35] F.M. Romero, Y. Pontillon, R. Ziessel, M. Bonnet, B. Delley, A. Grand, C. Paulsen, E. Ressouche, J. Schweizer, to appear in *J. Am. Chem. Soc.*
[36] R. Chiarelli, A. Rassat, and P. Rey, *J. Chem. Soc., Chem. Commun.* (**1992**) 1081.
[37] R. Chiarelli, M.A. Novak, A. Rassat, and J.L. Tholence, *Nature 363* (**1993**) 147.
[38] A. Zheludev, R. Chiarelli, B. Delley, B. Gillon, A. Rassat, E. Ressouche, and J. Schweizer, *J. Magn. Magn. Mater. 140–144* (**1995**) 1439.
[39] P. Fluekiger, J. Weber, R. Chiarelli, A. Rassat, and Y. Ellinger, *Int. J. Quant. Chem. 45* (**1993**) 649.
[40] E. Ressouche, J.X. Boucherle, B. Gillon, P. Rey, and J. Schweizer, *J. Am. Chem. Soc. 115* (**1993**) 3610.
[41] J. Laugier, P. Rey, C. Benelli, D. Gatteschi, and C. Zanchini, *J. Am. Chem. Soc. 108* (**1986**) 6931.
[42] *UniChem DGAUSS1.1*, Cray Research Inc., Cray Research Park, 655 Lone Oak Drive, Eagan, MN 55121.
[43] *DMOL*, Biosym Technologies Inc., 9686 Scranton Road, San Diego, CA 92121–2777.
[44] *B. Delley*, unpublished results, private communication.

Magnetism: Molecules to Materials I: Models and Experiments.
Edited by Joel S. Miller and Marc Drillon

ISBNs: 3-527-29772-3 (Hardback); 3-527-60084-1 (Electronic)

11 Spin Distributions in Molecular Systems with Interacting Transition Metal Ions

Béatrice Gillon

11.1 Introduction

The first applications of polarized neutron diffraction (PND) to metal-containing molecular systems were devoted to the study of covalence in the metal–ligand bonds of paramagnetic complexes of the first-series transition metals with monoatomic ligands, such as $[Cr^{III}F_6]^{3-}$ [1,2] and $Co^{II}X_4$ with $X = Br^-$ and Cl^- [3]. Detailed spin density determinations were then performed in larger molecules with polyatomic coordination groups, i. e. the nitro NO_2^- and ammonia NH_3 groups in $Ni^{II}(NH_3)_4(NO_2)_2$ [4] and the cyano ligand CN^- in $Cs_2K[M^{III}(CN)_6]$ complexes with $M = Cr^{3+}$ and Fe^{3+} [5], or the more extended ligands in $[Fe^{III}(bipy)_2Cl_2]$, $[Fe^{III}Cl_4]$ [6] and phtalocyaninato-Co^{II} and -Mn^{II} [7,8]. The family of octahedral Tutton salts of divalent transition metal ions $M^{II}(OH_2)_6$ has been thoroughly investigated for various 3d configurations with $M = Mn^{2+}$, Ni^{2+}, V^{2+}, Fe^{2+} and Cr^{2+} [9]. The most recent studies of spin distributions in paramagnetic transition metal mononuclear complexes concern second-series transition metal complexes (Mo^{3+}, Tc^{6+}, Re^{4+}, Ru^{3+}), which display enhanced covalence effects because of the larger radial extension of the 4d orbitals [10].

In PND studies of paramagnetic transition metal compounds, the unpaired electronic moments are aligned by an external magnetic field and the spin density is mostly positive; the regions with negative spin density are those where the majority of spins oppose the field. From a theoretical point of view, in order to account for the main features of experimental spin distributions, it is necessary to go beyond the restricted Hartree-Fock scheme, in which the spin density is given by the square of the singly occupied molecular orbital and is therefore always positive, and to take into account electron correlation, using the configuration interaction (CI) or the unrestricted Hartree-Fock (UHF) method. Density functional theory (DFT) has been revealed in the past fifteen years to be the most convenient method for spin density calculations in large molecules, such as organic free radicals as described in the previous chapter. The spin density is then given by the difference between the density of electrons with spin up and the density of electrons with spin down and may therefore be positive or negative.

The spin density observed on the ligand atoms in transition metal complexes results essentially from the sum of two contributions with opposite signs: the spin delocalization and the spin polarization of bonding or nonbonding, doubly-occupied molecular orbitals due to the unpaired electrons of the metallic ion [11]. The sign

of the spin density on the ligands is then governed by the sign of the dominating effect. An illustration of these general trends is given by the systematic study, both experimental [9] and theoretical [11], of octahedral $[M^{II}(OH_2)_6]^{2+}$ systems with σ-donor ligands OH_2, for different 3d configurations of the metal ion, leading to the following conclusions:

- the spin delocalization effect is dominant for σ-bonding compounds of an e_g^2 ion (i. e. Ni^{2+}) and leads to positive spin density of σ-type on the oxygen atom;
- the spin polarization effect is dominant for π-bonding systems of a t_{2g}^3 ion (i. e. V^{2+}) and is responsible for σ-type negative oxygen spin density;
- for a mixed occupation of the e_g and t_{2g} orbitals like in Mn^{2+}, the spin delocalization from the e_g orbital is stronger than for the t_{2g} orbitals and induces a positive spin population on the oxygen atom.

In the peculiar case of the octahedral π-bonding system of a t_{2g}^3 ion with unsaturated cyano ligands $[Cr^{III}(CN)_6]^{3-}$ [5a], a large positive π delocalization is found on the nitrogen atom together with a negative σ spin on the carbon atoms. This results from the particular topology of the singly occupied molecular orbital consisting of the combination between the t_{2g} orbital of Cr and the π and π^* orbitals of CN^- [11]. No contribution due to spin delocalization exists on the carbon atom and so a pure spin polarization effect occurs. The study of the related compound $[Co(NH_3)_5(OH_2)]\,[Cr(CN)_6]$ [12] deserves special attention as a spectacular example of spin and charge transfer from a magnetic ion, Cr^{III}, towards a nonmagnetic ion, Co^{III}, through hydrogen bonding via the Cr–C–N $\cdots$ H–N–Co pathway.

This chapter is devoted to molecular systems containing magnetic transition metal ions which interact through pure spin exchange mechanisms, i. e. excluding charge transfer [13]. Our first purpose is to show what the determination of spin density maps by PND brings to the understanding of the magnetic interaction mechanisms between magnetic transition metal ions through organic bridges.

The experimental spin distributions in binuclear compounds displaying either antiferro- or ferromagnetic intramolecular couplings will be discussed with the help of theoretical calculations involving the electron active model [14], or using the DFT method which allows ab initio spin density calculations on such extended molecules. Spin delocalization and spin polarization will be invoked in this discussion.

The investigations of bimetallic compounds displaying one-dimensional magnetic properties, ferrimagnetic as well as ferromagnetic, will also be reported. In particular the evolution of the spin distribution from a dimer of antiferromagnetic coupled ions to a ferrimagnetic chain will be followed, both experimentally and theoretically.

The second objective of this chapter is to show how PND allows us to elucidate the exact spin configuration in the spin ground state for large molecular clusters containing up to twelve metal ions.

Polarized neutron diffraction on single crystals [15], as described in the previous chapter, devoted to organic radicals, provides a set of experimental magnetic structure factors which are the Fourier components of the magnetization density. All the studies reported in this chapter concern paramagnetic materials, in which the magnetization density [16] is induced by an external magnetic field. The spin density is

reconstructed from these measurements either by the maximum of entropy method [17] or by refinement of a model based either on a multipole description of the spin density [18,19], or on the wave function [20,21].

11.2 Antiferromagnetic Intramolecular Coupling in Heterometallic Dimers

Heterometallic dinuclear species with two different local spin values S_A and S_B on the metal ions are of special interest in molecular magnetism because their spin ground state is never a singlet even in the most usual case of intramolecular antiferromagnetic coupling.

In the electron-active approximation, it is well established that the overlap between the magnetic orbitals centered on each metal ion favors antiferromagnetic coupling [14]. The experimental determination of the spin density allows us to quantitatively test the magnetic orbital model for heterometallic dimers having an intramolecular antiferromagnetic coupling, through different types of bridges, as well as more elaborate theoretical DFT wave function calculations.

11.2.1 Short Bridge in a $Cu^{II}Ni^{II}$ Dimer

The nonplanarity of the CuO_2Ni bridging network in the heterodinuclear compound $Cu^{II}(salen)Ni^{II}(hfa)_2$, with salen = N,N'-ethylenebis(oxosalicyldiiminato) and hfa = hexafluoroacetylacetonato, leads to a short Cu···Ni distance of 2.91 Å. The Ni^{2+} ion ($S_A = 1$) resides at the center of a slightly distorted octahedra of six oxygen atoms including the two bridging oxygen atoms. The Cu^{2+} ion ($S_B = 1/2$) lies in a square planar environment formed by the two bridging oxygen atoms and two nitrogen atoms. Because the Cu^{2+} and Ni^{2+} xy basal planes are not coplanar [22], the magnetic orbitals centered on each metal ion are not expected to strongly overlap, which is consistent with the relatively weak exchange coupling parameter $J = -23.6\,cm^{-1}$, the doublet-quartet energy gap of $35.4\,cm^{-1}$ being equal to $3|J|/2$ (the spin Hamiltonian is expressed in the form $-J\boldsymbol{S}_A \cdot \boldsymbol{S}_B$).

The induced spin density in the doublet ground state [23] represented in Fig. 1 with high density levels, shows a strong positive spin density on the Ni^{2+} ion and a weak negative density on Cu^{2+}, reflecting the antiferromagnetic nature of the intramolecular coupling [24]. The low density levels of Fig. 1 gives evidence for a positive spin transfer from the nickel ion towards the oxygen atoms outside of the bridge (the O3 and O6 atoms are superimposed onto Ni) together with a negative transfer from the copper ion towards the nitrogen atom N5, but no spin density appears on the bridging oxygen atoms. The corresponding spin populations are listed in Table 1. The sum of these populations amounts 1.13 μ_B which is in good agreement with the experimental magnetization close to saturation of 1.15 $\mu_B\,mol^{-1}$ at 2 K and under 5 Tesla [25].

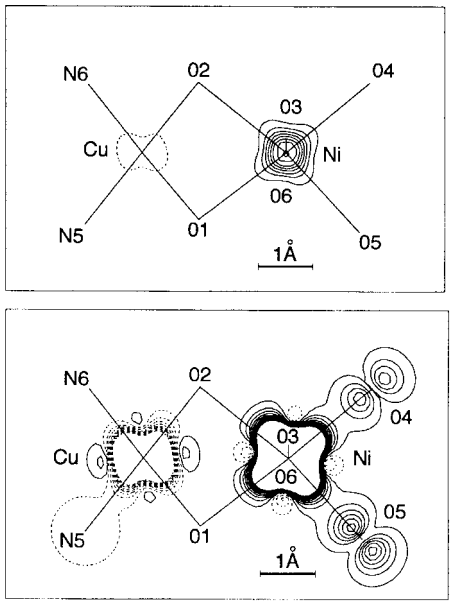

Fig. 1. Induced spin density map for Cu(salen)Ni(hfa)$_2$ at 2 K under 5 Tesla integrated along the Ni–O6 direction. The solid lines represent positive levels and dashed lines are negative levels. Top: high levels lines 0.2 μ_B Å^{-2} by steps of $\pm 0.4\,\mu_B$ Å^{-2}. Bottom: low-level lines 0.005 μ_B Å^{-2} in steps of $\pm 0.010\,\mu_B$ Å^{-2}

Table 1. Experimental (from PND) and calculated spin populations (in μ_B) using the (Heitler–London + Extended Hückel) method (H.L. + E.H.) for the $Cu^{II}Ni^{II}$ compound in the doublet ground state

Atom	PND	H.L. + E.H.
N5	−0.017(11)	−0.023
N6	−0.003(10)	−0.022
Cu	−0.250(10)	−0.285
O1	0.006(10)	0.002
O2	−0.003(10)	0.008
Ni	1.259(11)	1.288
O3	0.039(9)	0.032
O4	0.027(9)	0.025
O5	0.039(9)	0.034
O6	0.034(9)	0.039

The most striking feature of this map lies in the almost zero spin population found on the bridging oxygen atoms, within the experimental uncertainty (0.010 μ_B), in contrast with the nonbridging oxygen atoms bonded to nickel, which carry about 0.035(9) μ_B each.

A theoretical calculation of the spin density has been performed in the frame of the electron active model. Only the unpaired electrons in the magnetic orbitals centered on each metallic ion are taken into account in this approach, i. e. the spin delocalization mechanism alone is implied. Two magnetic orbitals originate from the $3d_{x^2-y^2}$ and $3d_{z^2}$ orbitals of Ni^{2+} and one from the $3d_{x^2-y^2}$ of Cu^{2+}. The magnetic

orbitals are determined by semi-empirical extended-Hückel calculations using the contracted orbital method [23]. The component $M_S = 1/2$ of the molecular doublet wave function $\psi_{1/2,1/2}$ is then built in the Heitler-London formalism for the system of antiferromagnetically coupled local spins ($S_{Ni^{2+}} = 1$, $S_{Cu^{2+}} = 1/2$) on the basis of the three magnetic orbitals a_1, a_2 and b, centered on nickel and copper, as given by Eq. (1):

$$\psi_{\frac{1}{2},\frac{1}{2}} = \frac{2}{\sqrt{6}}\left|a_1(1)a_2(2)\bar{b}(3)\right| - \frac{1}{\sqrt{6}}\left|\bar{a}_1(1)a_2(2)b(3)\right| - \frac{1}{\sqrt{6}}\left|a_1(1)\bar{a}_2(2)b(3)\right| \quad (1)$$

The spin populations p_i are calculated from the populations P_{ki} of atom i in the magnetic orbitals k by use of Eq. (2):

$$p_i = g_{\frac{1}{2}}\left[\frac{1}{3}P_{a_1 i} + \frac{1}{3}P_{a_2 i} - \frac{1}{6}P_{bi}\right] \quad (2)$$

where the g-factor is equal to 2.30.

As is apparent from Table 1, the experimental spin distribution is remarkably described in this approach, including the very weak spin populations on the bridging oxygen atoms. This allows us to the conclude that the positive spin density delocalized from the Ni^{2+} ion towards the bridging atoms is almost cancelled by the negative spin transferred from copper, although the Cu^{2+} moment is much smaller than the Ni^{2+} one, due to the strong covalent character of the Cu^{2+}–ligand interaction. This result confirms that the spin delocalization mechanism, which allows for the overlap between the copper and nickel magnetic orbitals, is responsible for the antiferromagnetic intramolecular interaction in this compound.

11.2.2 Extended Bridge in a $Mn^{II}Cu^{II}$ Dimer

Extended bisbidendate bridges such as oxamato, oxamido and other related bridges are the magnetic couplers which are the most widely used in molecular magnetism. One of the first molecular-based ferromagnetic compounds to be synthesized was an oxamato-bridged $Mn^{II}Cu^{II}$ system [26]. The spin distribution on such an extended bridge has been determined for the oxamido-bridged molecular compound $[Mn^{II}(cth)Cu^{II}(oxpn)](CF_3SO_3)_2$, where cth = ($Me_6$-[14]ane-$N_4$) and oxpn = *N*,*N*′-bis(3-aminopropyl)oxamido) [27]. The Mn^{2+} ion ($S_A = 5/2$) is surrounded by the two oxygens of the bridge and four external nitrogen atoms building a distorted octahedra. The square planar Cu^{2+} ($S_B = 1/2$) environment is formed by four nitrogen atoms, two of them belonging to the bridge. The coplanarity between *xy* basal planes of both transition ions and the oxamido plane, as well as the unsaturated character of the oxamido bridge favor antiferromagnetic coupling, which is characterized by a non-negligible coupling constant *J* of $-31.3\ cm^{-1}$ [28] although the distance between the ions is equal to 5.44 Å.

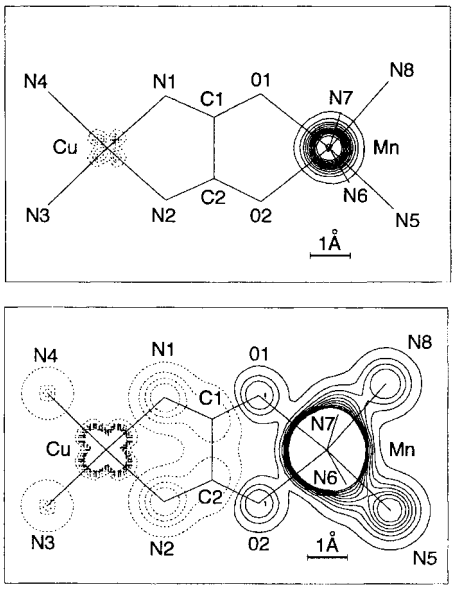

Fig. 2. Induced spin density map for $[Mn(cth)Cu(oxpn)](CF_3SO_3)_2$ at 2 K under 5 Tesla, integrated along the perpendicular to the oxamido mean plane. Same levels as in Fig. 1 (top: high levels, bottom: low levels)

Table 2. Atomic spin populations (in μ_B) for the $Mn^{II}Cu^{II}$ pair compound in the ground state ($S = 2$) from PND experiment and (H.L. + E.H.) calculations. DFT calculations are reported for the dimer $[Mn^{II}(cth)Cu^{II}(oxpn)]^{2+}$ ($S = 2$) and for the $[Cu^{II}(oxpn)]$ precursor

	PND	H.L.+E.H.	DFT	
			$[Mn^{II}(cth)Cu^{II}(oxpn)]^{2+}$	$[Cu^{II}(oxpn)]$
N_{ax}	0.07(1)	0.02	0.03	
N_{eq}	0.07(1)	0.02	0.02	
Mn	4.32(2)	4.47	4.41	
O	0.03(1)	0.05	0.02	−0.09
C	−0.03(1)	0.00	0.00	0.01
N	−0.05(1)	−0.12	−0.08	−0.15
Cu	−0.47(1)	−0.36	−0.27	−0.38
N	−0.02(1)	−0.02	−0.06	−0.06

The induced spin density maps in the quintet ground state ($S = 2$) shown in Fig. 2 visualize the spin delocalization over the whole molecule $[Mn(cth)Cu(oxpn)]^{2+}$: a region of strong positive spin density is observed on and around manganese, while negative spin resides on copper and its surroundings [29a]. The opposite signs of the spin densities associated to each magnetic center reflects the intramolecular negative coupling. The experimental populations are reported in Table 2 [29b]. The delocalization from the Cu^{2+} ion towards its first neighbors represents 30% of the total negative population while the spin transfer from Mn^{2+} amounts to only 7% of the total positive population. This again is a sign of the large covalent character of copper-ligand bonds.

The application of the Heitler-London formalism to the system of antiferromagnetically coupled local spins ($S_{Mn^{2+}} = 5/2$, $S_{Cu^{2+}} = 1/2$) leads to Eq. (3) of the $M_S = 2$ component of the wave function $\psi_{2,2}$ for the ground state $S = 2$, where a_1, a_2, a_3, a_4, a_5 are the five magnetic orbitals centered on manganese and b is the magnetic orbital centered on copper:

$$\psi_{2,2} = \sqrt{\frac{5}{6}}\,|a_1a_2a_3a_4a_5\bar{b}| - \sqrt{\frac{1}{30}}\,[|\bar{a}_1a_2a_3a_4a_5b| + |a_1\bar{a}_2a_3a_4a_5b| + |a_1a_2\bar{a}_3a_4a_5b| + |a_1a_2a_3\bar{a}_4a_5b| + |a_1a_2a_3a_4\bar{a}_5b|] \quad (3)$$

The spin populations p_i are then obtained from the populations P_{ki} of atom i in the magnetic orbitals k deduced from extended-Hückel calculations on a model molecule [27]:

$$p_i = g_2\left[\frac{7}{15}\left(P_{a_1i} + P_{a_2i} + P_{a_3i} + P_{a_4i} + P_{a_5i}\right) - \frac{1}{3}P_{bi}\right] \quad (4)$$

where the Zeeman factor g_2 is equal to 2.

The resulting populations reported in Table 2 are in relatively good agreement with the experimental spin distribution. No spin populations due to spin delocalization appear on the central carbon atoms.

DFT calculations were also performed, using the Dgauss program with a DZVP basis set (double-zeta split valence plus polarization). The DFT single determinant wave-function corresponding to the configuration with five unpaired electrons with spin up on Mn^{2+}, opposite to the unpaired spin on Cu^{2+}, is not an eigenstate of S^2, that is why the so-obtained state is called a broken symmetry (BS) state. The theoretical map for the BS state presented in Fig. 3 gives evidence for p_σ delocalized spin densities on the nitrogen atoms linked to copper while the spin density on the oxygen and nitrogen atoms surrounding manganese possess both p_σ and p_π characters. The DFT populations given in Table 2 for the dimer were corrected in order to reconstruct the $S = 2$ spin distribution from the BS spin distribution [27].

In the same table, the DFT results for the precursor Cu^{II}[oxpn] are reported, after changing all the signs for comparison with the pair compound in which the copper carries a negative spin population. The formation of molecular orbitals involving

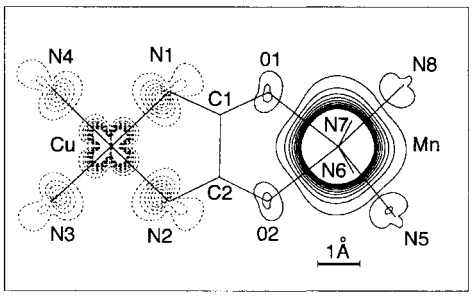

Fig. 3. Theoretical spin density map for the MnCu pair compound from DFT calculations. Same integration as in Fig. 2. Only the low levels lines are drawn: 0.005 μ_B Å^{-2} in steps of $\pm$0.010 μ_B Å^{-2}

the Cu^{2+} $3d_{x^2-y^2}$ orbital and the σ ligand atomic orbitals leads to a substantial delocalization of σ-symmetry on the nitrogen atoms as well as on the oxygen atoms at the extremities of the oxamido group [30]. The small positive population which can be noticed on the carbon atoms, is due to the spin polarization of the p_π carbon orbital, with a sign opposite to the sign of the Cu^{2+} population.

The comparison between the spin distributions in the Cu^{2+} precursor and the dimer shows that contributions of opposite signs arising from Mn^{2+} add to the populations on the O, C and N atoms of the bridge originating from Cu^{2+}. On the carbon atoms both contributions compensate in the calculated distribution, in contrast with the experimental distribution. The negative sign observed on the carbon atoms can then be attributed to a dominating negative spin polarization effect due to Mn^{2+}.

The strong delocalization at long distance from Cu^{2+} towards the bridge, due to the unsaturated nature of the oxamido group, is responsible for the strong overlap between the copper and manganese magnetic orbitals, giving rise to an antiferromagnetic coupling between the copper and manganese ions.

11.3 From a Molecule to a Chain of Antiferromagnetically Coupled $Mn^{II}Cu^{II}$ Ions

As pointed out in the previous section, the ground state of a pair of antiferromagnetically coupled ions with different spins S_A and S_B cannot be described by a single determinant wave function. The ground state wave function is expressed as a linear combination of determinants corresponding to different spin configurations as shown by Eq. (3) for a system of antiferromagnetically coupled spins (5/2, 1/2).

The spin populations P_A and P_B for a pair of local spins (5/2, 1/2) in the quintet ground state calculated from Eq. (4), are equal to:

$$P_A = 7\frac{g_2}{3} = 4.67 \quad \text{and} \quad P_B = -\frac{g_2}{3} = -0.67 \tag{5}$$

They differ from +5 and −1, because of the mixing of the spin configurations in the ground state wave function (Eq. 3).

The experimental populations associated to the manganese site and to the copper site in the $Mn^{II}Cu^{II}$ pair compound can be taken as the sum of the spin populations of the metallic ions and their first neighbors listed in Table 2, in order to take into account the spin delocalization towards the ligands. The so-obtained populations, equal to $4.67(8)\,\mu_B$ for the manganese site and $-0.67(8)\,\mu_B$ for the copper site, agree remarkably well with the calculated populations P_A and P_B given by Eq. (5).

When the number of coupled AB ions increases, the relative weights of the spin configurations in the ground state wave function change and the spin distribution is modified. What is the spin distribution that is reached when the number of AB units becomes infinite in a ferrimagnetic chain of alternating AB ions? To answer this question, the evolution of the spin distribution from a pair of antiferromagnet-

ically coupled ions to a ferrimagnetic chain, has been investigated for the system (Mn^{II}, Cu^{II}), with help of the combined spin density determinations in the isolated oxamido-bridged $Mn^{II}Cu^{II}$ molecular compound [27] (see previous section) and in the oxamato-bridged ferrimagnetic chain compound $Mn^{II}Cu^{II}(pba)(H_2O)_3.2H_2O$, with pba = 1,3-propylenebis(oxamato) [31].

The oxamato and oxamido bridge are very similar, one oxygen atom in the oxamato group replacing one nitrogen atom in the oxamido group. However, the Cu^{2+} environment is square pyramidal, due to the coordinated water molecule, in the chain compound, instead of square planar as in the molecule, which leads to a non-planar bridging network along the chain. The spin density maps projected along the perpendicular to the bridge for the chain compound in Fig. 4 and the molecule in Fig. 2 display very similar features [32a], i. e. the positive region of spin density on and around manganese, the negative spin density on and around copper and the weak negative spin densities on the carbon atoms of the bridge. The experimental spin populations in the chain compound are reported in Table 3 [32b]. No significant population was found on the oxygen belonging to the water molecule coordinated to copper.

The spin density is more localized on the metal ions in the chain than in the molecule: the Mn^{2+} ion carries 97.6% of the total positive spin density in the chain instead of 92.5% in the molecule and the Cu^{2+} population amounts 76.0% of the total negative spin instead of only 70.1% in the molecule. A point of note is that, in the oxamato bridge, the spin delocalization from copper towards the oxygen atom O_3 ($-0.05(1)\ \mu_B$) is smaller than that towards the nitrogen atom N1 ($-0.08(1)\ \mu_B$), which reflects the less covalent character of the Cu–O bond with respect to the Cu–N bond. The weaker spin delocalization in the oxamato-bridged compound with respect to

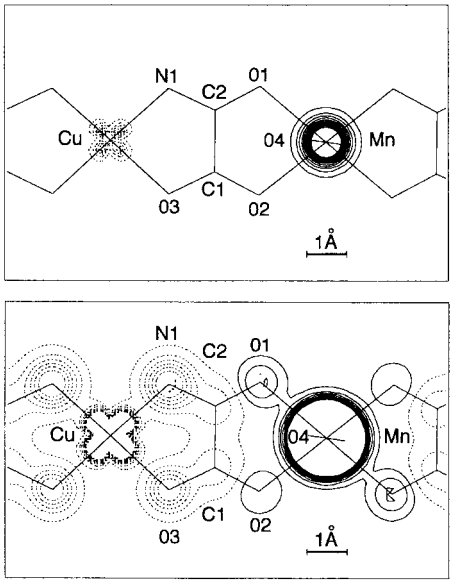

Fig. 4. Induced spin density map for $MnCu(pba)(H_2O)_3.2H_2O$ at 10 K under 5 Tesla integrated along the perpendicular to the oxamato mean plane. Same levels as in Fig. 1 (top: high levels, bottom: low levels)

Table 3. Atomic spin populations (in μ_B) for the $Mn^{II}Cu^{II}$ ferrimagnetic chain compound from polarized neutron diffraction and DFT(DMol-DSolid) calculations

Atom	PND	DFT
O4	0.02(1)	0.03
Mn	4.93(3)	4.56
O1	0.02(1)	0.02
O2	0.01(1)	0.02
C1	−0.03(2)	0.0
C2	−0.03(1)	0.0
N1	−0.08(1)	−0.08
O3	−0.05(1)	−0.07
Cu	−0.75(2)	−0.42
O5	0.01(2)	0.0

the oxamido-bridged one can be explained by the noncoplanarity between the Cu^{2+} xy basal plane and the oxamato plane, which reduces the spin delocalization from the $3d_{x^2-y^2}$ orbital towards the oxamato group as well as the overlap between the copper and manganese magnetic orbitals. The weaker delocalization on the oxamato bridge is directly correlated to the smaller value of the J parameter ($J = -23.4\,cm^{-1}$) [33] in comparison with the oxamido bridge ($J = -31.3\,cm^{-1}$).

The most striking difference between the chain and the molecular compound concerns the sum of the spin populations on each metal and its neighbors, 5.05(7) μ_B for the manganese site and −1.05(10) μ_B for the copper site for the chain, compared to 4.67(8) μ_B and −0.67(8) μ_B in the dimer.

DFT calculations performed for the chain compound using the DMol-DSolid program, which takes into account periodic boundary conditions, are reported in Table 3. While the DFT calculations agree relatively well with the experiment for the pair compound, the sum of the populations associated to the manganese and copper sites in the chain, equal to 4.72 and −0.72, are largely underestimated.

A quite different approach has been followed on an other side, in order to study the evolution of the spin distribution from the pair of antiferromagnetically coupled spins to the ferrimagnetic chain, using the DMRG (Density Matrix Renormalization Group) method [30]. This method originating in theoretical physics was revealed to be very successful for one-dimensional Heisenberg systems. The Hamiltonian for a chain of alternating spins S_A and S_B is given in Eq. (6):

$$H = -J \sum_{i} [S_{A,i} \cdot S_{B,i} + S_{B,i} \cdot S_{A,i+1}] \tag{6}$$

where J is the exchange coupling constant and the total number of sites is equal to $2N$, i. e. the number of AB units is equal to N. The properties of a long chain of $2N$ sites are reconstructed following an iterative process starting from a small system of $2n$ sites and adding two sites in the middle at each step [34].

The spin populations calculated by the DMRG method for a ferrimagnetic chain $(AB)_N$ of local spins S_A and $S_B = 1/2$ are reported in Table 4 for increasing values of S_A from 1 to 5/2 together with the spin populations obtained by exact diagonalization

Table 4. Spin populations for the A and B ($S_B = 1/2$) sites in the antiferromagnetically coupled pair (from exact diagonalization) and in the chain calculated by the DMRG method for increasing S_A values from 1 to 5/2. The experimental spin populations (in μ_B) from PND associated to the manganese ($S_{Mn^{2+}} = 5/2$) and copper ($S_{Cu^{2+}} = 1/2$) sites in the (Mn^{II}, Cu^{II}) pair and chain compounds are reported for comparison

S_A	S_B	Pair		Chain	
		P_A	P_B	P_A	P_B
1	1/2	1.333	−0.333	1.586	−0.586
3/2	1/2	2.500	−0.500	2.715	−0.715
2	1/2	3.600	−0.600	3.781	−0.781
5/2	1/2	4.667	−0.667	4.821	−0.821
(Mn^{II}, Cu^{II}) PND [27, 31]		4.67(8)	−0.67(8)	5.05(7)	−1.05(10)

of the Hamiltonian for a pair AB. The DRMG calculations demonstrate that for the chain $(AB)_N$, the spin population P_B becomes closer to −1 than in the pair; they also show that when S_A is larger, P_B becomes closer and closer to −1. The comparison of the calculated and experimental populations for the ($Mn^{II}Cu^{II}$) system reported in Table 4 shows that the DMRG method provides a rationalization of the evolution of the experimental populations from the pair to the chain.

11.4 Ferromagnetic Coupling in Copper(II) Dimers

Copper(II) dimers constitute the most extensively studied class of dinuclear compounds because they provide the simplest model for investigating the magnetic exchange interaction between transition metal ions, due to the presence of only one unpaired electron on each Cu^{2+} ion. Most of them are antiferromagnetically coupled, which is why the better understanding of the ferromagnetic coupling in the triplet ground states of one di-μ-hydroxo- and one di-μ-azido copper(II) dimer through spin density determinations, is particularly important.

11.4.1 Di-μ-hydroxo Bridged Dimer $Cu(OH)_2Cu$

The correlation between the nature of the magnetic coupling and the geometry of the bridging network in planar di-μ-hydroxo-bridged copper(II) dimers has been known for a long time. The first established empirical linear relationship between the exchange coupling constant J and the bridging angle α = (Cu–O–Cu) [35], shows that the intramolecular interaction is antiferromagnetic for α larger than $\alpha_0 = 97.5^\circ$ and ferromagnetic for smaller values of α, close to 90°. The geometrical dependence of J has been latter rationalized in the electron active approximation [14], involving the magnetic orbitals centered on each copper formed by the linear combination

of the $3d_{x^2-y^2}$ copper orbital and the $2p_\sigma$ orbitals on the bridging oxygen atoms and external ligand atoms. Only spin delocalization effects are accounted for in this approach. The arrival at a ferromagnetic coupling for $\alpha = \alpha_0$ close to 90° in that case is attributed to the "accidental orthogonality" of the magnetic orbitals.

The di-μ-hydroxo-bridged Cu^{II} dimer, $[(H_2O)(bipy)Cu(OH)_2Cu(bipy)(OSO_3)] \cdot 4H_2O$, with bipy = 2,2′bipyridine, characterized by a Cu···Cu distance of 2.9 Å and an angle α equal to 94°, takes place in the ferromagnetic-coupling range, with a singlet–triplet splitting of $49\,cm^{-1}$ [36]. The spin density model map [36] represented in Fig. 5 with logarithmic levels of isodensity, gives evidence for a $3d_{x^2-y^2}$ shape of the density on the copper atoms and a positive spin transfer onto the bridging oxygen atoms and onto the external nitrogen atoms [37]. The associated spin populations are respectively equal to 0.847(5)/0.810(5) μ_B on Cu(1)/Cu(2), 0.094(4)/0.121(4) μ_B on the bridging oxygen atoms O(1)/O(2) and 0.008(5) to 0.045(6) μ_B on the external nitrogen atoms. This spin distribution is consistent with a spin delocalization model, in which the positive population of the bridging oxygen atoms results from the sum of the positive spin contributions transferred from both copper ions. However the model map in Fig. 5 exhibits regions of negative spin density "behind" the oxygen atoms which cannot be interpreted by the spin delocalization only, but would imply some spin polarization effects.

Most of the theoretical ab initio studies on di-μ-hydroxo-bridged Cu^{II} dimers were dedicated to the calculation of the J coupling constant and its dependence upon the Cu···Cu distance, Cu–O–Cu angle and out-of-plane displacement of the H atom of the hydroxo group [38,39]. The calculated spin distribution for the related compound $[(bipy)Cu(OH)_2Cu(bipy)](NO_3)_2$ in the triplet state by DFT using the hybrid B3LYP method [39], qualitatively agrees with the above experimental distribution and no theoretical evidence for spin polarization in the bridging region was found [40]. These features confirm the spin delocalization mechanism for interpreting the ferromagnetic coupling in this compound [11].

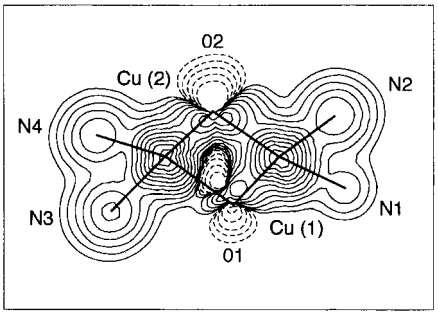

Fig. 5. Projection of the spin density along the c-axis in $[(H_2O)(bipy)Cu(OH)_2Cu(bipy)(OSO_3)] \cdot 4H_2O$ (from Ref. [36]). The contours are $\pm 2^n \times 10^{-3}$ e $Å^{-3}$ for $n = 1$ to 11 (the zero line is not drawn)

11.4.2 Di-μ-azido Bridged Copper Dimer $Cu(N_3)_2Cu$

The azido bridge N_3^- occupies a particular place in the large variety of organic bridges used in molecular magnetism. For all the symmetrical di-μ-azido copper(II) dimers synthesized up to now, either a strong ferromagnetic coupling, or alternatively a strong antiferromagnetic coupling occurs, depending on the way in which both azido groups are bridging, either in an "end-on" (μ-1,1-) or an "end-to-end" (μ-1,3-) fashion.

Until recently a long controversy had developed concerning the origin of the strong ferromagnetic coupling in "end-on" bridged di-μ-azido copper(II) dimers. The two principal mechanisms which were invoked are:

- the pure spin polarization mechanism [41], which implies the presence of negative spin density on the bridging atoms and predicts a ferromagnetic coupling whatever the bridging angle is,
- the spin delocalization mechanism, in a similar way to the di-μ-hydroxo-bridged copper(II) dimers. A magic angle of 108° was suggested, above which antiferromagnetic coupling should occur, from experimental data on copper dimers containing one azido bridge associated to another type of bridge [42].

Because these two mechanisms predict contradictory signs for the spin density on the bridging nitrogen atoms, the experimental spin density determination provides a deciding test for discriminating them.

The spin density in the triplet ground state of $[Cu_2(t\text{-Bupy})_4(N_3)_2](ClO_4)_2$, with ($t$-Bupy = *p-tert*-butylpyridine) is represented in Fig. 6 [43,44a]. The corresponding atomic spin populations are given in Table 5. The spin is mainly localized on the copper ions but positive spin density on the bridging and terminal nitrogen atoms of the azido bridge is observed as well as on the nitrogen atom of the pyridine rings. The positive sign on the bridging nitrogen atom N1 definitely rules out the spin polarization mechanism [44b] and demonstrates that the spin distribution is mainly

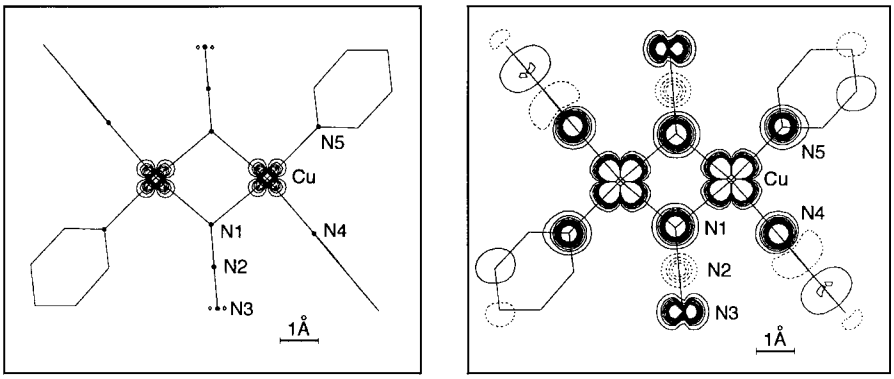

Fig. 6. Induced spin density projection for $[Cu_2(t\text{-Bupy})_4(N_3)_2](ClO_4)_2$ along a perpendicular to the (Cu–N1–Cu′) plane at 1.6 K under 4.6 Tesla. Same levels as in Fig. 1 (left: high levels, right: low levels)

Table 5. Spin populations (in μ_B) in the triplet ground state of $[Cu_2(t\text{-Bupy})_4(N_3)_2](ClO_4)_2$ from PND (normalized to $2\,\mu_B$ per molecule) and from density functional calculations using a Mulliken population analysis

Atom	PND [43]	DFT [45a]
Cu	0.783(7)	0.60
N1	0.069(6)	0.14
N2	−0.016(6)	−0.04
N3	0.057(7)	0.12
N4	0.067(8)	0.09
N5	0.049(7)	0.09

due to a spin delocalization mechanism. However, the spin density map also reveals the existence of some negative spin density on the central nitrogen atom N2, which can be assigned to the spin polarization of the doubly-occupied azido bridge π_g type orbital, which is superimposed upon the spin delocalization mechanism.

Both Hartree-Fock and DFT calculations using different density functional forms have been reported in the literature for various di-μ-azido bridged compounds [43,45a,b]. The spin populations calculated by the DFT-B3LYP method using the Gaussian 94 program for the triplet ground state of $[Cu_2(t\text{-Bupy})_4(N_3)_2](ClO_4)_2$ [45a] are given in Table 5. This method predicts a singlet ground state for an angle α larger than 104° in agreement with the spin delocalization mechanism. The spin delocalization is overestimated as always in DFT calculations on copper-containing compounds, but the spin alternation on the azido bridge, due to spin polarization, is in agreement with the experiment.

The ferromagnetic coupling constant in the above di-μ-azido dimer is much stronger ($J = 105(20)\,cm^{-1}$) [41] than in the di-μ-hydroxo dimer described in the previous section ($J = 49\,cm^{-1}$) [46] although the (Cu–N–Cu) angle equal to 100° is larger than the corresponding (Cu–O–Cu) angle of 94°. The comparison between the experimental spin distributions in the two compounds indicates that the spin delocalization in the di-μ-azido dimer is slightly stronger than in the di-μ-hydroxo dimer, as reflected by the smaller spin population of copper in the di-μ-azido dimer. This feature can be related to the relative strength of the ferromagnetic interactions.

11.5 Ferromagnetic Chain Bimetallic Compound

Up to now, to the best of our knowledge, only one bimetallic compound forming ferromagnetic chains has been entirely characterized from both the structural and magnetic point of view [47]. The compound $MnNi(NO_2)_4(en)_2$ (with en = ethylenediamine) forms zigzag chains of alternating Mn^{II} and Ni^{II} ions bridged by a bidentate NO_2^- group. The two oxygen atoms of the bridging nitro group are linked to the manganese ion while the nitrogen atom is bonded to the nickel ion, with an intrachain

Mn···Ni distance of 4.817 Å. The Ni^{II} ion is surrounded by four nitrogen atoms originating from two ethylenediamine groups and by two NO_2^- bridging nitrogen atoms. An unusual coordination sphere is observed for the Mn^{II} ion, consisting of eight oxygen atoms, of which two nonbonding oxygen atoms are at a slightly larger distance than the other six.

The Mn^{II} and Ni^{II} ions are ferromagnetically coupled, with a weak intrachain positive coupling $J = 1.33\,cm^{-1}$, as deduced from the magnetic susceptibility data using the spin Hamiltonian $-J \sum_i S_{Mn,i} \cdot S_{Cu,i}$ [47]. At $T_N = 2.35\,K$, a long range antiferromagnetic ordering occurs between the chains. The compound is actually metamagnetic, with a threshold field of 0.12 Tesla.

Fig. 7 displays the induced spin density in projection perpendicular to the N1–Ni–N3 plane [48]. The unpaired spin on Ni^{2+} is found to be essentially located in the $3d_{x^2-y^2}$ and $3d_{z^2}$ orbitals. For Mn^{2+} the five 3d orbitals were assumed to be equally populated [49]. The respective sum of the Mn^{2+} and Ni^{2+} spin populations and their neighbors are equal to $4.85(8)\,\mu_B$ and $2.15(8)\,\mu_B$, close to the idealized values of $5\,\mu_B$ and $2\,\mu_B$ [50]. The quantity of spin transferred from Mn^{2+} to its neighbors only amounts to 7% of the moment associated to the manganese region, while the spin delocalization from Ni^{2+} represents 24% of the total moment on the nickel site, reflecting the stronger covalent character of the nickel than the manganese ion.

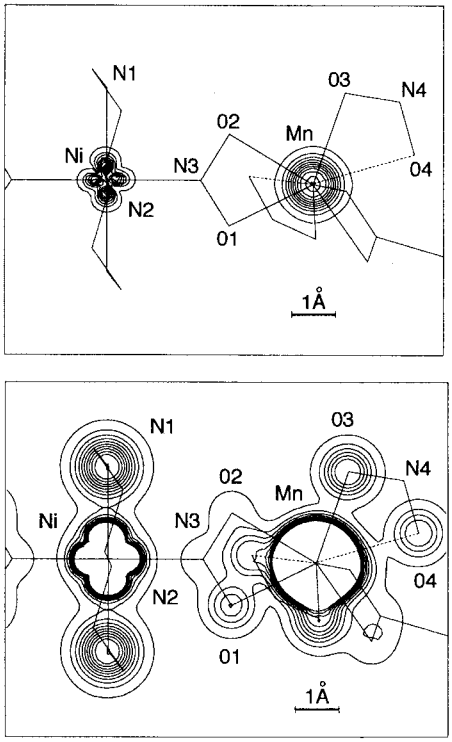

Fig. 7. Induced spin density integrated along the perpendicular to the N1-Ni-N3 plane in the ferromagnetic chain compound $MnNi(NO_2)_4(en)_2$ at 4 K under an applied field of 2 Tesla. Top: high levels lines. Bottom: low-level lines. Same levels as in Fig. 1

The amount of spin ($0.01(3)\,\mu_B$) carried by the bridging N_3 atom of the nitro group is significantly weaker than the moment found on each nitrogen atom of the ethylenediamine groups, N1 ($0.16(3)\,\mu_B$) and N2 ($0.09(3)\,\mu_B$). The spin populations of the oxygen atoms surrounding Mn^{2+} are not so contrasted and range from 0.01(2) to $0.08(2)\,\mu_B$, with slightly smaller values on both oxygen atoms of the bridge O1 and O2 than on the O3 and O4 atoms of the nonbridging NO_2^- groups.

The study of the spin delocalization in $Ni(NH_3)_4(NO_2)_2$ [4] gives evidence of a spin transfer of around $0.10\,\mu_B$ on the nitrogen atom of the nitro group from the Ni^{2+} ion, which carries about $2\,\mu_B$. This is the same order of magnitude as the moment transferred onto the ethylenediamine nitrogen atoms, but ten times more than the moment on the bridging nitrogen atoms. The apparent absence of spin transfer from Ni^{2+} towards the nitrogen atom of the NO_2^- bridge in the chain compound remains quite puzzling. This feature is not reproduced by recent DFT calculations of a binuclear $Mn^{II}Ni^{II}$ model in the $S = 7/2$ state, for which equivalent populations are found on all the nitrogen atoms linked to Nickel [51].

11.6 Clusters

Magnetic molecular clusters are formed by a large number of transition metal ions, strongly coupled through organic bridges. They have attracted much attention over recent years, particularly because they constitute single molecule magnets of nanometer size, each isolated from the others in the crystal and may be characterized by a strong Izing type anisotropy. Because the size of the clusters is intermediate between simple paramagnetic molecules and a bulk material, they may present both quantum mechanical and classical magnetic behaviors.

Magnetic measurements and ESR studies allow one only to propose a model for the configuration of the magnetic ground state of the cluster, resulting from the competition between various intra-cluster antiferromagnetic interactions. In contrast, PND allows one to determine the distribution of the spins in the ground state of large clusters without any ambiguity.

11.6.1 Mn_{12} Cluster

The paramagnetic Mn_{12} cluster, $Mn_{12}O_{12}(CH_2COO)_{16}(H_2O)_4{\cdot}2CH_3COOH{\cdot}4H_2O$ is formed by twelve manganese ions, of which eight are Mn^{III} ions ($S = 2$) and four are Mn^{IV} ions ($S = 3/2$), linked by oxo and carboxylato bridges. This cluster has been extensively studied, by various techniques: X-ray diffraction, magnetic measurements, ESR, inelastic neutron scattering [52], which have elucidated the spin structure of the magnetic ground state $S = 10$. The cluster is characterized by a strong magnetic anisotropy along the tetragonal c-axis.

A tentative method using unpolarized neutron diffraction on a deuterated powder sample was applied to determine the spin distribution in this cluster as no single

crystal of sufficient size was available [53]. This method could offer an alternative to the p.n.d. technique in the case of strongly magnetic materials where no large single crystals are available. The principle of this method is to measure the neutron diffraction pattern of the powder sample in which the magnetic moments are aligned by an applied magnetic field at low temperature [54] and then to subtract the purely nuclear spectrum obtained in zero-field at the same temperature, to yield the magnetic powder pattern. The model refinement based on the analysis of this diagram confirms the configuration proposed for the magnetic ground state $S = 10$ with positive magnetic moments on the eight Mn^{III} ions and negative moments on the four Mn^{IV} ions, but leads to unrealistic negative spin populations on the bridging ligands.

11.6.2 Mn_{10} Cluster

The first precise spin density study on a large cluster was realized by PND on the Mn_{10} cluster, $[Et_3NH]_2[Mn(CH_3CN)_4(H_2O)_2][Mn_{10}O_4(biphen)_4Br_{12}]$ [55]. A spin ground state $S = 12$ was proposed from magnetization measurements and ESR studies. The cluster exhibits a strong anisotropy, with the easy magnetization axis being the c-axis which is also a tetragonal symmetry axis. The structure of the cluster is schematized in Fig. 8. Six Mn^{II} ions ($S = 5/2$) occupy the Mn(1) and Mn(2) sites while four Mn^{III} ions ($S = 2$) lie in the Mn(3) sites. The metallic ions are bridged by oxo and bromide ligands. The maximum entropy reconstruction of the spin density represented in Fig. 8, in projection along the c-axis, gives evidence of isotropic spin distributions on the Mn^{II} ions and elongated shapes on the Mn^{III} ions, reflecting the local anisotropy of the $3d^4$ high spin ion. The negative spin density located on the site Mn(1) reveals a ferrimagnetic arrangement, with spins on the two Mn^{II} ions in

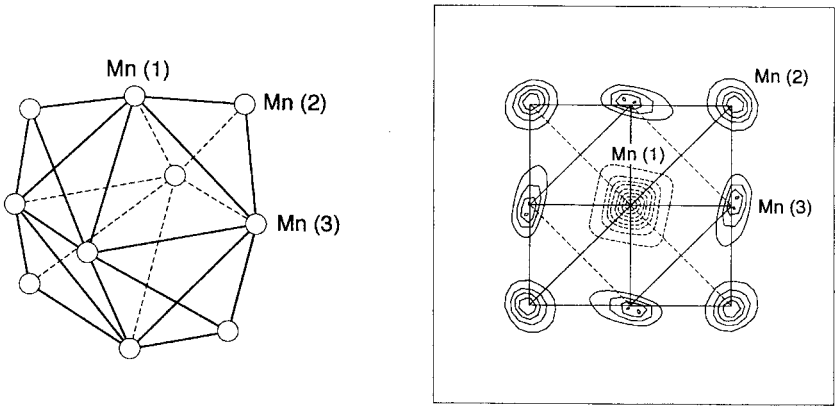

Fig. 8. Left: structure of the Mn_{10} cluster. Right: maximum entropy reconstruction of the induced spin density in the Mn_{10} cluster at 10 K in projection along the c-axis from reference [54]. A field of 4.8 Tesla was applied along the easy magnetization c-axis

Mn(1) sites opposite to the spins on the other Mn^{II} and Mn^{III} ions. The spins appear to be strongly localized on the metallic ions as no significant spin density is observed on the ligands, contrary to the results obtained on the Mn_{12} cluster.

11.6.3 Fe_8 Cluster

The Fe_8 cluster, $\{[Fe_8O_2(OH)_{12}(tacn)_6]Br_7 \cdot H_2O\}[Br.8H_2O]$, (with tacn = 1,4,7-triazacyclononane) [56], has attracted special attention in recent years as displaying pure quantum tunneling of the magnetization [57]. Another interesting feature is the strong magnetic anisotropy of the cluster, although each Fe^{III} ion ($S = 5/2$) is individually isotropic. This cluster, formed by eight Fe^{III} ions linked by oxo and hydroxo bridges, has the well-known "butterfly" structure [56] used to describe tetranuclear clusters Fe_4O_2: the body of the butterfly is formed by the ions 1 and 2, and the extremities of the wings are defined by the ions 3 and 4 as can be seen on Fig. 9. Four peripheral iron atoms 5, 6, 7, 8 are connected to the sides of the wings. A model with six spin up and two spin down irons was proposed for the spin configuration of the magnetic ground state $S = 10$ from magnetic susceptibility measurements. The magnetization density [58], reconstructed by the Maximum entropy method applied to noncentrosymmetric structures [59], is drawn in Fig. 9. The spin density map confirms that six ions carry spins parallel to the applied field, which are the body ions 1 and 2 and the four peripheral ions, while the ions 3 and 4 of the wings carry opposite spins. Similar to the Mn_{10} cluster, the spin density is strongly localized on the metallic ions.

The examination of the structure allows one to draw the following conclusions – the dominating antiferromagnetic interactions take place between the ions 4 and 8, 1, 2, 6 (and similarly between 3 and 5, 1, 2, 7) which are joined by single μ-oxo bridges – the ions connected by double bridges carry parallel spins while the ions connected by single bridges carry opposite spins. For the single μ-oxo bridges, the

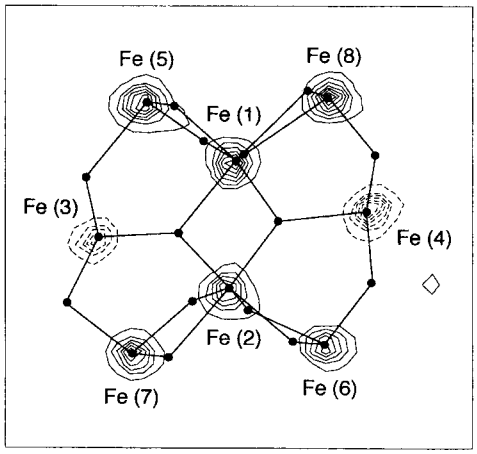

Fig. 9. Maximum entropy reconstructed induced magnetization density at 2 K under 4.6 Tesla projected onto the *bc* crystallographic plane of the Fe_8 cluster from reference [58]. Contours by steps of 0.7 μ_B $Å^{-2}$

Fe–O–Fe angles are larger (i. e. 128.8° for the 2–4 bridge) than for the double μ-oxo bridges (i. e. 96.8° for 1–2). The strength of the antiferromagnetic interaction then increases when the Fe–O–Fe angle increases, as already known for μ-oxo-bridged Fe^{III} binuclear compounds [60].

11.7 Conclusion

Experimental spin density maps, as given by polarized neutron diffraction, provide rich and detailed information about the spin ground state in magnetic molecular compounds: not only the visualization of the distribution in the space away from the metal ions which gives evidence for spin delocalization, but also the sign of the spin density which provides information on spin polarization. The spin density determination constitutes one of the best tests of a theoretical model for the mechanism of magnetic interaction between metal ions through an organic bridge. As a matter of fact, the spin density map alone has allowed us to definitely conclude the long controversy between the spin delocalization and the spin polarization mechanisms in the interpretation of the strong ferromagnetic coupling in "end-on" di-μ-azido copper dimers. In most of the compounds reported here, the spin delocalization mechanism is responsible for either antiferro- or ferromagnetic coupling but evidence of negative spin density regions shows that spin polarization is always subjacent.

It should be pointed out that the Heitler-London approach, using the magnetic orbital model, is remarkably convenient to describe the spin distribution in heterobimetallic compounds, in which the metal ions are antiferromagnetically coupled through di-μ-oxo bridges or extended bridges such as the oxamido bridge. However no spin polarization effect is accounted for in this approach. Density functional theory has proved to be very efficient to predict the spin distribution in the binuclear compounds reported here, either antiferro- or ferromagnetically coupled, and particularly the spin polarization effects on the bridge which can exist beside the dominating spin delocalization effect, even if this method systematically overestimates the spin delocalization for Cu^{II} complexes.

The density matrix renormalization group method allows one to rationalize the evolution of the experimental spin values associated to each magnetic ion, from an antiferromagnetically coupled dimer $Mn^{II}Cu^{II}$ to a ferrimagnetic chain. The DRMG calculations demonstrate that for a chain $(AB)_N$, with local spins S_A and $S_B = 1/2$, the spin population P_B is closer to -1 than in the pair AB, and that the spin population P_B in the chain is closer to -1 for larger S_A values.

An other interest of PND investigations for molecular-based magnetism is that the spin density map directly visualizes the arrangement of the spins in the ground state of polymetallic clusters which cannot be elucidated without ambiguity by other techniques.

Acknowledgments

The author expresses her gratitude to Professor O. Kahn, from the Institut de Chimie de la Matière Condensée de Bordeaux, who initiated most of the work on bimetallic compounds presented here and thanks him for many rich discussions. The author also sincerely thanks Dr J. Schweizer, from the Centre d'Etudes de Grenoble, for many helpful discussions.

References

[1] F. A. Wedgwood, *Proc. R. Soc. Lond.* **1976**, A *349*, 447.
[2] B. N. Figgis, P. A. Reynolds, G. A. Williams, *J. Chem. Soc. Dalton Trans.* **1980**, 2348.
[3] (a) G.S. Chandler, B. N. Figgis, R. A. Phillips, P. A. Reynolds, R. Mason, G. A. Williams, *Proc. R. Soc. Lond.* **1982**, A *384*, 31; (b) B. N. Figgis, P. A. Reynolds, R. Mason, *ibid.* **1982**, A *384*, 49.
[4] B.N. Figgis, P. A. Reynolds and R. Mason, *J. Am. Chem. Soc.* **1983**, *105*, 440.
[5] (a) B. N. Figgis, J. B. Forsyth, P. A. Reynolds, *Inorg. Chem.* **1987**, *26*, 101; (b) P. Day, C. D. Delfs, B. N. Figgis, P. A. Reynolds, F. Tasset, *Mol. Phys.* **1993**, *78*, 769.
[6] B. N. Figgis, P. A. Reynolds, J. B. Forsyth, *J. Chem. Soc. Dalton Trans.* **1988**, 117.
[7] (a) G. A. Williams, B. N. Figgis, R. Mason, *J. Chem. Soc. Dalton Trans.* **1981**, 734; (b) B. N. Figgis, G. A. Williams, J. B. Forsyth, R. Mason *ibid.* **1981**, 1837.
[8] In the case of MnPc which is the first known molecular ferromagnet ($T_C = 8.6\,K$) the spin distribution in the ferromagnetic state was determined.
[9] (a) B. E. F. Fender, B. N. Figgis, J. B. Forsyth, P. A. Reynolds, E. Stevens, *Proc. R. Soc. Lond.* **1986**, A *404*, 127; (b) B. E. F. Fender, B. N. Figgis, J. B. Forsyth, *ibid.* **1986**, A *404*, 139; (c) R. J. Deeth, B. N. Figgis, J. B. Forsyth, E. S. Kucharski, P. A. Reynolds, *ibid.* **1989**, A *421*, 153; (d) B. N. Figgis, J. B. Forsyth, E. S. Kucharski, P. A. Reynolds, F. Tasset, *ibid.* **1990**, A *428*, 113; (e) C. D. Delfs, B. N. Figgis, J. B. Forsyth, E. S. Kucharski, P. A. Reynolds, M. Vrtis, *ibid.* **1992**, A *436*, 417.
[10] (a) S. P. Best, B. N. Figgis, J. B. Forsyth, P. A. Reynolds, P. L. W. Tregenna-Piggott, *Inorg. Chem.* **1995**, *34*, 4605; (b) P. A. Reynolds, B. N. Figgis, J. B. Forsyth, F. Tasset, *J. Chem. Soc. Dalton Trans.* **1997**, 1447; (c) P. A. Reynolds, B. Moubarabi, K. S. Murray, J. W. Cable, L. M. Engelhardt, B. N. Figgis, *ibid.* **1997**, 263; (d) P. A. Reynolds, J. W. Cable, A. N. Sobolev, B. N. Figgis, *ibid.* **1998**, 559.
[11] J. Cano, E. Ruiz, S. Alvarez, M. Verdaguer, *Comments Inorg. Chem.* **1998**, *20*, 27.
[12] B. N. Figgis, E. S. Kucharski, M. Vrtis, *J. Am. Chem. Soc.* **1993**, *115*, 176.
[13] C. Kollmar, O. Kahn, *Acc. Chem. Res.* **1993**, *26*, 259.
[14] O. Kahn, in *Molecular Magnetism*, New York:VCH Publishers, Inc., **1993**.
[15] J. B. Forsyth, *Atomic Energy Review* **1979**, *172*, 345.
[16] The magnetization density is the sum of a pure spin contribution and an orbital contribution due to the interaction between the neutron magnetic moment and the magnetic field created by the unpaired electrons moving on their orbits. For metal-containing systems, the magnetization density is not identical to the spin density because of the orbital contribution (except in the case of systems with zero angular momentum like the Mn^{2+}

ion with half filled 3d shell). However for most of the transition metals ions like Cu^{2+} and Ni^{2+} the orbital moment is almost entirely quenched and the orbital contribution can be neglected or treated as a correction.
[17] R. J. Papoular, B. Gillon, *Europhys. Lett.* **1990**, *13*, 429.
[18] P. J. Brown, A. Capiomont, B. Gillon, J. Schweizer, *J. Magn. Magn. Mat.* **1979**, *14*, 289.
[19] J. N. Varghese, R. Mason, *Proc. R. Soc. Lond.* **1980**, A *372*, 1.
[20] E. Ressouche, thesis, Université J. Fourier, Grenoble (France), **1991**.
[21] B. N. Figgis, E. S. Kucharski, G. A. Williams, *J. Chem. Soc. Dalton Trans.* **1980**, 1515.
[22] The x, y, z axes are defined according to the metal-ligand bond directions for Cu^{2+} and Ni^{2+}.
[23] B. Gillon, C. Cavata, P. Schweiss, Y. Journaux, O. Kahn and D. Schneider, *J. Am. Chem. Soc.* **1989**, *111*, 7124.
[24] The spin density model was constrained to obey to the local symmetry of the Cu^{2+} and Ni^{2+} sites and the atomic densities on the terminal oxygen atoms were assumed to originate from p_σ-type orbitals. On all other atoms spherical densities were taken.
[25] The magnetization at saturation M (per mole), in $N\beta$ units (i. e. Bohr magneton units μ_B), is equal to $g_S S$, where S is the spin value, g_S is the Zeeman g-factor for the S state, N the Avogadro number and β the electronic Bohr magneton. For the $Cu^{II}Ni^{II}$ compound in the doublet ground state $S = 1/2$, $g_{1/2} = 2.30$ from the magnetic susceptibility data.
[26] O. Kahn, Y. Pei, M. Verdaguer, J. P. Renard, J. Sletten, *J. Am. Chem. Soc.* **1988**, *110*, 782.
[27] V. Baron, B. Gillon, O. Plantevin, A. Cousson, C. Mathonière, O. Kahn, A. Grand, L. Öhrström, B. Delley, *J. Am. Chem. Soc.* **1996**, *118*, 11822.
[28] The energy gap of $93.9\,cm^{-1}$ between the quintet ground state and the excited septet state is equal to $3|J|$ using the spin Hamiltonian $-J S_A S_B$.
[29] (a) The spin density was assumed to be spherical on all of the atoms excepted on Cu^{2+} for which the atomic density was constrained to originate from a $3d_{x^2-y^2}$ type orbital; (b) The experimental spin populations are normalized to $4\,\mu_B$ which is the magnetization at saturation for the ground state $S = 2$ taking g_2 equal to 2 (1.978 from the susceptibility data).
[30] O. Kahn, C. Mathonière, B. Srinavasan, B. Gillon, V. Baron, A. Grand, L. Öhrström, S. Ramashesha, *New J. Chem.* **1997**, *21*, 1037.
[31] V. Baron, B. Gillon, A. Cousson, C. Mathonière, O. Kahn, A. Grand, L. Öhrström, B. Delley, M. Bonnet, J. X. Boucherle, *J. Am. Chem. Soc.* **1997**, *119*, 3500.
[32] (a) The same type of spin density model as defined for the pair compound was taken for the chain compound; (b) The experimental spin populations are normalized to $4\,\mu_B$ per molecule.
[33] The spin Hamiltonian for the chain is written as $-J \sum_i (S_{Mn,i} \cdot S_{Cu,i} + S_{Mn,i+1} \cdot S_{Cu,i})$
[34] S. K. Pati, S. Ramashesha, D. Sen, *Phys. Rev. B* **1997**, *55*, 8894.
[35] W.H. Crawford, H.W. Richardson, J.R. Wasson, D.J. Hodgson, W.E. Hatfield, *Inorg. Chem.* **1976**, *15*, 2107.
[36] B. N. Figgis, R. Mason, A. R. P. Smith, J. N. Varghese, G. A. Williams, *J. Chem. Soc. Dalton Trans.* **1983**, 703.
[37] The multipole model includes multipoles up to hexadecapoles on copper and up to quadrupoles on oxygen. Spherical densities are taken for the nitrogen atoms.
[38] H. Astheimer, W. Haase, *J. Chem. Phys.* **1986**, *85*, 1427.
[39] E. Ruiz, P. Alemany, S. Alvarez, J. Cano, *Inorg. Chem.* **1997**, *36*, 3683; *J. Am. Chem. Soc.* **1997**, *119*, 1297.
[40] E. Ruiz, personal communication.
[41] S. Sikorav, I. Bkouche-Waksman and O. Kahn, *Inorg. Chem.* **1984**, *23*, 490.
[42] L. K. Thomson, S. S. Tandon, M. E. Manuel, *Inorg. Chem.* **1995**, *34*, 2356.

[43] M. A. Aebersold, O. Kahn, P. Bergerat, O. Plantevin, L. Pardi, B. Gillon, I. von Seggern, F. Tuczek, L. Öhrström, A. Grand and E. Lelièvre-Berna, *J. Am. Chem. Soc.* **1998**, *120*, 5238.
[44] (a) The best agreement with the experimental data was obtained for a model with constraints assuming a $3d_{x^2-y^2}$-type atomic density on copper and a p_z-type density for N_3. The density was assumed to be spherical for all other atoms. (b) The reconstruction of the spin density by the maximum of entropy method, i. e. without introducing any model, leads to the same conclusion about the sign of the bridging nitrogen spin population.
[45] (a) E. Ruiz, J. Cano, S. Alvarez, P. Alemany, *J. Am. Chem. Soc.* **1998**, *120*, 11122; (b) C. Adamo, V. Barone, A. Bencini, F. Totti, I. Ciofini, *Inorg. Chem.* **1999**, *38*, 1996.
[46] The spin hamiltonian being defined by $-J S_A S_B$, the triplet–singlet energy gap is equal to J.
[47] O. Kahn, E. Bakalbassis, C. Mathonière, M. Hagiwara, K. Katsumata and L. Ouahab, *Inorg. Chem.* **1997**, *36*, 1530.
[48] B. Gillon, *Mol. Cryst. and Liq. Cryst.*, **1999**, *335*, 53.
[49] Spherical densities were assumed for all atoms except Nickel, for which 3d orbital coefficients were refined.
[50] The refined spin populations are normalized to $7\,\mu_B$ for each MnNi unit which corresponds to a system of local spins $S_{Mn^{2+}} = +5/2$ and $S_{Ni^{2+}} = +1$, assuming a factor $g_{7/2} = 2$, instead of the experimental value of 2.07 deduced from the susceptibility data.
[51] E. Ruiz, S. Alvarez, B. Gillon, O. Kahn, to be published.
[52] A. Caneschi, D. Gatteschi, R. Sessoli, A. L. Barra, L. C. Brunel, M. Guillot, *J. Am. Chem. Soc.* **1991**, *113*, 5873; R. Sessoli, D. Gatteschi, A. Caneschi, M. Novak, *Nature* **1993**, *365*, 141; M. Hennion, L. Pardi, I. Mirebeau, E. Suard, R. Sessoli, A. Caneschi, *Phys. Rev. B* **1997**, *56*, 8819; I. Mirebeau, M. Hennion, H. Casalta, H. Andres, H. U. Güdel, A. V. Irodova, A. Caneschi, *ibid.* **1997**, *83*, 628.
[53] P. A. Reynolds, E. P. Gilbert, B. N. Figgis, *Inorg. Chem.* **1996**, *35*, 545.
[54] This method should be applied with caution in the case of a strongly anisotropic compound. It assumes that the magnetic moments in each grain of the powder are aligned along the easy magnetisation axis. This is valid if the easy axis is not far from the applied field direction, but not if it is nearly perpendicular to the field.
[55] A. Caneschi, D. Gatteschi, R. Sessoli, J. Schweizer, *Physica B* **1998**, *241–243*, 600.
[56] C. Delfs, D. Gatteschi, L. Pardi, R. Sessoli, K. Wieghard, D. Hanke, *Inorg. Chem.* **1993**, *32*, 3099.
[57] C. Sangregorio, T. Ohm, C. Paulsen, R. Sessoli, D Gatteschi, *Phys. Rev. Lett.* **1997**, *78*, 4645.
[58] Y. Pontillon, A. Caneschi, D. Gatteschi, R. Sessoli, E. Ressouche, J. Schweizer, E. Lelièvre-Berna, *J. Am. Chem. Soc.*, **1999**, *121*, 5342.
[59] P. Schleger, A. Puig-Molina, E. Ressouche, J. Schweizer, *Acta Cryst.* **1997**, A *53*, 426.
[60] F. Le Gall, F. Fabrizi de Biani, A. Caneschi, P. Cinelli, A. Cornia, A. C. Fabretti, D. Gatteschi, *Inorg. Chim. Acta* **1997**, *262*, 123.

Magnetism: Molecules to Materials I: Models and Experiments.
Edited by Joel S. Miller and Marc Drillon

ISBNs: 3-527-29772-3 (Hardback); 3-527-60084-1 (Electronic)

12 Probing Spin Densities by Use of NMR Spectroscopy

Frank H. Köhler

12.1 Introduction

In open-shell compounds the unpaired electrons are usually not concentrated at one or just a few atoms, regardless whether organic radicals, coordination compounds, organometallic molecules, or inorganic solids are concerned. Rather, there is a finite probability of finding the unpaired electrons at remote atoms of substituents, ligands, and counter ions. In other words, in molecule-based magnetic materials we are dealing with spin sources that give rise to spin density at various sites of a molecule in the lattice. How the spin density is transferred to these sites will be outlined below. Occasionally, the spin source is not well defined when the spin is equally distributed over the skeleton of a molecule like benzene radical anion and cation.

The appearance of spin density at sites other than the spin source is of paramount importance in materials because it is related to magnetic interaction. For instance, it has been known for long time that in di- and oligonuclear coordination compounds magnetic interaction is often mediated by *intramolecular* spin alignment. While the spin alignment energy of up to a few hundred cm^{-1} is much weaker than that of chemical bonds the alignment path follows the bonding skeleton, and hence, it is often regarded as *through-bond* interaction across the bridging ligands. Experimental evidence for this pathway, termed "superexchange" [1a], has been first presented for single diamagnetic ions intermediate between paramagnetic centers by Kramers and Becquerel et al. [1] while the theory has been developed by Anderson [2]. That some spin density can indeed be localized on lattice components originally introduced as diamagnetic species was first demonstrated by the EPR spectrum of $(NH_4)_2[IrCl_6]$ which did not only show the expected hyperfine interaction with the isotopes $^{191/193}Ir$ of the spin-1/2 metal center but also those with $^{35/37}Cl^-$ [3]. The concept of superexchange was soon introduced in transition metal chemistry where early examples are multi-atomic bridging ligands that mediate the magnetic interaction between copper(II) ions [4]. When the spin-transmitting ligands became larger the introduction of "magnetic orbitals" [5] proved useful for the understanding of magnetic interactions. Chemists are mainly using natural magnetic orbitals (as opposed to orthogonalized magnetic orbitals) which are defined as singly occupied orbitals of coupled fragments, each including a somewhat arbitrary number of atoms of the bridging ligand. A timely summary of this approach has been given by Kahn [6]. It is intuitively clear that the magnetic interaction modeled by combining magnetic orbitals will strongly depend on the sign and the amount of spin at the various atoms of the bridging

ligands. Any method that provides experimental spin density data would, therefore, be very helpful for understanding the mechanism(s) of magnetic interaction and for designing new magnetic materials derived from coordination compounds. The most popular approach in coordination chemistry for obtaining ferromagnetic interaction combines fragments [7] whose magnetic orbitals are orthogonal either by accident or by systematically choosing appropriate pairs of building blocks.

Spin alignment through bonds is an attractive topic in organic chemistry as well. Thus, numerous doublet (or higher multiplicity) radicals have been bridged or, in the organic chemist's language: linked by coupling units [8]. The basic features of ferromagnetic and antiferromagnetic coupling units are well understood. For instance, *m*-phenylene-bridged radicals usually afford ferromagnetic coupling whereas antiferromagnetic coupling results with *o*- and *p*-phenylene bridging. Nevertheless, there are exceptions where the expected ferromagnetic interaction could not be established [9] and where antiferromagnetic interaction has been found instead [10]. In these and other cases it would be very useful to know how the spin distribution in the coupling unit is modulated by steric and other constraints.

Another important general approach is based on *intermolecular* spin alignment. Since no additional bonding is present, it is also regarded as *through-space* interaction of spin densities at two (or more) radical centers held at short distance. For simplicity, a less strict meaning of through-space interaction is accepted here, which includes very weak hydrogen bonds (typically below 6 kJ mol^{-1} or about 500 cm^{-1}). This approach has been realized in solid organic radicals, mostly nitronyl nitroxides [7a,b,c,e,f,8f,11], by suitably stacking triplet-carbene-substituted benzenes in a paracyclophane [12], and in metallocenium tetracyanoethenides and the like [7e,f,13]. The important feature common to this sort of materials is that spin densities at neighboring interacting sites must have *different* signs in order to achieve ferromagnetic interaction. The interaction mechanism which has been proposed by McConnell [14b] (McConnell I mechanism) requires spin polarization to induce spin sign inversion at appropriate radical sites. Spin induction has been also discussed by Orgel [14a] and Anderson [14c], and magnetic polarization of closed shells has already been treated by Sternheimer [15]. It should be noted that the inter-ionic magnetic interaction in metallocenium tetracyanoethenides has not only been ascribed to the McConnell I mechanism [16] but also to charge transfer states (McConnell II mechanism) [7e, 16]. In any case, experimental methods are again highly desirable for probing spin densities including their sign. This would not only confirm the mechanism of the magnetic interaction but also establish the spin delocalization within the engaged radicals. Once the delocalization path is known it can be used as a guide for adjusting the spin density at given sites of a radical.

NMR spectroscopy is one of these methods. In what follows it will be shown how spin densities can be understood, how they are related to NMR spectroscopy, and what the experimental limitations are. Subsequently selected examples will be discussed.

12.2 The Spin Density and its Sign

In a paramagnetic molecule the unpaired electrons are normally delocalized over a number of atoms. The probability of finding the unpaired electron at a given atom may be expressed as the square of the amplitude of the wave function $|\psi(r)|^2$ at point r and by integrating over the electron coordinates. This probability is also known as spin density ρ_A at the atom A, and we can write:

$$\rho_A = |\psi(r)|^2 \tag{1}$$

The term spin density emphasizes the fact that we are dealing with electron density that has an uncompensated electron spin moment (to which the angular momentum must be added in many cases). The spin density is often given in $Å^{-3}$, i. e., we have to think in spaces, and chemists usually approximate this by drawing atomic and molecular orbitals (AOs and MOs, respectively). It is also useful to think of spin density in terms of the fraction of time the unpaired electron spends at a given atom of the radical. Because the electron spin gives rise to a magnetic moment that orients in an applied magnetic field, H_0, the spin density will also be associated with that moment. Its orientation relative to H_0 has been termed parallel and antiparallel, up and down, α and β, and positive and negative, respectively. "Positive" and "negative" spin density is used in this review in accord with the convention of theoretical calculations. There, the spin orientation is often accounted for by using the unrestricted Hartree–Fock (UHF) formalism, i. e., by assigning different orbitals to parallel and antiparallel electrons, and the sign of the spin density at a given atom follows from the difference between the average number of positive and negative spins including all occupied orbitals ψ_i.

12.3 Relating Spin Density to Magnetic Resonance

In principle, any magnetically active nucleus N can be used to study the spin density as far as the electron–nuclear interaction is measurable. The interaction, which may be also viewed as an electron–nuclear coupling by analogy to internuclear coupling, gives rise to an energy splitting that may be extracted from magnetic resonance experiments in the form of the hyperfine coupling constant, A(N), between the unpaired electron and the observed nucleus N. When A(N) is expressed in units of Hz (to underscore the coupling) it takes the form:

$$A(\mathrm{N}) = \frac{\mu_0}{3S} g_E \mu_B \gamma_N |\psi(0)|^2 \tag{2}$$

Here μ_0 is the vacuum permeability, g_E the electron g-factor, μ_B the Bohr magneton, γ_N the nuclear gyromagnetic ratio, S the electron spin quantum number, and $|\psi(0)|^2$ the probability of finding the unpaired electron at the observed nucleus.

Throughout this review parameters and symbols for use in NMR recommended by IUPAC have been considered as far as possible [17]. When Eq. (2) is applied to the hydrogen atom, $A(^1\mathrm{H}) = 1420\,\mathrm{MHz}$ is calculated in accord with the experiment [18]. When nuclei of larger molecules are considered g-factor anisotropy is taken into account by using the mean g-factor g_{av} instead of g_{E} and $|\psi(0)|^2$ is replaced by the spin density at the nucleus, ρ_{N}. Then the hyperfine coupling becomes

$$A(\mathrm{N}) = \frac{\mu_0}{3S} g_{\mathrm{av}} \mu_{\mathrm{B}} \gamma_{\mathrm{N}} \rho(\mathrm{N}) = F \sum_i \left[|\psi_i^+(0)|^2 - |\psi_i^-(0)|^2 \right] \tag{3}$$

by analogy with Eqs. (2) and (3) and by subsuming the constants under F. The calculation of $A(\mathrm{N})$ consists in evaluating the one-electron spin density matrix for which several approaches are available. Most recently, density functional methods have proven particularly useful [19].

It must be pointed out that magnetic resonance spectroscopies determine ρ_{N} rather than ρ_{A}. Thus the shape of the spin-containing orbital does not directly emerge although useful correlations between $A(\mathrm{N})$ and ρ_{A} have been established as we shall see later. The fact that ρ_{N} is strictly limited to the nucleus may be emphasized by quoting it in atomic units (a.u.) instead of $\mathrm{\AA}^{-3}$ ($1\ \mathrm{a.u.} = a_0^{-3}\ \mathrm{\AA}^{-3}$, a_0 = Bohr radius). As an important consequence, there may be differences between the spin density obtained from polarized neutron diffraction and spectroscopy.

Magnetic resonance methods that have been used for measuring hyperfine coupling constants include EPR [18], ENDOR (electron nuclear double resonance) [20], NMR [21], and μSR (muon spin resonance) [22]. Although μSR is a nonroutine method it provides important data, e. g., on radicals in the gas phase [22b]. Electron resonance-based methods are most popular for investigating organic radicals and transition metal compounds as far as the metals and their first coordination sphere are concerned. Here we focus on NMR studies which are well suited for the ligands of coordination and organometallic compounds as well as for organic radicals.

What appears in the NMR spectra as signal *shifts* are actually the hyperfine *couplings* (and additional components, see below) that are averaged by rapid electron spin relaxation to give one weighted mean signal per magnetically nonequivalent nucleus [21a]. This coupling is mediated through bonds and termed (Fermi) contact interaction. The corresponding contact shift of the nucleus N at the absolute temperature T, $\delta_T^{\mathrm{con}}(\mathrm{N})$, and $A(\mathrm{N})$ are related by Eq. (4):

$$\delta_T^{\mathrm{con}}(\mathrm{N}) = A(\mathrm{N}) \frac{g_{\mathrm{av}} \mu_{\mathrm{B}} S(S+1)}{3\gamma_{\mathrm{N}} kT} \tag{4}$$

where k is the Boltzmann factor. Substitution of Eq. (2) into Eq. (4) yields the formula for converting NMR contact shifts into spin densities in a.u.

$$\rho(\mathrm{N}) = \frac{9kT}{\mu_0 g_{\mathrm{av}}^2 \mu_{\mathrm{B}}^2 a_0^3 (S+1)} \delta_T^{\mathrm{con}} \tag{5}$$

Some useful conclusions may be drawn from Eq. (5): 1) Small spin densities can be detected. In these cases the signals are usually narrow, and shifts smaller than

1 ppm can be measured. For instance, for a spin-1/2 radical with $g = 2$ a contact shift of 1.2 ppm measured at 25 °C corresponds to 10^{-5} unpaired electrons. The precision of the signal shift depends on the line width and may be better than 0.12 ppm or $\rho_N = 10^{-6}$ a.u. 2) A given spin density is determined equally well for protons and other nuclei. In practice this is limited, however, by the lower signal-to-noise (S/N) ratio obtainable for other nuclei. 3) Some care must be devoted to the measurement of the temperature. Near room temperature an error of 3 K leads to a 1% difference in δ^{con} and hence in the spin density. 4) The spin densities may suffer from considerable errors when the g-factor is not well known experimentally. This is an issue for transition metal compounds which do not yield EPR spectra in X and Q band (e. g. owing to large zero field splitting) or at low temperature (where states having other g-factors may be populated). Even though there are some error sources that may render absolute spin densities unreliable, the trends of the spin distribution are well reproduced. 5) The measured shifts are not always pure contact shifts. Careful separation of other shift contributions (see below) is necessary, because for a spin density of 10^{-3} a.u., which is often encountered in paramagnetic compounds, a 6-ppm shift contamination of δ^{con} corresponds to an error of 5% in ρ_N.

12.4 The NMR Method: Effects of Unpaired Electrons

Paramagnetism adds some features to NMR spectroscopy which are illustrated in Fig. 1 [23]. The signal shifts are usually much larger than for diamagnetic compounds. The same is true for the signal widths which, in addition, may vary strongly. For instance, the solid-state ^{13}C NMR spectrum of the depicted nitronyl nitroxide shows signals in a range of about 1700 ppm. Those of the triazolyl substituent are narrow while the remaining ones are less well resolved owing partly to the larger widths and to similar spin densities on the respective carbon atoms.

12.4.1 Experimental Hints

Although the NMR spectra of many open-shell molecules can be recorded by using conventional spectrometers some precautions are useful. Thus the large shifts require the free induction decay (FID) to be sampled at high rates. For example, a proton signal shift of 700 ppm (almost arrived at by $(C_5H_5)_2VCH_3$ [24]) would require a rate of 280 kHz when recorded with a 400-MHz instrument. Analog-to-digital converters working at this rate often have a lower digital resolution of the signal amplitude thus deteriorating the detection of small signals in the presence of large solvent signals (dynamic range [25]).

Another issue of large signal shift ranges is signal excitement. The excitation bandwidth, $\Delta\nu_1$, is determined by the pulse as delivered by the emitter and by the properties of the probe head. When a 90 ° pulse of duration τ_{p90} is applied an estimate is $\Delta\nu_1 = 1/(4\tau_{p90})$. Thus for a typical minimal value of $\tau_{p90} = 5\,\mu s$ for a 400-MHz

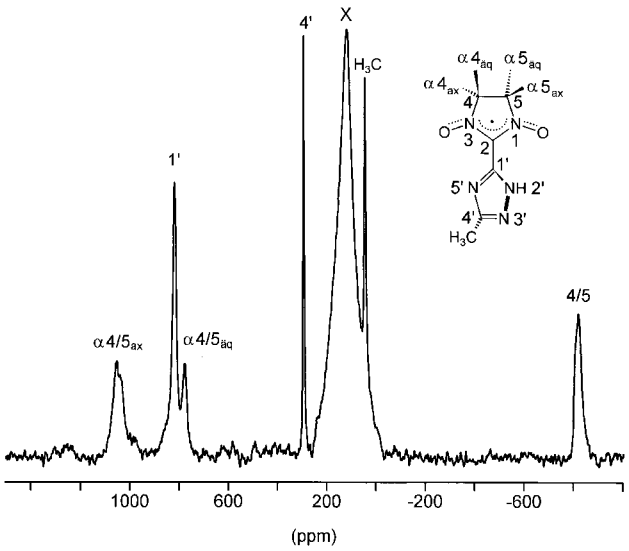

Fig. 1. ^{13}C Magic-angle spinning (MAS) NMR spectrum of the depicted nitroxyl nitroxide radical at 315 K. Spinning rate 15 kHz, X is the background signal of the probe head

instrument would yield $\Delta\nu_1 = \pm 50$ kHz or ± 50 ppm relative to the carrier frequency under quadrature detection. Of course, a more powerful emitter provides shorter pulses, but this is limited by the quality factor Q of the probe head circuit. The points at which the excitation has dropped to a value corresponding to 1/4 of the maximal signal height is given by $\Delta\nu_1 = \pm\nu_N/2Q$ where ν_N is the nuclear Larmor frequency. If we take the ^{13}C NMR signals of nickelocenes as an example which are very broad and cover a range of more than 2100 ppm [26] a probe head with $Q \sim 100$ (pushing the 1/4-height to 500 ppm) and $\tau_{p90} = 1.3$ μs would be desirable. Recording can be improved by moving the carrier frequency close to the signal in question while arranging for possible fold-over of the solvent signals (if a digital filter is not available). $\Delta\nu_1$ may be also increased by decreasing τ_p at maximum power level. This reduces S/N by $\sin\alpha$ (where α is the rotation angle of the nuclear magnetization in the rotating frame of reference). Note that for very rapid relaxation the optimal α stays close to 90° even at rapid pulse repetition [27].

Large line widths which are equivalent to fast nuclear relaxation have advantages and disadvantages. Thus spectrum accumulation may be also fast (often more than 20 times faster than for diamagnetic samples) thereby saving spectrometer time. But, usually, a compromise is necessary in order not to arrive at a duty cycle that would destroy the probe head. Disadvantages are possible errors in signal integration and difficulties in distinguishing broad signals from baseline rolling. Integration is particularly hampered when broad signals appear next to narrow ones, for the latter are easily saturated at high repetition rates. Baseline rolling is a widespread defect of NMR spectra which is most annoying for paramagnetic molecules. It is often due to the break-through of the excitation pulse, to a pre-sampling delay, and to

acoustic ringing [28]. In any case the amplitudes of the first data points of the FID are distorted. If the signals of interest are narrow, broad baseline distortions can be avoided by special pulse sequences which also affect broad signals [28,29]. Broad features are more difficult to separate, but reverse linear prediction of the first points of the FID and/or baseline correction routines are usually successful. Note that these procedures may affect the signal shape and lead to improper phasing.

The sample temperature has already been mentioned as an error source. Commercial controllers indicate the temperature close to the sample, but not in itself, and calibration [30] is indispensable. As for solid-state NMR spectroscopy special care is necessary as the sample temperature depends on the rotor spinning rate. Several external calibration methods have been proposed [31], while internal referencing can be realized by adding to the sample a paramagnetic solid and by measuring its ^{1}H NMR signal shift [32].

12.4.2 Relaxation Constraints

Not all compounds having unpaired electrons are susceptible to NMR spectroscopy. Actually, the possibility to detect a signal is determined by spin relaxation, and the nuclear relaxation rate, T_N^{-1} (in Hz), may be so fast that the NMR signals are broadened beyond the detection limit. The nuclear spin–lattice (or longitudinal) relaxation rate, T_{1N}^{-1}, and the spin–spin (or transverse) relaxation rate, T_{2N}^{-1}, have been first derived for the solution state by Solomon et al. [33], and elaborate treatments of the topic have been published more recently [34].

Here we are mainly interested in the signal width at half height, $\Delta\nu_{1/2}$ (in Hz), which is equal to $(\pi T_{2N})^{-1}$. When we restrict ourselves to small- and medium-sized molecules in solution, there are two contributions to T_{2N}^{-1}: the dipolar and the contact contribution, $(T_{2N}^{dip})^{-1}$ and $(T_{2N}^{con})^{-1}$, respectively. The latter arises from the delocalization of unpaired spin and thus from the local magnetic field at the observed nucleus. When the local field is modulated in such a way that frequency components correspond to ν_N efficient relaxation can occur. Note that, on the one hand, spin density at the nucleus is responsible for hyperfine coupling as measured by contact shifts; on the other hand, when time dependence is considered, it leads to contact relaxation. The latter is given by Eq. (6).

$$\frac{1}{T_{2N}^{con}} = \frac{1}{3}[A(N)]^2 S(S+1)\left(\frac{T_E}{1+\nu_E^2 T_E^2} + T_E\right) \tag{6}$$

This is a simplified version where the correlation time has been assumed to be dominated by the electron relaxation time, T_E, and that $T_{1E} \sim T_{2E} \sim T_E$. It has been further considered that the resonance frequency of the electron, ν_E, is much larger than that of the nuclei and that $\nu_N^2 T_E^2$ can be neglected for nuclear frequencies $\nu_N \leq 300$ MHz and in the range $T_E \leq 10^{-9}$ s (see below). For designing experiments one is interested in the signal width, $\Delta\nu_{1/2}$, which is associated with a given contact

shift (or spin density) and a given electron relaxation; it may be calculated after substituting Eq. (4) into Eq. (6):

$$\frac{1}{T_{2N}^{con}} = \Delta\nu_{1/2}^{con}(N) = F^{con}\frac{k^2T^2}{\mu_B^2}\,\frac{\gamma_N^2}{g_{av}^2S(S+1)}(\delta_T^{con})^2T_E \tag{7}$$

Here the electron relaxation term in Eq. (6) has been further simplified to $F^{con}T_E$ where the constant F^{con} is $9/2\pi$ if $\nu_E T_E$ equals one (e. g. for a 300-MHz instrument and $T_E = 5.1 \times 10^{-12}$ s) and increases up to $6/\pi$ if T_E decreases until $\nu_E T_E \ll 1$. For a spin-1/2 species with $g_{av} = 2$ investigated at 25 °C a proton contact shift of 100 ppm would lead to $\Delta\nu_{1/2}^{con}(^1H) \sim 2300$ Hz when T_E is 10^{-9} s. Clearly, faster electron relaxation is advantageous, while longer T_E values are acceptable for ^{13}C rather than ^1H; for instance $\Delta\nu_{1/2}^{con}(^{13}C) \sim 1400$ Hz for $T_E = 10^{-8}$ s.

The remaining dipolar relaxation results from time-dependent through-space interaction of the magnetic moments of the unpaired electron and a given nucleus. The corresponding signal width at half height is given by:

$$\Delta\nu_{1/2}^{dip}(N) = \left(\frac{\mu_0}{4\pi}\right)^2\frac{\mu_B^2}{15\pi}\,\frac{\gamma_N^2 g_{av}^2 S(S+1)}{r^6}\left(\frac{13T_E}{1+\nu_E^2T_E^2} + 7T_E\right) \tag{8}$$

All symbols have been stated previously except for r which is the distance between the spin source and the given nucleus. Eq. (8) is obtained by applying the same simplifications mentioned with Eq. (6). For estimating the signal half width the expression corresponding to Eq. (7) is:

$$\Delta\nu_{1/2}^{dip}(N) = F^{dip}\left(\frac{\mu_0}{4\pi}\right)^2\mu_B^2\,\frac{\gamma_N^2 g_{av}^2 S(S+1)}{r^6}T_E \tag{9}$$

where F^{dip} is $9/10\pi$ and $4/3\pi$ for $\nu_E^2T_E^2 = 1$ and $\ll 1$, respectively. It follows from Eq. (9) that the distance r is the most important parameter. Again for spin-1/2 species with $g_{av} = 2$ protons at 1 Å from the spin source can be detected only if T_E very short. For instance, the signal half width will exceed 7 kHz when T_E becomes longer than 10^{-11} s. When $\Delta\nu_{1/2}^{dip}(^1H) \sim 2.8$ kHz is assumed to be the detection limit and if $T_E = 10^{-9}$s the proton should be 2.5 Å away from the spin source. It should be noted that Eqs. (8) and (10) are only valid if the spin source can be approximated by a point and that the point–dipole model breaks down when spin delocalization occurs. In such a case ligand atoms become secondary spin sources, and for adjoining nuclei considerable signal broadening occurs even though the delocalized spin density is small. This is known as ligand-centered dipolar relaxation.

The general conclusion for relaxation restraints is summarized as follows: 1) It is difficult to record NMR signals of compounds having electron relaxation times longer than 10^{-9} s unless some other process leads to a shorter correlation time which replaces T_E. 2) Dipolar relaxation often dominates. Only if nuclei at the periphery of the molecule have large signal shifts, contact relaxation will be important [35]. But still the ligand-centered component of dipolar relaxation must be considered. 3) For a given molecule the signal half width decreases with γ_N^2 regardless whether

contact or dipolar relaxation is concerned (Eqs. 8 and 10). Therefore, low-γ nuclei, not least ^{13}C, are worth being studied provided that receptivity limitations can be overcome. An especially useful example is ^2H NMR spectroscopy. After deuteration the signal shift of a given molecule is virtually unchanged (although small primary isotope effects can be detected [36]) while the signal half width is decreased by a factor of up to $[\gamma(^1H)/\gamma(^2H)]^2 = 42.6$. In this way signals with shifts up to 1500 ppm have been recorded for Cr(III)–CD_2R fragments [37] whereas the corresponding proton signals could not be detected.

Because electron relaxation is often a decisive parameter some facts are in place; for details the reader is referred to the literature [38]. Electron relaxation in liquid solution and in the solid state are similar although the formalisms for describing them are different. In any case energy is exchanged between the spin moment and its surroundings which can be thought of as a thermal bath regardless whether the paramagnetic species is locked in a lattice or whether it is tumbling in a liquid.

NMR spectra are routinely recorded down to about $-120\,^\circ C$. In this temperature range the most efficient electron relaxation mechanism involves the uptake of a phonon (lattice vibration quantum) of an energy that allows the species to pass from the ground state (spin parallel to the field) to an excited state. From there a phonon of slightly smaller energy is emitted thus bringing the species back to a "near-ground state" with the spin antiparallel to the field and vice versa (Orbach process). Many paramagnetic transition metal compounds have low-lying electronic states and are thus suitable for NMR spectroscopy. As the energy of the closest excited state raises NMR signals become broader. When an angular momentum is coupled to the spin momentum (leading to large g-factor anisotropy) electron relaxation becomes more efficient. The same is true for large zero-field splitting for species having $S > 1/2$. In short, transition metal ions behave differently as can be seen from the T_E ranges listed in Table 1 [39]. Notoriously difficult cases are V(IV), Cu(II), and Gd(III), and molecules containing other ions may be close to the unfavorable limit of the T_E range. Diluted radicals which have spin centered at light main group elements experience only small spin-orbit coupling, and usually there are no low-lying excited states. These radicals are suitable for EPR rather than NMR spectroscopy.

From the foregoing it follows that slow electron relaxation can be accelerated in the following ways. 1) Chemical exchange. Radicals may be in equilibrium with their neutral counterparts (e. g. arene anions and arenes) or in dissolved paramagnetic transition metal derivatives coordinated ligands may rapidly change place with free ligands present in solution. These processes often shorten T_E. 2) Increasing the temperature. In solution the energy transfer from the spin system to the thermal bath is mediated by some reorientation process characterized by the correlation time, τ. If τ is dominated by the rotation time, τ_r, of the species it is given by $\tau_r = 4\pi\eta r'^3/kT$, where η is the viscosity and r' is the radius of the molecule. η is temperature-dependent in turn, and the overall dependence is $\tau_r \sim [\exp(\Delta E/kT)]/T$, where ΔE is the activation energy. Before choosing a solvent with a higher boiling point in order to make better use of the temperature dependence, it should be checked whether a higher viscosity of the solvent possibly counterbalances the temperature effect. In the solid state T_E^{-1} increases with temperature in a more complicated way, and the reader is referred to the literature [38]. 3) Inter-radical interaction. Electron

Table 1. Typical electron relaxation times of transition metal ions

Ion	(Spin state)	T_{1E} [s]	Ion	(Spin state)	T_{1E} [s]
Ti^{3+}	(1/2)	10^{-9}–10^{-10}	Co^{2+}	(1/2)	10^{-9}–10^{-10}
VO^{2+}	(1/2)	10^{-8}–10^{-9}	Ni^{2+}	(1)	10^{-10}–10^{-12}
V^{3+}	(1)	5×10^{-12}	Cu^{2+}	(1/2)	1–3 $\times 10^{-9}$
V^{2+}	(3/2)	5×10^{-10}	Ru^{3+}	(5/2)	10^{-11}–10^{-12}
Cr^{3+}	(3/2)	5×10^{-10}	Re^{3+}	(2)	10^{-11}
Cr^{2+}	(2)	10^{-11}			
Mn^{3+}	(2)	10^{-10}–10^{-11}	Gd^{3+}	(7/2)	10^{-8}–10^{-9}
Mn^{2+}	(5/2)	10^{-8}–10^{-9}	Tb^{3+}	(3)	8×10^{-13}
Fe^{3+}	(5/2)	10^{-10}–10^{-11}	Dy^{3+}	(5/2)	8×10^{-13}
Fe^{3+}	(1/2)	10^{-11}–10^{-12}	Ho^{3+}	(2)	7.5×10^{-13}
Fe^{2+}	(2)	10^{-12}	Tu^{3+}	(1)	8×10^{-13}
Co^{2+}	(3/2)	10^{-11}–10^{-12}	Yb^{3+}	(1/2)	10^{-12}

relaxation is also mediated by magnetic dipole–dipole interaction and by electron spin exchange [40] between overlapping singly-occupied orbitals of different radicals. Therefore, it is possible to pass from the EPR to the NMR regime by increasing the concentration, thereby shortening T_E up to several orders of magnitude; an example is given in Fig. 2 [23]. The shortest T_E would be expected for solid radicals, but often the narrowing of the NMR signals is thwarted by nuclear dipole interactions unless they are (partly) averaged out by magic angle spinning (MAS) [41] 4) Exchange coupling. If two (or more) spin centers A and B having short and long electron spin relaxation times, respectively, are present in a molecule the relaxation depends on the coupling energy J between A and B. Usually J is large enough so that A speeds up the relaxation of B [34b,c]. There are also cases where equal spin centers experience an increase of the electron relaxation rate for both strong and weak magnetic interaction [42]. Finally, it should be noted that instead of discussing the manipulation of electron spin relaxation times, the correlation time τ may be broken down into various components that are considered separately [34].

12.4.3 Contact, Dipolar, and Experimental Signal Shifts

The NMR signal shift of a paramagnetic compound recorded at temperature T, δ_T^{exp}, is the sum of three contributions:

$$\delta_T^{exp} = \delta_T^{con} + \delta_T^{dip} + \delta_T^{dia} \tag{10}$$

where δ_T^{con} is the contact shift mentioned previously, δ_T^{dip} is the dipolar (or pseudocontact) shift, and δ_T^{dia} is the shift (usually independent of T) that the signal would have if the molecule were diamagnetic. In addition, the shift due to the bulk susceptibility, δ^{susc}, must be considered in solution but not in the solid state [43]. It is eliminated by referencing to the internal signal of a diamagnetic molecule, most

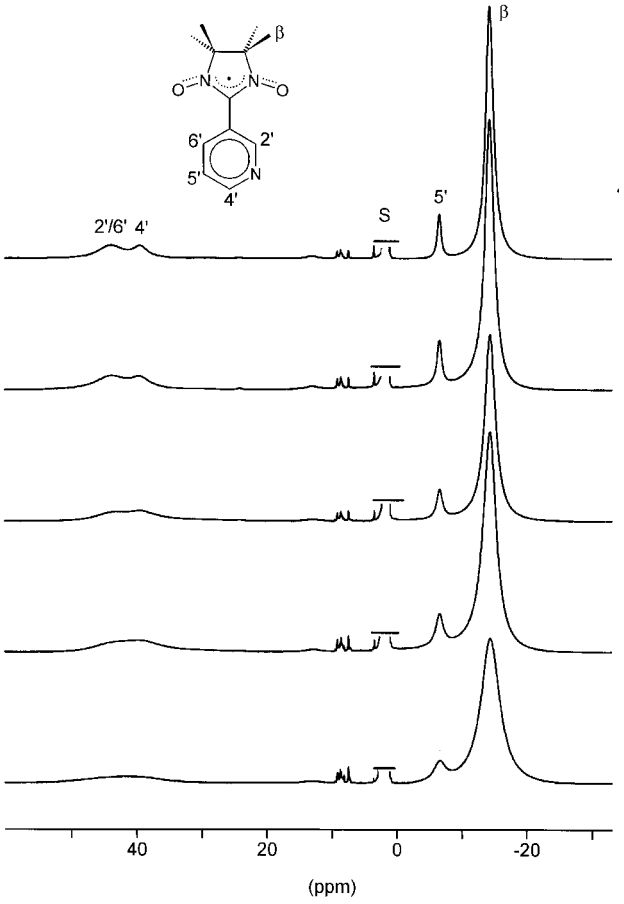

Fig. 2. ^{1}H NMR spectra of m-pyridylnitronyl nitroxide dissolved in acetone-d_6 at 300 K [23]; the concentration decreases from top to bottom. S = solvent. Small peaks close to S are due to impurities

often the solvent, which experiences the same bulk susceptibility. Therefore, external referencing of solution NMR spectra [44] cannot be recommended unless the susceptibility is known. There are also cases where organic [45a] and organometallic [45b] radicals cause paramagnetic signal shifts of supposedly inert solvents. Proper referencing is then achieved by concentration-dependent measurements. The sign convention of the signal shifts is the same as for diamagnetic compounds, i. e., shifts to high frequency are positive. Note that in the earlier literature reversed signs have been used.

The shift δ^{dia} is eliminated by referencing each signal to the corresponding signal of an isostructural diamagnetic molecule. Often δ^{dia} is taken from the literature while the shift of the solvent signal, δ^{solv}, is used as intermediate reference. Then the signal

shift which is exclusively due to the paramagnetism of the molecule under study, δ_T^{para}, is given by

$$\delta_T^{\text{para}} = \delta_T^{\text{con}} + \delta_T^{\text{dip}} = \delta_T^{\text{exp}} + \delta^{\text{solv}} - \delta_T^{\text{dia}} \tag{11}$$

Alternatively, temperature-dependent spectra may be recorded. When the data are plotted in a δ^{exp}-over-T diagram (see Eq. (4) the intercepts of the straight lines are δ^{dia}. This is a particularly elegant method when closely related diamagnetic species are not available. However, serious errors arise when the temperature range is narrow, when δ^{exp} is difficult to determine (e. g. for broad noisy signals), and when dynamic effects like geometric changes and high-spin/low-spin equilibria are present.

Finally, the dipolar shift must be eliminated to obtain δ_T^{con} and thus the spin density. For an axially symmetric species δ_T^{dip} is given by [46]:

$$\delta_T^{\text{dip}}(\text{N}) = \frac{\mu_0}{4\pi} \frac{\mu_{\text{B}}^2 S(S+1)}{9kT} \frac{(3\cos^2\theta - 1)}{r^3} (g_\parallel^2 - g_\perp^2) f(g, D) \tag{12}$$

The last term is a function of the g-factor and the zero-field splitting, D; it depends on S and becomes unity for $S = 1/2$. The last but one term considers the g-factor anisotropy, where $g_\parallel$ and $g_\perp$ are the g-factors parallel and perpendicular to the magnetic axis, respectively. The third last term is the geometric factor where r is the vector relating the spin center and the nucleus under study, and θ is the angle between r and the magnetic axis of the species. The g-factor anisotropy of organic radicals is usually so small that δ_T^{dip} can be neglected. When transition metal ions are involved $g_\parallel^2 - g_\perp^2$ is often smaller than 2 and hence δ_T^{dip} is also small. So even if the g-factors are not known experimentally, estimates of δ_T^{dip} are helpful. The term $f(g, D)$ is close to unity when $D < 20\,\text{cm}^{-1}$ which applies in many cases.

For studies in solution the geometric term is calculated from (symmetrized) X-ray and calculated minimum-energy structures, or reasonable estimates of bond lengths and angles are made. δ_T^{dip} can be neglected when θ is close to 54.7° and/or when the distance of the nucleus from the spin center is large. As an example, assume that we have a spin-1/2 compound with a medium-sized g-factor anisotropy leading to $g_\parallel^2 - g_\perp^2 = 1$. If we consider nuclei at $\theta = 35°$ or 0°, and if we accept δ_T^{con} to be in error by $\delta_T^{\text{dip}} = \pm 1$ ppm at 298 K the nucleus should be at $r \geq 5.6$ Å. For $35° > \theta > 0°$ and the ±1-ppm limit the nucleus may be closer to the spin center. Note, however, that Eq. (12) must be corrected for small r [47].

12.4.4 Signal Assignment Strategy

Owing to the special features of NMR spectroscopy of paramagnetic molecules described in the previous sections, some signal assignment procedures known for diamagnetic molecules are not (or not fully) applicable to paramagnetic ones. On the other hand, there are additional methods that are based on the paramagnetism.

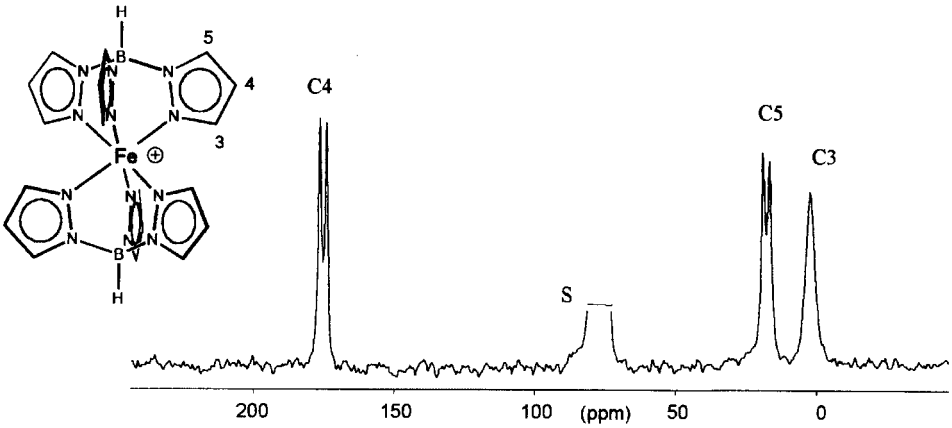

Fig. 3. ^{13}C NMR spectrum of bis[hydrotris(pyrazol-1-yl)borato]iron hexafluorophosphate dissolved in $CDCl_3$ at 305 K [48a] (S = solvent)

Important methods of assignment are: 1) Signal areas. Special care is necessary with regard to distorted base lines and signals of different widths in the same spectrum (see Section 3.1). 2) Internuclear coupling. Normally proton signals are too broad as to detect H, H couplings, but exceptions are known [48b]. By contrast, one-bond C, H multiplets are more often resolved (see Fig. 3) and thus of great help for the assignment of ^{13}C NMR signals. But even if a carbon signals is narrow it may not show the expected C, H coupling owing to excessive proton relaxation [48a,c]. In any case, $\Delta\nu_{1/2}$ of all nuclei engaged in the coupling should be smaller than about twice the coupling constant. 3) Signal shifts. In many cases a spin delocalization mechanism can be assumed (see Section 5) which predicts the sign and the orders of magnitudes of the signal shifts. High-level spin density calculations may guide more detailed assignments. 3) (Isotopic) Substitution. Exchangeable protons are easily assigned after deuteration by ^{1}H and ^{2}H NMR spectroscopy. Also, upon selectively changing the substitution pattern (mostly CH_3 for H) signals can be identified. 4) Temperature variation. It is often difficult to distinguish weakly shifted signals of a paramagnetic compound from those of diamagnetic impurities. As can be seen from Eqs. (5) and (11) the signals of the first should move with temperature whereas those of the latter should not. A precise δ_T^{exp}-over-T plot enables correlation of the signals of a paramagnetic molecule and its diamagnetic analog whose signal assignment is known. 5) Redox titration. Many paramagnetic species are synthesized by oxidizing or reducing diamagnetic precursors. When the electron transfer between both is rapid on the NMR time scale mean signals are observed, and the signals of the *para*- and diamagnetic compounds can be correlated. In this way the proton signals of a paramagnetic triple-decker sandwich have been assigned [49]. 6) Signal half widths. As stated in Section 3.2, dipolar relaxation is usually predominant, and hence $\Delta\nu_{1/2}$ is proportional to r^{-6} (Eq. 5). Precise correlations of $\Delta\nu_{1/2}$ and r^{-6} may be disturbed by ligand-centered dipolar relaxation. But usually, the broader of two similarly shifted signals can be safely assigned to the nucleus which is closer to the spin source. An

example is given in Fig. 3, where all carbon signals should be doublets and have the same area. Since $r(C3) < r(C5) < (C4)$ the signal widths are rather different thus establishing the assignment. This is confirmed by the spin delocalization which should place the signal of C4 on one frequency side and C3/5 on the other as actually found. 7) NOE, saturation transfer, and correlation spectra. These techniques are applicable to relatively narrow signals and have been worked out in great detail for bioinorganic molecules [50].

12.5 Spin Delocalization Mechanisms

Through recent progress in theoretical calculations spin density distributions of various molecules are available which are in good accord with the results of, e. g., polarized neutron diffraction. These data must be interpreted in order to understand why a certain spin delocalization pattern is obtained and how it can be changed deliberately by chemically modifying the compound. Simple qualitative and semiquantitative mechanisms have been proposed which explain how spin is transferred from one molecular fragment or from a given atom to the next. Most of these mechanisms have been developed to explain EPR spectra. It is not attempted to give a comprehensive overview here; rather, examples are selected that can be adopted to other compounds.

12.5.1 Spin Distribution in π Orbitals

Spin density is found in π orbitals, if the molecule itself is a radical, like allyl and benzene anion radical, or if spin is transferred from an adjacent source into π orbitals. These sources may be either limited areas of purely organic compounds where the unpaired electron is concentrated, or they may be transition metals to which ligands are π-bonded (polyhapto-bonded) like in arene and cyclopentadienyl (Cp) complexes. This section selects delocalization mechanisms which are relevant for compounds studied by NMR spectroscopy.

12.5.1.1 Direct Spin Delocalization

Figure 4 shows a generalized MO scheme for the bonding of conjugated cyclic ligands $C_xR_x^{+/-/0}$ (for instance, $C_5H_5^-$, C_6H_6, $C_7H_7^+$) to a transition metal ion M^{n+}. In any case and to a good approximation, only the five lowest ligand π orbitals interact with the metal d and s (not shown) orbitals to yield MOs which are relevant for spin delocalization. They have been labeled e_1, e_2, a, and e_1^* to refer to the type of ligand orbital that is mixed in. Depending on M^{n+}, the unpaired electrons occupy the front orbitals given in the frame. Only two, e_1^*, have a considerable ligand content and thus mediate direct spin delocalization from the metal to the ligand when they are singly

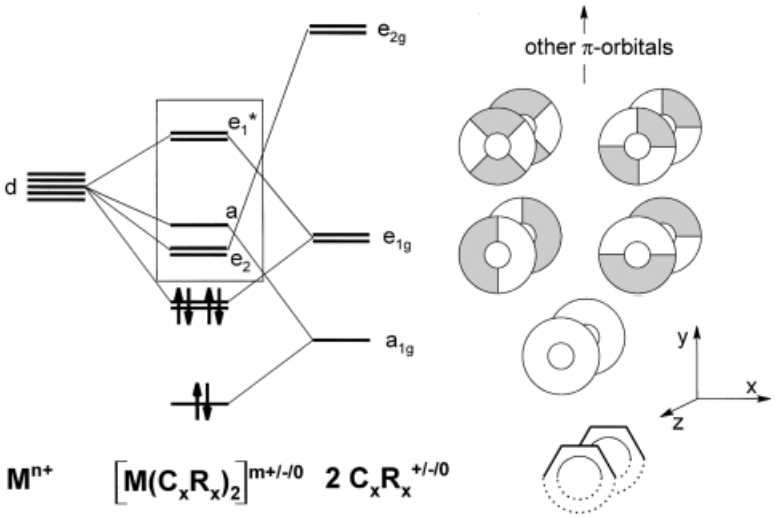

Fig. 4. Simplified MO scheme relevant for spin delocalization in paramagnetic π compounds. $C_xR_x^{+/-/0}$ might be $C_5H_5^-$, C_6H_6, and $C_7H_7^+$. The generalized MO phases are those parts of the MO shapes seen by the d orbitals which are sandwiched between the ligands

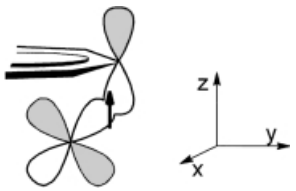

Fig. 5. Direct delocalization of spin in a MO that extends from the metal to the ligand

occupied. Here "direct" means that the spin sign remains unchanged. It follows that in symmetric low-spin sandwich compounds, $(C_xR_x)_2M^{m+/-/0}$, direct delocalization is expected for $d^{>6}$ compounds, i. e., for M = Fe, Co, and Ni. A similar reasoning applies for compounds having two different π ligands (mixed sandwich compounds) and high-spin congeners. A simplified view of direct spin delocalization is given in Fig. 5.

12.5.1.2 Adjusting the Spin Distribution in π Radicals and π-bonded Ligands

Conceptually it does not matter whether spin appears in π orbitals because they belong to genuine π radicals [51] or because it has been delocalized from (or induced by, see below) a transition metal source. Consequently, π ligands can be regarded as *spin-reduced radicals* carrying less than one unpaired electron.

As already mentioned, only e_1^* orbitals and thus e_1-type ligand orbitals (see Fig. 4) are engaged in delocalization. A more detailed but still general view of these orbitals is given in Fig. 6. The carbon $2p_z$ coefficients of e_{1s} and e_{1a} orbitals (symmetric and

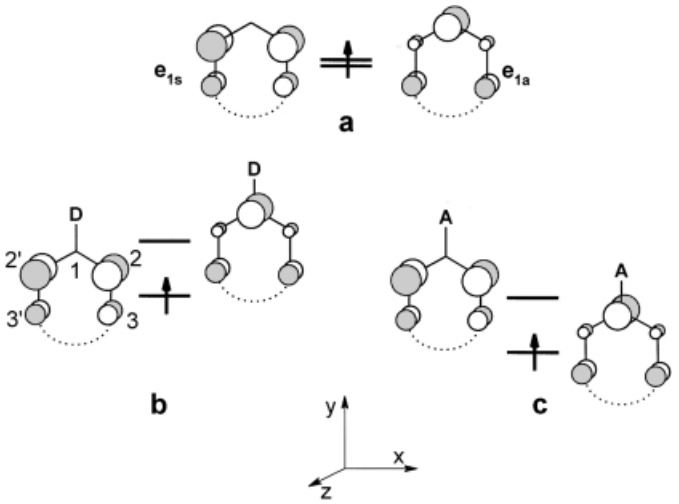

Fig. 6. Spin density changes resulting from orbital splitting; only the $C_x R_x^{+/-/0}$ ligand contributions of the MOs are given. (a) Degenerate e_1-type orbitals. (b) and (c) Orbital splitting after introducing donor and acceptor substituents D and A, respectively

antisymmetric with respect to the C_2 axis) are different as indicated qualitatively by the different size of the lobes. Yet each ring carbon has the same spin density as both orbitals are degenerate (Fig. 6a). When a donor substituent is introduced (Fig. 6b) the orbital degeneracy is lifted, the e_{1s} orbital will be more populated, and the spin density at C1 will be smaller than at C3/3′ and C2/2′. When an acceptor substituent is introduced (Fig. 6c) the orbital population is inverted and C1 will have more spin density than the other carbons. The energy gap between the e_{1s} and e_{1a} orbitals can be adjusted by choosing an appropriate substituent; most efficient will be the replacement of a CR fragment by heteroatoms like N, P, As, and B. Once the orbital degeneracy is lifted, the energy gap will also depend on the strength of the metal–ligand bond which normally changes upon substitution.

12.5.1.3 Spin Delocalization into π Orbitals of σ-bonded Aryls

Instead of being π-bonded, an unsaturated molecule may also serve as a monohapto substituent, R, of a spin source and still receive spin density in its π orbitals. The sources may be very different if only they have spin in a π-type orbital at the site to which R is bonded. Some examples shown in Fig. 7 are transition metal fragments L_nM, amine oxide residues R′NO, and π-bonded ligands (Fig. 7a, b, and c, respectively). Here we take R = phenyl as an example and assume that R and the fragments a, b, and c of Fig. 7 are conjugated.

Figure 8 demonstrates that the spin-carrying fragment can interact with four of the six phenyl π orbitals in a bonding (π_1, π_2) and antibonding (π_4, π_6) fashion. When these interactions are summarized the orbital contributions at C1 and C3/5 subtract,

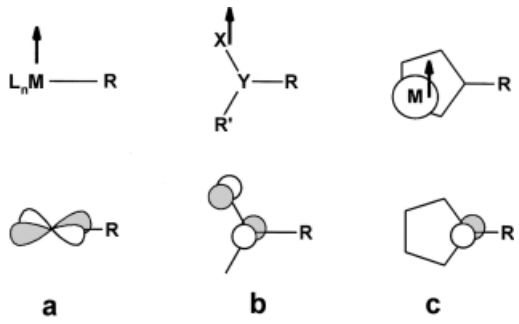

Fig. 7. Examples of monohapto binding of R to spin sources. Shown at the bottom are relevant spin-containing orbitals at the binding site

at C2/6 and C4 they add, and the spin-containing MO looks like in Fig. 8a; examples are phenylated metallocenes [52]. As we pass to benzylidene and phenylacetylide the same procedure yields the MOs shown in Figs 8b and 8c, respectively. In this way the phenyl positions with large positive spin density can be predetermined. Note that the MOs in Fig. 8a–c are oversimplified; "empty" positions mean that there is finite but little positive spin density which is overcompensated by negative spin density induced by polarization as we shall see below. A more detailed treatment of cases similar to those in Figs. 8a and 8c with the spin source being a bent $(Cp)_2V$ fragment have been published [24,53].

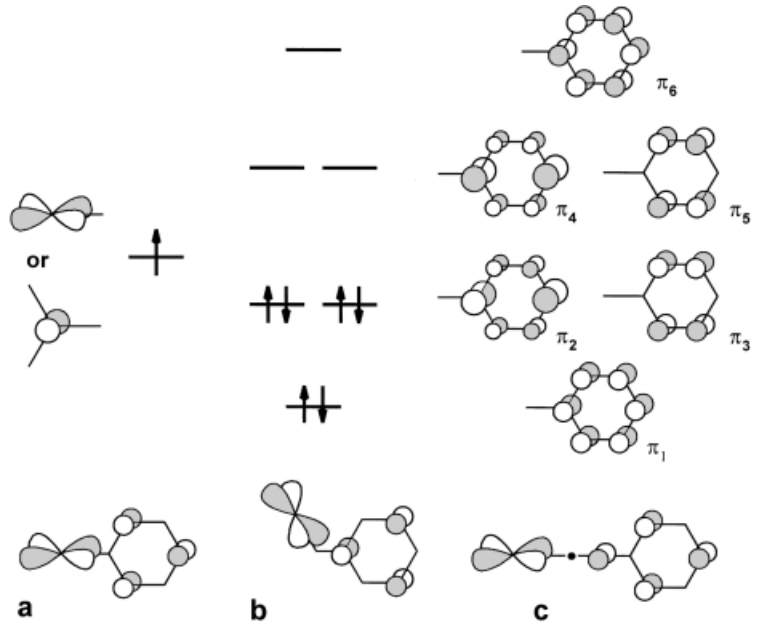

Fig. 8. Phenyl orbitals π_1, π_2, π_4, and π_6 interact with a spin-containing orbitals of Fig. 7 to yield orbital (a). Other examples are (b) and (c) (see text)

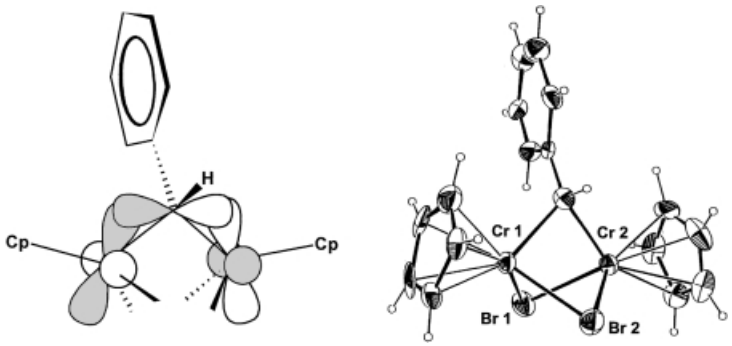

Fig. 9. Molecular structure of $[(C_5H_5)CrBr]_2(\mu\text{-}CHC_6H_5)$ and spin transfer from two d orbitals to the π orbitals of the bridging benzylidene. For clarity only the $2p_z$ orbital of the bridging carbon is given

The examples in Fig. 8 are special cases in so far as the substituents see π-faced orbitals from which they receive spin. Other cases are conceivable where just one lobe of a spin-carrying d orbital is engaged. For instance, benzylidene may not only be a monohapto ligand (Fig. 8b) but also serve as a bridge as shown in Fig. 9 [54]. Often the π substituent cannot be fixed with respect to the spin source as assumed here. Then the spin distribution is modulated according to the population of the rotamers and σ delocalization (see below) comes into play.

12.5.1.4 Spin Polarization

Spin density may be found in both localized and delocalized orbitals of radicals and ligands even if they are not mixed in the singly occupied MO, i. e., when direct delocalization is negligible. This is quite common for paramagnetic π complexes with less than six d electrons. As can be seen in Fig. 4 these electron occupy e_2 and a orbitals which have a small ligand content. However, unpaired spins in these MOs can polarize the paired spins in lower-lying orbitals as has been suggested early for metallocenes [55]. The treatment is based on electron exchange interaction and has been applied to similar problems [56]. Qualitatively, in the present case, a spin in an e_2 orbital can polarize the electrons in the lower e_1 orbitals which have a considerable ligand content and which are allowed to have different orbital energies (UHF formalism). This rests on the fact that Coulomb exchange stabilizes a system when spins are parallel. Hence paired e_1-type electrons with positive spins spend more time close to the unpaired spin at the metal than do e_1-type electrons with negative spins. This is compensated by a higher probability of finding the latter electrons in an orbital region distant from the metal. As a result positive spin density at the source is increased while negative spin is induced on the ligand π orbital. This is illustrated in Fig. 10 which resembles Fig. 5 except that now the unpaired electron is in the $d_{x^2-y^2}$ orbital which has a bad overlap with the ligand π orbital. Polarization is experienced by the bonding electron pair in the MO which has d_{yz} and carbon $2p_z$ contributions. Note that for clarity the spin arrows in Fig. 10 have similar size while the induced spin is actually small.

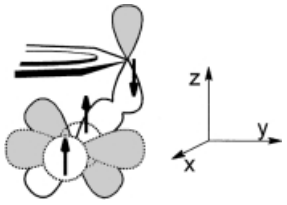

Fig. 10. Metal-localized *unpaired* electrons (e. g. in the dotted $d_{x^2-y^2}$ orbital) induce negative spin density in ligand π orbitals through polarization of *paired* metal–ligand bonding electrons (e. g. in the MO which has some d_{yz} character)

Alternatively, polarization can be described by starting from paired electrons which are not allowed to have different orbital energies (restricted Hartree–Fock (RHF) formalism). The delocalization of positive spin is accounted for by the singly occupied MO, and negative spin density is introduced by configuration interaction. The latter method considers excited states of the molecule which have the same symmetry as the ground state so that they can mix in. When applied to metallocenium ions [16b,c] this leads to negative spin in the e_1-type π orbitals of the Cp ligands. Similarly negative spin density at the central carbon of allyl radical, the most simple example of odd alternant radicals, has been explained [57].

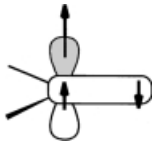

Fig. 11. Polarization of the C–H bonding electrons by spin in the carbon 2p orbital

The most simple case of spin polarization is met in the CH fragment of a π radical where the carbon is sp^2-hybridized and spin density, $\rho(^{13}C)$, sits in the remaining p orbital (Fig. 11). Owing to polarization of the C–H bond, positive spin density on the carbon is enhanced and negative spin density, $\rho(^1H)$, is induced at the proton. Clearly, $\rho(^1H)$ must be proportional to $\rho(^{13}C)$, and since $\rho(^1H)$ is measured via the hyperfine coupling constant the so-called McConnell relationship [58] applies

$$A(^1H) = Q\rho(^{13}C) \tag{13}$$

where the constant Q is -64.5 MHz for the benzene radical anion.

For π radicals and spin-reduced analogs it is straightforward to approximate the spin densities by the squared coefficients, c_i^2, of the carbon $2p_z$ orbitals obtained by MO calculations. This approach has been applied to nuclei other than protons by Karplus and Fraenkel [56a], and their work has been extended by Yonezawa et al. [56b]. For instance, when we are interested in the hyperfine coupling constant, $A(^{13}C)$, of the carbon C in Fig. 11 we must not only consider polarization of the C–H bond but also that of the bonds to the adjacent sp^2 carbons C′ and C″ of the enlarged fragment shown in Fig. 12a. The following spin contributions are induced at the nucleus of C. π-Spin at C polarizes: 1) the bonds C–C′, C–C″ (Fig. 12b,c), and C–H (Fig. 11) inducing positive spin; and 2) the 1s electron pair of C (Fig. 12f) inducing negative spin. 3) π-Spin at C′ and C″ polarizes the bonds C–C′ and C–C″

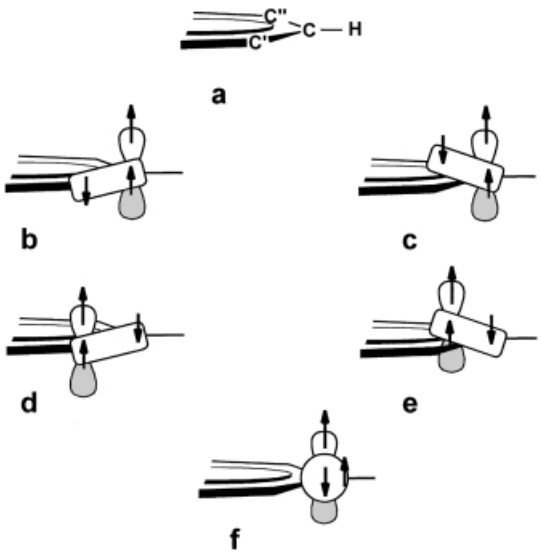

Fig. 12. Polarization of paired electrons in a C″C′CH fragment. The sum of the contributions of (b) through (f) is the spin induced on carbon C (see text)

(Fig. 12d, e), respectively, thus inducing additional negative spin. For the C″C′CH fragment the contributions can be summarized by Eq. (14):

$$A(^{13}\mathrm{C}) = Q_{\mathrm{C}} p^0_{\mathrm{CC}} + \sum_{i=1}^{3} Q_{\mathrm{X}_i} p^0_{ii} + \sum_{i=1}^{3} R_{\mathrm{CX}_i} p^0_{\mathrm{C}_i} \tag{14}$$

where $X_i = C'$, C″, H and where p^0_{CC}, p^0_{ii}, and p^0_{Ci} are elements of the spin matrix obtained from MO calculations. Here we follow Yonezawa et al. [56b] who have given a more general treatment and determined the polarization constants Q and R.

For spin in ligand π orbitals it follows qualitatively, that negative spin is induced at all carbon atoms which have a small $2p_z$ orbital coefficient. In Fig. 8a–c we have seen that the alternation of large and small AO coefficients is characteristic of π ligands. Owing to polarization this is transformed into alternating positive and negative spin at the respective carbon nuclei. On passing to the adjacent proton the spin sign is inverted (see Fig. 11). The result is illustrated in Fig. 13 where the expected sign patterns of the signal shifts are given for the examples in Fig. 8b,c. In summary, the spin signs in aryls can be switched in two ways: 1) The spin source can be chosen to have negative or positive spin as in phenylated metallocenes [52]. 2) The number of nuclei between the spin source and the aryl can be adjusted as shown in Figs. 8 and 13.

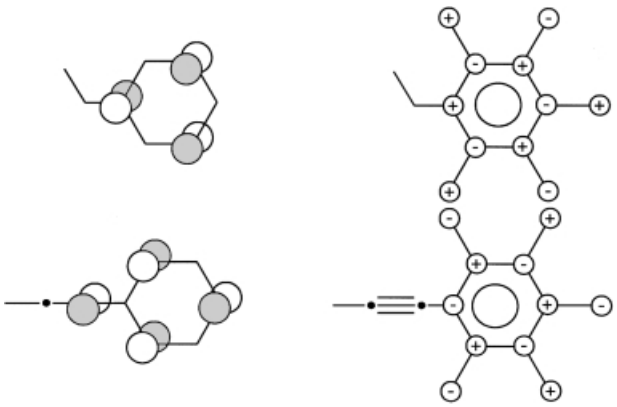

Fig. 13. Relevant MOs for π delocalization (left) and spin sign patterns (right) expected for the signal shifts of the phenyl carbons and protons of benzyl (top) and phenylacetylide (bottom) substituents

12.5.2 Spin Delocalization into σ Orbitals

When the ligand content of a spin-containing orbital has σ symmetry all nuclei experience positive spin density and hence have positive contact shifts unless they are lying in a nodal plane of the orbital. The hyperfine coupling constant is again proportional to the corresponding squared AO coefficient, this time of the s orbital. As the coupling is now a first order process it is more efficient, and Q is much larger: 1420 MHz and 3338 MHz for the unpaired hydrogen 1s and carbon 2s electron, respectively [18,56a].

For instance, in π complexes ligand orbitals of a_1 and e_2 nodal properties but σ character [59] (which are lying below the ligand π orbitals shown in Fig. 4) may mix into the e_2-type front orbitals. This leads to additional σ delocalization which will be considered further in Section 6.2. Other instructive examples are iron porphyrins whose spin state determines whether σ or π delocalization dominates. For instance, pentacoordinate iron(II) porphyrins like those shown in Fig. 14a have a $S = 2$ ground state [60]. It can be seen in Fig. 14a′ that two spins are occupying σ-type ($d_{x^2-y^2}$ and d_{z^2} content) and π-type (d_{xz} and d_{yz} content) MOs, respectively. Of the possible σ and π MOs [61] those relevant for the reasoning are given in Figs. 14a″ and 14b″. As stated above, a given spin density in σ MOs yields much larger hyperfine couplings and hence contact shifts than if it were in π MOs. Actually, in the present case σ delocalization dominates, and this is verified by a large positive signal shift of the pyrrole protons [60] (Fig. 14a, $\delta^{con}(H4) = 46.5$). In addition, σ delocalization is confirmed by the signal shift of the adjacent CH_2 protons which is also positive (Fig. 14a, $\delta^{con}(CH_2) = 10.5$). Note that this shift would be negative if π spin at C3 were dominating as we shall see below.

In contrast, the hexacoordinate iron(IV) porphyrins shown in Fig. 14b have a $S = 1$ ground state [62] with spin exclusively in π-type orbitals (Fig. 14b′, d_{xz} and d_{yz} content). The most important MO is that given in Fig. 14b″, and, therefore, considerable positive spin must be in the $2p_z$ orbitals of the outer pyrrole carbons like C3/4. Subsequent C–H-bond polarization as shown in Fig. 11 must lead to negative

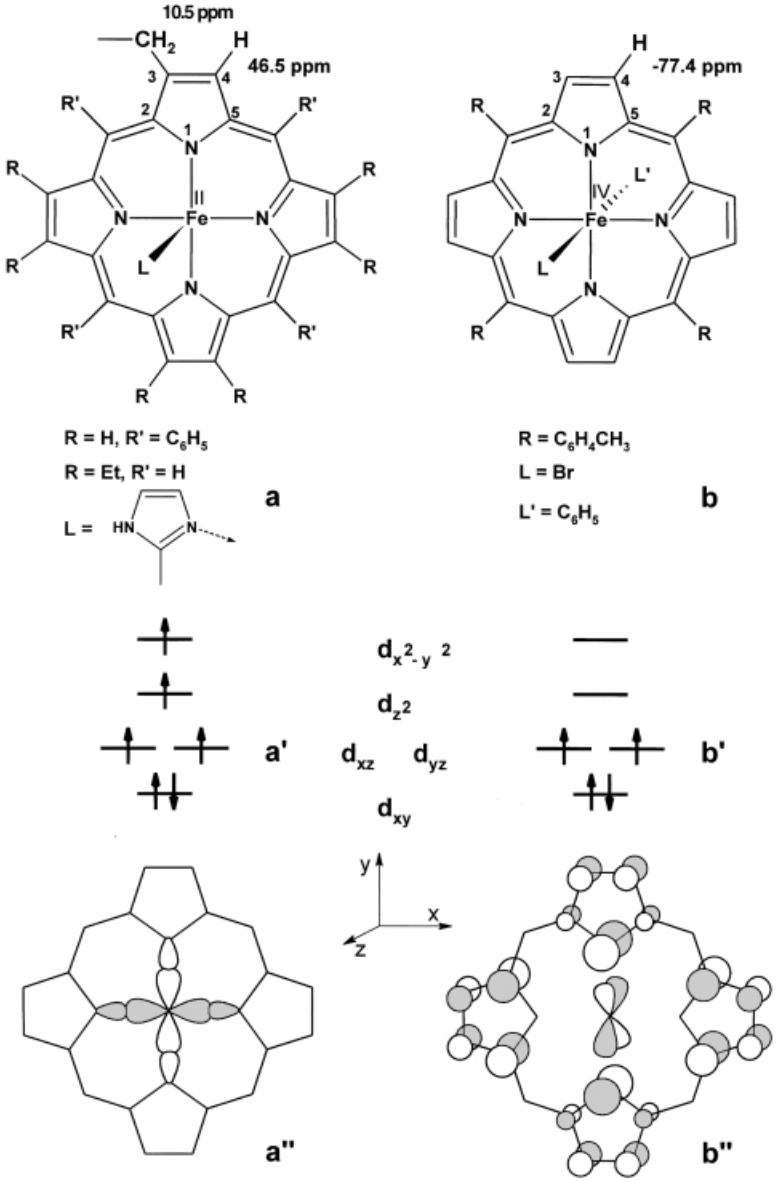

Fig. 14. Spin delocalization in iron porphyrins. (a) Dominating σ delocalization in $S = 2$ iron(II) derivatives leads to positive contact shifts for pyrrole-H and pyrrole-CH_2. (b) π Delocalization in $S = 1$ iron(IV) derivatives leads to negative contact shifts for pyrrole-H. See text for more details

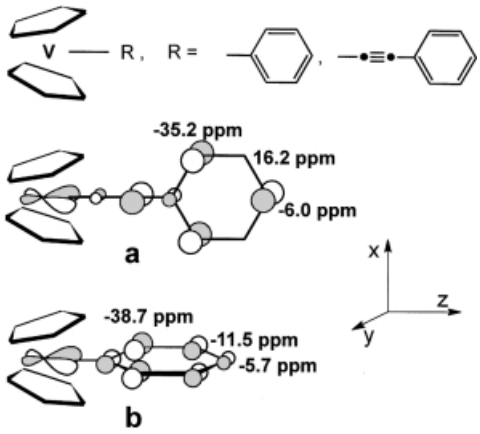

Fig. 15. MOs relevant for spin delocalization into R = phenylacetylide and phenyl of Cp_2VR derivatives ($S = 1$) and signs of the contact shifts of the phenyl protons. (a) π Delocalization leads to alternating signs. (b) σ Delocalization leads to equal signs

spin at the pyrrole protons. This is confirmed by a large negative signal shift [62] (Fig. 14b, $\delta^{\text{con}}(\text{H4}) = -77.4$).

Switching from π to σ delocalization cannot only be realized by choosing an appropriate ground state of a molecule but also by adjusting the orientation of ligands. This is illustrated with bent vanadocenes, Cp_2VR [24], ($S = 1$) in Fig. 15. When R is phenylethinyl the rotamer in Fig. 15a is favored and hence spin transfer from the (rehybridized) d_{yz} orbital into the π system of the phenyl. Indeed, the proton signal shifts given in Fig. 15a confirm the pattern of alternating signs predicted in Fig. 13. By contrast, when R is phenyl (Fig. 15b) steric hindrance by the Cp ligands force the phenyl at right angles to the Cp–V–Cp plane. Now spin transfer proceeds into the σ orbital (represented by the carbon $2p_y$ contributions), and this is confirmed by *equal* signs of the proton signal shifts given in Fig. 15b.

In many cases the symmetry of the molecule does not allow to separate σ and π orbitals [63]. Yet it is often possible to establish σ besides π delocalization as will be shown below.

12.5.3 Spin Delocalization from π Orbitals to Nuclei of Substituents

Spin density can be also detected on various nuclei of substituents other than phenyls and other aryls which are bonded directly to transition metals of a paramagnetic fragment or to the skeleton of π radicals and π ligands of paramagnetic complexes. How the spin gets there depends on the number of bonds by which the nucleus is separated from the spin-carrying π orbital. According to a widely-used convention $\alpha, \beta, \gamma \ldots$ nuclei are one, two, three … bonds away, respectively.

12.5.3.1 α Nuclei

The prototype is the proton of a C, H fragment shown in Fig. 11 where sign inversion of the spin occurs on passing from C to H. In much the same way α nuclei other than

protons should experience, e. g., negative spin if it is positive at carbon and unless σ delocalization takes over (see Figs. 14a and 15b) or the α nucleus is engaged in π bonding (as in the case of fluorine).

12.5.3.2 β Nuclei

Once spin has been induced at a nucleus in α position it is obvious to continue so that consecutive polarization of σ bonds (Fig. 16a) would induce spin at a nucleus in β position; the sign would be the same as that of the spin in the starting π orbital. It is also conceivable that direct polarization of the α–β bond through spin in the π orbital (Fig. 16b) induces spin at the β nucleus. Finally, hyperconjugation leads to spin transfer. The orbitals relevant for hyperconjugation are visualized in Fig. 16c. In a three-orbital interaction the spin-containing orbital of the π ligand as well as the bonding and antibonding C–H orbital of appropriate symmetry yield the fragment orbital given in the box of Fig. 16c. It can be seen that little spin is transferred to α nuclei and much to β nuclei, so that hyperconjugation is a selective mechanism. The relative importance of polarization and hyperconjugation has been investigated [64]. There is general agreement that hyperconjugation dominates, but polarization

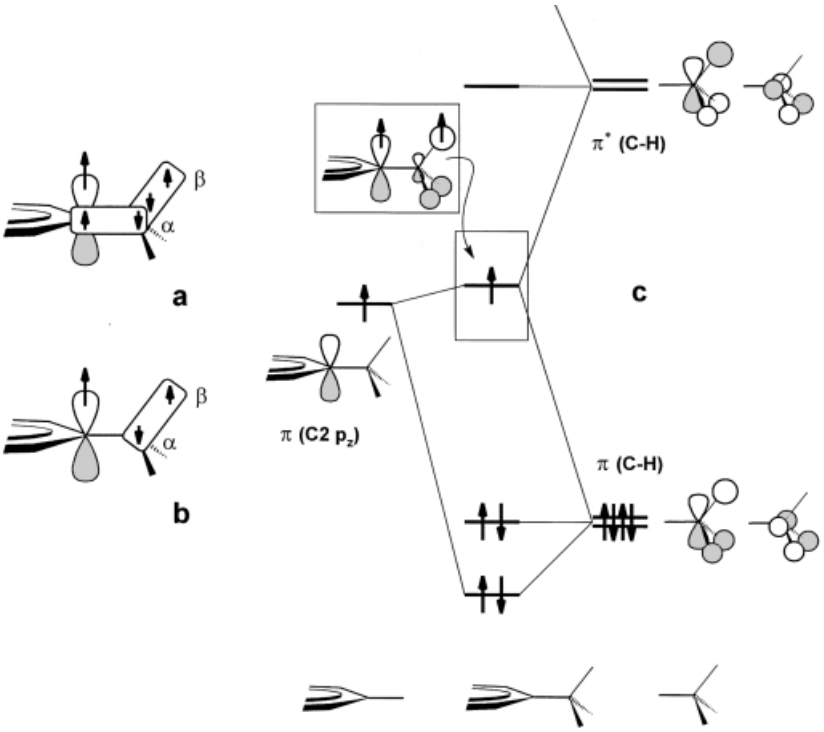

Fig. 16. Spin transfer from the π orbital of a sp^2 center to β nuclei. (a) Consecutive polarization of σ bonds. (b) Direct polarization of the α–β bond. (c) Hyperconjugation

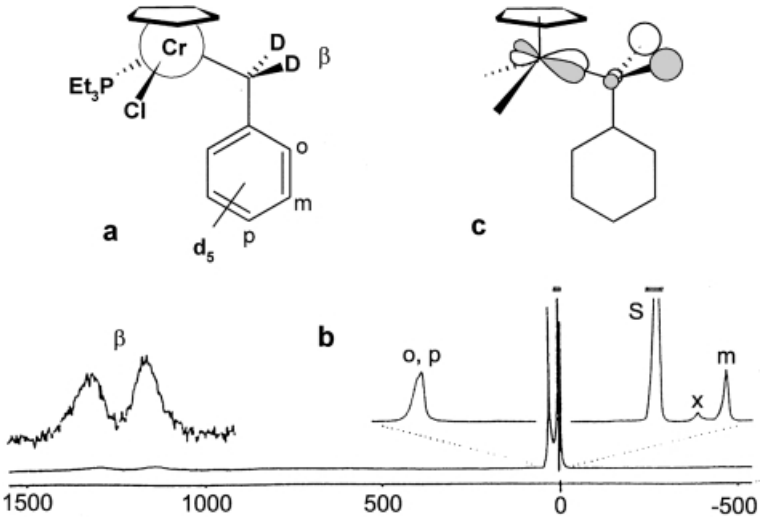

Fig. 17. Selective spin transfer from chromium to β deuterons of CpCr(benzyl-d_7)Cl(PEt_3) (a). In the ^2H NMR spectrum (b) large signal shifts of the β deuterons are due to hyperconjugation; $S = C_6H_6$, X = impurity. Part (c) shows the MO relevant for selective spin transfer to βD

(sometimes restricted to direct polarization) is considered more [64b, d] or less [64a,c] important.

The example in Fig. 16c which combines a π ligand like benzene or Cp and a methyl group may be generalized. Thus, the methyl nuclei may be replaced by others (thereby possibly switching from a donor to an acceptor group), and the spin-containing π orbital may be a metal orbital. For example, chromium-deuterium hyperconjugation is illustrated in Fig. 17. In the ^2H NMR spectrum of the $S = 3/2$ compound (benzyl-d_7)CpCr(PEt_3)Cl [54b,37] the signals of the phenyl deuterons are weekly shifted (inset of Fig. 17b) while those of the diastereotopic benzylic deuterons have extremely large shifts. The latter establish selective hyperconjugational spin transfer to the β deuterons of the benzyl group reflected by the MO in Fig. 17c.

The spin delocalization to β nuclei depends on the dihedral angle θ between the spin-containing π-type orbital and the α–β bond as illustrated in Fig. 18a,b. This has been suggested early [65], and the most simple NMR-adapted relationship is:

$$\delta^{\mathrm{con}}(\mathrm{N}) = \delta_0(\mathrm{N}) + B(\mathrm{N})\cos^2\theta \tag{15}$$

Thus, the contact shift of nucleus N is the sum of an angular-dependent shift reflecting hyperconjugation (plus some direct polarization) and δ_0(N) which accounts for all other shift contributions. The constants B(N) and δ_0(N) may differ even for closely related molecules. Fixing of θ is straightforward, e. g., by investigating bicyclic molecules. When rotation occurs as for (substituted) methyl groups θ depends on the population of the rotational isomers. In the most simple case equal population

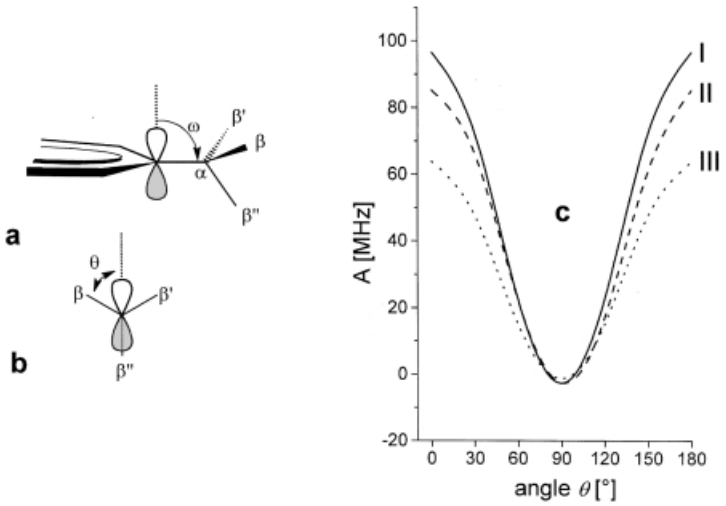

Fig. 18. Spin transfer from a π-type orbital to nuclei in β position. (a) Perspective view and (b) Newman projection. (c) Calculated angular dependence of the spin transfer expressed as hyperfine couplings for the β protons of ethyl radical (curve I) and for the β protons (curve II) and β carbon (curve III) of *n*-propyl radical. Adapted from Ref. 64d

(sometimes incorrectly called "free rotation") gives $\delta^{\mathrm{con}} = \delta_0 + 0.5B$, and maximum spin transfer occurs for $\theta = 0$, e. g., nucleus β'' in Fig. 18b.

The trends of the contact shifts can be derived from the hyperfine coupling constants calculated [64d] for the β protons of the ethyl radical and the β carbon of the *n*-propyl radical (curves I and III of Fig. 18c). The curves correspond to Eq. (15) and apply also to spin-reduced (e. g. organometallic) radicals after scaling. When the symmetry of the molecule is lowered the curves become asymmetric. For instance, on passing from ethyl to *n*-propyl radical CH_3 is replaced by CH_2R, and the curve for the β protons (curve II, Fig. 18c) is described by

$$A(^1\mathrm{H}\beta) = A_0(^1\mathrm{H}\beta) + B'(^1\mathrm{H}\beta)\, cos^2\theta + C\ \sin\theta\ \cos\theta \tag{16}$$

More sophisticated approaches include bending [64d] of the radical by an angle ω as illustrated in Fig. 18a and the variation of substituents [66].

12.5.3.3 γ Nuclei

When proceeding one bond further to nuclei in γ position the spin transfer depends on the angle φ in addition to θ. This is illustrated by the Newman projection in Fig. 19b which is obtained when looking down the α–β bond of the radical in Fig. 19a. Fig. 19c shows how $A(^1\mathrm{H}\gamma)$ of *n*-propyl radical varies with φ and that different curves result depending on θ [64d]. Efficient transfer of positive spin is limited to a small range of angles with a maximum at $\varphi = 180^\circ$ and $\theta = 0^\circ$ which is much smaller than in the case of β protons (see Fig. 18c). The optimum path resembles the letter W [67] formed by the direction of the π orbital and the bonds leading to the investigated γ nucleus

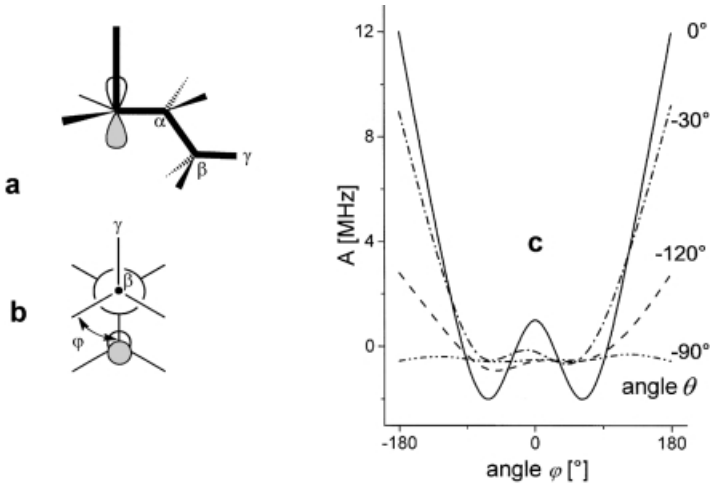

Fig. 19. Spin transfer from a π-type orbital to nuclei in γ position. (a) Perspective view emphasizing the "W path" (see text) and (b) Newman projection looking down the α–β bond. (c) Calculated dependence of the spin transfer on the angles φ and θ of expressed as hyperfine couplings for the γ protons of *n*-propyl radical. Adapted from Ref. 64d

(bold lines in Fig. 19a). For nonrigid chains the mean angles are $\varphi = \theta = 45°$, and hence little spin is transferred. This is why the contact shifts of γ (and more distant) nuclei is usually much smaller than that of β nuclei. Note that around $\varphi = \pm 60°$ the spin at γ nuclei becomes always negative. For more details the reader is referred to the literature [63,68].

12.6 Experimental Examples

The number of paramagnetic compounds investigated by NMR spectroscopy is legion. Most often the mere classification as paramagnets, confirmation of the structure, magnetic exchange, and spin crossover have been the focus of interest. As for spin densities, the method has been applied to quantitative analysis in many cases, but most often its distribution and the mechanisms of delocalization have been discussed qualitatively or briefly mentioned. Therefore, it is not intended to present a comprehensive compilation but to select representative examples of various classes of compounds ranging from pure organic radicals to inorganic solids.

12.6.1 Organic Radicals

Important types of stable radicals that have been investigated by NMR spectroscopy are listed in Fig. 20. Early examples are diphenylpicrylhydrazyl (DPPH, **1**) and its derivatives which have been studied as static powders or single crystals [69a–d] and

in solution [69e,f]. These studies include the first experimental proof of negative spin density on a carbon adjacent to the investigated proton of an organic radical [69a] and the use of ^{2}H NMR spectroscopy for the precise measurement of hyperfine coupling constants [69e]. It is gratifying that the NMR data are in good accord with the results obtained by applying ENDOR and triple resonance. In all DPPH derivatives the spin is positive at H3/5 and H3′/5′, while it is negative at H2/6 and H4. The alternating sign is clear evidence for spin in the aryl π systems (see Section 5.1) with more spin at the *ortho* and *para* positions than at the *meta* position.

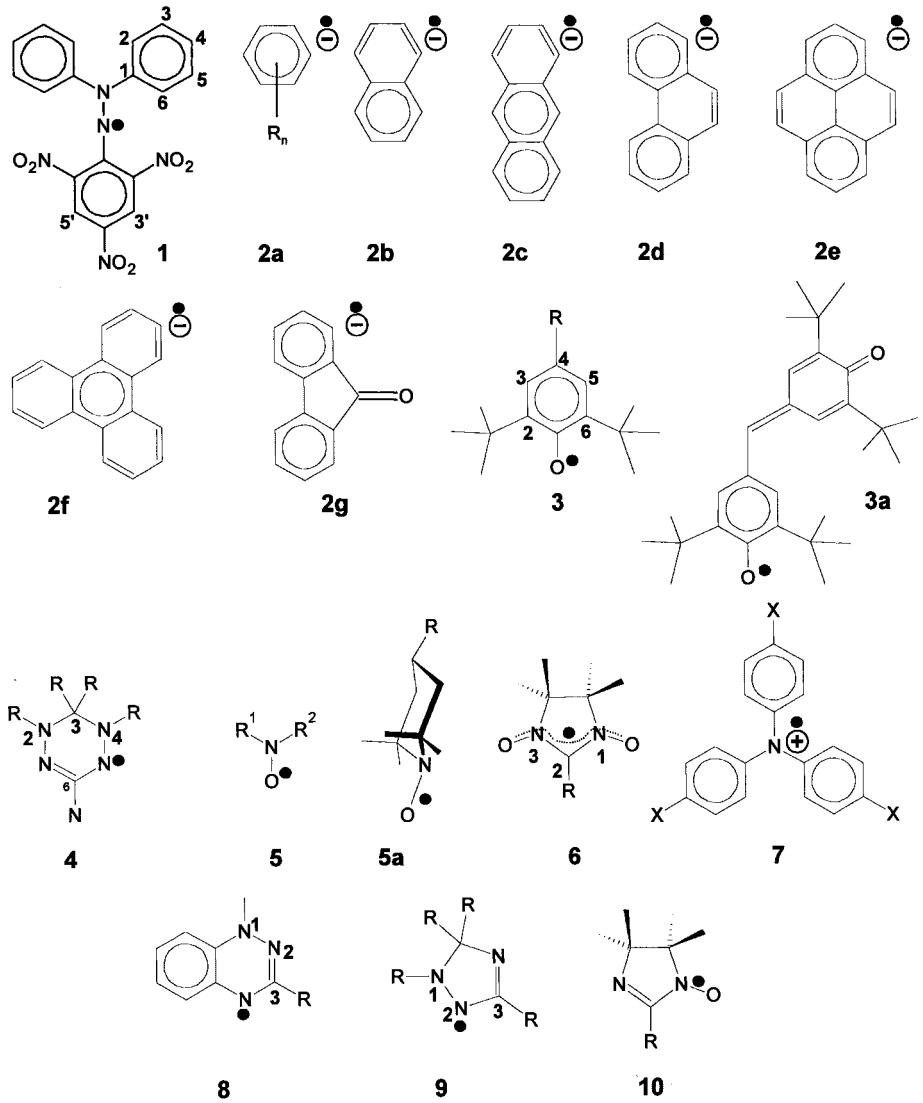

Fig. 20. Selected organic radicals studied by NMR spectroscopy

The radical anions of aromatic hydrocarbons (Fig. 20, **2a–g**) have also been investigated in detail [70a–j]. Among these solid pyrene radical anion (**2e**) is another early example for which negative spin has been detected by ^{1}H NMR spectroscopy [70a]. The spin distribution in radical anions of alkylated benzenes (**2a**) and condensed aromatic species (**2b–g**, partly deuterated) have been studied by de Boer's group in solution by using ^{1}H and ^{2}H NMR spectroscopies, respectively [70b–j]. While the magnitude of the resulting spin densities is virtually the same as that calculated from the EPR data, NMR spectroscopy has added complete sign information. The results can be well reproduced by theoretical calculations, and often the LUMO of the aryl accommodating the excess electron satisfactorily explains the data. For instance, the LUMO of biphenyl given in Fig. 21 approximates (after squaring the MO coefficients) the spin density distribution in the corresponding radical anion. Much positive spin is expected at C2/4/6 and negative spin at H2/4/6 after C–H bond polarization (see Fig. 11). Also, the spin density at H4 should be slightly less than half that at H2/6 which agrees with experiment [70e]. Because only little positive spin is delocalized directly to C3/5, C–C bond polarization (see Fig. 12d,e) takes over, the overall spin density at C3/5 is negative, and hence that at H3/5 is positive. Again, this has been shown experimentally [70e].

Phenoxy radicals (Fig. 20, **3**) are good candidates for NMR investigations when they are stabilized by bulky groups at C2/6 and, most often, by substituents R at C4 which improve delocalization of the unpaired electron. ^{1}H and ^{19}F NMR spectra of various substituted derivatives have been recorded in solution [71a–i]. They show that the species are π radicals with much negative spin at H2/6, less at H4, and even less positive spin at H3/5. Delocalization into aliphatic substituents R is governed by hyperconjugation [71c], the hyperfine coupling constants may depend on the temperature owing to molecular motion [71g], and the spin density at fluorine is about 7.5% of that at carbon [71i]. A particular stable derivative is glavinoxyl radical (**3a**) which yields positively shifted proton signals for H3/5 as expected [71a,d].

The ^{1}H and ^{2}H NMR spectra of (selectively deuterated) verdazyl radicals (Fig. 20, **4**) [72a–h], mostly obtained by Neugebauer's group, have revealed that the spin is delocalized in the π system including phenyl substituents in positions 2, 4, and 6. This follows from the NMR signal pattern which establishes alternating spin signs on passing from *ortho* to *meta* and *para* positions. Aliphatic substituents at these phenyl groups have shown hyperconjugation to be most efficient for delocalization to β-type protons (see Fig. 18), while the W arrangement (see Fig. 19) is important for

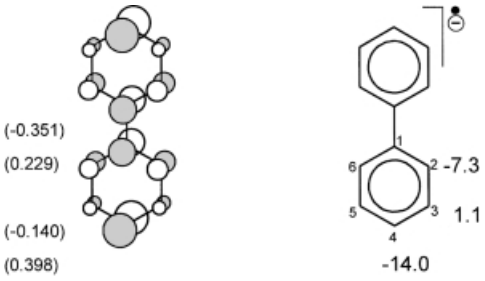

Fig. 21. Experimental $A(^1\text{H})$ values in MHz of biphenyl radical anion (right) and singly occupied molecular orbital (left). The relative size of the atomic orbital lobes reflect the MO coefficients

γ-type protons [72e]. Spin transfer across the bridges of paracyclophane introduced as substituents at N4 of **4** turned out to be negligible [72g].

N-oxides (Fig. 20, **5**) constitute another family of stable radicals which have been studied thoroughly for the most part by ^{1}H [71a,h,73a–g,j–p,s], but also by ^{2}H [73o], ^{13}C [73h,i,q], ^{15}N [73r], ^{19}F [73j], and ^{31}P [73l] NMR spectroscopies. After revision of early data [73a] by Torssell [73g] it turned out that considerable spin density is delocalized to both aliphatic and aromatic substituents at nitrogen. As for phenyl substituents, alternating signs of ^{1}H NMR signal shifts indicate π delocalization. However, after methylating the phenyl, steric congestion may twist the π system of the NO group relative to that of the phenyl so that σ delocalization comes into play. This is most evident at the *meta* positions [73f]. As for aliphatic substituents, cyclic N-oxides such as **5a** and bicyclic congeners have been used to relate the spin delocalization to the stereochemistry [73c,e,m,n]. For instance, at low temperature ring inversion of **5a** is slow enough as to distinguish equatorial and axial methyl groups. The latter receive more spin as reflected by the signal shifts of the γ protons. This is due to the axial methyl's smaller dihedral angle θ (see Figs. 18 and 19) while φ (see Fig. 19) is 45° for all methyl groups owing to equally populated rotamers. The dihedral-angle dependence of spin delocalization in **5a** has been confirmed by solution-state ^{13}C NMR data which are more difficult to obtain but easier to interpret [73h,i].

Nitronyl nitroxides (Fig. 20, **6**) have been investigated by ^{1}H, ^{13}C, and ^{19}F NMR spectroscopies [73d,j,74a–c]. On the one hand, they resemble N-oxides with the spin residing essentially on NO. On the other hand, changing the substituent directly at nitrogen is possible for **5** while for **6** the substituent is always separated from N by C2. The consequences are easily seen by NMR spectroscopy. If R of **6** and R^1 of **5** is phenyl the sign pattern of the spin at the *ortho*, *meta*, and *para* protons for **6** is $+/-/+$, respectively, whereas for **5** it is $-/+/-$. This corresponds to what has been illustrated in Figs. 8 and 13. Furthermore, the magnitude of the spin density at the *ortho* and *meta* protons of **6** is smaller than that of **5**, while at the *para* protons it is similar.

Some other radicals for which the spin density distribution has been determined by NMR spectroscopy are triarylaminium cations [75] (Fig. 20, **7**), dihydrobenzotriazinyl radicals [76] (**8**), 3-triazolinyl radicals [77] (**9**), and 2-imidazoline-1-oxide radicals [78] (**10**). In **7** like in **5**, where the phenyl is directly connected to the spin source, the sign pattern of the spin is $-/+/-$ as just mentioned. By contrast, the situation of R in position 3 of **8**, **9**, and **10** resembles that in nitronyl nitroxides (**6**). Correspondingly, when R is phenyl, the sign pattern of the spin is $+/-/+$, but the amount of spin induced in the phenyls is larger for **6** than for **8**, **9**, and **10**.

12.6.2 Organometallic Radicals

Compounds having metal–carbon bonds are commonly called organometallics in contrast with coordination compounds where metal–ligand bonding occurs through atoms other than carbon. Of course, there are also many mixed species like the porphyrin derivative in Fig. 14a which has an iron–phenyl fragment. In these cases the

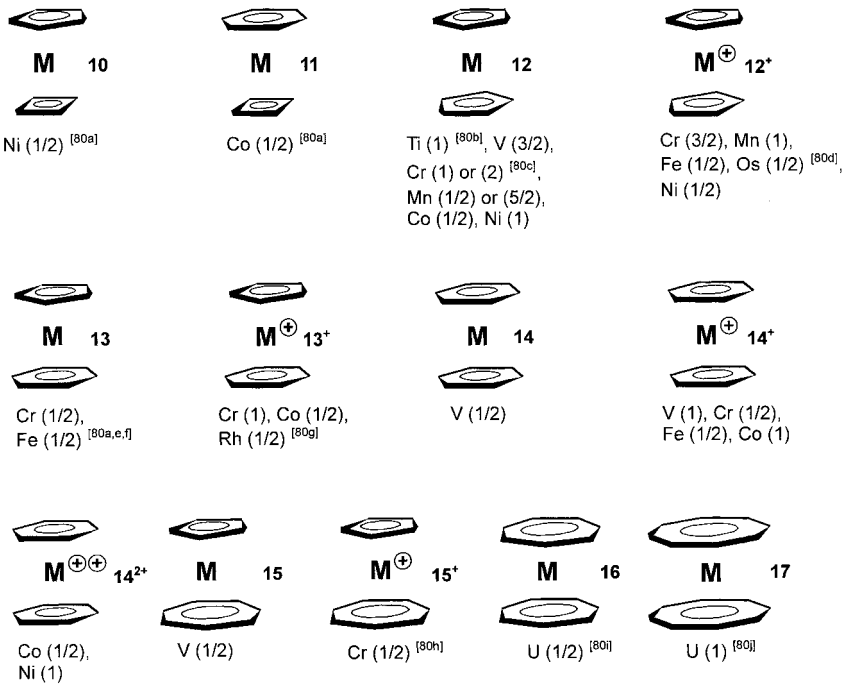

Fig. 22. Paramagnetic sandwich compounds investigated by NMR spectroscopy; the spin state is given in parentheses. Compounds labeled by references have not been analyzed with regard to spin delocalization, the others are discussed in Section 6.2.1

classification corresponds to the most important part of the molecules. The following discussion will be mainly concerned with open d-shell compounds; reviews on paramagnetic f-element molecules exist [79].

12.6.2.1 Sandwich Compounds

The various types of paramagnetic sandwiches for which NMR signals have been recorded are listed in Fig. 22. Note that not all parent compounds are stable so that substituted congeners have been investigated instead. In many cases the spin delocalization problem has not been addressed. The spin distribution can be deduced, however, by applying the principles outlined in Section 5; some examples are given below.

For sandwiches having more than six d electrons positive spin is transferred from the metal to the ligand. This has been first demonstrated for the neutral metallocenes [81] (Cp_2M, **12**) and the neutral and cationic bis(benzene)metal compounds [81f] (**14**, $\mathbf{14}^+$, $\mathbf{14}^{2+}$). Experimental evidence came from *negative* ^{1}H NMR signal shifts which can be explained by two delocalization steps: direct delocalization (Fig. 5) followed by C–H bond polarization (Fig. 11). The *positive* ^{1}H NMR signal shifts

of sandwiches having less than six d electrons were more difficult to understand. Besides two successive polarization steps of the metal–ligand and the C–H bond [55,81c] (Figs. 10 and 11) direct metal–hydrogen interaction [82a,b], also termed "metal–hydrogen hyperconjugation" [82c] (not well understood and different from that outlined in Section 5.3.2) and σ delocalization [80c,e,f] have been proposed. Things became more complicated when polarization of electrons in the σ skeleton and direct delocalization via a higher, thermally accessible state were proposed [83] to operate in ferrocenium ions (**12**$^+$Fe) besides metal–ligand bond π polarization. Much progress in the understanding of spin distribution was achieved by introducing ^{13}C NMR spectroscopy [35,84]. Negative shifts of the ring carbon signals proved that metal–ligand bond polarization dominates for $d^{<6}$ sandwiches while corresponding positive shifts confirmed direct metal–ligand delocalization for $d^{>6}$ sandwiches. Some early work has been reviewed [85].

The precise knowledge of the spin distribution is important in connection with molecular magnets of the type [sandwich]$^+$ [TCNE]$^-$ as mentioned in the Introduction. As for the two concurring models for magnetic interaction in these materials: the McConnell mechanisms I [16] and II [7e,13]; the first one has to assume negative and positive spin in the ligand π system, respectively, in order to explain ferro- and antiferromagnetism. NMR spectroscopy allows to selectively monitor spin in π orbitals by making use of hyperconjugation [86] (see Section 5.3.2). The approach relies on nuclei (preferably carbons) in β position of the π system. When the α–β bond makes up a dihedral angle (θ in Fig. 18) close to 90° hyperconjugation and thus π spin will not affect the NMR signal shift. When θ is adjusted close to 0 ° or 180 ° the effect of π spin on the β nucleus is switched on, and its NMR signal shift becomes more negative if the π spin is negative and vice versa. This has been realized by introducing rotating and blocked substituents (Fig. 23a,b), respectively, leading to $\theta = 45°$ and 0°. In this way negative π spin has been established for the sandwiches, **12**$^+$Mn, **12**$^+$Fe, and **13**Cr and positive π spin for **12**$^+$Ni [86b,c].

Even better model compounds have β nuclei with two different dihedral angles in the same molecule (Fig. 23c), because perturbation through changes in the metal–ligand bonding of different molecules (Fig. 23a,b) can be excluded. The dihedral angles visualized in Fig. 23d yield negative signal shift differences $\delta(^{13}C\beta') - \delta(^{13}C\beta)$ and

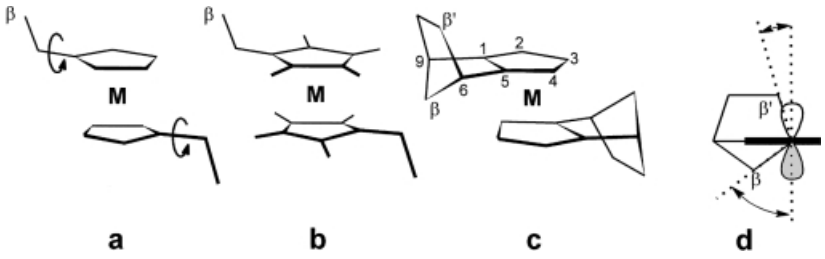

Fig. 23. Probing spin density in π systems of sandwiches. (a) and (b) Two different molecules whose β nuclei sense little (a) and much (b) π spin, respectively. (c) Metallocene having nuclei β and β'. (d) Side view looking down the bond C6–C5 of (c) showing different dihedral angles associated with β and β'

hence prove (or confirm) negative π spin for **12**V, **12**Cr, **12**$^+$Cr, and **12**$^+$Fe whereas a positive sign applies for **12**Co, **12**Ni, and **12**$^+$Ni [86d]. In addition σ delocalization can be analyzed. It turns out to be more effective in **12**V than in **12**Cr, **12**$^+$Cr, and **12**$^+$Fe. In general σ spin (see Section 5.2) shifts the signals of the ring and, less so, α and β nuclei to more positive values. When combined with metal–ligand bond polarization this leads to smaller spin density at the ring carbons and β nuclei and to increased spin at α nuclei (Fig. 24a). Opposite trends are expected for joint action of σ and direct π delocalization (Fig. 24b). Experimental evidence for this kind of spin density modulation is provided by the ^{13}C NMR spectra of polyalkylated metallocenes [86a,b,87] (**12**), metallocenium cations [83b,84c,86a,b] (**12**$^+$), neutral CpCr(arene) derivatives (**13**Cr) and CpCr(arene) cations [88] (**13**$^+$Cr). The combination of σ delocalization and metal–ligand bond polarization, which has been also discussed for CpV(C_7H_7) [89] (**15**), may even lead to equal signs of the spin density at ring and α carbons of low-spin manganocenes [90] (**12**Mn). Particularly interesting are high-spin manganocenes because each front orbital (Fig. 4) accommodates an unpaired electron so that all three mechanisms of spin delocalization are expected to operate. It has been shown by ^{13}C NMR spectroscopy [90] that considerable positive spin sits on the ring and β carbons while little negative spin is found at the α carbons. This means that direct metal–ligand π delocalization is more important than π polarization and that σ delocalization modulates the spin distribution as illustrated in Fig. 24b.

There are still other possibilities of varying the *overall* spin density on the ligands of sandwich compounds which can be controlled by the chemist. For a given number of unpaired electrons these are: 1) the ring size; 2) substitution of the ligand; and 3) the charge of the molecule. With increasing ring size the energies of the π orbitals decrease [91], while they increase upon alkylating a given ligand. Also, the energy of the d orbitals decreases when a metal is ionized. In a MO diagram like that in Fig. 4 this entails changes in the energy match and thus the ligand content of the spin-carrying MO. In addition, the orbital overlap changes with the ring size of the ligand. Discussion of the details is outside the scope of this review. However, some general consequences for the spin distribution is uncovered by the NMR data. 1) In a mixed-ligand d$^{<6}$ sandwich more spin is found on the larger ring; examples are **13**Cr [80h,88], **13**$^+$Cr [88], **13**$^+$Co [92], and **15**$^+$ [80h]. 2) The spin density on the ligands increases slightly when the sandwich is alkylated as in the series **12** [86a] and **13**$^+$Co. 3) Passing from neutral to cationic isoelectronic sandwiches is accompanied by an increase of spin at the ligands of d$^{<6}$ species and a decrease in the case of d$^{>6}$ species.

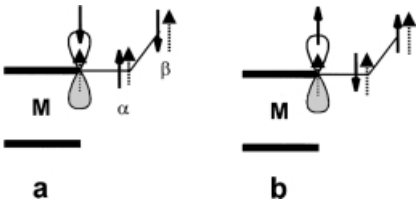

Fig. 24. Combined effect of spin delocalization via σ (dotted arrows) and π orbitals (normal arrows). (a) σ delocalization plus metal–ligand bond polarization, (b) σ delocalization plus direct π delocalization

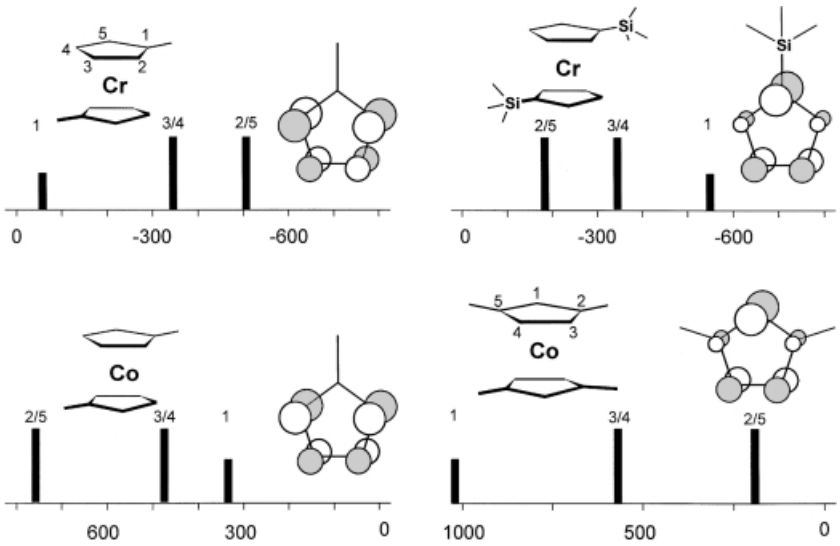

Fig. 25. Spin density changes in sandwich ligands visualized by ^{13}C NMR data (scales in ppm). Only C1–5 (symmetry-adapted numbering) are shown as stick spectra. (a) and (b) Change of π acceptor for donor substituent. (c) and (d) Change of the substitution pattern of π donor substituents. Also shown is the ligand content of the MOs which are most important for spin delocalization

Changes of the spin density *within* the ligands of sandwiches can be also detected by NMR spectroscopy. Examples are given in Fig. 25; they follow the principles outlined in Section 5.1.2 and Fig. 6. Thus in chromocene the unique carbon receives minimal or maximal spin depending on whether the substituent is a π donor or acceptor, respectively [26,87,93]. The same is true for cobaltocenes when going from mono to 1,3-dimethylated ligands [94]. Since these spin density changes depend on the relative population of the front orbitals of sandwiches (Fig. 4), they are temperature-dependent [93a,95], and they are much less pronounced if there are two unpaired electrons in the e orbitals as in the case of nickelocenes and vanadocenes [26,87,93] The stronger the perturbation of a substituted ligand, the larger will be the energy splitting of the e_{1s} and e_{1a} orbitals in Fig. 6, and eventually only one e-type orbital of chromocenes and cobaltocenes will receive spin density. Regardless whether e_{1s} or e_{1a} is concerned, both have $2p_z$ functions with small coefficients so that negative next to positive spin will be found on the ring atoms of a given ligand; an example is 1,1′-diphosphachromocene [96]. In interconnected sandwich compounds like bimetallocenes the spin distribution may be determined by more than two ligand orbitals [97].

As already mentioned spin delocalization has not been analyzed for a number of molecules studied previously. This can be done following the principles outlined above. For instance, (substituted) mixed-ligand sandwiches of type **10**, **11** [80a], and $\mathbf{13}^{+}$Rh [80g] should have positive spin in their ligand π system as indicated by negative and positive signal shifts of the ring and methyl protons, respectively.

Decamethyltitanocene [80b] seems to behave like polyalkylvanadocenes [86a,b,87] as both show methyl proton signals which have positive shifts. Interestingly, the proton signals of decamethylferrocenium [83b] and decamethylosmocenium [80d] ion have different shift signs (−38.3 and 22.5 ppm, respectively). This does not necessarily mean that the sign of the spin in the ligand π system is also different, because dipolar signal shifts and σ delocalization may be responsible. Other sandwiches such as triple-deckers [49,98] and sandwiches having carborane [99] and dienyl [100a] or trienyl [100b,c] ligands can be rationalized along these lines.

12.6.2.2 Bent Sandwiches and Half-sandwiches

Electron-deficient sandwiches may accommodate additional ligands to yield bent sandwiches. Paramagnetic representatives derived from the 3d metals are **18**–**20** in Fig. 26 where Cp_2TiX is a monomer or dimer depending on the ligands. Moreover, one of the pentahapto Cp ligands may be replaced by an anionic and two neutral donor ligands so that half-sandwiches are obtained which are paramagnetic in many cases [101]. The examples **21**–**31** listed in Fig. 26 are generalized; many derivatives are known where the spin density distribution may be of interest. These may be charged, the number of donor ligands (L) may vary, their ligands may be chelates,

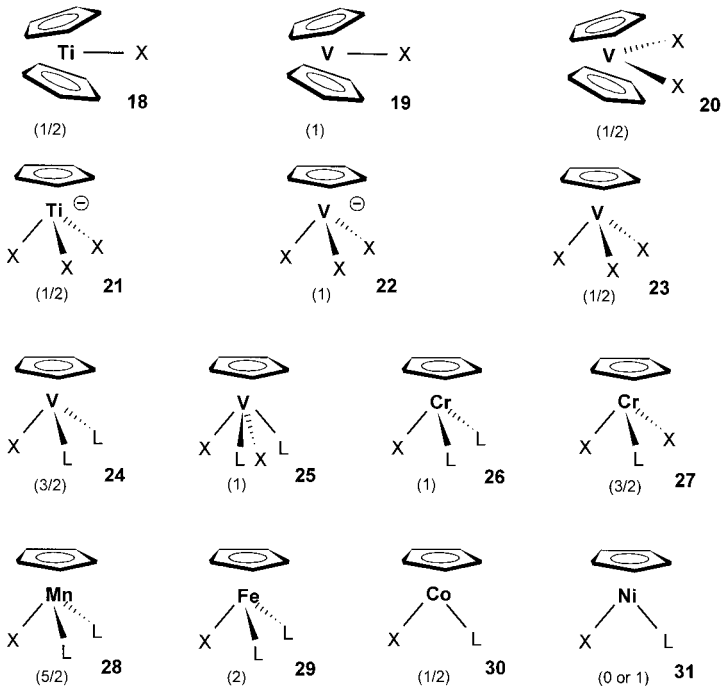

Fig. 26. Paramagnetic bent sandwiches (**18**–**20**) and half-sandwiches (**21**–**31**) of the 3d metals. The spin state is given in parentheses

and they may be dinuclear species featuring magnetic interaction. Paramagnetic half-sandwich fragments may also form oligonuclear species through metal-metal bonds and through bridging by oxygen and sulfur.

While NMR investigation of Cp_2VX (**19**) is straightforward, Cp_2TiX (**18**) and Cp_2VX_2 (**20**) have less favorable electron relaxation. Usually Cp_2VX_2 yields useful signals only for substituents at Cp. For Cp_2TiX mostly ^1H and ^2H NMR spectra have been recorded without considering spin densities [80b,102]. Joint ^{13}C and ^1H NMR data known for Cp_2TiX have established negative spin density in the Cp π system as a result of combined metal–ligand bond polarization and σ delocalization [103].

The ^{13}C and ^1H NMR data of Cp_2VX derivatives [24,53,104] have shown that, similar to Cp_2TiX, negative spin resides at the Cp ligands. The signal shifts and thus the spin densities at the Cps of Cp_2VX are larger than those of (monomeric) Cp_2TiX in accord with the number of unpaired electrons. Quantitative analysis has not been performed, because partly the zero-field splitting and g-factors and thus the dipolar shifts are unknown. Spin delocalization in Cp_2VX seems to resemble that in chromocenes and vanadocenes, but actually there are symmetry-imposed differences. On going from parent to bent sandwiches the symmetry is lowered (e. g. from D_{5d} to C_{2v}) thereby mixing some e_1 orbital content of the ligands into the spin-containing MO. As a result negative spin induced by metal-ligand bond polarization is reduced not only by σ delocalization but also by direct π delocalization [86a]. This corresponds to the scenario in the high-spin manganocenes mentioned above (although the origin is different), and it should apply to any paramagnetic bent sandwich.

The frontier orbitals of half-sandwich compounds [105] (**21**–**31**) are similar to those of the sandwiches (Fig. 4). Therefore, the spin density on the ring ligands should depend on the d-electron count in the same way as described in the previous section. This is best confirmed by analyzing both ^{13}C and ^1H NMR data. For instance, chromium(III) half-sandwiches (**27**) show signal shifts between -30 and 90 ppm for Cp ring carbons, α protons and carbons have large positive signal shifts, and those of β protons are negative [106]. This has been attributed to the effect of combined metal-ligand bond polarization and σ delocalization [106c]. (Fig. 24a) so that the spin in the Cp π system should be negative. Manganese(II) half-sandwiches are another example for which ample data are available [107]. They indicate that the spin delocalization parallels that in high-spin manganocenes [107c], i. e., negative spin sits in the Cp π system.

By contrast, in the case of nickel(II) half-sandwiches the spin at the Cps should be positive. (C_5Me_5)Ni(acetylacetonate) is an intriguing example as it undergoes spin crossover near room temperature ($S = 0 \rightarrow 1$). At high temperature the proton signal of C_5Me_5 has a positive shift [108] while the carbon signal shifts of C_5Me_5 and C_5Me_5 are strongly positive and negative, respectively, as shown in Fig. 27.

The discussion presented so far can be applied to the ^1H NMR data which have been published for numerous half-sandwiches of the type $CpTiX_3^-$ [109a], $CpVX_3^-$ [109a], $CpVX_3$ [109a], $CpVXL_2$ [109b], $CpVX_2L_2$ [109c], $CpNbX_2L_2$ [109d], $CpMoXL_2$ [109e], $CpMoX_3L$ [109f], $CpWX_4$ [109g], $CpFeXL_2$ [109h,i], and Cp-CoXL [109j] and which have not been analyzed in view of spin distribution.

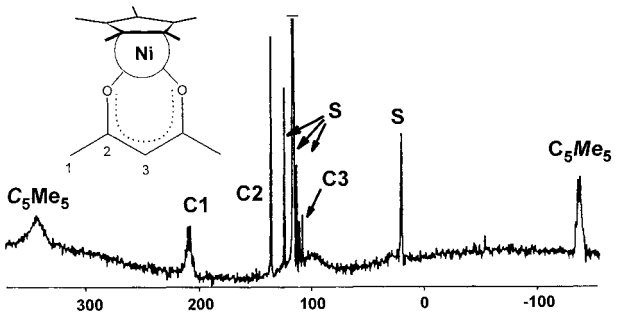

Fig. 27. ^{13}C NMR spectrum of $(C_5Me_5)Ni$(acetylacetonate) dissolved in toluene-d_8 at 333 K. *S* = solvent signals

12.6.2.3 Metal Alkyl and Aryl Compounds

Spin delocalization from paramagnetic organometallic fragments into monohapto (η^1) hydrocarbon ligands, R, has been investigated for bent vanadocenes [24,53,104], Cp_2VR, and chromium half-sandwiches [37,54a], $CpCrR_2L$, or CpCrXRL. Normally, α carbons cannot be observed because of the relaxation constraints described in Section 4.2. Exceptions are molecules where the spin at the carbon is strongly reduced, e. g., by dynamic phenomena like metallatropic shifts of the η^1-ligand in $(\eta^5\text{-}Cp)_2V(\eta^1\text{-}Cp)$ [104c].

The spin distribution in alkyl ligands is dominated by hyperconjugation which transmits much spin to β nuclei (Section 5.3.2). This has been established for the β protons of $R = CH_2R'$ ($R' = H$, $n\text{-}C_3H_7$, C_5H_6, and $Si(CH_3)_3$ which have signal shifts of up to 700 ppm (^1H NMR [24]) and 1500 ppm (^2H NMR [37]). For a given type of compounds the spin on π nuclei may vary considerably when R is susceptible to steric hindrance and when it receives spin preferably from one π-faced d orbital. An example are the of the β-proton signals of $Cp_2VCH_2R($ which appear between 389 and 686 ppm. This is another variant of the dihedral-angle dependence illustrated in Fig. 18. Nuclei that are more distant from the metal receive much less spin (see Section 5.3.3) as has been found for $Cp_2V(n\text{-}Bu)$ and $Cp_2V(CH_2SiMe_3)$ [24].

Aryl substituents may have spin in their σ and/or π orbitals depending on the stereochemistry as has been outlined in Section 5.2. Apart from the examples given there predominating σ spin has been found on the *p*-phenylene bridge of $Cp_2V(C_6H_4)VCp_2$ [104b] while π spin takes over when the bridge is longer as in $Cp_2V(CCC_6H_4CC)VCp_2$, when R in Cp_2VR is ferrocenyl, and in the case of $CpCr(CH_2C_6H_5)_2(PEt_3)$ [37].

12.6.3 Paramagnetic Coordination Compounds of Organic Ligands

Spin density distribution in coordination compound has been investigated for a long time, and the basic theory has been deduced essentially from ^1H NMR results [110]. In more recent years interest has shifted to paramagnetic ions in biological systems where structure rather than spin distribution is the main issue as can be seen in recent reviews on metalloproteins and the like [111]. In particular much work has

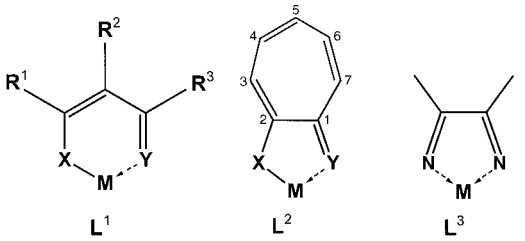

Fig. 28. Typical chelating ligands of coordination compounds (see text for details)

been devoted to metal porphyrin complexes [112] because of their close relation to heme proteins. Paramagnetic coordination compounds are much more abundant than organometallics, because derivatives of the heavier d-block metals are more easily accessible and because there is a plethora of mono-, bi-, and oligodentate ligands. Therefore, only selected examples are given.

12.6.3.1 Simple Metal Chelates

Some general and common types of chelating ligands are given in Fig. 28 where L^1 may be, for instance, acetylacetonate-type ligands (X, Y = O, S, NR) having various substituents R^{1-3}. Alternatively, L^1 represents the large variety of Schiff-base ligands with X = O, Y = NR and $R^{1,2}$ being part of an aryl. Surprisingly few compounds have been investigated by ^{13}C alongside ^1H NMR spectroscopy. An example are Schiff-base iron(III) compounds, L^1_2FeX, where L^1 is salicylideneiminate and X is a bridging oxygen [113]. Alternating signs of both ^1H and ^{13}C NMR signals of the aryl part are clear evidence of dominating π delocalization. However, comparison of experimental and expected magnitudes of the shifts points to additional σ delocalization. Efficient tuning of the spin distribution in L^1_2FeX (L^1_2 = substituted salene) has been realized by substituting X = Cl for phenolates and thiophenolates; a decrease of the spin density on L^1_2 up to a factor of two has been achieved [114]. Independent of this effect the spin distribution in the aryl part of L^1_2 is unsymmetrical with less spin close to X = O than close to Y = NR. Similarly, π delocalization has been claimed for L^1_2Co although different ground states have been assumed [115]. Many other Schiff-base complexes of transition-metal ions have been discussed previously [21a].

^{13}C NMR data have also proven to be important for the analysis of spin delocalization in aminotroponiminato (L^2 with X = Y = NR in Fig. 28) complexes of Ni(II). While proton NMR results alone pointed to π delocalization, ^{13}C NMR spectroscopy has shown that additional σ delocalization augments positive spin density at C3/7 and (less so) C5 while negative spin density at C4/6 is diminished [116]. The measured spin densities are actually mean values resulting from rapid interconversion of tetrahedral $S = 1$ and square planar $S = 0$ isomers which can be tuned by the size of R in X = Y = NR [116].

Among transition-metal diimine (L^3 in Fig. 28) complexes those of substituted bipyridines (bipy) have been studied most intensively for $[L^3_3M]^{2+}$ (M = Cr, Co, Ni) and $[L^3_3M]^{3+}$ (M = Fe, Ru, Os) [21a,117]. In the case of d^5 species the spin delocal-

ization mechanism has been subject of some controversy because π delocalization [117] and σ delocalization [118] have been claimed to dominate. More recently it has been shown that in $[L_3^3M]^-$ (M = Ru, Os; L^3 = bipy) all carbons of the ligand receive positive spin except for those next to nitrogen [119].

As has been mentioned in the Introduction, it is necessary to know the spin distribution within molecules in order to understand and to design magnetic interaction between them. In particular, it matters whether the spin is located in σ or π orbitals because intermolecular interaction is usually mediated more efficiently through π orbitals. Therefore, a more detailed investigation of supposedly well-known compounds is advisable. For instance, in some of the coordination compounds mentioned above π-spin density may be probed selectively as described for sandwich compounds in Section 6.2.1 and Fig. 23.

The spin distribution in a large number of monodentate nitrogen-donor ligands bonded to bis(acetylacetonato)nickel ($Ni(acac)_2$) has been investigated by ^1H, ^{13}C, and ^{14}N NMR spectroscopies. The spectra have been recorded at low concentration of $Ni(acac)_2$ with rapidly exchanging monodentate ligands so that the mean spin densities at the nuclei and hence the signal shifts were small. Representative papers [68a,120] demonstrate that it is not always clear which delocalization mechanisms lead to the observed spin distribution. Aromatic amines like aniline feature alternating signs of both ^1H and ^{13}C NMR signal shifts so that π delocalization should prevail [120d,h]. "σ-Electron effects" have been claimed to operate in pyridine-type donors [120b], but polarization of bonding electrons has also been favored [120a,g]. Mono- and bicyclic amines seem to be more complicated, because alternation of signal shift signs is found for ^{13}C but not for protons. Again σ delocalization [120a,e,f] and spin polarization [120a,f] has been suggested. Yet there are still differences between expected and experimental data which have been explained by direct spin transfer from nickel to carbons [120b] and through space [120f]. Other important issues were how the spin transfer is determined by steric arrangement of α, β, γ, and δ nuclei (see Section 5.3), by the orientation of the lone-pair at sp^3-nitrogen donors [120e], and by the hybridization of the nitrogen [120g].

These basic findings on spin distribution and spin delocalization mechanisms have been applied to many other coordination compounds. In view of magnetic materials this is of particular interest for polynuclear compounds for which recent examples exist. Thus, in a tetranuclear vanadium(III) compound with $S = 3$ ground state spin is delocalized into the π system of bipyridine ligands as derived from ^1H NMR spectroscopy [121]. Bipyridine-type ligands have also been studied in tetranuclear chromium(III) compounds by using ^1H and ^2H NMR spectroscopy. Again π delocalization has been found to be prevalent [122]. ^1H NMR results have been obtained for acetato-bridged di- and trimetallic compounds containing high-spin tris(imidazol)iron(II) fragments [123]. The fact that all signals of the imidazoles have positive shifts has been ascribed to σ delocalization. In addition, corresponding mononuclear low-spin iron(III) and high-spin iron(II) compounds have been shown to experience π and σ delocalization, respectively.

12.6.3.2 Metal Porphyrins

Porphyrin complexes are another type of coordination compounds that have been widely studied by NMR spectroscopy [112] and that have been applied successfully to the design of molecule-bases magnets [7i]. With respect to intermolecular interaction the knowledge of the spin density at various sites of these disc-shaped molecules (see Fig. 14) is of interest. Thus, when these discs are assembled in stacks, spin in the porphyrin π system determines interaction. If stacking is achieved through bridges spin delocalization into axial ligands must be studied. Finally, inter-stack interaction is controlled by spin at the periphery of the porphyrin discs. As has been outlined in Section 5.2, spin can be canalized predominately into the porphyrin σ or π orbitals by selecting the spin state of the metal. Details on other spin states can be found in a recent review by Walker and Simonis [112d]. By switching between σ and π delocalization it is not only possible to adjust the spin above and below the porphyrin plane, but also to change the sign of the spin at the periphery (see Fig. 14). Besides, the periphery is generally controlled by varying the substituents at C3/4 of the individual pyrrole and the *meso* position of the porphyrin as we shall see below.

Whenever an impair number of electrons is accommodated by degenerate orbitals of a metal porphyrin, it is possible to change the spin distribution within the ligand by selecting one of the orbitals for spin transfer through appropriate substitution. The principle has been demonstrated with organometallic π compounds in Section 6.2.1 (Fig. 25). For instance, it has been found that the spin density on the pyrroles of low-spin iron(III) porphyrins can be shifted arbitrarily between C3 and C4 (see Fig. 14 for numbering) depending on whether one of the *meso* substituents is more electron-withdrawing (or -donating) than the others [124]. Changing the substitution pattern of the pyrroles [125] and of the stereochemistry adopted by axial ligands of porphyrin complexes [126] also entail redistribution of the spin density. For a long time only ^{1}H NMR spectroscopy has been applied for this sort of studies. More recently the influence of axial ligands on the spin distribution of $S = 2$ manganese(III) porphyrins has also been determined by ^{13}C NMR spectroscopy [127]. For instance, appropriate choice of the axial ligands can be used for spin density changes by switching the spin state of the manganese(III) center between $S = 1$ and $S = 2$ [128]. A particularly strong perturbation of the spin distribution is realized by variation of the porphyrin donor centers by reducing one of the pyrroles (yielding chlorine ligands [112d]) and by substituting the nitrogen for other donors. The latter approach is illustrated by tetraphenyldithiaporphyrin whose high-spin nickel(II) derivative experiences prevailing π and σ delocalization into the thiophene and pyrrole rings, respectively, yielding negative and positive spin at the respective protons [129].

Spin delocalization into axial ligands, which is of interest for magnetic interaction between metal porphyrin building blocks across axial bridges, has been investigated mostly for iron derivatives. The CN^- ligand is a prominent example owing to biological implications. In the ^{13}C NMR spectra of biscyano adducts of $S = 1/2$ iron(III) porphyrins the cyanide resonance is found at roughly -2500 ppm relative to analogous diamagnetic molecules [130]. This can be understood as arising from π interaction between the spin-carrying iron d_{xz} and d_{yz} orbitals with the cyanide π and π^* orbitals. Similar to the acetylide ligand in Fig. 13, this leads to much positive spin at

nitrogen and little at carbon. The latter is largely overcompensated by negative spin induced by polarization of metal-carbon and C-N bonding electrons. The negative spin at carbon varies strongly depending on the *meso* substituents. Evidence has been presented that this arises from a shift of the unpaired electron from the iron d_{xz} and d_{yz} orbitals to the d_{xy} orbital owing to substituent-induced distortion of the molecule [130b]. At nitrogen positive spin density has actually been established by ^{15}N NMR signal shifts in a range of 550–1180 ppm relative to uncoordinated CN^- [131]. The shift range does no seem to reflect large spin density changes; rather it must be attributed to changes of the dipolar shift as a result of hydrogen-bond formation with the cyano ligands [131b].

Many other ligands bonded to $S = 1/2$ iron(III) porphyrin complexes have been reported, but in most cases the NMR data of the porphyrin and not the axial ligands have been discussed [112d]. Representative exceptions include axial amines [132a,b], phosphanes [132c], and alkyls [132d,e]. Although little emphasis has been laid on spin delocalization in the literature the results can be analyzed by following the principles outlined in Section 5.3. Thus, the large signal shifts of protons in β position (ca. 240 ppm and 530 ppm for the fragments Fe-NH_3 [132b] and Fe-CD_3 [132e] respectively) should be due to hyperconjugation. The selective spin transfer is confirmed by the fact that the signal shifts decrease abruptly when passing to more distant protons of amines [132a] and alkyls [132d]. Nothing seems to be known for β protons of coordinated phosphanes. Surprisingly, however, the spin at γ protons of phosphane ligands is negative [132c] while it is positive for amine ligands [132a]. This might have to do with the fact that amines are σ donors while phosphanes have additional π-acceptor capabilities. The ^1H NMR signal shifts of imidazole coordinated to $S = 1$ manganese(III) porphyrins indicate negative spin at the protons [128a] while pyridine coordinated to $S = 2$ congeners experiences positive spin at all protons [128b]. Only in the latter case does the manganese d_{z^2} orbital (which directs toward the axial pyridine) accommodate an unpaired electron so that σ delocalization becomes efficient.

12.6.4 Inorganic Compounds

Typical paramagnetic inorganic compounds such as transition metal oxides, halides, salts of oxo-acids and mixed compounds thereof are particularly worth being studied because a large number of NMR-active nuclei is accessible, the structure is often simple, and hence spin delocalization mechanisms are easier to establish. Representative examples are given in Table 2.

Many compounds have been studied in the solid state which offers additional information. It turns out that spin is not only found at the paramagnetic transition metal ion but also at all other nuclei of, e. g., halo- and oxo-salts. The spin densities (previously termed "fractional spin") are obtained from the experimental shift data after subtraction of the classical dipolar contribution from adjoining spin centers in the lattice. This contribution vanishes if the environment is cubic, otherwise it can be calculated based on crystal structure data. In addition, second-order quadrupolar shifts must be determined and subtracted when nuclei with $I > 1/2$ are concerned

Table 2. Spin density in selected inorganic compounds investigated by NMR spectroscopy

Nucleus	Compound	Experimental conditions	Ref.
$^{1/2}H$	$CuCl_2(H_2O)_2$	Solid, MAS	[133]
$^{6/7}Li$	Li_6VCl_6	Solid, static	[134a]
	Li_2MnO_3	Solid, static + MAS	[134b]
	$LiMn_2O_4$	Solid, static + MAS	[134b,c]
	$LiMn_{2-x}M_xO_4$ [(a)]	Solid, static	[134c]
	$Li_4Mn_5O_{12}$	Solid, static	[134c,d]
	$LiMnO_4$	Solid, MAS	[134d]
	$Li_2Mn_4O_9$	Solid, MAS	[134d]
^{9}Be	$BeCr_2O_4$	Solid, static	[135]
^{13}C	$K_3[Fe(CN)_6]$	Solution; solid, static	[136a,b]
	$K_3[Mn(CN)_6]$	Solution; solid, static	[136b]
	$K_4[Mn(CN)_6]$	Solution; solid, static	[136b]
^{14}N	$K_3[Fe(CN)_6]$	Solution	[136a,c]
	$K_3[Mn(CN)_6]$	Solution	[136a,c]
	$K_4[Mn(CN)_6]$	Solution	[136a]
	$K_3[Cr(CN)_6]$	Solution	[136a,c,d]
	$Na_2[Fe(CN)_5(NH_3)]$	Solution	[136d]
	$Na_2[Fe(CN)_5(H_2O)]$	Solution	[136d]
	$Na_3[Fe(CN)_5(NO_2)]$	Solution	[136d]
	$K_3[Cr(CN)_5(NO)]$	Solution	[136d]
^{17}O	MnO, CoO	Solid, static	[137a]
	$M_2CuX_4(H_2O)_2$ [(b)]	Solid, static	[137b]
^{19}F	$RbMnF_3$	Solid, static	[138a]
	$RbCoF_3$	Solid, static	[138b]
	$RbFeF_3$	Solid, static	[138c]
	$NaMnF_3$	Solid, static	[138d]
^{23}Na	$NaMnF_3$	Solid, static	[138d]
^{27}Al	$Na_8[Si_6Al_6O_{24}]$	Solid, MAS	[139]
^{29}Si	$Na_8[Si_6Al_6O_{24}]$	Solid, MAS	[139]
^{31}P	MPO_4 [(c)]	Solid, static	[140a]
	$VO(HPO_4)(H_2O)_2$	Solid, static	[140b]
^{39}K	$KNiF_3$	Solid, MAS	[138e]
^{51}V	MVO_4 [(c)]	Solid, static	[141]
^{59}Co	$RbCoF_3$	Solid, static	[138b]
$^{85/87}Rb$	$RbMnF_3$	Solid, static	[138a]
	$RbCoF_3$	Solid, static	[138b]
	$RbFeF_3$	Solid, static	[138c]
^{133}Cs	$CsMnCl_3$	Solid, static	[138f]
^{205}Tl	$Tl_3[Fe(CN)_6]$	Solid, static	[136e]

(a) M = Co, Ni.
(b) M = K, Rb, Cs, NH_4; X = Cl, Br.
(c) M = lanthanide.

[138d]. What results are signals whose shifts and shapes reflect hyperfine interaction. The shift is related to the spin density as described in Section 3. For instance, typical spin densities in the fluorine 2s orbital of fluorometalates (Table 2) are in the order of 10^{-4} [138a–c]. This has played an important role in assigning a small covalent contribution to ionic bonding commonly accepted for these compounds. Analysis of the signal shape obtained from static powders or spinning side-band patterns of MAS experiments as well as single-crystal studies yield anisotropic hyperfine interactions which may be converted into spin densities in p orbitals [133,134a,137b,138a–d].

The sign of the spin density at the fluorides and oxides is positive while for the counter ions of the fluorometalates negative spin has been reported [137a,138a–d] and attributed to spin polarization. It follows that in the lattice the spin densities show a periodic change of sign which has been viewed as spin oscillation or spin waves. The spin at alkali counter ions must not necessarily be negative; positive spin density has been detected, for instance, at lithium in Li_6VCl_8 [134a] and various lithium manganates [134b–d].

In the context of recent progress in magnetic materials based on cyanometalates [142] NMR studies on this type of compounds are of interest. ^{13}C and ^{14}N NMR spectroscopies in solution and in the solid state have established spin density on the CN^- ligand; it is negative at carbon and positive at nitrogen for all examples of Table 2. The spin density pattern can be traced to the general MO scheme of octahedral species $[ML_6]^{n+/-}$ with L being a σ-donor/π-acceptor ligand [143] which has been recently extended to halo- and cyanometalates [56c]. The frontier orbitals consist of the familiar two-over-three orbital set representing σ and π interaction, respectively. It follows that for $d^{>6}$ metal centers σ delocalization and hence positive spin at both carbon and nitrogen of the cyanide ligands is expected. This does not seem to have been established by NMR spectroscopy yet. In contrast, the observed alternation of the spin sign at CN^- is indicative of π delocalization in keeping with the fact that the cyanometalates studied so far are $d^{<6}$ metal derivatives (Table 2). For the latter the spin-carrying MOs result from three-orbital interactions (metal-d, cyano-π, and -π^* orbitals) similar to the situation of CN^- coordinated to porphyrin complexes which has been described in Section 6.3.2. From the MO model it is clear that the spin density at CN^- can be tuned by shifting the d-orbital energy relative to that of the cyanide π and π^* orbitals. This may be realized by changing the metal and/or the external charge of $[M(CN)_6]^{n-}$ and by substituting some cyanides for other ligands. As for the counter ions of hexacyanometalates positive spin has been reported at thallium in $Tl_3[Fe(CN)_6]$ [136e].

12.7 Concluding Comments (Knight Shifts, Evaluation of the NMR Method)

This review has been restricted to compounds that are not metallically conducting. It must be noted, however, that one goal of research on molecule-based magnetic materials is to combine useful magnetic properties with others, not least conduct-

ing behavior [144]. In the case of metallic conductance hyperfine interaction occurs between the magnetic moment of the observed nucleus and conducting electrons giving rise to so-called Knight shifts [145]. Most often the conducting electrons are in s states, they align parallel to the external field and hence the shifts (of typically several hundred ppm) are positive. These shifts are also related to the spin density at the respective nucleus. The conducting electrons may be also in d states. Then negative Knight shifts are observed due to polarization of core s-state electrons by d-state electrons. Most notably, these shifts do not depend on the temperature unless some indirect process is effective. It follows that temperature-dependent measurements can be used to distinguish Knight shifts from paramagnetic signal shifts considered so far and, should both be present, to separate them. While Knight shifts have long been studied with genuine metallic phases, molecule-oriented chemists are mainly interested in materials that contain ordered π compounds such as tetrachalcogenofulvalenides, tetracyanoethenide, tetracyanoquinodimethanides and the like combined with suitable organic and metal cations. The resulting organic conductors and superconductors also yield (mostly ^{1}H and ^{13}C) Knight shifts which have been discussed in a recent review [146].

Most of the paramagnetic NMR spectra have been recorded for molecules in solution. Although the available data yield precise spin density maps solid-state investigations are more appropriate, because the magnetic properties of materials depend strongly on intermolecular or inter-ionic interactions and because structural changes upon passing from solutions to the solids are usually accompanied by spin density changes. Almost all solid-state studies mentioned so far have been carried out with static powders and single crystals. These experiments are restricted to simple compounds, because most often spin densities of different nuclei cannot be resolved. A solution of this problem is MAS NMR spectroscopy. Besides some examples given in Table 2 which have one or only few signals the method is particularly well suited for resolving the spin densities of many different nuclei of complicated molecules. This has been exemplified with the ^{13}C, ^{2}H, and ^{1}H MAS NMR spectra of nitronyl nitroxides [11] as well as the ^{2}H, and ^{1}H MAS NMR spectra of similar organic radicals [147]. The results suggest that MAS NMR spectroscopy is also promising for all sorts of compounds discussed in Section 6 as has been verified for metallocenes [32,148].

Determination of spin densities by the NMR method has advantages and limitations. Advantages are: 1) costs are relatively low; 2) small spin densities can be detected; 3) the sign of the spin is easy to determine; 4) nuclei with rather low natural abundance are accessible; and 5) high-resolution data may be obtained from (even undiluted) solutions and solids. Points 1 and 2 makes NMR more favorable than polarized neutron diffraction, while the others are advantageous as against EPR. An interesting option is temperature-dependent NMR spectroscopy, but routine work is limited to temperatures above about $-120\,^{\circ}C$. Other limitations are: 1) signal assignment is not always simple; 2) compounds with long electron relaxation times cannot be studied; 3) molecular sites with large spin densities and/or very close to the spin source are not accessible; and 4) the spatial spin distribution at atoms must be deduced indirectly.

Acknowledgment

Part of this review was been written during a stay at the Instut de Physique et Chimie des Matériaux de Strasbourg; I am grateful to Professor Marc Drillon and his team for the hospitality. I'm also indebted to Drs A. Schell and, partly, H. Heise for drawings.

References

[1] (a) H. A. Kramers, *Physica* **1934**, *1*, 182. (b) J. Becquerel, W. J. Haas, J. van der Handel, *Physica* **1934**, *1*, 383.
[2] (a) P. W. Anderson, *Phys. Rev*. **1950**, *79*, 350. (b) P. W. Anderson, *Phys*. *Rev*. **1959**, *115*, 2.
[3] J. Owen, K. W. H. Stevens, *Nature* **1953**, *171*, 836.
[4] M. Kato, H. B. Jonasson, *Chem*. *Rev*. **1964**, *64*, 99.
[5] P. W. Anderson in *Solid State Physics* (Eds.: F. Seitz, D. Turnbull) Academic Press, New York, **1963**, Vol. 14, p. 99.
[6] O. Kahn, *Molecular Magnetism*, VCH, Weinheim, **1993**, Chapter 8.
[7] (a) O. Kahn, *Angew. Chem., Int. Ed. Engl*. **1985**, *24*. 834. (b) O. Kahn, *Struct. Bonding (Berlin)* **1987**, *68*, 89. (c) A. Caneschi, D. Gatteschi, R. Sessoli, P. Rey, *Acc. Chem. Res*. **1990**, *22*, 392. (d) A. Caneschi, D. Gatteschi, P. Rey, *Progr. Inorg.* Chem. **1991**, *39*, 331. (e) J. S. Miller, A. J. Epstein, *Angew. Chem., Int. Ed. Engl* **1994**, *33*, 385. (f) J. S. Miller, A. J. Epstein, *Chem. Eng. News* **1995**, Oct. 2, 30. (g) S. Decurtins, R. Pellaux, *Comments Inorg*. *Chem*. **1998**, *20*. 143. (h) R. E. P. Winpenny, *Chem. Soc. Rev*. **1998**, *27*, 447. (i) J. A. McCleverty, M. D. Ward, *Acc. Chem. Res.* **1998**, *31*, 842. (j) J. S. Miller, A. J. Epstein, *Chem. Commun.* **1998**, 1319. (k) L. Ouahab, *Coord*. *Chem. Rev.* **1998**, *180*, 1501.
[8] (a) A. L. Buchachenko, *Russ. Chem. Rev.* **1990**, *59*, 307. (b) H. Iwamura, *Adv. Phys. Org. Chem.* **1990**, *26*, 179. (c) D. A. Dougherty, *Acc. Chem Res.* **1991**, *24*, 88. (d) A. Rajca, *Chem. Rev.* **1994**, *94*, 871. (e) H. Nishide, *Adv. Mater.* **1995**, *7*, 221. (f) P. M. Lahti (Ed*.), Magnetic Properties of Organic Materials*, Marcel Dekker, New York, **1999**.
[9] D. Shiomi, M. Tamura, H. A. Katori, T. Goto, A. Hayashi, Y. Ueda, H. Sawa, R. Kato, M. Kinoshita, *J. Mater., Chem.*, **1994**, *4*, 915.
[10] (a) F. Kanno, K. Inoue, N. Koga, H. Iwamura, *J. Am. Chem. Soc.* **1993**, *115*, 847. (b) R. Chiarelli, S. Gambarelli, A. Rassat, *Mol. Cryst. Liqu. Cryst.* **1997**, *305*, 455.
[11] H. Heise, F. H. Köhler, F. Mota. J. J. Novoa, J. Veciana, *J. Am. Chem. Soc.* **1999**, *121*, 9659.
[12] A. Uzuoka, S. Murata, T. Sagawara, H. Iwamura, *J. Am. Chem. Soc.* **1987**, *109*, 2631.
[13] (a) J. S. Miller, A. J. Epstein, W. M. Reiff, *Science* **1988**, *240*, 40. (b) J. S. Miller, A. J. Epstein, W. M. Reiff, *Acc. Chem. Res.* **1988**, *21*, 114. (c) J. S. Miller, A. J. Epstein, W. M. Reiff, *Chem. Rev.* **1988**, *88*, 201.
[14] (a) L. E. Orgel, *J. Chem. Phys.* **1959**, *30*, 1617. (b) H. M. McConnell, *J. Chem. Phys*. **1963**, *39*, 1910. (c) P. W. Anderson in *Magnetism*, Vol.1 (Eds.: G. T. Rado, H. Suhl) Academic Press, New York, **1963**, p. 25.
[15] R. M. Sternheimer, *Phys. Rev.* **1951**, *84*, 244.
[16] (a) C; Kollmar, O. Kahn, *J. Am. Chem. Soc*., **1991**, *113*, 7987. (b) C. Kollmar, M. Couty, O. Kahn, J. *Am. Chem; Soc*, **1991**, *113*, 7994. (c) C. Kollmar, O. Kahn, *J. Chem. Phys*. **1992**, *96*, 2988.

[17] R. K. Harris, J. Kowalewski, S. Cabral de Menezes, *Magn. Reson. Chem.* **1998**, *36*, 145.
[18] J. S. Tiedeman, H. G. Robinson, Phys. *Rev. Lett.* **1977**, *39*, 602.
[19] (a) V. G. Malkin, O. L. Malkina, L. A. Erikson, D. R. Salahub in *Modern Density Functional Theory* (Eds. J. M. Seminario, P. Politzer) Elsevier, Amsterdam, **1995**. (b) V. Barone in *Recent Advances in Density Functional Methods, Part I* (Ed. D. P. Chong) World Scientific, Singapore, **1995**. (c) *Chemical Applications of Density Functional Theory* (Eds. B. B. Laird, R. B. Ross, T. Ziegler) ACS Symposium Series 629, American Chemical Society, Washington DC, **1996**.
[20] H. Kurreck, B. Kirste, W. Lubitz, *Electron Nuclear Double Resonance Spectroscopy of Radicals in Solution,* VCH Publishers, New York, **1988**.
[21] (a) G. N. La Mar, W. DeW. Horrocks, Jr., R. H. Holm, *NMR of Paramagnetic Molecules,* Academic Press, New York, **1973**. (b) R. S. Drago, *Physical Methods for Chemists*, Saunders College Publishing, Ft. Worth, **1992**, Chapter 12.
[22] (a) S. J. Blundell in *Magnetism: Molecules to Materials* (Eds.: M. Drillon, J. S. Miller) Wiley-VCH, Weinheim, **2000**, Chapter 7. (b) E. Roduner, *Chem. Soc. Rev.* **1993**, 337.
[23] H. Heise, PhD thesis, Technische Universität München (Germany), **1999**.
[24] F. H. Köhler, P. Hofmann, W. Prössdorf, *J. Am. Chem. Soc.* **1981**, *103*, 6359.
[25] J. W. Cooper, *Comput. Chem.* **1965**, *1*, 55.
[26] F. H. Köhler, K.-H. Doll, W. Prössdorf, *Angew. Chem., In. Ed. Engl.* **1980**, *19*, 479.
[27] R. R. Ernst, W. A. Anderson, *Rev. Sci. Sci. Instrum.* **1966**, *37*, 93.
[28] I. P. Gerothanassis, *Progr. NMR Spectrosc.* **1987**, *19*, 267.
[29] P. S. Belton, I. J. Cox, R. K. Harris, *J. Chem. Soc., Faraday Trans. 2* **1985**, *81*, 63.
[30] H. Ulbrich, PhD thesis, Universität Bochum (Germany), **1996**.
[31] A.-R. Grimmer, A. Kretschmer, V. B. Cajipe, *Magn. Reson. Chem.* **1997**, *35*, 824, and cited literature.
[32] F. H. Köhler, X. Xie, *Magn. Reson. Chem.* **1997**, *35*, 487.
[33] I. Solomon, *Phys. Rev.* **1955**, *99*, 559.
[34] (a) J. Kowalewski, L. Nordenskiöld, N. Benetis, P. O. Westlund, *Progr. Nucl. Magn. Reson. Spectrosc.* **1985**, *17*, 141. (b) L. Banci, I. Bertini, C. Lucinat, *Nuclear and Electron Relaxation*, VCH, Weinheim, **1991**. (c) L. Banci in *NMR of Paramagnetic Molecules* (Eds. L. J. Berliner, J. Reuben) Plenum Press, New York, **1993**.
[35] F. H. Köhler, *Z. Naturforsch. B* **1974**, *29*, 708.
[36] N. Hebendanz, F. H. Köhler, F. Scherbaum, B. Schlesinger, *Magn. Reson. Chem.* **1989**, *27*, 789.
[37] A. Grohmann, F. H. Köhler, G. Müller, H. Zeh, *Chem. Ber.* **1989**, *122*, 897.
[38] (a) F. E. Mabbs, D. Collison, *Electron Paramagnetic Resonance*, Elsevier, Amsterdam, **1992**, Chapter 18.5. (b) J. R. Pilbrow, *Transition Ion Electron Paramagnetic Resonance,* Clarendon Press, Oxford, **1990**, Chapter 8. (c) I. Bertini, G. Martini, C. Luchinat in *Handbook of Electron Spin Resonance*, Eds. C. P. Poole, Jr., H. A. Farach, AIP Press, New York, **1994**, Chapter III.
[39] I. Bertini, G. Martini, C. Luchinat in *Handbook of Electron Spin Resonance* (Eds.: C. P. Poole, Jr.,H. A. Farach) AIP Press, New York, **1994,** Chapter IV.
[40] Yu. N. Molin, K. M. Salikhov, K. I. Zamaraev, *Spin Exchange,* Springer Verlag, Berlin, **1980**.
[41] E. O. Stejskal, J. D. Memory, *High Resolution NMR in the Solid State,* Oxford University Press, New York, **1994**, Chapter IV.
[42] N. N. Murthy, K. D. Karlin, I. Bertini, C. Luchinat, *J. Am. Chem. Soc.* **1997**, *119*, 2156.
[43] A. N. Garroway, *J. Magn. Reson.* **1982**, *49*, 168.
[44] P. A. Petillo, J. De Felippis, S. F. Nelson, *J. Org. Chem*., **1991**, *56*, 6496.

[45] (a) J.-A. K Bonesteel, B. Borah, R. D. Bates, *J. Magn. Reson.* **1992**, *98*, 475. (b) B. L. Bales R. A. Blum, D. Mareno, M. Peric, H. J. Halpern, *J. Magn. Reson.* **1992**, *98*, 299 and references cited therein. (c) F. H. Köhler, *Z. Naturforsch. B* **1980**, *35*, 199.
[46] R. J. Kurland, B. R. McGarvey, *J. Magn. Reson.* **1970**, *2*, 286.
[47] (a) R. M. Golding, R. O. Pasqual, J. Vrbancich, *Mol. Phys.* **1976**, *31*, 731. (b) R. M. Golding, L. C. Stubbs, J. *Magn. Reson.* **1979**, *33*, 627.
[48] (a) R. Feher, PhD thesis, Technische Universität München, **1996**. (b) A. I. Breikss, T. Nicholson, A. G. Jones, A. Davison, *Inorg. Chem.* **1990**, *29*, 640. (c) F. H. Köhler, *J. Organomet. Chem.* **1975**, *91*, 57.
[49] F. H. Köhler, U. Zenneck, J, Edwin, W. Siebert, *J. Organomet. Chem.* **1981**, *208*, 137.
[50] (a) G. N. La Mar, J. S. de Ropp in *NMR of Paramagnetic Molecules*, Eds. L. J. Berliner, J. Reuben, Plenum Press, New York, **1993**, Chapter I. (b) I. Bertini, P. Turano, A. J. Vila, *Chem. Rev.* **1993**, *93*, 2833.
[51] (a) E. T. Kaiser, L. Kevan, *Radical Ions,* Interscience Publishers, New York, **1968**, Chapters 4, 5, and 6. (b) E.G. Janzen, *Acc. Chem. Res.* **1969**, *2*, 279.
[52] F. H. Köhler, G. Matsubayashi, *Z. Naturforsch. B* **1976**, *31*, 1153.
[53] F. H. Köhler, W. A. Geike, P. Hofmann, U. Schubert, P. Stauffert, *Chem. Ber.* **1984**, *117*, 904.
[54] (a) F. H. Köhler, C. Krüger, H. Zeh, *J. Organomet. Chem.* **1991**, *386*, C13. (b) H. Zeh, PhD thesis, Technische Universität München (Germany), **1989**.
[55] D. A. Levy, L. E. Orgel, *Mol. Phys.* **1961**, *3*, 583.
[56] (a) M. Karplus, G. K. Fraenkel, *J. Chem. Phys.* **1961**, *35*, 1312. (b) T. Yonezawa, T. Kawamura, H. Kato, *J. Chem. Phys.* **1969**, *50*, 3482. (c) J. Cano, E. Ruiz, S. Alvarez, M. Verdaguer, *Comments Inorg. Chem.* **1998**, *20*, 27.
[57] A. Carrington, A. D. McLachlan, *Introduction to Magnetic Resonance*, Harper & Row, New York, **1969**, Chapter 6.
[58] H. M. McConnell, D. B. Chesnut, *J. Chem. Phys.* **1956**, *24*, 764 and cited literature.
[59] H. Preuss, G. Diercksen, *Int. J. Quant. Chem.* **1976**, *1*, 349.
[60] H. Goff, G. N. La Mar, *J. Am. Chem. Soc.* **1977**, *99*, 6599.
[61] H. C. Longuet-Higgins, C. W. Rector, J. R. Platt, *J. Chem. Phys.* **1950**, *18*, 1174.
[62] A. L. Balch, M. W. Renner, *J. Am. Chem. Soc.* **1986**, *108*, 2603.
[63] F. W. King, Chem. Rev. 1976, 76, 157.
[64] (a) J. P. Colpa. E. De Boer, *Mol. Phys*. **1964**, *7*, 333. (b) Z. Luz, *J. Chem. Phys*. **1968**, *48*, 4186. (c) F. C. Adams, F. W. King, *J. Chem. Phys*. **1973**, *58*, 2446. (d) Y. Ellinger, R. Subra, P. Millie, G. Bertier, *J. Chem. Phys*. **1975**, *62*, 10.
[65] (a) M. C. R. Symons, *J. Chem. Soc*. **1959**, 277. (b) C. Heller, H. M. McConnell, *J. Chem. Phys*. **1960**, *32*, 1535. (c) E. W. Stone, A. H. Maki, *J. Chem. Phys*. **1962**, *37*, 1326.
[66] J. Maruani, A. Hernándes Laguna, D. Bahier, *J. Mol. Struct*. **1983**, *92*, 303.
[67] (a) G. A. Russel, K.-Y. Chang, *J. Am. Chem. Soc*. **1965**, *87*, 4381. (b) G. A. Russel, K.-Y. Chang, C. W. Jefford, *J. Am. Chem. Soc*. **1965**, *87*, 4383.
[68] (a) G. A. Underwood, H. S. Friedman, *J. Am. Chem. Soc*. **1974**, *96*, 4089. (b) G. R. Underwood, K. El Bayoumy, *J. Am. Chem. Soc*. **1982**, *104*, 3007.
[69] (a) H. S. Gutowsky H. Kusumoto T. H. Brown D. H. Anderson, *J. Chem. Phys.* **1959**, *30*, 860. (b) M. E. Anderson, G. E. Pake, T. R. Tuttle, Jr. *J. Chem. Phys.* **1960**, *30*, 1581. (c) R. Verlinden, P. Grobert, L. Van Gerven, *Chem. Phys. Lett.* **1974**, *27*, 535. (d) P. Grobert, J. Burg, L. Van Gerven, *J. Magn. Reson.* **1977**, *28*. 163. (e) R. Biehl, K. Möbius, S. E. O'Connor, R. I. Walter, H. Zimmermann, *J. Phys. Chem*. **1979**, *83*, 3449. (f) R. E. Sagdeev, Yu. N. Molin, V. I. Koryakov, A. K. Chirkow, R. O. Matevosyan, *Org. Magn. Reson.* **1972**, *4*, 365.

[70] (a) M. E. Anderson, P. J. Zandstra. T. R. Tuttle, *J. Chem. Phys.* **1960**, *33*, 1591. (b) E. de Boer, C. McLean, *Mol. Phys.* **1965**, *9*, 191. (c) E. de Boer, C. McLean, *J. Chem. Phys.* **1966**, *44*, 1334. (d) E. de Boer, J. P. Colpa, *J. Phys. Chem.* **1967**, *71*, 21. (e) G. W. Canters, E. de Boer, *Mol. Phys.* **1967**, *13*, 395. (f) G. W. Canters, B. M. P. Hendricks, E. de Boer, *J. Chem. Phys.* **1970**, *53*, 445. (g) J. A. M. Brockhaven B. M. P. Hendricks, E. de Boer, *J. Chem. Phys.* **1971**, *54*, 1988. (h) B. M. P. Hendricks, G. W. Canters, C. Corvaja, J. W. M. de Boer, E. de Boer, *Mol. Phys.* **1971**, *20*, 193. (i) G. W. Canters, B. M. P. Hendricks, J. W. M. de Boer, E. de Boer, *Mol. Phys.* **1973**, *25*, 1135. (j) B. M. P. Hendricks, E. de Boer, *Mol. Phys.* **1975**, *29*, 129.

[71] (a) K. H. Hauser, H. Brunner, J. C. Jochims, *Mol. Phys.* **1966**, *10*, 253. (b) R. W. Kreilick, *J. Am. Chem. Soc.* **1968**, *90*, 2711. (c) R. W. Kreilick, *J. Am. Chem. Soc.* **1968**, *90*, 5991. (d) R. W. Kreilick, *Mol. Phys.* **1968**, *14*, 459. (e) F. Yamauchi, R. W. Kreilick, *J. Am. Chem. Soc.* **1969**, *91*, 3429. (f) W. G. Esperson, R. W. Kreilick, *Mol. Phys.* **1969**, *16*, 577. (g) W. G. Esperson, R. W. Kreilick, *J. Phys. Chem.* **1969**, *73*, 3370. (h) P. W. Kopf, R. W. Kreilick, *J. Am. Chem. Soc.* **1969**, *91*, 6569. (i) S. Icli, R. W. Kreilick, *J. Phys. Chem.* **1971**, *75*, 3465.

[72] (a) F. A. Neugebauer, H. Trischmann, G. Taigel, *Monatsh. Chem.* **1967**, *98*, 713. (b) H. Brunner, K. H. Hauser, F. A. Neugebauer, *Tetrahedron*, **1971**, *27*, 3611. (c) F. A. Neugebauer, H. Brunner, K. H. Hauser, *Tetrahedron*, **1971**, *27*, 3623. (d) P. W. Kopf, K. Morokuma, R. W. Kreilick, *J. Chem. Phys.* **1971**, *54*, 105. (e) F. A. Neugebauer, H. Brunner, *Tetrahedron*, **1974**, *30*, 2841. (f) F. A. Neugebauer, H. Fischer, R. Bernhardt, *Chem. Ber.* **1976**, *109*, 2389. (g) F. A. Neugebauer, H. Fischer, *Tetrahedron Lett.*, **1977**, 3345. (h) F. A. Neugebauer, R. Bernhardt, H. Fischer, *Chem. Ber.* **1977**, *110*, 2254.

[73] (a) R. W. Kreilick, *J. Chem. Phys. 1966, 45,* 1922. (b) R. W. Kreilick, *J. Chem. Phys. 1967,46,* 4260. (c) R. Brière, H. Lemaire, A. Rassat, P. Rey, A. Rousseau, *Bull. Soc. Chim. France* **1967**, *12*, 4479. (d) P. W. Kopf, R. W. Kreilick, D. G. B. Boocock, E. F. Ullman, *J. Am. Chem. Soc.* **1970**, *92*, 4531. (e) R. Brière, H. Lemaire, A. Rassat, J.-J. Dunand, *Bull. Soc. Chim. France* **1970**, *15*, 4220. (f) A. Calder, A. R. Forster, J. W. Emsley, G. R. Luckhurst, R. A. Storey, *Mol. Phys.* **1970**, *18*, 481. (g) H. J. Jakobsen, K. Torssell, *Tetrahedron Lett.*, **1970**, 5003. (h) G. F. Hatch, R. Kreilick, *Chem. Phys. Lett.* **1971**, *10*, 490. (i) G. F. Hatch, R. Kreilick, *J. Chem. Phys.* **1972**, *57*, 3676. (j) J. Goldman, T. E. Petersen, K. Torssell, *Tetrahedron* **1973**, *29*, 3833. (k) K. Torssell, J. Goldman, T. E. Petersen, *Liebigs Ann. Chem.* **1973**, *95*, 231. (l) K. Torssell, *Tetrahedron* **1977**, *23*, 2287. (m) R. M. Dupeyre, A. Rassat, *Bull. Soc. Chim. France* **1978**, *23*, 612. (n) R. M. Dupeyre, A. Rassat, *Tetrahedron* **1978**, *34*, 1501. (o) A. R. Forrester, F. A. Neugebauer, H. Fischer, *J. Chem. Soc., Perkin Trans. 2* **1978**, 1014. (p) D. Ondercin, T. Sandreczki, R. W. Kreilick, *J. Magn. Reson.* **1979**, *34*, 151.(q) I. A. Grigor'ev, L. B. Volodarsky, A. Z. Gogolev, R. Z. Sagdeev, *Chem. Phys. Lett.* **1985**, *122*, 46. (r) I. A. Grigor'ev, L. B. Volodarsky, A. Z. Gogolev, R. Z. Sagdeev, *Chem. Phys. Lett.* **1983**, *100*, 19. (s) B. L. Bales, D. Mareno, F. L. Harris, *J. Magn. Reson., Ser. A* **1993**, *104*, 37.

[74] (a) R. W. Kreilick, J. Becher, E. F. Ullman *J. Am. Chem. Soc.* **1969**, *91*, 5121. (b) M. S. Davis, K. Morokuma, R. W. Kreilick, *J. Am. Chem. Soc.* **1972**, *94*, 5588. (c) J. W. Neely, G. F. Hatch R. W. Kreilick, *J. Am. Chem. Soc.* **1974**, *96*, 652.

[75] (a) T. H. Brown, D. H. Anderson, H. S. Gutowsky, *J. Chem. Phys.* **1960**, *33,* 720. (b) G. A. Pearson, R. I. Walter, *J. Am. Chem. Soc.* **1977**, *99*, 5262. (c) S. J. G. Linkletter, G. A. Pearson, R. I. Walter, *J. Am. Chem. Soc.* **1977**, *99*, 5269.

[76] F. A. Neugebauer, I. Umminger, *Chem. Ber.* **1980**, *113*, 1205.

[77] F. A. Neugebauer, H. Fischer, *Tetrahedron*, **1995**, *51*, 12883.

[78] J. W. Neely, C. H. Lam, R. W. Kreilick, *Mol. Phys.* **1975**, *29*, 1663.

[79] (a) R. D. Fischer in *Fundamental and Technological Aspects of Organo-f-Element Chemistry* (Eds.: T. J. Marks, I. L. Fragalà), D. Reidel Publishing Company, Dordrecht **1985**. (b) W. Jahn, W. Oroschin, H.-D. Amberger, R. D. Fischer, *Inorg. Chim. Acta* **1984**, *95*, 85 and earlier reviews cited therein.

[80] (a) G. E. Herberich, W. Klein, U. Kölle, D. Spiliotis, *Chem. Ber.* **1992**, *125*, 1589. (b) J. E. Bercaw, *J. Am. Chem. Soc.* **1974**, *96*, 5087. (c) H. Sitzmann, M. Schär, E. Dormann, M. Kelemen, *Z. Anorg. Allg. Chem.* **1997**, *623*, 1850. (d) D. O'Hare, J. C. Green, T. Chadwick, J. S. Miller, *Organometallics* **1988**, *7*, 1335. (e) D. Astruc, J.-R. Hamon, G. Althoff, E. Roman, P. Batail, P. Michaud, J. P. Mariot, F. Varret, D. Cozak, *J. Am. Chem. Soc.* **1979**, *101*, 5445. (f) J.-R. Hamon, D. Astruc, P. Michaud, *J. Am. Chem. Soc.* **1981**, *103*, 758. (g) J. Merkert, R. M. Nielson, M. J. Weaver, W. E. Geiger, *J. Am. Chem. Soc.* **1989**, *111*, 7084. (h) Ch. Elschenbroich, F. Gerson, *J. Organomet. Chem.* **1973**, *49*, 445. (i) T. Arlignie, M. Lance, M. Nierlich, J. Vigner, M. Ephritikhine, *J. Chem. Soc., Chem. Commun.* **1995**, 183. (j) N. Edelstein, G. N. La Mar, F. Mares, A. Streitweiser, *Chem. Phys. Lett.* **1971**, *8*, 399.

[81] (a) H. M. McConnell, C. H. Holm *J. Chem. Phys.* **1957**, *27*, 314. (b) R. E. Robertson, H. M. McConnell, *J. Chem. Phys.* **1960**, **64**, 70. (c) R. Prins, *J. Chem. Phys.* **1969**, *50*, 4804. (d) M. F. Rettig, R. S. Drago, *J. Am. Chem. Soc.* **1969**, *91*, 1361. (e) M. F. Rettig, R. S. Drago, *J. Am. Chem. Soc.* **1969**, *91*, 3432. (f) S. E. Anderson, R. S. Drago, *J. Am. Chem. Soc.* **1970**, *92*, 4244.

[82] (a) H. P. Fritz, H. J. Keller, K. E. Schwarzhans, *Z. Naturforsch. B* **1967**, *22*, 891. (b) H. P. Fritz, H. J. Keller, K. E. Schwarzhans, *Z. Naturforsch. B* **1968**, *23*, 298. (c) Yu. S. Karimov, V. M. Chibrikin, I. F. Shchegolev, *J. Phys. Chem. Solids* 1963, 24, 1683.

[83] (a) I. R. Lyatifov, S. P. Solodvnikov, V. N. Babin, R. B. Materikova, *Z. Naturforsch B* **1979**, *34*, 863. (b) R. B. Materikova, V. N. Babin, S. P. Solodvnikov, I. R. Lyatifov, P. V. Petrovskii, E. I. Fedin, *Z. Naturforsch B* **1980**, *35*, 1415.

[84] (a) P. K. Burkert, H. P. Fritz, F. H. Köhler, *J. Organomet. Chem.* **1970**, *24*, C59. (b) S. E. Anderson, N. A. Matwiyoff, *Chem. Phys. Lett.* **1972**, *13*, 150. (c) F. H. Köhler, *J. Organomet. Chem.* **1974**, *64*, C27.

[85] (a) M. F. Rettig in *NMR of Paramagnetic Molecules* (Eds.: G. N. La Mar, W. DeW. Horrocks, Jr., R. H. Holm) Academic Press, New York, **1973**, Chapter 6. (b) S. P. Solodovnikov, *Russ. Chem. Rev.* **1982**, *51*, 961.

[86] (a) F. H. Köhler, K.-H. Doll, W. Prössdorf, *J. Organomet. Chem.* **1982**, *224*, 341. (b) J. Blümel, N. Hebendanz, P. Hudeczek, F. H. Koehler, W. Strauss, *J. Am. Chem. Soc.* **1992**, *114*, 4223. (c) J. Blümel, N. Hebendanz, P. Hudeczek, F. H. Köhler, A. Steck W. Strauss, *Mol. Cryst. Liqu. Cryst.* **1993**, *233*, 153. (d) I. Gattinger, M. A. Herker, W. Hiller, F. H. Köhler, *Inorg. Chem.* **1999**, *38*, 2359.

[87] F. H. Köhler, K.-H. Doll, *Z. Naturforsch B* **1982**, *37*, 144.

[88] F. H. Köhler, B. Metz, W. Strauss, *Inorg. Chem.* **1995**, *34*, 4402

[89] M. F. Rettig, C. D. Stout, A. King, P. Farnham, *J. Am. Chem. Soc.* **1970**, *92*, 5100.

[90] N. Hebendanz, F. H. Köhler, G. Müller, J. Riede, *J. Am. Chem. Soc.* **1986**, *108*, 3281.

[91] M. Elian, M. M. L. Chen, D. M. P. Mingos, R. Hoffmann, *Inorg. Chem.* **1976**, *5*, 1148.

[92] U. Kölle, B. Fuss, M. V. Rajasekharan, B. L. Ramakrishna, J. H. Ammeter, M. C. Böhm, *J. Am. Chem. Soc.* **1984**, *106*, 4152.

[93] (a) F. H. Köhler, W. A. Geike, *J. Organomet. Chem.* **1987**, *328*, 35. (b) J. Blümel, P. Hofmann, F. H. Köhler, *Magn. Reson. Chem.* **1993**, *31*, 2.

[94] H. Eicher, F. H. Köhler, *Chem. Phys.* **1988**, *128*, 297.

[95] (a) F. H. Köhler, W. A. Geike, *J. Magn. Reson.* **1983**, *53*, 297. (b) F. H. Köhler, R. D. Cao, G. Manlik, *Inorg. Chim. Acta.* **1984**, *91*, L1.

[96] R. Feher, F. H. Köhler, F. Nief, L. Ricard, *Organometallics,* **1997**, *16*, 4606.

[97] (a) H. Hilbig, P. Hudeczek, F. H. Köhler, X. Xie, P. Bergerat, O. Kahn, *Inorg. Chem.* **1998**, *37*, 4246. (b) P. Hudeczek, F. H. Köhler, P. Bergerat, O. Kahn, *Chem. Eur. J.* **1999**, *5*, 70.

[98] (a) J. Edwin, M. Bochmann, M. C. Böhm, D. E. Brennan, W. E. Geiger, C. Krüger, J. Pebler, H. Pritzkow, W. Siebert, W. Swiridoff, H. Wadepohl, J. Weiss, U. Zenneck, *J. Am. Chem. Soc.* **1983**, *105*, 2582. (b) J. Zwecker. T. Kuhlmann, H. Pritzkow, W. Siebert. U. Zenneck, *Organometallics,* **1988**, *7*, 2316. (c) M. Stephan, P. Müller, U. Zenneck, H. Pritzkow, W. Siebert, R. N. Grimes *Inorg. Chem.* **1995**, *34*, 2058.

[99] (a) L. G. Sneddon D. C. Beer, R. N. Grimes, *J. Am. Chem. Soc.* **1973**, *95*, 6623. (b) R. J. Wiersema, M. F. Hawthorne, *J. Am. Chem. Soc.* **1974**, *96*, 761. (c) M. Stephan, J. Hauss, U. Zenneck,W. Siebert, R. N. Grimes *Inorg. Chem.* **1994**, *33*, 4211.

[100] (a) J. Müller, W. Holzinger, F. H. Köhler, *Chem. Ber.* **1976**, *109*, 1222. (b) J. Heck, G. Rist. *J. Organomet. Chem.* **1988**, *342*, 45. (c) B. Bachmann, J. Heck, *Organometallics* **1991** *10*, 1373.

[101] R. Poli, *Chem. Rev.* **1996**, *96*, 2135.

[102] J. M. de Wolf, A. Meetsma, J. H. Teuben, *Organometallics* **1995**, *14*, 5466 and cited literature of this group.

[103] F. H. Köhler, D. Cozak, *Z. Naturforsch. B* **1978**, *33*, 1274.

[104] (a) F. H. Köhler, W. Prössdorf, U. Schubert, *Angew. Chem., Int. Ed. Engl.* **1978**, *17*, 850. (b) F. H. Köhler, W. Prössdorf, U. Schubert, *Inorg. Chem.* **1981**, *20*, 4096. (c) F. H. Köhler, W. A. Geike, *J. Organomet. Chem.* **1983**, *256*, C27.

[105] T. A. Albright, J. K. Burdett, M.-H. Wangbo, *Orbital Interactions in Chemistry*, Wiley, New York, **1985**, Chapter 20.

[106] (a) F. H. Köhler, R. D. Cao, K. Ackermann, J. Sedlmair. *Z. Naturforsch. B* **1983**, *38*, 1406. (b) F. H. Köhler, J. Lachmann, G. Müller, H. Zeh, H. Brunner, J. Pfaunsch, J. Wachter *J. Organomet. Chem.* **1989**, *365*, C15. (c) B. Bräunlein, F. H. Köhler, W. Strauss, H. Zeh, *Z. Naturforsch. B* **1995**, *50*, 1739.

[107] (a) F. H. Köhler, N. Hebendanz, U. Thewalt, B. Kannelakopulos,R. Klenze, *Angew. Chem., Int. Ed. Engl.* **1984**, *23*, 721. (b) J. Heck, W. Massa, P. Weinig *Angew. Chem., Int. Ed. Engl.* **1984**, *23*, 722. (c) F. H. Köhler, N. Hebendanz, G. Müller U. Thewalt, B. Kannelakopulos, R. Klenze, *Organometallics* **1987**, *6*, 115.

[108] (a) M. E. Smith, R. A. Anderson, *J. Am. Chem. Soc.* **1996**, *118*, 11119. (b) N. Hertkorn, PhD thesis, Technische Universität München (Germany), **1987**.

[109] (a) D. B. Morse, D. N. Hendrickson, T. B. Rauchfuss, S. R. Wilson*Organometallics* **1988**, *7*, 496. (b) J. Nieman, J. H. Teuben, *Organometallics* **1986**, *5*, 1149. (c) B. Hessen, J. H. Teuben, T. H. Lemmen, J. C. Huffman. K. G. Caulton, *Organometallics* **1985**, *4*, 946. (d) U. Siemeling, V. C. Gibson, *J. Organomet. Chem.* **1992**, *424*, 159. (e) F. Abugideiri, D. W. Keog, R. Poli, *J. Chem. Soc., Chem. Commun.* **1994**, 2317. (f) F. Abugideiri, J. C. Gordon, R. Poli, E. E. Owens-Watermire, A. L. Rheingold, *Organometallics* **1993**, *12*, 1575. (g) J. F. Buzinkai, R. R. Schrock, *Organometallics* **1987**, *6*, 1447. (h) A. de la Jara Leal, M. J. Tenorio, M. C. Puerta, P. Valerg, *Organometallics* **1995** *14*, 3839. (i) T. Weyland, K. Costuas, A. Mari, J.-F. Halet, C. Lapinte, *Organometallics* **1998**, *17*, 5569. (j) U. Kölle, B. Fuss, M. Belting, E. Raabe, *Organometallics* **1986**, *5*, 980.

[110] (a) G. N. La Mar in Ref. [21a], Chapter 3, (b) W. DeW Horrocks, Jr. in Ref. [21a], Chapter 4, D. R. Eaton, in Ref. [21a], Chapter 5.

[111] (a) L. Banci, M. Piccioli, A. Scozzafava, *Coord. Chem. Rev.* **1992**, *120*, 1. (b) J. D. Satterlee, S. Alam, Q. Yi, J. E. Erman. I. Constantinidis, J. D. Russell, S. J. Moench in *NMR of Paramagnetic Molecules* (Eds.: L. J. Berliner, J. Reuben) Plenum Press, New York, **1993**, Chapter 5. (c) C. Lucinat, S. Ciurli, Ref. [110b], Chapter 7. (d) I. Bertini,

P. Turano, A. J. Vila, *Chem. Rev.* **1993**, *93*, 2833. (e) Y. Yamamoto, *Ann. Reports NMR Spectrosc.* **1998**, *36*, 1.
[112] (a) G. N. La Mar in *Biological Applications of Magnetic Resonance* (Ed.: G. Shulman), Academic Press, New York, **1979**, p 305. (b) G. N. La Mar, F. A. Walker in *The Porphyrins* (Ed.: D. Dolphin), Academic Press, New York, **1979**, Vol. IVB, p 61. (c) H. Goff in *Iron Porphyrins* (Eds.: A. B. P. Lever, H. B. Gray), Addison-Wesley Publ. Comp., Reading (Mass.), **1983**, Part I, p 239. (d) F. A. Walker, U. Simonis, Ref. [110b], Chapter 4. (e) J. Mispelter, M. Momentau, J.-M. Lhoste, Ref. [110b], Chapter 6.
[113] K. S. Murray, *J. Chem. Soc., Dalton Trans.* **1975**, 1538.
[114] R. H. Heistand II, R. B. Laufer, E. Fikrig, L. Que, *J. Am. Chem. Soc.* **1982**, *104*, 2789.
[115] (a) K. Migita, M. Iwaizumi, T. Isobe, *J. Am. Chem. Soc.* **1975**, *97*, 4228. (b) C. Srivanavit, D. G. Brown, *J. Am. Chem. Soc.* **1976**, *98*, 4447.
[116] D. Doddrell, R. D. Roberts, *J. Am. Chem. Soc.* **1970**, *92*, 4484 and 5256.
[117] R. E. DeSimone, R. S. Drago, *Inorg. Chem.* **1972**, *11*, 668.
[118] G. N. LaMar, G. R. van Hecke, *Inorg. Chem.* **1970**, *9*, 1546.
[119] Y. Ohsawa, M. K. DeArmond, K. W. Hanck, C. G. Moreland, *J. Am. Chem. Soc.* **1985**, *107*, 5383.
[120] (a) I. Morishima, K. Okada, T. Yonezawa, K. Goto, *J. Am. Chem. Soc.* **1971**, *93*, 3922. (b) I. Morishima, K. Okada, T. Yonezawa, *J. Am. Chem. Soc.* **1972**, *94*, 1425. (c) G. R. Underwood, H. S. Friedman, *J. Am. Chem. Soc.* **1974**, *96*, 4089. (d) C. Chachaty, A. Forchioni J. Virlet, J. C. Ronfard-Haret, *Chem. Phys. Lett.* **1974**, *29*, 436. (e) I. Morishima, K. Yoshikawa, *J. Am. Chem. Soc.* **1975**, *97*, 2950. (f) I. Morishima, K. Yoshikawa, K. Okada, *J. Am. Chem. Soc.* **1976**, *98*, 3787. (g) K. Yoshikawa, M. Hashimoto, H. Masuda, I. Morishima, *J. Chem. Soc., Perkin II* **1977**, 809. (h) L. M. Stock, M. R. Wasielewski, *J. Am. Chem. Soc.* **1977**, *99*, 50.
[121] S. L. Castro, Z. Sun, C. M. Grant, J. C. Bollinger, D. N. Hendrickson, G. Christou, *J. Am. Chem. Soc.* **1998**, *120*, 2365.
[122] T. Ellis, M. Glass, A. Harton, K. Folting, J. C. Huffman, J. B. Vincent, *Inorg. Cchem*. **1994**, *33*, 5522.
[123] F.-J. Wu, D. M. Kurtz, Jr, *J. Am. Chem. Soc.* **1989**, *111*, 6563.
[124] H. Tan, U. Simonis, N. V. Shokhirev, F. A. Walker, *J. Am. Chem. Soc.* **1994**, *116*, 5784.
[125] (a) G. N. La Mar, D. B. Viscio, K. M. Smith, W. S. Caughey, M. L. Smith, *J. Am. Chem. Soc.* **1978**, *100*, 8065. (b) M. F. Isaac, Q. Lin, U. Simonis, D. J. Suffian, D. L. Wilson, F. A. Walker, *Inorg. Chem.* **1993**, *32*, 4030. (c) K. Rachlewicz, L. Latos-Grażyński, *Inorg. Chem. 1995*, *34*, 718.
[126] (a) M. K. Safo, F. A. Walker, A. M. Raisimiring, W. P. Walters, D. P. Dolata, P. G. Debrunner, W. R. Scheidt, *J. Am. Chem. Soc.* **1994**, *116*, 7760. (b) F. A. Walker, U. Simonis, H. Zang, J. M. Walker, T. McDonald Rusciti, C. Kipp, M. A. Amptuch, B. V. Castillo III, S. H. Cody, D. L. Wilson, R. E. Graul, G. J. Jong, K. Tobin, T. J. West, B. A. Barichiewich, *New. J. Chem.* **1992**, *16*, 609.
[127] (a) P. Turner, M. J. Gunter, Inorg. Chem.**1994**, *33*, 1406. (b) P. Turner, M. J. Gunter, B. W. Skelton, A. H. White, T. W. Hambley, *J. Chem Research (S)* **1996**, 18; *J. Chem Research (M)* **1996**, 220.
[128] (a) A. P. Hansen, H. M. Goff, *Inorg. Chem.* **1984**, *23*, 4519. (b) H. M. Goff, A. P. Hansen, *Inorg. Chem.* **1984**, *23*, 321.
[129] J. Lisowski, L. Latos-Grażyński, L. Szterenberg, *Inorg. Chem.* **1992**, *31*, 1933.
[130] (a) H. Goff, *J. Am. Chem. Soc.* **1977**, *99*, 7723. (b) M. Nakamura, T. Ikeue, H. Fujii, T. Yoshimura, *J. Am. Chem. Soc.* **1997**, *119*, 6284.
[131] (a) I. Morishima, T. Inubishi *J. Am. Chem. Soc.* **1978**, *100*, 3568. (b) D. V. Behere, E. Gonzales-Vergara, H. M. Goff, *Biochim. Biophys. Acta.* **1985**, *832*, 319.

[132] (a) Y. C. Hwang, D. W. Dixon, *Inorg. Chem.* **1986**, *25*, 3716. (b) Y. O. Kim, H. M. Goff, *Inorg. Chem.* **1990**, *29*, 3907. (c) G. Simmoneaux, P. Sodane, *Inorg. Chem.* **1988**, *27*, 3956. (d) D. Lexa, J. Mispelter, J.-M. Savéant, *J. Am. Chem. Soc.* **1981**, *103*, 6806. (e) Z. Li, H. M. Goff, *Inorg. Chem.* **1992**, *31*, 1548.
[133] A. Nayeem, J. P. Jesinowski, *J. Chem. Phys.* **1988**, *89*, 4600.
[134] (a) G. Villeneuve, L. Latié, C. Cros, P. Hagenmuller, *Mat. Res. Bull.* **1984**, *19*, 1515. (b) P. Mustarelli, V. Massarotti, M. Bini, D. Capsoni, *Phys. Rev. B* **1997**, *55*, 12018. (c) B. Gee, C. R. Horne, E. J. Cairns, J. A. Reimer, *J. Phys. Chem. B* **1998**, *102*, 10142. (d) Y. J. Lee, F. Wang, C. P. Grey, *J. Am. Chem. Soc.* **1998**, *120*, 12601.
[135] H. Saji, T. Yamadaya, *Phys. Status Solidi* **1974**, *63*, K103.
[136] (a) M. Sporer, G. Ron, A. Loewenstein, G. Navon, *Inorg. Chem.* **1965**, *4*, 358. (b) D. G. Davis, R. J. Kurland, *J. Chem. Phys.* **1967**, *46*, 388. (c) R. G. Shulman, *J. Chem. Phys.* **1958**, *29*, 945. (d) B. R. McGarvey, J. Pearlman, *J. Magn. Reson.* **1969**, *1*, 178. (e) D. Herbison-Evans, P. B. P. Phipps, R. J. P. Williams, *J. Chem. Soc.* **1965**, 6170.
[137] (a) D. E. O'Reilly, T. Tsang, *J. Chem. Phys.* **1964**, *40*, 734. (b) W. L. Looyestijn, T. O. Klaassen, N. J. Poulis, *Physica B*, **1978**, *93*, 349.
[138] (a) M. B. Walker, R. W. H. Stevenson, *Proc. Phys. Soc.* **1966**, *87*, 35. (b) M. P. Petrov, G. M. Nedlin, *J. Appl. Phys.* **1968**, *39*, 1012. (c) M. P. Petrov, G. M. Nedlin, *Sov. Phys. Solid State* **1968**, *9*, 2556. (d) E. A. Vopilov, V. M. Buznik, V. N. Voronov, *Sov. Phys. Solid State* **1982**, *24*, 1017. (e) D. Markgraber, G. Engelhardt, *Chem. Phys. Lett.* **1999**, *300*, 701. (f) A. R. Lim, S. H. Choh, S.-Y. Yeong, *Physica B*, **1997**, *239*, 299.
[139] G. Engelhardt, M. Feuerstein, P. Sieger, D. Markgraber, G. Stucky, V. Srdanov, *J. Chem. Soc., Chem. Commun.* **1996**, 729.
[140] (a) G. Villeneuve, K. S. Suh, P. Amorós, N. Casañ-Pastor, D. Beltrán-Porter, *Chem. Mater.* **1992**, *4*, 108. (b) M. Bose, M. Bhattacharya, S. Ganguli, *Phys. Rev. B* **1979**, *19*, 72.
[141] M. Bose, S. Ganguli, M. Bhattacharya, *Phys. Rev. B* **1979**, *19*, 5535.
[142] M. Verdaguer, A. Bleuzen, V. Marvaud, J. Vaissermann, M. Seuleiman, C. Desplanches, A. Scuiller, C. Train, R. Garde, G. Gelly, C. Lomenech, I. Rosenman, P. Veillet, C. Cartier, F. Villain, *Coord. Chem. Rev.* **1999**, *192*, 1023.
[143] T. A. Albright, J. K. Burdett, M.-H. Whangbo, *Orbital Interactions in Chemistry*, Wiley-Interscience, New York, **1985**, Chapter 15.
[144] (a) E. Coronado, C. J. Gómez-García *Comments Inorg. Chem.* **1995**, *17*, 255. (b) P. Day, M. Kurmoo *J. Mater. Chem.* **1997**, *7*, 1291.
[145] (a) W. D. Knight, *Solid State Phys.* **1956**, *2*, 93. (b) C. P. Slichter, *Principles of Magnetic Resonance*, Springer, New York, **1989**, Chapter 4.
[146] P. Wzietek H. Mayaffre, D. Jérome, S. Brazovskii, *J. Phys. I France* **1996**, *6*, 2011.
[147] (a) G. Maruta, S. Takeda, R. Imachi, T. Ishida, T. Nogami, K. Yamaguchi, *J. Am. Chem. Soc.* **1999**, *121*, 424. (b) G. Maruta, S. Takeda, A. Yamaguchi, T. Okuno, K. Awaga, K. Yamaguchi, *Mol. Cryst. Liq. Cryst.* **1999**, *334*, 295.
[148] J. Blümel, M. Herker, W. Hiller, F. H. Köhler, *Organometallics* **1996**, *15*, 3474.